

UNCLASSIFIED

**AD NUMBER**

AD344925

**CLASSIFICATION CHANGES**

**TO:** unclassified

**FROM:** confidential

**LIMITATION CHANGES**

**TO:**

Approved for public release, distribution  
unlimited

**FROM:**

Controlling Office: Advanced Research  
Projects Agency, Washington, DC.

**AUTHORITY**

OCA; 6 Nov 1975 IAW document markings;  
DARPA ltr 15 Sep 1980

**THIS PAGE IS UNCLASSIFIED**

UNCLASSIFIED

AD 3 4 4 9 2 5

DEFENSE DOCUMENTATION CENTER  
FOR  
SCIENTIFIC AND TECHNICAL INFORMATION  
CAMERON STATION, ALEXANDRIA, VIRGINIA



NOTICE: When government or other drawings, specifications or other data are used for any purpose other than in connection with a definitely related government procurement operation, the U. S. Government thereby incurs no responsibility, nor any obligation whatsoever; and the fact that the Government may have formulated, furnished, or in any way supplied the said drawings, specifications, or other data is not to be regarded by implication or otherwise as in any manner licensing the holder or any other person or corporation, or conveying any rights or permission to manufacture, use or sell any patented invention that may in any way be related thereto.

NOTICE:

THIS DOCUMENT CONTAINS INFORMATION  
AFFECTING THE NATIONAL DEFENSE OF  
THE UNITED STATES WITHIN THE MEAN-  
ING OF THE ESPIONAGE LAWS, TITLE 18,  
U.S.C., SECTIONS 793 and 794. THE  
TRANSMISSION OR THE REVELATION OF  
ITS CONTENTS IN ANY MANNER TO AN  
UNAUTHORIZED PERSON IS PROHIBITED  
BY LAW.

344925

8424-6018-RS000

344925L

FINAL REPORT  
SATELLITE INTERCEPTION SYSTEM  
FEASIBILITY STUDY (U)

Volume II  
8 NOVEMBER 1963

Contract No. SD-177

Prepared for  
ADVANCED RESEARCH PROJECTS AGENCY  
Washington, D.C.

CATALOGED BY DDC

AS AD NO.



SPACE TECHNOLOGY LABORATORIES, INC.  
a subsidiary of Thomson Radio-Video Inc.  
ONE SPACE PARK • REDWOOD BEACH, CALIFORNIA





8424-e018-R5000  
Copy 77 of 102  
Total Pages: 442

FINAL REPORT  
SATELLITE INTERCEPTION SYSTEM  
FEASIBILITY STUDY (U)

Volume II

Project Manager: John Mandrow  
Phone: 478-5411, Ext. 24015

Prepared for  
ADVANCED RESEARCH PROJECTS AGENCY  
Washington, D.C.  
Under Contract No. SD-177

1 November 1963

SPACE TECHNOLOGY LABORATORIES, INC.  
A Subsidiary of Thompson Radio Waltham Inc.  
One Space Park - Redwood Beach, California

DOWNGRADED AT 2 YEAR INTERVALS;  
DECLASSIFIED AFTER 12 YEARS.  
DDO 018 10010

This document contains information which is exempt from automatic declassification under the provisions of the Executive Order 11652, U.S.C. Section 552, and the information is being controlled and released in accordance with the policy of the Department of Defense.

"U.S. military agencies may obtain copies of this report directly from DDC. Other qualified DDC users shall request through ARPA Defender."

## ABSTRACT

This is the final report of an Antisatellite System Feasibility Study sponsored by the Advanced Research Projects Agency under Contract SD-177. The contract performance period extended from 30 April to 31 October 1963.

The systems studied depends upon SPAD/TS to establish a location and time of target kill. This information is used to target a modified ICBM/IRBM boost vehicle, which is launched and guided to place a homing stage on a collision course against the nominal target. Errors in forecast target position and errors in booster powered flight guidance introduce the need for a homing stage in order to achieve hypervelocity pellet kill.

Radar, infrared, and sunlight reflection homing stage sensors were studied and found feasible, subject to the solution of problems in infrared detector array availability and cooling. Depending upon sensor selection and target hardness, homing stage weights range from 600 to 1300 pounds for Set 2 ephemeris errors.

Polaris, Minuteman, and Titan II boost vehicles were studied for the mission. All boost vehicles and their guidance systems require some modification, but these are minor until one combines large warheads with radar sensing (with Set 2 ephemeris errors). Resulting stage weights in that case require structural modification of small or medium size boost vehicles.

The antisatellite approach studied was found feasible and attractive as long as ephemeris errors are not larger than Set 2. If a system is to achieve fast reaction, or if it is to have growth capability towards fast reaction, radar and/or infrared sensing appears most promising. In this case medium to large boost vehicles (Minuteman or larger) appear most suitable.

"Catalog cards with an unclassified abstract may be found in the back of this document."

## CONTENTS

### CHAPTER

- 9. HOMING STAGE COMPUTER
- 10. WARHEAD AND FUZE
- 11. HOMING STAGE CONFIGURATION
- 12. BOOSTER SELECTION AND RANGE PAYLOAD CAPABILITY
- 13. BOOST VEHICLE GUIDANCE ACCURACY AND REQUIRED SYSTEM MODIFICATIONS
- 14. DEPLOYMENT ANALYSIS AND SYSTEM PERFORMANCE
- 15. PROJECTED SYSTEM COSTS

### APPENDICES

- A. LINEAR ANALYSIS OF BODY FIXED TRACKING GYRO MISALIGNMENT
- B. STATISTICAL ANALYSIS OF MISS DISTANCE
- C. DEPLOYMENT OF RADAR PARAMETRIC EQUATIONS
- D. RADAR ANGLE ERRORS
- E. CALCULATION OF TRACKER NOISE EQUIVALENT FLEX DENSITY
- F. THE EFFECTS OF EARTHSHINE ON TARGET INTENSITY
- G. TRACKER ACCURACY AS A FUNCTION OF TELESCOPE APERTURE DIAMETER
- H. TYPICAL TARGETING PROGRAM MODIFICATIONS
- I. STRUCTURAL CONSTRAINTS ON MINUTEMAN TRAJECTORIES
- J. POLARIS TARGETING ALTERNATIVES
- K. HOMING STAGE GEOMETRY
- L. A BOOST-HOME SYSTEM USING A RADAR SENSOR

Total pages: 442

## ILLUSTRATIONS

Figure	Page
9-1 Target Identification Block Diagram .....	9-6
9-2 Target Identification Block Diagram .....	9-7
9-3 Guidance and Control Block Diagram .....	9-11
10-1 Explosive Warhead Concept—"Soft" Targets .....	10-5
10-2 Warhead—Oriented Rod Concept .....	10-9
10-3 Warhead—Heavy Fragment Concept .....	10-11
10-4 General Arrangement—Passive Kill Mechanism .....	10-13
10-5 Torus Longitudinal Stress Versus Torus Wall Thickness..	10-20
10-6 Warhead Weight and Torus Pressure Versus Torus Wall Thickness .....	10-21
10-7 Torus Pressure Hoop Stress Versus Position on Torus ..	10-22
10-8 Passive Warhead Inflation Procedure .....	10-24
11-1 Outboard Profile of Homing Stage With Electro-Optical Tracker .....	11-3
11-2 Outboard Profile of Homing Stage With Radar Tracker ...	11-5
11-3 $I_{sp}$ Versus $F$ and $P_c$ for $P_c = 100$ to $500$ psia .....	11-10
11-4 $I_{sp}$ Versus $F$ and $P_c$ for $P_c = 600$ to $1400$ psia .....	11-10
11-5 $\frac{W_P}{W_G}$ Versus $I_{sp}$ and $\Delta V$ .....	11-11
11-6 $\frac{W_I}{W_P}$ Versus $P_c$ .....	11-11
11-7 $W_E$ Versus $F$ and $P_c$ for $P_c = 100$ to $500$ psia .....	11-12
11-8 $W_E$ Versus $F$ and $P_c$ for $P_c = 600$ to $1400$ psia .....	11-12
11-9 $\frac{W_S}{W_G}$ Versus $W_G$ .....	11-13
11-10 $W_{AC}$ Versus $W_G$ .....	11-13

# ILLUSTRATIONS (Continued)

Figure		Page
11-11	$W_{PL}$ Versus $P_c$ and $W_G$ for $F/W_G = 2$ and $\Delta V = 1000$ . . .	11-17
11-12	$W_{PL}$ Versus $P_c$ and $W_G$ for $F/W_G = 7$ and $\Delta V = 1000$ . . .	11-17
11-13	$W_{PL}$ Versus $P_c$ and $W_G$ for $F/W_G = 10$ and $\Delta V = 1000$ . . .	11-18
11-14	$W_{PL}$ Versus $P_c$ and $W_G$ for $F/W_G = 2$ and $\Delta V = 3000$ . . .	11-18
11-15	$W_{PL}$ Versus $P_c$ and $W_G$ for $F/W_G = 7$ and $\Delta V = 3000$ . . .	11-19
11-16	$W_{PL}$ Versus $P_c$ and $W_G$ for $F/W_G = 10$ and $\Delta V = 3000$ . . .	11-19
11-17	$W_{PL}$ Versus $P_c$ and $W_G$ for $F/W_G = 2$ and $\Delta V = 7000$ . . .	11-20
11-18	$W_{PL}$ Versus $P_c$ and $W_G$ for $F/W_G = 7$ and $\Delta V = 7000$ . . .	11-20
11-19	$W_{PL}$ Versus $P_c$ and $W_G$ for $F/W_G = 10$ and $\Delta V = 7000$ . . .	11-21
11-20	$W_{PL}$ Versus $P_c$ and $W_G$ for $F/W_G = 2$ and $\Delta V = 11,000$ . .	11-21
11-21	$W_{PL}$ Versus $P_c$ and $W_G$ for $F/W_G = 7$ and $\Delta V = 11,000$ . .	11-22
11-22	$W_{PL}$ Versus $P_c$ and $W_G$ for $F/W_G = 10$ and $\Delta V = 11,000$ . .	11-22
11-23	$\frac{-\Delta W_{PL}}{+\Delta P_c}$ Versus $\Delta V$ and $W_G$ for $F/W_G = 2$ . . . . .	11-23
11-24	$\frac{-\Delta W_{PL}}{+\Delta P_c}$ Versus $\Delta V$ and $W_G$ for $F/W_G = 7$ . . . . .	11-23
11-25	$W_{PL}$ Versus $F/W_G$ and $W_G$ for $\Delta V = 1000$ . . . . .	11-24
11-26	$W_{PL}$ Versus $F/W_G$ and $W_G$ for $\Delta V = 3000$ . . . . .	11-24
11-27	$W_{PL}$ Versus $F/W_G$ and $W_G$ for $\Delta V = 7000$ . . . . .	11-25
11-28	$W_{PL}$ Versus $F/W_G$ and $W_G$ for $\Delta V = 11,000$ . . . . .	11-25
11-29	$W_{PL}$ Versus $W_G$ for $F/W_G = 3.5$ and $\Delta V = 3250$ . . . . .	11-26
11-30	$W_{PL}$ Versus $W_G$ for $F/W_G = 3.5$ and $\Delta V = 3500$ . . . . .	11-27
11-31	$W_{PL}$ Versus $W_G$ for $F/W_G = 5$ and $\Delta V = 3500$ . . . . .	11-27
11-32	$W_{PL}$ Versus $W_G$ for $F/W_G = 6$ and $\Delta V = 4000$ . . . . .	11-27
11-33	$W_{PL}$ Versus $\Delta V$ and $W_G$ for $F/W_G = 3.5$ . . . . .	11-28

# ILLUSTRATIONS (Continued)

Figure		Page
11-34	$W_{PL}$ Versus $\Delta V$ and $W_G$ for $F/W_G = 5$ .....	11-28
11-35	$W_{PL}$ Versus $\Delta V$ and $W_G$ for $F/W_G = 6$ .....	11-29
11-36	$W_{PL}$ Versus $\Delta V$ and $W_G$ for $F/W_G = 7$ .....	11-29
11-37	General Arrangement—Homing Stage With Electro-Optical Tracker .....	11-31
11-38	General Arrangement—Homing Stage With Radar Tracker .....	11-33
11-39	Propulsion System Schematic .....	11-43
11-40	Injector Element Schematic .....	11-47
11-41	Positive Orientation and Expulsion Device .....	11-53
11-42	Propellant Expulsion Device .....	11-54
11-43	Gimbal Platform Perspective—Electro-Optical Tracker .....	11-72
11-44	Gimbal Platform—Electro-Optical Tracker .....	11-73
11-45	Starting Torque Versus Bearing Preload .....	11-77
11-46	Electric Lead Wrap-up .....	11-80
11-47	Lead Wrap-up Versus Torque .....	11-81
11-48	Platform Orientation Rate and Acceleration .....	11-82
11-49	Gimbal Platform Prospective Radar Tracker .....	11-90
11-50	Gimbal Platform Radar Tracker .....	11-91
11-51	Radar Tracking Antenna .....	11-93
11-52	Homing Stage Fairing and Adapter—Minuteman .....	11-101
11-53	Homing Stage Fairing, Minuteman Limit Axial Loads ...	11-103
11-54	Homing Stage Fairing, Minuteman Limit Shear and Bending Moment .....	11-104
11-55	Homing Stage Fairing, Minuteman Limit Pressure Distribution .....	11-105

# ILLUSTRATIONS (Continued)

Figure		Page
11-56	Radar Equipped Homing Stage with Large Warhead . . .	11-108
12-1	Vertical Flight Capability of Booster Vehicles . . . . .	12-21
12-2	Polaris—Maximum Capability Envelopes—North Launch . . . . .	12-22
12-3	Minuteman—Maximum Capability Envelopes—North Launch—2.5 Percent Propellant Residual . . . . .	12-22
12-4	Titan II—Elliptical Earth Orbit Payload Capabilities . .	12-23
12-5	Titan II—Maximum Capability Envelopes . . . . .	12-24
12-6	Minuteman Wing II—Altitude Versus Surface Range Envelopes—1000 lb Payload—North Launch . . . . .	12-24
12-7	Plain View of Launch Geometry Against Low Altitude Targets . . . . .	12-25
12-8	Minuteman Intercept Geometry for 100 n mi Altitude Targets—Nonrotating Earth—1000 lb Payload . . . . .	12-26
12-9	Minuteman Intercept Geometry for 100 n mi Altitude Targets—Nonrotating Earth—1500 lb Payload . . . . .	12-27
12-10	Minuteman Intercept Geometry for 500 n mi Altitude Targets—Nonrotating Earth—1000 lb Payload . . . . .	12-27
12-11	Minuteman Intercept Geometry for 500 n mi Altitude Targets—Nonrotating Earth—1500 lb Payload . . . . .	12-28
12-12	Minuteman Intercept Geometry for 1000 n mi Altitude Targets—Nonrotating Earth—1000 lb Payload . . . . .	12-28
12-13	Minuteman Intercept Geometry for 1000 n mi Altitude Targets—Nonrotating Earth—1500 lb Payload . . . . .	12-29
12-14	Minuteman Wing II—1000 lb Payload—North Launch—2.5 Percent Propellant Residual . . . . .	12-30
12-15	Minuteman Wing II—1500 lb Payload—Altitude Versus Surface Range—2.5 Percent Propellant Residual . . . . .	12-30
12-16	Titan II Intercept Geometry for 100 n mi Altitude Targets—Nonrotating Earth—5000 lb Payload . . . . .	12-31
12-17	Titan II Intercept Geometry for 500 n mi Altitude Targets—Nonrotating Earth—5000 lb Payload . . . . .	12-31



# ILLUSTRATIONS (Continued)

Figure		Page
12-18	Titan II Intercept Geometry for 1000 n mi Altitude Targets—Nonrotating Earth—5000 lb Payload . . . . .	12-32
12-19	Titan II Altitude Versus Surface Range—North Launch—5000 lb Payload . . . . .	12-32
12-20	Titan II—Relative Velocity Contours for 500 n mi Altitude Target—Nonrotating Earth—5000 Pound Payload . . . . .	12-33
12-21	Titan II—Relative Velocity Contours for 1000 n mi Altitude Target—Nonrotating Earth—5000 lb Payload . . . . .	12-34
12-22	Polaris A3—Altitude Versus Surface Range Envelopes—1000 lb Payload . . . . .	12-35
12-23	Polaris A3—Intercept Geometry for 100 n mi Altitude Targets—Nonrotating Earth—1000 lb Payload . . . . .	12-36
13-1	System Information Flow and Task Description . . . . .	13-7
13-2	Minimum System Reaction Time with Wing II Minuteman . . . . .	13-18
13-3	Minimum System Reaction Time with Wing II Minuteman . . . . .	13-22
13-4	Minimum System Reaction Time with Titan II . . . . .	13-27
13-5	Polaris Guidance Coordinate System . . . . .	13-30
13-6	Schematic of Polaris Countdown . . . . .	13-34
13-7	Minimum System Reaction Time with Polaris . . . . .	13-34
14-1	Maximum Possible Closest Approach Surface Range Within 24 Hours . . . . .	14-27
14-2	Maximum Possible Closest Approach Surface Range Within 24 Hours . . . . .	14-28
14-3	Maximum Possible Closest Approach Surface Range Within 24 Hours . . . . .	14-29
14-4	Maximum Possible Closest Approach Surface Range Within 24 Hours . . . . .	14-30
14-5	Possible Areas for Interceptor Launch Sites . . . . .	14-31

# ILLUSTRATIONS (Continued)

Figure		Page
14-6	Lateral Reach Required for Interception Within One Orbit Revolution from One Launch Site. . . . .	14-32
14-7	Required Lateral Reach for Interception Within One Orbit Revolution for All Orbital Inclinations . . . . .	14-33
14-8	Lateral Reach Requirement for AMR and A Second Interceptor Launch Site . . . . .	14-34
14-9	Lateral Reach Requirement for PMR and A Second Interceptor Launch Site . . . . .	14-34
14-10	AMR Interceptor Footprint for Target Orbit Altitude = 100 n mi and Target Orbit Inclination = 30 Degrees . . .	14-35
14-11	AMR Intercept Footprint for Target Orbit Altitude = 100 n mi and Target Orbit Inclination = 45 Degrees . . .	14-36
14-12	AMR Interceptor Footprint for Target Orbit Altitude = 100 n mi and Target Orbit Inclination = 60 Degrees . . .	14-37
14-13	AMR Interceptor Footprint for Target Orbit Altitude = 100 n mi and Target Orbit Inclination = 75 Degrees . . .	14-38
14-14	AMR Interceptor Footprints for Target Orbit Altitude = 1000 n mi and Target Orbit Inclination = 30 Degrees . .	14-39
14-15	AMR Interceptor Footprints for Target Orbit Altitude = 1000 n mi and Target Orbit Inclination = 45 Degrees . .	14-40
14-16	AMR Interceptor Footprints for Target Orbit Altitude = 1000 n mi and Target Orbit Inclination = 60 Degrees . .	14-41
14-17	AMR Interceptor Footprints for Target Orbit Altitude = 1000 n mi and Target Orbit Inclination = 75 Degrees . .	14-42
14-18	AMR Interceptor Footprints for Target Orbit Altitude = 1000 n mi and Target Orbit Inclination = 90 Degrees . .	14-43
14-19	AMR Interceptor Footprint for Target Orbit Altitude = 2500 n mi and Target Orbit Inclination = 45 Degrees . .	14-44
14-20	AMR Interceptor Footprint for Target Orbit Altitude = 2500 n mi and Target Orbit Inclination = 60 Degrees . .	14-45
14-21	AMR Interceptor Footprint for Target Orbit Altitude = 2500 n mi and Target Orbit Inclination = 75 Degrees . .	14-46
14-22	AMR Interceptor Footprint for Target Orbit Altitude = 2500 n mi and Target Orbit Inclination = 90 Degrees . .	14-47

# ILLUSTRATIONS (Continued)

Figure		Page
14-23	PMR Interceptor Footprints for Target Orbit Altitude = 100 n mi	14-48
14-24	PMR Interceptor Footprints for Target Orbit Altitude = 1000 n mi	14-49
14-25	PMR Interceptor Footprints for Target Orbit Altitude = 2500 n mi	14-50
14-26	Johnston Island Interceptor Footprints for Target Orbit Altitude = 100 n mi	14-51
14-27	Johnston Island Interceptor Footprints for Target Orbit Altitude = 100 n mi	14-52
14-28	Kodiak Alaska Interceptor Footprints for Target Orbit Altitude = 100 n mi	14-53
14-29	Puerto Rico Interceptor Footprints for Target Orbit Altitude = 100 n mi	14-54
14-30	Puerto Rico Interceptor Footprints for Target Orbit Altitude = 100 n mi	14-55
14-31	AMR Interceptor Footprints for Target Orbit Altitude = 100 n mi	14-56
14-32	AMR Interceptor Footprints for Target Orbit Altitude = 100 n mi	14-57
14-33	AMR Launch Opportunities Against Targets in 100 n mi Altitude Circular Orbits—No $V_R$ Restrictions	14-58
14-34	AMR Launch Opportunities Against Targets in 1000 n mi Altitude Circular Orbits—No $V_R$ Restrictions	14-59
14-35	AMR Launch Opportunities Against Targets in 2500 n mi Altitude Circular Orbits—No $V_R$ Restrictions	14-60
14-36	PMR Launch Opportunities Against Targets in 100 n mi Altitude Circular Orbits—No $V_R$ Restrictions	14-61
14-37	PMR Launch Opportunities Against Targets in 1000 n mi Altitude Circular Orbits—No $V_R$ Restrictions	14-62
14-38	PMR Launch Opportunities Against Targets in 2500 n mi Altitude Circular Orbits—No $V_R$ Restrictions	14-63
14-39	Johnston Island Launch Opportunities Against Targets in 100 n mi Altitude Circular Orbits—No $V_R$ Restrictions	14-64

# ILLUSTRATIONS (Continued)

Figure		Page
14-40	AMR and PMR Launch Opportunities Against Targets in 100 n mi Altitude Circular Orbits—No $V_R$ Restrictions . . . . .	14-65
14-41	AMR and PMR Launch Opportunities Against Targets in 1000 n mi Altitude Circular Orbits—No $V_R$ Restrictions . . . . .	14-66
14-42	AMR and Johnston Island Launch Opportunities Against Targets in 100 n mi Altitude Circular Orbits—No $V_R$ Restrictions . . . . .	14-67
14-43	AMR Launch Opportunities Against Targets in 100 n mi Altitude Circular Orbits—with $V_R$ Restrictions . . . . .	14-68
14-44	AMR Launch Opportunities Against Targets in 1000 n mi Altitude Circular Orbits—with $V_R$ Restrictions . . . . .	14-69
14-45	AMR Launch Opportunities Against Targets in 2500 n mi Altitude Circular Orbits—with $V_R$ Restrictions . . . . .	14-70
14-46	PMR Launch Opportunities Against Targets in 100 n mi Altitude Circular Orbits—with $V_R$ Restrictions . . . . .	14-71
14-47	PMR Launch Opportunities Against Targets in 1000 n mi Altitude Circular Orbits—with $V_R$ Restrictions . . . . .	14-72
14-48	PMR Launch Opportunities Against Targets in 2500 n mi Altitude Circular Orbits—with $V_R$ Restrictions . . . . .	14-73
14-49	Johnston Island Launch Opportunities Against Targets in 100 n mi Altitude Circular Orbits—with $V_R$ Restrictions . . . . .	14-74
14-50	AMR and PMR Launch Opportunities Against Targets in 100 n mi Altitude Circular Orbits—with $V_R$ Restrictions . . . . .	14-75
14-51	AMR and PMR Launch Opportunities Against Targets in 1000 n mi Altitude Circular Orbits—with $V_R$ Restrictions . . . . .	14-76
14-52	AMR and PMR Launch Opportunities Against Targets in 2500 n mi Altitude Circular Orbits—with $V_R$ Restrictions . . . . .	14-77
14-53	Locust of Satellite Orbits that can be Intercepted from AMR within one Orbital Revolution . . . . .	14-78
14-54	Locust of Satellite Orbits that can be Intercepted from PMR within one Orbital Revolution . . . . .	14-79

# ILLUSTRATIONS (Continued)

Figure		Page
14-55	Locust of Satellite Orbits that can be Intercepted From Johnston Island Within One Orbital Revolution . . . . .	14-80
14-56	Locust of Satellite Orbits that can be Intercepted From Kodiak, Alaska Within One Orbital Revolution . . . . .	14-81
14-57	Locust of Satellite Orbits that can be Intercepted From Puerto Rico Within One Orbital Revolution . . . . .	14-82
14-58	Locust of Satellite Orbits that can be Intercepted From AMR Within One Orbital Revolution (No Launch Azimuth Restrictions) . . . . .	14-83
14-59	Locust of Satellite Orbits that can be Intercepted From AMR Within One Orbital Revolution . . . . .	14-84
14-60	Locust of Satellite Orbits that can be Intercepted From PMR Within One Orbital Revolution . . . . .	14-85
14-61	Locust of Satellite Orbits that can be Intercepted From Johnston Island Within One Orbital Revolution . . . . .	14-86
14-62	Locust of Satellite Orbits that can be Intercepted From Kodiak, Alaska Within One Orbital Revolution . . . . .	14-87
14-63	Locust of Satellite Orbits that can be Intercepted From Puerto Rico Within One Orbital Revolution . . . . .	14-88
14-64	Locust of Satellite Orbits that can be Intercepted From AMR Within One Orbital Revolution (No Launch Azimuth Restrictions) . . . . .	14-89
14-65	AMR Launch Opportunities Against Targets in 100 n mi Altitude Circular Orbits—with $V_R$ and $S_m$ Look Angle Restrictions for Midnight of December 25 . . . . .	14-90
14-66	Johnston Island Launch Opportunities Against Targets in 100 n mi Altitude Circular Orbits—with $V_R$ and Sun-Look Angle Restrictions for Midnight of December 20 . . . . .	14-91

## ILLUSTRATIONS

Figure	Page
A-1 Coordinate System for Gyro Misalignment Analysis . . . .	A-2
B-1 Ratio of Miss Distance to Target Standard Deviation as a Function of Interception Probability . . . . .	B-4
B-2 Ratio of Miss Radius to Target Standard Deviation for 90 Percent Interception Probability . . . . .	B-8
C-1 Typical Geometry at Target Acquisition . . . . .	C-7
D-1 Target Geometry . . . . .	D-5
D-2 Spectral Density of Angle Scintillation for Closing Range . . . . .	D-7
D-3 Spectral Density of Angle Noise for a 10-foot Target Rotating at 2 mr/sec . . . . .	D-8
E-1 Noise Equivalent Flux Density Versus Aperture Diameter for Thermal Tracker . . . . .	E-6
E-2 Noise Equivalent Flux Density for Photomultiplier Tracker Versus Aperture Diameter . . . . .	E-8
F-1 Geometry for Determining the Effect of Earthshine . . . .	F-2
F-2 Geometry Showing Plane Specular Satellite Surface Reflecting Earthshine . . . . .	F-4
F-3 Effective Irradiance Produced by Earth-Reflected Sunlight From a Plane Specular Surface on a Satellite (S-20 Photocathode) . . . . .	F-5
G-1 Aperture Diameter for Single Channel FM Tracker with Cone Condenser Versus Target Effective Area for Thermal Target, Ge: Cu Detector and 0.125 Milliradian Tracking Accuracy . . . . .	G-4
G-2 Required S-20 Photomultiplier Tracking Telescope Aperture Diameter Versus $\rho A_T$ for Spherical Diffuse Reflecting Target in Sunlight . . . . .	G-6
I-1 Configurations, Mass and Aero Data . . . . .	I-2
I-2 Trajectory Parameters at Max q for a Wing II Minuteman with a Payload of 1500 Pounds . . . . .	I-3

# ILLUSTRATIONS (Continued).

Figure		Page
K-1	Homing Phase Geometry . . . . .	K-1
L-1	Miss Distance Vector Diagram (In Plane to Normal to Normal Relative Velocity Vector) . . . . .	L-5
L-2	A Possible Boost Law (Command Miss Distance Correction Versus Measured Miss Distance). . . . .	L-6
L-3	Boost Phase Velocity Gain Versus Command Miss Distance Correction (Contact Thrust Boost Phase). . . . .	L-10

## CHAPTER 9

### HOMING STAGE COMPUTER

#### 9.1 INTRODUCTION

A central digital computer will be used in the homing stage. The computer will perform computing functions required by the various subsystems in the homing stage from approximately the time of separation from the launch vehicle until the end of the mission. The functions to be performed include:

- Target identification
- Guidance computations
- Gyro torquing control
- ACS subsystem computation and control
- Generation of discrete signals required for systems operations.

A brief study has been made of the major functions the computer will perform and it appears that the computing requirements can be met by a modification of an existing computer, the Univac 1824. This computer is a parallel, binary, general purpose machine having a 24 bit word length. Its add time (single word operation time) is 8 microseconds giving it a capability of 125,000 single word operations per second. Multiply time is 40 to 72 microseconds depending on the bits in the words. The 1824 uses a thin film memory and integrated circuitry. The computer weight with a 9000 word memory and the additional input-output required for the SIS system is estimated at 27 pounds. The 1824 is now in production and the modifications required for the SIS system are minor and may in fact already be incorporated in newer versions.

The computer functions performed in the EO sensor homing stage and the radar sensor homing stage differ primarily in the treatment of sensor data. The guidance and control functions for example are essentially the same. The following two sections will describe the computer functions in the two versions and give estimates of the computing load imposed. The final section discusses the modifications that will be required in the 1824 computer.



## 9.2 COMPUTER FUNCTIONS IN ELECTRO-OPTICAL TRACKING STAGE

In the EO system the basic source of information about the target is the output of the EO subsystem. Each time the orthicon detects a signal it will provide a pulse to the computer. The computer interrupt system will sense when a signal occurs and read the contents of a counter into buffer storage. The count will be initiated at the start of each scan and the count at any given time will give the coordinates of the scanning beam at that time. (It is probable that the initiation of the scan will be under control of the computer.) The coordinates of each sighting will be stored in a buffer storage in order of arrival. The entire set of inputs on one scan will be stored prior to operation on those inputs. In the target identification phase of operations there will be many inputs per scan.

During the early part of the track phase, the computer will set gates so as to limit the input from the scanning system to a small region surrounding the target. Therefore, there will be only one input per scan at this time. In the end game when the target appears as an extended source there will be many inputs per scan.

### 9.2.1 End Game Sensor Considerations

When the target appears as an extended source, the output of the orthicon sensor will be treated in a different fashion than when the target is a point source.

One approach would be to take the first input signal from the sensor as the target position. However, this point might vary considerably over successive scans and furthermore would in general be away from the centroid.

An alternative approach that appears more desirable would be to determine the centroid of the target as it appears to the sensor. Now when the target appears as an extended source, the sensor when scanning it will have an output at each grid point where the target is seen. However, much of the information in such a case is redundant. Therefore, one can eliminate much of the redundancy and greatly reduce the input data rate. To perform this one could employ one flip-flop which would be set when a scan line crossed the target initially and reset when the scan line left the target. The computer would read in the scan

coordinates at the time of the set and reset pulses. This would be done for each scan line on which the target was seen. At the end of the scan the computer would determine the centroid of the target based on this outline information. This is a simple operation. It has the advantage of getting a centroid which is highly desirable for two reasons. First the centroid is a more desirable point at which to aim than an outlying point on the target insofar as target kill is concerned. Secondly, the centroid would not be as subject to variation as the first point of the target that is seen on a scan. Therefore, it is felt that this approach or one similar to it should be implemented.

The major computing functions in the EO system are:

- Target identification
- Target tracking operations
- Guidance and control of the homing stage

These will be described in the following sections.

#### 9.2.2. Target Identification

The procedure for target identification is to discriminate between the star background and the target on the basis of target motion. The sightings seen over a 3 second interval will be stored in the computer memory and the computer will then analyze the data to determine which sightings correspond to stars, i.e., have no velocity, and which sightings correspond to targets. In order to do this, it is necessary to establish a time history for each signal source. This will be done by correlation of the data seen on one scan with the data seen on previous scans.

The basic procedure involved in the correlation is to check whether a signal appearing on a given scan appeared near the same place on a previous scan. The stars are fixed; therefore, they should always appear at the same place on successive scans. However, there is a small amount of jitter in the scanning system so the stars will have small motions in the field-of-view. Therefore, it is necessary to establish a bin about each sighting that is large enough to account for the uncertainty in a sighting. This is plus or minus one scan element. The procedure is then to check whether a sighting made on a given scan lies within the bin for any

sighting of the previous scan. When a correlation is found, then the new position data is stored with the data from the correlated sighting for analysis when the set of 10 scans is complete.

Target motion between scans can be larger than the uncertainty in star positions and therefore a sighting on a target may not correlate with any sighting from a previous scan based on the bin size for stars. Therefore, the sightings that do not match previous sightings (within the tolerances of the system on star motion) are checked against previous sightings using the tolerance limits for a possible target motion. These limits will be larger than that of a star due to the possible motion of the target during a scan time. Any sighting which satisfies this criterion will be stored with its matching data in a separate location. Any sighting not meeting any of the above criteria will be considered as a new sighting.

After 10 scans of data have been correlated all data are checked to see if there is indication of a target. Each set of data points corresponding to a given source will be checked to see if the maximum separation of inputs exceeds the limits on star sighting imposed by jitter. For those in which this is the case a mean squares angular velocity estimate will be made. The velocity estimate will then be compared against a threshold to see if it corresponds to a reasonable target motion. Further tests can be made to see if the motion is in the proper direction.

When a target is found, the gyros will be torqued so as to cause the tracking telescope to be centered on the target.

Although the bin size is small, it is possible that more than one sighting will correlate with a given sighting from a previous scan. This would be particularly true for the actual target which will move in the field of view. When this happens, the computer would note the occurrence and use data from prior and succeeding scans to resolve the ambiguity. For example, it could check to see if extrapolation of previous points in the time history of one sighting could correspond to one of the correlating points.

There are a number of ways in which the correlation processing can be done. The actual way to do it should be determined on the basis of the actual characteristics of star distribution. One approach to doing this

is developed in flow chart form in Figures 9-1 and 9-2. This approach has the basic advantage that it is relatively insensitive to the number of stars that must be handled. That is, the computing rates determined here should not be affected greatly by some increase in the number of stars in the field-of-view.

In this system, the sightings are stored according to the elevation region in which they lie. Then correlation is done only on previous sightings in that region. The neighboring region is searched (for sightings lying on the boundary) if there is no correlation in the first region searched. If no correlation is found using the bin size corresponding to a star, then the target checking routine is initiated. This is the same as the basic correlation routine except that a larger bin size is used to account for possible target motion. When the correlation has been done on all the inputs for a given scan, the stored data on each sighting is checked. Any sighting for which there is no data on at least one of the last two scans is deleted.

The raster is on the order of  $100 \times 300$  elements. Since  $2^6 < 100 < 2^7$  and  $2^8 < 300 < 2^9$  we need only have 16 bit words to store the position of a sighting. Therefore, it is desirable to store both the X and Y coordinates of a sighting in one word. This requires unpacking the word, i.e., separating the azimuth and elevation, prior to performing arithmetic operations. Unpacking can be done with little computation and will cut the requirements for input storage in half.

By far the major part of the time spent in this phase of operations is taken up in the loop having the starred blocks. This loop involves the testing of targets seen on the present scan against those seen on the previous scans.

We will assume that there are 150 stars that appear in the field-of-view on at least one of the scans. Further, it is assumed that the stars have a uniform distribution over the field-of-view. The field-of-view is taken as having 100 lines in elevation, 300 lines in azimuth. The elevation range will be divided into 20 regions each consisting of five lines of elevation. The expected number of stars per region is then  $150/20 = 7.5$ .

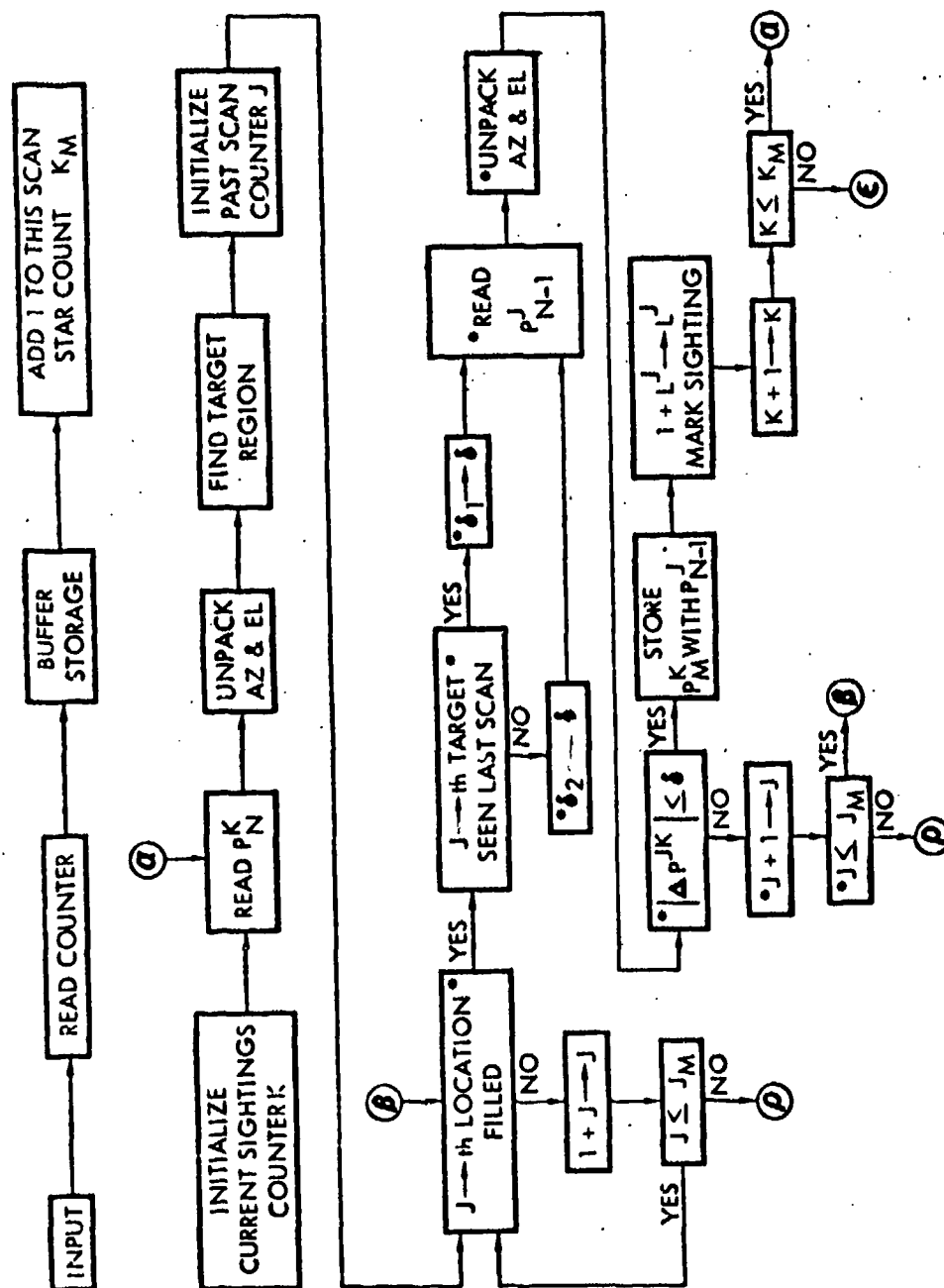


**Figure 9-1. Target Identification Block Diagram.**

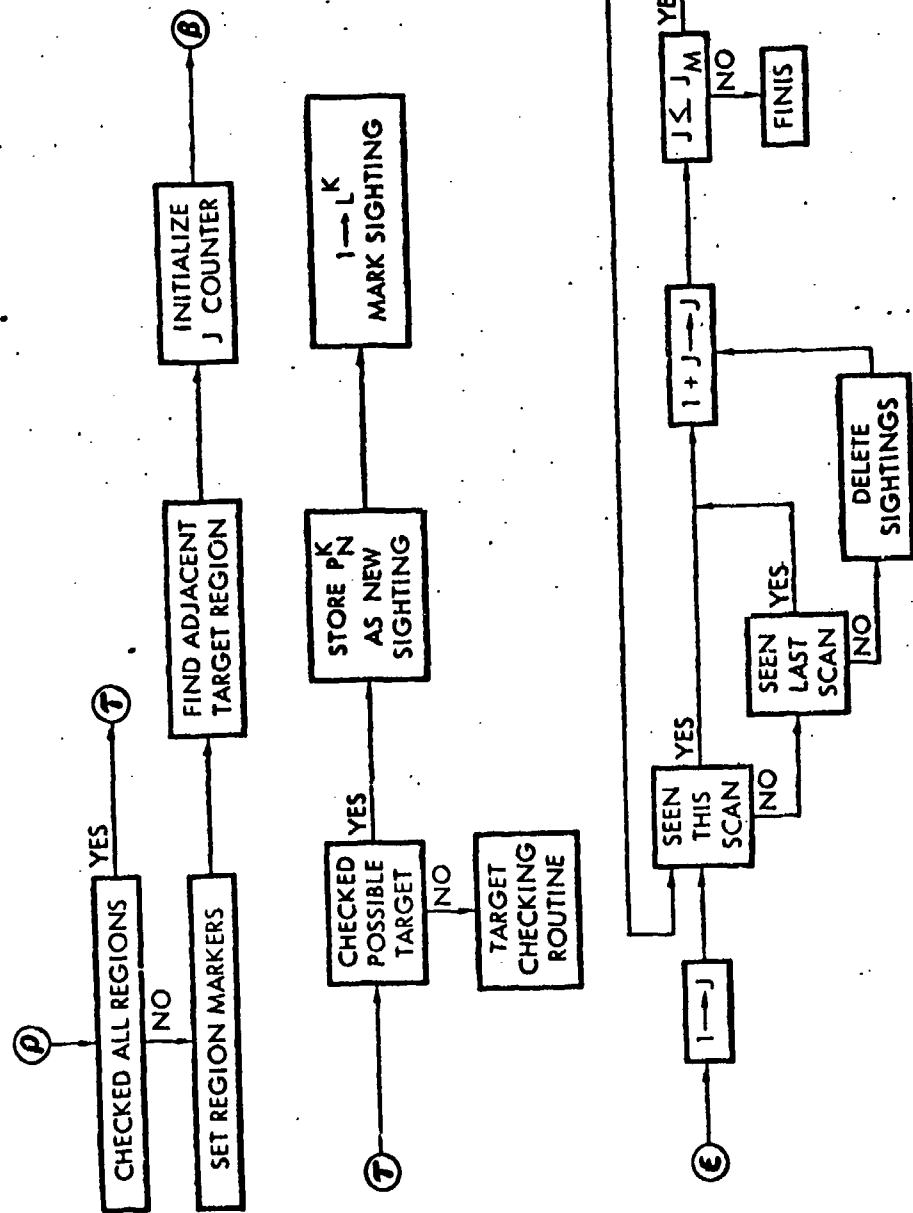


Figure 9-2. Target Identification Block Diagram

Since the probability of any single star lying in a region is  $1/20 = 0.05$  and there are 150 stars, the standard deviation on the number of stars in a region is given by

$$\begin{aligned}\sigma^2 &= Np(1-p) \\ &= (150)(0.05)(0.95) = 7.125 \\ \sigma &\approx 2.7 \\ 3\sigma &= 3 \times 2.7 = 8.1\end{aligned}$$

Thus the number of stars in a region within a  $3\sigma$  region of the mean is  $7.5 + 8.1 \approx 16$ . Therefore, we will assume a maximum of 16 stars per region.

We have assumed that there are a total of 150 stars seen on at least one scan of a set of 10. We will assume that the maximum number of stars seen on any one scan is 75. On the assumption that only 50 stars are above threshold, i.e., seen at least one out of two times, this appears reasonable.

Now the loop having the starred blocks requires 28 instructions per cycle. For 16 stars in a region the loop would be traversed a maximum of 16 times. The average number would be only eight times. Thus we have

$$8 \times 28 = 224 \text{ add times/target/scan}$$

For 75 targets this is then

$$224 \times 75 = 16,800 \text{ add times/scan}$$

Considering three scans/second gives

$$16,800 \times 3 = 50,400 \text{ adds/sec}$$

In some cases, there will be additional loops to check plus there is a small amount of additional work that must be done for each target. However, it should be noted that the number of times used for looping is based on maxima rather than mean values, giving a conservative estimate. In addition including a safety factor of 50 percent gives an estimate of 75,600 adds/sec for this part of the work. The duty cycle is then approximately 0.6 for the 1824 computer.

### 6.2.3 Gyro Torquing

The computer can provide a number of different types of gyro torquing signals to the gyros. The system described in Section V—Homing Stage G and C—will require only that the computer determine and measure three time intervals per axis for the torquing to orient the system and for the torquing to acquire the target in the track field-of-view. The torquing during tracking is part of a closed loop operation so the computer will develop two analog voltages (one for each axis) for driving the torquers during tracking.

As an alternative to the above, the computer could provide pulse torquing signals. These would be pulse width modulated signals of fixed amplitude, giving a fixed turning rate when on, with the duty cycle serving to define the average turning rate. In this mode the computer will determine the required duty cycle and from this determine the times at which to turn the torquers on and off. The computer will set the time interval required into a counter and count down the time. A d-c signal will be provided to the gyro torquers for the duration of the countdown.

The computing required in a countdown for pulse torquing is that of accepting counting signals, decrementing the counter by one each time a signal is received and then making a zero test. When the zero test is satisfied, a subroutine is entered that is used to terminate the d-c signal. The subroutine can also provide more precise interval control than the counter which is assumed to count time intervals on the order of half a millisecond. From the computer manual, it appears that during the counting interval two single word commands are required per count. The duty cycle then required per torquer when giving a rate of 2000 pulses per second, each pulse being accurate to  $1/20,000$  second or  $50 \mu\text{sec}$ , would be  $20,000 \times 16 \times 10^{-6} = 0.32$ . On the other hand, if the pulse rate required is only 500 pulses per second, as for example during target tracking, with each pulse accurate to  $1/5000$  second or  $200 \mu\text{sec}$ , then the duty cycle per torquer is only

$$5000 \times 2 \times 8 \times 10^{-6} = 0.08$$

By utilizing a counting interval every pulse time the accuracy of the pulses can be increased to on the order of one word time ( $8 \mu\text{sec}$ ).



This would require an additional duty cycle of 0.1 when the counter accuracy is 10 percent of the pulse width.

#### 9.2.4 Guidance and Control

The guidance and control functions to be performed in the SIS with optical sensor are shown in block diagram form in Figure 9-3. The computer accepts inputs from the EO subsystem, a roll angle sensor, a roll rate gyro and the gyro gimbal pickoffs. The computer generates the gyro torquing signals, the thrust control, and control signals for the ACS subsystem. It performs all filtering and function generation required. The nominal rate of operation is 30 times per second which is the rate of information input from the infrared subsystem.

The total computation load per cycle for guidance and control is estimated at 570 equivalent single word operations. Putting in a safety factor of 2 we have 1140 equivalent operations. On the basis of 30 operation cycles per second this requires -

$$30 \times 1140 = 34,200 \text{ operations/sec}$$

A single word operation requires 8  $\mu$ sec giving a duty cycle of

$$34,200 \times 8 \times 10^{-6} = 0.28$$

for the guidance and control functions during target tracking.

#### 9.2.5 Other Computing Functions

The computer will perform a number of other functions in the course of the mission. These do not noticeably affect the computer load. These will include:

- Generation of pulses at specified points for such things as unpinning the gimbals, initiating scan operations, etc.
- Computation of angles through which to torque the gyros for target acquisition.
- Control of the part of the scan of the EO system on which data are accepted
- Variation of gain settings with mission phase.



### 9.3 RADAR FUNCTIONS

The computer will perform a number of functions internally to the radar system. These will be essentially low frequency logical functions which can be done by the computer on a time-shared basis, thus eliminating a number of analog components; e.g., integrators, that would be required if there were no digital computer.

#### 9.3.1 Computer Functions

##### 9.3.1.1 Target Detection

The computer will sample the output of each of the 30 filters in the filter bank periodically (approximately 20 times per second). The sampled output will be digitized and compared against a threshold value. When an output is found that exceeds the threshold value, the body motion of the satellite will be halted.

The computer will then drive the frequency of the oscillator used for the frequency locked loop to the frequency band detected from the target so that the frequency locked loop can lock on the input signal.

Since there will be outputs from the filter bank removed from the center frequency by harmonics of the PRF rate, it will be necessary to decide which signal corresponds to the true center frequency. The computer will increase the PRF rate as range decreases to prevent eclipsing loss, thus causing the frequency due to the PRF harmonics to vary. The resultant variation in output of the various filter bands will be analyzed to pick out the center frequency and frequency lock will be transferred to the center frequency and then maintained there.

##### 9.3.1.2 Intermediate Frequency Offset Oscillator Control (Local Oscillator)

In order to set the local oscillator to the proper frequency band for acquisition, the computer will control the local oscillator frequency. The computer will predict the value of closing velocity  $V_R$  on the basis of the satellite and missile trajectories. It will then solve the equation

$$F = AV_R + B \quad (9.1)$$

where  $F$  is the desired offset oscillator control frequency and  $A$  and  $B$  are constants. The computer will sample the offset frequency and drive the oscillator to the desired frequency. The frequency sampled by the computer will be in the range 0 to 50 kc. A counter will count a prescribed number of cycles and, from the time interval required, determine the oscillator frequency. The computer will then generate a control signal to drive the frequency to the desired value and continually control the frequency according to Equation (9.1) until a target is detected.

Frequency measurement is specified by the equation

$$F\tau = N \quad (9.2)$$

where  $F$  is the actual frequency,  $\tau$  is the time interval of the count and  $N$  is the total cycle count. Taking the variation, assuming  $N$  is known, we have

$$\Delta N = 0 = F\Delta\tau + \tau\Delta F \quad (9.3)$$

$$\Delta F = -\frac{F^2\Delta\tau}{N} \quad (9.4)$$

Note that  $\Delta F$  varies as  $F^2$  and also we are concerned only with magnitude of  $\Delta F$ . The largest error occurs at  $F = F_{\text{maximum}}$ . Let  $F_{\text{maximum}} = 50,000$  cps. Then

$$|\Delta F| = 25 \times 10^8 \frac{\Delta\tau}{N} \quad (9.5)$$

Now a minimum  $\Delta\tau$  would be on the order of 16  $\mu\text{sec}$  for the presently considered computer. For an allowable error of 12.5 cps corresponding to a range rate accuracy of 5 ft/sec we have to count

$$N = 25 \times 10^8 \frac{\Delta\tau}{|\Delta F|} \quad (9.6)$$

$$N = \frac{25 \times 10^8 \times 16 \times 10^{-6}}{12.5} = 3200 \text{ cycles} \quad (9.7)$$

This would require a time interval of

$$\frac{3,200}{50,000} = 0.064 \text{ sec} \quad (9.8)$$

Thus, this would be satisfactory if the time rate of change of range rate is less than

$$\frac{5 \text{ ft/sec}}{0.064 \text{ sec}} \approx 80 \text{ ft/sec}^2. \quad (9.9)$$

This is true since  $\dot{V}_R \approx 2.5 \text{ ft/sec}^2$ .

#### 9.3.1.3 PRF Signal

The computer will generate a PRF signal as a square wave which will be provided to the transmitter and the local oscillator. The frequency will be a function of range to target and be variable from 200 cps to 4000 cps.

#### 9.3.1.4 Guidance and Control Functions

The computer will accept a voltage signal from the rate integrating gyro. The voltage will be digitized, then filtered and a control signal will be generated for the lateral steering control setting.

Yaw and pitch error signals will be provided by the radar and operated upon by the computer in a manner similar to that discussed for the optical system. The computer will use this to generate control signals for the ACS subsystem.

#### 9.3.1.5 Scan Pattern

The computer will generate the required control signals for torquing the body to provide the desired scan pattern for the radar.

#### 9.3.2 Effect on Computer

The functions described above will provide a small load for the computer. The guidance and control functions are essentially the same as in the optical system. The target detection problem involves a sampling rate of 300 samples per second and performing a simple comparison on

each sample. Assuming the 10 single word operations were required per sample this would involve 3000 operations per second which is less than 0.025 of the capacity of the computer.

The frequency measurement will require a 50 kc counter of about 5 bits length. The computer clock may be sufficiently accurate or it may be necessary to provide a better clock.

#### 9.4 COMPUTING REQUIREMENTS SUMMARY

##### 9.4.1 Computing Requirements

The major requirements will now be summarized.

##### Electro-optical System

Acquisition	Duty Cycle	Var.	Memory
Target Identification	0.60		1820
Attitude Control	0.14		
	0.74		1820
Tracking			
Target Input	<0.10		
Guidance and Control	0.28		
Pulse Torquing Gyros (500/sec)	0.08		
	0.46		

##### Radar System

The major computing load in the radar SIS is the guidance and control which will be essentially the same as that for the electro-optical system.

##### 9.4.2 Computer Modifications Required

The input-output (see Table 9-1 for input-output requirements) system will require an analog-digital and digital-analog converter of about 1 percent accuracy capable of operating at approximately 500 samples per second. A 50 kc counter about 5 bits long will be needed for frequency measurement in the radar system. A 16 bit counter

Table 9-1. Electro-Optical System Input-Output Requirements

<u>Type</u>	<u>Form</u>	<u>Rate (sec<sup>-1</sup>)</u>	<u>Accuracy</u>
<u>Inputs</u>			
Sighting Signals			
Acquisition	Pulse	~500	
Homing Initial	Pulse	30	
Homing Terminal	Pulse	<2400	
Roll Angle Increments	Pulse	200	1/2 degree
Gimbal Angles			
Yaw	Voltage	30	1 percent
Pitch	Voltage	30	1 percent
Roll Rate	Voltage	30	1 percent
Digital Data			
Prelaunch	Pulses		
Separation	Pulses		
<u>Outputs</u>			
Thrust	Voltage	30	1 percent
Gyro Torquers			
Yaw	Voltage	30	1 percent
Pitch	Voltage	30	1 percent
Roll	Voltage	30	1 percent
ACS			
Yaw	DC Pulse	30	
Pitch	DC Pulse	30	
Roll	DC Pulse	30	
Miscellaneous Sequencing and Control Signals Pulses			

operating at about 200 kc will be required for the infrared input system (this may be part of the EO subsystem). These should require relatively minor modifications to the computer design.

The input requirement of the electro-optical system necessitates an increase in the variable memory from 500 to approximately 2000 words. We have been informed that much larger increases can be made in variable memory if desired.

A cursory look at the equations to be solved indicates that a few thousand words of permanent memory (electrically alterable) would be sufficient. Therefore, the weight estimate for the computer was based on a 9000 word memory, about 2000 words variable and 7000 (which is exceedingly conservative for present requirements) fixed.



## CHAPTER 10

### WARHEAD AND FUZE

#### 10.1 INTRODUCTION AND SUMMARY

The required radius of the kill pattern at the instant when the target penetrates the plane of the pattern is a function of the expected terminal miss. In particular, at the instant of kill, the lethal pattern should have a radius of not much less than the  $3\sigma$  terminal miss. Thus, when one is concerned with a homing stage which utilizes a low noise tracking sensor (i.e., infrared) terminal miss performance might be very good,  $1\sigma$  values of 3 feet. For this case the warhead pattern should have a radius of 9 feet at the instant of kill.

The amount and nature of lethal material of which this 18 foot diameter circle is composed, is primarily a function of target hardness. For example, if the target is characterized by the kind of construction typically found in current U.S. satellite designs, a plate slap warhead would be lethal. In this case the warhead can be a balloon structure and, if desired, small pellets can be embedded in this balloon structure.

On the other hand, if the target is hard, plate slap mechanisms may not be lethal and larger metallic fragments are required. If the target is armored enough, each fragment may have to be as massive as 100 grams. The number of such fragments required in the lethal pattern has to do with the target's vulnerable cross section and with the number of hits required to achieve a satisfactory kill probability.

Returning to our sample computation for a low terminal miss ( $1\sigma$  of 3 feet), the lethal pattern must have an 18 foot diameter and therefore represents an area of about  $250 \text{ ft}^2$ . Now suppose the target were heavily armored (required pellet mass 100 grams) and had a vulnerable cross section of  $10 \text{ ft}^2$ . Suppose furthermore that two hits were required to achieve the desired kill probability. In that case, the warhead pattern must include at least 50 fragments at a total pellet weight of about 10 pounds, provided that the pellets are uniformly spaced. An additional factor of two must be allowed for pellet bunching (nonuniform deployment), thus increasing pellet weight to 20 pounds and this weight corresponded to a  $1\sigma$  miss of 3 feet.

Noting that the required number of pellets varies with the square of the terminal miss, it follows that if the 1 $\sigma$  miss against an armored target rises to 10 feet, the resulting required pellet mass rises to 200 pounds. Allowing weight for the explosive charge necessary to impart separation velocity to the pellets, it is not hard to see how such warheads can easily weigh 250 pounds. Observe that the warhead weight fluctuates by a factor of 10 as the rms miss goes from 3 to 10 feet. It must be emphasized, however, that the warhead weight is an even more sensitive function of the assumptions made relative to target hardness. If one wishes to emphasize heavily armored targets, as was the case during terminal portions of the SIS study, then heavy warheads become a necessity.

During the SIS study, STL studied three warhead concepts—a relatively light pellet warhead effective against soft targets with rms miss distance larger than 3 feet; an even lighter plate slap warhead effective against soft targets at rms miss distances of 3 feet or less; and a heavy pellet warhead effective against hard targets with rms miss distances of about 8 to 10 feet. These warhead concepts are described in the next portions of this discussion.

## 10.2 EXPLOSIVE WARHEAD CONCEPTS

To accommodate large miss distances (in excess of 8 feet, 3 $\sigma$ ), and to defeat hardened targets a directional type explosive warhead appears most attractive. Preliminary design and development of a similar device was conducted during the STL BAMBI studies and are reported in Reference 1. During the BAMBI study, the feasibility of obtaining circular fragment patterns was established by limited fabrication and test firing of smaller ( $\sim 3$  lb) warheads.

### 10.2.1 Target Considerations

A review of the suggested threat models presented in the Battelle Second Interim Report (Reference 2) shows that targets can be categorized in two general classes of widely differing vulnerability. The reconnaissance vehicles are characterized by moderate size, i. e., projected areas of 16 to 80 square feet and are generally of soft construction: 0.1 or 0.2-inch double steel skins with spacing between layers. Orbital bombs are larger, presenting areas of 160 to 360 square feet, and may have some hard as well as soft areas.

The kill mechanism consists of the hypervelocity collision of metallic fragments with the target. Since the relative velocity between the homing stage and the target at the instant of warhead deployment is between 10,000 and 20,000 ft/sec, the pellet deployment velocity can be kept relatively low. For armored targets, the lethal pellet mass required may be as high as 100 grams, while a one gram pellet is probably lethal against soft targets.

#### 10.2.2 Soft Target Warhead Concept

For soft targets, it seems reasonable to use a fragmentation warhead with a dense and carefully controlled circular fragment pattern. The requirements are not very different from those previously encountered in the BAMBI study and the BAMBI study results are applicable here. It is assumed that the interceptor-target closing velocities will vary between 8000 and 20,000 ft/sec and that the warhead axis of symmetry is oriented in the direction of the relative velocity.

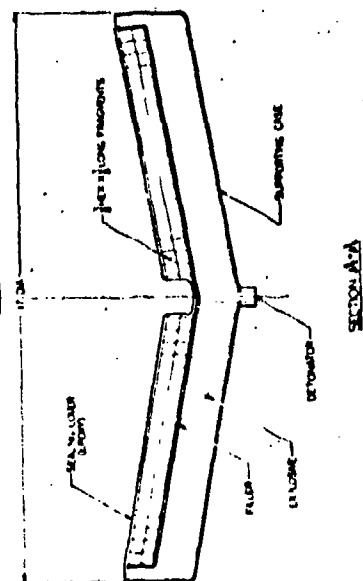
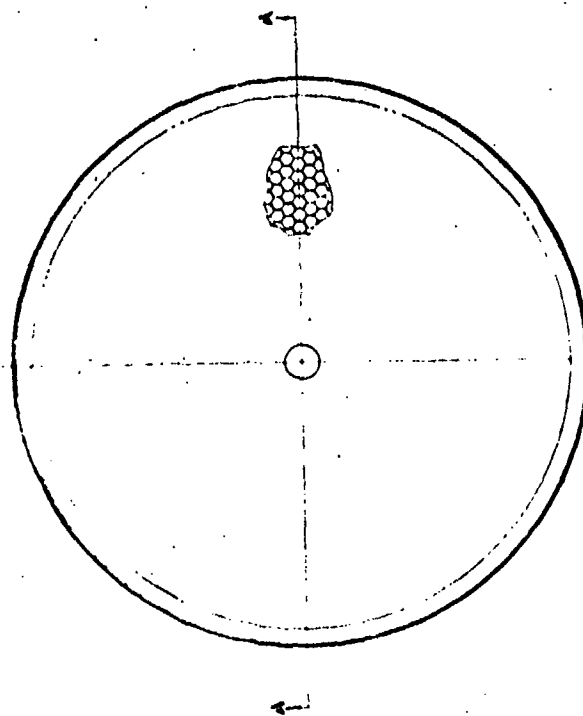
The characteristics of the soft target warhead shown in Figure 10-1 are as follows:

Weight	66 lb
Size of fragment	3/8 hex x 3/8 lg steel
Weight of fragment	90 grains
Number of fragments	about 3000
Desired size of pattern	60 ft diameter
Included angle of fragment projection beam	20 deg (approximately)
Fragment static velocity	2000 ft/sec (approximately)

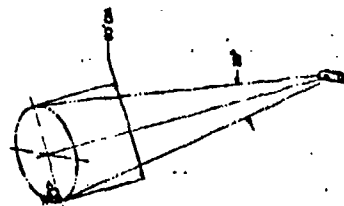
The proper warhead configuration to achieve required fragment projection angle and velocity is a matter for experimentation and the configuration shown should be regarded as approximate. It is estimated that perhaps 40 or more test samples would be required to determine a final configuration.

#### 10.2.3 Hard Target Warhead Concepts

Some parts or all of the "orbital bomb" targets are quite hard and the 90 grain fragments of the warhead discussed in Paragraph 10.2.2 will not be effective. The hardest part of the re-entering orbital bomb, for example, consists of layers of 0.5-inch steel, 0.5-inch aluminum,



WARHEAD WEIGHT — 650 LBS  
 PATTERN SIZE AT INTERCEPT — 60' DIA  
 PROJECTION CONE ANGLE — APPROX 20°  
 PATTERN DENSITY — 10/FT<sup>2</sup>  
 NUMBER OF FRAGMENTS — APPROX 3000  
 FRAGMENT MATERIAL — STEEL  
 FRAGMENT WEIGHT — 50 GRAMS



PROJECT INTERCEPT



Figure 10-1. Explosive Warhead Concept

1.0-inch lead and "several" inches of tuballoy. If one assumes "several inches" to be, say, 3 inches, a multiplate, composite target 5 inches thick is encountered. Furthermore, it is not clear what degree of "over perforation" must be obtained against this very thick vehicle case in order to do killing damage to the inside.

There is some question as to the wisdom of attempting to defeat hard target areas—as opposed to causing mission frustration by damaging softer target parts. However, it is of interest to examine what might be required to perforate the hard shell devices. First, it should be noted that only a approximations can be made of the terminal ballistic effects involved since pertinent data for these targets are very sparse.

The following preliminary warhead designs, which may be effective against such targets, have been examined.

#### 10.2.3.1 Clustered Shaped Charges

The average density of the composite (say 5 inches thick) target is about 0.52 lb/in<sup>3</sup>. Therefore, if one uses the approximate formula

$$P = \frac{1.6}{\rho_t 0.898}$$

where P is penetration in cone diameters and  $\rho_t$  is target density, a shaped charge with a cone diameter of 2 inches should perforate the target wall.

If one further assumes that the probability of killing, given a hit, for a single hollow charge is 0.5 and the desired overall warhead  $P_k$  is, say, 0.97, the number of hits required is five. For a target whose hard part has 60 ft<sup>2</sup> of area (maximum) the hit density is, thus, 0.0833. If the 3 $\sigma$  miss distance is 30 feet (any direction), the number of shaped charges required is 236. To accommodate such an array would require a warhead assembly roughly 4 feet in diameter. Even if such a large weapon could be carried, there are certain problems associated with fuzing. It is not clear as to the maximum standoff that could be tolerated in a shaped charge of this size operating in a vacuum. In any case the tolerance on fuzing time would need to be rather tight. If the maximum tolerable standoff were small, the angle of the outermost charge with respect to the cluster axis would be objectionably large resulting in a "wiping" action at the target. This would

tend to reduce the ability to perforate. Thus, one is led to the conclusion that utilization of shaped charges depends upon solution of a number of serious problems. Nonetheless, the shaped charge approach has attractive possibilities for attacking very tough targets and merits further investigation.

#### 10.2.3.2 Oriented Rod Warhead

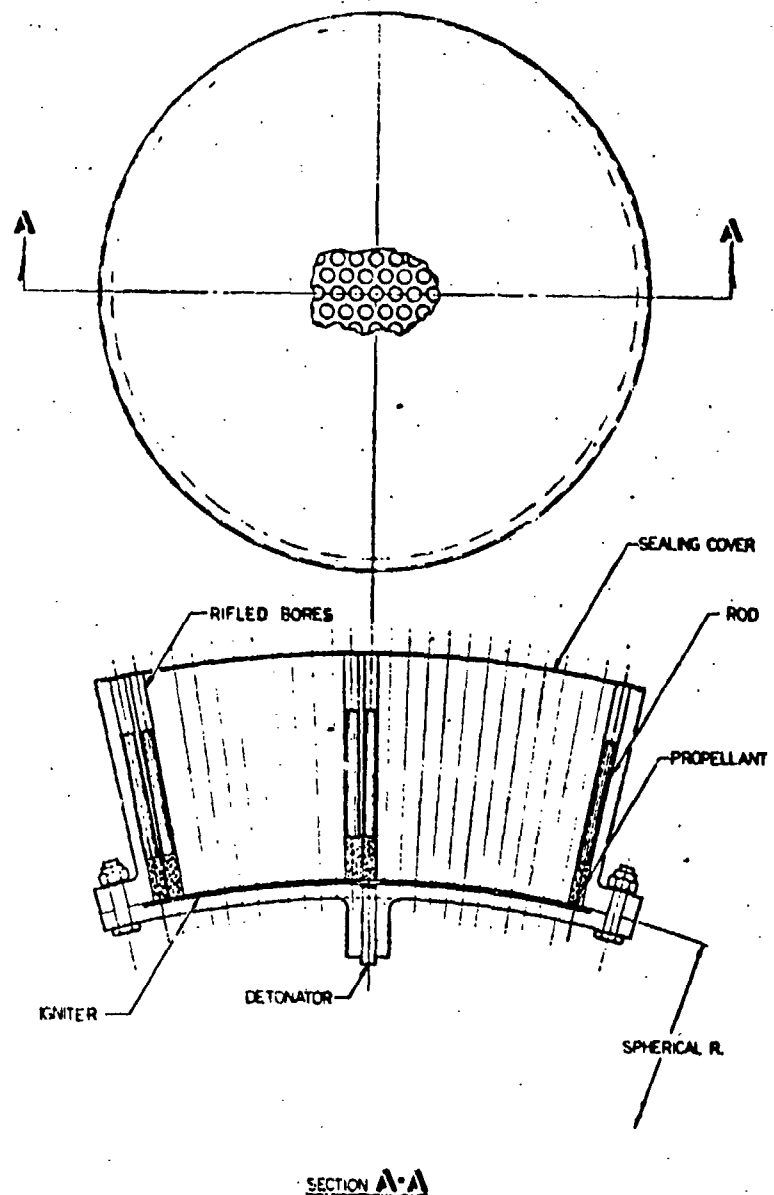
On a weight basis, the use of rods as "fragments" has advantages. If the rod can be induced to strike the target in an unyawed attitude, the advantage in weight for the same penetration depth is of the order of 8 or 10 to one when compared with compact steel fragments. (Rod  $L/D = 9$ .)

It has been estimated that a steel rod 0.250-inch in diameter x 2.25-inches long would be sufficient to perforate the 5-inch thick target postulated above. If the  $p_k$  for a single rod is assumed to be 0.3, and the same assumptions used as for the shaped charge above, it can be shown that about 566 rods will be required. The rods could be projected from a multitube holder (see Figure 10-2).

There are two difficult problems associated with this design: In order to maintain the rod orientation, spin up will be necessary. It is anticipated that this could be accomplished either by rifled tubes or by integral "fin-grooves" to be acted upon by the propellant gases. The other problem is that of yawed impact. Even though the original tube orientation is maintained, the rods from the outer part of the cluster will tend toward yawed impact because of the "built-in" angle. This angle is necessary to obtain the required pattern size (60 feet diameter). Of course, this condition diminishes to zero at the center of the cluster. A long fuzing time tends to reduce the required maximum angle for the rod projection beam and thus reduces the yawed impact condition for the outer rods. There is little question that rods are extremely attractive, but their proper exploitation hinges upon solution of the orientation problem.

#### 10.2.3.3 Fragmentation Warhead

The warhead discussed in 10.2.2 was based upon previous work done in connection with the BAMBI project. For very thick hardened targets, much larger fragments are required to obtain the same penetration as was



ROD SIZE .....250 DIA X 2.25  
 ROD WEIGHT .....218.5 GRAINS  
 TOTAL NUMBER OF RODS.....566

0 1 2 3  
 SCALE IN INCHES

Figure 10-2. Warhead - Oriented Rod Concept

calculated for the above rods. Fragments cut from hexagonal bars ( $L/D = 1$ ) were chosen because of weight advantage over square fragments for the same penetrating ability and because of packing efficiency. As an example, a fragment 15/16 (across flats) hex x 15/16 long was chosen (weight: 1405 grains). The ballistic limit for this fragment against the composite target is estimated to be about 15,000 ft/sec which lies within the expected range of striking velocities. A warhead containing about 800 of these fragments is estimated to weigh 220 pounds. In order to achieve an overall  $P_k$  of 0.97, the  $p_k$  for this fragment should be about 0.2 (pattern density = 0.282 frags/ft<sup>2</sup>).

A possible configuration using these fragments is shown in Figure 10-3. This is the warhead configuration tested as part of the BAMBI study. This design basically depends upon the use of a fairly thin explosive layer either peripherally or centrally initiated. Since the static fragment velocity required is low (requiring a low C/M) and the fragment weight (in the BAMBI case) is also low, the thin layer of explosive tends to function in a "two dimensional" manner.

In the case of the larger warhead, however, maintaining the same C/M (charge to metal ratio) results in an explosive layer which is fairly thick and tends toward a "3-dimensional" configuration. Also, in order to provide enough fragments within a reasonable space, a double layer fragment pack is necessary. For these reasons confidence in the performance of this warhead is somewhat reduced. However, it is believed that with a proper development program a heavy fragment weapon could be developed.

Since the postulated targets are neither all thick or all thin, it is not unreasonable to consider a mixed fragment pack with both large and small fragments. While this technique is feasible and has been used in the past, careful study of the target should be made to determine if an overall advantage really exists. There would be some complication in the manufacture of a mixed pack but for the small quantities involved this should not be a serious consideration.

In summary, it may be stated that either the rod or shaped charge would probably be more effective per unit weight than the large compact fragments. The design problems are greater for rods or shaped charges



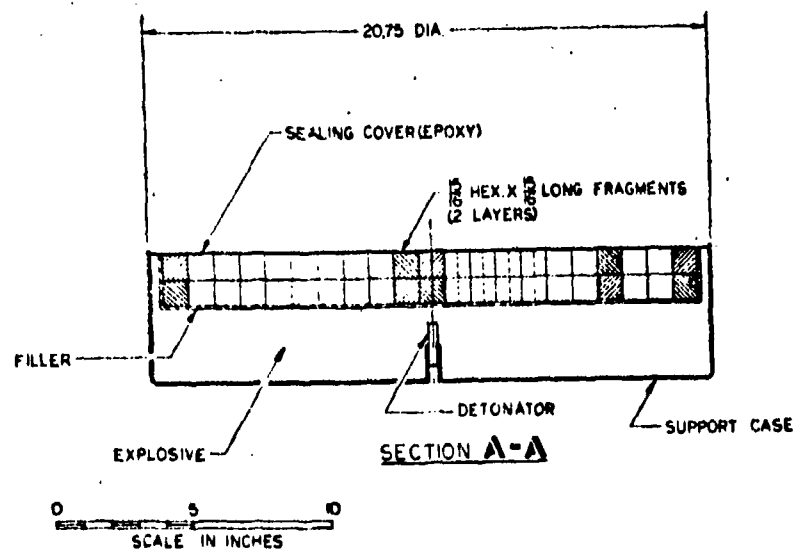
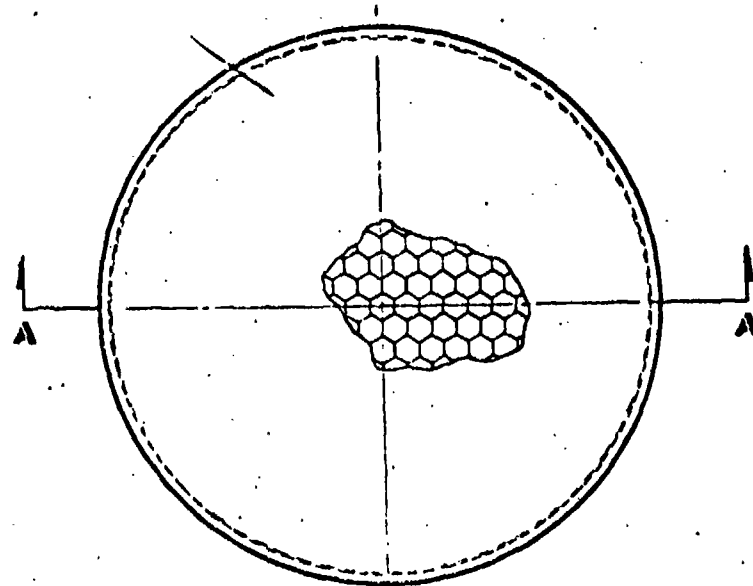


Figure 10-3. Warhead - Heavy Fragment Concept

and size becomes a problem for a clustered shaped charge. While the large fragment weapon is probably easier to develop, it is less efficient on a per fragment basis. Also, due to its size and mass it presents a constraint upon homing stage configurational design.

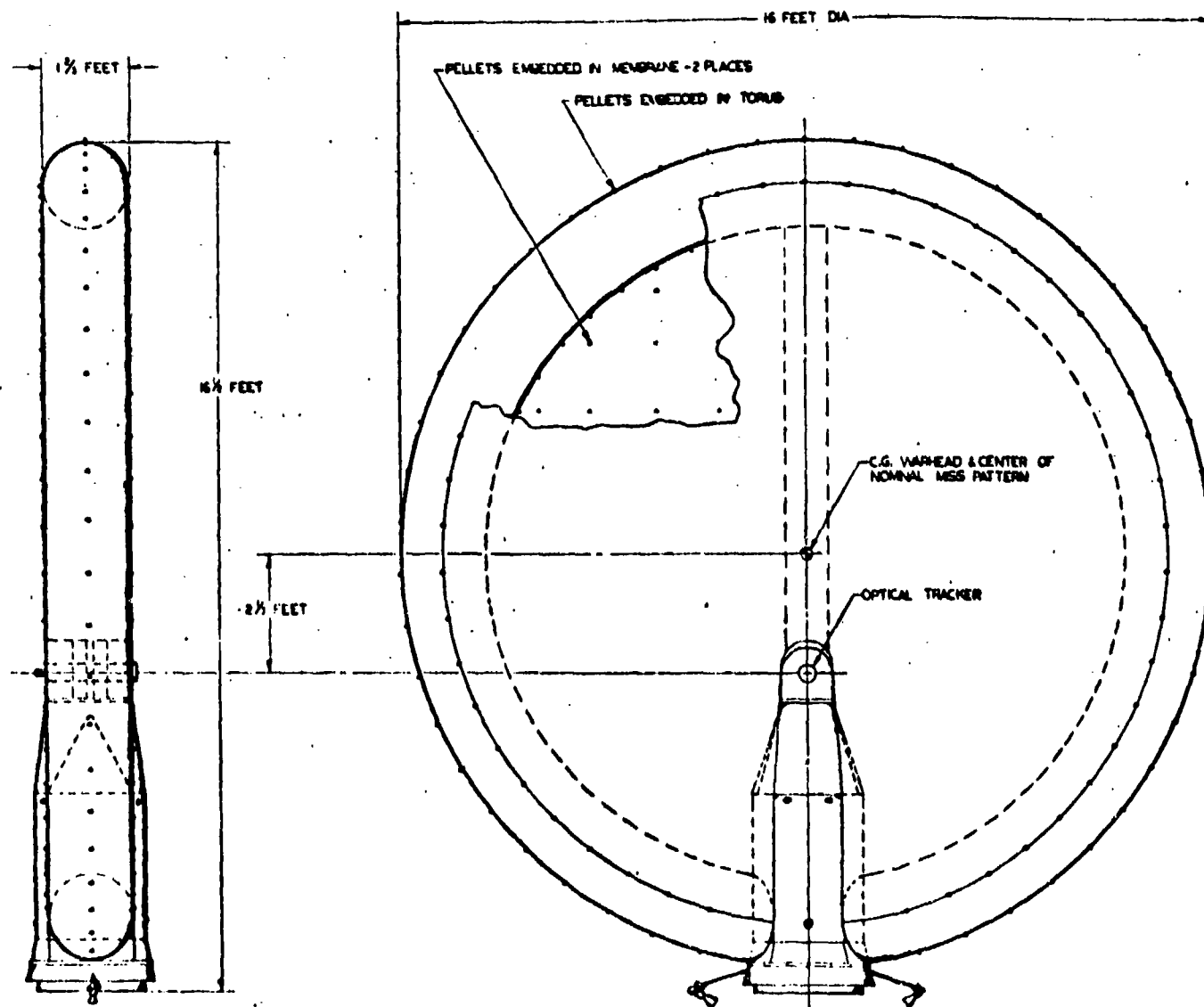
### 10.3 UNFURLABLE PASSIVE KILL MECHANISM

As reported in the Second Interim Report (Reference 3), it became evident that practical considerations limit the size of an unfurlable mechanism to a radius approximately equal to the overall length of the homing stage. A feasible design is shown in Figure 10-4. Larger devices are unattractive because of the following factors:

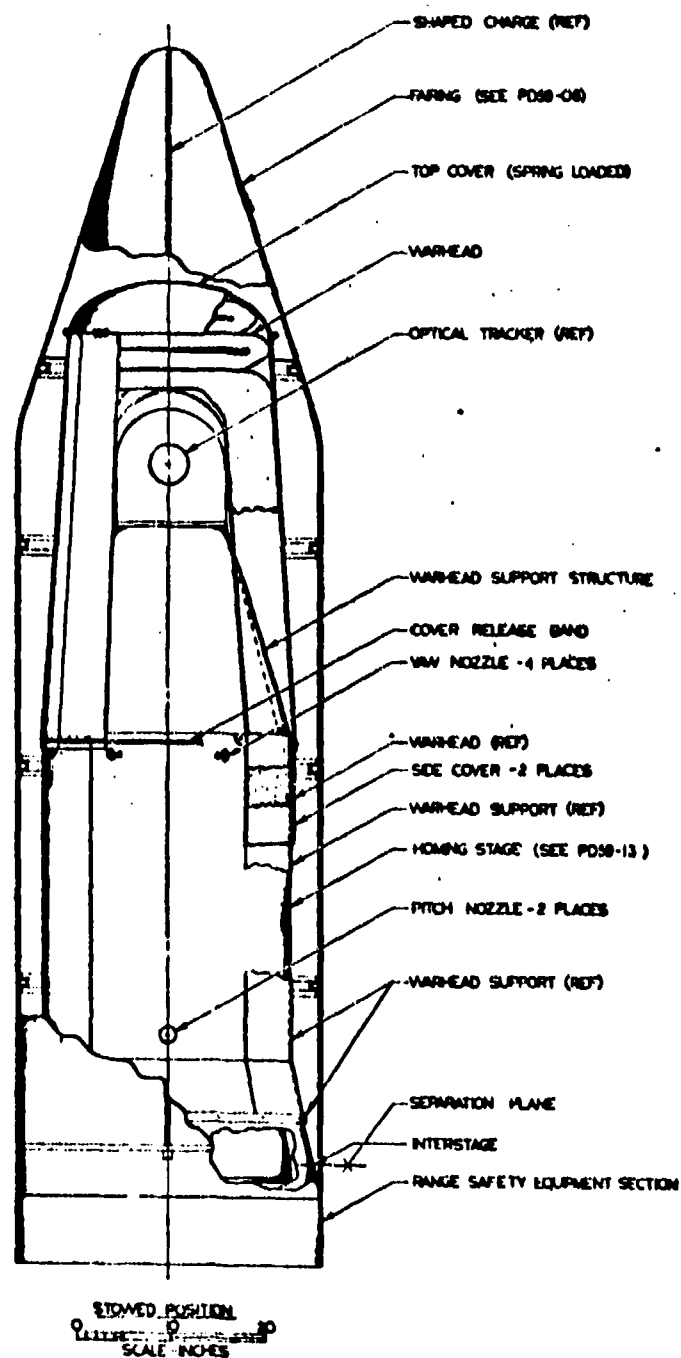
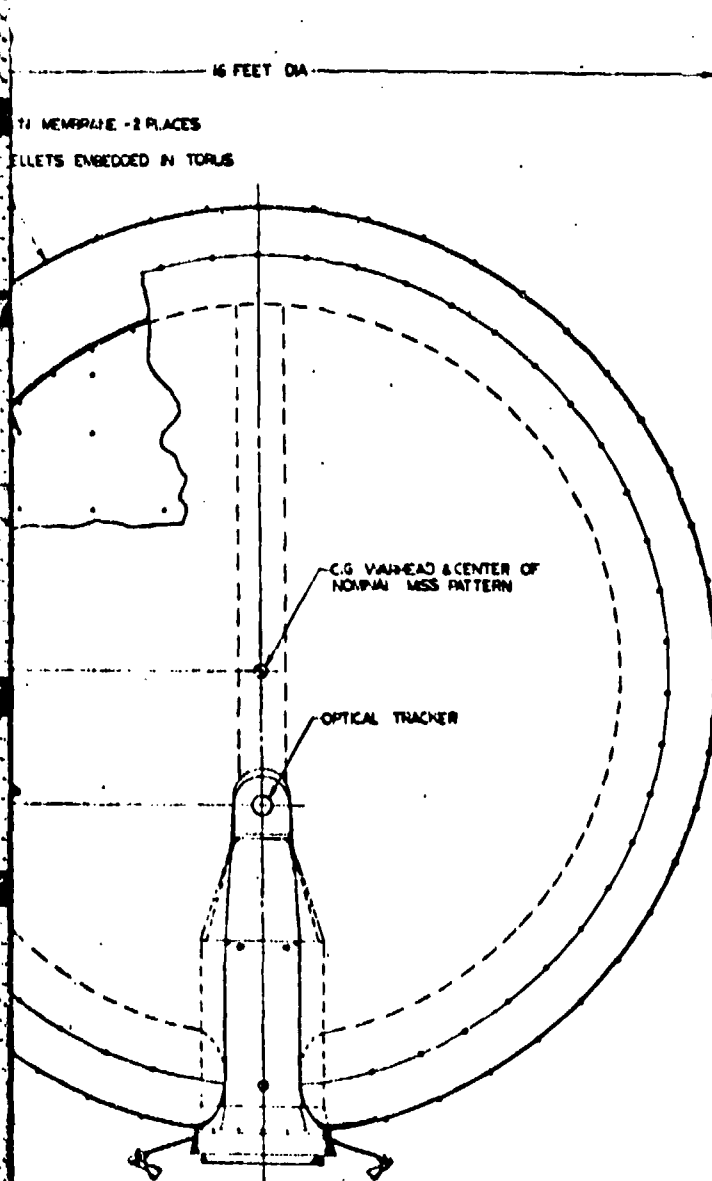
- Main engine plume impingement on the warhead
- Difficulty in placing the attitude control system thrusters to avoid their plume impingement on the unfurled structure
- Maintenance of structural continuity of unfurled mechanism
- Increased "packed volume"
- Increased inflation gas volume, unfurlable structural weight, and deployment reaction time
- Increased homing stage moment of inertia
- Increased interaction with homing stage attitude control system due to warhead deformations

The proposed unfurlable passive kill mechanism utilizes a combination of plate slap by the membranes and pellet impingement as a kill mechanism. This warhead's probability of target hit for a  $\pm$  miss of 4 feet is approximately 0.95 if the target's vulnerable cross section is 4 feet in diameter and 0.90 if the target's vulnerable cross section is only 1 foot in diameter.

Since one "face" of the homing stage is aligned along the  $V_R$  vector, a one dimensional or planar array is geometrically sufficient. If an 8 foot radius is sufficient for a hit ( $\text{rms miss} \leq 3 \text{ ft}$ ), the chosen torus with dual membranes which are oriented normal to the closing velocity vector (see Figure 10-4) has advantages over other shapes such as a sphere of the same radius. When volumes are compared it is apparent that the sphere has approximately 66 times the volume of the proposed torus. If



1



2

Figure 10-4. General Arrangement -  
Passive Kill Mechanism  
10-11

the sphere pressure is 1 psi and the torus pressure is 5.6 psi the weight of torus inflation gas is 1/12 that required by the sphere. It also appears that the inflation period of the sphere would be greater than that for the equivalent torus.

Possible impingement of the hot gas attitude control engine plumes on the proposed torus design was avoided by deploying the roll engines on arms. The body mounted pitch engines, which thrust normal to the plane of the warhead, would also require deployment if a spherical warhead were used. Increased pitch torque levels would be needed to provide the equivalent pitch acceleration since the pitch moment of inertia would increase by a factor of  $\sim 2.0$ .

Other serious disadvantages of the spherical design appear when full consideration is given to the interaction between its stowed condition and the homing stage. When installed on the vehicle, it forms a cocoon which completely surrounds the vehicle, thereby eliminating all on-stand access to the vehicle and possibly creating a serious thermal problem.

The present concept allows for packing volume on two sides of the vehicle and over the long tracker in a saddle-fashion. The major portion of the vehicle's sides are left open for access and the tracker's line-of-sight is unobstructed at all times. Packing space in front or behind the tracker is presently unavailable as the tracker extends to the fairing clearance line. The outside covers, which presently consist of two segments along the sides of the vehicle, would also need to be extended around the periphery of the vehicle resulting in a weight increase and complexity of jettisoning.

The torus and membranes are designed to withstand vehicle acceleration without wrinkling. The membranes are continuously attached at their intersection with the support structure. A torus internal pressure has been selected which prevents relief of torus or membrane tensile loads under maximum vehicle thrust condition. No wrinkling or buckling is tolerated, in order to provide as stiff a system as possible to minimize vehicle attitude control problem. Point loading of a sphere is associated with large membrane deflection and consequently results in a softness or response lag during engine on-off cycling or vehicle control maneuvers.

this structure is required to maintain its shape during powered flight or attitude maneuvers of the homing stage.

The material selection is based on the requirement for flexibility and pressure tightness inherent with inflatable structures. When structural rigidity is provided by pressure, the higher material strength allows increased internal pressure resulting in a corresponding increase in load capacity. Based on these factors, Mylar film was selected as the best available material. Table 10-1 summarizes the mechanical properties of Mylar film.

The critical design load condition after inflation is the 6 g's along the thrust axis of the homing stage. The design pressure for the torus was set such that the average hoop stress (i. e., around the cross section through the torus) is 8000 psi. The ultimate tensile strength of Mylar is 20,000 psi resulting in an elongation of 100 percent. At 8000 psi stress, the elongation is reduced to approximately 1 percent.

The previous parametric analysis (Reference 3) indicated minimum structural weight is obtained by using as large a torus cross section as possible. Based on this conclusion, the torus cross section radius was set at 10 inches, the recommended maximum for the selected configuration. Ninety-grain pellets are added to the torus and membranes on 1 foot spacing. This added weight represents a substantial increase over the weights associated with the torus and membranes and therefore require increased torus thicknesses for the selected design. The critical load condition was modified to the requirement that the torus would not wrinkle at limit load which is defined as 1.1 times the design load (i. e., the maximum load predicted in service). This modification was made because an inflated structure has reserve strength above its wrinkling. This is analogous to the advantage taken of plastic bending in stress analysis of beams. Tests of an inflated pressurized cylinder in the form of a cantilever beam with a tip load showed that collapsing occurred at a bending moment twice the bending moment that causes wrinkling. This factor of two, although possibly reduced for the case of a torus because of the effect of curvature, is considered adequate to cover the ultimate load condition of 1.5 times design load. The design pressure was set in the same manner as for the parametric analysis (i. e., design pressure is such that the average hoop

Table 10-1. Mechanical Properties of Mylar Film

Typical values (1 mil film)

Tensile strength	20,000 psi	} Instron tester
Tensile modulus	550,000 psi	
Break elongation	100 percent	
Impact strength	60 kgm-cm	Dupont falling ball
Burst strength	45 pounds	Mullen test method
Tear strength	15 grams	Dupont single sheet tear tester
Flex life	20,000 cycles	Dupont flex tester at 25 percent
Bend recovery	43 percent	Immediate 180 degree bend recovery
Bend recovery	51 percent	60-second bend recovery
Density	1.39 grams/cc	
Melting point	250-255°C	
Service temperature	-60 to 150°C	Has been used as bladder for cryogenic tankage
Thermal expansion coefficient	15 x 10 <sup>-6</sup> in/in/°F	from 70 to 120°F
Gauge	25 35 50 100 150 200 300 500 700 1000	
Thickness, mils	0.25 0.35 0.5 1.0 1.50 2 3 5 7 10	
Thickness, in.	0.00025 0.00035 0.0005 0.001 0.0015 0.002 0.003 0.005 0.007 0.01	
Area factor, in <sup>2</sup> /lb	80,000 57,150 40,000 20,000 13,300 10,000 6650 4000 2650 2000	

stress in the torus is 8000 psi). Hence, the critical condition is that there will be no wrinkling at the limit load condition when the torus is pressurized to the design pressure.

The torus was analyzed as a ring loaded by the total weight of the unfurled passive kill mechanism. The critical point is at the maximum bending moment position, which is at the support structure joint adjacent to the homing stage. The total maximum compressive stress from this ring analysis, the bending stress plus the end load stress, is plotted against torus wall thickness in Figure 10-5. The intersection of this curve with the tension stress due to pressure gives the point for zero compressive stress and therefore, no wrinkling. The range of values for Poisson's ratio 0.25 to 0.4 covers the probable range for Mylar. Based on the results of Figure 10-5, the next available Mylar film thickness is 0.007 inch which has been used for the torus design. The minimum thickness required for no wrinkling is 0.0062 inch. The torus internal pressure and total unfurlable mechanism weight are given by Figure 10-6. The hoop stress in the torus at the design pressure is plotted in Figure 10-7 and shows the maximum torus stress of 8530 psi. The tensile stress in the membranes for values for Poisson's ratio of 0.4 and 0.25 are 805 psi and 1750 psi, respectively.

When a curved tube is subjected to a bending moment, the initially circular cross section is deformed into an oval configuration. Among the effects of this ovalization is that the stress distribution differs from that computed by the simple beam theory formula,  $\sigma = M_c/I$ , used in the present analysis where the effect of curvature was neglected. The maximum longitudinal stress due to bending can then be expressed as  $\sigma_{\max} = B(M_c/I)$  where the value of B varies from a maximum at zero internal pressure to approximately 1.0 with large internal pressures.

In any extensive analysis of the unfurlable structure these factors should be considered. However, it is felt that such an analysis would not yield values of B greater than 1.22. This is the value which would show a wrinkled condition for the torus at the design load with a torus thickness of 0.007 inch including the B factor on the bending stress component. Further, the initial assumption that the torus carries all the



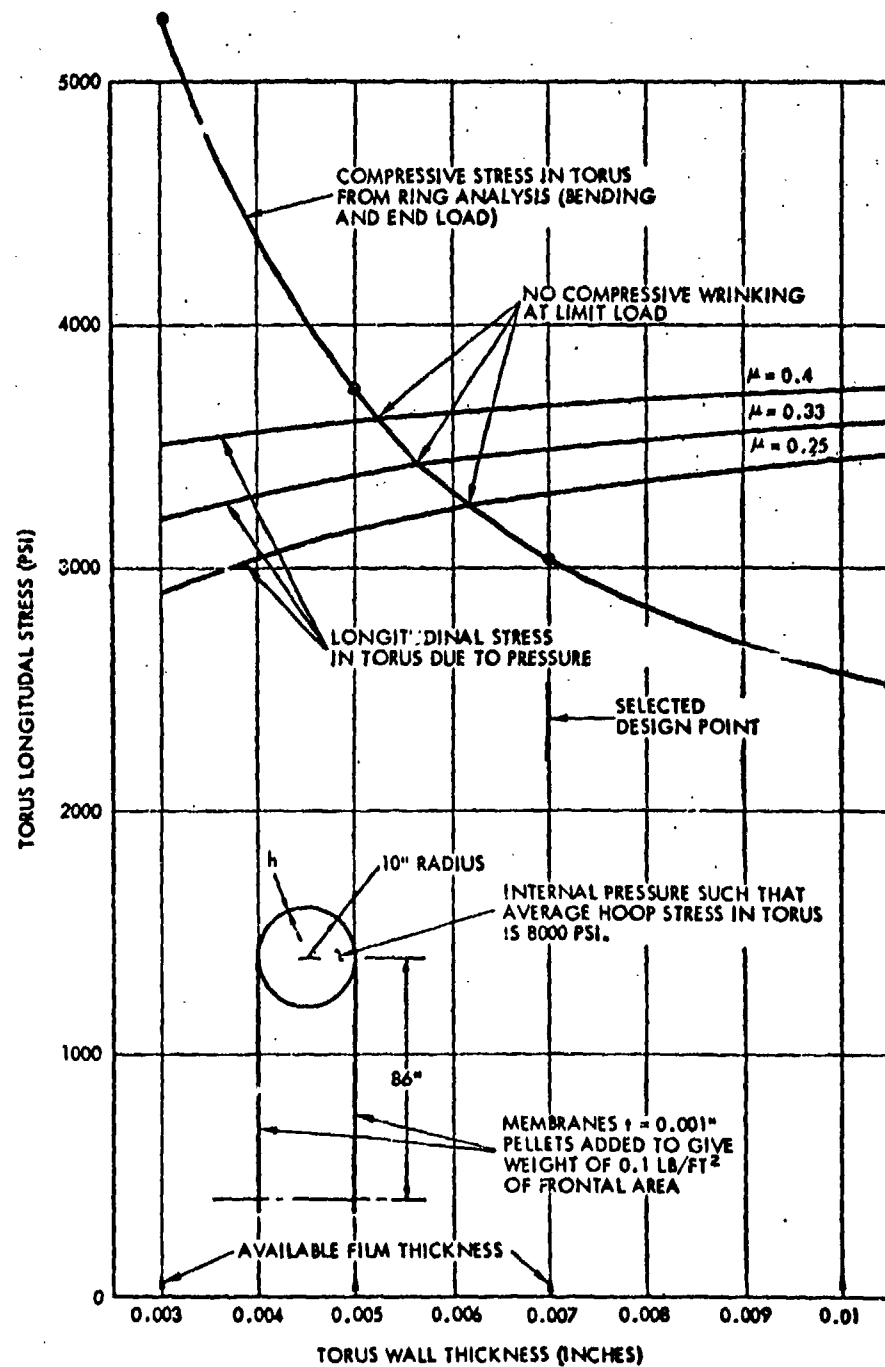


Figure 10-5. Torus Longitudinal Stress Versus Torus Wall Thickness

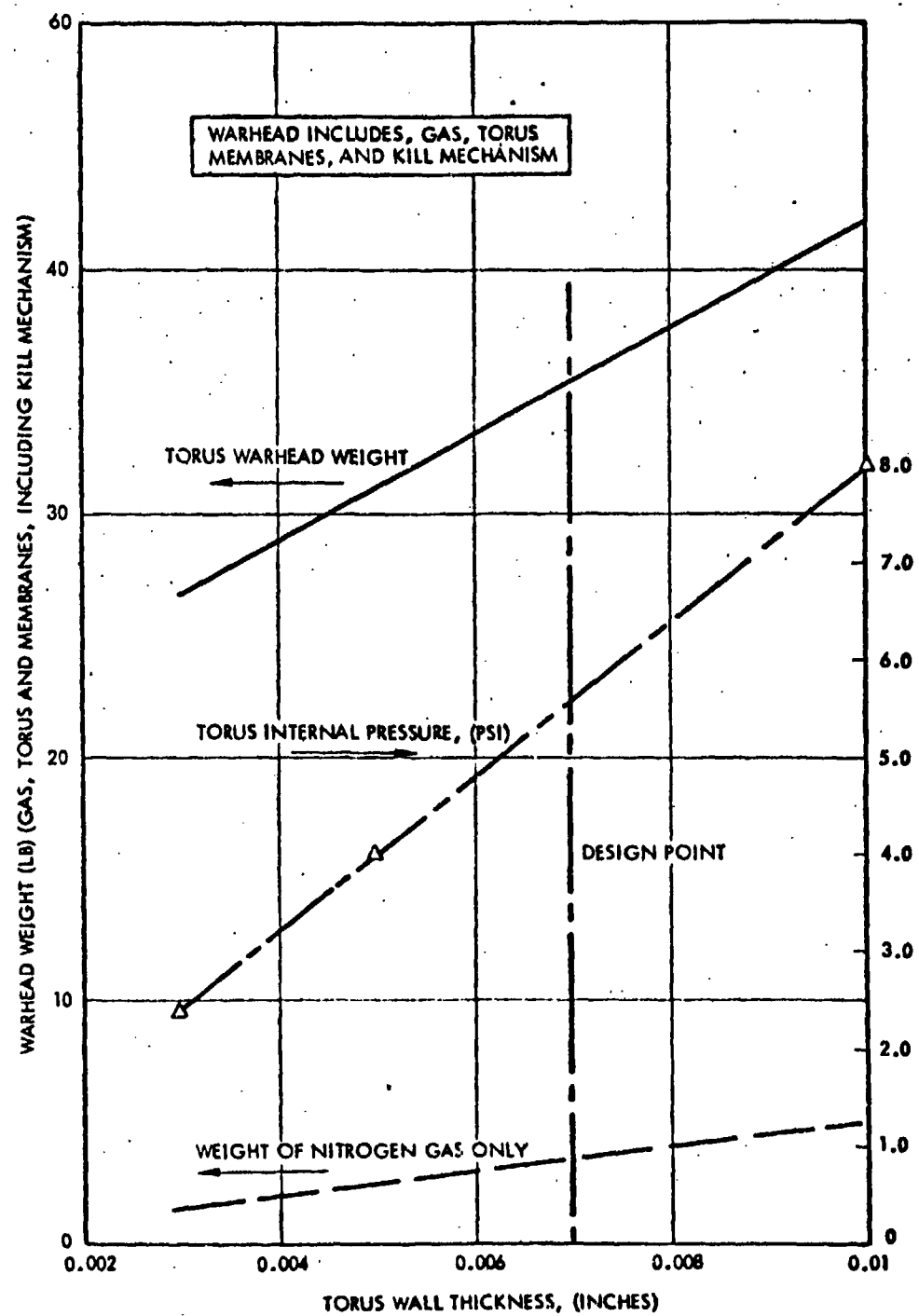


Figure 10-6. Warhead Weight and Torus Pressure Versus Torus Wall Thickness

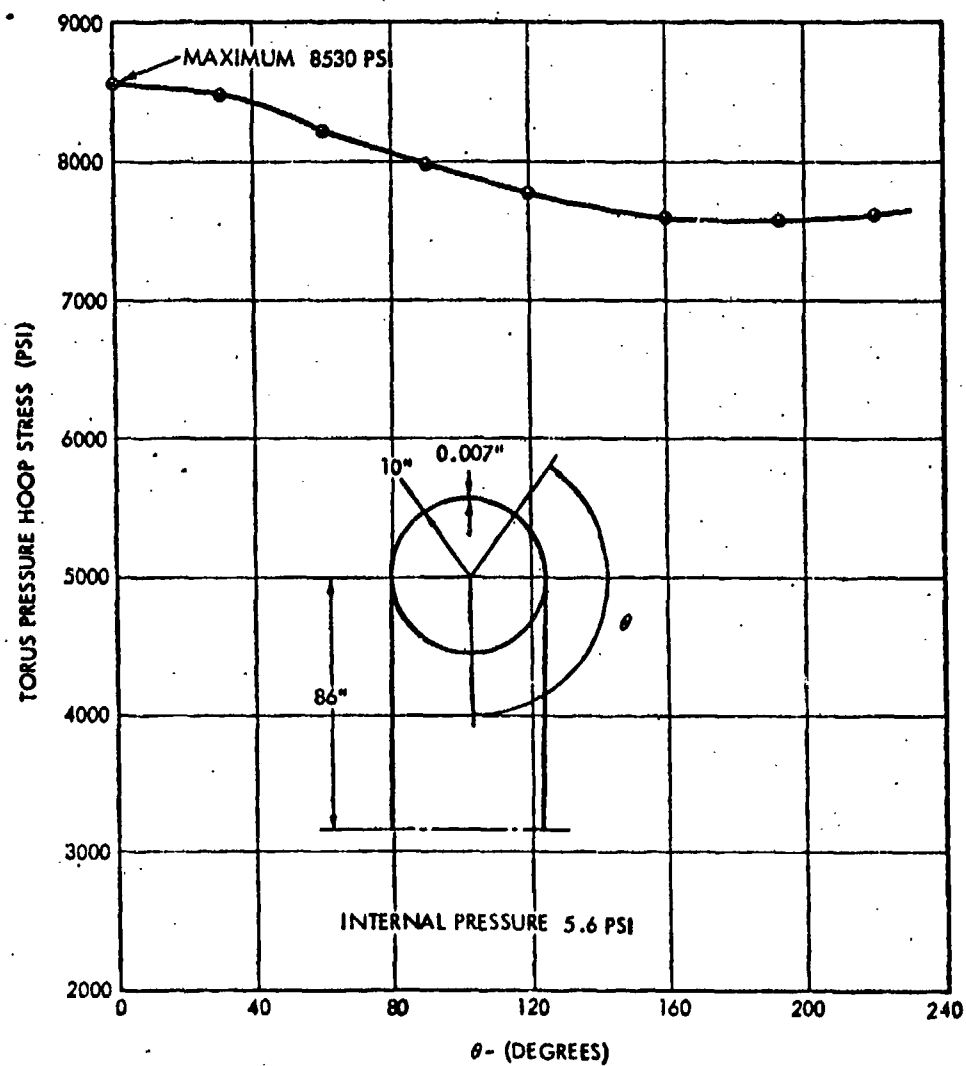


Figure 10-7. Torus Pressure Hoop Stress Versus Position on Torus

weight was conservative as a portion will transfer directly from the membranes to the support structure and then to the homing stage structure.

The 90-grain steel pellets are mounted on the torus circumference and along the intersection of the torus and membrane as well as embedded in the membranes in a rectangular pattern on one foot centers.

#### 10.3.2.1 Side Covers

The two magnesium side covers are cylindrical segments that retain the unfurlable structure (when "packed") and are retained themselves by the top cover. The bottom end has a lip that mates with a groove on the support structure and forms a semicaptive pivot joint. The top end has a lip that mates with an internal groove on the top cover and is retained by it. The inner surface of these covers are coated with emerolon or its equivalent to prevent damage to the unfurlable structure due to flight vibrations.

#### 10.3.2.2 Top Cover

The top cover, also made of magnesium, is a hemispherical dome with eight spring loaded petals attached. The petals are in two diametrically opposite groups of four each. Each group, when stowed against their spring load, forms a cylindrical segment covering the "packed" unfurlable structure and retains one of the side covers. All internal surfaces of the top cover are covered with emerolon or its equivalent to protect the unfurlable structure during flight vibrations.

#### 10.3.3 Retention and Release System

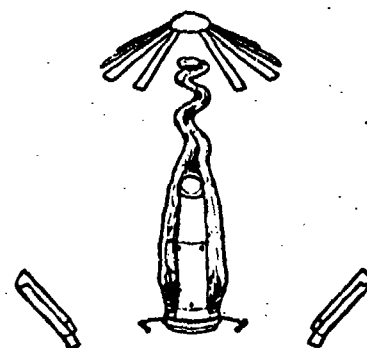
An explosively actuated separation band retains the unfurlable device by being drawn tight in grooves on the external surfaces of the eight petals of the top cover. The explosive actuated device releases the band which in turn releases the outwardly spring loaded petals. Since the petals retain the side covers, the one separation band releases all covers allowing the unfurling process to begin.

#### 10.3.4 "Packing" Procedure

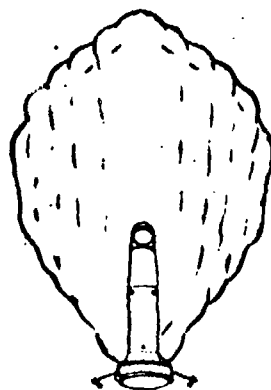
With the unfurlable structure deployed and attached to the support structure, the following procedure can be used to "pack" the unfurlable structure (see Figure 10-4 and Figure 10-8):



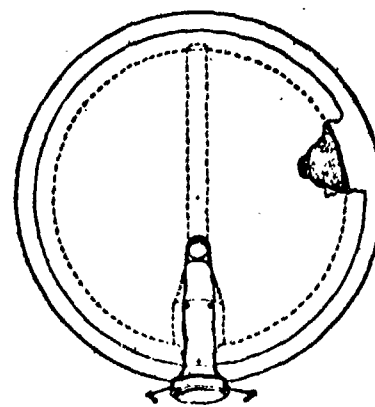
STORED CONDITION



STEP 1



STEP 2



STEP 3

Figure 10-8. Passive Warhead Inflation Procedure

- Use a vacuum pump to evacuate the air from the torus and fill-tube until they are fully collapsed.
- Start an accordian type fold on each side of the unfurlable structure, maintaining the fold line approximately parallel to the centerline of the support structure. The folded width should be approximately 20 inches. This will yield 5-1/2 folds on each side. It is desirable to reverse the folding direction on opposite sides of the assembly (i. e., first fold up on one side, and down on the other).
- With the side folding complete, a center section of approximately 26 inches in width will remain between the two 20-inch wide folded sides. This center section should now be pleated to allow the two sides to come together at the top.
- Start an accordian fold of the folded sides with the new fold line normal to the previous folds, but in the same plane. The fold width should again be 20 inches. Continue folding until the top of the support structure is reached. This should yield 6-1/2 folds. This folded package, 20-inches square, will then be shaped to the contour of the support structure and/or the covers.
- Install the two side covers
- Install the top cover, bring the eight petals into the down position and retain with the separation band
- The unfurlable passive kill mechanism with support structure is now ready for installation on the homing stage.

#### 10.3.5 Deployment Sequence

After third stage separation and the deployment of the roll control engines, the kill mechanism is ready to deploy. The following procedure accomplishes deployment (see Figure 10-4 and Figure 10-8):

- Actuate the separation band. This allows the band to separate and the spring loaded petals of the top cover to swing open. This action removes the top cover and releases the two side covers which fall outward. The unfurlable structure is now ready for inflation.
- Start pressurizing the fill tube. This unfolds the top accordian folds and unfurls the structure forward.
- Start pressurizing the torus at the support structure. This flow, along with flow from the fill tube, unfurls the two side accordian folds.

- Relief valves will maintain this pressure to intercept. Pressurizing continues until 5.6 psi is reached in the torus and fill tube which pulls the membranes into correct position. The total elapsed time from separation of the covers to full pressurization is estimated to be 20 seconds, based on experience with the Echo satellite series.

#### 10.4 FUZE

As mentioned in the previous discussion, relatively soft targets, such as current U.S. satellite designs, can be destroyed by body fixed (i.e., nondeployed) warheads. Such warheads can be implemented by means of balloon structures, or by any other technique which effectively increases the homing stage cross section. To the extent that such warheads provide the required lethality, they are attractive for two reasons; a) they are light, and b) they do not require fuzing. It needs to be added, however, that STL studies indicate that configurational constraints limit body fixed warhead radii to 8 feet or less. Since this radius must correspond to 2 to 3 $\sigma$  values of the terminal miss, it follows that body fixed warheads are effective only in situations where the terminal rms miss is of the order of 3 feet or less. Such miss performance can be achieved only with low noise electro optical tracking sensors. It therefore appears that a homing stage which operates with electro-optical sensing against a soft target might make use of a body fixed warhead, and in this case no fuze is required.

Unfortunately, one cannot depend upon the existence of only soft targets. Against armored targets of the kind postulated by Battelle, metallic fragments must be deployed, thus introducing a fuzing problem. First consideration was given to range fuzing based upon radar derived range information. The range at which fuzing and warhead deployment takes place is entirely a function of the expected miss and the velocity with which pellets are deployed with respect to the interceptor. Two cases can be considered. In the first case, the separation velocity is applied entirely in a plane normal to the line-of-sight. With explosive pellet deployment, which is deemed much more reliable than a mechanical deployment technique, typical separation velocities of the outermost pellets are 2000 ft/sec. Such a warhead therefore gives rise to a pellet cloud whose radius grows at a rate of 2000 ft/sec.

In the time interval between explosive deployment and the instant when the target penetrates the warhead plane, the pellet cloud should grow to a radius equal to about the 3 $\sigma$  terminal miss. With a 1 $\sigma$  miss of 10 feet (typical for radar sensing stages) the radius must therefore be 30 feet and the warhead should therefore be fuzed at 0.015 second to go. That time to go value corresponds to a fuzing range of 300 feet if the relative velocity,  $V_R$ , is 20,000 ft/sec and 150 feet if  $V_R$  is 10,000 ft/sec.

The radar fuze could be simply implemented by merely noting the time at which an a priori chosen range, say 0.5 n mi, is passed. The measurement could start a clock, with the warhead being deployed at a preset time instead passing the 0.5 n mi range value. In that case the the fuzing range  $R_f$  is

$$R_f = R_o - V_R t$$

where

$$R_o = 0.5 \text{ n mi}$$

$$V_R = \text{relative velocity}$$

$$t = \text{time between 1/2 mile range and deployment.}$$

Differentiating,

$$\Delta R_f = \Delta R_o - V_R \Delta t - t \Delta V_R$$

With a 1 percent range accuracy, a 1 millisecond timing accuracy, and assuming a knowledge of  $V_R$  to 1 percent of its actual value, the rms error in fuzing range is approximately 50 feet. Note that this error in fuzing range would, at most, require one to deploy the warhead slightly earlier, and let it grow to a radius slightly larger than 30 feet against the nominal target. In short, the fuzing error can be compensated by a slight increase in warhead weight. In this case, the deployment velocity is added normal to  $V_R$  with the result that the relative velocity between pellets and targets is very nearly the same as the  $V_R$  value of the homing stage with respect to the target.

An alternate approach to warhead design and deployment consists of explosively deploying the pellets in a fairly narrow cone centered about the



$V_R$  vector. In this case the deployment velocity is again 2000 ft/sec but with a 6 degree cone half angle, only 200 ft/sec cause growth of the pellet cloud, and now typical fuzing times are about 0.15 seconds-to-go, which correspond to ranges of 1500 and 3000 ft for  $V_R$ 's of 10,000 and 20,000 ft/sec respectively. With a range marker at 1 n mi and making the same conservative assumptions relative to errors, the rms fuzing range error is about 100 feet, insignificant compared to the fuzing range.

The design of pellet warheads which are deployed in fairly narrow cones was studied by Aerojet-General under subcontract to STL as part of the BAMBI study. This approach was found to be feasible and, in fact, successful test firings of models were conducted. This approach appears more attractive than deployment normal to  $V_R$  for two reasons. First, by fuzing at a longer time to go, the fuzing error becomes insignificant. Second, and perhaps more important, most of the 2000 ft/sec deployment velocity is applied along  $V_R$ , with the result that the relative velocity between pellets and target is 2000 ft/sec higher than that of the homing stage. In summary, a simple radar fuzing scheme appears entirely feasible and requires merely a radar fuze which is capable of generating one accurate range marker at a range of about 1 n mi.

Late in the SIS study program, interest was expressed in kinematic line-of-sight rate fuzing. This topic was studied by STL in considerable detail as part of the BAMBI study, and a comprehensive summary of these findings is available in the STL BAMBI Final Report (Reference 1). While no effort is made to repeat the details of this presentation here, the following summary may be of interest.

There can be little question that a successful fuze can be built by deriving a fuzing signal when the measured rate of rotation of the line-of-sight,  $W_{LS}$ , exceeds a previously chosen threshold. A number of significant points need to be emphasized however.

Note first that the growth of  $W_{LS}$  at low times-to-go is a very strong function of the terminal miss. For low misses,  $W_{LS}$  remains almost constant until, at a very small range, it rises extremely rapidly, implying a high line-of-sight rate acceleration. The fuzing signal can only be derived from measured values of  $W_{LS}$  and these measurements will inevitably

reflect bandwidth limitations in the angular tracking loops. The net result is the strong possibility that the kinematic fuze will not operate properly with a small terminal miss, 2 feet or less.

This problem may be somewhat aggravated by sensor blind range performance. The problem here has to do with the minimum range to which an angle tracking sensor can operate. If the sensor ceases to angle track before  $W_{LS}$  has built up to the fuzing threshold, the warhead may not deploy. In short, the kinematic fuze is beset by problems if the terminal miss is small.

It can be argued with considerable justification that if the miss is that small, there is an excellent chance that some portion of the homing stage may physically collide with the target, in which case the question of whether the warhead has or has not been deployed becomes highly academic.

Another point may be of interest, and it concerns selection of the fuzing threshold level. The first question in this area must inquire into the minimum fuzing threshold level, and that level is dictated by the angle tracking noise level. If that threshold is set too low, the fuze may be activated prematurely by a noise peak rather than the kinematic growth of  $W_{LS}$ . It follows that for radar derived  $W_{LS}$  values the minimum fuzing threshold must be higher than for a lower noise electro-optical tracker. This consideration generally places the minimum fuzing threshold near 10 mr/sec. That level can be made higher, of course, but now one must be concerned with the following error (i. e. bandwidth limitations) of the angular rate measuring system. Generally speaking, it appears that in the SIS application, optimum fuzing thresholds lie between 20 and 30 mr/sec. A thorough quantitative treatment of this topic is presented in Reference 1.

#### REFERENCES

1. "Final Technical Summary Report, BAMBI Phase II Technical Investigations, Single Interceptor Satellite (U)," 8637-609D-RL000, Space Technology Laboratories, Inc., 2 November 1962 (S), Vol II, Chapter 18.
2. "Second Interim Report on Antisatellite Support Study," Battelle Memorial Inst, 16 August 1963.
3. "Second Interim Progress Report Satellite Interception System Feasibility Study (U)," 8424-6007-RS000, Space Technology Laboratories, Inc., 15 August 1963.

## CHAPTER 11

### HOMING STAGE CONFIGURATION

#### 11.1 INTRODUCTION AND SUMMARY

This chapter presents a summary of homing stage design studies carried out during the SIS program. Historically, the first two months of the program were concerned with studies of gross size and weight of the major subsystems which, in combination, constitute the homing stage. By the beginning of the third program month, enough preliminary information had been generated to allow initiation of fairly detailed configurational design studies of various homing stages.

In view of the highly parameterized nature of the SIS study program, one is concerned with many conceptual homing stage designs, where one design represents each combination of parameters. Note that three sensor techniques, all found feasible, were explored. Ephemeris errors were quantized by the ARPA Program Guide into three sets. The kill effectiveness of hypervelocity pellets was parameterized over a wide range, depending upon target hardness, etc.

In order to gain maximum utility from the effort and time available, it was decided to select particular parameter combinations and to design the resulting homing stage configurations in some detail. Information relating to other stages can then be obtained by extrapolation or interpretation. The foregoing decision reflects the feeling that more useful information results from designing a few configurations in some depth, than from designing many configurations superficially.

For design purposes, it was decided to concentrate on Set 2 ephemeris errors. This choice was made for two reasons. First, it was the median set (i.e., it was neither the most optimistic nor the most pessimistic set of values), and second, STL studies indicate that, with available improvements, SPADETS can achieve that accuracy in the near future. It should therefore be kept in mind that substantially all of the information presented in this chapter refers to homing stages which are sized for Set 2 ephemeris errors.

Three homing stage sensor techniques were explored—active radar, sunlight reflection sensing, and passive infrared sensing. As is discussed in Chapters 4, 5, and 6 of this report, all of these sensing approaches appear feasible, subject to the availability of suitable infrared detector arrays and detector cooling techniques. From a configurational design point-of-view the sunlight reflection tracker and the infrared tracker are so similar with respect to size and weight of the subsystem package that the resulting homing stage designs would be so similar to each other that separate design efforts did not seem warranted. The ensuing discussion will therefore be concerned with a radar sensing stage, and an electro-optical sensing stage, where information relating to the latter is applicable to either sunlight sensing or infrared sensing stages.

Finally, a design ground rule had to be adopted with respect to the required warhead. Generally, two kinds of warheads were considered: body fixed, nonfuzed plate slap warheads, and fuzed pellet warheads. Configurational studies indicate that body fixed warheads are confined to radii near 8 feet, suggesting that this warhead approach is suited only to homing stages which achieve low terminal miss values (of the order to 3 feet or less). Since such miss performance can be achieved, if at all, only by a homing stage equipped with an extremely low noise level tracker, the plate slap warhead concept was explored in context with the electro-optical sensing homing stage, the resulting stage design is summarized in Figure 11-1.

The deployed pellet warhead approach is suitable to situations where the rms terminal miss exceeds 3 feet, as is the case with the radar sensing homing stage which achieves an rms miss of 8 to 10 feet. For this reason, the radar sensing stage design included a fuzed and deployed pellet warhead.

As is discussed in Chapter 10, the size of plate slap warhead, or the size of the deployed pellet cloud at the instant of target kill, is a function of the attack geometry, and most important, it is a function of the expected miss. The composition of the warhead (i.e., how many pellets and what individual pellet mass) is a function of target size and target hardness. The target size assumptions made correspond to the data included in the ARPA Program Guide.

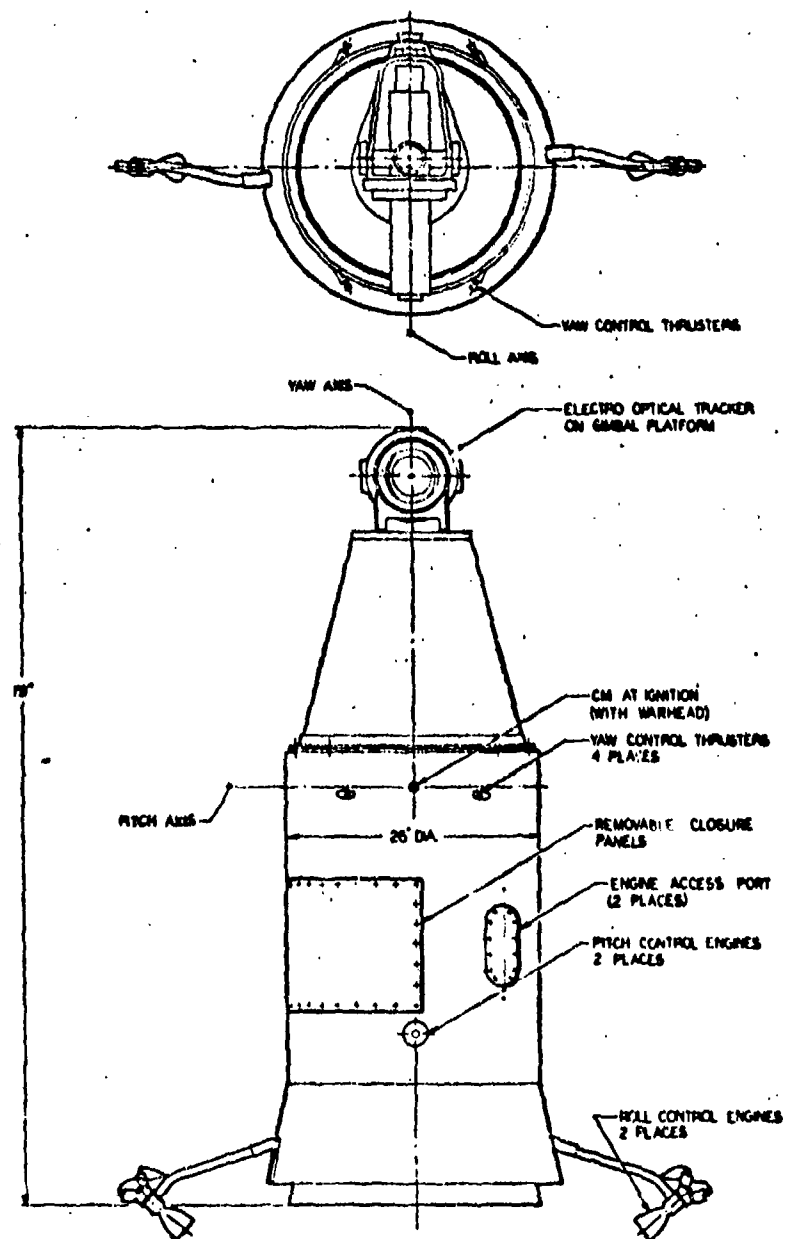


Figure 11-1. Outboard Profile of Homing Stage With Electro-optical Tracker

The bulk of the radar sensing configurational design effort centered around a pellet warhead weighing 66 pounds. This warhead consisted of 6 g metallic pellets deployed explosively in a conical shape, as discussed in Chapter 10. A 6 g pellet impacting at relative velocities ranging from 10,000 to 22,000 ft/sec is lethal against all but extremely hard targets. Much lighter pellets would be lethal against current U.S. satellite designs. Indeed, some data suggest that 6 g pellets impacting at such velocities are lethal against current U.S. re-entry vehicles. Thus, the 66 pound pellet warhead appears adequate against all but the hardest targets. The resulting stage design is summarized in Figure 11-2.

Late in the SIS study emphasis shifted to heavily armored target vehicles which require pellet masses as high as 100 g to achieve kill. Corresponding warhead weights for radar sensing homing stages rise to about 250 pounds. Information presented near the end of this chapter and pertaining to a radar sensing homing stage with a 250 pound warhead was obtained by extrapolation from the radar stage design with a 66 pound pellet warhead.

In summary, the electro-optical homing stage with plate slap warhead is estimated to weight 597.4 pounds. The radar sensing stage with a 66 pound pellet warhead is estimated to weight 961 pounds. The radar sensing stage with a 250 pound pellet warhead is estimated to weight 1290 pounds. All of the foregoing estimates apply to stages designed to cope with Set 2 ephemeris errors.

The utilization of any of the above mentioned homing stages requires the use of a suitable fairing to protect the homing stage during the powered flight portion of the boost trajectory. The requirements placed upon this fairing are a function of the ascent trajectory and become fairly severe when one wishes to fly a very depressed trajectory to achieve maximum lateral reach against low altitude targets. A preliminary design study of such a fairing and the adapter was carried out for a Minuteman boost vehicle. This study is summarized in Section 11.5 of this chapter where it is shown that the fairing weight is estimated at 217 pounds. It should be kept in mind that this fairing weight is payload to the boost vehicle, no less so than the homing stage itself.

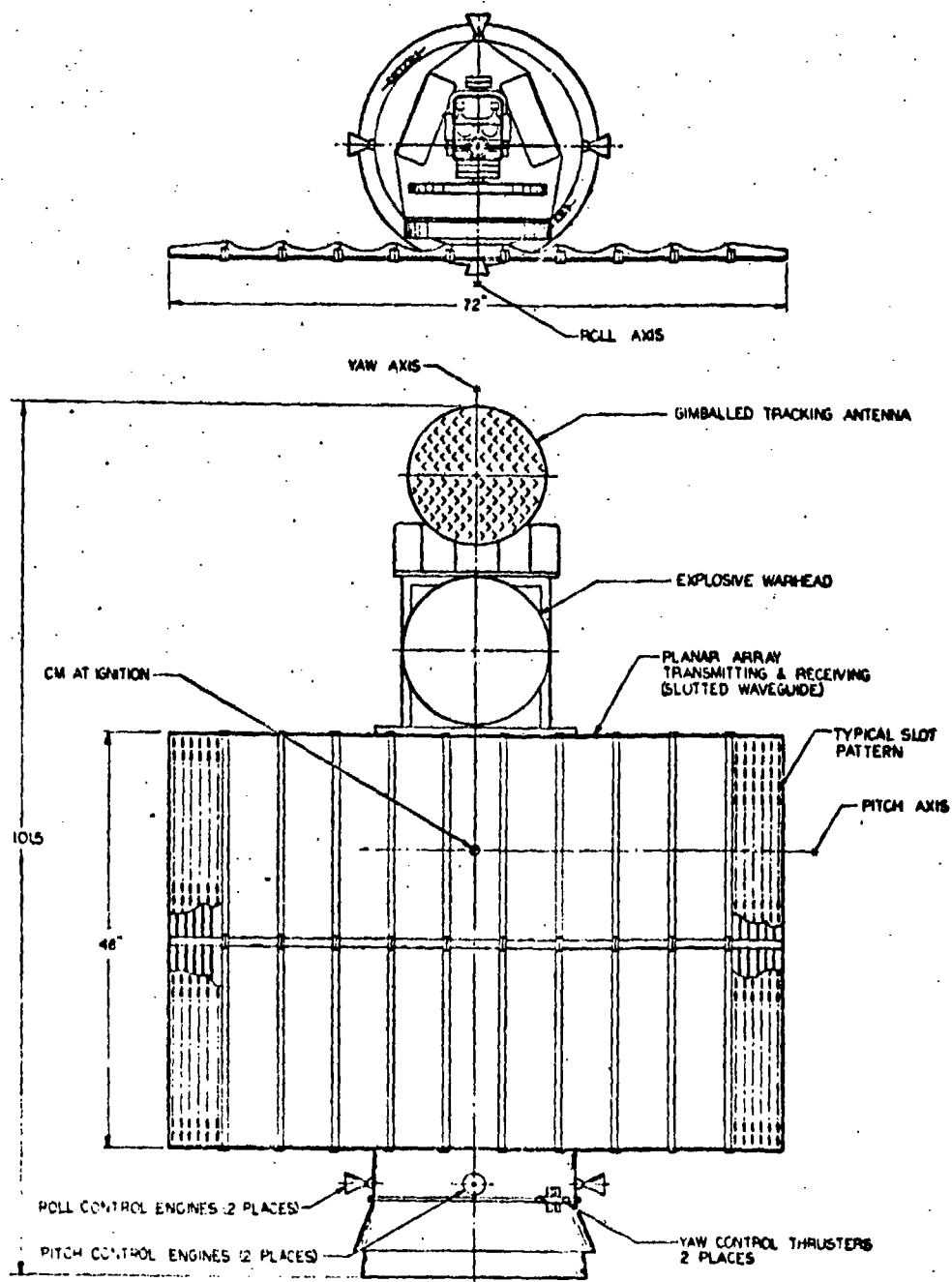


Figure 11-2. Outboard Profile of Homing Stage With Radar Tracker



Effort was expended to investigate the structural compatibility between the various homing stage designs and the boost vehicles considered. With respect to Polaris, this effort was hampered by the lack of sufficient information. With respect to Minuteman, the following facts emerged. No significant difficulties arise from increase in pure payload weights. Were one able to package a 1500 pound payload into the present re-entry vehicle (R/V) envelope, no significant Minuteman structural modifications would be necessary.

Unfortunately, it is not possible to package the homing stage into precisely the present R/V envelope. As a result, the fairing would not conform to the present R/V contour. As shown in this chapter, homing stage fairings are shorter but maintain maximum diameter longer than is the case for the weapon system R/V. To the extent that problems can be expected, they will occur as a result of shifts in the center of pressure, since such shifts can create structural problems due to aerodynamics which arise when peak side winds induce angle of attack at conditions of maximum  $q$ . In short, structural problems come about due to aerodynamics and not due to pure payload weight increases.

Study indicates that no severe problems are to be expected with either the electro-optical stage or the radar stage with a 66 pound pellet warhead. When one gets to the 1300 pound stage, however (radar and 250 pound warhead), the fairing must be elongated by about 14 inches and now structural problems can be expected. These problems would require strengthening of the guidance and control compartment and strengthening of the upper end of the third stage. Of these two modifications, the first is easily achieved, but the second is not and conceivably could require a fairly comprehensive Stage 3 redesign.

It is probably obvious that no structural problems exist in connection with Titan II. On the contrary, certain guidance changes would be required because even a 1500 pound payload is too low for the Titan II boost vehicle.

## 11.2 GENERAL VEHICLE CONSIDERATIONS

The homing stage concepts that appear in this report are vehicles tailored and sized to satisfy the satellite intercept mission requirements with Set 2 ephemeris errors. The proposed guidance technique, bias

proportional navigation, is best satisfied by the use of a variable thrust engine which can introduce thrust in any commanded direction normal to the tracker line-of-sight (LOS). To accomplish this with a single engine, the vehicle is equipped with a reaction control subsystem capable of rolling the vehicle around the nominal LOS to properly position the engine thrust vector. The tracker is gimbal mounted with full freedom in roll and limited freedom in pitch and yaw.

Two widely differing acquisition and tracking techniques were selected: an electro-optical system and a radar system. The electro-optical system utilizes an orthicon camera with simple optics mounted on a gimbaled platform which is designed to measure target tracking angular rates, from which desired thrust magnitude and direction are computed. The radar vehicle utilizes two antennas, a large planar array for target acquisition, subsequent target illumination and a small gimbaled dish for angle tracking. The two tracking systems require different vehicle configurations because of a wide variation in payload weight, and subsystem requirements, such as the unfurlable radar antenna.

Of the two warhead concepts investigated and reported in Chapter 10, the passive device was deemed appropriate to the smaller electro-optical homing stage which achieves lower miss and where warhead stowage space was available. The densely-packed (66 pounds) explosive warhead was appropriate to the larger radar equipped homing stage which is surrounded by an unfurlable planar array antenna. In the stowed position, this antenna uses the space occupied by the passive warhead on the other vehicle. The explosive warhead could easily be adapted to the electro-optical vehicle but considerable difficulties would arise from a passive warhead/radar tracker combination.

The homing stage was primarily shaped to fit on Wing II or Wing IV Minuteman. A fairing and adapter section were designed to complete the interface definition. With modifications, these vehicles could be adapted to other boosters such as the Polaris A-2 or A-3. Although the Polaris A-3 length constraint (Reference 1) was exceeded to satisfy the passive warhead stowage requirements, this constraint could be satisfied by a somewhat modified electro-optical vehicle equipped with an internally mounted explosive warhead, such as proposed for use on the radar equipped vehicle. The payloads, could easily be adapted to the Titan II.

The selected fairing shape is a cylinder-cone hemisphere with its maximum diameter matching the upper end of the Minuteman Guidance and Control Section. Overall fairing length of 119 inches is well within the constraints set forth in the Boeing Booster Symposium document (Reference 1). A preliminary load analysis, based on the proposed fairing shape subjected to the most severe trajectory, shows that the maximum permissible weapons systems Minuteman loads are not exceeded thereby precluding the need for any major Minuteman structural modifications. A 7-inch long range safety equipment section between the payload and Minuteman Guidance and Control Section was also accounted for in the loads analysis. The foregoing statement refers to the electro-optical stage and the radar stage with a 66 pound pellet warhead.

#### 11.2.1 Performance Requirements

Vehicle acceleration and  $\Delta V$  requirements are mostly determined by the selected guidance technique, stage optimization and target ephemeris errors. Implementation of the electro-optical guidance technique is accomplished by means of an orthicon camera or a radar target tracking device resulting in two basically different vehicle configurations because of differences in payload weight and payload requirements. Also, the vehicles optimized at slightly different  $\Delta V$  and thrust to weights ratios. Engine throttling requirements, however, are the same for both vehicles. The following criteria formed the basis for these designs:

	<u>Electro-Optical</u>	<u>Radar</u>
$\Delta V$ (ft/sec)	4000	3250
$F/W_G$ (lb/lb)	6	4
$W_{PL}$ (lb)	160	400
Engine throttling range	10/1	10/1
Warhead type	Passive	Explosive

Since both vehicles utilized the same basic guidance technique they both required roll-to-control capability. This maneuver may be commanded and needs to be accomplished with the main engine off.

Also, since the vehicle requires attitude control during main engine off operation, an attitude control system is required. In general, greater guidance accuracy is expected with the electro-optical tracker subsystem resulting in reduced miss at intercept. For this reason, the passive kill mechanism which is size limited was associated with this vehicle. Since it was desired to also investigate an explosive warhead, it was utilized on the radar equipped vehicle, which requires a larger fragment pattern at intercept because of larger miss distances.

#### 11.2.2 Parametric Weight Analysis

A versatile tool for vehicle sizing and performance analysis is a parametric weight analysis. Such an analysis can be initiated with a minimum of vehicle design criteria, such as approximate payload weight range, estimated vehicle  $\Delta V$  and acceleration requirements, engine type, propellant tank shape and any vehicle shape or size constraints. The results of earlier vehicle subsystem designs provide a background of parametric data which is used to size the new vehicle. Upon completion of vehicle design layouts, a refined physical properties study can then be conducted.

Such a parametric study was undertaken for the homing stage in question to establish approximate payload capability. The following range of design parameters was assumed:

Vehicle Gross Weight	500 to 4000 lb
Thrust to Weight Ratio	5 to 10
Ideal Velocity Capability	1000 to 11,000 ft/sec
Chamber Pressure	100 to 1400 psia
Engine Exit Diameter	28 inches
Propellant Tank Shape	Spherical

Subsystem weight and performance relationships used for this study are shown in Figures 11-3 to 11-10, and were obtained from Reference 2 and 3.

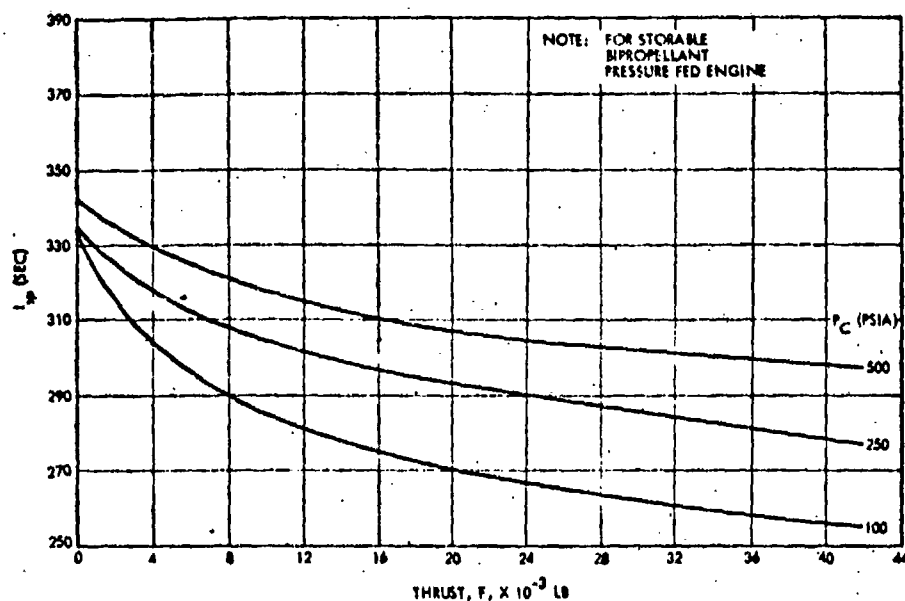


Figure 11-3.  $I_{sp}$  Versus  $F$  and  $P_c$  for  $P_c = 100$  to 500 psia

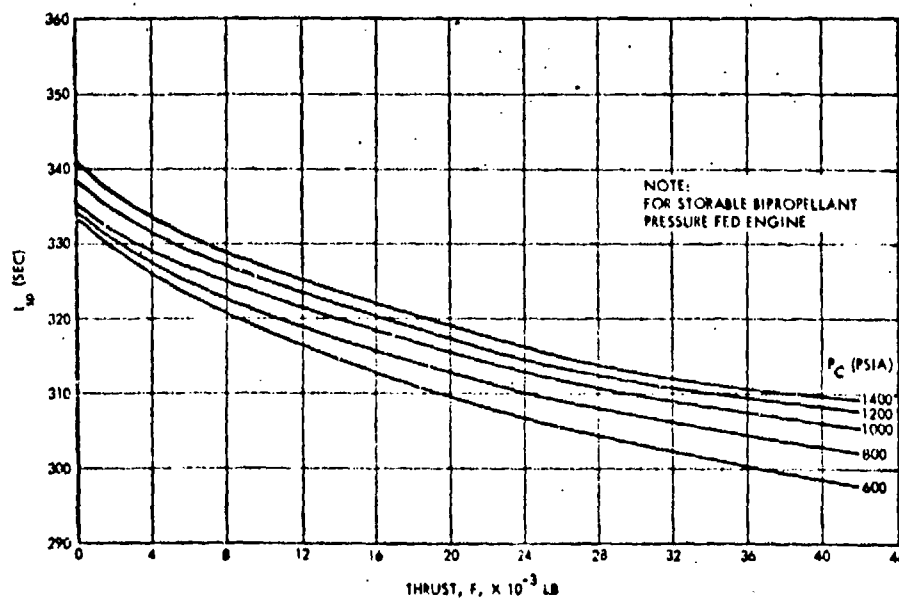


Figure 11-4.  $I_{sp}$  Versus  $F$  and  $P_c$  for  $P_c = 600$  to 1400 psia

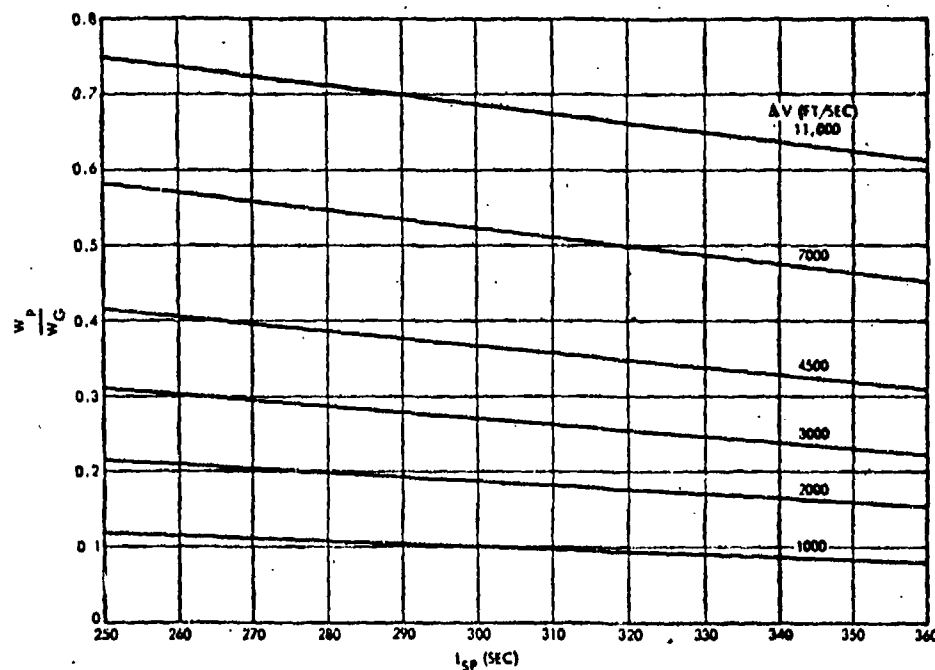


Figure 11-5.  $W_P/W_G$  Versus  $I_{SP}$  and  $\Delta V$

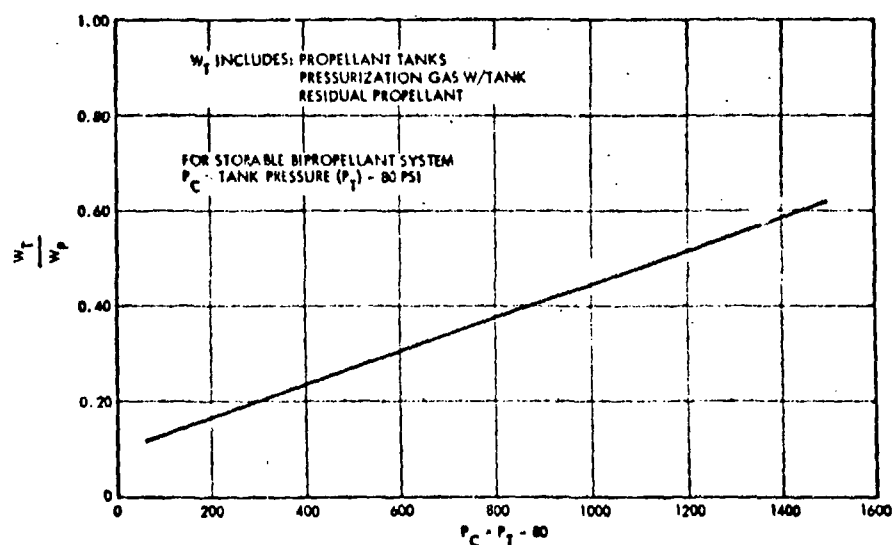


Figure 11-6.  $W_T/W_G$  Versus  $P_C$

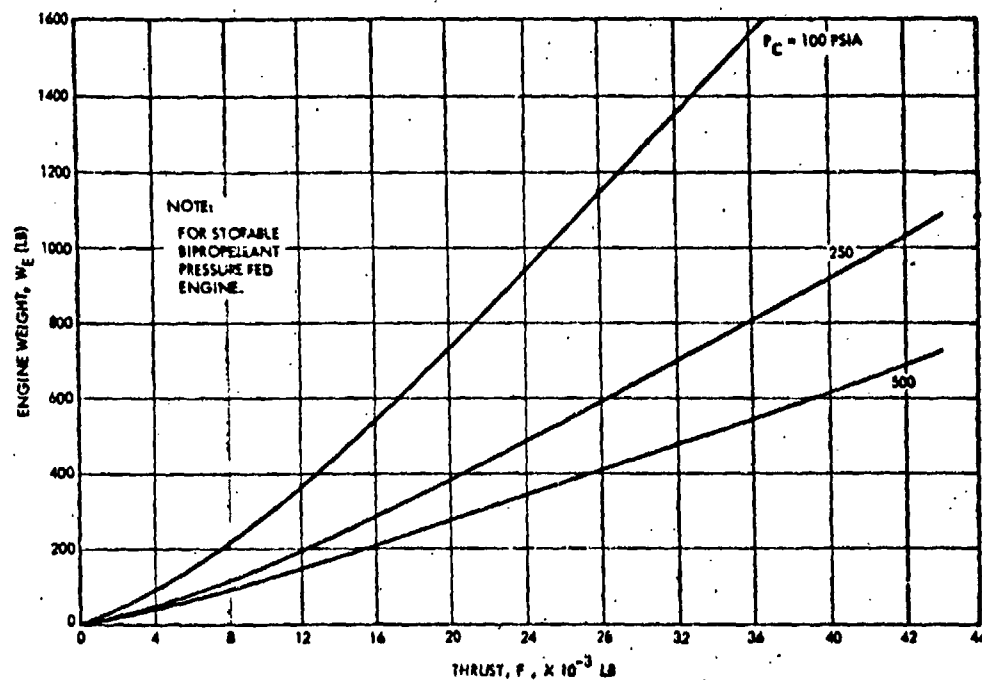


Figure 11-7.  $W_E$  Versus  $F$  and  $P_C$  for  $P_C = 100$  to 500 psia

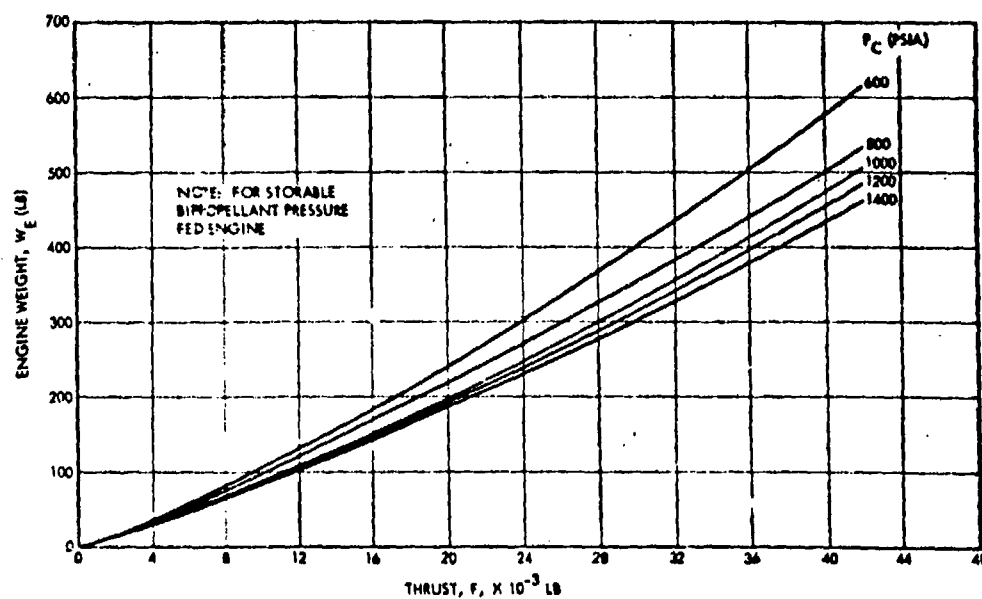


Figure 11-8.  $W_E$  Versus  $F$  and  $P_C$  for  $P_C = 600$  to 1400 psia

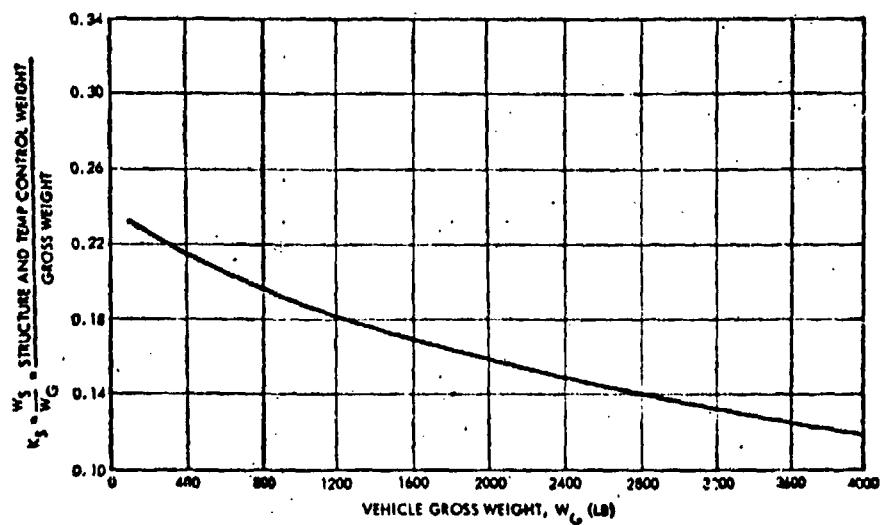


Figure 11-9.  $W_S/W_G$  Versus  $W_G$

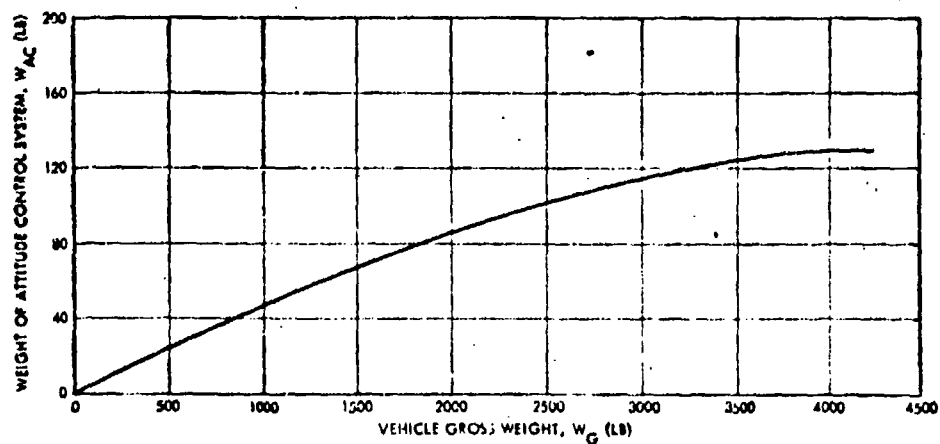


Figure 11-10.  $W_{AC}$  Versus  $W_G$



Payload ( $W_{PL}$ ) is defined as that weight remaining for a given gross weight, after accounting for the weight of structure, propellant, tankage, engine, and attitude control subsystem (less electronics). Other nomenclature is as follows:

Nomenclature

$W_G$	= Vehicle gross weight	lb
$W_{PL}$	= Payload weight	lb
$W_P$	= Propellant weight	lb
$W_T$	= Tankage, pressurization, residual propellant weight	lb
$W_E$	= Engine weight	lb
$W_S$	= Structure and temperature control weight	lb
$W_{AC}$	= Attitude control subsystem weight (less electronics)	lb
$\Delta V$	= Ideal velocity capability	ft/sec
$F$	= Thrust	lb
$I_{SP}$	= Specific impulse	sec
$D_e$	= Engine exit diameter	Inch
$P_C$	= Chamber pressure	psia
$P_T$	= Propellant tank pressure	psia

To illustrate the usefulness of this analysis, an example starting with payload weight derivation for a given set of design criteria follows:

$$\begin{aligned}
 W_G &= 1000 \text{ lb} \\
 \Delta V &= 3000 \text{ ft/sec} \\
 F/W_G &= 7 \\
 P_C &= 400 \text{ psia}
 \end{aligned}$$

### Payload Weight Derivation

From Figure 11-3 at  $F = 7000$  and  $P_C = 400$

$$I_{SP} = 318$$

From Figure 11-5 at  $V = 3000$  and  $I_{SP} = 318$

$$\frac{W_P}{W_G} = 0.257$$

$$W_P = 0.257 \times 1000 = 257$$

From Figure 11-6 at  $P_C = 400$

$$\frac{W_T}{W_P} = 0.235$$

$$W_T = 0.235 \times 257 = 60$$

From Figure 11-7 at  $F = 7000$  and  $P_C = 400$

$$W_E = 80$$

From Figure 11-9 at  $W_G = 1000$

$$\frac{W_S}{W_G} = 0.188$$

$$W_S = 0.188 \times 1000 = 188$$

From Figure 11-10 at  $W_G = 1000$

$$W_{AC} = 46$$

$$\begin{aligned} W_{PL} &= W_G - W_P - W_T - W_E - W_S - W_{AC} \\ &= 1000 - 257 - 60 - 80 - 188 - 46 = 369 \text{ lb} \end{aligned}$$

Chamber pressure optimizations resulted from plotting payload weight ( $W_{PL}$ ) versus chamber pressure ( $P_C$ ) and gross weight ( $W_G$ ) for various combinations of vehicle design criteria as shown in Figures 11-11 through 11-22. Figure 11-15 indicates that the chamber pressure of 400 psia is optimum for the above derived example payload weight of 369 pounds. Exchange ratios showing the effect on payload of designing for other than

optimum chamber pressure are given in Figures 11-23 and 11-24. For the above example, Figure 11-24 shows that only 0.06 pound of payload loss per psia increase will be incurred if it is desired to design to a higher chamber pressure to, say, reduce engine envelope requirements.

Payload weight ( $W_{PL}$ ) versus thrust to weight ratios ( $F/W_G$ ) for optimum chamber pressures are shown in Figures 11-25 through 11-28. Similar cross plots of  $W_{PL}$  versus  $W_G$  and  $W_{PL}$  versus  $\Delta V$  appear in Figures 11-29 through 11-36.

Results obtained from the parametric weight analysis served as a basis for vehicle sizing and system optimization.

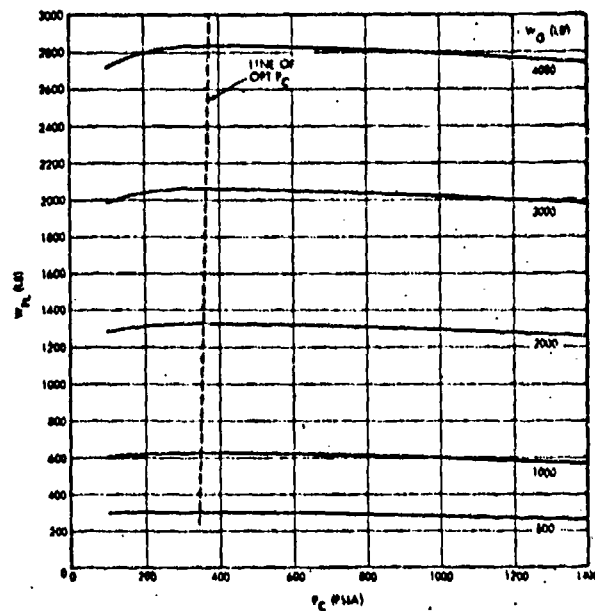


Figure 11-11.  $W_{PL}$  Versus  $P_C$  and  $W_G$  for  $F/W_G = 2$  and  $\Delta V = 1000$

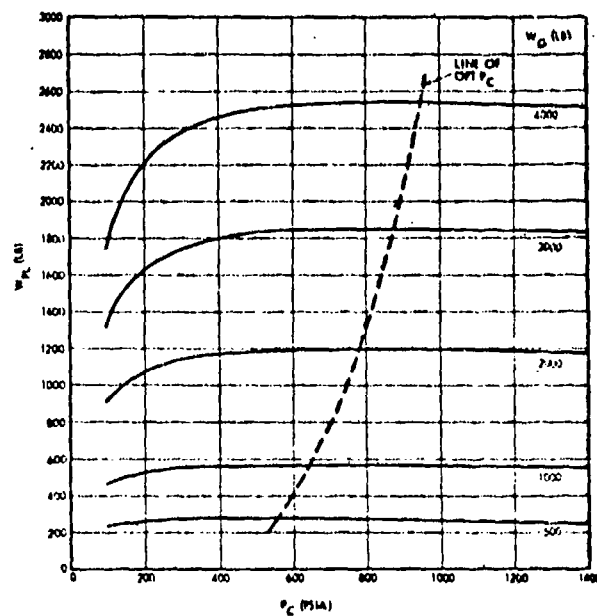


Figure 11-12.  $W_{PL}$  Versus  $P_C$  and  $W_G$  for  $F/W_G = 7$  and  $\Delta V = 1000$

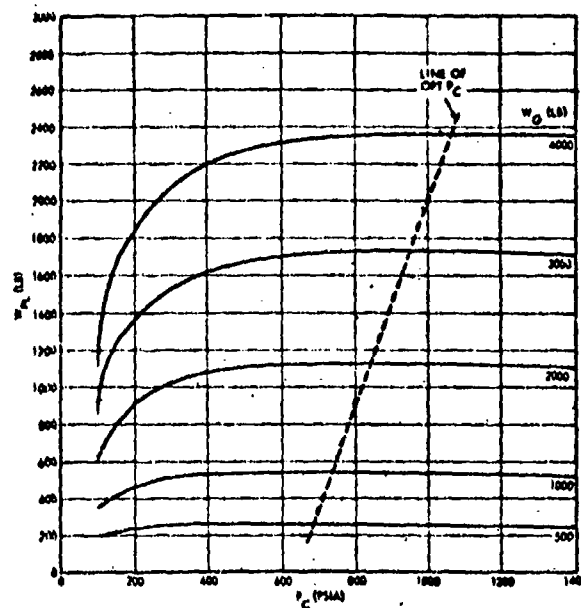


Figure 11-13.  $W_{PL}$  Versus  $P_C$  and  $W_G$  for  $F/W_G = 10$  and  $\Delta V = 1000$

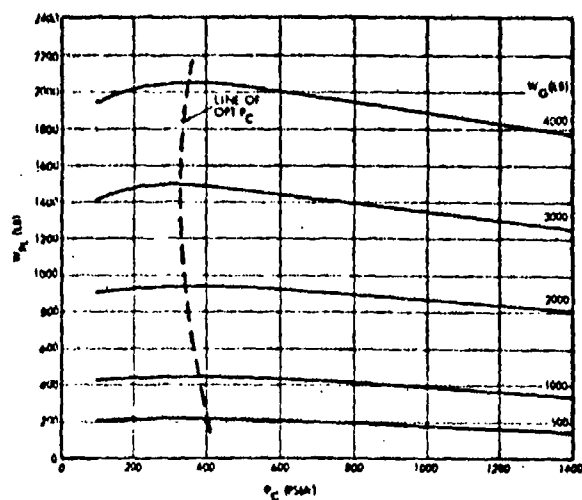


Figure 11-14.  $W_{PL}$  Versus  $P_C$  and  $W_G$  for  $F/W_G = 2$  and  $\Delta V = 3000$

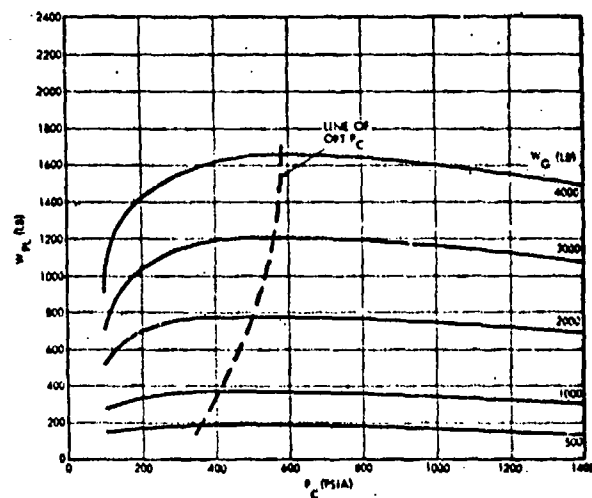


Figure 11-15.  $W_{pL}$  Versus  $P_c$  and  $W_G$  for  $F/W_G = 7$  and  $\Delta V = 3000$

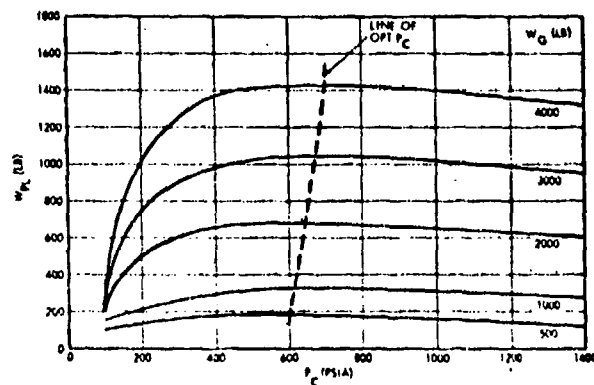


Figure 11-16.  $W_{pL}$  Versus  $P_c$  and  $W_G$  for  $F/W_G = 10$  and  $\Delta V = 3000$

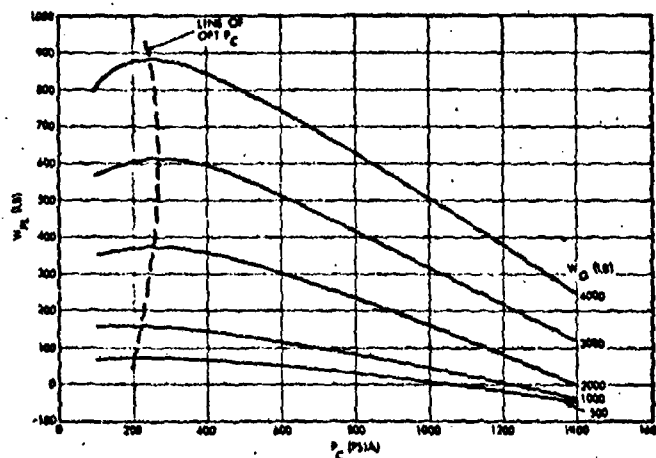


Figure 11-17.  $W_{PL}$  Versus  $P_C$  and  $W_G$  for  $F/W_G = 2$  and  $\Delta V = 7000$

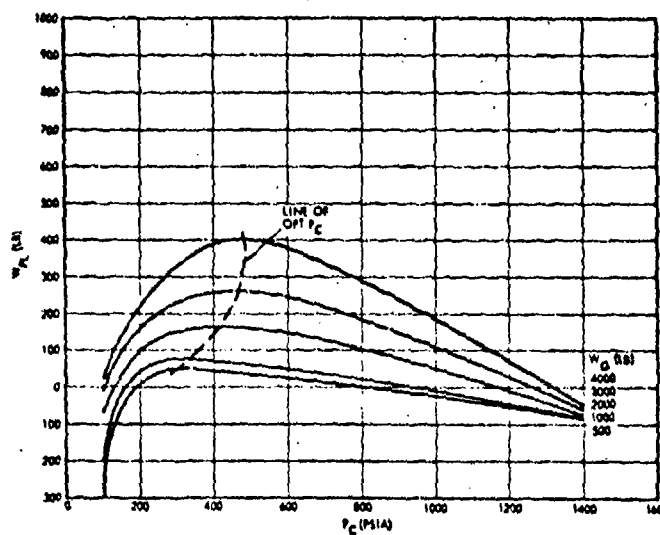


Figure 11-18.  $W_{PL}$  Versus  $P_C$  and  $W_G$  for  $F/W_G = 7$  and  $\Delta V = 7000$

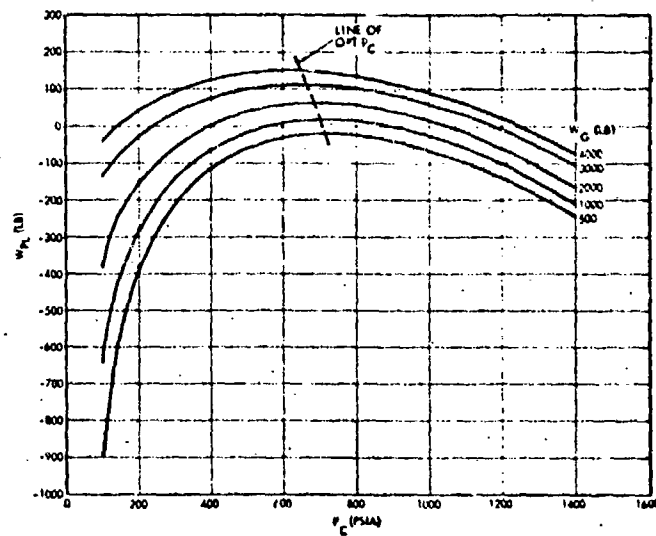


Figure 11-19.  $W_{PL}$  Versus  $P_C$  and  $W_G$  for  $F/W_G = 10$  and  $\Delta V = 7000$

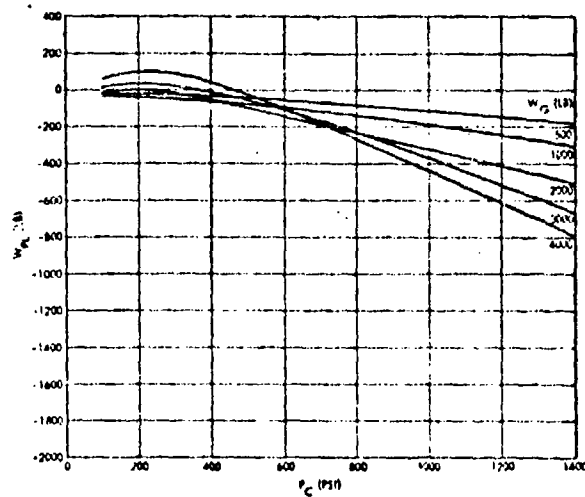


Figure 11-20.  $W_{PL}$  Versus  $P_C$  and  $W_G$  for  $F/W_G = 2$  and  $\Delta V = 11,000$



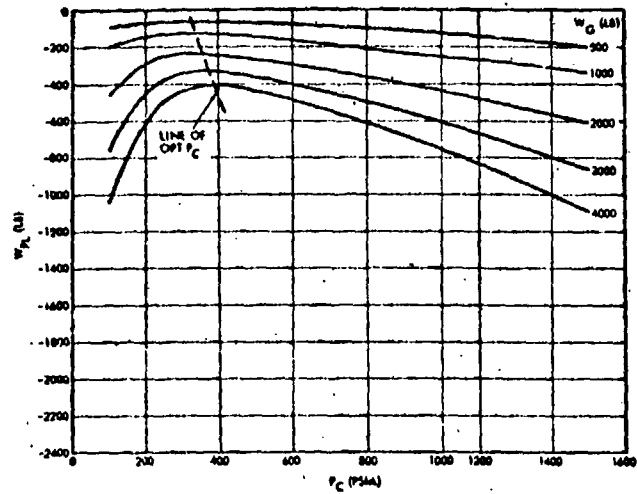


Figure 11-21.  $W_{pL}$  Versus  $P_c$  and  $W_G$  for  $F/W_G = 7$  and  $\Delta V = 11,000$

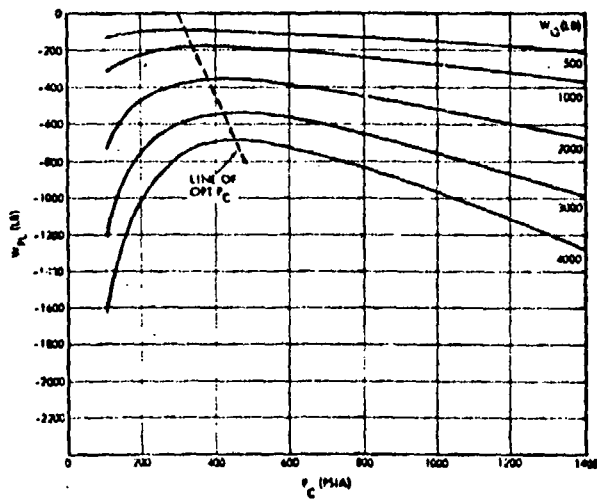


Figure 11-22.  $W_{pL}$  Versus  $P_c$  and  $W_G$  for  $F/W_G = 10$  and  $\Delta V = 11,000$

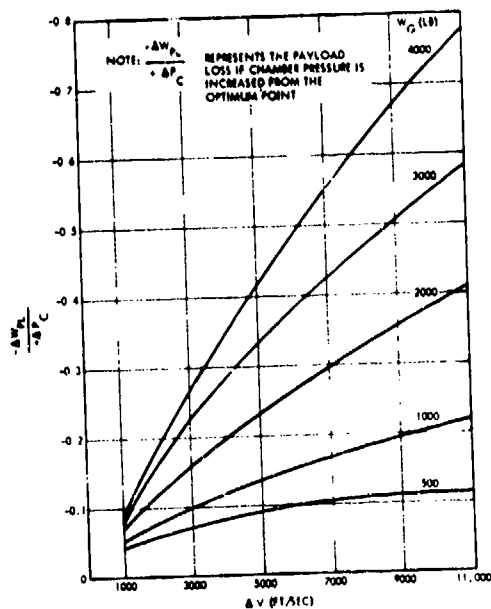


Figure 11-23.  $-\Delta W_{PL}/\Delta P_C$  Versus  $\Delta V$  and  $W_G$  for  $F/W_G = 2$

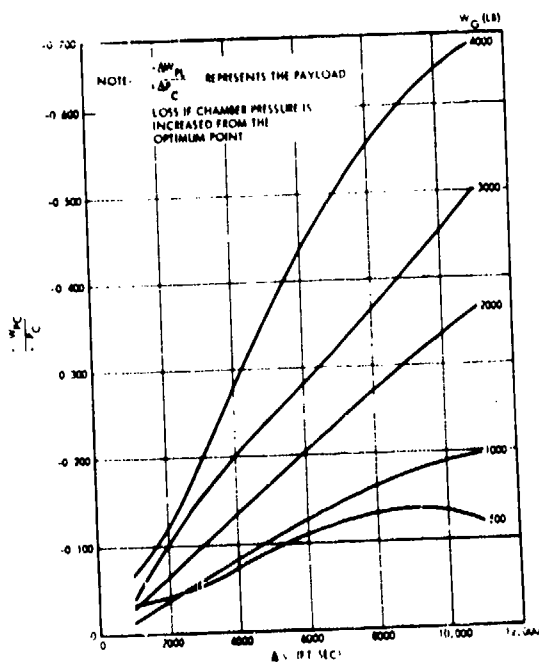


Figure 11-24.  $-\Delta W_{PL}/\Delta P_C$  Versus  $\Delta V$  and  $W_G$  for  $F/W_G = 7$

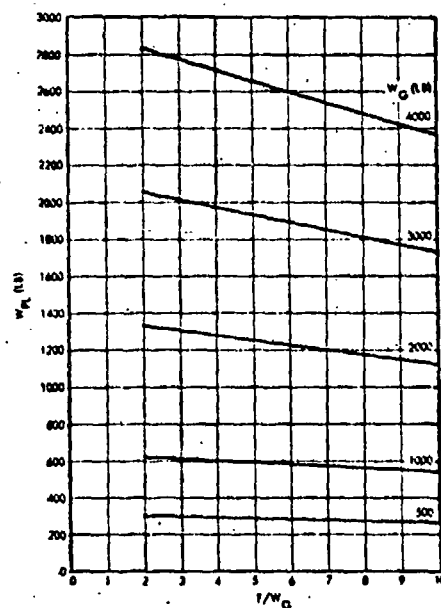


Figure 11-25.  $W_{pL}$  Versus  $F/W_G$  and  $W_G$  for  $\Delta V = 1000$

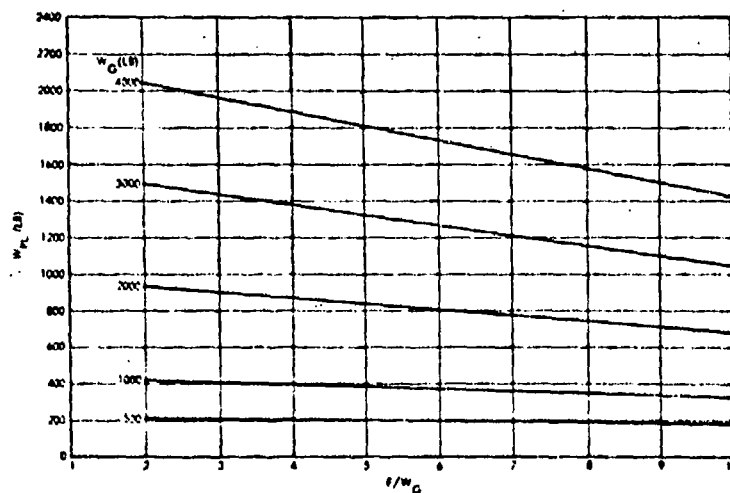


Figure 11-26.  $W_{pL}$  Versus  $F/W_G$  and  $W_G$  for  $\Delta V = 3000$

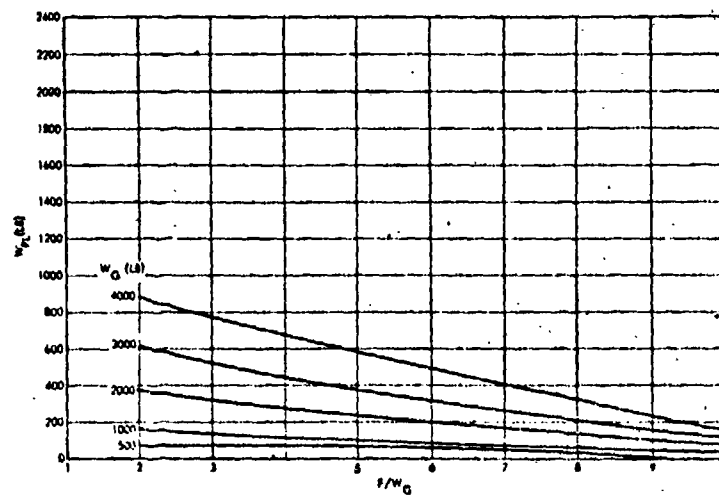


Figure 11-27.  $W_{PL}$  Versus  $F/W_G$  and  $W_G$  for  $\Delta V = 7000$

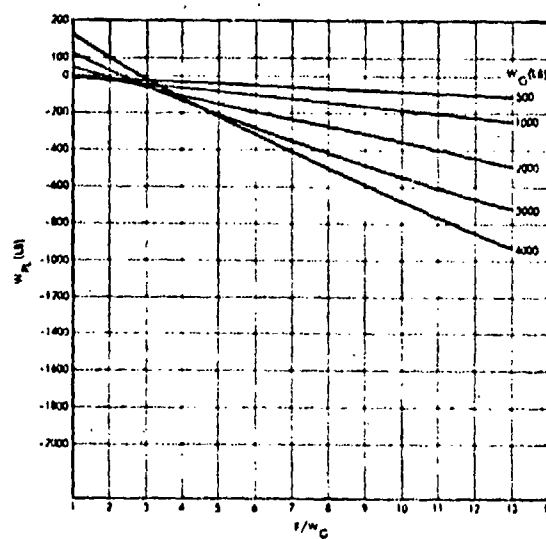


Figure 11-28.  $W_{PL}$  Versus  $F/W_G$  and  $W_G$  for  $\Delta V = 11,000$

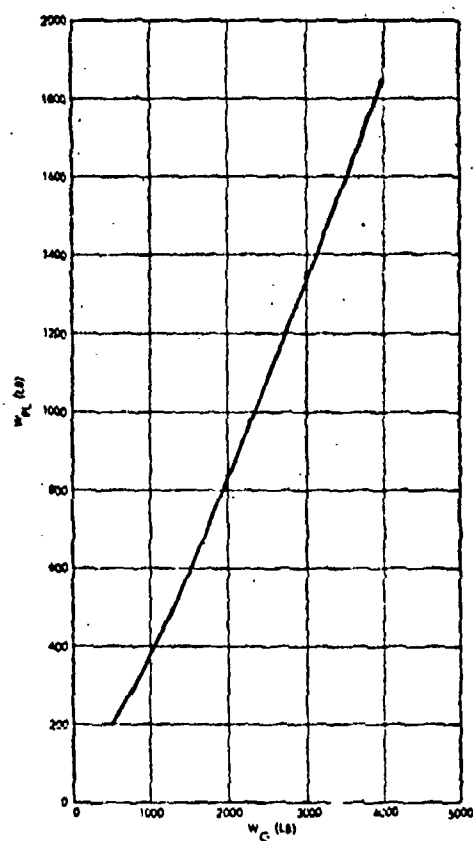


Figure 11-29.  $W_{pl}$  Versus  $W_G$  for  $F/W_G = 3.5$  and  $\Delta V = 3250$

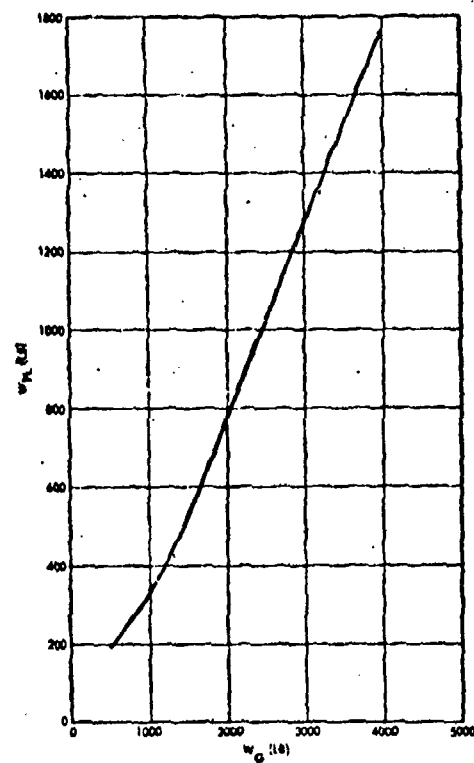


Figure 11-30.  $W_{pl}$  Versus  $W_G$  for  $F/W_G = 3.5$  and  $\Delta V = 3500$

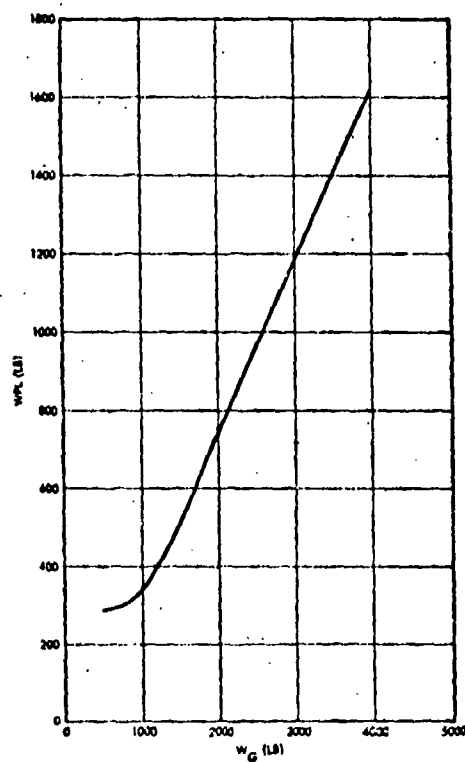


Figure 11-31.  $W_{PL}$  Versus  $W_G$  for  $F/W_G = 5$  and  $\Delta V = 3500$

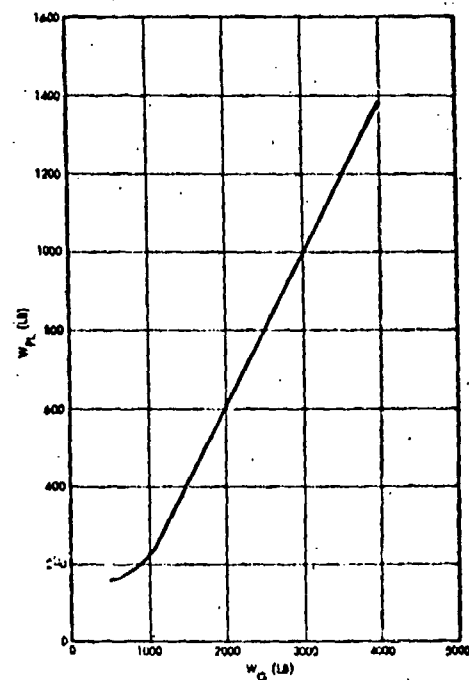


Figure 11-32.  $W_{PL}$  Versus  $W_G$  for  $F/W_G = 6$  and  $\Delta V = 4000$

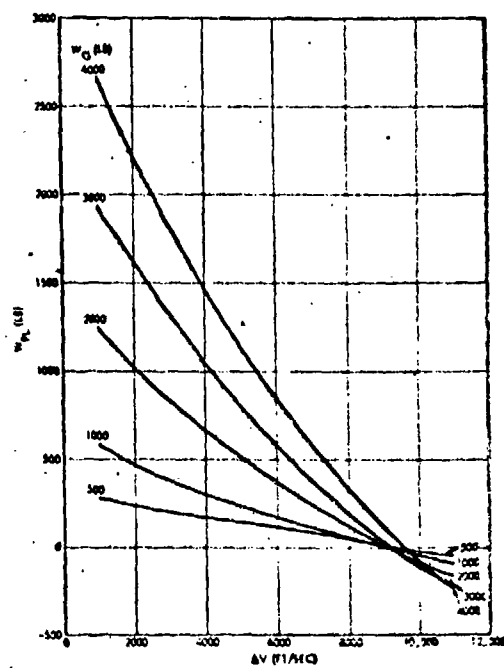


Figure 11-33.  $W_{PL}$  Versus  $\Delta V$  and  $W_G$  for  $F/W_G = 3.5$

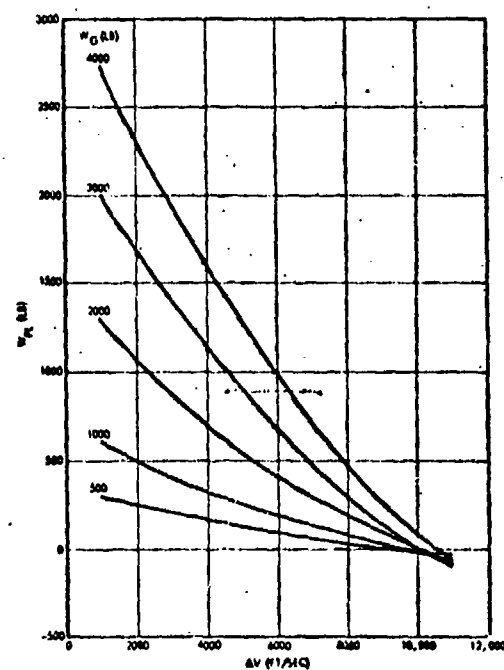


Figure 11-34.  $W_{PL}$  Versus  $\Delta V$  and  $W_G$  for  $F/W_G = 5$

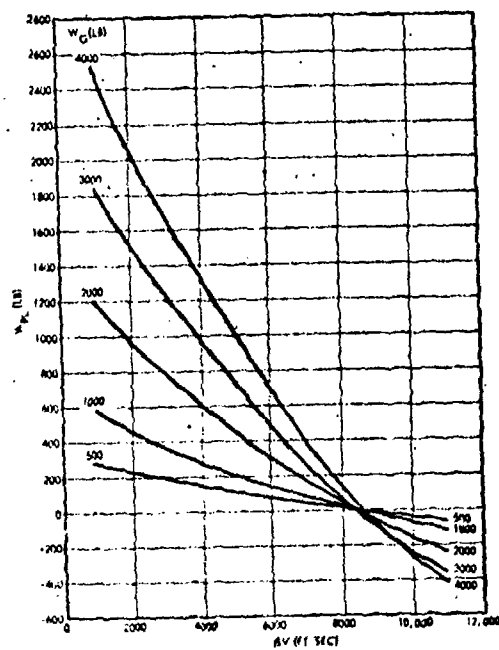


Figure 11-35.  $W_{PL}$  Versus  $\Delta V$  and  $W_G$  for  $F/W_G = 6$

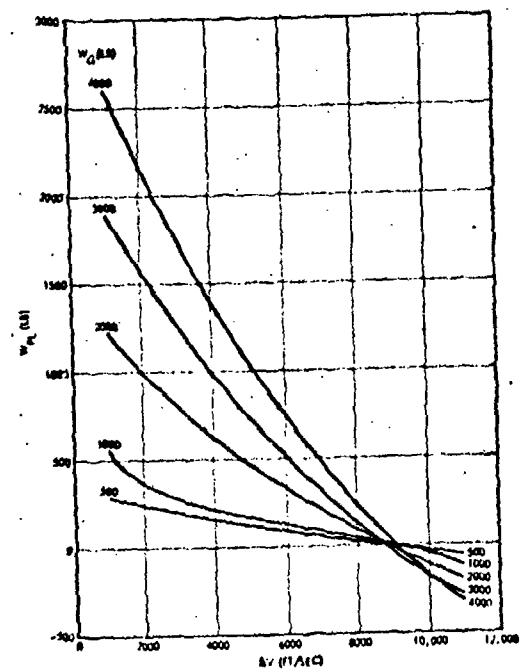


Figure 11-36.  $W_{PL}$  Versus  $\Delta V$  and  $W_G$  for  $F/W_G = 7$



### 11.2.3 Vehicle Structure

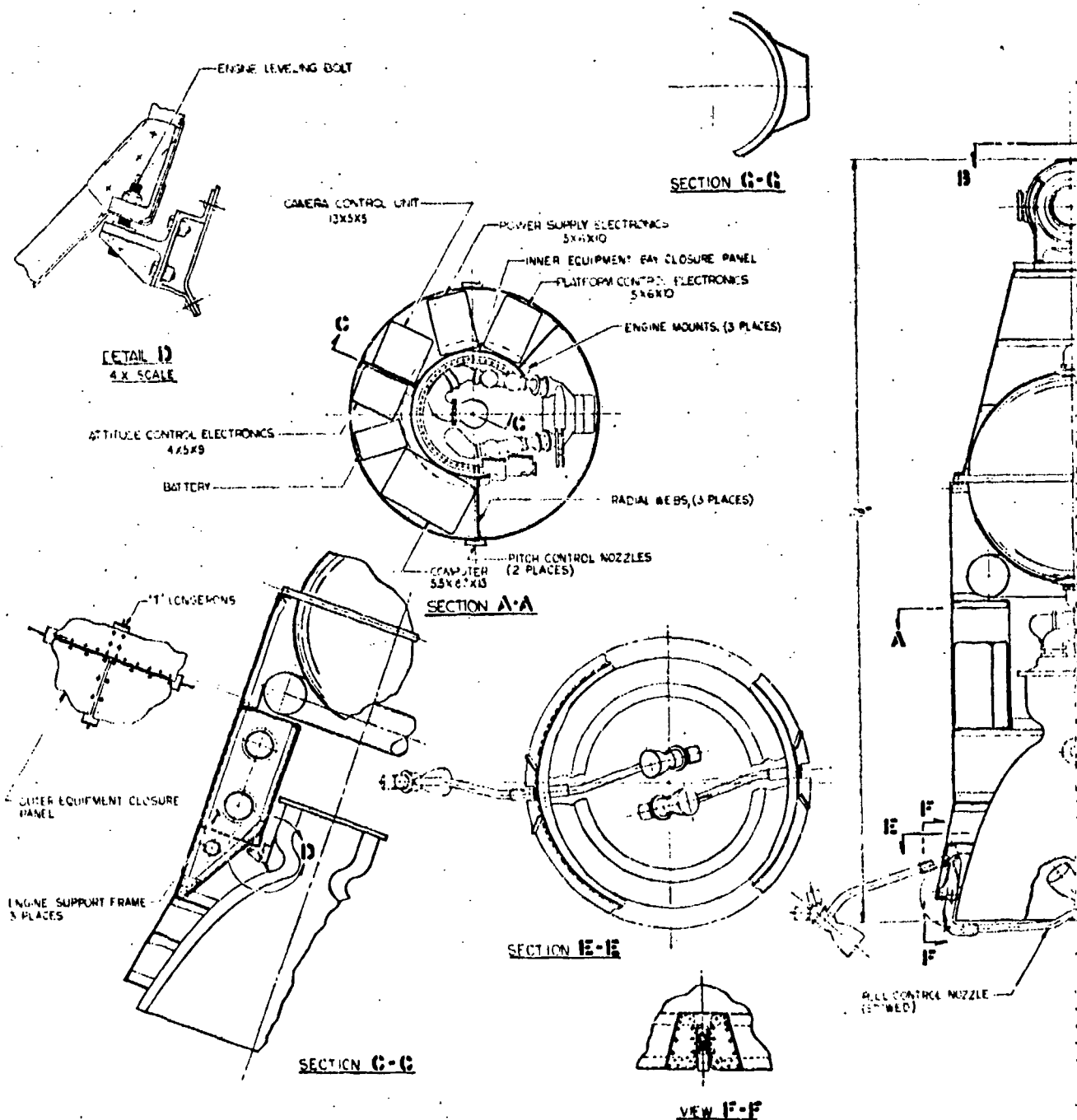
The basic structure for the electro-optical homing stage is a primary outer shell of monocoque construction. The engine, equipment panels, tanks, attitude control engines and tracker support structure as well as the aft cone are secured to this structure through appropriate rings, webs, flanges, etc., as shown in Figure 11-37.

The gimbaled tracker mounting panel is of sandwich construction and mounts on the forward end of the tracker support structure. A "V" shaped sheet metal bracket attached to the tracker support structure provides additional support for the overhanging portion of the tracker mounting panel.

The two roll control engines, which deploy after separation from the boost vehicle, are mounted on arms hinged from brackets secured to the vehicle's aft cone structure. The hinge brackets are located just above the shaped charge separation device. These brackets, with doublers, serve to reinforce the discontinuous aft cone's lower structural ring which is interrupted to allow clearance for the extended arms. The arms are shaped such that the roll control engines stow, cross-arm, in the cavity of the main engine nozzle extension. They are deployed by means of torsion spring motors and latch in the extended position.

The aft cone provides the structural connection to the booster (Minuteman). Separation is accomplished by means of a shaped charge which severs the aft cone a few inches above the main engine exit.

The radar equipped vehicle utilizes a similar structural arrangement below the main propellant tank but its structure differs considerably above the tank to accommodate the radar subsystem as shown in Figure 11-38. Both vehicles utilize the space around the main engine for equipment mounting panels. Access to these panels is provided by the use of structural doors in the outer shell. The engine is mounted on three points equipped with leveling screws for ease of engine alignment. Engine thrust load is fed into the primary outer shell through three sloping radial tension members which join the shell at the aft cone to cylinder transition frame.



1

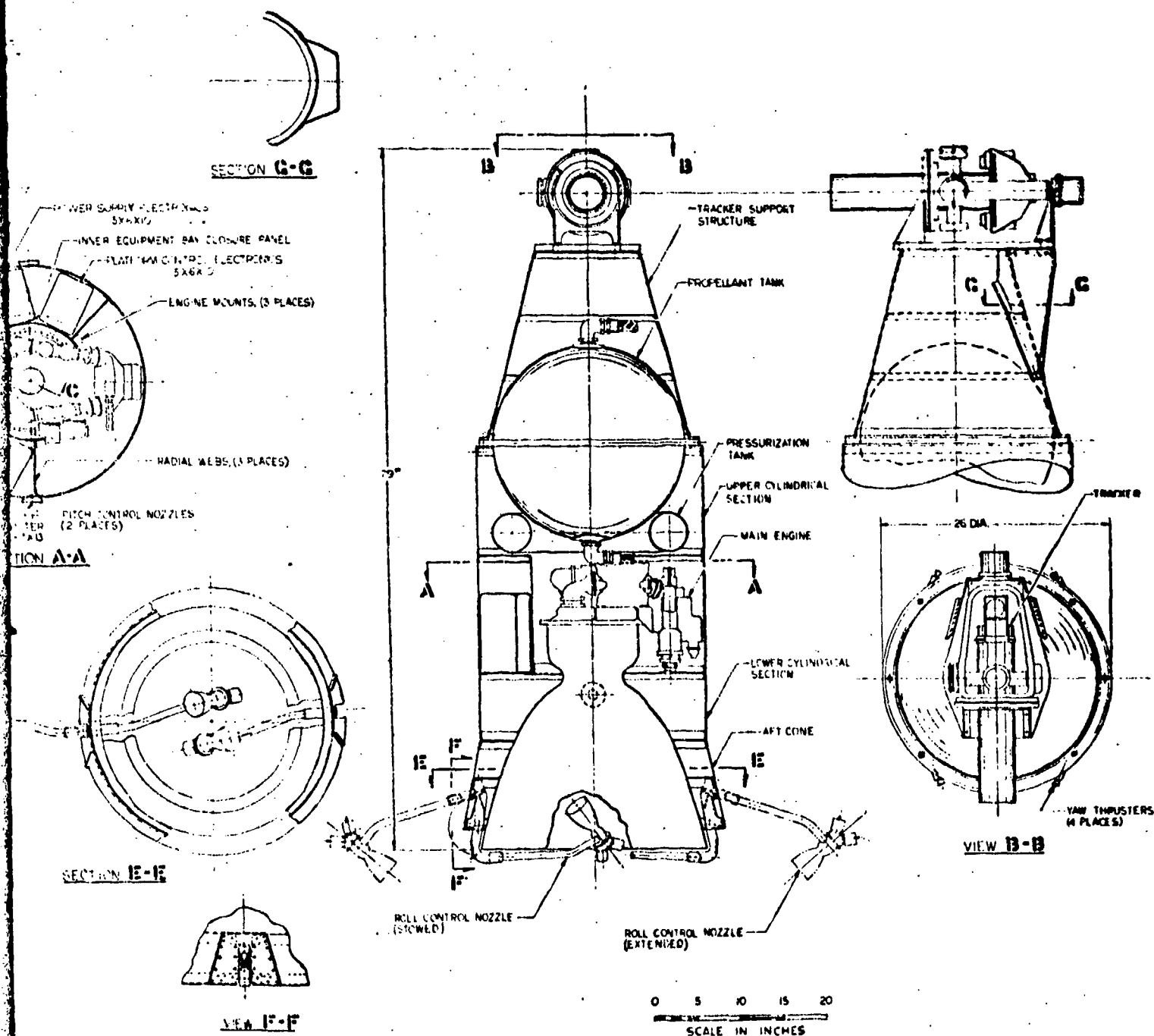
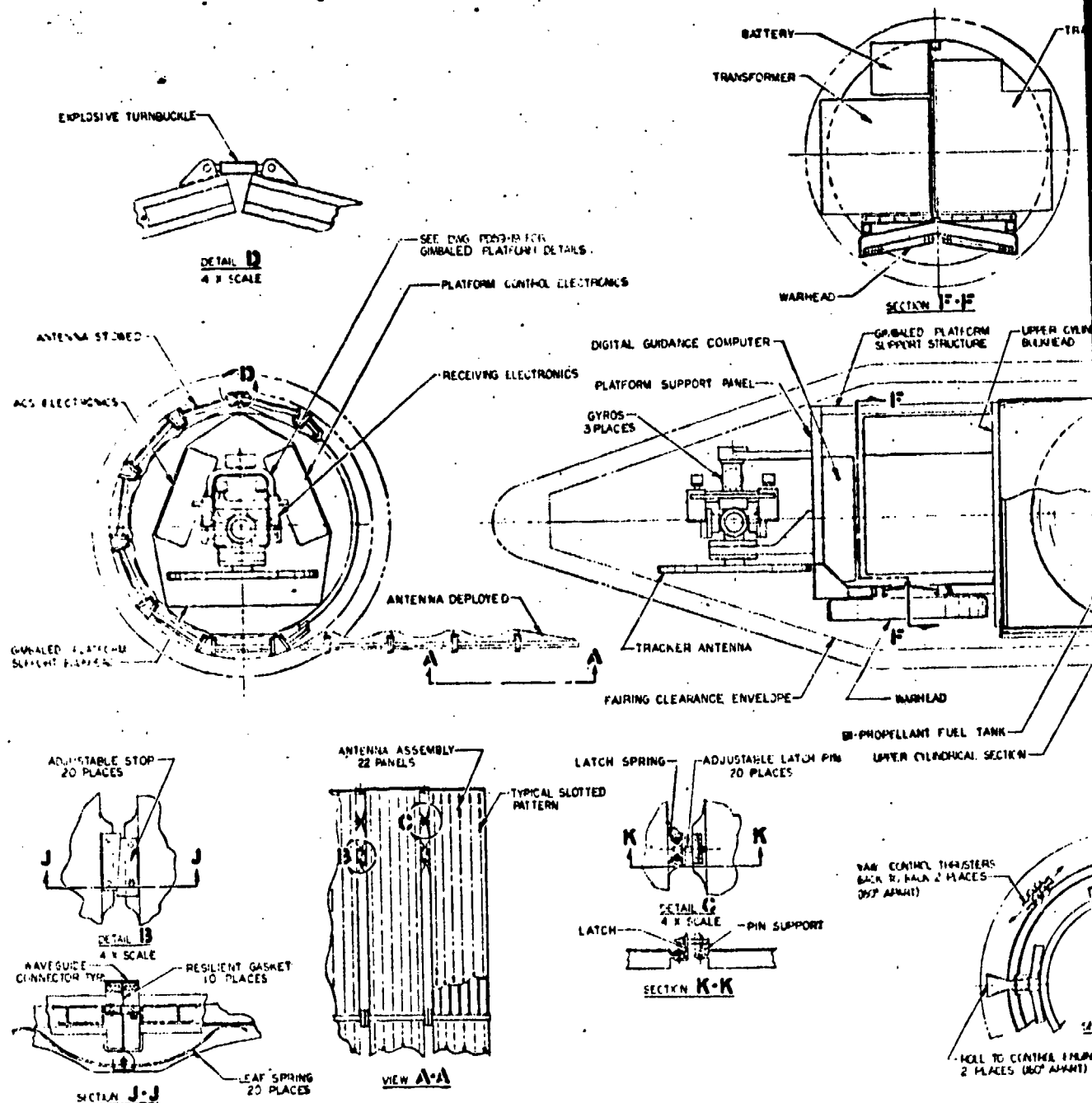


Figure 11-37. General Arrangement—Homing Stage With Electro-optical Tracker



1

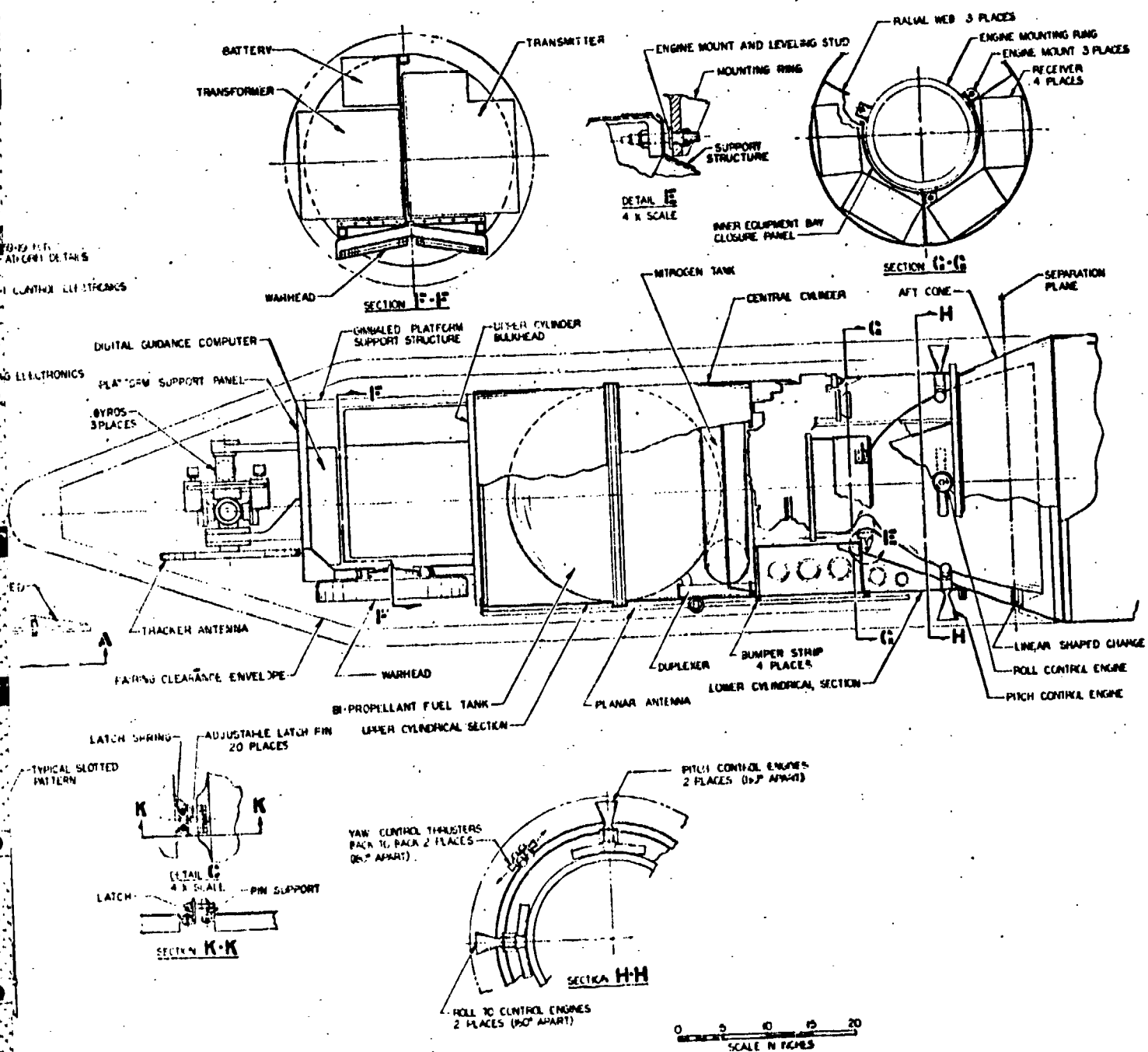


Figure 11-38. General Arrangement—Homing Stage With Radar Tracker

A preliminary stress analysis of the basic primary structure was performed using the vehicle physical properties defined in the appropriate section. The analysis was conducted with sufficient detail to accomplish the following objectives:

- Establish that adequate structural strength and rigidity has been provided in the vehicle designs.
- Establish structural member sizes with sufficient accuracy to permit realistic weight estimates.

The critical structural design conditions, load factors, and results of the stress analysis follow. Included are definitions of major load paths, material selection criteria, and the basis for establishing structural member sizes. The two subject vehicle structural designs appear in Figures 11-37 and 11-38 where the essential structural elements are defined:

- Limit Loads are defined as the maximum loads expected in service, including uncertainties.
- Ultimate Loads are those used for design and analysis to assure design adequacy for limit loads. They are equal to the product of limit load and the ultimate factor of safety. Failure must not occur at ultimate load.
- Factors of Safety are used to account for all uncertainties in the design analysis, material properties and variations in fabrication. The values used in this analysis are as follows:
  - Ultimate Factors of Safety:
    - Primary Structures 1.25
    - Pressure Vessels (for burst) 1.50

Material design mechanical properties selected for the basic primary structure are summarized in Table 11-1.

Minimum gauge in each structural member was selected as the maximum thickness based on three separate requirements:

- Minimum thickness for manufacturing and processing
- Minimum thickness to insure ruggedness during handling, transportation, and prelaunch conditions
- Minimum thickness to obtain required strength and rigidity

Table 11-1. Material Design Mechanical Properties

Alloy	Magnesium AZ31B	Magnesium ZK60A	Titanium 6Al 4V	Epoxy Glass Laminate
Form	Sheet	Hollow Extrusion	Sheet	
Condition	H24	T5	Heat Treated	
Temperature	RT	RT	RT	400° F
F <sub>tu</sub> ksi	39	46	160	
F <sub>ty</sub> ksi	29	38	145	
F <sub>cy</sub> ksi	24	26		35
Elong (in 2") %	6	4	4	
E 10 <sup>6</sup> psi	6.5	6.5	16.5	2.5

The design limit load factors for this vehicle's primary structure are as follows:

- Powered Flight of Minuteman Booster

- Along booster axis 15.4 g's
- Normal to booster axis 1.0 g's

The critical condition during the powered flight of the Minuteman booster occurs during third stage burnout.

- Homing Stage Main Engine Firing

- Engine thrust (maximum) 3600 lb

One basic internal load analysis was conducted for the primary structure of both the electro-optical and the radar vehicle. Combinations of mass distributions from both designs were chosen such that maximum envelope loads resulted. This approach is admittedly conservative but was used to minimize detailed analysis.

For ease of presentation, each major structural element is discussed separately. Unless otherwise stated, the structural element is applicable to both the electro-optical as well as the radar vehicle.

#### 11.2.3.1 Aft Cone

The aft cone is located just forward of the Minuteman booster interface and supports the entire homing stage. Integral with the aft cone is the linear shape charge separation system. Critical loading of the aft cone occurs during burnout of the third stage Minuteman booster. At this time, the aft cone is subjected to an ultimate maximum axial load of 17,850 pounds combined with an ultimate bending moment of 62,800 in-lb. The selected design is a monocoque structure of AZ 31B-H24 magnesium alloy whose thickness is 0.053 inch. The allowable compressive working stress is 5970 pounds per square inch and the allowable axial load equivalent is 25,800 pounds. With straight line interaction between axial and bending the corresponding ultimate margin of safety is slightly above 0 percent. Monocoque standard aircraft type construction was selected because of its simplicity and ease of fabrication. Magnesium alloy AZ 31B-H24 was selected because of its favorable strength, stiffness, and low density.

#### 11.2.3.2 Central Cylinder

11.2.3.2.1 Lower Cylindrical Section and Equipment Bay. The central cylinder's lower cylindrical section and equipment bay houses the main engine and all or a portion of the required electronic equipment.

In addition, in the electro-optical vehicle the same regions provide support for the external payload (passive kill mechanism) while in the radar vehicle the same regions provide support for the external planar array antenna. Critical loading for the basic structure occurs during the burnout of the third stage Minuteman booster. At this time the lower cylindrical section is subjected to an ultimate maximum axial load of 17,850 pounds combined with an ultimate bending moment of 49,600 inch pounds. Following the same design philosophy as the aft cone structure, the lower cylindrical section and equipment bay consist of a magnesium alloy AZ 31B-H24 monocoque design of 0.050 inch. The allowable compressive working stress is 7280 pounds per square inch and the allowable axial load



equivalent is 27,400 pounds. The corresponding ultimate margin of safety is 5 percent. Since the equipment bay external closure panels must be removed for access to the internal compartments, three basic tee long-rons and two rings have been provided for structural support when the panels are removed. In addition, structural type fasteners are supplied at all attach points for proper load transfer through the equipment bay shell sections.

The homing stage main engine is mounted on three points at the inner equipment bay closure panel. Engine thrust loads are reacted directly through the three engine mounts down through the three sloping radial members located within the lower cylindrical section. Engine firing loads are not critical except for local attach structures.

The equipment platform is presently designed to be of sandwich construction and is stabilized and structurally supported by the three equally spaced radial webs which extend and taper into the lower cylindrical section. These webs also form part of the engine reaction members.

11.2.3.2.2 Upper Cylindrical Section. The upper cylindrical section houses the pressurization tank as well as the lower half of the propellant tank on the radar vehicle. In the electro-optical vehicle the upper cylinder houses the pressurization tank and the lower half of the propellant tank. In addition, the upper cylindrical section also helps support the external planar antenna of the radar vehicle and the external payload of the electro-optical vehicle. Critical loading occurs during burnout of the third stage Minuteman booster. At this time the upper cylindrical section is subjected to an ultimate maximum axial load of 14,330 pounds combined with an ultimate bending moment of 24,400 inch pounds. Following the same design philosophy as the aft cone structure, the upper cylindrical section consists of a magnesium alloy AZ 31B-H24 monocoque design of 0.042 inch. The allowable compressive working stress is 5780 pounds per square inch and the allowable axial load equivalent is 18,320 pounds. Determining the margin as in the aft cone, the corresponding ultimate margin of safety is slightly above 0 percent.

#### 11.2.3.3 Bipropellant Tank

The spherical bipropellant tank is mounted at its circumference on the upper cylindrical section. The tank diameter is 24 inches and is fabricated from heat treated 6Al-4V titanium alloy. Critical design condition for the bipropellant tank is the 750 psi ultimate burst pressure. Corresponding basic tank wall thickness for this pressure is 0.029 inch based on a heat treated material tensile ultimate strength of 160,000 psi. Local thickening to 0.035 inch will be required at the circumferential weld land and support ring due to discontinuity stresses and local annealing.

#### 11.2.3.4 Pressurization Tank

The toroidal pressurization tank is mounted at its outer circumference on the upper equipment bay. The tank has an outer diameter of 21 inches and a cross-sectional radius of 2.5 inches. The tank is fabricated from heat treated 6Al-4V titanium alloy. The critical design condition for this tank is the 6000 psi ultimate burst pressure. Corresponding basic tank wall thickness for this pressure varies from 0.116 inch at the inner radius to 0.083 inch at the outer radius. These thicknesses are based on a heat treated material tensile ultimate strength of 160,000 psi. Local thickening to 0.142 inch and 0.102 inch for the inner and outer radii respectively will be required at the weld lands and support ring due to discontinuity stresses and local annealing.

#### 11.2.3.5 Tracker Support Structure for Electro-Optical Vehicle

The tracker support structure for the electro-optical vehicle is located over the forward half of the propellant tank. Critical loading of the tracker support structure occurs during the burnout of the third stage Minuteman booster. At this time the tracker support structure is subjected to an ultimate maximum axial load of 771 pounds combined with an ultimate bending moment of 1400 in-lb. Following a similar design philosophy as the aft cone structure, the tracker support structure consists of a magnesium alloy AZ 31B-H24 monocoque design of 0.025 inch minimum gage. The allowable compressive working stress is 3120 psi and the allowable axial load equivalent is 4910 pounds. Being of minimum gage design, the corresponding ultimate margin of safety is high.

#### 11.2.3.6 Tracker Support Structure for the Radar Vehicle

The tracker support structure for the radar vehicle is located forward of the upper cylindrical section. Critical loading of this structure occurs during the burnout of the third stage Minuteman booster. At this time, it is subjected to an ultimate maximum axial load of 1240 pounds combined with an ultimate bending moment of 2110 in-lb. Component mounting allowed only clearance for a deep tee-type cross section design structure. Minimum gage extruded square sections were chosen as cap members for this tee section. Square sections were selected for ease of attachment while at the same time maintaining good column stability characteristics. Sections selected consist of 1 inch square by 0.035 inch thick extruded and chemical milled magnesium alloy ZK 60A-T5 tubes. The critical tube compressive stress is 21,500 pounds per square inch based on column failure assuming pinned ends. The maximum applied compressive stress under the aforementioned booster burnout environment is 12,120 psi. Thus, the ultimate margin of safety is high.

#### 11.2.3.7 Other Structural Elements

An analysis of the gimbaled platform structural components was conducted to establish structural stiffness requirements (see Section 11.2.4). The results of a structural analysis of the unfurlable passive kill mechanism were included in Chapter 10, Paragraph 10.1.2.

#### 11.2.4 Propulsion Systems

Propulsion systems for the homing stage mission, based on documented rocket engine technologies at STL, are defined in this section. Three principles of impulse reaction are utilized: bipropellant variable thrust, bipropellant pulse modulation, and cold nitrogen jets. Augmenting the thrust units are propellant tankage, positive expulsion devices, a pressurization subsystem, and associated controls.

Coincidentally, the two basic vehicles under study, a homing stage equipped with an electro-optical tracker and one equipped with a radar tracker, require nearly identical thrust levels and, therefore, utilize the same main engine. Restartable, variable thrust engines in this thrust range are feasible; in fact, engines with somewhat higher thrust (5000 and

10,000 lb) are presently under development at STL as part of the Lunar Excursion Module program. Lower thrust level prototype engines of this type have already been satisfactorily tested at STL. Based on an optimized selection of specific impulse and thrust requirements for the homing stage and preliminary design analysis of the selected thrust units, the following approach is suggested.

The main engine will be an ablatively cooled, solenoid-actuated, bipropellant variable-thrust (10:1) engine utilizing direct liquid injection. Vehicle pitch and roll control is provided by radiation-cooled pulse-modulated bipropellant engines. Yaw attitude control is provided by four cold gas reaction nozzles. The engines are designed to respond in an automatic control loop. If necessary, the system can be provided with external propellant dump devices for missions requiring such capability. Spherical propellant tanks with positive expulsion devices and nitrogen pressurization are utilized.

Many specific problems associated with the development of the main engine for this application were solved or are being solved in support of STL's variable thrust LEM engine for the Apollo mission, and the STL 150 pound variable thrust chamber assembly for the Surveyor engine which is now in its final phase of development at STL. Use of the Surveyor and LEM engine technology can result in considerable reduction in this engine's development time and cost.

Mission criteria utilized in the analysis of the optimum propulsion configuration for a typical intercept trajectory gave consideration to the total energy required by the vehicle for homing  $\Delta V$  and attitude control. Thrust selection for attitude control was based on vehicle angular acceleration requirements and/or predicted main engine thrust to vehicle center of gravity misalignment. A total homing period of 90 seconds was assumed a conservative estimate.

Parametric weight and mission error analysis yield an optimum thrust of 3600 pounds for the main engine, at 400 psi chamber pressure. The engine is required to deliver 4000 ft/sec  $\Delta V$  for the electro-optical vehicle, and 3250 ft/sec for the radar configuration. Table 11-2 is a list of criteria for pitch, yaw, and roll attitude control engine analysis.

Table 11-2. Attitude Control Subsystem Design Criteria

<u>Electro-Optical Vehicle</u>	<u>Roll</u>	<u>Pitch</u>	<u>Yaw</u>
Thrust, lb each	55	43.0	5.0*
Moment Arm, ft	4.2	2.1	1.8**
Torque lb-ft	230	90.0	9.0
Initial Moment of Inertia, slug-ft <sup>2</sup>	115	35	93
Total Energy, lb-ft sec	8000	3800	500
<u>Radar Vehicle</u>	<u>Roll</u>	<u>Pitch</u>	<u>Yaw</u>
Thrust, lb			
Moment Arm, ft	3.25	32.5	1.05
Torque, lb-ft	204	36.0	4.0
Initial Moment of Inertia, slug-ft <sup>2</sup>	102	100	15
Total work, ft-lb/sec	8000	1700	200

\* Each Thruster

\*\* Couple lever arm (two thrusters)

#### 11.2.4.1 System Description

A number of previous STL conducted studies of propulsion system requirements for similar vehicles and the results of those studies are applicable to the homing stage. Typical STL low-thrust hot and cold gas propulsion systems are used as the basis for this homing stage attitude control design. The bipropellant and cold gas propulsion flow diagram, Figure 11-39, shows the energy conversion portion of an all-pressure-fed system. All components, exclusive of the electronic controls which are discussed elsewhere in this report, are included.

A torus type pressurization tank supplies nitrogen at 480 psi for propellant tank pressurization, and for the yaw control nozzles. The pressure regulator reduces pressure from an initial 4000 psi to a continuous 480 psi supply at the required discharge flow rates.

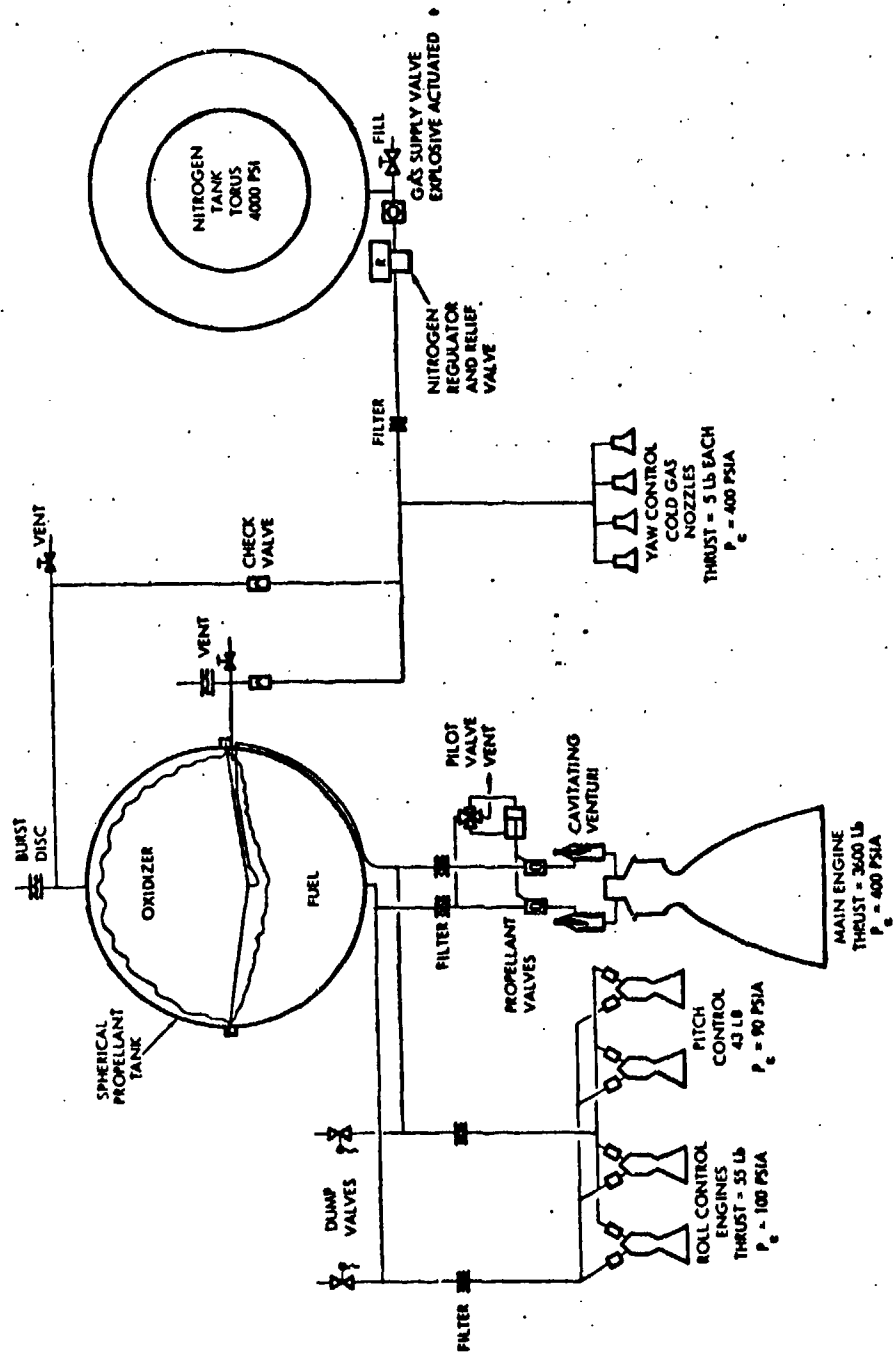


Figure 11-39. Propulsion System Schematic

The bipropellant fuel and oxidizer tank is equipped with positive expulsion devices and a metal separation bulkhead clamped between the flanged hemispheres. Plumbing elements shown are shutoff valves for each fill and purge line, nitrogen regulator and relief valve, filters, and check valves.

The tanks are filled as follows: Make connection to propellant loading equipment at the dump valves; open the tank vent valves; load propellant one at a time as indicated by the equipment loading procedures. After both sides of the spherical tank are filled or evacuated, the fill connections are closed and capped. Propellant loading can be accomplished prior to or after the homing stage is installed on the boost vehicle.

#### 11.2.4.2 Propellants and Performance

The mission requires reasonably high performance, storable, liquid propellant. Hypergolic ignition for the bipropellant engines is also desirable for reliable on-off operation. The same propellant must also be augmented by high boiling temperatures and must be consistent with engine selection and availability. Since those requirements can best be met with Aerozine-50 and nitrogen tetroxide, no detailed propellant tradeoff study was conducted in conjunction with this program. Such a study for a somewhat similar mission was conducted for BAMBI and reported in detail in Reference 4. Aerozine and  $N_2O_4$ , for which the STL engine is designed, easily satisfy the homing stage mission requirements and result in a simple, reliable propulsion system without concern of special system development programs. Propellant physical and chemical properties are listed in Table 11-3.

Table 11-3. Propellant Physical and Chemical Properties

<u>Properties</u>	<u>A-50</u>	<u><math>N_2O_4</math></u>
Boiling Point, °F	170	70
Freezing Point, °F	18	11.8
Density at 70°F, lb/ft <sup>3</sup>	53.6	92.0
Vapor Pressure at 70°F, psi	2.5	14.4

#### 11.2.4.3 Main Engine

The main engine is an STL design and consists of a single element variable area injector, mechanically linked bipropellant shutoff valves, and full ablative chamber and nozzle. An oxidizer to fuel mixture ratio of 1.6 was selected based on theoretical calculations of performance using kinetic reaction data for the expansion process. The data indicate that only partial equilibrium nozzle flow can be expected. Therefore, higher mixture ratios would not provide any performance advantages, but would greatly decrease ablative chamber life and reliability. Engine performance parameters are summarized in Table 11-4. Of greatest significance is the nozzle thrust coefficient. STL's tests have repeatedly demonstrated  $C^*$  values of 97 percent of equilibrium flow. The predicted specific impulse of 318 seconds, which is considered conservative, will be verified by simulated altitude testing. Further system and subsystem optimizations will provide tradeoffs of specific impulse, engine operating pressure and nozzle length versus vehicle weight.

Table 11-4. Main Engine Characteristics

Thrust, lb	3600
Chamber Pressure, psia	400
Expansion Ratio	50.1
Mixture Ratio	1.6
$I_{SP}$ , sec	318
Burning Time, sec (intermittent)	20 to 90
Engine Weight, lb	38
Thrust Coefficient	1.805

The thrust chamber consists of a composite ablative cooled chamber, graphite nozzle throat insert, and ablative divergent section. The ablative material is encased in a continuous titanium shell which provides containment of the ablative material and thrust transmission into the vehicle thrust structure. The throat insert allows the use of ablative material at the 400 psia chamber pressure.



A major engine component is the variable area coaxial injector, shown in Figure 11-40. It is a rugged, precise, and mechanically simple device which provides a stable symmetric flame pattern and high combustion efficiency. The injector consists of a face plate and fuel manifold assembly, a propellant metering sleeve, and the oxidizer feed tube assembly as shown in Figure 11-40. The fuel enters the chamber through the annular gap formed by the face plate and the sleeve; oxidizer enters the chamber through the radial slots located in the oxidizer feed tube and the sleeve. The sleeve is actuated to an optimum position with an external actuator and linkage.

The variable injector is augmented by a combined cavitating venturi and flow control valve in each propellant line. The venturi provides sufficient cavitation to allow optimum injection area adjustment during the throttling process.

The propellant shutoff valves are attached to the injector to minimize propellant dribble volume. The main propellant valve is fluid actuated, controlled by a solenoid actuated pilot. The basic element of the pilot valve is a caged free ball which alternately seats against the actuation fuel inlet port and the overboard vent. In the normally closed position, the ball is held in place by a small spring loaded plunger, and the actuator pistons are vented to space. Energizing the solenoid causes the plunger to retract. The actuator fuel pressure unseats the ball from the inlet port and holds it in place against the vent port. The fuel then flows into the actuator pistons opening the main valves. Valve actuation is independent of throttle actuation.

#### 11.2.4.4 Attitude Control Engine

The pitch and two roll control units are radiation cooled, solenoid actuated bipropellant engines utilizing direct liquid injection (see Table 11-5). These units are designed to perform upon command in an automatic control loop. They are the same as, or similar to, commercially available engines.

Extensive sea level and simulated altitude development work has been conducted on radiation cooled thrust chambers, especially at this thrust level. Chambers were developed to operate for durations in excess of 30 minutes in a space environment. The chambers are constructed of

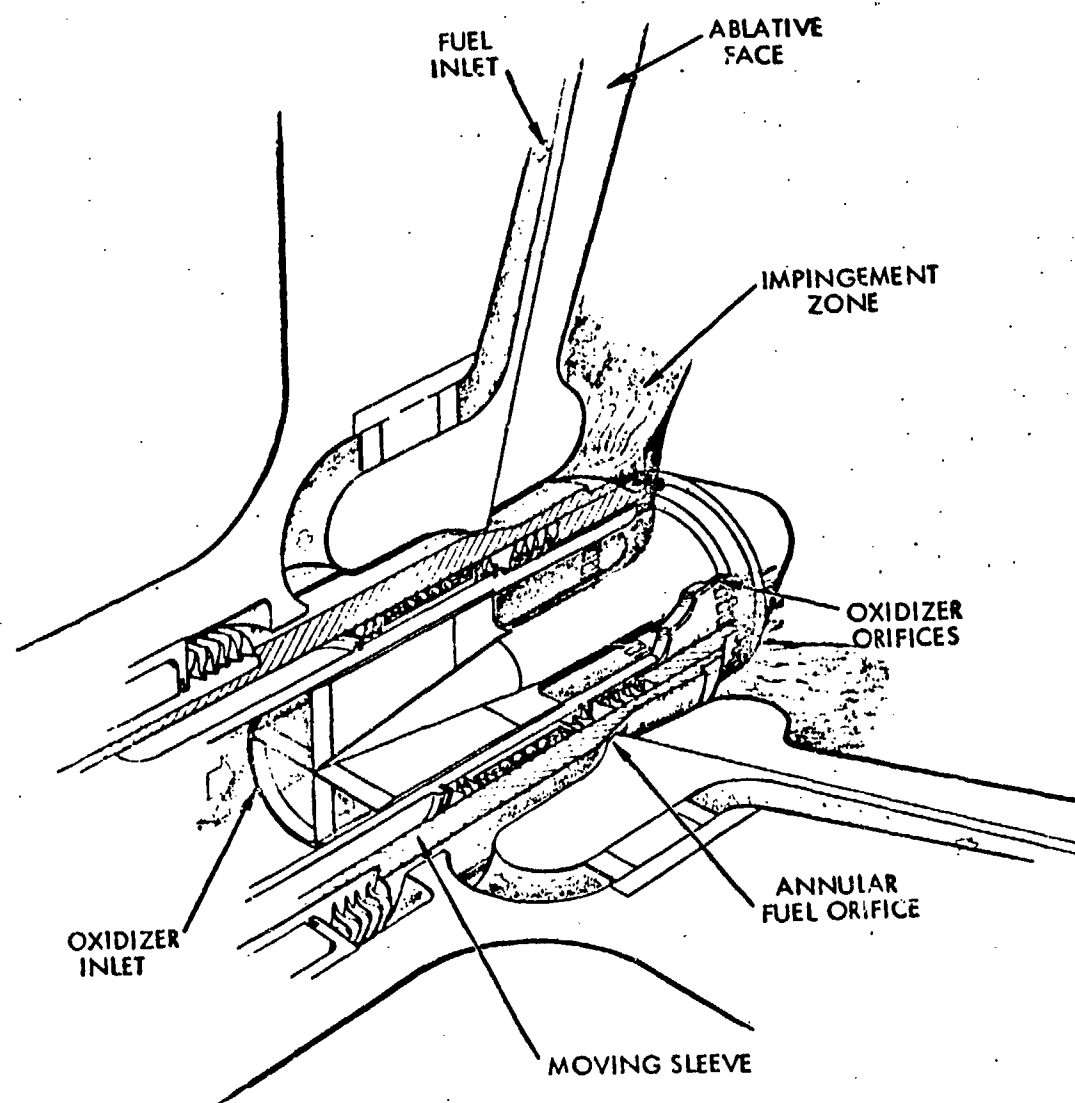


Figure 11-40. Injector Element Schematic

Table 11-5. Homing Stage Attitude Control  
Subsystem Design Criteria

	Electro-Optical Vehicle			Radar Vehicle		
	Roll	Pitch	Yaw(1)	Roll	Pitch	Yaw(1)
Thrust (lb)	55	43	5(2)	63	11	2(2)
Chamber Pressure (psia)	90	90	400	90	90	400
Specific Impulse (sec)	305	305	60-90	305	305	60-90
Obtainable Minimum Impulse Bit (lb-sec)	0.30	0.25		0.30	0.25	
Propellant	$N_2O_4/A-50$	$N_2O_4/A-50$	$N_2$ (3)	$N_2O_4/A-50$	$N_2O_4/A-50$	$N_2$ (3)
Homing Phase (sec)	90	90	90	90	90	90
Minute On-time (msec)	60	60	50	60	60	50

(1) Four thrusters in pairs to produce purr couple.

(2) Each thruster.

(3) Main propellant pressurant.

molybdenum, with an oxidation resistant coating on both inside and outside surfaces. The coating insures a high emissivity on the outside surface which reduces wall temperatures. The actual combustion gas-to-wall film coefficient for the optimized motor is approximately two times lower than theoretical convection coefficient. The difference, together with intelligent chamber design, has permitted the use of coated molybdenum nozzles. Actual  $I_{sp}$  values based on test data are:

Steady State = 310 seconds

Pulse Modulation = 304 seconds

Single Pulse = 285 seconds

Pulse rate modulated engine suppliers have conducted extensive tests on many different injector configurations in arriving at configurations which result in the best compromise between high  $I_{sp}$  efficiency, combustion stability, repeatable performance, long life and realistic manufacturing tolerances. Injector variables have been investigated in hundreds of tests and are based on conclusive results; single impinging pencil streams of fuel and oxidizer are provided for this engine. The pressure drop required for propellant injection is approximately 50 to 75 psi.

The roll control engines for the electro-optical configuration are mounted on retractable thrust levers and are deployed prior to main engine firing. The location and arrangement of these engines are shown on Figures 11-1 and 11-37. For the radar vehicle, which utilizes an internally mounted warhead, these engines are body mounted as shown in Figures 11-2 and 11-38.

Four cold gas thrusters are provided for yaw control. These nozzles are also commercially available and can be easily adapted to this vehicle. Nozzle design characteristics are as shown in Table 11-5. The low yaw torque requirements and the high reliability and tight weight of the cold gas system offset the low specific impulse provided by nitrogen. The mission may consume as much as 4.5 pounds of  $N_2$  (0.225 ft<sup>3</sup> stored at 4000 psi).

#### 11.2.4.5 Pressurization and Propellant Feed System

A pressurization system is required to supply pressure for warhead inflation (electro-optical vehicle) and for propellant expulsion as well as cold gas for the yaw jets. The quantities provided for each are listed below:

	<u>EO Vehicle</u>	<u>Radar Vehicle</u>
Warhead Inflation	3.4	None
Propellant Expulsion	8.5	11.7
Yaw Jets	4.5	5.4
Total	16.4 (lb)	17.1 (lb)

The system consists of one toroidal nitrogen supply tank, a single stage pressure regulator (containing an integral relief valve), and an explosively actuated supply valve. Gaseous nitrogen is specified and stored at a nominal pressure of 4000 psia and 70°F. (See Section 11.2.3 for tank structural design criteria.)

A single stage gas regulator with an integral relief valve is used to regulate the flow of nitrogen gas from the pressurant tank to the respective components upon demand.

The gas regulator effects a pressure reduction from 4000 psia in the nitrogen tanks to 480 psia distribution. The relief valve will operate at a preset 530 psia. The regulator will automatically compensate for the increase or decrease of nitrogen pressure in the propellant tank. Such variation in pressure might be caused by a change in propellant volume, temperature fluctuation, or propellant equilibrium shift. Leakage through the regulator will be restricted to 0.008 cubic inches per minute. The weights of the regulator and other components are listed in the propulsion subsystem weight Table 11-6.

The gas supply valve will be a normally closed, explosively actuated, aluminum alloy valve. To minimize leakage points and connections, the tubing connecting this unit into the system will be an integral part of the valve body.

Table 11-6. Propulsion Subsystems Weight Summary

<u>Component</u>	<u>Weight (lb)</u>	
	<u>EO Vehicle</u>	<u>Radar Vehicle</u>
<b>Engines</b>		
Main (one)	38.00	38.00
Roll (two)	6.2	6.2
Yaw (four)	0.75	0.75
Pitch (two)	4.40	4.40
<b>Propellant Tank</b>	32.90	36.38
<b>Pressurization System</b>		
Tank	14.94	13.99
Regulator	2.90	2.90
Supply Valves (one required)	0.20	0.20
Check Valves (two required)	0.50	0.50
<b>Plumbing and Fittings</b>		
Lines and Miscellaneous	3.15	3.00
Burst Diaphragm (two required)	0.25	0.25
<b>Electrical</b>	2.20	2.20
<b>Residual Propellants</b>	5.80	8.1
<b>Dry Weight</b>		
Propellants	188.2	261.5
Pressurant	16.4	17.1

The proposed propellant tank is a spherical tank containing positive expulsion devices similar to those shown in Figures 11-41 and 11-42. The upper hemisphere contains the oxidizer and the lower contains fuel. The tank and expulsion device are designed to be fabricated from materials compatible with storable propellants. The upper and lower hemispheres with flanges are fabricated separately. The tank bulkhead and expulsion devices are independently assembled. Final bolting of the flanged hemispheres and expulsion devices makes for a unique spherical propellant tank. The tank design criteria are outlined in Section 11.2.3.

The positive expulsion devices consist of dual-membrane, ring-stiffened metallic diaphragms which provide propellant orientation control as well as positive zero-gravity expulsion. Propellant orientation control is required on this highly maneuverable vehicle to prevent large center of mass shifts due to propellant motion during the roll maneuvers. Such devices were investigated and found feasible as part of the BAMBI Continuation Study (Reference 5).

#### 11.2.5 Engine Alignment and CM Position Control

The primary source of homing stage disturbance torques, which must be reacted by the vehicle's attitude control thrusters, is main engine thrust vector to center-of-mass (CM) offset resulting from assembly misalignments or mass shifts during engine operation. Factors known to contribute to this misalignment and possible corrective measures were discussed in detail in the Second Interim Report (Reference 2). The major factors and corrective measures are summarized below:

<u>Factors</u>	<u>Corrective Measures</u>
Lateral and angular misalignment of the nozzle centerline to CM of the dry stage due to assembly tolerances and lateral center of mass shift resulting from propellant loading.	Assembly techniques can be utilized to provide balance of the stage in the dry condition with the propellant tank so positioned that the predetermined CM of the usable propellant will be on the nozzle centerline or theoretical thrust line at ignition. A high degree of accuracy is possible with a relatively small expenditure for assembly and measuring equipment and time.

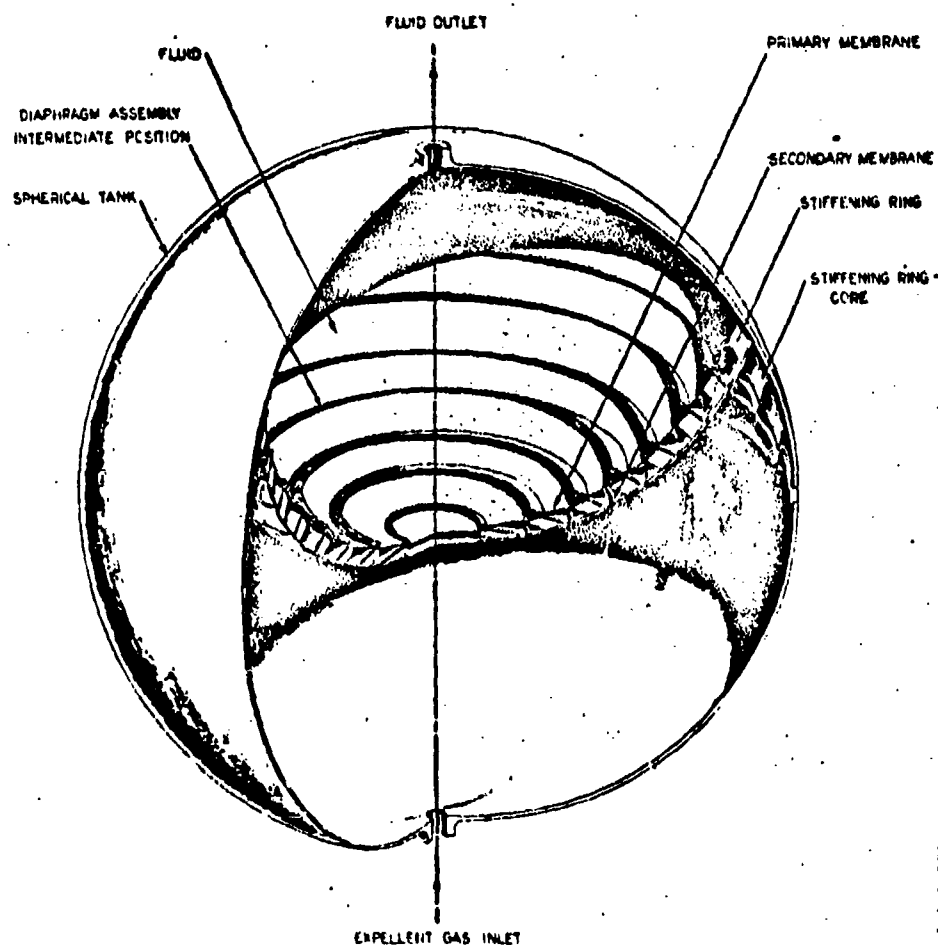


Figure 11-41. Positive Orientation and Expulsion Device



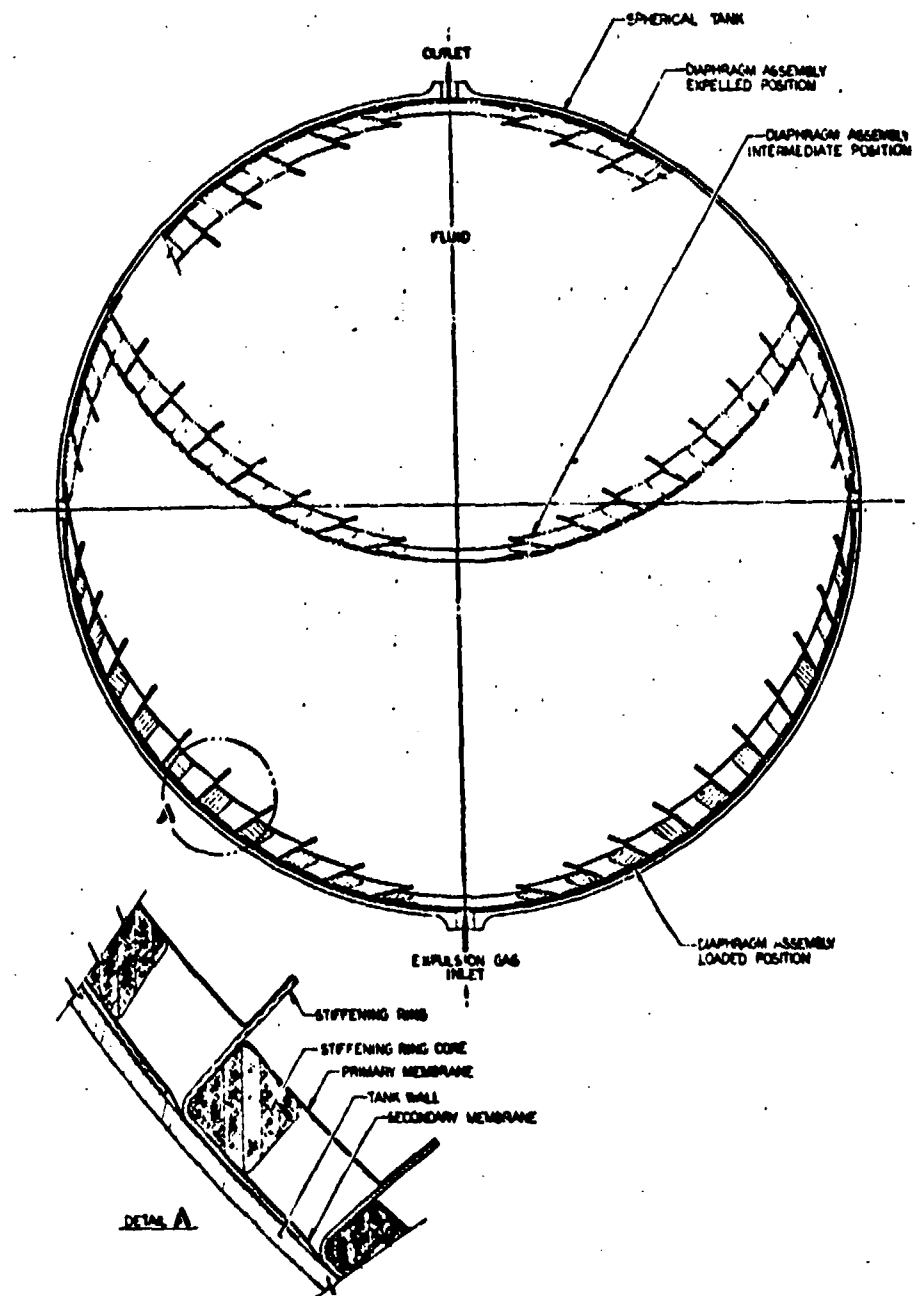


Figure 11-42. Propellant Expulsion Device

### Factors

Center of propellant mass shift during propellant depletion or lateral center of mass shift induced by fluid slosh during the "roll-to-control" maneuver.

Center of mass lateral shift resulting from asymmetric deflections of the deployed warhead while the vehicle is under thrust.

### Corrective Measures

The design and development of a positive expulsion device that provides lateral propellant position control was initiated as part of the BAMBI Phase II Continuation Effort (Reference 5) and resulted in a device which utilizes dual walled, convoluted diaphragms. (see Figures 11-41 and 11-42) These diaphragms are designed to resist tipping or buckling when the vehicle is subjected to angular velocities and acceleration which induce unsymmetrical fluid loads on the diaphragms.

This source of CM to true thrust line offset in the electro-optical vehicle is considered the most difficult one to predict and control. Although inflatable structures can be made relatively accurate, fairly large deflections are common. Such deflections, though structurally acceptable, could result in large center of mass shifts.

The inflated warhead appears to be the predominant source of induced offset for the electro-optical vehicle. It is estimated that the maximum CM shift due to deflection of the 16 foot diameter warhead under the influence of maximum engine thrust is approximately 0.05 inch (1 $\sigma$  value). This offset results in a torque around the pitch axis, thereby sizing the pitch thrusters. Since the warhead is symmetrical with respect to roll and yaw axes, warhead deflections produce little, if any, disturbance torque around these axes.

A vehicle, such as the radar vehicle, equipped with an internally mounted explosive warhead, in place of the inflated device, would be subject to somewhat reduced disturbance torques estimated to be less than 0.05 inch (3 $\sigma$  value). In either case, careful design and balancing techniques can minimize thrust vector misalignment to acceptable levels.

#### 11.2.6 Dynamic Considerations

The scope of the present study does not justify detailed dynamic analyses of the proposed vehicle concepts. A general summary of the

potential problem areas and a brief description of the methods that would be used to attack these problems is considered appropriate at this time. The following summary of dynamic problem areas includes consideration of all phases of the satellite interceptor flight from prelaunch to intercept.

#### 11.2.6.1 Prelaunch

11.2.6.1.1 Lateral Loads due to Wind-Induced Oscillations. Ground winds load the vehicle, causing lateral oscillations. Loads induced in the payload are calculated by obtaining analytically the modes of vibration of the elastic vehicle and applying the ground wind loads as a generalized force, taking into account the effects of random vortex-shedding.

11.2.6.1.2 Payload-Fairing Interference due to Wind-Induced Oscillations. Lateral oscillations caused by ground winds produce relative deflection of the payload with respect to the fairing. This deflection is calculated by obtaining, analytically, the modes of vibration of the elastic vehicle, treating the fairing as a separate branch, and applying the ground wind loads as a generalized force, again accounting for the effects of random vortex-shedding.

11.2.6.1.3 Longitudinal Loads due to Thrust Buildup and Liftoff Transients. Thrust buildup and liftoff transients cause longitudinal oscillations of the vehicle. Using a lumped-mass axial model of the vehicle, loads induced in the payload are calculated by obtaining the modes of vibration of the model and applying the thrust buildup and liftoff transients as generalized forces.

#### 11.2.6.2 Booster Flight

11.2.6.2.1 Lateral Loads due to Wind Gusts. Lateral loads induced in the payload by wind gusts during booster operation are calculated using a modal analysis which treats the vehicle as an elastic body and takes into account the effects of possible fuel slosh and engine gimbaling.

11.2.6.2.2 Payload-Fairing Interference due to Wind Gusts. Relative deflection of the payload with respect to the fairing as a result of wind gusts is calculated using a modal analysis, which treats the vehicle as an elastic body, simulating the fairing as a separate branch, and also accounting for the effects of sloshing and engine gimbaling.

11.2.6.2.3 Lateral Loads due to Transonic Buffeting. Lateral loads induced in the payload by transonic buffeting are calculated using a modal analysis which treats the vehicle as an elastic body. The generalized force to be applied to the vehicle makes use of the power spectrum of the fluctuating pressures acting on the vehicle during transonic buffeting. The power spectrum data are obtained from wind-tunnel tests on a scale model of the vehicle.

11.2.6.2.4 Payload-Fairing Interference due to Transonic Buffeting. Relative deflection of the payload with respect to the fairing as a result of transonic buffeting is calculated using a modal analysis which treats the vehicle as an elastic body and simulates the fairing as a separate branch. As noted above, wind tunnel tests are necessary to obtain power spectrum data.

11.2.6.2.5 Longitudinal Loads due to Thrust Buildup and Decay Transients. Thrust buildup and decay transients of the boosters various stages cause longitudinal oscillations of the vehicle. Using a lumped-mass axial model of the vehicle, loads induced in the payload are calculated using a modal analysis.

#### 11.2.6.3 Staging and Separation

11.2.6.3.1 Fairing Separation and Clearance. Our analysis of separation of the payload fairing from the vehicle must determine the adequacy of the separation mechanism, assuring that there is no interference between fairing and vehicle as separation occurs. Rigid body techniques are utilized for this analysis. A separation test would be needed to verify the separation technique.

11.2.6.3.2 Payload-Booster Separation. An analysis of the separation of the payload from the booster must be performed to verify adequacy of the separation technique, primarily that there is no interference between payload and booster as separation occurs. Angular tipoff rates of the payload must also be calculated to determine that they are small enough to be overcome by the payload attitude control system. Rigid body techniques are utilized for these analyses.

11.2.6.3.3 Separation of Passive Warhead Cover (applies to electro-optical vehicle only). An analysis to determine adequate clearance of the passive warhead cover when it separates from the warhead is required. The analysis can treat the cover as a rigid body and can utilize momentum and energy techniques to verify that interference with the warhead will not occur. Since the separation mechanism utilized for this cover is somewhat unusual, a test is needed to verify its adequacy.

11.2.6.4 Deployment

11.2.6.4.1 Planar Antenna Deployment (applies to radar vehicle only).

An analysis is required to determine loads induced in the planar antenna due to deployment. Energy techniques can be used to approximate the forces which the adjustable stops apply to the antenna elements. These forces are then used in a modal analysis to calculate the loads induced in the antenna. Deployment tests are required to determine adequacy of the deployment scheme.

11.2.6.4.2 Attitude Control System Deployment (applies to electro-optical vehicle only). An analysis is required to determine loads induced in the attitude control system booms due to deployment. The method used for the analysis is similar to that of 11.2.6.4.1. Deployment tests are required.

11.6.2.5 Vehicle Maneuvers

11.6.2.5.1 Loads due to Vehicle Maneuvers. The various maneuvers which the interceptor can accomplish impose angular and axial accelerations on the vehicle. Because the vehicle is flexible, these accelerations excite the natural frequencies. Hence, a modal analysis which treats the interceptor as an elastic body is necessary to calculate loads in the vehicle. Engine plume impingement must be considered when the loads are calculated.

11.6.2.5.2 Deflections due to Vehicle Maneuvers. Because several of the vehicle components, for example, the antenna and the attitude control system booms, are quite flexible and because oscillations of these components beyond certain limits seriously affects the interceptors proper operation, a modal analysis is required to calculate deflections caused by vehicle maneuvers.

The problem areas and the overall approaches to solution of the problems for 11.6.2.5.1 and 11.6.2.5.2 are the same for both types of vehicles. However, the electro-optical vehicle with its inflatable structure is somewhat more difficult to analyze, the reason for this being that modal analysis of a structure, a portion of which is inflatable, could become a state-of-the-art matter.

#### 11.2.7 Thermal Considerations

A brief investigation of the internal thermal problems of the subject vehicles indicated that the passive technique of the equipment absorbing its own dissipated energy would be adequate to hold allowable temperatures. Short vehicle life from launch to intercept justifies this thermal control technique. Prelaunch conditioning can be used to avoid overheating on the launch stand and internal insulation can be used to eliminate adverse heating during boost.

Thermally, the two homing stages considered are similar except for different tracker components. For the radar vehicle the radar equipment replaces the camera and camera control unit of the electro-optical vehicle. Special provisions for radar klystron cooling are included in the radar equipment and weigh approximately 8 pounds. No special camera cooling requirements are known to exist. The temperature rise results shown in Table 11-6 are based on the assumption that the heat dissipating component absorb the energy uniformly throughout its mass. Internal hot spots were not investigated since the assumption that the component can achieve adequate internal thermal coupling appears valid. It was further assumed that the mass of the vehicle, extraneous of the component, was not available as a heat sink.

The operation of the vehicle is assumed to require warm-up of the electronic systems such that steady state temperatures are achieved before launch. Aerodynamic heating effects would be eliminated by insulating the components singly or in groups. The temperature sensitive equipments would therefore be made thermally independent of their surroundings, and subject only to their own heat dissipation. With the temperature rise of each component fixed by its power, time of operation, and thermal capacity it is necessary only to pick an upper allowable temperature limit based on

the most critical component. The digital computer has the largest temperature rise ( $35^{\circ}\text{F}$ ) and would have a high reliability if its mean temperature were around  $120^{\circ}\text{F}$ . A prelaunch conditioning air temperature of  $70^{\circ}\text{F}$  with corresponding equipment temperatures of about  $80^{\circ}\text{F}$  would result in  $115^{\circ}\text{F}$  mean temperature of the computer and temperatures ranging from near  $80^{\circ}\text{F}$  to  $95^{\circ}\text{F}$  for the remainder of the components at the end of a maximum of 30 minutes mission time from launch. The one close temperature tolerance requirement is that of the camera unit with a  $\pm 5^{\circ}\text{C}$  limit about any design point between  $0^{\circ}$  and  $55^{\circ}\text{C}$ . Table 11-7 shows a  $+5^{\circ}\text{F}$  ( $2.8^{\circ}\text{C}$ ) increase after starting from the prelaunch conditioning temperature of say  $80^{\circ}\text{F}$  ( $25^{\circ}\text{C}$ ).

The provisions for temperature control, therefore, consist of the prelaunch conditioning and insulation to eliminate adverse thermal effects from the vehicle.

### 11.3 HOMING STAGE WITH ELECTRO-OPTICAL TRACKER

#### 11.3.1 General Description

The electro-optical homing stage is a cylindrically shaped vehicle approximately two feet in diameter and 7 feet long equipped with a body-fixed variable thrust engine. (Figure 11-1 and 11-37). A divided spherical propellant tank equipped with positive expulsion devices contains the Aerozine fuel and  $\text{N}_2\text{O}_4$  oxidizer. The electronic equipment is mounted on panels surrounding the main engine. A toroidal tank, mounted immediately below the propellant tank, contains  $\text{N}_2$  at 4000 psia which serves as the propellant pressurant, warhead inflation gas and yaw control thruster gas. A pressure regulator maintains pressurant at 480 psia to supply the main engine tank and yaw nozzles.

The vehicle's outer shell which extends from the boost vehicle adapter to the propellant tank, serves to carry the primary loads which are maximum at booster burnout. A conical superstructure above the propellant tank supports the girded platform on which the acquisition and tracking camera is mounted.

The four yaw control nozzles which operate on  $\text{N}_2$  are mounted on the vehicle's upper cylinder structure. The two hot gas pitch engines are mounted on the vehicle's outer shell near the main engine nozzle exit.

Table 11-7. Components Temperature Rise

Item	Power (watts)	Time (min)	Energy (Btu)	$W_c^*$ Btu/°R	$\Delta T$ °R	$\Sigma \Delta T$ °R	Location
<u>Electro-Optical Vehicle</u>							
** Camera ** and gyros	10 25.5	26 4	14.8 5.8	21(.15) 21(.15)	4.6 1.8	6.4	On platform
Gimbal torquers, inner ring	25	4	5.7	6.5(.15)	5.8	5.8	Inner gimbal ring
Gimbal torquers, shell	50	4	11.4	8.5(.15)	8.8	8.8	Outer gimbal ring
Digital computer	61	30	104.0	20(.15)	34.8	34.8	Around engine
Digital gear	10	30	17.0	10(.15)	11.3	11.3	
Camera control unit**	15	30	25.6	12(.15)	14.2	14.2	
ACS	6	30	10.2	5(.15)	13.6	21.2	
ACS	25	4	5.7	5(.15)	7.6		
<u>Radar Vehicle</u>							
Radar unit	6850	3	(cooled with 8 pounds of cooling provisions)				
Remainder of units same as Configuration A, above, minus camera and camera control.							

Note:  
Weight used is that thermally coupled with the energy dissipated.

\* Specific heat of equipment assumed to be 0.15 Btu/lb °R.

\*\* Not in Configuration "B"



Special provisions were necessary to stow and deploy the roll engines to avoid interaction of their plume with the inflated warhead. These engines are mounted on arms that permit stowing the engines inside the main engine nozzle until separation from the booster at which time they deploy and lock in position outboard of the main engine. Their line of thrust is away from the warhead to avoid flame impingement on the inflated structure.

A summary of vehicle subsystem parameters follows:

**Lifetime**

Coast Period	10 min max
Tracking Phase	90 sec max
$\Delta V$ Requirements	4000 ft/sec
Envelope Volume	33 ft <sup>3</sup>
Thrust to Weight Ratio	6

**Weights**

At Ignition	594.5
At Burnout	397.3
Payload	160.6

**Mass Moments of Inertia (At Ignition)**

Roll	115
Pitch	93
Yaw	35

**Structural Materials**

Primary	Magnesium
Tanks	6Al-4V Titanium

Thermal Control Techniques	Passive
----------------------------	---------

**Main Engine**

Type	Liquid Bipropellant
Throttling	10/1
Mounting	Body Fixed
Nozzle Cooling	Ablative
Chamber Pressure	400 psia
Fuel	Aerozine
Oxidizer	N <sub>2</sub> O <sub>4</sub>
Feed System	Pressure

Pressurant	N <sub>2</sub> Stored at 4000 psi	
Propellant tank pressure	500 psia	
I <sub>SP</sub>	315	
Expansion Ratio	50	
Thrust, Vacuum	3600 lb	
Vehicle Stabilization		
Type	Attitude Controlled	
Thruster Fuel		
Roll	Aerozine-N <sub>2</sub> O <sub>4</sub>	
Pitch	Aerozine-N <sub>2</sub> O <sub>4</sub>	
Yaw	N <sub>2</sub> Cold Gas (Propellant Pressurant)	
Thrust Levels and Lever Arms	Thrust, lb	Lever Arm, ft
Roll	55	4.2
Pitch	43	2.1
Yaw	5	0.9
Number of Thrusters		
Roll	2	
Pitch	2	
Yaw	4	

The following preliminary operational sequence serves as an additional vehicle descriptive aid:

- Jettison Fairing at about 300,000 ft altitude
- Uncage all gyros just prior to booster burnout
- Staging sequence
  - Initiate booster cutoff
  - Disconnect electrical circuits between booster and homing stage
  - Stage with shaped charge when thrust decays to zero
- Deploy Roll control engines
- Activate all ACS engines
- Initiate warhead deployment sequence (see Chapter 10 for details)
- Coast period—fully attitude controlled
- Initiate turns for vehicle reorientation
- Uncage stabilized platform

- Perform acquisition tasks
- Initiate angle tracking mode
- Activate homing stage engine
- Proceed with homing phase
- Target intercept

### 11.3.2 Vehicle Physical Properties (Electro-Optical Homing Stage)

The ground rules and the results of a detailed vehicle weight and mass properties analysis of the homing stage equipped with an electro-optical acquisition and tracking subsystem are presented in this section. This vehicle utilizes an unfurlable, passive kill mechanism consisting of pellet-embedded membranes stretched tight by an inflated torus extending to a 16 ft diameter which was discussed in detail in Chapter 10. The subject homing stage appears in Figure 11-37.

The estimated weights summary appears in Table 11-8 and includes a 5 percent contingency to account for weight growth. The ground rules for this study are delineated below.

#### 11.3.2.1 Structure and Temperature Control Subsystem

The basic structural elements are sheet metal, extruded sections, rolled rings and some use of sandwich structure. Gauges for all items are based on the results of the preliminary stress analysis. No specific provisions were necessary for temperature control or heat shielding.

#### 11.3.2.2 Payload

The inflated kill mechanism for this vehicle is a 0.007 inch wall thickness Mylar torus with a 172 inch major diameter and a 20 inch minor diameter weighing 18.5 pounds. The two double Mylar membranes across the major diameter weigh about 6 pounds and contain about 3 pounds of steel pellets. About 3.4 pounds of  $N_2$  at 5.7 psia are required to inflate the warhead.

Table 11-8. Summary Weight Statement Elector-Optical Homing Stage

<b>PAYLOAD</b>			<b>149.7</b>
<u>Warhead</u>			<b>47.7</b>
Torus, Membranes, and Pellets		28.7	
Support Structure		12.0	
Retainer		7.0	
<u>Gimbaled Platform Assembly</u>			<b>28.1</b>
Platform		16.2	
Camera w/optics	13.0		
Gyros (3)	2.7		
Gyros support	0.3		
Camera yoke	0.2		
Gimbal-yaw		3.7	
Ring	1.6		
Torquer	0.9		
Resolver and Trim Weight	0.9		
Bearings	0.3		
Gimbal-pitch		3.7	
Yoke	1.6		
Torquer	0.9		
Resolver and Trim Weight	0.9		
Bearings	0.3		
Gimbal-roll		3.3	
Structure	1.2		
Torquer	1.2		
Resolver	0.3		
Bearings	0.6		
Flex Leads		1.2	
Platform Control Electronics			6.0
Attitude Control System Electronics			3.7
Camera Control Unit			16.0
Digital Guidance Computer			27.0
Integrated Power Supply			8.0
Batteries	4.0		
Electronics	4.0		
Junction Boxes and Intercabling			10.0
Supports and Hardware			3.2
<b>HOMING STAGE</b>			<b>331.3</b>
Propellant Tank Assembly		27.5	
Propellant Plumbing System		11.0	
Propellant - Impulse		189.7	
Propellant - Residual		5.9	
Engine		38.0	
Pressurization Tank N <sub>2</sub>		21.8	
Pressurization Gas N <sub>2</sub>		16.4	
Pressurization Plumbing		5.0	
Attitude Control Engines w/Valves, Lines and Brackets		16.0	
<b>STRUCTURE</b>			<b>88.0</b>
Attitude Nozzle Booms (2)		10.0	
Stage Structure		78.0	
<b>Total</b>			<b>569.0</b>
<b>RECOMMENDED CONTINGENCY 5 PERCENT</b>			<b>28.4</b>
<b>VEHICLE GROSS WEIGHT</b>			<b>597.4</b>

### 11.3.2.3 Tanks

Tank weights were computed for a tank pressure of 480 psia, which is 80 psia above main engine chamber pressure. The propellant tank is made of 6A-4V Titanium. The expulsion device weight estimate is based on BAMBI (Reference 5) experience and proportioned by spherical surface area.

Propellant weight was calculated to provide a vehicle  $\Delta V$  of 4000 ft/sec. In addition, 7.5 percent has been added to propellant weight for hot gas attitude control, and 3 percent for expulsion efficiency. Excess tank volume of 9 percent for volumetric efficiency has been allowed. Table 11-9 shows a detailed propellant tank weight statement.

Table 11-9. Propellant Tank Weight Summary

<u>Item</u>	<u>Weight - (lb)</u>
Spherical Shell	5.76
Flanges (2)	6.82
Bolts (72) 1.0" grip	4.03
Partition (0.010 Aluminum)	0.46
Expulsion Devices	4.20
Flanges for Expulsion Devices and Partitions (4) 0.1" Aluminum	4.32
Bosses, Welds, and Contingency	<u>1.92</u>
Total	27.5 lb

Nitrogen tanks are sized to contain enough nitrogen to inflate the warhead and pressurize the propellant tanks as well as supply the yaw control thrusters. Volume for  $N_2$  is based on storage at 4000 psia. Tanks are Titanium. Calculation indicated gauges of 0.094 and 0.092, so the next larger standard gauge of 0.100 was used for weight calculation.

Table 11-10. Nitrogen Tank Weight Summary

<u>Item</u>	<u>Weight - (lb)</u>
Toroidal Shell (0.100 Gauge)	20.3
Bosses, Welds, and Contingency	<u>1.5</u>
Total	21.8 lb

#### 11.3.2.4 Engines

Engine weight of 38 pounds includes all valves and manifolding. Propellant lines are included in the propellant plumbing system.

Major engine design criteria are shown below:

$$D_e = 24 \text{ inch}$$

$$P_c = 400 \text{ psia}$$

$$F = 3600 \text{ pound}$$

$$t_b = 16 \text{ sec (min)}$$

$$\epsilon = 50$$

$$I_{sp} = 315$$

Propellants :  $N_2O_4$ /Aerozene

Mixture Ratio = 1.6 to 1

Throttle Ratio = 10 to 1

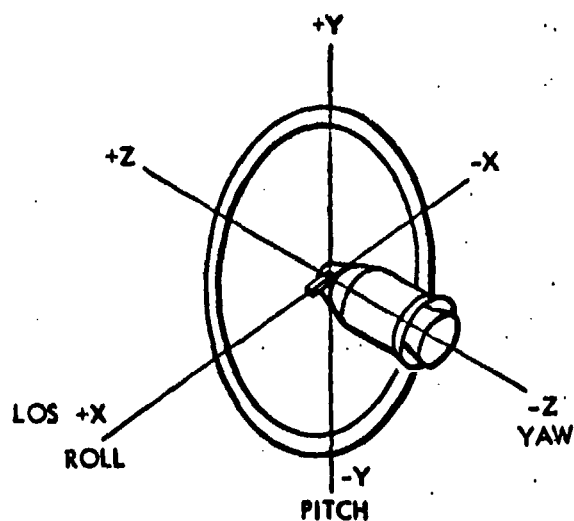
The attitude control subsystem consists of the two hot gas roll and two pitch control engines and four cold gas yaw thrusters. Valves, plumbing and mounting brackets are also included. The basic items appear in Table 11-11.

Table 11-11. Major Attitude Control Subsystem Items

<u>Item</u>	<u>Weight (lb)</u>
Roll Engine (2) (w/valves)	6.2
Pitch Engines (2) (w/valves)	4.4
Yaw Thrusters (4) (w/valves)	0.8
Plumbing, brackets, etc.	4.4
Total	16.0

Table 11-2 shows center of gravity location and moments of inertia which were computed on the basis that all items shown in Figure 11-37 are homogenous bodies. Structural weights were distributed generally as shown in Figure 11-37. Properties at engine ignition and burnout were determined to show possible shifts in center of mass during engine operation. The indicated location of center of gravity along the yaw axis could be eliminated on the next design iteration.

Table 11-12. Mass Properties of Electro-Optical Homing Stage



Properties of Vehicle at Ignition

<u>Weight (lb)</u>	<u>Center of Gravity</u>			<u>Inertia About Center of Gravity (slug ft.<sup>2</sup>)</u>		
	X	Y	Z	X-X	Y-Y	Z-Z
590.4	0.0	-0.3	42.9	115	93	35

Properties of Vehicle at Burnout

<u>Weight (lb)</u>	<u>Center of Gravity</u>			<u>Inertia About Center of Gravity (slug ft.<sup>2</sup>)</u>		
	X	Y	Z	X-X	Y-Y	Z-Z
387.7	0.0	-0.4	41.5	115	90	35

### 11.3.3 Attitude Control Subsystem

The homing stage attitude control subsystem is designed to provide muscles for vehicle stabilization during the coast period, vehicle re-orientation at target acquisition and attitude control during homing. All functions are satisfied by one subsystem consisting of two roll engines, two pitch engines, and four yaw thrusters. Hot gas engines, fed from the main propellant supply, were selected for the roll and pitch function. Yaw control, which requires a much lower torque, is satisfied by 4 cold gas thrusters fed from the  $N_2$  pressurant gas supply.

Design criteria for the attitude control subsystem are summarized in Table 11-13. Engine locations and arrangement are shown in Figure 11-1 and 11-37. The roll engines were necessarily deployed to avoid flame impingement on the inflated warhead. These engines are deployed immediately following separation from the boost vehicle and prior to warhead deployment. All control engines are then activated to provide immediate vehicle stabilization.

The roll engine thrust level was established by an angular roll acceleration requirement of 2 radians/sec<sup>2</sup>. The pitch engines were sized to overcome the disturbance torque emanating from an estimated thrust vector to center of gravity offset of 0.01 ft (3 sigma value). The yaw thrust requirements are estimated to be an order of magnitude less than the pitch torque. Engine design is discussed in Section 11.2.5 of this chapter.

Table 11-13. Reaction Control Subsystem Design Criteria Homing Stage W/Electro-Optical Tracker

	<u>Roll</u>	<u>Pitch</u>	<u>Yaw</u>
Required Torque (ft lb) <sup>1</sup>	230	90	9
Thruster Lever Arm (ft)	4.2	2.1	1.8 <sup>2</sup>
Engine Thrust (lb)	55	43	5 <sup>3</sup>
Homing Phase (seconds)	90	90	90
Total Energy (ft-lb-sec)	8000	3300	500
Total Impulse (lb sec)	1900	1800	280
Limit Cycle Frequency (cps)(max)	--	8	8

<sup>1</sup>Established in Chapter 5

<sup>2</sup>Couple lever arm (two thrusters)

<sup>3</sup>Each Thruster



#### 11.3.4 Power Supply

A preliminary estimate of power requirements appear in Table 11-14. The total requirements are estimated at 85 watt hours which are consumed at a low standby rate for approximately 26 minutes and at a peak rate for about 4 minutes. This type of operation is typical of ballistic missile requirements and also resembles the STL BAMBI homing stage power subsystem requirements reported in Reference 4. Silver-zinc batteries, which are low in weight and capable of high discharge rates, have been used extensively in such cases and have been selected for this application. Battery weight estimates were based on a conservative rating of 30 w-hr which is assumed to include battery activation mechanism and electrolyte. Since these batteries have a short activated life measured in terms of hours, activation is not initiated until just prior to launch. Activation is accomplished automatically by squib and is completed in about 2 seconds. Converter and inverter weight estimates, were based on previous experience, scaled in proportion to the total power requirements.

Table 11-14. Electric Power Requirements for Electro-Optical Homing Stage

Unit	Electric Power Requirements		
	26 Min	4 Min	Total (W-Hr)
Camera Unit Plus Optics and Shielding		20.5	3.54
Gyros	5.0 <sup>(1)</sup>	5.0	2.50
Platform Torquer (yaw)	0	10 <sup>(2)</sup>	0.67
Platform Torquer (pitch)	0	10 <sup>(2)</sup>	0.67
Platform Torquer (roll)	0	56	3.73
Platform Control Electronics	5	5	2.50
Attitude Control Electronics	6	25	4.26
Camera Control Unit	10	25	10.36
Digital Guidance Computer	70	70	35.0
Integrated Power Supply Electronics	5	5	2.50
Main Engine		129	8.6
Attitude Control Engines			
Roll	6 <sup>(3)</sup>	30	4.6
Pitch	6 <sup>(3)</sup>	30	4.6
Yaw	3 <sup>(3)</sup>	15	2.3

(1) Includes 20 watt intermittent heaters

(2) 35 watt peak

(3) 20 percent duty cycle assumed

85.8

### 11.3.5 Gimbaled Electro-Optical Tracker

The acquisition and tracking subsystem consists of an orthicon camera mounted on a gimbaled platform. Associated electronics, gyros, etc., are either body mounted on the vehicle or mounted on the platform. A platform with three degrees of freedom is required to satisfy the selected vehicle guidance technique which depends on angle tracking data to establish the direction and magnitude of commanded thrust. The platform mechanical design requirements are governed by this target tracking technique and the vehicle attitude control requirements, as established in Chapter 8 as well as vehicle configuration and anticipated loads. These criteria are summarized below:

- Roll freedom (around the tracker LOS) of  $\pm 360$  degrees minimum
- Pitch and yaw freedom of  $\pm 6$  degrees minimum
- Vehicle acceleration along the yaw axis during tracker operation of 6 g's. (Maximum design limit load.)
- Angular acceleration of the vehicle around the LOS  $\sim 2 \text{ rad/sec}^2$
- A mechanical gimbal lock during the boost phase (15.4 g's max.) to avoid excessive torquer loads
- Resonant frequencies of the gimbal structure of about 200 cps
- Life of 30 minutes maximum in a space environment
- Pitch and yaw axis inboard of the roll bearings to avoid trigonometric transformation during roll maneuvers

The selected design takes advantage of a conventional gimbaled platform approach using a three-axis, bearing-mounted gimbal system as shown in Figure 11-43 and 11-44. The gimbal order from inside-out is yaw, pitch and roll. The stabilized platform consists of the orthicon camera with optics as described in Chapter 6.

Three mutually perpendicular, wide angle, miniature integrating (IMIC) gyros are mounted on a three axis support bracket attached to the base of the camera. The inner gimbal ring contains the yaw axis bearings, torquer and resolver and the fore and aft supports contain the roll axis

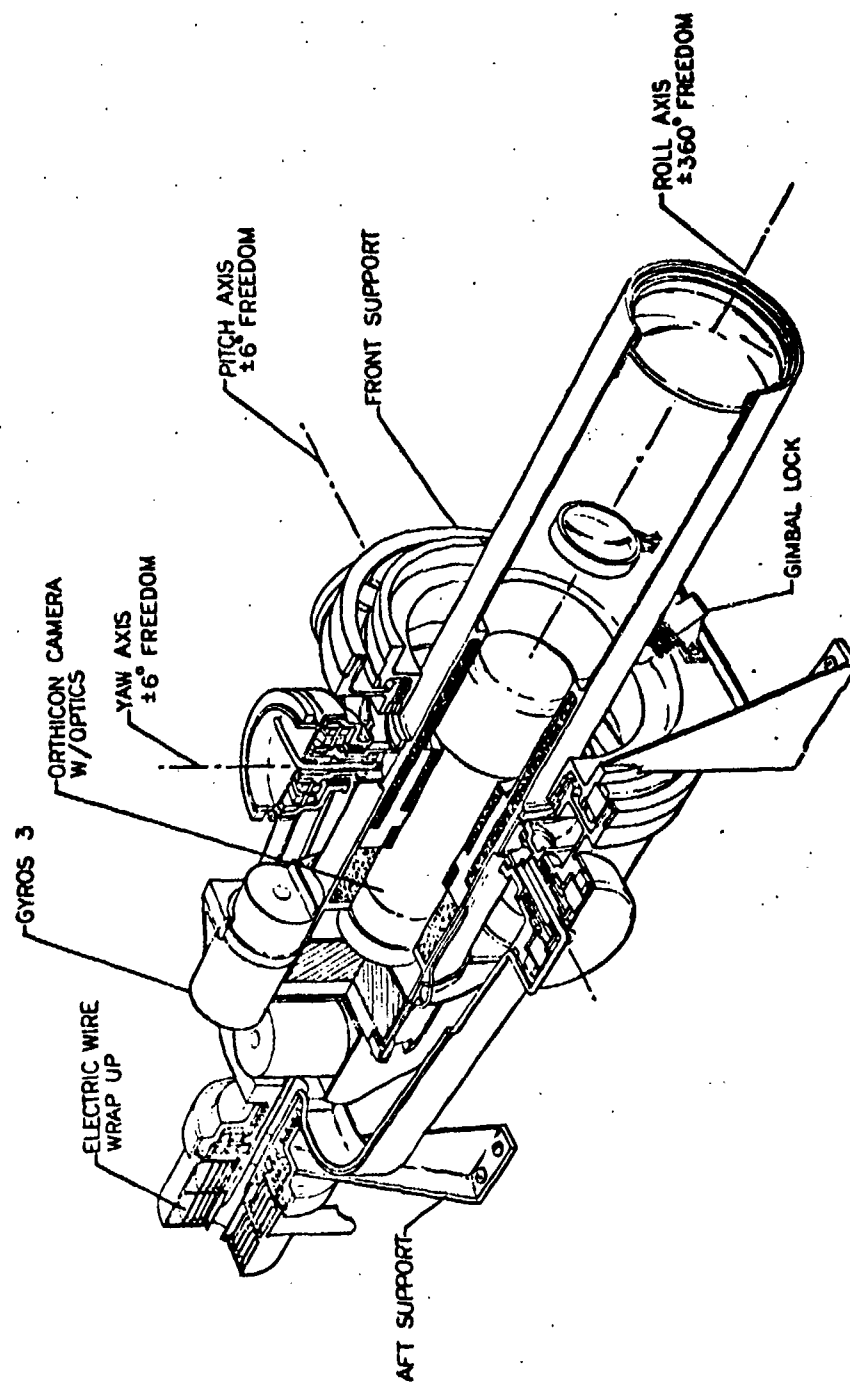
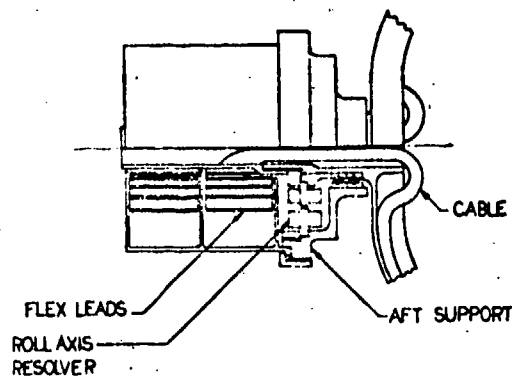
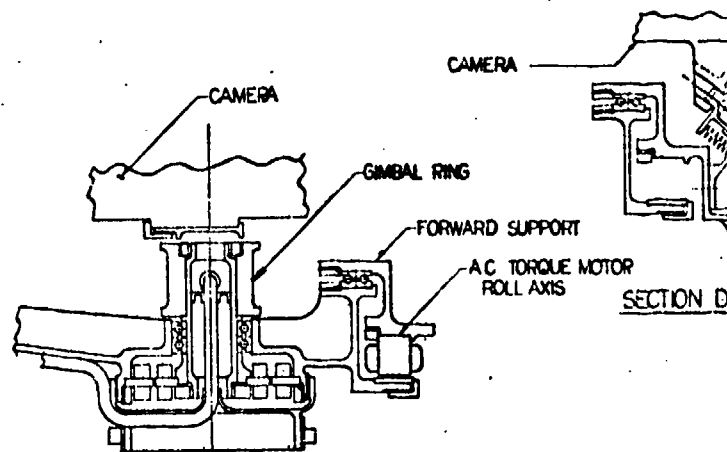


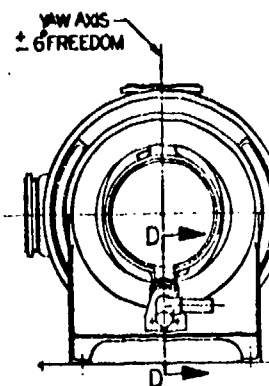
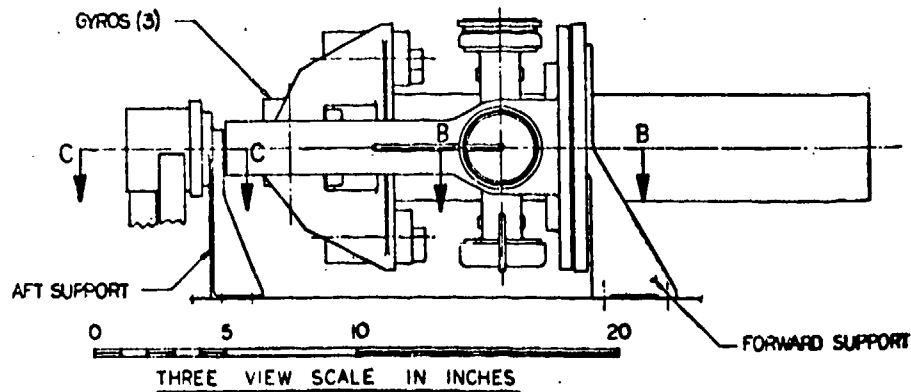
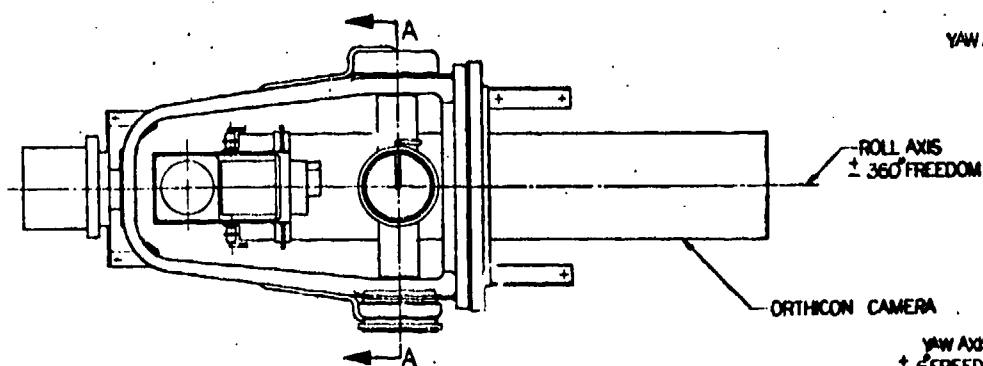
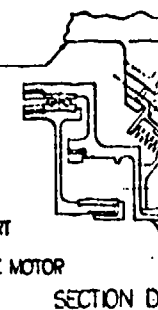
Figure 11-43. Gimbal Platform Perspective—Electro-optical Tracker



SECTION C-C



SECTION B-B



1

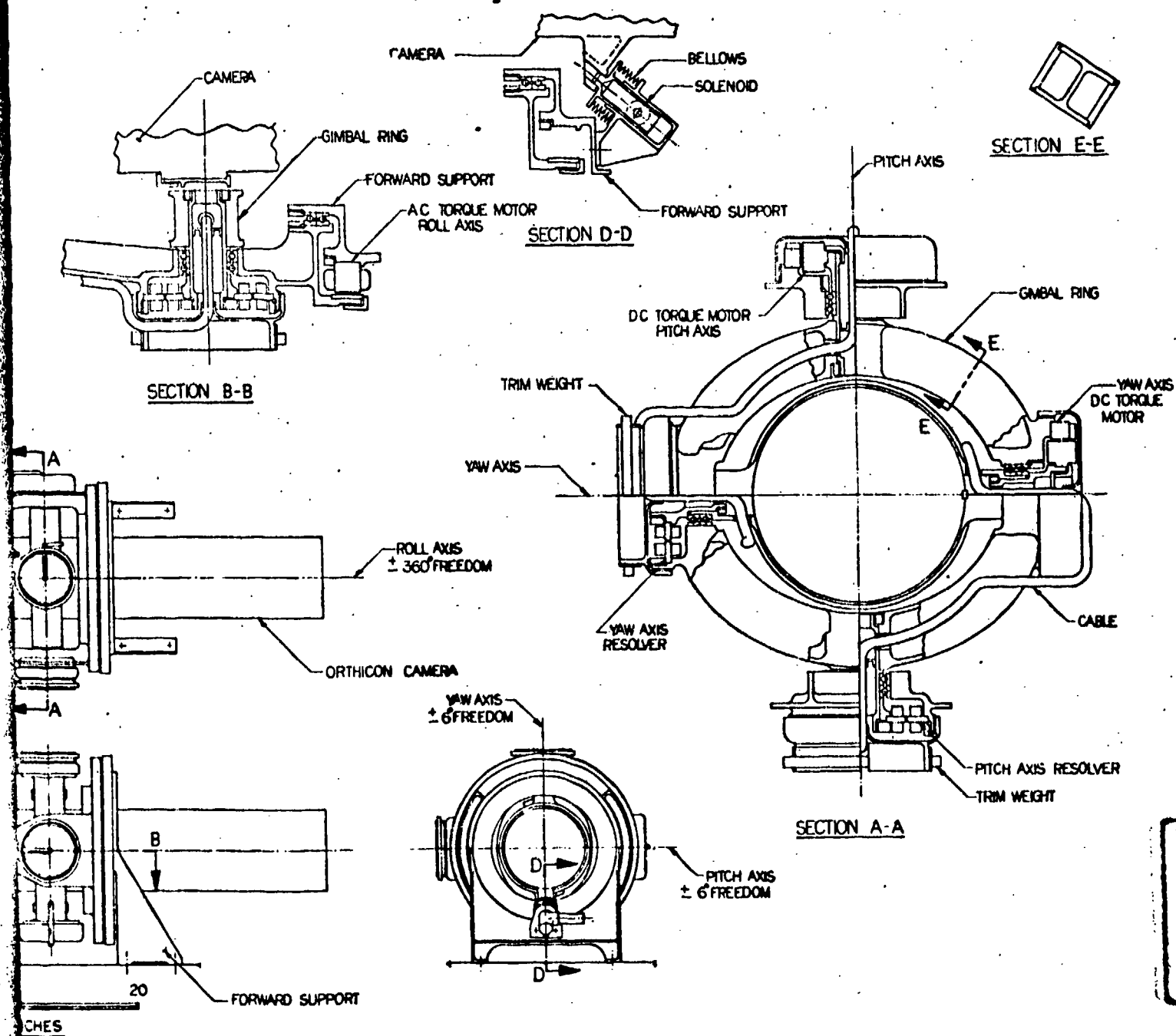


Figure 11-44. Gimbal Platform—Electro-optical Tracker

bearings, torquer and resolver. All structural elements, such as the gimbal ring and yoke, are made of beryllium for maximum stiffness to weight ratio and maximum thermal stability.

The electrical connection between the stabilized platform and the vehicle is through two flex leads each containing approximately 30 electrical wires. The platform is securely locked to the craft during boost when high g loads are encountered. An electric solenoid released locking mechanism is used as shown in Figure 11-44. The unit is hermetically sealed with a bellows held in tension until released by the solenoid operated trigger, permitting the mechanism to retract thereby freeing the platform about all three axes.

#### 11.3.5.1 Bearing Selection and Design

The selected bearings are large bore, extra thin, deep groove roller bearings which are designed for duplex mounting in preloaded pairs to provide high rigidity and low friction torque. The bearing arrangement is identical for all three axes, in that axial expansion is accommodated by allowing one duplex pair to float in the housing.

##### Bearing Loads

###### Yaw Axis

Initial Platform Weight

Camera 13.0

Gyros 2.7

Support Structure 0.3

Miscellaneous 0.98

Total 16.98 lb + 10 percent

= 18.68 lb

###### Pitch Axis

Initial Platform Weight = 18.68 lb

Gimbal Ring + Miscellaneous = 2.3 lb + 10 percent = 2.53 lb

21.21 lb

###### Roll Axis

Platform + Gimbal Ring, etc. = 21.21 lb

Yoke Fitting + Miscellaneous + 10 percent = 3.79 lb

25.00 lb

Forward Bearing takes 20.7 lb radially

Rear Bearing takes 4.3 lb radially

The design ultimate accelerations are:

Boost Phase (Bearings static)	20 g's axial
	1-1/4 g's lateral
Homing Phase (Bearings Operative)	7-1/2 g's axial

Table 11-15. Bearing Design Loads Summary

Bearing		*Static Lbs		*Running Lbs	
		Axial	Radial	Axial	Radial
Yaw		374	12	140	10(70)**
Pitch		27	212	22(160)**	80
Roll	Fwd	32	414	26	155
	Aft	0	96	0	33

\* Loads are per duplex pair

\*\* Loads in parenthesis occur when gimbal is rolled 90 degrees, i.e., when pitch axis parallels vehicle thrust axis.

#### 11.3.5.2 Bearing Preload

The preload designed into the duplex pairs must be optimized to give lowest starting torque in combination with the unbalance torques due to center of gravity shift resulting from axial or radial compliance in the bearings. The compliance (yield) rate of the bearings is decreased by increased preload which in turn increases the initial starting torque; hence, an optimum preload can be obtained which yield a minimum total torque as shown graphically in Figure 11-45.

The increment torques  $\Delta T$  varies linearly with the bearing yield rate (N), i.e.,  $\Delta T = CN$  where  $C = 17 \times 10^3$  in oz for yaw and  $C = 118 \times 10^3$  in oz for pitch.

One restriction to the above is that the bearing yield rate (inches/lb) be kept below a certain level to avoid jeopardizing the platform natural frequency. The bearings are of isoelastic design in that the yield rate (N) is the same for both radial and axial loads.

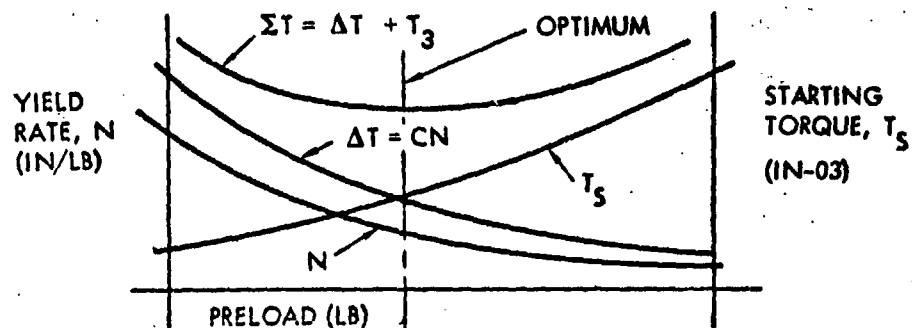


Figure 11-46. Starting Torque Versus Bearing Preload

For the design study the bearing preloads were arbitrarily set at 50 pounds which resulted in the following starting torques:

Yaw and Pitch axis bearings	6.6 in oz per pair
Roll axis bearings	8.0 in oz per pair

These torques were supplied upon request from bearing manufacturers and assumed oil lubrication.

#### 11.3.5.3 Lubrication

Due to the short platform life requirements in the spare environment, the bearings can use conventional oil or grease lubricants in conjunction with a labyrinth seal. Justification for this approach is as follows:

- Outgassing of the lubricant would represent a problem only if particles deposited on sensitive elements such as on the camera lens. This is improbable due to the difficult geometric path between lubricant molecules and the lens. The molecules would have to bounce to attach themselves to the lens face. Even if some molecules were to take such a path, it is improbable that there would be critical deposition in the 30 minutes maximum operating period.
- Plated races and balls, which might offer an alternate approach, tend to give increased ball race diameters and increased breakout torques.
- The oiled bearings is much smoother in operation than plated races and balls. Burnished MoS<sub>2</sub> coatings and gold plated balls, another alternate, tend to have peaked torque levels.



#### 11.3.5.4 Platform Natural Frequency

Of major concern in the design of a gimbaled platform, is the inherent structural resonant frequency. It is desirable to maintain a minimum resonant frequency from five to ten times greater than the maximum platform limit cycle frequency which, in this case, is estimated to be approximately 20 cps (Reference Chapter 5). An approximate natural frequency for the platform is given by:

$$F_N = \frac{1}{2\pi} \sqrt{\frac{g}{\sum \delta}}$$

Where  $\sum \delta$  is the summation of static deflections under a one g acceleration field.

Consider bending stiffness in the plane of the gimbal ring (Normal to the camera roll axis). The major deflections ( $\delta$ ) under one g are:

	<u>Inches</u>
Axial deflection of yaw axis bearings	0.000140
Deflection of gimbal ring	0.000020*
Radial deflection of pitch axis bearings	0.000070
Deflection of roll axis fitting	0.000035
Radial deflection of roll axis bearings	<u>0.000131</u>
$\sum \delta$	0.000396

\* Based on an "I" section one inch high x 1.5 inches wide x 0.06 inch thickness.

$$F_N = \frac{1}{2\pi} \sqrt{\frac{386}{0.000396}}$$

157 cps

The above deflection estimates are based on the following ground rules:

- Yield rate in all bearings is assumed to be 7 micro inches per pound both axially and radially.
- Structural material is beryllium
- The deflection of the inner platform (camera barrel and yoke) is negligible.

Because of high torsional deflections, the above "I" section does not provide sufficient gimbal ring stiffness normal to the plane of the ring; hence, a box section (1.5 x 1.0 x 0.06) was selected. As noted in Table 11-16, an equivalent stiffness could be obtained with an increased "I" section at the cost of about 0.5 lb as compared to the above box section. Though structurally inefficient as a torsional member, the heavy "I" section can be readily obtained by conventional machining from a solid block. The box section, however, requires the use of a bolted, brazed, welded or bonded joint to close out the cross section.

Table 11-16. Gimbal Ring Resonant Frequency Summary

	Natural Frequency $F_N$ in cps	
	In the plane of the ring	Normal to the plane of the ring
"I" Section (1.5 x 1 x 0.06)	157	Unacceptable
"I" Section (Beefed-up) (1.5 x 1 x 0.25)	> 157	156
Box Section (1.5 x 1 x 0.08)	> 157	163
Box Section (1.5 x 1 x 0.08)	> 157	175
Infinity Stiff Gimbal Ring	165	183

A bonded joint was selected since beryllium bonding techniques are well established with joint strengths of 10,000 psi readily obtainable. Since stiffness is the design criteria for this part, actual stresses in the part are probably an order of magnitude below this level; therefore, confidence in the design is not degraded by the use of a bonded structure. Conventional quality control techniques can insure a highly reliable structural element.

The major portion of the spring rate of the platform in any direction is contributed by the bearings. If increased stiffness is required, improvement can be obtained through a bearing redesign.

#### 11.3.5.5 Electrical Flex Leads

The anticipated wiring budget for the platform is as follows:

	<u>Number of wires</u>	<u>Gage</u>
Camera	18	24*
Gyros	27	24
	2	22
DC Servos	4	24
Resolvers	<u>10</u>	30
Total	61	

\* Two of these wires must be shielded.

For the pitch and yaw axis the flex leads rotate through  $\pm 6$  degrees. This simplifies the flex lead design since a straight torsional cable can be used as shown on Figure 11-44. To balance the cable weights on the platform, the cable is split into two branches and wired symmetrically as shown.

Approximate torque figures have been obtained for this configuration by the use of a simple model made of 28 - No. 24 gage wire with 1-1/2 inches free length. The result obtained was 1-1/4 in oz torque for 6 degrees of movement. This gives a total of 2.5 in oz torque around the pitch or the yaw axis.

The flex lead configuration for the roll axis is in the form of opposed spiral springs. This type of flex lead is proposed due to its compactness and small variations in torque over the extreme roll movement of  $\pm 360$  degrees. The concept is shown on Figure 11-43 and diagrammatically in Figure 11-46.

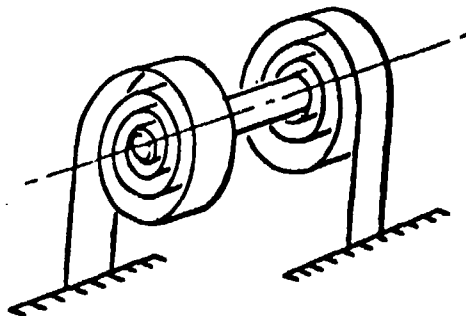


Figure 11-46. Electric Lead Wrap-up

The electrical cable is transformed into two flexible bands, one wire thickness and approximately one inch wide. This can be achieved by either bonding together standard insulated wires or by etched circuits on mylar film. Theoretically, as the spring force of the wire wraps are opposing each other, the torque required for movement is zero, providing that the spring rate remains constant as in Figure 11-47, and that the springs are preloaded.

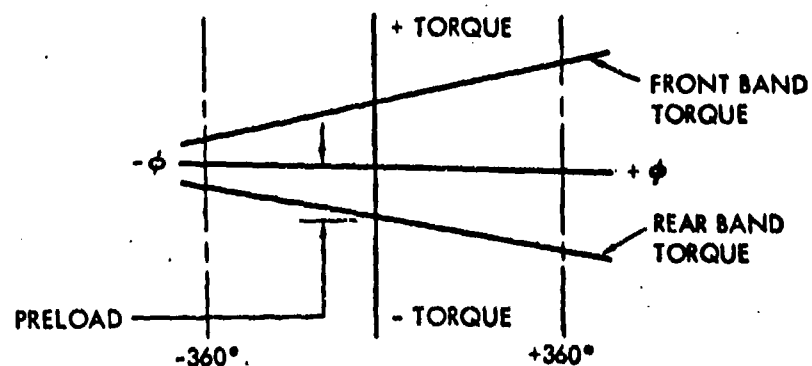


Figure 11-47. Lead Wrap-up Versus Torque

However, as the spring rate will change and since hysteresis effects are unknown, it is proposed to use 50 percent of the torque required to rotate one of the bands through 720 degrees. This was found to be 2.80 in oz by a simple test using conventional insulated 24 gage wires. It should be noted that these figures are preliminary and that further substantiation would be required for any hardware application.

#### 11.3.5.6 Platform Inertia Orientation Torques

Platform inertias have been calculated and are as follows:

Yaw	25.1 oz in sec <sup>2</sup>
Pitch	26.5 oz in sec <sup>2</sup>
Roll	5.4 oz in sec <sup>2</sup>

The platform inertia torques are as follows:

11.3.5.6.1 Yaw Axis. The platform is to be reorientated about the yaw axis a maximum of 6 degrees in 1.2 sec with constant angular acceleration.

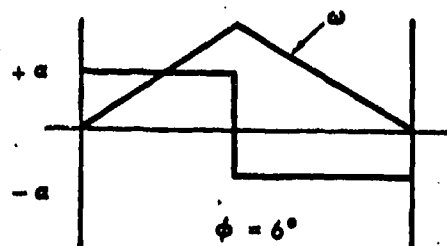


Figure 11-48. Platform Orientation Rate and Acceleration

For the velocity diagram as shown in Figure 11-48, angular acceleration  $a = 0.29 \text{ rads/sec}^2$ .

$$\text{Platform yaw torque} = I a = 25.1 \times 0.29 = 7.29 \text{ oz in.}$$

11.3.5.6.2 Pitch Axis. Angular acceleration about the pitch axis is identical to that for yaw, i.e.,  $a = 0.29 \text{ rads/sec}^2$ .

$$\text{Platform pitch torque, } I a = 26.5 \times 0.29 = 7.7 \text{ oz in.}$$

11.3.5.6.3 Roll Axis. Angular acceleration about the roll axis during the target acquisition mode is assumed to be identical to that of the above yaw and pitch axis tracking mode accelerations, i.e.,  $a = 0.29 \text{ rads/sec}$ .

$$\text{Platform roll torque} = I a = 5.4 \times 0.29 = 1.57 \text{ oz in.}$$

11.3.5.6.4 Thermal Center of Gravity Shift. The center of gravity of the camera moves along the yaw axis 0.00211 inches with respect to the platform when the camera, initially at room temperature, reaches its maximum operating temperature of  $55^\circ\text{C}$ . Assuming that the structure remains at room temperature, the incremental torque due to this center of gravity movement is approximately 0.7 oz in about the pitch and roll axis only. With the platform rolled 90 degrees, i.e., platform pitch axis parallel to the vehicle's thrust axis, a roll torque of approximately 3.0 oz in results from this offset.

11.3.5.6.5 Mass Unbalance. The platform will be dynamically balanced using trim weights as shown in Figure 11-44, i.e., threaded collars locked in position. More trim weights will be required than those shown, these being omitted from the drawing for clarity. The camera will be in the tracking mode during dynamic balancing of the platform to account for the center of gravity shift that occurs due to a camera lens shift from acquisition to the tracking mode. There will be other mass unbalance which cannot be trimmed out and are at present incalculable such as:

- o Variation of camera longitudinal center of gravity with temperature
- o Thermal warpage of gimbal rings due to unsymmetrical heating
- o Misalignments due to material creep, etc.

However, it is to be expected that the sum of these and other unknown effects will be small and by the use of a conservative factor applied to the values in Table 11-17 in sizing the torque motors these side effects can be ignored. It is felt that this reserve factor should be at least 1.5 or preferably 2 times the calculable torque requirements, which for a small weight penalty considerably increases the platform confidence level. Increased electric power requirements for the larger torquers are negligible because of the short operating time.

Table 11-17. Platform Torque Requirements Summary

Yaw Axis

Bearing friction	13.2 oz in
Reorientation torque	7.3 oz in
Flex leads	2.5 oz in
Servo friction	1.5 oz in
Total	24.5 oz in

Pitch Axis

Bearing Friction	13.2 oz in
Reorientation torque	7.7 oz in
Flex leads	2.5 oz in
Thermal center of gravity shift	0.7 oz in
Servo friction	1.5 oz in
Total	25.6 oz in

Roll Axis

Bearing Friction	13.0 oz in
Reorientation torque	1.6 oz in
Flex leads	2.8 oz in
Thermal center of gravity shift	3.0 oz in
Total	20.4 oz in

#### **11.3.5.7 Platform Assembly Procedure**

As an additional platform descriptive aid, the following assembly sequence is presented:

- Assemble camera supporting yoke to gimbal ring
- Install yaw axis bearings, torque motor, resolver, attach nuts and electric cabling.
- Assemble above subassembly to roll yoke fitting
- Install pitch axis shafts, bearings, torque motor, resolver, nuts and cabling
- Assemble gyros to their support structure and checkout their mutual alignment then install on camera
- Assemble camera subassembly to supporting yoke; make electrical connection.
- Install forward and aft support assemblies complete with torque motors, bearings, resolvers, locking mechanism and cabling.
- Assemble flex lead assembly
- Proceed with dynamic balancing, proof test, etc.

## 11.4 HOMING STAGE WITH RADAR TRACKER

### 11.4.1 Vehicle Description

The radar equipped homing stage which appears in Figures 11-2 and 11-38 is similar to the electro-optical homing stage in many respects and, in fact, shares many common subsystems such as the main engine, attitude control electronics, computer, etc. The vehicle, also interfaces with the booster in a similar fashion and uses the same fairing and a similar adapter. The use of a different tracking subsystem and warhead prompted the need for several subsystem changes and resulted in a vehicle weighing about 950 pounds which is about 350 pounds heavier than the electro-optical vehicle. Other differences appear in the vehicles upper structure where major modifications were necessary to accommodate the radar components. Also, all attitude control engines are body mounted which was not possible on the other vehicle due to interaction with the unfurlable kill mechanism.

The acquisition and tracking subsystems differ completely from the electro-optical vehicle. A large (4 x 6 ft) planar array which is wrapped around the vehicle's outer shell in the stowed position and deployed after booster separation provides target illumination during the acquisition and subsequent tracking mode. A 16 inch diameter dish on a stable platform provides angle tracking data during the homing phase. A brief description of the antenna and gimbaled platform appears in Section 11.4.4.

To avoid duplication, only the subsystems and features peculiar to the radar vehicle will be discussed in this section with all other vehicle subsystems defined in Section 11.3. Comparison of vehicle outboard drawings, Figures 11-2 and 11-3 and the general arrangement drawings, Figures 11-37 and 11-38, are a further aid in establishing vehicle differences.

### 11.4.2 Vehicle Physical Properties

The ground rules for the detailed weight and mass properties analysis for this vehicle are identical to those stated in Section 11.3.2. The radar subsystem replaces the electro-optical subsystem used on the other vehicle and the unfurlable warhead is replaced by an internally mounted explosive warhead. A detailed weight summary appears in Table 11-18. Ignition

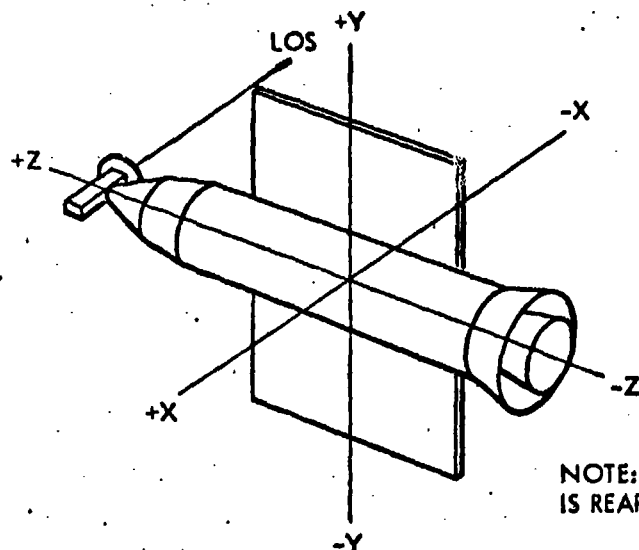


and burnout mass properties are summarized in Table 11-19. The indicated center of gravity offset along the x and y axes could be eliminated by component rearrangement during a next design iteration.

Table 11-18. Summary Weight Statement Homing Stage W/Radar Tracker

<u>Payload</u>		<u>396.3</u>
Warhead	66.0	
Fuse	4.0	
Radar (Body Mounted)		
Transmitter Assembly	65.0	
Power Supply	65.0	
Receiver Assembly	48.0	
Duplexer	5.0	
Acquisition Antenna (4 x 6 ft Planar)		36.0
Gimbaled Tracking Antenna		26.4
Receiving Electronics	3.5	
Wave Guide Tubing	1.8	
Gyros (3)	3.0	
Torquers (3)	3.0	
Bearings (3)	1.3	
Resolvers (3)	3.0	
Yoke	2.4	
Structure	2.3	
Gimbal Ring	1.9	
Flex Leads	2.0	
Antenna (16 inch diameter)	2.2	
Platform Control Electronics		6.0
ACS Electronics		3.7
Digital Guidance Computer		27.0
Power Supply		21.0
Batteries	15.0	
Electronics	6.0	
Wiring and Boxes		15.0
Supports and Hardware		8.2
<u>Homing Stage</u>		<u>409.9</u>
Propellant Tank Assembly	31.8	
Propellant Plumbing System	11.0	
Propellant—Impulse	262.6	
Propellant—Residual	8.1	
Engine	38.0	
Pressurization Tank N <sub>2</sub>	20.3	
Pressurization Gas N <sub>2</sub>	17.1	
Pressurization Plumbing	5.0	
Attitude Control Engines w/valves, Lines and Brackets	16.0	
<u>Structure</u>		<u>109.0</u>
Stage Structure	109.0	
	Total	<u>915.2</u>
Recommended Contingency 5 percent		45.8
<u>Vehicle Gross Weight</u>		<u>961.0</u>

Table 11-19. Homing Stage W/Radar Tracker Mass Properties



NOTE: STATION Z-Z = 0.0  
IS REAR EDGE OF NOZZLE

Properties of Vehicle at Ignition

Weight (lb)	Center of Gravity			Inertia About Center of Gravity (Slug ft <sup>2</sup> )		
	X	Y	Z	X-X	Y-Y	Z-Z
961.0	-1.1	-0.1	49.9	102	100	15

Properties of Vehicle at Burnout

Weight (lb)	Center of Gravity			Inertia About Center of Gravity (Slug ft <sup>2</sup> )		
	X	Y	Z	X-X	Y-Y	Z-Z
681.3	-1.5	-0.2	51.1	97	94	15

11.4.3 Attitude Control Subsystem

The attitude control subsystem for the radar vehicle utilizes the same basic type of control engines as the electro-optical homing stage. All engines are body mounted as shown on Figures 11-2 and 11-38 since the use of the internally mounted warhead in place of the unfurlable device negates the need for deployed roll engines. The design criteria for this subsystem is summarized in Table 11-20 which show torques and total energy requirements somewhat reduced from the electro-optical vehicle again, due to the elimination of the unfurled kill mechanism.

Table 11-20. Attitude Control Subsystem Design Criteria  
Homing Stage W/Radar Tracker

	<u>Roll</u>	<u>Pitch</u>	<u>Yaw</u>
Required Torque (est) (ft-lb) <sup>1</sup>	204	36	4
Thruster Lever Arm (ft)	3.25	3.25	2.1 <sup>(2)</sup>
Engine Thrust (lb)	63	11	2 <sup>(3)</sup>
Homing Phase (seconds)	90	90	90
Total Energy (Est) (ft-lb-sec)	8000	1700	200
Total Impulse (Est) (lb sec)	2460	520	95

(1) Established in Chapter 6

(2) Couple lever arm (two thrusters)

(3) Each Thruster

A more detailed definition of this subsystem appears in the propulsion Section 11.2.4 and in Section 11.3.3.

#### 11.4.2 Gimbaled Radar Tracker

The radar tracking subsystem consists of a slotted wave guide radar antenna mounted on a gimbaled platform. Associated electronics, gyros, etc. are either body mounted on the vehicle or mounted on the platform. A platform with three degrees of freedom is required to satisfy the selected vehicle guidance technique which depends on angle tracking data to establish the direction and magnitude of commanded thrust. The platform mechanical design requirements are governed by this target tracking technique and the vehicle attitude control requirements as established in Chapter 8 as well as the vehicle configuration and anticipated loads. These criteria are summarized below:

- Roll freedom (around the tracker LOS) of  $\pm 360^\circ$  minimum.
- Pitch and yaw freedom of  $\pm 4^\circ$  minimum
- Vehicle acceleration (maximum design limit load) along the yaw axis during tracker operation of 4 g's
- Angular acceleration of the vehicle around the LOS - 2 rad/sec<sup>2</sup>

- A mechanical gimbal lock during the boost phase (15.4 g's maximum limit load)
- Resonant frequencies of the gimbal structure of about 200 cps
- Life of 30 minutes maximum in a space environment
- Gimbal order from the inside out is yaw; pitch and roll to avoid trigonometric transformation during the roll maneuvers
- Design ultimate accelerations are:

Boost Phase (bearings static)	20 g's axial 1-1/4 g's lateral
Homing Phase (bearings operative)	5 g's axial 1 g lateral

The selected design takes advantage of a conventional gimballed platform approach using a three-axis, bearing-mounted gimbal system as shown in Figures 11-49 and 11-50. The gimbal order from inside-out is yaw, pitch and roll. The inner platform is a slotted wave guide planar array antenna with associated electronic wave guide components arranged to provide dynamic balance around gimbal centerline. (See Figure 11-51.)

The MIG gyros are mounted on a three axis support bracket attached to the base of the antenna. The inner gimbal ring contains the yaw axis bearings, torquer and resolver and the fore and aft supports contain the roll axis bearings, torquer and resolver. All structural elements, such as the gimbal ring and yoke, are made of beryllium for maximum stiffness to weight ratio and maximum thermal stability.

The electrical connection between the stabilized platform and the vehicle is thru flex leads. The platform is securely locked to the craft during boost when high acceleration loads are encountered.

#### 11.4.2.1 Bearings

The selected bearings are large bore, extra thin, deep groove roller bearings which are designed for duplex mounting in preloaded pairs to provide high rigidity and low friction torque. The bearing arrangement is identical for all three axes in that axial expansion is accommodated by allowing one duplex pair to float in the housing. The bearing preloads were arbitrarily set at 50 pounds which resulted in the following estimated starting torques supplied by the bearing manufacturer.

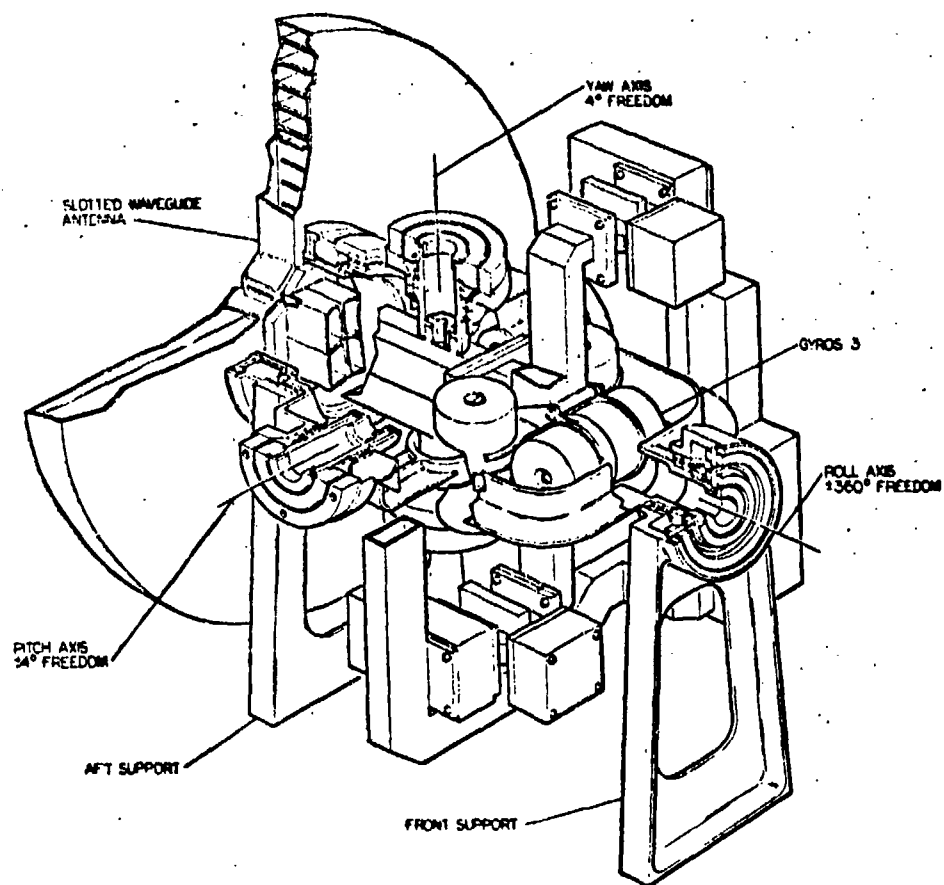
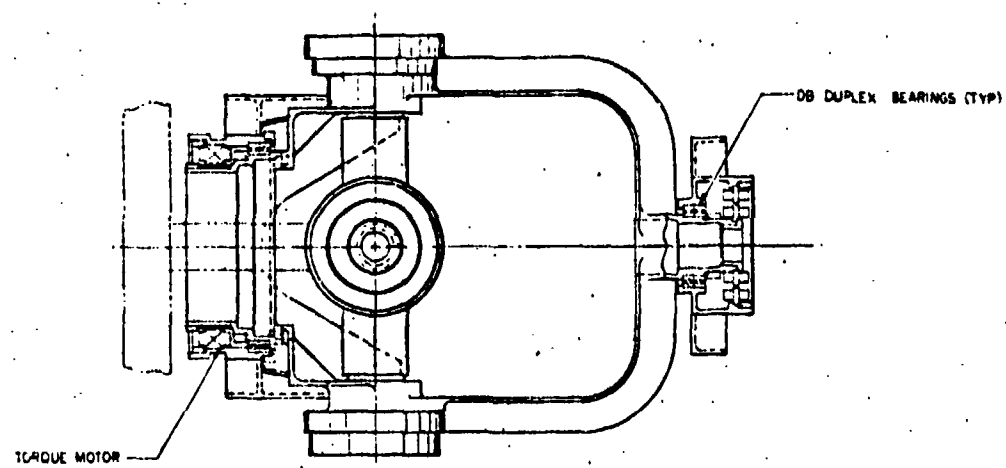
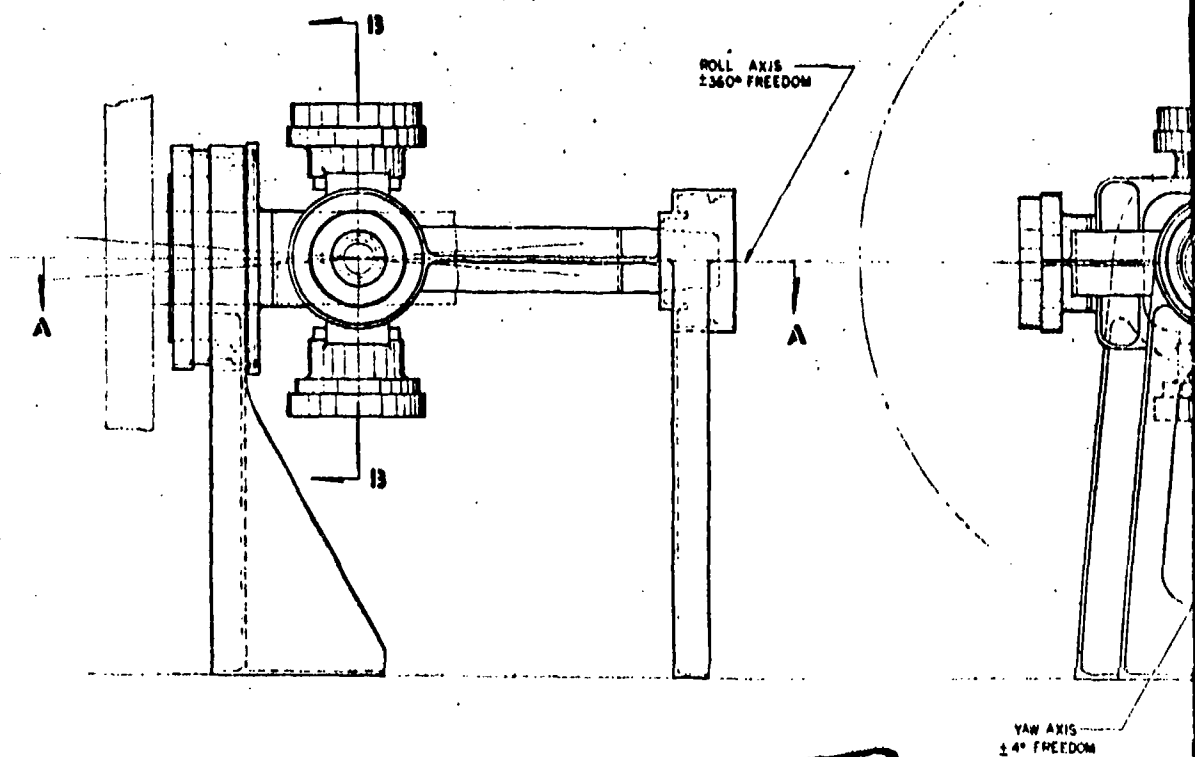


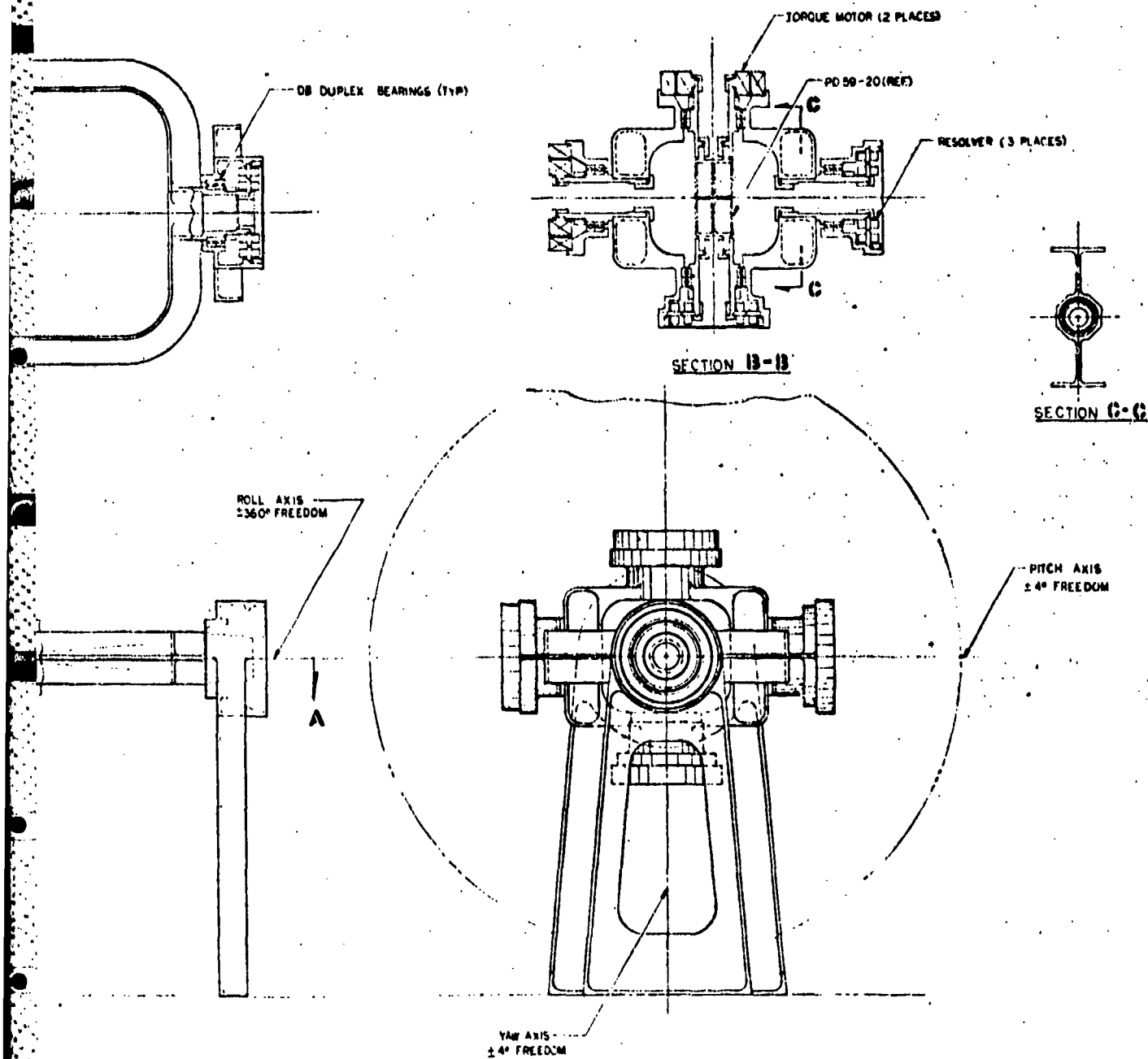
Figure 11-49. Gimbal Platform Perspective—Radar Tracker



SECTION A-A

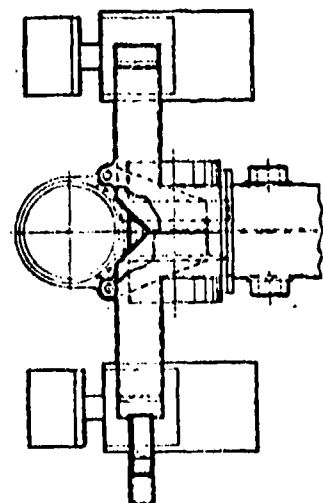
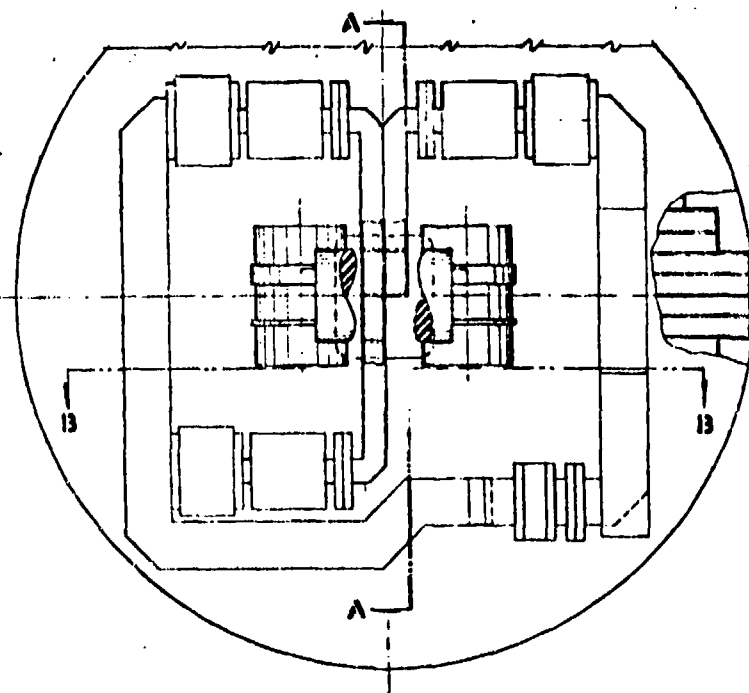
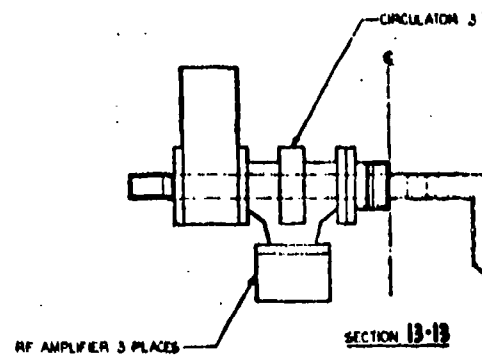
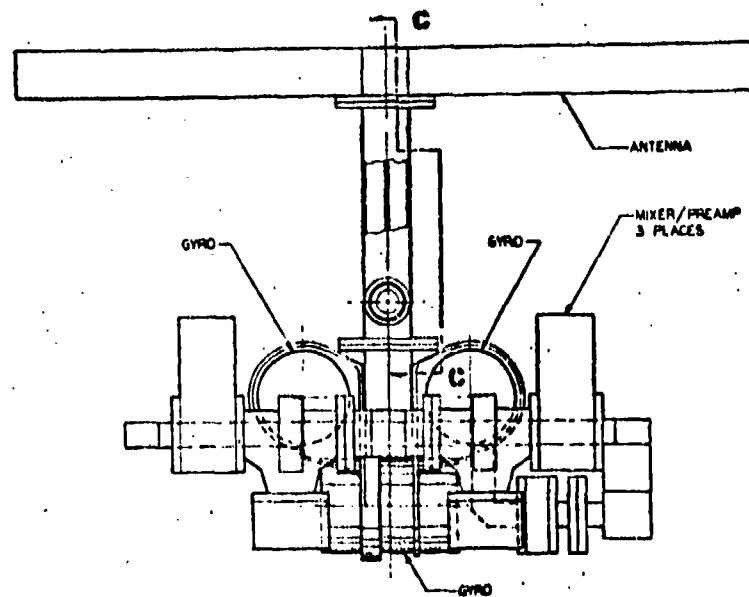


1



2

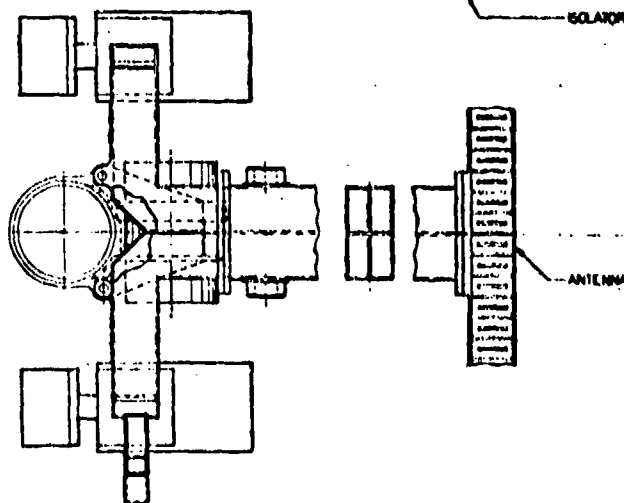
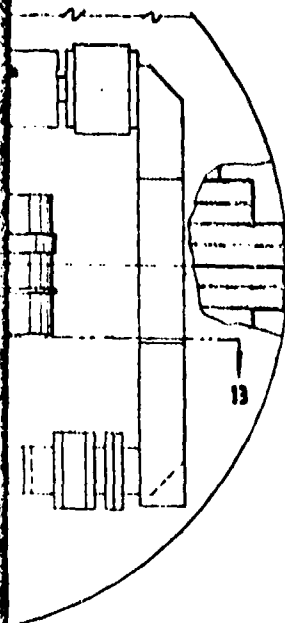
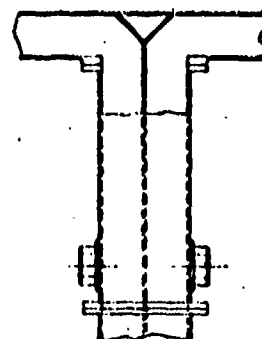
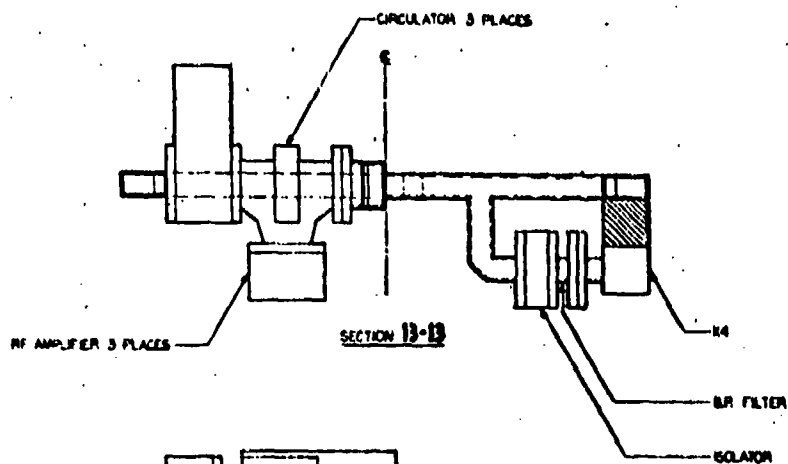
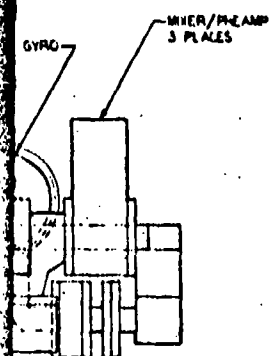
Figure 11-50. Gimbal Platform Radar Tracker



SECTION A-A  
(SEE GYRO UNIT FOR CLARITY)

1





SECTION A-A  
(ONE GYRO OMITTED FOR CLARITY)

2

Figure 11-51. Radar Tracking Antenna

11-93

Yaw and Pitch axis bearings 6.6 in oz per pair

Roll axis bearings 8.0 in oz per pair

Due to the short platform life in the space environment, it is proposed that the bearings use conventional oil or grease lubricants in conjunction with a labyrinth seal. Justification for this approach was outlined in Section 11.3.4.3 of this chapter.

#### 11.4.4.2 Platform Natural Frequency

Of major concern in the design of a gimbale platform, is the inherent structural resonant frequency. It is considered desirable to maintain a minimum resonant frequency from five to ten times greater than the maximum platform limit cycle frequency which in this case is estimated to be approximately 20 cps (see Chapter 8). Although a detailed loads and deflection analysis of this design was not undertaken at this time, the analysis associated with the electro-optical gimbale platform (Section 11.3.4.4), which is similar in many respects, indicated that the required natural frequencies were indeed attainable provided beryllium is used as the structural material and reasonable bearing yield rates are maintained.

#### 11.4.4.3 Electrical Flex Leads

For the pitch and yaw axis, the flex leads rotate through  $\pm 4^\circ$ . This simplifies the flex lead design since a straight torsional cable can be used. To balance the cable weights on the platform, the cable is split in two branches and wired symmetrically.

The flex lead configuration for the roll axis is in the form of opposed spiral springs. This type of flex lead is proposed due to its compactness and small variations in torque over the extreme roll movement of  $\pm 360^\circ$ . The concept is shown diagrammatically in Figure 11-46, Section 11.3.4.4.

The electrical cable is transformed into 2 flexible bands, one wire thickness and approximate 1 inch wide. This can be achieved by either bonding together standard insulated wires or by etched circuits on Mylar film. Theoretically, as the spring force of the wire wraps are opposing each other, the torque required for movement is zero providing that the spring rate remains constant as in Figure 11-47, Section 11.3.4.4 and that the springs are preloaded.

#### **11.4.4.4 Platform Orientation Torques**

Orientation torque requirements are established by platform angular acceleration, bearing friction, electrical lead wrap up, servo friction, and unaccountable platform center of gravity shifts. These effects are minimized by careful design and by dynamically balancing the platform with trim weights on all axes. Torque estimates appearing in Section 11.3.4.6 are considered applicable here and were used as a basis for selecting the following platform torque levels.

Roll Torque                      70 in oz

Pitch and Yaw Torque        35 in oz

As was the case with the electro-optical platform, it is felt that a reserve factor of at least 1.5 or preferably 2 times the calculable torque requirements is a small weight penalty for a considerably increased platform confidence level. Increased electric power requirements for the larger torquers is negligible because of the short operating time.

As an additional descriptive aid, the platform assembly sequence is outlined below: (see Figure 11-45)

- Install bearings in front and rear supports
- Assemble both supports to roll axis yoke
- Install roll torque motor in front support and resolver in rear support
- Install bearings on both pitch axis shafts
- Install shafts with bearings in pitch axis supports in yoke and secure to gimbal ring with retainers
- Install bearings on both yaw axis shafts
- Slip forward portion of wave guide with antenna attached through hole in forward end of roll axis yoke. Install shafts with bearings in yaw axis supports in gimbal ring and secure to bosses on wave guide with retainers
- Install pitch and yaw torque motors and resolvers
- Assemble aft section of wave guide, gyros and electronics to forward section of wave guide.

#### 11.4.5 Alternate Antenna Considerations

A single transmitting and receiving parabolic radar antenna was suggested for use as a target acquisition and tracking device. Such an antenna would replace the proposed dual hybrid antenna system for the radar equipped homing stage which utilizes a body fixed array transmitting antenna for target acquisition and a small gimbaled antenna for target angle tracking. The design criteria for the suggested system is as follows:

- o To satisfy the angle tracking requirements, the antenna must be fully gimbaled with  $\pm 360$  degree roll freedom and approximately  $\pm 4$  degree pitch and yaw freedom.
- o Rotary wave guide joints are required to provide r-f connections between the body mounted transmitter and the antenna feed.
- o High dish stiffness is required to minimize deflections under load (approximately 5 g's limit load) which would degrade the antenna's performance.
- o A 5 foot diameter parabolic dish with multiple horn feeds is required.
- o The dish must be collapsable to accommodate stowage in the payload clearance envelope for Minuteman.

A cursory look at the stowage problems revealed that the collapsed dish must be stowed with its axis coincident with or parallel to the fairing centerline. A 90 degree hinge action is therefore required to place the antenna in operating position. Without further study, it is not clear whether it would be best to hinge outboard (between the dish and gimbals), or inboard (between gimbal and vehicle) of the gimbal system. In either case, wave guide hinge or rotary joints are required as well as a positive locking system. An inboard hinge would seem preferred to avoid degrading

the platform stiffness by use of an outboard hinge. Furthermore there would be inherent c.g. platform shift associated with the inboard hinge.

Preliminary design studies show that a fairing length increase of about 2 feet would be required to accommodate the collapsed antenna regardless of the collapsing technique.

Two unfurlable concepts were considered. One utilizes hinged pedals on the largest possible rigid center on which the four feed horns and cassegrain secondary are mounted. Because of close tolerance requirements between the secondary and horns, it is not considered practical to collapse and unfurl these elements. It appears that the unfurled pedals must be mutually supported or structurally joined at the periphery to maintain the required antenna surface accuracy under load. A satisfactory means of accomplishing this with a simple and reliable system is not evident.

An alternate concept utilizes a light weight inflatable structure to deploy and support the parabolic reflector. A concept that appears feasible is an inflatable torus which is used to stretch the two parabolic diaphragms; one is a metalized reflective surface which serves as the active parabolic reflector and the other serves passively. The parabolic shape is obtained by the use of drop cords which maintain the parabolic diaphragm shape. Again, a rigid center for cassegrain secondary reflector and feed horn mounting would be used. Torus pressure would be established to maintain tension in the membranes under the anticipated load conditions.

Many unfurlable antennas have been designed and fabricated but primarily for use on nonmaneuverable spacecraft. Stabilized dish antenna designs also exist as well as refined gimbal systems with sufficient structural stiffness to meet this system's angle tracking limit cycle frequency requirements. Antenna or platform deployment through 90 degrees is not considered a problem.

## 11.5 FAIRING AND ADAPTER DESIGNS

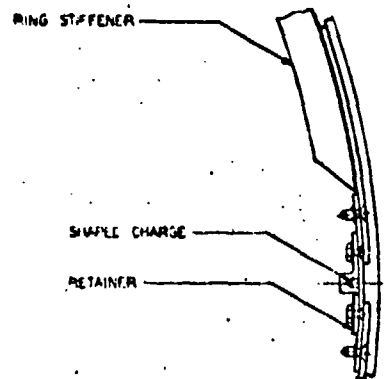
A preliminary design study of the fairing and adapter section was conducted to provide a basis for a rough weight estimate and to determine the loads induced on the Minuteman structure by the fairing aerodynamic loads. The fairing configuration was tailored to house the subject homing stages and designed to satisfy the envelope constraints delineated in the Boeing Booster Symposium Document (Reference 1).

The adapter section was designed to mate with the Minuteman G and C section or with the range safety equipment section: assumed to be required for flights from the continent. The adapter is essentially an extension of the homing stage structure which is fabricated of magnesium. A peripheral shaped charge separation system is employed for disengaging the homing stage from the adapter section.

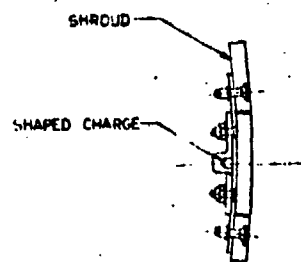
A shaped charge fairing separation system is utilized, in lieu of a presplit fairing with explosive actuators, to maintain maximum fairing structural integrity during the boost phase. Lateral  $\Delta V$  to the separated shells is provided by a preloaded spring plunger system. The fairing structural design shown in Figure 11-52 was based on the estimated loads appearing in Figures 11-53, 11-54 and 11-55. These loads are based on maximum  $q_a$  conditions for the most depressed mission trajectory under consideration. The basic fiberglass structure consists of ring stiffened half-shells tied together by a doubler frame. The fairing is made in two halves to facilitate assembly, and installation of the separation system in the otherwise inaccessible forward portion of the fairing.

The estimated weight of the fairing including structure, insulation, separation systems, etc. is 217 pounds and 21 pounds for the adapter section.

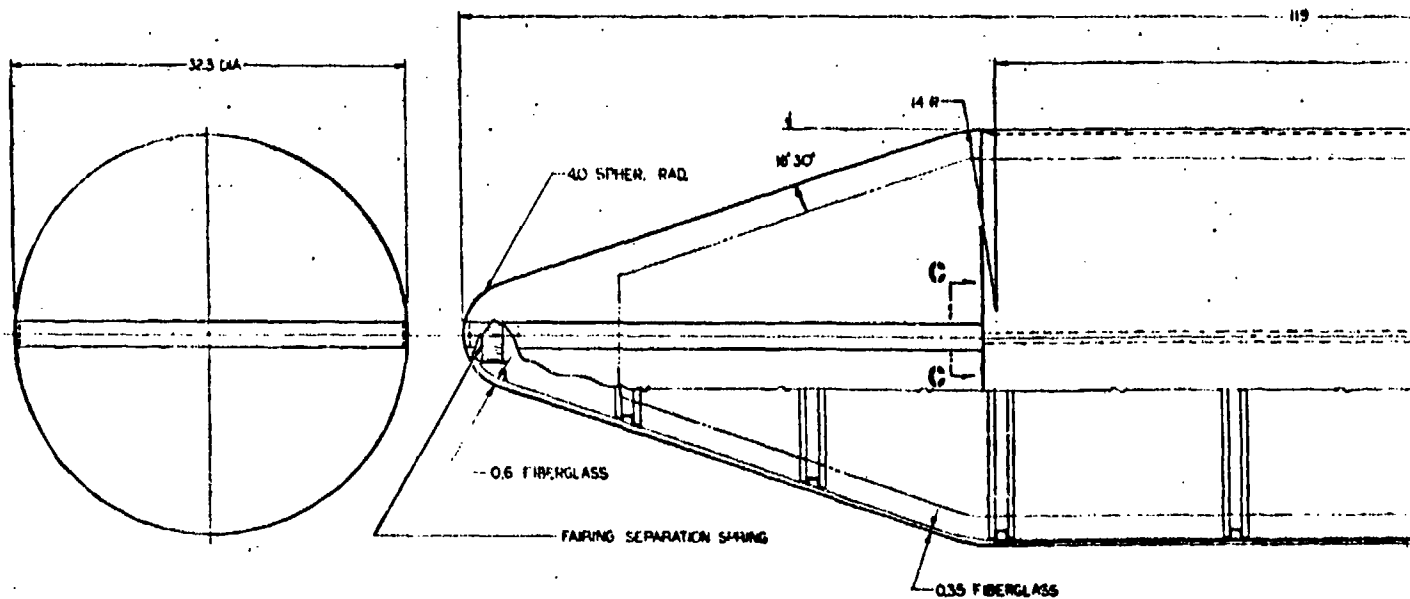
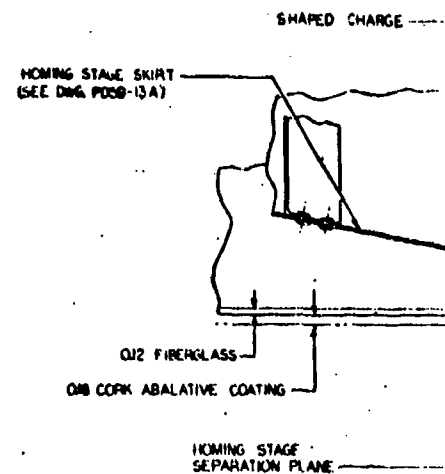
A preliminary structural analysis was conducted of the external fairing provided to aerodynamically shield the homing stage during the Minuteman booster flight through the atmosphere. The external fairing is designed to be structurally independent of the homing stage. Critical loading on the fairing occurs during the maximum  $q_a$  flight environment. At this time the cylindrical portion of the fairing is subjected to an ultimate maximum axial load of 8,940 pounds combined with an ultimate

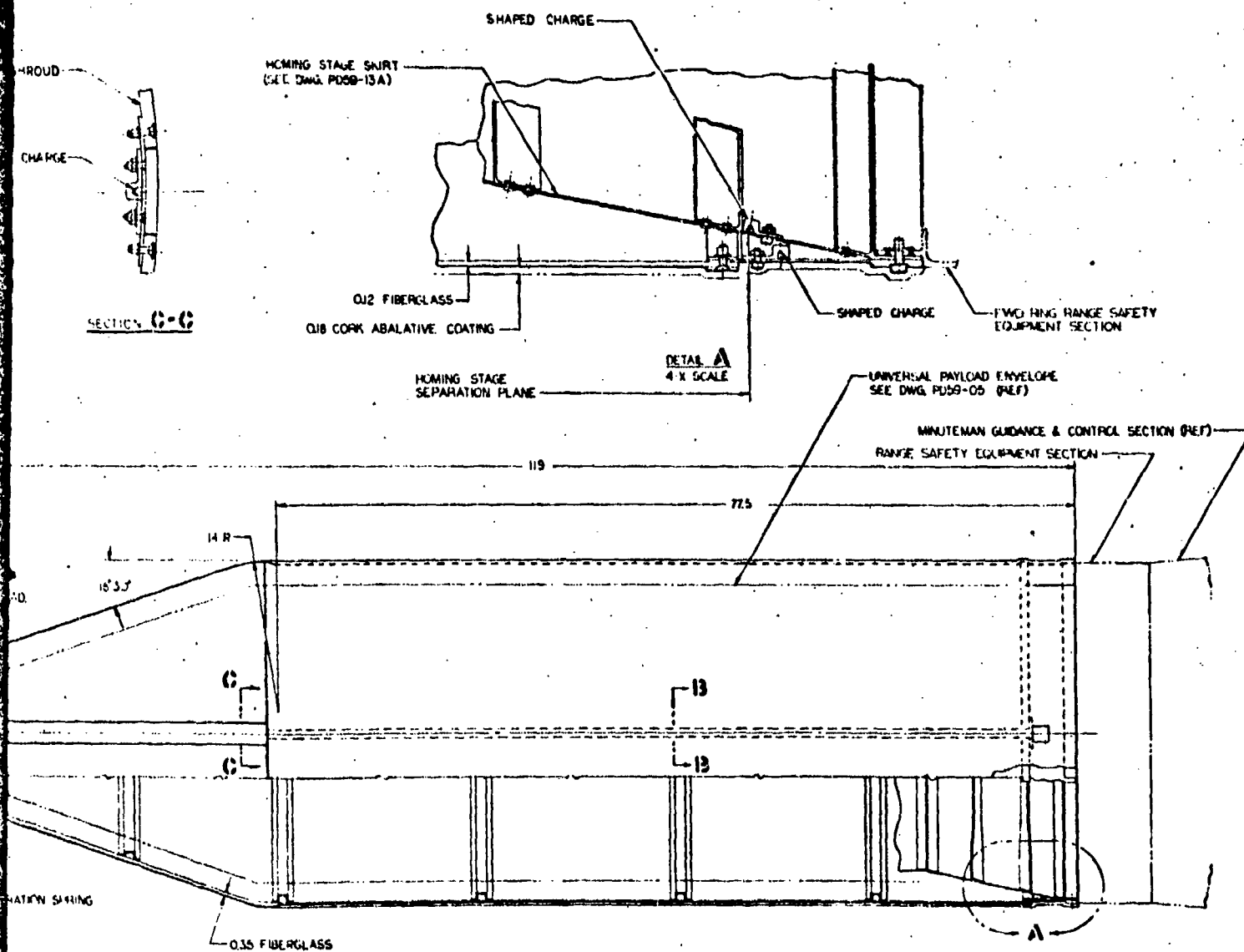


SECTION B-B  
4 X SCALE



SECTION C-C

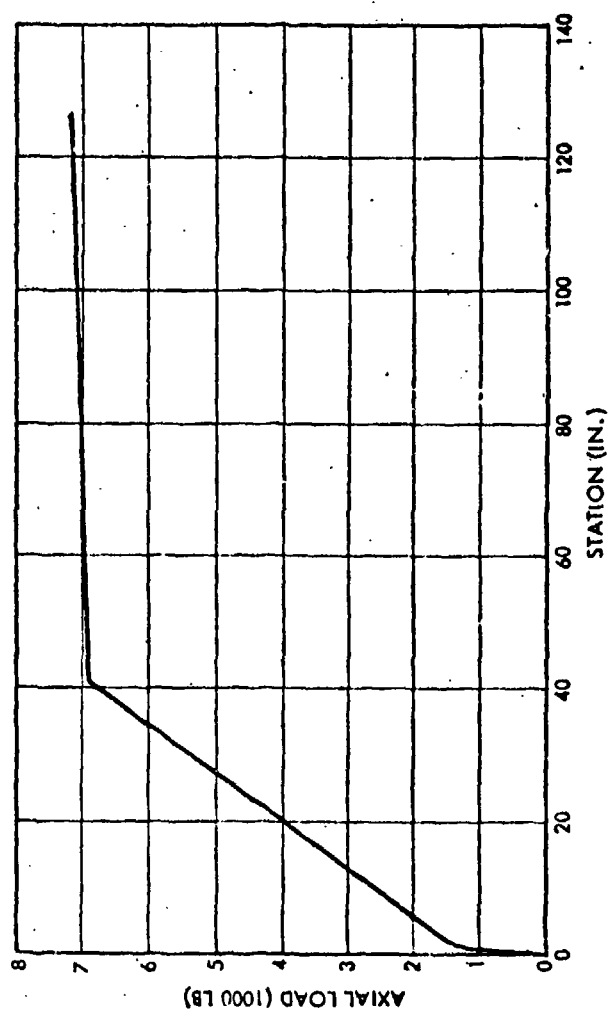




2

Figure 11-52. Homing Stage Fairing and Adapter—Minuteman





$q = 4250 \text{ LB/FT}^2$

Figure 11-53. Minuteman Homing Stage Fairing, Limit Axial Load  
(Maximum  $q_a$  Condition)

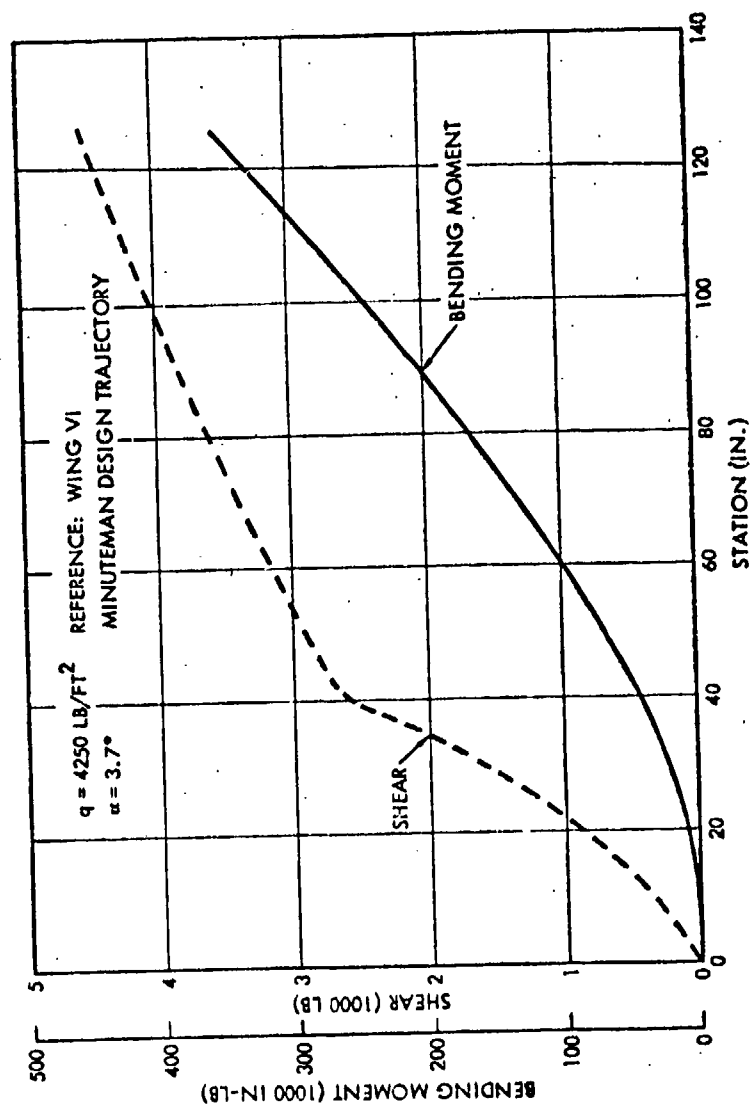


Figure 11-54. Minuteman Forming Stage, Limit Shear and  
 Bending Moment (Maximum  $q_a$  Condition)

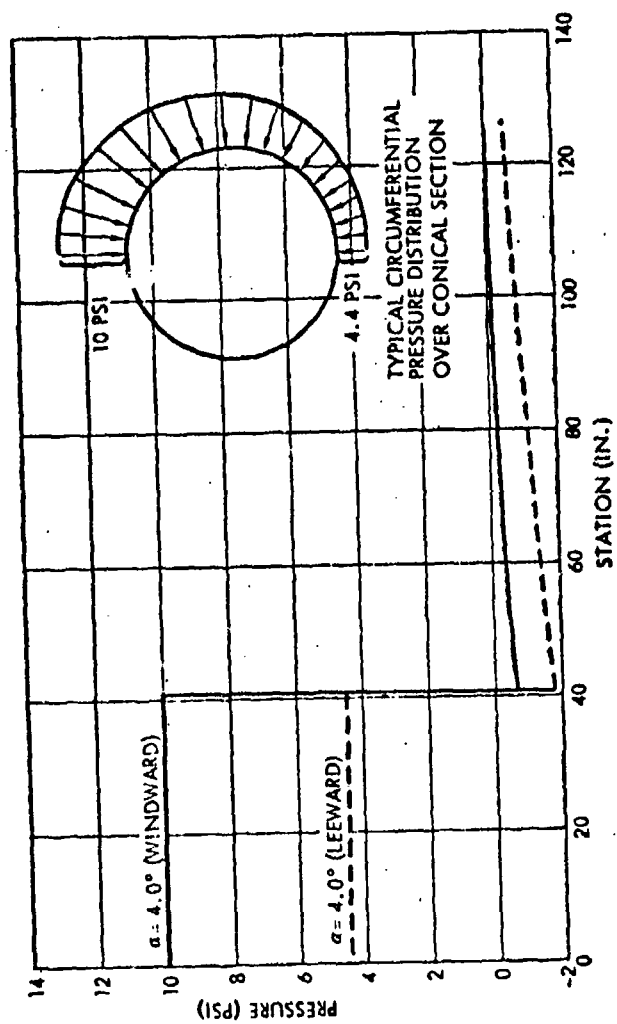


Figure 11-55. Minuteman Homing Stage, Limit Pressure Distribution (Maximum  $q_a$  Condition)

bending moment of 444,000 inch pounds with negligible aerodynamic pressures. The conical portion of the fairing is subjected to a corresponding ultimate axial load of 8,620 pounds, an ultimate bending moment of 56,200 inch pounds and an ultimate external crushing pressure of 12.5 pounds per square inch. The design selected for these loading environments is a ring stiffened monocoque structure of epoxy glass construction whose structural thickness, independent of insulation thickness requirements, range from 0.12 inch in the cylindrical portion to 0.15 inch in the conical portion. The allowable axial compressive working stresses are 6,000 pounds per square inch in the cylindrical section and 8,250 pounds per square inch in the conical section. Corresponding allowable axial load equivalents are 72,4000 pounds and 124,300 pounds respectively. The allowable hoop compressive working stress for the given ring spacing in the conical section is 2,260 pounds per square inch equaling an external crushing pressure of 22.7 pounds per square inch. All fairing structural allowables are based on a conservative maximum operating structural thickness temperature of 400° F during the maximum qa condition. The resulting ultimate margins of safety are 12 percent for the cylindrical portion and 47 percent for the conical portion. Straight line type interactions between axial, bending and crushing external pressure loads were assumed for the fairing structure in arriving at the margins of safety. Ring stiffened monocoque type construction was selected because of its simplicity, consistent with good axial and external pressure load carrying capabilities. Epoxy glass material was selected because of its favorable strength at moderate temperatures consistent with good insulative characteristics. Margins of safety for the fairing structure was purposely kept high due to the preliminary nature of the structural analysis which did not include the influences of thermal differential stresses. However, at this time it is felt that this design approach is conservative and therefore satisfactory for initial weight estimation purposes.

For thermal protection of the payload during the ascent through the atmosphere, an insulated fairing capable of resisting the aerodynamic loads is required. The insulation must be of a thickness great enough to prevent the structure from exceeding temperatures which would excessively degrade the strength of the fairing. An additional requirement is the thermal protection of payload components prior to fairing jettison.

The nose fairing differs somewhat from conventional fairing design because of the use of a Minuteman booster. The higher acceleration of Minuteman creates considerably greater ascent heating than that from liquid propellant boosters. In this environment of high heating, a satisfactory design is obtained by utilizing materials which ablate at comparatively low temperature. The thermal energy stored in the fairing wall and the associated temperatures are reduced in this way as compared to a solid nonablating wall made of fiberglass, for example.

The materials selected for the cylindrical portion of the fairing are fiberglass (0.120 inches) with an outer cork insulation (0.180 inches). A similar construction utilizing a magnesium substructure is in use on the Minuteman missile and has been demonstrated to be adequate in flight tests. Because of the questionable performance of cork in environments of high aerodynamic shear stress, the nose and forecone material are assumed to be made of fiberglass (-0.6 inches). This design will maintain the load bearing portion of the fairing at a temperature of 400° F or less during the design heating and load trajectory for the Minuteman booster.

#### 11.6 RADAR EQUIPPED HOMING STAGE WITH A LARGE WARHEAD

Consideration of attacks against "hardened" targets implies the need for large (approximately 1,500 grain) fragments for effective kill (see Chapter 10). To obtain a reasonable pattern density (approximately 0.2 to 0.5 pellets/ft<sup>2</sup>) in conjunction with an estimated pattern diameter of 60 ft, the warhead weight increases to approximately 250 pounds as compared to 66 pounds for a "soft" target warhead. A preliminary vehicle configuration (Figure 11-56 and weight estimate (Table 11-21) were generated based on the radar equipped vehicle design parameters. Although it appears that such a vehicle could be physically adapted to the Minuteman, fairing length increase of about 14 inches is necessary. Analysis shows that this increase in fairing length gives use to a severe structural problem due to aerodynamic loads, induced by side winds at maximum  $q$ . Solution of this structural problem requires strengthening of the GC component (a simple modification) and strengthening of the top of the third stage, a possible extensive modification.

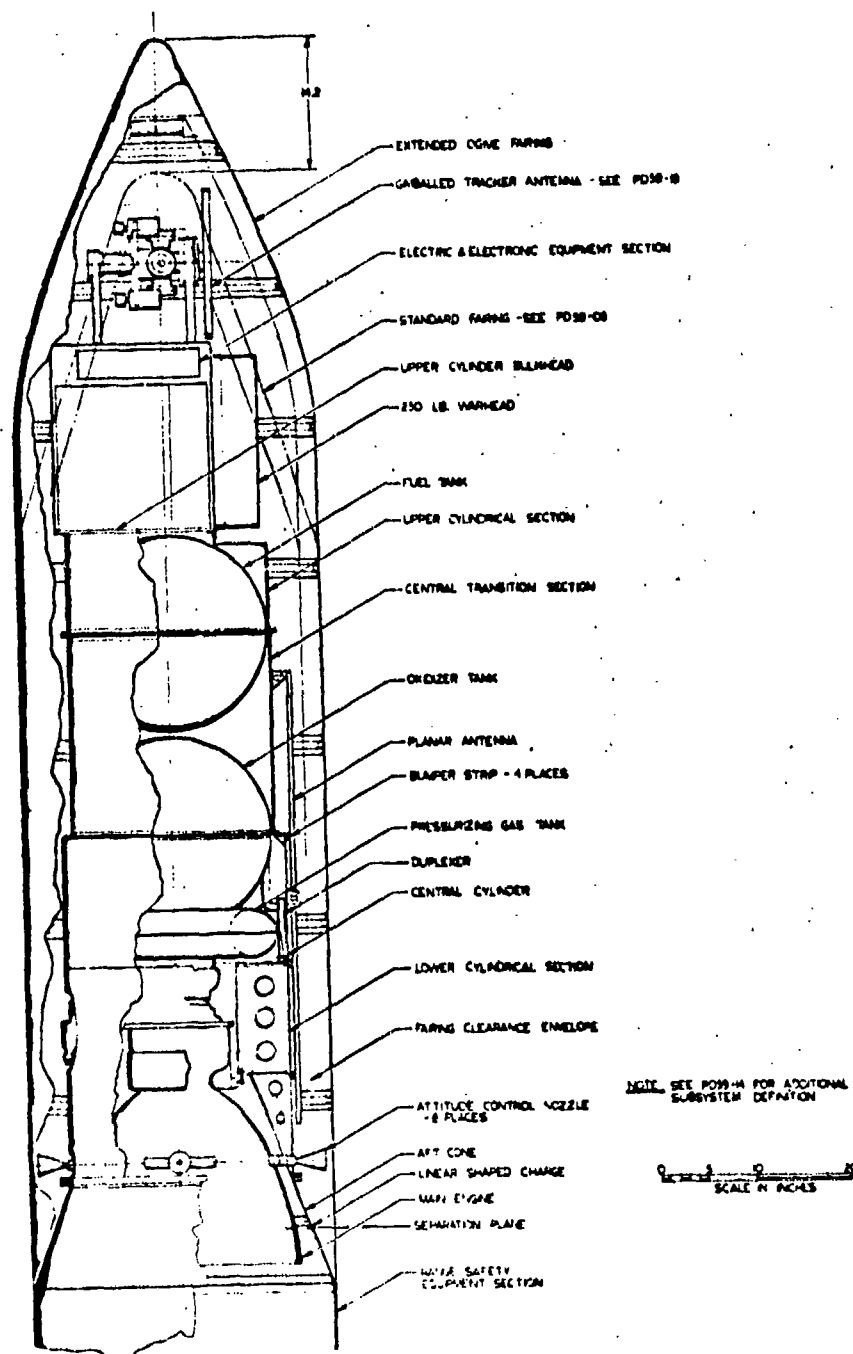


Figure 11-56. Radar Equipped Homing Stage With Large Warhead

Table 11-21. Radar Equipped Homing Stage with a  
250 lb Explosive Warhead

Vehicle Gross Weight	1290
Propellant Weight	376
Tankage, Pressurization, Residual Weight	50
Attitude Control System Weight (less electronics)	58
Engine Weight	52
Structure and Temperature Control Weight	140
Payload Weight	579

#### REFERENCES

1. "Answer to Some Questions for ARPS Anti-Satellite Symposium," Boeing, Seattle, Washington, DZ-3579, 1 May 1963.
2. "Second Interim Progress Report Satellite Interception System Feasibility Study (U)," Space Technology Laboratories, Inc., 8424-6007-RS000, 15 August 1963.
3. "A Semi-Analytical Method for Spacecraft Weight Estimation," D.R. Pence, Space Technology Laboratories, Inc., SAWE Paper, No. 240, May 1961.
4. "Final Technical Summary Report, BAMBI Phase II, Technical Investigations Single Interceptor Satellite," Space Technology Laboratories, Inc., 8637-6090-RA000, 2 November 1962.
5. "Final Technical Summary Report, Continuation Effort, SIS BAMBI Phase II Feasibility Study," vol. I, Space Technology Laboratories, Inc., SSD-TDR-63-24, 28 February 1963.



## CHAPTER 12

### BOOSTER SELECTION AND RANGE-PAYLOAD CAPABILITY

#### 12.1 SELECTION OF PREFERRED BOOSTER SYSTEMS

The selection of a boost vehicle for the satellite intercept mission is not a simple task; all of the candidate vehicles examined originally were developed as ballistic missile weapon systems and as such are not directly applicable without minor or major modifications. The problem, therefore, becomes one of determining the criteria by which to measure the capability of the candidate vehicles for the mission, evaluating each of the vehicles against these criteria, determining the extent of the modifications required for the mission, and estimating the cost and development time required to effect the modifications and implement the boost vehicle subsystem portion of an antisatellite interceptor.

The various boost vehicles studied for the satellite intercept mission have been generally evaluated in order to select from among them a promising, but lesser number for detailed study. The original vehicles included the Atlas D, E, and F; the Titan I and II; the Minuteman, Wings II and VI; the Polaris A2 and A3; the Thor with BTL and ACSP guidance systems; and the thrust-augmented Thor (with BTL guidance) by itself, with the Agena as a second stage, and with the Delta upper stages. From this group five boost vehicles were selected for further study although all are more or less appropriate for the mission. The five selected were the Titan II, the Minuteman (Wings II and VI), and the Polaris (A2 and A3). The reasons for selecting these in preference to the other vehicles are discussed below.

##### 12.1.1 Boost Vehicle Criteria

The characteristics of boost vehicles which are of prime concern to this mission are the performance capability, guidance system adaptability, cost, reliability, availability, launch site requirements, and payload size and weight constraints.

##### 12.1.1.1 Performance Capability

The boost vehicle performance capabilities are measured most readily in terms of range-altitude coverage volumes for given payload

weights. The payload weight range initially being considered is 500 to 2500 pounds; however, higher payload weights are not eliminated from consideration (especially for the Titan II). Altitudes of interest extend from 75 to 2500 n mi.

#### 12.1.1.2 Guidance System Adaptability

The guidance systems for all of the boost vehicle systems under present consideration were developed for ballistic missile weapon system application. The requirements for these systems included rapid reaction time (with a preselected target) and highly accurate impact point prediction and control. Later requirements also included a multiple (preselected) target capability and a prescribed time of flight or time-on-target-control (TOTC) capability for possible salvo operations.

The booster guidance system to be used for the satellite interception mission must be capable of reaction against a target satellite whose position is not known until shortly before the interceptor is to be launched. This requirement can be met with existing guidance systems by providing; a) a rapid retargeting capability which allows a sufficient azimuthal coverage and which can be operated so that the total retargeting plus countdown time satisfies the reaction time requirements, and b) a guidance program and equation set which allows an accurate intercept with the moving satellite target.

12.1.1.2.1 Retargeting Time. The allowable retargeting time is a function of the required system reaction time, the countdown time, the tracking station coverage, the command and control response time, the speed of determination and transmission of target satellite ephemeris data, the exact nature of the threat, and the number and locations of interceptor launch sites. The most relaxed level of system reaction time is represented by the requirement for interception within 24 hours of launch. The most stringent level of system reaction time is the requirement for interception within one orbital period after a satellite is designated as a hostile target.

12.1.1.2.2 Azimuthal Coverage. The azimuthal coverage necessary to allow a favorable downrange intercept of any target satellite from a single launch site is 360 degrees. This coverage can be provided by a boost

vehicle with a 360 degree azimuthal capability, two boost vehicles with 180 degree azimuthal capability, or generally  $n$  boost vehicles with 360 deg/ $n$  azimuthal capability. Range safety limitations on the permissible attack sector will obviate the requirement for a 360 degree coverage in some cases, but in general, broad azimuth coverage by a single vehicle is desirable.

12.1.1.2.3 Guidance Program and Evaluation. The guidance program and equation set must be designed to allow intercept of the target satellite at a prescribed time and point in space. This means that the guidance input must include an intercept time (in terms of GMT), as well as a latitude, longitude, and altitude of intercept.

12.1.1.3 Other Considerations

In addition to the criteria discussed above, major items to be considered are cost, reliability, availability, launch site requirements, and the payload size and weight constraints. For purposes of boost vehicle selections, some approximate costs for the Atlas, Titan and Minuteman weapon systems were obtained.

The mission reliability of a boost vehicle is strongly dependent on the maintenance policy which is employed. The boost vehicle reliability for the satellite interception mission will be the product of the readiness, retargeting, countdown and flight reliabilities. A cursory examination of the quoted reliability figures for the boost vehicles considered shows that if the retargeting operation can be successfully modified, no significant reliability differences may exist between boost vehicles.

The special launch site requirements of the various boost vehicles include radio baselines, freedom from radio interference in certain frequency regions, and storage facilities for the propellants. The solid-fueled vehicles require a fairly rigidly controlled temperature-humidity environment; the cryogenics require special storage facilities for LOX; and the storable liquids are toxic and require special handling.

The payload size and weight constraints for each boost vehicle will be treated as payload design constraints, since the payload design is not fixed.

## 12.1.2 Evaluation of Candidate Vehicles

### 12.1.2.1 Performance

The vertical flight capabilities of the selected vehicles, assuming burning to propellant depletion and then coasting to apogee, are presented in Figure 12-1\* as a function of payload weight. These curves show the maximum altitude capabilities of the less energetic boosters such as Polaris, Thor, and Minuteman with payload weights greater than 500 pounds; however, for the large booster vehicles which have orbital capabilities, higher apogee altitudes can be achieved by flying a more optimum ascent trajectory profile. The utility of these curves is further limited because they do not reflect certain system constraints nor do they indicate the range capability associated with a given altitude. These shortcomings notwithstanding, the curves are useful for an initial performance ranking of the selected vehicles as an indication of their maximum altitude capabilities.

The curves show that on a payload performance basis all of the selected vehicles have some capability for the SIS mission, but as would be expected, a large differential exists between the capabilities of a Polaris or Thor and an Atlas or Titan. For example, for a payload weight between 500 to 1000 pounds and a maximum altitude capability requirement of approximately 1500 n mi, one might choose between a Polaris or Thor although any of the more energetic boosters could operate at this altitude. For the same payload weight and a maximum altitude capability requirement between 2000 and 3000 n mi, one could select from either a Minuteman, Atlas, Titan I or TAT plus second stage. Clearly for this case the selection of the booster vehicle would have to be based on operational considerations rather than payload performance. For maximum altitudes much above 3000 n mi the Titan II is the only possible choice.

However, if one were selecting a booster for a much heavier payload, a different booster choice would probably be made for the lower altitude threats because of the differences in payload sensitivity of the various

---

\* For convenience all illustrations in Chapter 12 are placed at the end of the chapter.

vehicles. The performance capabilities of the second generation multistage vehicles are degraded more rapidly by an increase in payload weight than that of a single stage Thor or one and one-half stage TAT or Atlas.

#### 12.1.2.2 Guidance System Considerations

12.1.2.2.1 Retargeting. The present retargeting operation for the Atlas, Titan and Minuteman weapon systems begins at SAC headquarters with the assignment of a specific target. Input cards are prepared for the operational targeting program and the target data required by the missile guidance computer are computed on an IBM 7090. A punched tape is then manufactured and transported from SAC headquarters to the missile launch site, where it is read-in to the guidance computer. (In the case of the Atlas E and F, transfluxor and ground operating equipment (GOE) diode boards must be prepared, transported and installed.) If repositioning of the missile and/or inertial platform is not required, countdown may then be initiated.

For the satellite interception application, the desired reaction time may necessitate a major departure from the targeting procedure described above. It is assumed that the target data required by the guidance computer can be calculated from the satellite ephemeris data and from information regarding the interceptor launch site locations, reaction time and trajectory characteristics. Assuming a 7090 or similar computer to be available to the system for these calculations, the remaining time to retarget will be used to transmit the calculated inputs to the missile guidance computer. Since the present method of preparing, transporting, and reading-in punched tape inputs to the guidance computer requires excessive time, a direct electrical input from the 7090 output into the boost vehicle guidance computer is desirable. It is estimated that the necessary targeting data could be calculated in approximately 7 minutes, with launch azimuth available after approximately 2 minutes. If a direct electrical input were used, the time required to transmit these data would be negligible.

The following paragraphs discuss the various boost vehicles and their individual targeting problems:

- Thor. The flight control system on the Thor versions, which controls the roll and pitch programs for the first 90 seconds of flight (before BTL guidance takes over), presently requires 24 hours to reprogram. Douglas is conducting a design study of a solid state first stage flight controller which provides the capability of changing steering commands through the use of plug-in modules, thereby reducing the retargeting time to 1 to 2 hours. The retargeting time for the BTL system itself could be reduced from the present 1 to 2 hours by modifying the BTL ground system to allow steering requirements and target tracking data to be stored in the ground computer.
- Atlas E and F. The Atlas E and F Arma guidance system retargeting operation presently requires approximately 4 hours, not including the time required to transport the airborne transfluxor board and GOE diode board from the targeting center to the launch site. Of this time, approximately 1 hour is required for computation and for preparation of these boards, and approximately three hours are required to install the boards and perform an alignment and calibration. This retargeting time could be reduced by redesigning the airborne computer and targeting insertion methods.
- Titan I and II. The Titan I and II guidance systems presently require approximately 1 hour for targeting calculations and punched tape manufacture, additional time for transporting the punched tape from the targeting center to the launch site, and approximately 20 minutes for the punched tape readin and subsequent countdown. The radio-guided Titan I requires 5 minutes for tape readin to the ground guidance computer and has a 15-minute countdown, while the Titan II requires about 20 minutes for tape readin to the missile guidance computer and 1 minute for countdown. By providing a direct electrical interface between the targeting computer and the guidance computer, the retargeting time could conceivably be reduced to about 7 minutes as discussed above. The Titan I is limited by radar look angles to an azimuthal coverage of about 200 degrees, while the Titan II has an all azimuth capability.
- Minuteman Wing II. The Minuteman Wing II retargeting operation at the targeting center provides a Mylar punched tape which requires about 30 minutes to prepare. This tape then must be transported to the launch site, where it requires about 3 minutes or less to readin the new tape. This retargeting operation could be reduced to about 7 minutes for the satellite intercept application. The subsequent countdown requires approximately 30 seconds.

If the target azimuth is changed by more than 10 degrees from the previous target (existing) azimuth, seven to 8 hours are required to shut the computer down, reposition the missile, umbilicals and auto-collimator, restart and fill the computer.

and perform platform erection, alignment and calibration. About 2-1/2 hours could be saved by omitting the calibration cycle, resulting in a degradation in accuracy. The weapon system is limited in azimuth to a 120 degrees sector. The sector could be increased by extending the auto-collimator bench and the umbilicals.

- Minuteman Wing VI. The Minuteman Wing VI retargeting operation is similar to that of the Minuteman Wing II, except that no repositioning of the missile is required for a 360 degree azimuthal coverage. If the new target azimuth is more than 10 degrees from the previous azimuth setting, 15 minutes are required to reposition the inertial platform. This time could be reduced to about 1 minute with minor modifications discussed in the next chapter. The Wing VI countdown is also about 30 seconds.

Wing VI has radio and cable inputs directly to the airborne computer from a remote location which could be used as a direct link to the targeting center of the satellite interception system. The data rate is 8 bits per second for radio inputs and 64 bits per second for cable. These rates could be increased to 16 and 256 bits per second, respectively.

- Polaris. The Polaris weapon system targeting is presently accomplished using a firing table approach discussed in the following chapter. The countdown requires a maximum of 13 minutes and includes a 4 minute allowance for realignment of the guidance platform to a new azimuth. The airborne computer may be filled during the countdown. The Fire Control Computer has a direct electrical interface with the airborne guidance computer.

**12.1.2.2.2 Guidance Program and Equations.** In order to allow intercept of the target satellite at a prescribed time and point in space, the guidance program and equation set of the boost vehicle selected will require certain modifications. It appears that guidance equations with prescribed time of flight would allow the greatest flexibility of operation and accuracy of intercept. It is also desirable that information regarding vehicle attitude be available for use by the homing stage, which will require this information in order to orient itself for the acquisition mode.

The Titan II, Minuteman (Wing VI) and Polaris A2 guidance systems employ prescribed time of flight guidance techniques. The Titan II, Minuteman (Wings II and VI) and Polaris guidance systems also provide the capability of transmitting attitude information to the payload, although some modifications will be required.

The Atlas E and F guidance system has the capability of providing coarse attitude information to the payload. Special procedures would be required to provide accurate attitude information to the payload.

The Atlas D, Titan I and one version of Thor use radio guidance systems and, therefore, information not directly available in the boost vehicle conceivably could be supplied from the ground. The inertial guidance system used in Thor is comparatively outdated, containing a large number of obsolete components of low accuracy. It is doubted that this system could satisfy the requirements of the SIS mission even with major hardware modifications.

#### 12.1.2.3 Cost

Crude cost estimates for the Atlas, Titan, and Minuteman weapon systems are presented in Table 12-1. These coarse estimates are obtained by amortizing total costs (exclusive of R and D) over the number of deployed missiles. The missile costs shown in this table are not necessarily meaningful if existing launch facilities could be used.

Table 12-1. Estimated Weapon System Initial Investment Costs (Millions Dollars)

	<u>Atlas</u>	<u>Titan I</u>	<u>Titan II</u>	<u>Wing II Minuteman</u>
Missile plus spares	2.0	2.6	2.8	1.8
Support equipment plus spares	9.4	24.7	15.0	1.7
Site acquisition and base construction	3.2	4.0	5.6	0.7
Personnel training	0.1	0.1	0.1	0.1
Miscellaneous	<u>0.3</u>	<u>0.6</u>	<u>0.5</u>	<u>-</u>
Total	15.0	32.0	24.0	4.3

#### 12.1.2.4 Summary

It is believed that none of the studied boost vehicles can be rejected on the grounds of inability to perform the satellite interception mission if certain modifications are allowed. It is also believed that none of the boost vehicles can perform the mission without some modification.



Inasmuch as STL desired to avoid a dilution of effort resulting from studying all of the boost vehicles, five were selected for further study. These five are the Titan II; the Minuteman, Wings II and VI; and the Polaris A2 and A3. The choice was based upon two factors; a) those booster systems which appear to be the most promising ones for the satellite interception system application, and b) vertical flight performance. The vehicles chosen cover the complete spectrum rather well. If very high altitudes and/or heavy payloads are considered, the Titan II is clearly superior from the performance point of view. If lower altitudes and lighter payloads are considered, Polaris appears to have an adequate performance capability. For the middle altitude ranges, the choice of Minuteman was made over the Thor and its offspring, Atlas and Titan I, primarily on the basis of apparently simpler operation or lesser guidance modifications and a possible cost savings.

## 12.2 EVALUATION OF BOOSTER PERFORMANCE

Detailed studies have been conducted in order to evaluate the performance capabilities of the five boost vehicles which were selected as most promising for the SIS mission. Initial studies were conducted to determine the maximum range-altitude capability envelopes for these vehicles as a function of payload weight without regard to the resultant interceptor-target trajectory geometry at intercept. Later studies were concerned with evaluating vehicle intercept capabilities when intercept geometry constraints are considered. The effects of aerodynamic heating, loads, and guidance constraints on interceptor ascent trajectories were considered in all studies. In some cases these constraints were not well defined so that their effect could only be estimated.

### 12.2.1 Range-Altitude Capability Envelopes

Presented in this section are the altitude versus surface range capabilities of the five boost vehicles selected for detailed study; namely, Polaris A2 and A3, Minuteman Wings II and VI, and Titan II. Where available, the performance data presented by the respective booster vehicle contractors have been utilized; however, for the most part the results are based on STL trajectory simulations because of the incompleteness of the data presented by the contractors. In the case of Polaris, lack of definitive configuration data and information pertaining to trajectory constraints made

it impossible to simulate exactly the performance capabilities of the missile. However, it is believed that any discrepancies between contractor missile performance estimates and the estimates presented in this report will be relatively small. A final definition of booster performance is also dependent on the payload design since it will affect booster weights, aerodynamic characteristics, and may impose additional constraints on the ascent trajectory.

Range-altitude capabilities are presented for Polaris and Minuteman for payloads of 500, 1000, and 1500 pounds. Because of the greater capability of Titan II, data are presented corresponding to payload weights of 622, 3000, 5000, and 6000 pounds. Payload weight for all vehicles is defined as the weight above an adapter and therefore includes the payload weight plus shroud if required. All booster ascent trajectories are based on an estimated 3 $\sigma$  propellant reserve to insure that the capabilities presented can be achieved by a booster with non-nominal performance characteristics.

A detailed description of the trajectory simulation and constraints considered in computing vehicle performance is presented in Appendix A of Reference 12-1. Also presented there is a summary of configuration data for all five boosters.

#### 12.2.1.1 Polaris A2 and A3

Polaris A2 and A3 maximum range-altitude capability envelopes are presented in Figure 12-2 for payloads of 500, 1000 and 1500 pounds. Each curve in the figure was generated by simulating several trajectories ranging from vertical flight to maximum range capability, plotting the resultant range-altitude loci, and then drawing an envelope tangent to these curves. A comparison of these trajectories with Polaris weapon system trajectories indicated that aerodynamic heating and loads constraints were not exceeded; however, the near vertical trajectories do violate a guidance constraint which restricts the vehicle attitude at burnout.

#### 12.2.1.2 Minuteman Wings II and VI

Presented in Figure 12-3 are Minuteman maximum capability envelopes for 500, 1000, and 1500 pound payloads. STL and Boeing performance estimates for Wing VI were in close agreement, hence Boeing

### 12.2.2 Interceptor-Target Trajectory Geometry Considerations

Of critical importance to the homing stage designer is the relative interceptor-target geometry at the initiation of the acquisition phase. If the homing stage design limits the satellite intercept to apogee or near apogee attacks which permit favorable homing geometry, then the interception of targets in low altitude orbits at maximum range may present some special problems for a boost vehicle designed for an IRBM or ICBM mission. This point is illustrated in Figure 12-6 in which range-altitude envelopes for a Minuteman are presented. Curve A in the figure shows the range versus altitude attained using typical ICBM trajectory shaping. This shaping is characterized by a three second vertical rise followed by a simulated "kick" gravity turn until approximately 90 seconds, after which a constant inertial attitude is maintained until Stage 3 burnout. Note that at Stage III burnout the missile is at an altitude of 112 n mi and that the resultant apogee altitude is approximately 660 n mi. At a re-entry altitude of 100 to 200 n mi the interceptor is descending very steeply so that if intercept was to occur at this point of the trajectory the interceptor-target relative velocity would be very high even for an in-plane intercept. Furthermore, the tracker field-of-view would include the earth since the target would be below the interceptor at initial acquisition.

It is apparent therefore, that the ICBM trajectory shaping is not suitable for intercepting low altitude targets unless one is content with kills at short range from the launch site. A simple method of attaining a low altitude apogee would be to cut off the Stage 3 motor early, thereby severely limiting the range capability. It appears that the best trajectory shaping for intercepting low altitude targets at maximum range is to depress the trajectory by pitching the interceptor nose down during Stage II burning rather than holding a constant attitude. The effect of this pitch maneuver on the range-altitude envelope is illustrated by curves B, C, and D in Figure 12-6. Using the ICBM trajectory shaping (curve A), at 90 seconds the vehicle has pitched to an attitude of 67 degrees relative to the launch vertical which was maintained until Stage 3 burnout. The trajectories for curves B, C, and D were identical to the trajectory for curve A up until 90 seconds of flight, at which time a pitch

rate of 10 deg/sec was simulated until the indicated attitudes were attained. All trajectories are based on full Stage III burn. The effect of the pitch maneuver is seen to be a reduction of the burnout and apogee altitudes and the surface range attained. However, the re-entry angle is not nearly as steep and because of this, postapogee attacks will be possible over a considerable range with tolerable interceptor-target relative velocities and without the tracker's field-of-view intersecting the earth.

Based on the above method of trajectory shaping and other systems considerations, a plan has been devised for intercepting low altitude targets. This plan is illustrated schematically in Figure 12-7. For targets which pass close to the launch site in Region 1, short range apogee attacks will be used, resulting in the most favorable interceptor-target closing geometry. The desired apogee altitude will be achieved by using early upper stage cutoff or, for Polaris A3, homing stage separation prior to Stage II burnout. The desired lateral reach,  $d$ , will be achieved by varying the launch azimuth. In Regions 2, 3, and 4 postapogee intercepts will be utilized. Intercepts in Region 2 will utilize a fixed launch azimuth and a variable upper stage cutoff time to achieve greater ranges. Intercepts in Region 3 will utilize the maximum range capability of the booster for a specified trajectory shaping and a variable launch azimuth to achieve greater lateral reaches. Thus the same trajectory shaping is used for intercepting targets in Regions 1, 2, or 3 with the cutoff time and launch azimuth being varied to achieve greater lateral reaches. However, to achieve the maximum possible lateral reaches it may be necessary to change the shaping, since a highly depressed trajectory does not result in maximum range capability (see Figure 12-6). This would correspond to intercepts occurring in Region 4.

The same general launch scheme can be used to intercept targets in high altitude orbits. The only difference is that as the target altitude increases, more of the intercepts will occur at or near apogee.

This proposed launch scheme is not intended to preclude preapogee intercepts. Additional analysis is required to determine if preapogee intercept is more optimal than an apogee intercept for targets passing close to the launch site. Launch azimuth and range restrictions for specific launch sites would also influence the choice of launch geometry.

### 12.2.3 Boost Vehicle Lateral Reach Capabilities

As can be seen from Figure 12-7, the effectiveness of a single unrestricted launch site depends largely upon the width of the defended corridor. This corridor width is twice the interceptor lateral reach, where lateral reach is defined as the distance of closest approach between the ground trace of a target orbit and the launch site of an interceptor which can kill that target. In this section the lateral reach capabilities that can be achieved by Minuteman Wing II, Titan II, and Polaris A3, are presented as a function of some pertinent interceptor target geometry parameters. In the deployment analysis presented in Chapter 14, interceptor lateral reach will be related to system reaction time.

The following parameters are evaluated as a function of lateral reach:

$V_R$  = Magnitude of relative velocity vector

$\alpha$  = Angle between target and interceptor velocity vectors

$\psi$  = Angle between target velocity vector and relative velocity vector

TCA = Track crossing angle, angle between target and interceptor ground traces

ELA = Earth look angle, angle between line-of-sight from interceptor to target and local horizon

These parameters are related to lateral reach ( $d$ ), target velocity ( $V_T$ ), interceptor velocity ( $V_I$ ), interceptor surface range ( $R_I$ ), and interceptor flight path angle ( $\beta'_I = \beta_I - 90$ ) through geometry as follows:

$$TCA = \sin^{-1} \left[ \sin \left( \frac{d}{60} \right) / \sin \left( \frac{R_I}{60} \right) \right]$$

$$\alpha = \cos^{-1} \left[ \cos TCA \cos \beta'_I \right]$$

$$V_R = \left[ V_T^2 + V_I^2 - 2V_TV_I \cos \alpha \right]^{1/2}$$

$$\psi = \sin^{-1} \left( V_I \sin \alpha / V_R \right)$$

$$ELA = \cos^{-1} \left( V_I \sin \beta' / V_R \right) - 76.4^\circ \quad (\text{target altitude} = 100 \text{ n mi})$$

#### 12.2.3.1 Minuteman Wing II

The lateral reach capabilities of a Minuteman Wing II booster with 1000 and 1500 pound payloads were evaluated for intercepting targets in 100, 500, and 1000 n mi circular orbits. The resultant capabilities are presented in Figures 12-8 through 12-13 as a function of the intercept geometry. The principal criteria used in computing these data was to keep the relative velocity less than 20,000 feet per second and the earth look angle greater than four degrees over as wide a range of lateral reaches as possible. This was achieved for each altitude by selecting different interceptor ascent trajectories and by varying the interceptor launch geometry as described in Section 12.2.2. Noted on some of the Figures are the regions corresponding to the launch plan used. For the 1500 pound payload, only one set of initial conditions ( $V_I$ ,  $R_I$ ,  $\beta_I$ ) was used to evaluate lateral reach capabilities for each altitude. In each case, conditions were selected which would result in maximum lateral reaches for the specified  $V_R$  and ELA criteria.

Range-altitude envelopes for the ascent trajectories on which these capabilities are based are presented in Figures 12-14 and 12-15. All trajectories were shaped so as not to exceed the constraints specified for the operational Minuteman. However, as was previously mentioned structural modifications are required in the Minuteman third stage if these constraints are to be applicable for an intercept mission with large homing stages. The weight of these modifications will subtract directly from the payload weights considered.

From Figures 12-8 through 12-13 it is seen that for  $V_R \leq 20,000$  feet per second and  $ELA \geq 4$  degree, a Minuteman Wing II booster has the following lateral reach capabilities:

Target Altitude, n miLateral Reach, n mi $W_{PL} = 1000 \text{ lb}$      $W_{PL} = 1500 \text{ lb}$ 

100	2160	1720
500	2640	2000
1000	2300	1380

For a target altitude of 100 n mi, Minuteman lateral reach is limited by the minimum look angle constraint. In order to satisfy this constraint, a depressed trajectory must be flown which has a resultant range considerably less than the maximum range capability of the booster. If the ELA constraint is relaxed so that the tracker field-of-view can include a portion of the earth, the maximum lateral reach for a 1000 pound payload and  $V_R \leq 20,000 \text{ ft/sec}$  would be increased from 2160 to 2630 n mi. For target altitudes of 500 n mi and higher, Minuteman lateral reach is limited by the relative velocity constraint. At these altitudes, the ascent trajectories, which result in maximum lateral reach, generally correspond to maximum booster range capability.

12.2.3.2 Titan II

The lateral reach capabilities of a Titan II booster with 5000 pound payload were evaluated for target altitudes of 100, 500 and 1000 n mi. These capabilities are presented in Figures 12-16, 12-17, and 12-18, and range-altitude envelopes for the ascent trajectories on which they are based are presented in Figure 12-19. All operational Titan II trajectory constraints were satisfied in generating each of these curves.

The geometry presented in Figure 12-16 for a target altitude of 100 n mi is based on the interceptor being injected into a circular orbit at that altitude. In this case the earth angle is a function only of the altitude, and curves of intercept range versus lateral reach can be drawn for a specified relative velocity and track crossing angle. Curves are presented for relative velocities of 20,000, 30,000, and 36,190 ft/sec, the latter case corresponding to a cross plane intercept. It can be seen that orbital intercepts alleviate problems associated with the minimum earth look angle constraint, but lead to higher relative velocities at intermediate lateral reaches. The data presented for target altitudes of 500 and 1000 n mi are based on ballistic type ascent trajectories and are similar in form

to those presented for Minuteman. These data show that with a 5000 pound payload and  $V_R \leq 20,000$  ft/sec, Titan II has the following maximum lateral reach capabilities:

<u>Target Altitude, n mi</u>	<u>Lateral Reach, n mi</u>
100	2750
500	3000
1000	3280

The intercept geometry presented in Figures 12-17 and 12-18 plus similar data based on other ascent trajectories were used to draw  $V_R$  contours. The results are presented in Figures 12-20, and 12-21 for target altitudes of 500 and 1000 n mi respectively. In these figures, target motion is assumed to be in a downrange direction, thus crossrange distance corresponds to lateral reach. For a given  $V_R$ , these contours represent the intercept footprint that can be achieved by Titan II neglecting launch azimuth, impact range, and tracker field-of-view constraints. Shown on each figure is a constraint line corresponding to a tracker line-of-sight tangent to an altitude of 400,000 feet. For a specified launch site, launch azimuth and impact range constraint lines could also be added; however, the reader is cautioned that angles are not generally preserved in the projection shown.

#### 12.2.3.3 Polaris A3

A preliminary analysis was made to determine the Polaris A3 lateral reach capabilities utilizing the launch plan previously described. Since sufficient detailed information regarding Polaris configuration data and trajectory constraints was not available, confidence in these estimates is not as great as that for the Minuteman estimates.

Typical range-altitude envelopes for the Polaris A3 with a 1000 pound payload are presented in Figure 12-22. The curve labeled "no pitch maneuver" is roughly representative of a weapon system trajectory. This trajectory was shaped by simulating a short vertical rise period followed by a gravity turn until 90 seconds, after which a constant inertial attitude was maintained. The atmospheric portion of the trajectory was very similar to that described by Lockheed in Reference 12-3 as being acceptable for aerodynamic heating and loads. As can be seen from the



figure, this shaping results in an apogee altitude of approximately 450 n mi with a steep re-entry angle in the altitude range from 100-150 n mi. In order to depress the trajectory, the vehicle was pitched at 84 seconds to attitudes of 67, 77, and 87 degrees as noted in the figure. According to a statement made in Reference 12-3, a pitch maneuver at this time is permissible; however, the angle through which the vehicle can be pitched is constrained by the guidance system. If the vehicle is pitched past an attitude of approximately 78 degrees, one of the guidance accelerometers will saturate and the guidance accuracy will be degraded accordingly unless suitable guidance system modifications are made. Thus the trajectory profiles shown represent varying degrees of guidance degradation.

Using initial conditions for apogee and postapogee attacks from the depressed trajectories, intercept geometry was computed for attacking targets in 100 n mi circular orbits. From this it was determined that only the ascent trajectory which was depressed by pitching the vehicle to an attitude of 87 degrees resulted in favorable closing velocities and earth look angles at a re-entry altitude of 100 n mi and a range corresponding to full Stage 2 burn. These data are presented in Figure 12-23. Using this trajectory shaping, a lateral reach capability of 940 n mi was attained for  $V_R = 20,000$  ft/sec and  $ELA = 5$  degrees. From a comparison of the intercept geometry for the trajectories which were not as severely depressed, it appeared that the optimal pitch attitude to maximize lateral reach was between 77 and 87 degrees, so that the Polaris A3 lateral reach can probably be extended to 1000 n mi.

#### 12.2.4 Minuteman Heating and Loads Trajectory Analysis

Since the trajectory shaping recommended for intercepting targets in low altitude orbits differs considerably from that previously analyzed for weapon system application a study of the sensitivity of these trajectories to non-nominal missile performance was performed to determine the effect on aerodynamic heating and loads. Current operational Minuteman nominal and perturbed trajectories were used for comparative purposes since these trajectories had already been generated for another purpose (Reference 12-4). Using identical configuration data (corresponding to a payload weight of approximately 900 pounds) and

simulation models, nominal and perturbed trajectories were computed for a satellite intercept mission. The powered flight trajectory shape was controlled by the pitch plane velocity steering method used for the weapon system, and therefore it was necessary to evaluate coefficients for the pitch steering polynomials prior to making simulations. These were evaluated for a SIS trajectory which was depressed to an apogee altitude of 130 n mi with full Stage 3 burn.

In the perturbed trajectory simulations for both ICBM and satellite intercept missions, the Stage 1 thrust was increased 5.3 percent, drag decreased by 15 percent, normal force increased 7 percent, and a Maritime Tropical atmosphere used throughout flight so as to result in the combination of non-nominal performance which would maximize aerodynamic heating and loads. These trajectories result in pseudo  $3\sigma$  plus conditions for design heating and loads.

A summary of pertinent parameters from these trajectories is presented in Table 12-2. Comparison of these data show that the nominal or perturbed trajectories for both missions are essentially identical at the times corresponding to maximum dynamic pressure and Stage 1 burn-out. At approximately 80 seconds a nose-down pitch maneuver was simulated in the trajectories for the interceptor so that by the end of Stage 2 the intercept trajectories are more depressed. However, at this time the vehicles are at a sufficiently high altitude so that the magnitude of the aerodynamic heating indicator is essentially the same for both missions.

The results of the study did show that the Stage 2 interstage must be jettisoned prior to performing the pitch maneuver or the interstage jettison time delayed approximately 15 seconds to avoid excessive aerodynamic loading at separation. The interstage jettison time was 80.4 and 77.4 seconds respectively for the nominal and perturbed trajectories so that the pitch maneuver can be performed after interstage separation and still achieve a low altitude apogee. If this shaping technique is used for an intercept mission, ascent trajectories based on non-nominal booster performance will be no more sensitive to aerodynamic heating and loads than those for the current operational Minuteman.

Table 12-2. Comparison of Minuteman Wing II Nominal and Perturbed Trajectories for Satellite Intercept and ICBM

	<u>Satellite Intercept</u>		<u>ICBM</u>	
	Nominal	Perturbed	Nominal	Perturbed
<u>At Maximum Dynamic Pressure</u>				
Time, $t$ (sec)	36.96	38.46	36.51	38.46
Dynamic Pressure, $q$ (lb/ft <sup>2</sup> )	4,160	4,806	4,163	4,801
Angle-of-Attack, $\alpha$ (deg)	0.04	0.12	0.04	0.13
Heating Parameter, $\int q V_a dt \times 10^{-8}$	1.54	2.23	1.48	2.23
Velocity, $V$ (ft/sec)	3,740	4,373	3,678	4,375
Altitude, $h$ (ft)	37,275	43,729	36,424	43,783
Flight Path Angle, $\beta$ (deg)	56.80	57.70	56.80	57.70
<u>At Stage I Burnout</u>				
$t$	60.36	57.36	60.36	57.36
$q$	622	749	623	750
$\alpha$	0.19	0.29	0.15	0.25
$\int q V_a dt \times 10^{-8}$	4.65	5.28	4.65	5.28
$V$	7,443	7,553	7,446	7,556
$h$	106,938	103,548	106,925	103,532
$\beta$	61.40	61.40	61.40	61.40
<u>At Stage 2 Burnout</u>				
$t$	121.53	118.53	121.53	118.53
$q$	0.70	1.20	0	0
$\alpha$	8.00	8.00		
$\int q V_a dt \times 10^{-8}$	5.03	5.73	5.00	5.70
$V$	14,309	14,418	14,394	14,506
$h$	291,861	287,395	363,153	361,363
$\beta$	80.80	80.90	69.50	69.60
<u>At Stage 3 Burnout</u>				
$t$	176.55	173.55	176.55	173.55
$q$	0	0	0	0
$\alpha$	2.90	2.90		
$\int q V_a dt \times 10^{-8}$	5.03	5.73	5.00	5.70
$V$	23,549	23,663	23,272	23,385
$h$	404,022	399,044	694,210	693,866
$\beta$	85.20	85.20	71.30	71.30
<u>At Apogee</u>				
Altitude, $h$ (n mi)	129.50	132.40	696	714
Range, $R$ (n mi)	1,519	1,647	2,949	3,039

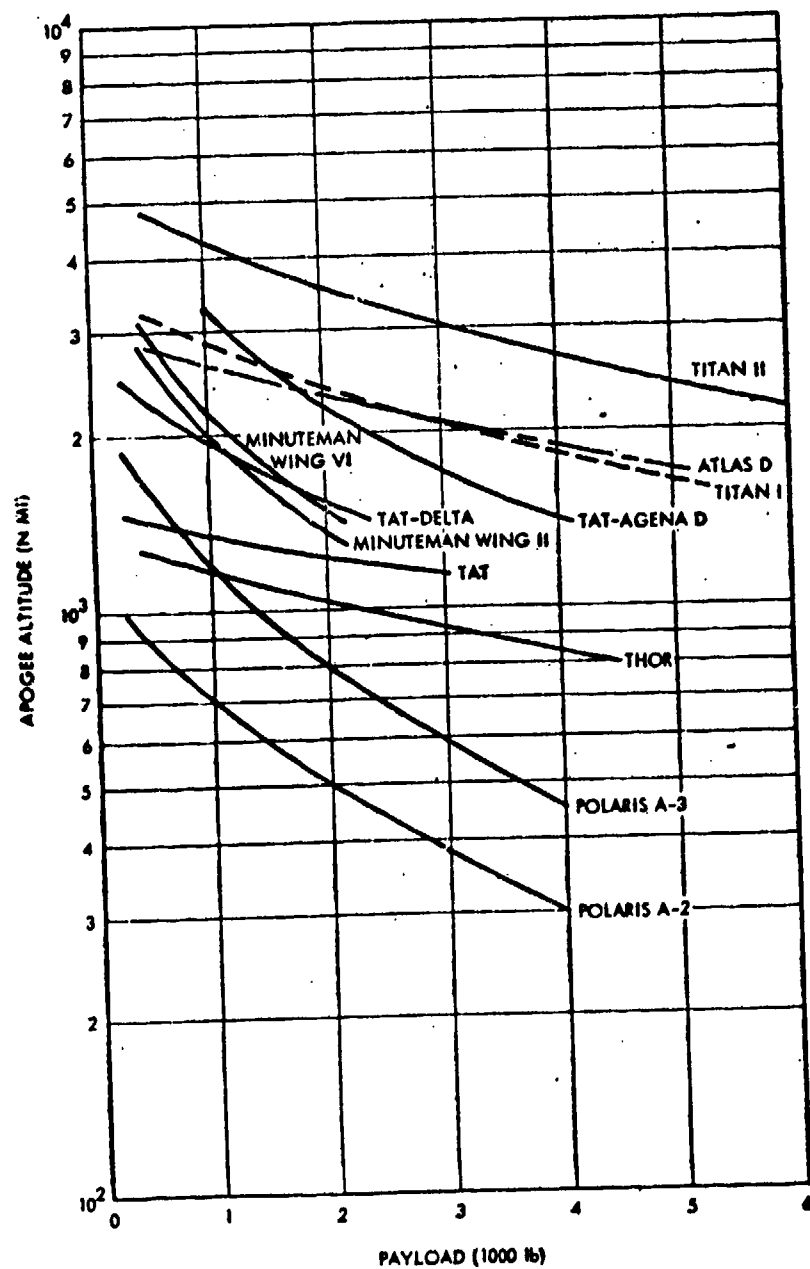


Figure 12-1. Vertical Flight Capability of Booster Vehicles

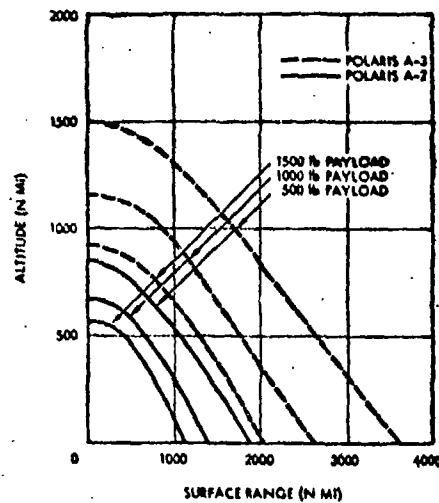


Figure 12-2. Polaris Maximum Capability Envelopes (North Launch).

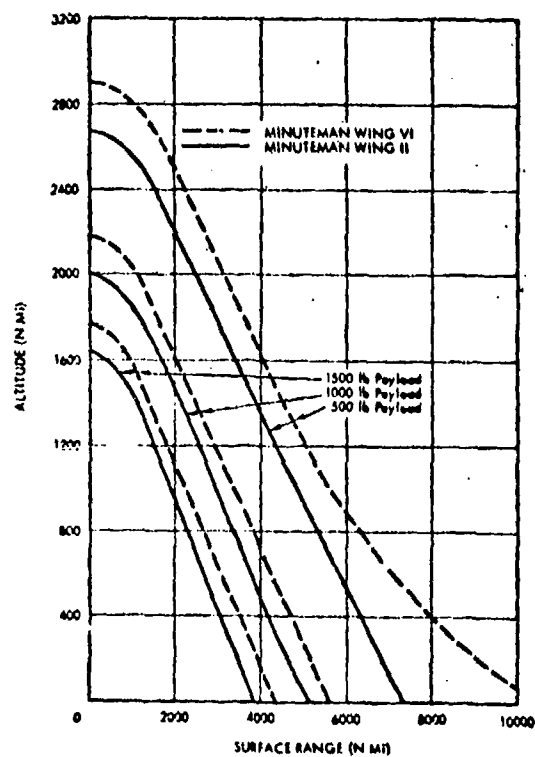


Figure 12-3. Minuteman Maximum Capability Envelopes (North Launch, 2.5 Percent Propellant Residual)

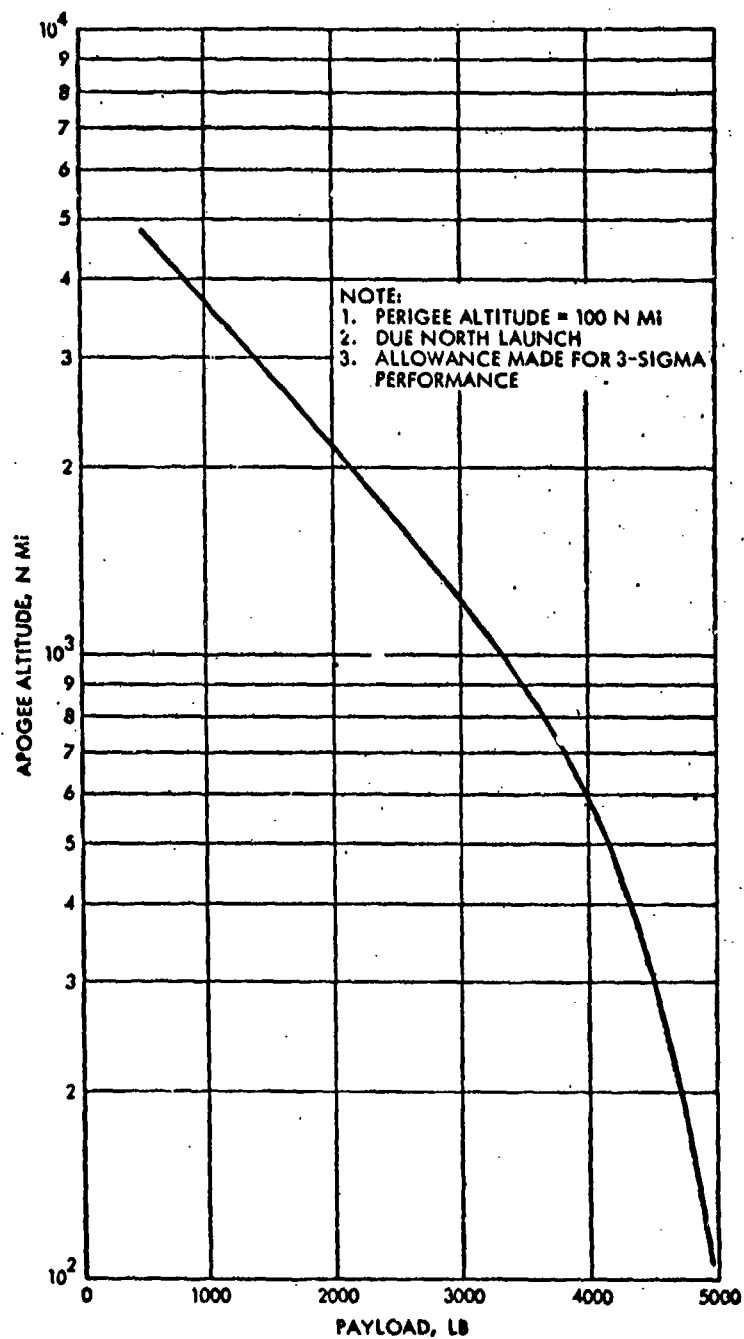


Figure 12-4. Titan II Elliptical Earth Orbit Payload Capabilities

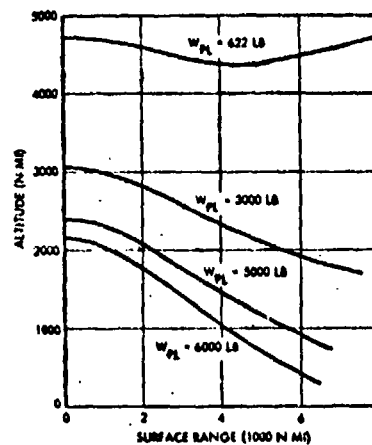


Figure 12-5. Titan II Maximum Capability Envelopes (North Launch, 3-Sigma Capabilities)

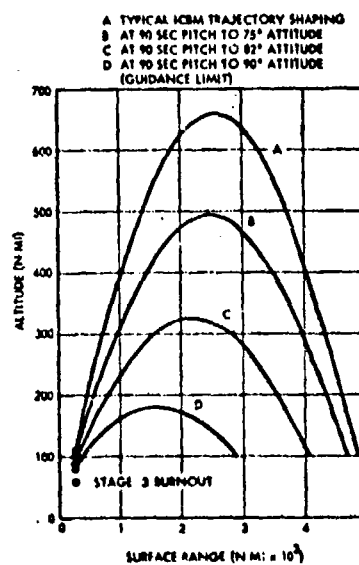


Figure 12-6. Minuteman Wing II Altitude Versus Surface Range Envelopes (1000-Pound Payload, North Launch)

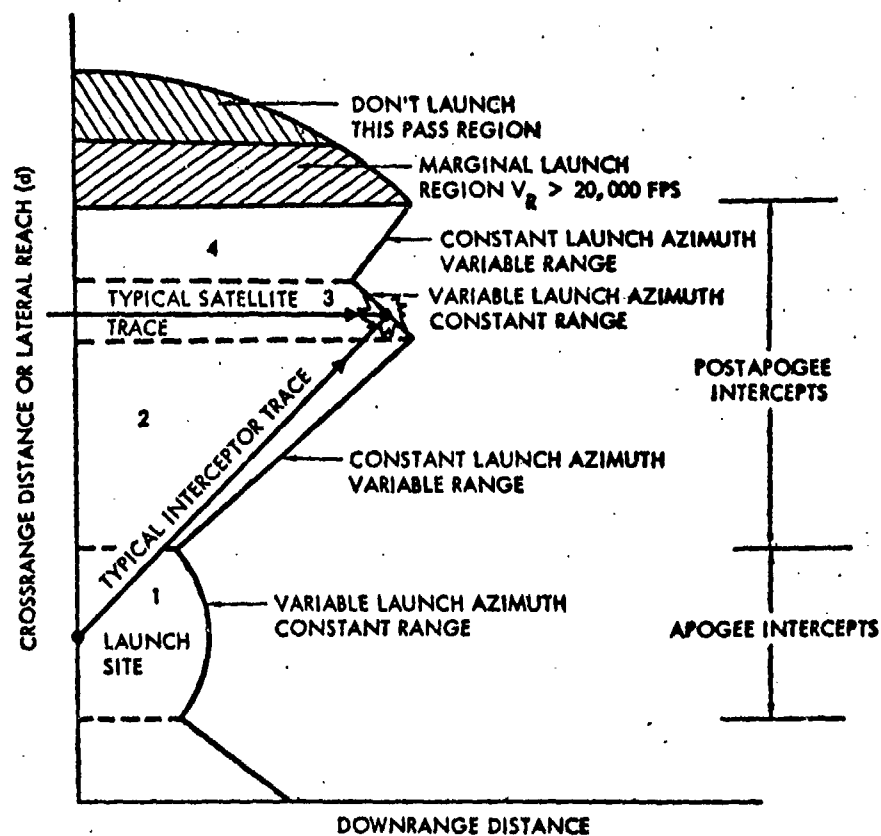


Figure 12-7. Plan View of Launch Geometry Against Low Altitude Targets



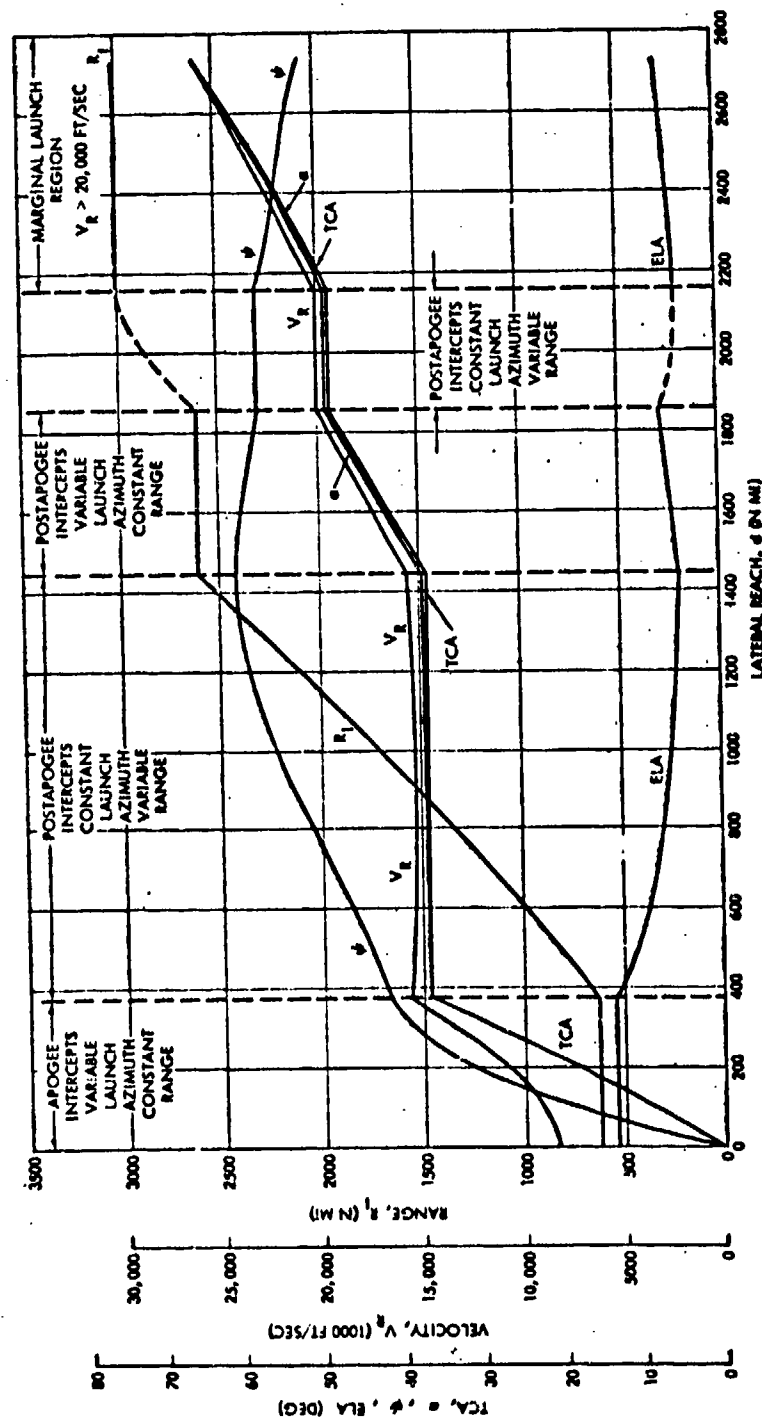


Figure 12-8. Minuteman Intercept Geometry for 100 n mi Altitude Targets (Nonrotating Earth, 1000-Pound Payload)

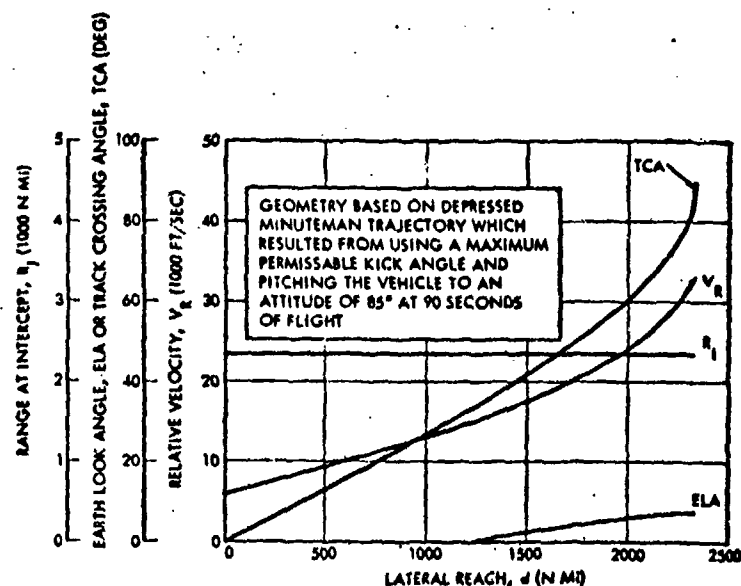


Figure 12-9. Minuteman Intercept Geometry for 100 n mi Altitude Targets (Nonrotating Earth, 1500-Pound Payload)

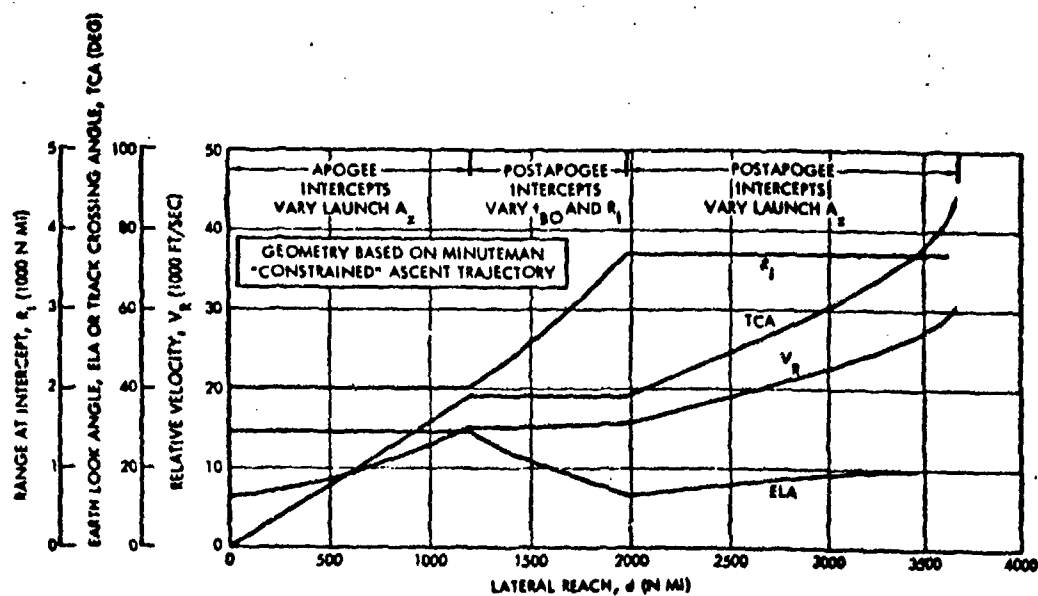


Figure 12-10. Minuteman Intercept Geometry for 500 n mi Altitude Targets (Nonrotating Earth, 1000-Pound Payload)

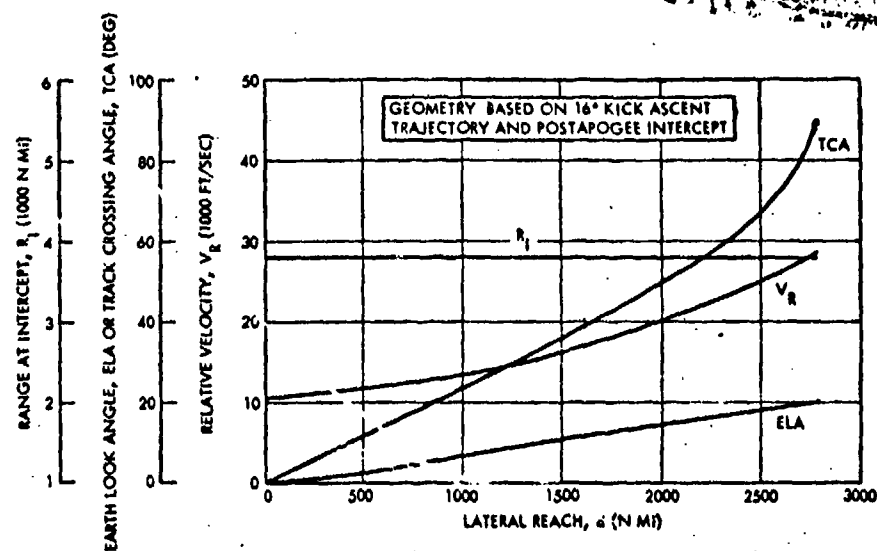


Figure 12-11. Minuteman Intercept Geometry for 500 n mi Altitude Targets (Nonrotating Earth, 1500-Pound Payload)

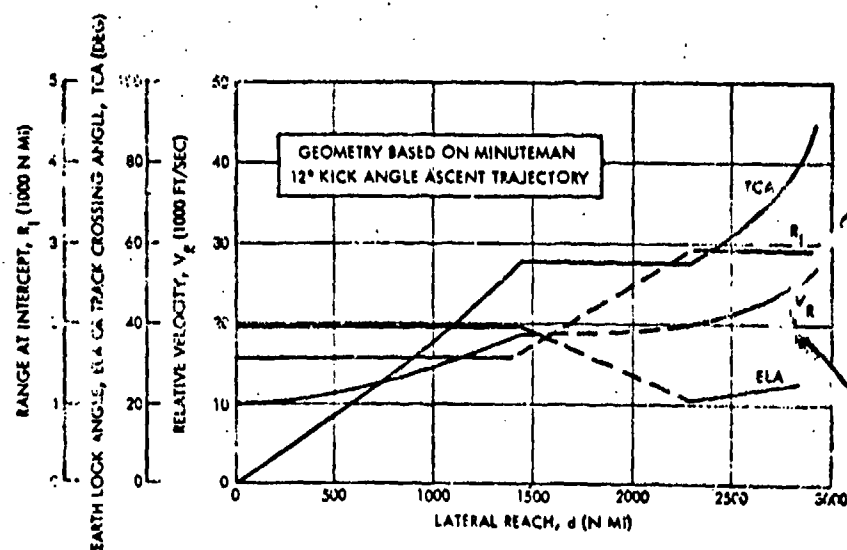


Figure 12-12. Minuteman Intercept Geometry for 1000 n mi Altitude Targets (Nonrotating Earth, 1000-Pound Payload)

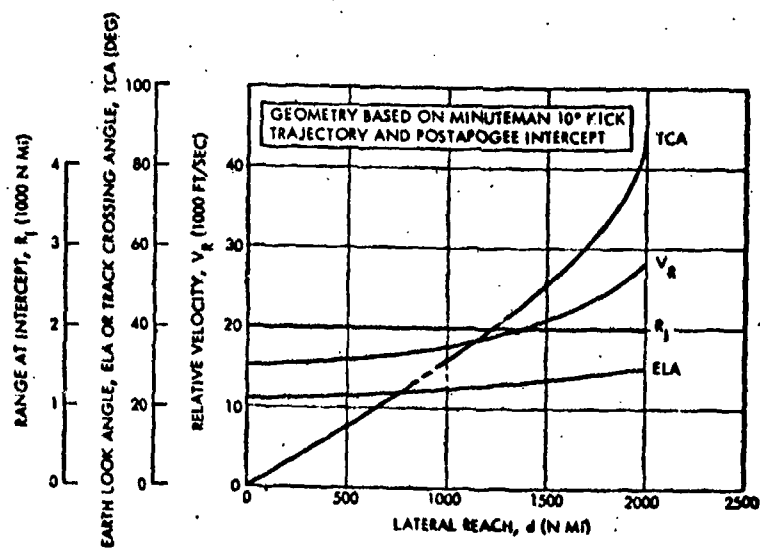


Figure 12-13. Minuteman Intercept Geometry for 1000 n mi Altitude Targets (Nonrotating Earth, 1500-Pound Payload)

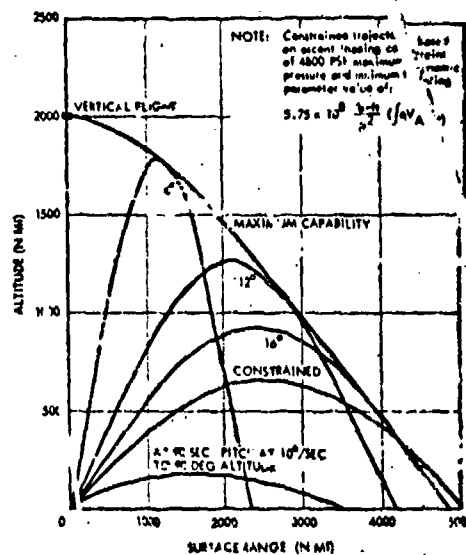


Figure 12-14. Minuteman Wing II Altitude Versus Surface Range (1000-Pound Payload, North Launch, 2.5 Percent Propellant Residual)

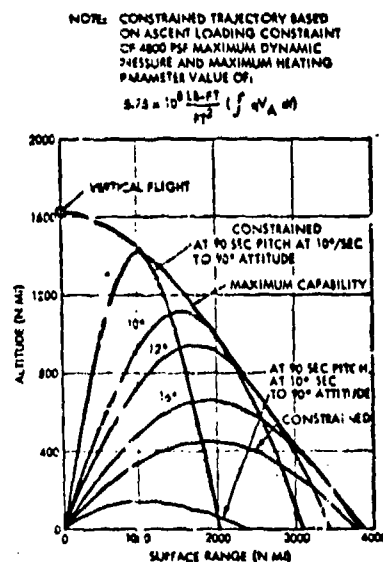


Figure 12-15. Minuteman Wing II Altitude Versus Surface Range (1500-Pound Payload, 2.5 Percent Propellant Residual)

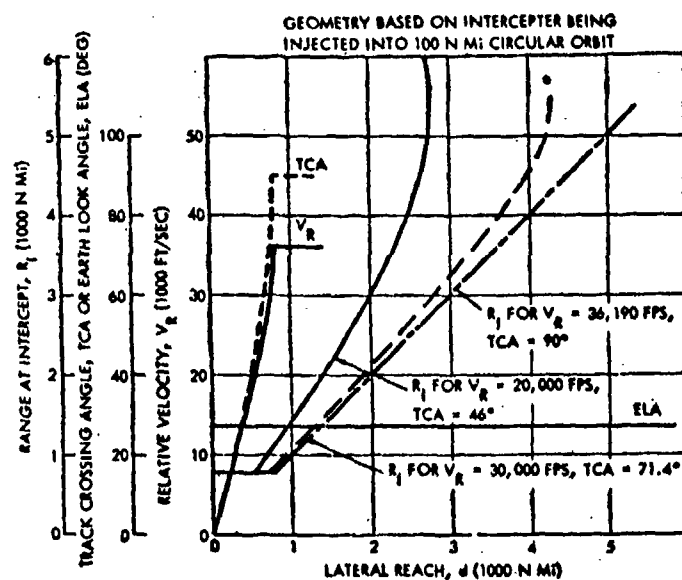


Figure 12-16. Titan II Intercept Geometry for 100 n mi Altitude Targets (Nonrotating Earth, 5000-Pound Payload)

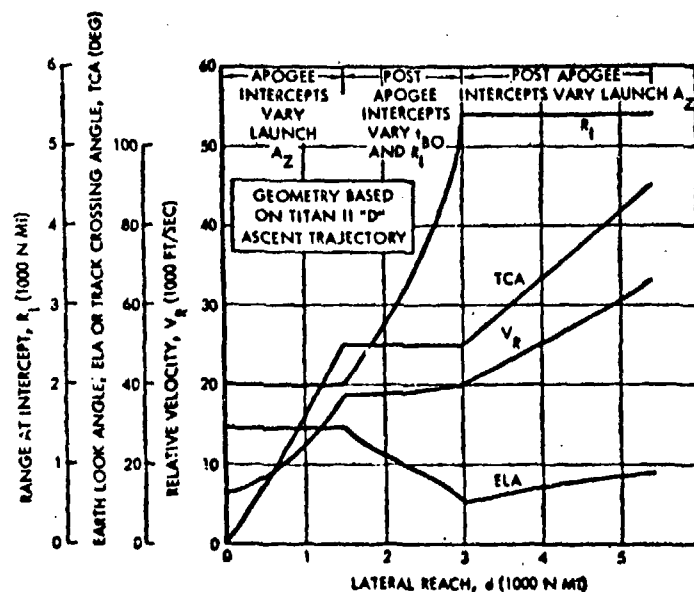


Figure 12-17. Titan II Intercept Geometry for 500 n mi Altitude Targets (Nonrotating Earth, 5000-Pound Payload)

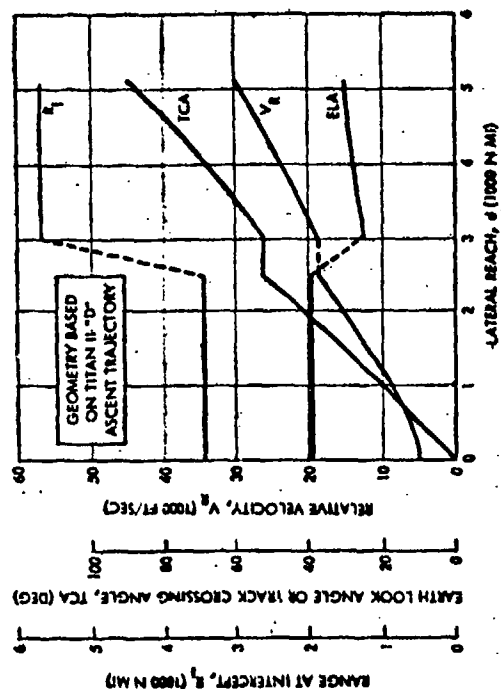


Figure 12-18. Titan II Intercept Geometry for 1000 n mi Altitude Targets (Nonrotating Earth, 5000-Pound Payload)

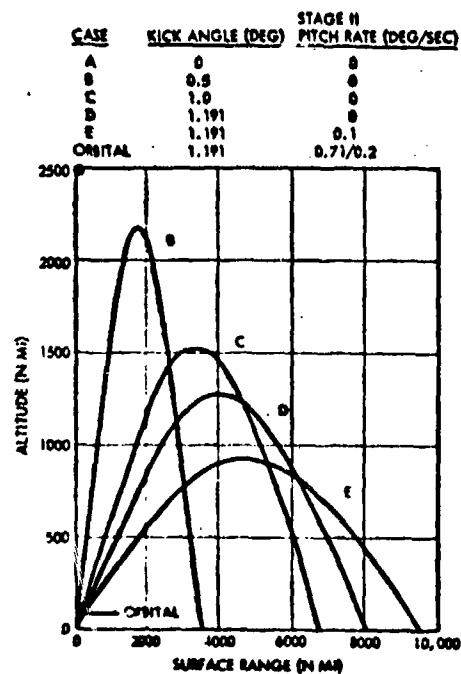


Figure 12-19. Titan II Altitude Versus Surface Range (North Launch, 5000-Pound Payload)

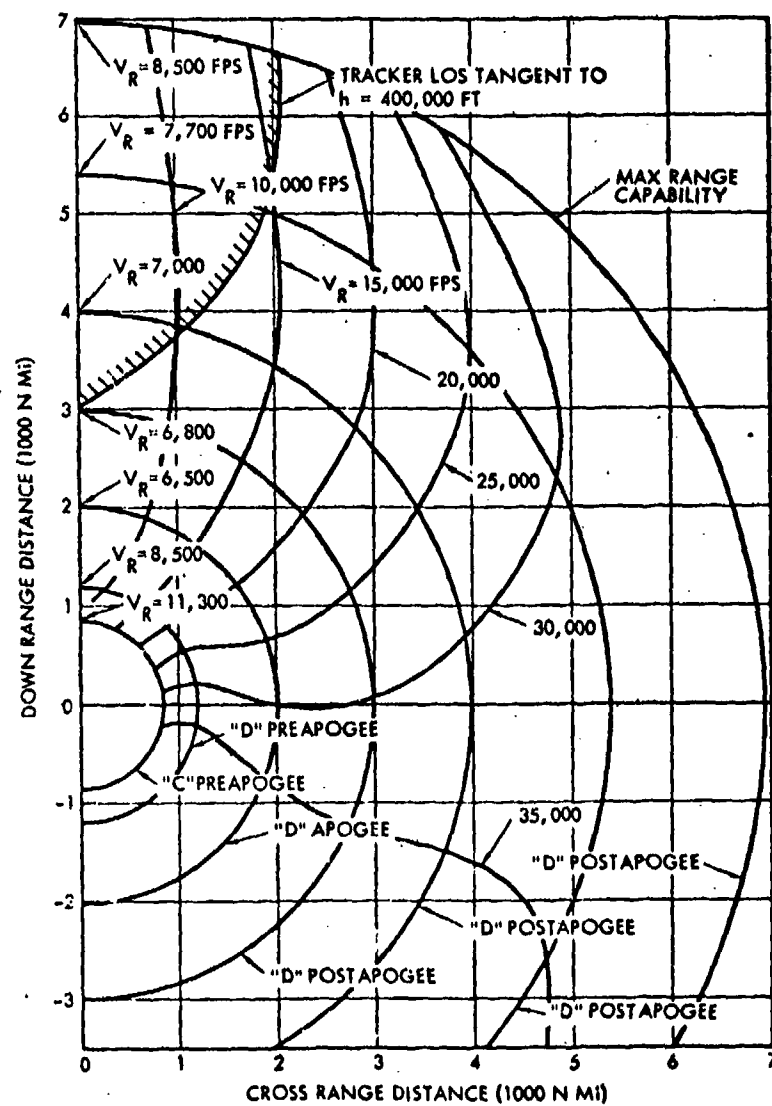


Figure 12-20. Titan II Relative Velocity Contours for 500 n mi Altitude Target (Nonrotating Earth, 5000-Pound Payload)



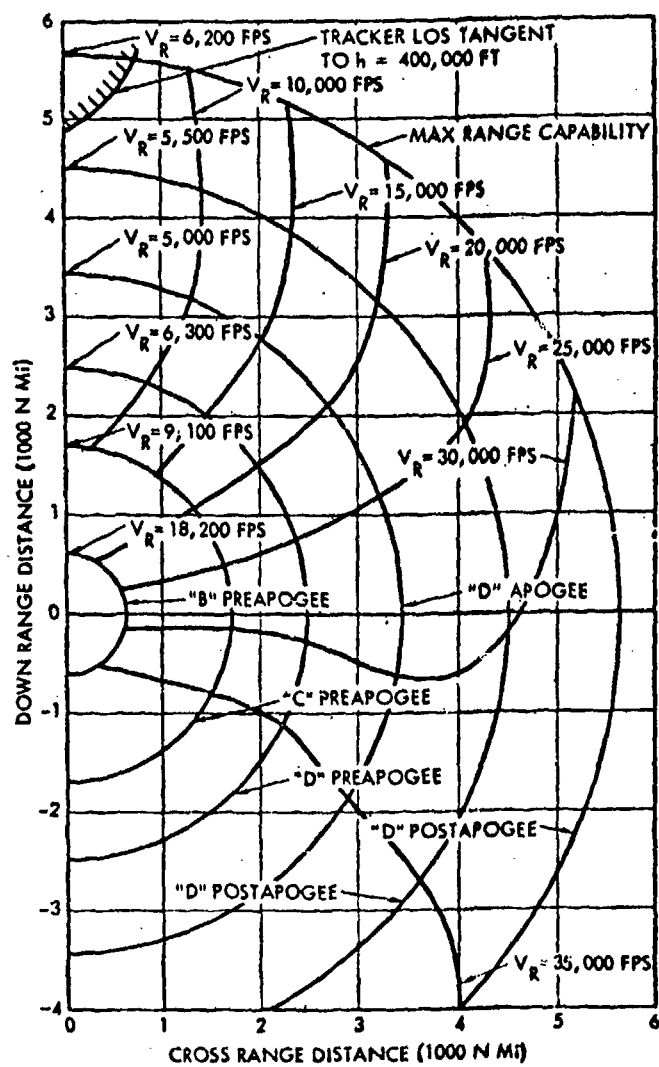


Figure 12-21. Titan II Relative Velocity Contours for 1000 n mi Altitude Target (Nonrotating Earth, 5000-Pound Payload)

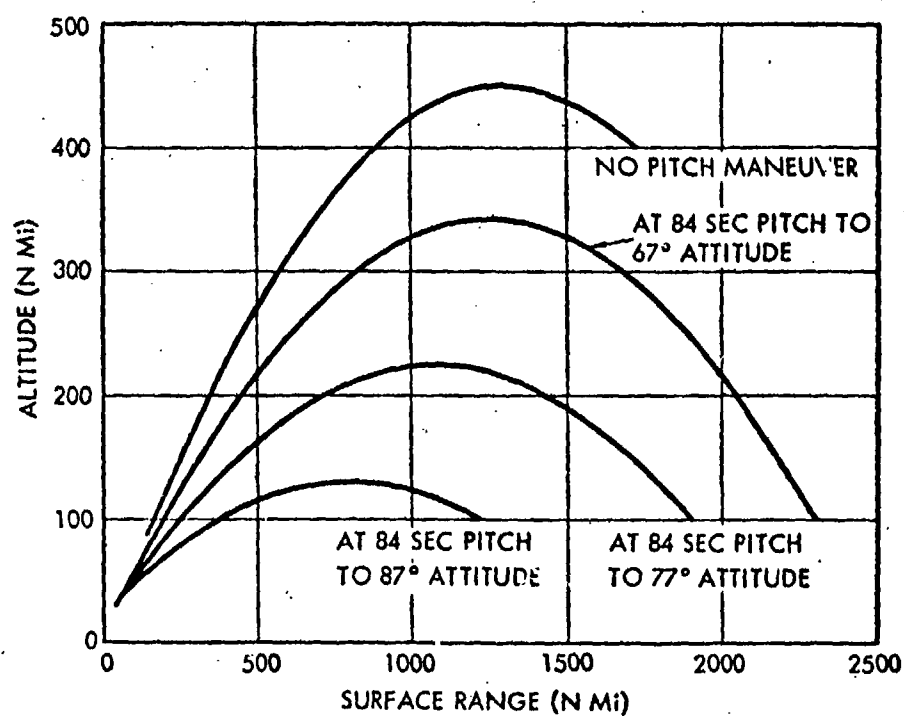


Figure 12-22. Polaris A-3 Altitude Versus Surface Range (1000-Pound Payload)

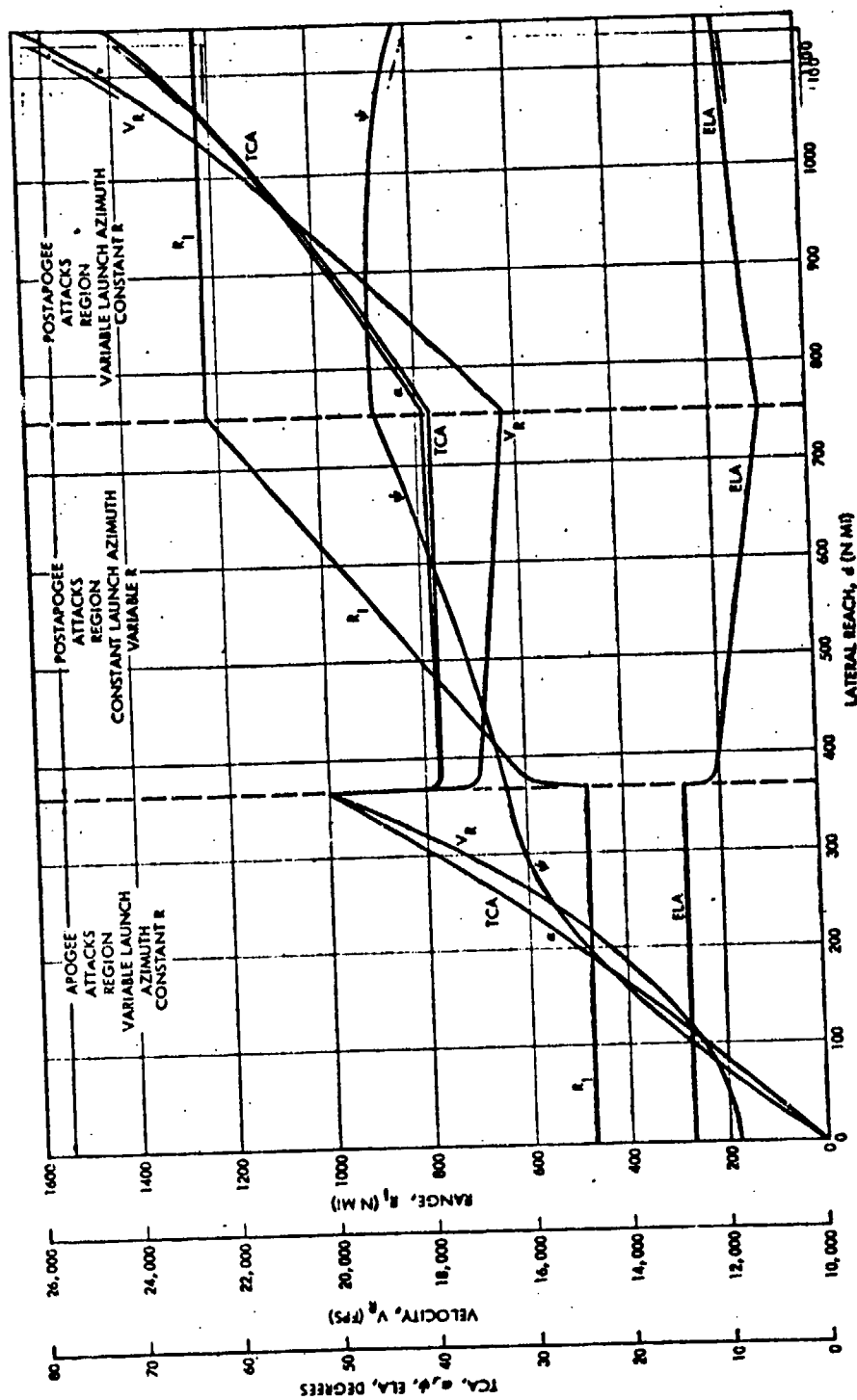


Figure 12-23. Polaris A-3 Intercept Geometry for 100 n mi Altitude Targets (Nonrotating Earth, 1000-Pound Payload)

#### REFERENCES

1. "First Interim Progress Report Satellite Interception System Feasibility Study," (U), Space Technology Laboratories, Inc., 8424-6003-RS000, dated 27 June 1963, (S).
2. "Second Interim Progress Report Satellite Interception System Feasibility Study, Volume II," Space Technology Laboratories, Inc., 8424-6007-RS000, dated 15 August 1963.
3. Transmittal of Polaris Information—Letter to Columbia, LMSC/A370456.
4. "Minuteman Wing II Range-Payload Nominal and Perturbed Trajectories," (U), Space Technology Laboratories, Inc., 9862.4-479, R. J. Meyer, 29 August 1963, (C).

## CHAPTER 13

### BOOST VEHICLE GUIDANCE ACCURACY AND REQUIRED SYSTEM MODIFICATIONS

This chapter presents the results of boost vehicle studies in the areas of guidance accuracy and required system modifications. As explained in Chapter 12, these studies have concentrated on Minuteman Wings II and VI, Polaris A2 and A3, and the Titan II boost vehicle systems.

Boost vehicle system modifications required for the satellite interception mission generally fall into two categories:

- Those modifications which are necessary to accommodate the mission, independent of the reaction time requirement imposed on the system.
- Those modifications required to achieve a fast reaction time.

In summary, only two of the required modifications appear to be major. These have to do with the Polaris guidance system and the use of large, heavy homing stages on the Minuteman boost vehicle.

The Polaris guidance system suitability is dependent upon the use of a modified accelerometer which has not been adequately evaluated for this mission.

In the event that large, heavy homing stage designs (1500 pounds or more) are required, Minuteman (both wings) would require major structural modifications. The elongated payload fairing required for such designs creates excessive aerodynamic loads in the third stage motor casing, requiring structural beef-up of the third stage. The smaller homing stage designs, with their corresponding smaller payload fairings, do not give rise to structural problems.

The majority of the required modifications are relatively minor. Guidance and control modifications include airborne computer program changes for all of the boost vehicles considered, and a minor hardware change to the Titan II potted autopilot module to accommodate lighter payloads. The provision of means to transfer data from the booster guidance system to the homing stage is required for all vehicles studied. Additions to the ground support equipment include a data receiver, a punch

unit or direct input to the airborne computer, and a precise GMT clock linked to the launch control equipment (except for Minuteman Wing VI, which already has one). The Polaris A3 payload separation mechanism must be modified to allow the homing stage to be accelerated away from the still-burning second stage.

The guidance accuracies of the modified Minuteman and Titan II boost vehicles are presented in Table 13-1, along with the current weapon system accuracy figures. The guidance accuracies in this table are expressed in terms of time-of-arrival uncertainties at the intercept point on a typical intercept trajectory. These results will vary with range, launch azimuth and trajectory shape, but generally will not exceed 0.4 second. These figures are comparable to Set 1 ephemeris errors, which were 0.3 second error in track and 0.3 n mi radially. Polaris accuracy figures are expected to be similar for typical intercept trajectories if the potential accelerometer problems do not arise.

Table 13-1. Time-of-Arrival Uncertainties at Intercept ( $1\sigma$ ) for a Nonmaneuvering Payload

Source of Uncertainty	Minuteman-Wing II		Minuteman-Wing VI	Titan II	
	Current	Modified	Current	Current	Modified
Command Generation	0.5	0.07	0.10	0.5	0.10
Command Transmission	-	-	-	-	-
Command Interpretation	0.3	-	-	-	-
Countdown	0.13	0.01	0.01	3.0	0.01
Liftoff	0.06	-	-	-	-
Guidance Control	<u>3.0</u>	<u>0.10</u>	<u>0.10</u>	<u>0.06</u>	<u>0.06</u>
RSS Subtotal	3.1	0.12	0.14	3.04	0.12
Guidance Measurement	<u>0.16</u>	<u>0.16</u>	<u>0.08</u>	<u>0.16</u>	<u>0.16</u>
RSS Total	3.1	0.20	0.16	3.04	0.20

The minimum reaction time that can be achieved for the Minuteman or Titan II is approximately 8 minutes, assuming a maximum azimuth change is required. The corresponding minimum reaction time for Polaris is 14 minutes. These reaction times are measured from target ephemeris availability to launch.

### 13.1 MISSION-DEPENDENT MODIFICATIONS

Mission-dependent boost vehicle modifications are required primarily for the following purposes:

- Providing the homing stage with information necessary to perform intercept. At the very least, attitude information and a time reference must be transferred in-flight from the booster guidance system to the homing stage.
- Providing the boost vehicle guidance necessary to insure that the homing stage will be placed on a trajectory which will cause it to achieve desired acquisition conditions. Other modifications in this category include possible changes to flight control systems and payload separation techniques, as required by the payload characteristics and the booster vehicle.

Mission dependent booster and booster guidance modifications are, of course, a reflection of the detailed choices made in implementing an antisatellite capability. The following discussion presents one possible set of choices, but many variations could be considered.

Assume that a target satellite has been detected and declared hostile. Assume furthermore that a precise determination of threat orbital elements has been carried out by a U. S. facility, i. e., SPADATS. This computation must be based upon data inputs from a suitable SPACE TRACK network. The resulting ephemeris data permits one to forecast future positions of the target, but it is clear that the error in the forecast will always increase as the target position is forecast further into the future. For this very reason the forecast time should be minimized and this is true independently of the desired reaction time.

Put into other words, the antisatellite interceptor should have the benefit of as up-to-date target data as possible. The implications of this factor can be demonstrated as follows. Imagine that, for one reason or another, one were content with 24 hour reaction capability. Suppose that

at the time origin from which reaction time is measured, ephemeris data were available. Now one possibility would consist of forecasting the position of the satellite at some suitable time in the prospective 24 hour period, when the target is within reach of a launch site. Targeting program constants can now be generated and inserted into the interceptor guidance system. Since many hours are available, this entire exercise could take place leisurely, but this leisure extracts a stiff price. That homing stage must be sized to cope with ephemeris uncertainties which result from a long forecast time.

A much more preferable mode of operation would be to take advantage of allowable reaction time to absorb more tracking data to establish orbital elements. More important, the forecast time would be cut and thus, the expected uncertainty of target position at the time of homing stage acquisition would be much smaller, permitting operation with smaller, simpler homing stages. This feature requires, however, a capability for rapid targeting. This capability appears highly desirable independently of whether the overall system must react rapidly or not.

Returning to a possible operational sequence, ephemeris data were generated by SPADATS and from these data a suitable kill point and kill time were selected. At this point two possibilities need investigation. First, SPADATS could generate the booster guidance program constants and relay them to the launch site. This approach requires much data transfer between SPADATS and the site, but obviates the need for on-site targeting computations. Alternatively, SPADATS could relay only the position and time of kill to a launch site with the targeting computations being performed at the site. In this case, the communication traffic is of low volume, but on-site computation is required.

The choice between the foregoing alternatives seems to depend on launch site location, the principal question being whether the site is connected to SPADATS by wire lines. In this case, central SPADATS targeting appears reasonable. If, however, the site is remote (in a communication sense), on-site targeting may be the preferable alternative.

The targeting program for the boost vehicle must be based on a constant time of flight guidance scheme, in order for the homing stage



to arrive at the nominal point of kill at a chosen Greenwich Mean Time (GMT). This requirement implies two things. First, the guidance equations must be constant time of flight. Second, a precise clock must be startable on the pad at a chosen time. Only Wing VI Minuteman provides these features in its weapon system configuration. All other boost vehicle guidance systems must undergo some degree of modification to achieve these features.

The targeting program must also calculate a number of parameters to be inserted into the homing stage computer. These parameters include the inertial orientation of the nominal LOS at acquisition, the time of acquisition, a forecast of relative velocity,  $V_R$ , and possibly some fuzing parameters. Shortly before booster thrust termination, the booster guidance system must provide the homing stage with attitude information and a time reference, in order to enable the homing stage to assume attitude memory and to carry out its operational sequence in the proper time frame of reference.

### 13.2 MODIFICATIONS TO REDUCE REACTION TIME

The second category of modifications is required to assure an acceptable system reaction time. This includes modifications to procedures and hardware necessary to receive the targeting constants and information, direct the targeting constants to the boost vehicle guidance computer, direct targeting information to the homing stage, realign the boost vehicle or its platform in azimuth (if required), conduct the necessary launch control operations to specify the precise GMT for guidance function initiation, and conduct the terminal countdown; all of these functions must be performed within the required reaction time. It has been assumed here that the satellite ephemeris determination, mission analysis, and targeting calculations are all being performed at a point remote from the launch site and that the required targeting constants and additional information will be transmitted in the proper format to the launch site.

#### 13.2.1 Current Targeting Procedure

The current procedure used by SAC to target the Minuteman and Titan II missiles is described below. The SAC Director of Intelligence is responsible for the production and distribution of all target trajectory

materials requested by the SAC Missile Force. The Targets Division of the SAC Directorate of Intelligence selects the target and assigns the launch-target combination. The Target Materials Division obtains the precise geodetic data for the launch site and target, and then programs the production and distribution of the target trajectory kit, which consists of several sheets of information and a Mylar punched launch-target tape. The SAC Trajectory Center (TJC), upon receipt of the proper information forms, produces and distributes the trajectory materials. The TJC transcribes the information onto IBM keypunch forms and then keypunches the launch-target data into IBM cards. Normally there are only 15 cards used. These cards are required by the IBM 7090 missile targeting program to generate the launch-target guidance constants. To generate, verify, and assemble the guidance constants, the program requires from 3 to 5 minutes, depending slightly on the target range and, for Titan, slightly on the trajectory shaping requirements.

The output of the targeting program is two magnetic tapes—one for printing the target kit instruction and information sheets, and one for punching the Mylar target tape. The target kit sheets can be printed directly by the 7090 but they are usually printed by a separate equipment item for reasons of economy; however, the 7090 cannot punch the Mylar tape. This is performed in less than 2 minutes by a Digitronics D-105, which is a bi-directional magnetic-to-punched tape converter. The target trajectory kit materials are assembled and transmitted to the launch site.

#### 13.2.2 Proposed Targeting Procedure

For the satellite interception application, the desired reaction time necessitates a major departure from the weapon system targeting procedure. The basic targeting procedure proposed is shown in Figure 13-1, which also includes the command, control, and task descriptions. If the mission analysis and targeting calculations were performed on an IBM 7090 linked directly with the output of the computer which determines the target satellite orbital data, the combined mission analysis and targeting calculations could probably be completed within 5 to 7 minutes, with launch azimuth available after about two minutes. The targeting constants and additional information should then be transmitted to the launch site by a direct secure data link in order to avoid the delays associated with transporting the

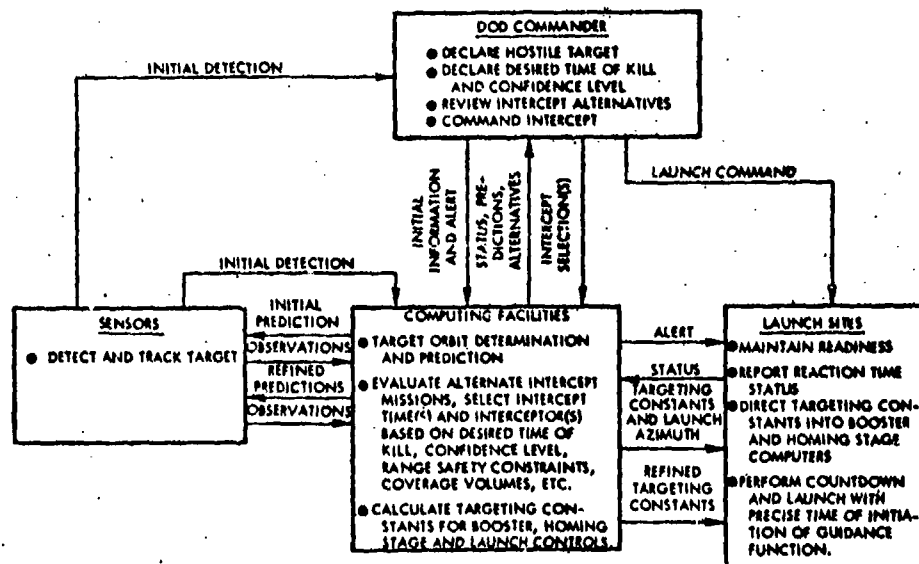


Figure 13-1. System Information Flow and Task Description

target kit to the site. The targeting constants would be either punched on Mylar tape at the launch site or transmitted directly to the airborne computer, depending on reaction time requirements. As soon as the guidance platform is properly aligned in azimuth and the targeting constants are entered into the airborne guidance computer and appropriate launch control ground equipment, countdown may be initiated.

For purposes of evaluating reaction times, it will be assumed that:

- Reaction time is measured from the availability of target ephemeris data in the mission analysis and targeting computer to the moment of liftoff
- Launch azimuth information is available at the launch site after two minutes
- Targeting constants are available at the launch site after seven minutes.

### 13.2.3 Targeting Program Modifications

To illustrate a typical targeting program and its required modifications, the Titan Operational Targeting Program (TOTP) is examined in Appendix H. Similar logic and modifications would be required for the other missile system targeting programs.

### 13.3 MINUTEMAN, WING II

#### 13.3.1 Summary

The guidance equations for Wing II Minuteman must be changed to constant time of flight for the SIS mission. The Wing VI equations can be used for this purpose. Other changes to the airborne guidance computer program will also be necessary. All of these changes involve software modifications only and can easily be incorporated into the present Wing II D17 airborne digital computer (ADC) memory.

The guidance computer must be started at the appropriate precise GMT, requiring the addition of an accurate GMT clock at the launch control facility. This clock must be linked to the GSE in order to initiate the countdown and to achieve precise timing of entry into the ADC flight mode.

Analysis of the Minuteman Wing II arrival time ( $t_a$ ) uncertainty for satellite interception indicates that, with the indicated ground support equipment (GSE) and airborne digital computer program modifications, the  $t_a$  uncertainty may be reduced from 3.1 seconds to 0.20 second (1 $\sigma$ ) for a typical intercept trajectory. Large variations in the above results can occur because of guidance measurement errors which vary with range, azimuth, and trajectory shape.

A major structural modification may be required for the bulkier homing stage designs employing radar sensors and 250 pound explosively-deployed pellet warheads.

When the launch azimuth is more than 10 degrees away from the inertial platform azimuth alignment, the Wing II Minuteman must be realigned. The current realignment procedure requires 8 hours. In order to provide a faster reaction capability, special procedures must be followed. Using these procedures, it is possible to perform the target-ing operation, realign, and complete the terminal countdown in less than 8 minutes after the target ephemeris data are available in the targeting computer. A slight loss of alignment accuracy would result but this loss would be partially offset by the probable improvement in target ephemeris data as a result of using later tracking data.

### 13.3.2 Current Guidance Equations

The Wing II guidance equations are delta equations which do not control the time of flight. The powered flight trajectory shape is controlled by a pitch plane velocity steering method utilizing polynomials with arbitrary coefficients. Thus, the reference trajectory may be reshaped easily by changing the coefficients. The flight control system is a "digital" control system, i.e., the system is mechanized by equations in the airborne digital computer. This enables the control system to be modified by only software changes. A feature of the Wing II guidance equations is that of being able to choose the guidance (target) azimuth as much as 10 degrees away from the inertial platform azimuth alignment. Although the yaw gimbal limit is  $\pm 18$  degrees, the azimuth offset is currently limited to  $\pm 10$  degrees to enable the attitude control system to correct for missile performance and environmental perturbations.

### 13.3.3 Guidance Equation Changes

The satellite intercept mission requires constant time of flight (CTOF) guidance equations, which will always affect interception at a time and position predetermined by the targeting program. The CTOF guidance equations which have been developed for Wing VI Minuteman are recommended for incorporation into the Wing II flight program for the antisatellite mission.

For the highly lofted trajectories needed to intercept high altitude targets, several of the flight program equations require modification. The control system gain change criteria should be based on a combination of downrange ( $\dot{x}$ ) and vertical ( $\dot{z}$ ) velocities instead of just  $\dot{x}$ , which is not precise enough for nearly vertical trajectories. Another change required by nearly vertical trajectories is a rescaling of all the guidance equations because of the larger variation in the magnitudes of their coefficients. Further investigation of the nearly vertical trajectories revealed a need for more terms in the equations for pitch command and both downrange and time-of-flight velocity-to-be-gained guidance equations. The third stage must be cut off by a combination of downrange and vertical velocities since the present method of cutting off on only downrange velocity loses its effectiveness for nearly vertical trajectories.

For extremely depressed (flattened) trajectories, the current guidance equations require no additional modification. The reference trajectory may be obtained simply by changing the arbitrary coefficients of the pitch plane velocity steering polynomial. The criteria remain unaltered for changing the missile attitude control system gains and for staging the missile. The proposed Wing VI equations for pitch command and CTOF guidance are also acceptable without change.

Once the guidance system is aligned, the missile may fly downrange or backrange. This is accomplished by using positive or negative pitch commands. The weapon system trajectory is designed to always fly downrange. If siting considerations require a missile to fly backrange, then some alterations in the flight program are required. The flight equations must be capable of accepting negative values of  $\dot{x}$  (downrange velocity) in the control system gain change criteria. The flight equations must also be capable of accepting a negative value of acceleration experienced by the  $x$  accelerometer,  $\ddot{x}_a$ , which is used in the missile staging criteria. A further problem in the missile  $\ddot{x}_a$  staging criteria exists for some of the backrange trajectories because the missile  $\ddot{x}_a$  may be zero or very nearly zero. This problem may be solved by always staging on a combination of  $\ddot{x}_a$  and  $\ddot{z}_a$ . The downrange guidance equation ( $V_{gx}$ ) must be changed to include an arbitrary coefficient for  $\dot{x}$ .

The flight program will require a routine<sup>\*</sup> to execute the initiation of the guidance computations prior to launch. Further additions to the flight program may be required by additional flight safety checks or by a need for a routine to remotely read new launch-target guidance constants into the computer.

Preliminary investigation indicates that all of the above could easily be incorporated into the Wing II airborne digital computer (D17) memory as shown in Table 13-2. The post-attack emergency alert mode and the two-target capability do not apply to the satellite intercept mission; the same is true of certain monitor checks which are presently performed.

<sup>\*</sup>This routine is simply a repetitive test performed in the airborne computer which continues to look for the signal to initiate guidance computations ("go inertial").

Table 13-2. Minuteman Wing II D17 Computer Memory Budget

	<u>Memory Cells</u>
Wing II D17 ground and flight program utilization	2560
Unused cells in D17 Wing II program	0
Additional cells required by CTOF guidance	50
Required for near vertical trajectories by control system and guidance equations	50
"Initiate guidance" routine	15
Additional flight safety checks	25
Routine for remotely reading launch-target guidance constants	50
Deletion of monitor checks which are unnecessary for satellite intercept mission	-50
Deletion of emergency alert mode	-194
Deletion of two-target capability	-50
Total Budget	2456
Unused cells in D17 satellite intercept program	<u>104</u>
Total D17 Memory Cells	<u>2560</u>

#### 13.3.4 Launch Control Timing Accuracy

The major contributors to time-of-arrival,  $t_a$ , uncertainty are:

- The command and launch control timing errors prior to entry into the airborne computer flight mode
- The variations in the time of flight,  $t_f$ , from entry into the flight mode to the desired intercept point.

The first set is considered in this subsection and the second set in the next. Entry into the flight mode, which occurs prior to liftoff, is chosen as the start of  $t_f$  since the ADC commences solution of the guidance equations at this time. The missile guidance system attempts to control the  $t_f$  to the nominal value determined by the targeting program. Modifications to the ground support equipment (GSE) and the airborne digital computer program are required to reduce  $t_a$  uncertainties.

An error analysis of the missile guidance must consider both the position and time errors. However, position errors can be converted to timing errors by dividing them by the velocity of the homing stage. Thus a total  $t_a$  uncertainty may be computed as the root-sum-square (rss) of the timing error which is computed from the position miss and the time measurement errors. Since the guidance miss is required to size the homing stage engine and the satellite homing tracker, the miss may be determined by multiplying the total  $t_a$  uncertainty by the homing stage velocity at intercept.

The launch control errors which affect the miss are:

- Command generation to initiate the launch countdown
- Command transmission
- Command interpretation
- Countdown.

#### 13.3.4.1 Command Generation

The current Minuteman Wing II command generation uncertainties in Table 13-1 include estimated errors from visual clock reading and manual launch key actuation. The modified uncertainties occur when a command generation system such as that employed by Minuteman Wing VI is incorporated. This may be accomplished by replacing the clock reading and the launch key by an electronic device to initiate the launch countdown at a prescribed GMT, quantized to 0.25 second or better.

#### 13.3.4.2 Command Transmission

The transmission system does not add any  $t_a$  uncertainty for a single missile launch.

#### 13.3.4.3 Command Reception and Interpretation

The Wing II Minuteman command is received by a mechanical decoder which then transmits the signal to the Autonetics coupler, C53, with a time accuracy of  $\pm 0.1$  second. The ADC is synchronized with the C53 clock which has an accuracy of 1 part in  $10^8$ . However, the clock pulses occur only once every 1.04 seconds and the countdown is not started until it senses a clock pulse. Thus the interpretation of the command signal has



a 1σ uncertainty of 0.3 second. At a prescribed time later, the "enter flight mode" signal is sent from the C53 with an accuracy of 1 part in  $10^8$ . Both of the above errors may be eliminated by using the current "enter flight mode" signal from the C53 to activate the ADC to look for a new "enter flight mode" signal, which will be generated at a prescribed time interval after the nominal initiation of the launch countdown. The prescribed interval must allow for both uncertainties above, but it must not hold the missile on missile battery power for more than 2 seconds longer than it is presently held.

#### 13.3.4.4 Countdown

The Minuteman Wing II countdown is controlled with an accuracy of 1 part in  $10^8$  by the Autonetics GSE. However, the ADC currently determines the end of the countdown with a time quantization of 0.45 second. The modified accuracy in Table 13-1 can be accomplished by changing the quantization in the ADC to 0.03 second by software reprogramming of the ADC.

#### 13.3.5 Booster Guidance Accuracy

The second set of errors which result in time-of-arrival uncertainty (or target miss) are those errors resulting from:

- Liftoff
- Guidance control
- Guidance measurement.

Table 13-1 also summarizes the  $t_a$  uncertainties of the above errors.

##### 13.3.5.1 Liftoff

Normal liftoff variations contribute insignificant uncertainties when CTOF guidance is employed. CTOF guidance is used in Titan II and Minuteman Wing VI and is recommended for Minuteman Wing II, primarily for reduction of guidance control variations.

##### 13.3.5.2 Guidance Control Accuracy

Propulsion and mass uncertainties contribute the most to the inaccuracy of the current guidance control. With CTOF guidance the inaccuracies are reduced to the levels indicated in Table 13-1, or about 0.1 second.

Use of CTOF guidance for Minuteman Wing II has been estimated to be about as accurate as the Wing VI equations, since they are recommended for incorporation into the Wing II ADC. The  $t_a$  uncertainty is thereby reduced from 3.0 to 0.1 second. It has been assumed that environmental control comparable to that in the weapon system silos is maintained.

#### 13.3.5.3 Guidance Measurement

In order to augment the Autonetics SEP data presented in Reference 5, Spherical Error Probable (SEP) miss distances were computed and presented in Table 13-3 for five trajectories. The meaning of the miss distance associated with SEP is that 50 percent of the missiles will be closer to the desired point than the given distance. SEP's were derived from the combined effects of the following: gyro drift and compensation errors; velocity meter bias, scale factor, nonlinearity, calibration, and miscellaneous errors; platform initial alignment, component alignment, and servo errors; approximations for the airborne computer and guidance equations; control system errors; cutoff impulse; geodetic and geophysical uncertainties (target errors not included). The resultant inertial guidance system error volumes were computed.

Guidance measurement uncertainties propagate into position miss at the prescribed intercept time. However, they may be related to timing errors by dividing them by the homing stage velocity at the intercept time. The guidance measurement uncertainty included in Table 13-1 has been estimated from a guidance SEP for Minuteman Wing II of 0.5 n mi. The actual SEP varies from 0.2 to 1.8 n mi depending on range, azimuth, and trajectory shape, as can be seen in Table 13-3. It can be seen that the largest guidance errors occur for highly flattened trajectories used to maximize lateral reach against low altitude targets; and even these errors are not significant compared to Set 2 ephemeris errors.

The accuracies are based on guidance system mechanizations which compensate for both liftoff time delays and booster engine burning rate dispersions. This implies that the guidance equations will control the nominal time to satellite intercept as recommended in Section 13.3.3.

Table 13-3. Minuteman, Wing II SIS Guidance Miss From IMU Errors Only

Kick Angle (degrees)	Trajectory Point Description	Time (sec)	Altitude (n mi)	Range (n mi)	③ $\overline{\text{SEP}}$ (ft)	④ $\overline{\text{SEP}}$ (ft)	Local Vertical Coordinates		
							x 1 $\sigma$	y 1 $\sigma$	z 1 $\sigma$
0	Apogee	1385.5	2000	0	3,135	3,450	2040	1382	2725
6	Apogee	1337.2	1780	1200	3,900	4,290	3165	1827	2657
12	Apogee	1500.	1260	2100	3,420	3,760	2411	2184	2112
12	Post-apogee	2200.4	70	4100	5,339	5,870	4041	4200	2228
① 18F	Apogee	664.0	280	1800	1,204	1,320	591	826	945
18F	Post-apogee	1206.2	70	3500	2,528	2,780	1730	1674	1553
② 18F	Apogee	540.	131	1630	3,297	3,627	1361	2424	2638
18F	Post-apogee	802.	105	2570	10,149	11,164	5796	6356	7620

① The vehicle pitch attitude was flattened to and held at 90 degrees after the middle of second stage burning.

② The vehicle pitch attitude was flattened to and held at 90 degrees early in second stage burning.

③  $\overline{\text{SEP}} \approx 1.54 (\sigma_x + \sigma_y + \sigma_z) \div 3$

④  $\text{SEP} = 1.1 (\overline{\text{SEP}})$  to account for applicable geodetic and IMU errors which could not be simulated.

### 13.3.6 Other Required Modifications

As discussed in Section 13.1, an electrical cable from the ADC output to the homing stage computer will be required to provide an attitude information and a time reference to the homing stage just prior to boost vehicle thrust termination.

A major structural modification to the boost vehicle may be required for the bulkier homing stage designs employing radar sensors and 250 pound explosively-deployed payload warheads with ephemeris errors corresponding to Set 2 or larger. A preliminary analysis of structural loads for the largest homing stage considered for Minuteman indicates that the allowable bending moments in the guidance and control section and in the third stage are exceeded due to aerodynamic wind loading on the payload fairing. (See Appendix I.) This critical aerodynamic loading occurs due to a maximum  $q_0$  condition, based on the 1959 Sissenwine wind profile criteria, at a point in the trajectory very near maximum dynamic pressure ( $q$ ). This condition is less severe for highly lofted trajectories than for the depressed trajectories necessary to intercept low altitude satellites at long ranges. While a structural modification of the guidance and control section would not be a major modification, modification of the third stage structure must be considered major.

### 13.3.7 Reaction Time

The general targeting operation outlined in Section 13.2.2 can be used for the Wing II Minuteman. However, Minuteman can be brought to launch readiness by only specifying the guidance system alignment azimuth and the launch site dependent constants. Since the launch site dependent constants are fixed and can be stored at the launch site, only the coarse alignment azimuth needs to be transmitted (by voice if permitted) for early missile guidance system alignment and calibration. The precise target dependent guidance constants can be transmitted later, after more precise ephemeris data is obtained. The difference between the coarse alignment azimuth and the precise target azimuth, which may be as large as 10 degrees, can be handled by an azimuth offset matrix in the ADC.

When the launch azimuth is more than 10 degrees away from the inertial platform azimuth alignment, the Wing II Minuteman must be

realigned. The current realignment procedure requires 8 hours. In order to provide a faster reaction capability, special procedures must be followed. Using these procedures, it is possible to perform the targeting operation, realign, and complete the terminal countdown in less than 8 minutes after the target ephemeris data are available in the targeting computer. A slight loss of alignment accuracy would result but this loss would be partially offset by the probable improvement in target ephemeris data as a result of using later tracking data.

When the missile was placed on the launch pad, its pitch plane would be aligned to within 0.5 degree of a fixed azimuth,  $A_1$ , determined by the anticipated launch azimuth probability density function. The precise alignment in azimuth would be conducted with an accurate gyrocompass and a "twist autocollimator." Calibration of the inertial measurement unit (IMU) would follow. When the coarse launch azimuth became available, the following procedure would be followed:

- The platform would be torqued in azimuth at a known rate to determine the relationship of the current alignment azimuth,  $A_1$ , with respect to an adjacent roll gimbal pickoff. These pickoffs are located 72 arc seconds apart, and at earth rate this would require 5 seconds.
- The platform would be then slewed at 2-deg/sec to the roll gimbal pickoff nearest to the coarse launch azimuth. The maximum slew would be 60 degrees and would require 30 seconds for slewing.
- The airborne digital computer (ADC) would next compute the difference between the gimbal pickoff azimuth and the coarse launch azimuth and store this difference in the current target azimuth offset matrix. The ADC would then transform the platform torquing rates and the IMU calibration biases into the new azimuth alignment plane.
- Four minutes would then be allowed for settling of the platform leveling loops and refinement of the gyro biases.
- When the targeting constants are received, a launch azimuth offset matrix will be included which will compensate for the difference between the coarse and final launch azimuth. This matrix must be combined by the ADC with the offset matrix computed earlier.

This procedure must be performed within a few minutes of launch, because of the open loop platform drift incorporated with aligning to a roll gimbal pickoff. This drift does not exist when aligning to the autocollimator.

The accuracy of this scheme is about 30 arc seconds (1 $\sigma$ ). Changes must be made in the booster guidance steering equations to allow a roll maneuver of  $\pm 60$  degrees during a four second vertical rise after liftoff. The Wing VI Minuteman steering equations (for Stage 1) could be used for this purpose. The additional D17 ADC memory requirements imposed by the above procedures could be accommodated by eliminating the present automatic ground calibration program. This program is only utilized when the missile is emplaced and every 3 months thereafter.

The quick reaction azimuthal coverage for the Wing II Minuteman, using the above procedure, would be  $A_1 \pm 60$  degrees. By reversing pitch polarity, the sector  $A_1 + 180$  degrees  $\pm 60$  degrees would also be covered, for a total coverage of 240 degrees.

The minimum system reaction time, using this procedure for a maximum azimuth change, is presented in Figure 13-2. The reaction time shown assumes a direct input from the targeting data receiver to the airborne guidance computer. If a punched tape is generated and read in at the launch site, an additional 7 minutes would be required. Furthermore, targets which correspond to launch azimuths outside of the two 120-degree sectors could not be attacked without an 8 hour delay for the normal Wing II realignment. Range safety restrictions on launch azimuth would reduce the effect of this limitation. In the absence of range safety restrictions, a second interceptor could be used to cover the remaining two 60-degree sectors.

	TIME (MINUTES)								
	8	7	6	5	4	3	2	1	0
TARGET EPHEMERIS DATA AVAILABLE	*								
INTERCEPTOR LAUNCH AZIMUTH TRANSMITTED				*					
GENERATE TARGETING CONSTANTS									
REALIGNMENT, LEVELING AND BIASING									
ENTER TARGETING CONSTANTS								*	
TERMINAL COUNTDOWN									*
LAUNCH									*

Figure 13-2. Minimum System Reaction Time With Wing II Minuteman

### 13.4 MINUTEMAN, WING VI

#### 13.4.1 Summary

The guidance equations for Wing VI Minuteman are constant time of flight equations, as required by the SIS mission. For highly lofted trajectories, minor software changes would be required in the airborne computer program. These changes can easily be incorporated into the Wing VI D37 airborne digital computer memory.

The Wing VI launch control timing accuracy is adequate for the SIS mission, as shown in Table 13-1. Without any changes to the weapon system, Wing VI Minuteman can achieve a time-of-arrival uncertainty of 0.16 second ( $1\sigma$ ) for a typical intercept trajectory.

A major structural modification may be required for the bulkier homing stage designs employing radar sensors and 250 pound explosively-deployed pellet warheads.

Azimuth realignment presently requires 15 minutes when the required azimuth is more than 10 degrees from the existing alignment, but 14 minutes of this time are required for the airborne computer to compute the biases for the earth rate components associated with the realigned platform axes. These biases can be computed in the targeting computer in a few seconds, and slight changes to the airborne computer program can then reduce the realignment time to one minute.

The minimum system reaction time, assuming a direct input to the airborne guidance computer, would be less than 8 minutes.

#### 13.4.2 Current Guidance Equations

The Wing VI guidance system will have all of the features mentioned in Section 13.3.2 except that the guidance equations are to be CTOF equations and the computer memory is to be greater. Realignment of the platform will require only 15 minutes, and a 360-degree azimuth coverage is provided.

#### 13.4.3 Guidance Equations Changes

The changes recommended for Wing II in Section 13.3.3 for nearly vertical trajectories, depressed trajectories, flight safety checks, and

remote read-in are also applicable to Wing VI. The Wing VI D37 ADC can easily handle the required SIS changes.

Wing VI trajectories will not require the missile to fly backrange, since the guidance system can be realigned quickly to any azimuth.

#### 13.4.4 Launch Control Timing Accuracy

The Wing VI launch control errors which affect miss are:

- Command generation to initiate the launch countdown
- The countdown.

Table 13-1 summarizes the current Wing VI time-of-arrival uncertainties.

##### 13.4.4.1 Command Generation

Minuteman Wing VI command generation contributes 0.1 second to  $t_a$  uncertainty because GMT launch prescription is obtained from two numbers, each quantized to 0.25 second.

##### 13.4.4.2 Command Transmission and Interpretation

Command transmission and interpretation do not add any  $t_a$  uncertainty for a single missile launch.

##### 13.4.4.3 Countdown

The Minuteman Wing VI countdown is synchronized by the ADC with a time quantization of 0.03 second.

#### 13.4.5 Booster Guidance Accuracy

Table 13-1 also summarizes the  $t_a$  uncertainties resulting from:

- Liftoff
- Guidance control
- Guidance measurement.

##### 13.4.5.1 Liftoff

Normal liftoff variations cause insignificant  $t_a$  uncertainties with the use of the Wing VI CTOF guidance equations.



#### 13.4.5.2 Guidance Control Accuracy

For a 5500 n mi trajectory, the Wing VI guidance control contribution to  $t_a$  is about 0.1 second.

#### 13.4.5.3 Guidance Measurement

According to Autonetics information in Reference 1, the SEP's for Wing VI were about one-half to one-fourth as large as Wing II SEP's for the same intercept trajectory. Thus, in light of the Wing II SEP presentation in Table 13-3, the Wing VI one sigma uncertainties in position at intercept will always be less than Set 1 satellite ephemeris errors.

The accuracies are based on guidance system mechanizations which compensate for both liftoff time delays and booster engine burning rate dispersions. The current proposed Wing VI (WS-133B) guidance equations perform these tasks.

An SEP of 0.25 n mi was assumed for use in Table 13-1. However, the actual SEP will probably vary from 0.1 to 0.6 n mi depending on range, azimuth, and trajectory shape. The Wing II variations are shown in Table 13-3.

#### 13.4.6 Other Required Modifications

Other required modifications for Wing VI are similar to those discussed in Section 13.3.6 and Appendix I.

#### 13.4.7 Reaction Time

The general targeting operation outlined in Section 13.2.2 can also be used by the Wing VI Minuteman.

The Wing VI Minuteman is capable of 360 degrees of azimuth coverage without repositioning the missile. This is accomplished by rolling the missile after liftoff through an angle of  $\pm 180$  degrees.

Presently, if the new target azimuth is more than 10 degrees from the guidance system alignment azimuth setting, 15 minutes are to be required to realign the inertial platform. The realignment time could be reduced to 1 minute with little loss in accuracy, especially if the targeting program were implemented to compensate for the errors associated with the 1 minute realignment. The platform is actually realigned in about

1 minute but it takes 14 minutes for the airborne computer to compute the biases for the earth rate components associated with the realigned platform axes. Computing these biases in the targeting computer would probably add (at most) a few seconds to the time required for the targeting calculations. It is also possible to perform a simple matrix transformation in the airborne computer in a few seconds. This modification would require additional changes to the airborne computer program involving software changes only. The D37 computer memory is sufficient to allow all of the modifications considered, since it is twice that of the Wing II D17 computer memory.

Wing VI has radio and cable inputs directly to the airborne computer from a remote location which could be used as a direct link to the targeting center of the satellite interception system. The data rates are 8 bits per second for radio inputs and 64 bits per second for cable. These rates can be increased to 16 and 256 bits per second, respectively, with minor modifications. Thus, a message consisting of 40 constants can be transmitted in less than 4 seconds by cable.

The minimum system reaction time for Wing VI Minuteman, assuming a maximum azimuth change, is presented in Figure 13-3. The reaction time shown also assumes a direct input from the targeting data receiver to the airborne guidance computer. If a punched tape is generated and read in at the launch site, an additional 7 minutes would be required.

	TIME (MINUTES)								
	8	7	6	5	4	3	2	1	0
TARGET EPHEMERIS DATA AVAILABLE	*								
INTERCEPTOR LAUNCH AZIMUTH TRANSMITTED				*					
PLATFORM ALIGNMENT, LEVELING AND BIASING									
GENERATE TARGETING CONSTANTS									
ENTER TARGETING CONSTANTS								*	
TERMINAL COUNTDOWN									
LAUNCH									*

Figure 13-3. Minimum System Reaction Time with Wing VI Minuteman

### 13.5 TITAN II

#### 13.5.1 Summary

The Titan II guidance equations are constant time of flight equations, as required by the SIS mission. Minor airborne computer changes will be required, as described below. The potted autopilot module will also require slight modification for payload weights of less than about 4000 pounds.

An accurate GMT clock is needed for precise timing of the initiation of countdown and entry into the ADC flight mode. This clock must be linked to the GSE.

Arrival time uncertainty for a typical intercept trajectory would be about 0.2 second (1 $\sigma$ ) after the indicated modifications were made. Large variations could occur because of guidance measurement error variations.

The Titan II does not require realignment in azimuth and has a 1-minute terminal countdown. The minimum system reaction time, assuming a direct input to the airborne guidance computer, would be 8 minutes.

#### 13.5.2 Current Guidance Equations

The Titan II guidance equations are delta equations which control the time of flight (CTOF). The powered flight trajectory shape is controlled by a pitch plane velocity steering method utilizing polynomials with arbitrary coefficients. Thus, the reference trajectory may be reshaped easily by changing the coefficients. The guidance platform does not require realignment when the launch azimuth is changed.

#### 13.5.3 Guidance Equation Changes

The Titan II steering equations require almost no change for the SIS mission, primarily for two reasons: first, they are already constant-time-of-flight; and, second, the definition of the guidance coordinate system will keep the form of the steering equations invariant for almost any SIS mission. As a result, the only change anticipated is the possible addition of a  $(\dot{z})^2$  term to the booster steering pitch command equation for extremely depressed trajectories. If this addition is necessary, its inclusion into both the targeting and flight programs can be easily accomplished.

The flight program will require additional features in the form of a routine to test for the precise time to initiate guidance computations prior to launch, additional flight safety checks, and a routine to remotely enter targeting constants into the airborne computer. All of these changes can be accommodated within the present flight computer by deleting the three-target capability or parts of the ground program which are needed only for the operational weapon system.

A homing stage weight of less than 4000 pounds would also require modifications to the potted autopilot module in order to change the control system gains to assure dynamic flight stability.

#### 13.5.4 Launch Control Timing Accuracy

The Titan II launch control errors which affect miss are:

- Command generation to initiate both the launch countdown and the entry into the flight mode
- The countdown.

Table 13-1 summarizes the Titan II current and modified time of arrival uncertainties.

##### 13.5.4.1 Command Generation, Transmission and Interpretation

The current Titan II command generation errors are similar to the current Wing II Minuteman errors (see Section 13.3.4.1). These can also be reduced by an electronic device which initiates both the launch countdown and the entry into the flight mode with only 0.25 second quantizations.

Transmission and interpretation do not add to  $t_a$  uncertainty.

##### 13.5.4.2 Countdown

The Titan II one minute terminal countdown is "event sequenced" and controlled by the Martin GSE. Timing variations occur for many of the events in the countdown. Since each event must be completed before sequencing to the next event, the entry into the flight mode (the last event) has almost a 3 second one sigma variation (see Table 13-1). This error can be reduced by placing an electronic switch in series with the "enter flight mode" signal in the A-C Spark Plug GSE. The signal can then be transmitted to the ADC electronically at a prescribed GMT. The countdown initiation must allow for 3 $\sigma$  variations in the countdown duration.

The ADC only looks for the flight mode entry signal once every 0.5 second. However, the quantization error in the ADC can be reduced to 0.05 second by software reprogramming of the ADC.

#### 13.5.5 Booster Guidance Accuracy

Table 13-1 also summarizes the  $t_a$  uncertainties resulting from:

- Liftoff
- Guidance control
- Guidance measurement.

##### 13.5.5.1 Liftoff

The use of CTOF guidance equations causes insignificant  $t_a$  uncertainty for normal liftoff variations.

##### 13.5.5.2 Guidance Control Accuracy

For a 5500 n mi trajectory, the guidance control contribution to  $t_a$  uncertainty is about 0.06 second.

##### 13.5.5.3 Guidance Measurement

Spherical Error Probable (SEP) miss distances were computed and are presented in Table 13-4 for typical trajectories. SEP's were derived from the combined effects of the following: gyro drift and compensation errors; accelerometer zero set, scale factor, nonlinearity, and other sources; platform initial alignment with a 1-hour hold, component alignment, and servo errors; computer approximations; control system errors; cutoff impulse; geodetic and geophysical uncertainties (target errors not included).

Guidance measurement uncertainties propagate into position miss at the prescribed intercept time. However, they may be related to timing errors by dividing them by the homing stage velocity at the intercept time. The guidance measurement uncertainty included in Table 13-1 has been based on a guidance SEP for Titan II of 0.5 n mi. The actual SEP varies from 0.2 to 1.7 n mi depending on range, azimuth, and trajectory shape as can be seen in Table 13-4.

The accuracies are based on guidance system mechanizations which compensate for both liftoff time delays and booster engine burning rate dispersions. The current Titan II guidance equations perform these tasks.

Table 13-4. Titan II SIS Guidance Miss From IMU Errors Only

Kick Angle (degrees)	Trajectory Point Description	Time (sec)	Altitude (n mi)	Range (n mi)	① SEP (ft)	② SEP (ft)	Local Vertical Coordinates		
							x 1σ	y 1σ	z 1σ
1.191	Pre-apogee	1050	1000	2486	4490	4,715	3,897	2338	2738
1.191	Post-apogee	2505	1000	5672	9580	10,060	11,368	3347	4443
1.191	Post-apogee	2990	500	6947	9970	10,470	12,391	3923	3624
1.191	In orbit	1500	100	5250	6960	7,310	6,898	3618	3404

① SEP  $1.54 (\sigma_x + \sigma_y + \sigma_z) \div 3$

② SEP = 1.05 (SEP) to account for applicable geodetic and IMU errors which could not be simulated.

### 13.5.6 Other Required Modifications

The only other required modification for Titan II will be the addition of an electrical cable from the ADC output to the homing stage computer, as previously discussed in Section 13.1.

### 13.5.7 Reaction Time

The general targeting operation outlined in Section 13.2.2 can be used by Titan II.

The Titan II is capable of 360 degrees of azimuth coverage without repositioning the missile. This is accomplished by rolling the missile after liftoff through an angle of  $\pm 90$  degrees and then by flying downrange or backrange according to the pitch attitude polarity.

The minimum system reaction time for the Titan II is presented in Figure 13-4. The reaction time shown assumes a direct input from the targeting data receiver to the airborne guidance computer. If a punched tape is generated and read in at the launch site, an additional 7 minutes would be required.

	TIME (MINUTES)								
	8	7	6	5	4	3	2	1	0
TARGET EPHEMERIS DATA AVAILABLE	*								
GENERATE TARGETING CONSTANTS									
ENTER TARGETING CONSTANTS									
TERMINAL COUNTDOWN									
LAUNCH									*

Figure 13-4. Minimum System Reaction Time with Titan II

## 13.6 POLARIS

### 13.6.1 Summary

The guidance equations proposed by General Electric should accomplish the SIS mission, although some improvement in accuracy may be desirable and easily obtainable. The hardware changes to the guidance computer will use the same basic circuit design, packaging, and production procedures as presently used. The additions to the computer should not seriously affect its electrical, mechanical, or thermal environment.

An accurate, absolute time of entry into the computer flight mode can be achieved using the Ship's Inertial Navigation System (SINS) time reference.

The inertial measurement unit (IMU) is a potential source of problems for Polaris in the SIS mission. To make efficient use of the booster's capability by flying lofted or very depressed trajectories, the Z-axis accelerometer must have its saturation level increased. This may be done with relatively little trouble. However, the characteristics of this accelerometer at high accelerations (5 g's) are virtually unknown. Furthermore, the stability of the known characteristics between calibration periods is questionable in light of the limited experimental test data available to STL on the type of accelerometer used. More frequent calibration might reduce this latter problem.

With the modifications indicated, the Polaris should be capable of reaction times only slightly longer than the minimum reaction times for the Titan II or Minuteman.

### 13.6.2 Current Guidance Equations

The Polaris guidance equations are based upon the Q concept. This means that steering and prediction are based upon the solution of the vector equation

$$\dot{\vec{V}}_g = -Q \vec{V}_g - \vec{a}_T$$

where  $\vec{V}_g$  is the velocity-to-be-gained, Q is a time-varying matrix, and  $\vec{a}_T$  is the acceleration vector. The steering equation controls the direction of  $\vec{a}_T$  so that  $\vec{V}_g = 0$  is attained. For Polaris A-3, the pitch steering



equation follows a gravity turn during the atmosphere, and terminal steering causes the missile to fly perpendicular to an axis in the pitch plane defined by a scalar quantity called skew. This is the means by which the pitch profile is varied, and corresponds roughly to kick angle in other missile systems.

### 13.6.3 Proposed Guidance Equations

The proposed formulation for Polaris for this mission is

$$\dot{V}_{gy} = -a_y$$

$$\dot{V}_{gx} = -a_x - Q_{xx} V_{gx} - Q_{xz} V_{gz}$$

$$\dot{V}_{gz} = -[a_z - Aa_x - Q_{zx} V_{gx}]$$

The yaw channel becomes a nulling loop. In the pitch plane equations, the term  $-Aa_x$  in the equation for  $\dot{V}_{gz}$  is unusual. This is the skew term which reflects into the pitch steering equation

$$\dot{\theta}_p = -K_p [\tau_p \dot{V}_{gz} + V_{gz}]$$

Figure 13-5 defines the guidance coordinate system. It can be shown that  $V_{gz}$  goes to zero before burnout and  $V_{gx}$  becomes small near burnout. Hence

$$\dot{\theta}_c = K(a_z - Aa_x) = 0$$

when

$$a_z = Aa_x$$

Therefore, skew effects the burnout attitude, and by varying  $A$ , the pitch profile is varied (since its presence is felt earlier in flight as well).

The proposed mechanization uses a time varying term for  $Q_{xx}$ , namely

$$Q_{xx} = K_0 + K_1 t$$

while the other  $Q$ 's would be constants.

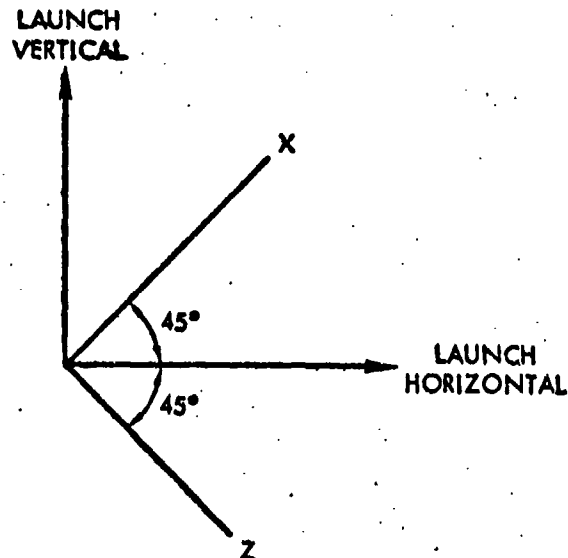


Figure 13-5. Polaris Guidance Coordinate System

A General Electric simulation of these equations resulted in a Spherical Error Probable (SEP) due to the equations alone of about 2000 feet. Burnout attitude was 15 degrees above the x-axis and the target was about 900 n mi downrange at an altitude of about 700 n mi (slightly past apogee). Improvement could be made using "optimum" Q's and a linear time term for  $Q_{zx}$ . The Q's used for these simulation results were not optimized, but corresponded to "optimum" Q's for a burnout attitude very near to the x-axis.

#### 13.6.4 Guidance Computer Changes

The guidance computer hardware changes require the addition of 3 or 4 computer sticks to the present 13, using the same basic circuit elements, design and production as presently used in the Polaris computer. General Electric reports that there is sufficient space for these additions, and they would not upset the thermal, mechanical, and electrical systems presently in the Polaris missile. Hence, there is little reason to believe that suitable guidance equations could not be mechanized for the SIS mission.

#### 13.6.5 Launch Control Timing Accuracy

The go-inertial time may be closely controlled (within 20 milliseconds) using SINS to update the Fire Control Computer (FCC) clock. SINS is very accurate with a drift rate of  $10^{-7}$  sec/sec, and is synchronized with GMT every 8 hours. Some minor additions to FCC hardware are necessary to allow it (rather than an operator) to send the go-inertial signal.

#### 13.6.6 Inertial Measurement Unit Accuracy

The present Polaris missile constrains its thrust attitude to be within about  $\pm 30$  degrees of the x-axis at burnout. This is because the z-axis PIPA saturates at about 4.5 g's and the total acceleration is about 7 g's at burnout. This precludes very lofted trajectories and, more important, very depressed trajectories, which would give about 5 g's to the PIPA.

To remove this limitation, General Electric proposes to increase the PIPA range by a factor of three by reducing the pendulosity of the sensor float by the same factor. This technique would undoubtedly be the simplest way to increase the range of this PIPA. It would require a redesign of the float (which could be readily accomplished) and a rescaling of the computer processing of the input from this accelerometer (also a minor change). The present caging electronics for the accelerometer could be used without modification.

The accelerometer scale factor, bias and quantization level will increase three-fold as a result of this change. The bias uncertainty will also increase by a factor of three. The scale factor uncertainty, when expressed as a ratio (i.e., ppm, etc.) will remain the same except that the bias uncertainty will decrease the measurement repeatability associated with two point scale factor calibrations. This effect is probably negligible when compared to the long term scale factor uncertainties.

There are, however, two other important problems. The first has to do with the rms uncertainty of the PIPA scale factor from its initial calibration. The current recalibration period is one year. General Electric asserts that this value is 150 ppm and that the bias uncertainty is  $0.1 \text{ cm/sec}^2$ . In STL's experience with the testing of one such PIPA, and based on comments of various manufacturers of these instruments, STL feels that these numbers are grossly optimistic. This instrument

suffers from a torquer ferrite rotor magnetization problem whereby shutdown, cooldown, and certain types of open loop operation result in changes in both bias and scale factor which considerably exceed the above uncertainty numbers. Development effort is being expended by various organizations in an effort to improve or correct this defect, and it is reasonable to assume that at least a partial improvement will eventually be accomplished.

The second problem is with the PIPA characteristics above 1 g. The scale factor is quoted up to 1 g, but at higher accelerations no accurate and extensive measurement of the PIPA linearity has been made. An absolute specification is  $\pm 1000$  ppm for scale factor at  $\pm 3.5$  g's. A limited number of these instruments have been tested at this point and have been found to be satisfactory. However, the limits at 5 g's (for the modified PIPA) is not known. If nonlinearities exist, it would be important to test an appropriate sample in order to determine whether the values are essentially the same throughout the accelerometer population or vary from unit to unit. If the latter situation arose, expensive calibration on a precision centrifuge would be necessary.

In summary, the performance of the modified PIPA at high accelerations is not known, and its stability between calibrations is rather uncertain. An error analysis was performed by General Electric using the trajectory mentioned in Section 13.6.3, and a SEP of about 3800 feet resulted. This analysis used their estimates of the stability of the instruments and neglected initial position errors. The SEP would be about 5800 feet using a 0.5 n mi navigation error in both horizontal directions.

#### 13.6.7 Other Required Modifications

Attitude information to the homing stage must be provided through a direct link from the IMU to the homing stage. The sines and cosines of gimbal angles are available, and they may be transmitted via cable provided the impedance is high so that negligible loading results.

The present Polaris A3 R/V separation is accomplished by accelerating the payload away from the still-burning second stage. Some modification to the booster-payload interface will therefore be necessary to

accommodate the homing stage and a small rocket motor which will be necessary to provide the required acceleration.

#### 13.6.8 Reaction Time

The general targeting operation outlined in Section 13.2.2 can be used for Polaris. A detailed discussion of alternate methods of calculating the targeting constants is presented in Appendix J.

The Polaris launch site, be it a surface ship, submarine, or on land, must be provided with a data receiver capable of receiving 10 to 20 parameters (depending on the targeting) and of reading this directly into the FCC. This could be done without modifying the FCC hardware since it has a tape reader now and only the program need be made receptive to the particular format.

The Polaris countdown procedure is indicated in Figure 13-6. The guidance platform may be realigned in azimuth at a rate of 0.75 deg/sec, for a maximum required realignment time of 4 minutes. The targeting constants are not required to be entered into the airborne guidance computer until about one minute before launch. Launch azimuth corrections as large as 0.5 degree may also be made at this time. The resulting system reaction time would be as shown in Figure 13-7.

#### REFERENCES

1. Autonetics EM-0663-142, "Autonetics Presentation at ARPA Satellite Interception Symposium, " 1 May 1963. (U)
2. W. Plumb and J. Culbertson, "An Evaluation of Booster Inertial Guidance Systems for the ARPA Satellite Intercept System," (U) STL Memo No. 8424-6023-TS-000, 28 October 1963. (S)

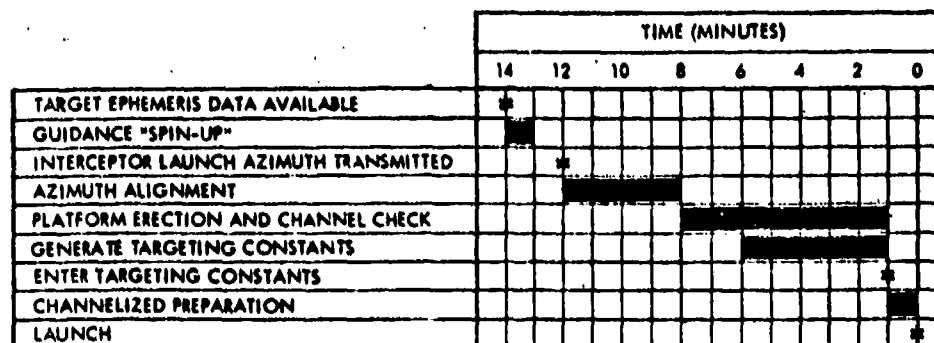


Figure 13-6. Schematic of Polaris Countdown

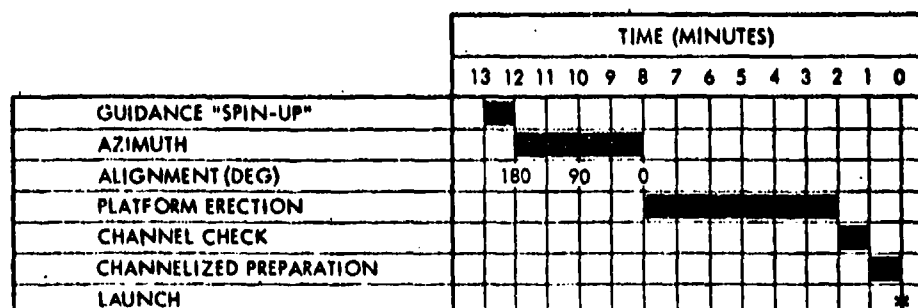


Figure 13-7. Minimum System Reaction Time with Polaris

## CHAPTER 14

### DEPLOYMENT ANALYSIS AND SYSTEM PERFORMANCE

#### 14.1 INTRODUCTION

The specific reaction time requirements considered in the deployment analysis were those provided in the ARPA Study Guide. For orbit altitudes ranging from 75 to 2500 n mi and for all orbital inclinations, those requirements are:

- Interception within 24 hours of launch
- Interception during first orbit (with emphasis on target launches from present Russian launch sites)
- Interception before first pass over the continental United States
- Interception within one orbital period after a satellite is designated as a hostile target.

Based upon the foregoing reaction time requirements, a deployment analysis was performed and this chapter presents a summary of the results generated by this effort. The deployment analysis was carried out in two steps. First, consideration was given to unrestricted launch sites, i.e., sites which are not limited by any range safety considerations. Next, attention was shifted to system performance levels which can be achieved by the use of specific launch sites which are subject to range safety limitations. Further analysis was devoted to the examination of the impact of interceptor constraints upon reaction time. Such constraints result from limits on the relative velocity,  $V_R$ , and the imposition of a requirement that the homing phase tracking sensor cannot "look" at the earth or its sensible atmosphere.

#### 14.2 INTERCEPTOR REQUIREMENTS WITHOUT REGARD TO CONSTRAINTS

As was discussed previously in Chapter 12, the effectiveness of a single launch site depends largely upon the width of the defended corridor. If no interceptor launch azimuth, impact range, or intercept geometry constraints are imposed, this corridor width is twice the interceptor

lateral reach where lateral reach is defined as the distance of closest approach between the ground trace of a target orbit and the launch site of an interceptor which can kill that target. Therefore, the lateral reach required from a specific launch site to counter the target threats posed in the ARPA Study Guide is a good measure of the effectiveness of that launch site. In later sections it will be shown how these requirements are affected by system constraints.

#### 14.2.1 An Approximate Method for Obtaining Required Number of Interceptor Sites

The following method is useful for determining the number of interceptor launch sites required on the equator (and their position) for a given interceptor lateral reach capability, and a given waiting time within which interception must occur.

Assume that all interceptor sites are on the equator, that there is unrestricted azimuth coverage from each site, and that the target is in a polar orbit (an example of a geometrically worst case).

Right ascension swath of ascending nodes covered by one launch site is

$$\frac{2d}{60} + \omega_e T \text{ (deg)}$$

where

$d$  = Interceptor lateral reach (n mi).

$\omega_e$  = Rotation rate of earth (approximately equal to 15 deg/hr)

$T$  = Waiting time (hr)

A total of 180 degrees must be covered by an integral number of sites,  $N$ , so that

$$n = \frac{180}{\frac{2d}{60} + 15T}$$

where  $N$  is the smallest integer larger than  $n$ .

A correction to the above formula is required to account for the phasing of satellite position relative to its ascending node. Since it is



possible that almost one full revolution may be required for the satellite to enter the attack zone after its node has entered the attack zone, the total formula is now

$$n = \frac{5400}{d + 450(T - 1.5)}$$

using 1.5 hours as an approximation to one revolution (for a 100 n mi circular orbit altitude).

For multiple sites ( $N > 1$ ) the location for the case in question must be such that in time  $T$  the 180 degrees of ascending nodes are covered. Thus, equal longitudinal spacing, 180 deg/ $N$  apart, is required such that in time  $T$ , the right ascension of the eastern most edge of the attack zone of one site just reaches the right ascension of the western most boundary of the attack zone of the next easterly station, as it was at the beginning.

Nothing is different for  $N$  equal 1, but it is a trivial case.

#### 14.2.2 Interception Within 24 Hours of Launch

The most relaxed reaction time requirement is the one requiring satellite interception within 24 hours. Figures 14-1 through 14-4\* present the lateral reach requirement for one interceptor base for orbit altitudes of 100, 500, 1000, and 2500 as a function of interceptor launch site latitude. Thus, for an orbit altitude of 100 n mi, an interceptor base at latitude 11 degrees or less would result in a lateral reach requirement of approximately 650 n mi for all orbit inclinations. Using AMR or PMR would result in reach requirements of 1700 and 2100 n mi, respectively.

For a 2500 n mi orbit altitude the ideal latitude for an interceptor base would be at latitude 23 degrees, resulting in a reach requirements of 1320 n mi. Here the minimum is more pronounced, although the use of lower latitudes still costs, at most, less than 100 n mi. Thus for coverage of all orbit inclinations and all orbit altitudes through 2500 n mi, it can be seen that the use of AMR as an interceptor base results in a reach requirements of approximately 400 n mi more than the ideal latitude of 23 degrees.

\* For convenience all tables and illustrations in Chapter 14 are placed at the end of the chapter.

#### 14.2.3 Interception During First Orbit After Launch

Presently, the most probable locations for a satellite launch site are Kapustin Yar (slightly east of the northern tip of the Aral Sea) and Tyuratam (slightly northwest of the northern part of the Caspian Sea). Figure 14-5 shows the band of orbit traces for orbital inclination between 48 and 75 degrees for satellites launches from the launch site situated at Tyuratam. (All past Russian satellite launch azimuths were less than or equal to 90 degrees with inclination of either 65 degrees or 49 degrees). Assuming the existence of an interceptor launch site within this band of orbit traces, the time interval from satellite orbit injection to intercept would be on the order of one-half of the satellites orbital period. For orbit altitudes ranging from 100 to 2500 n mi, that interval ranges from about 44 to 96 minutes. This statement presumes that the target has been detected, declared hostile, adequate ephemeris has been computed, the interceptor was targeted—all in time to exploit the first launch opportunity.

#### 14.2.4 Interception Before First Passage Over the Continental United States

Also shown in Figure 14-5 is the band of orbit traces for passage over the continental United States during the first revolution. This band has been drawn by assuming that the enemy uses his present site locations, but launches at an azimuth which minimizes the time to satellite crossing over the United States (such a launch probably falls outside the azimuth limits of enemy launch sites.) In case of interest, it may be noted that an unrestricted antisatellite launch site located on the northeast coast of Greenland and operating with a lateral reach of about 1000 n mi could destroy such satellites.

Such statements, however, are academic answers to unrealistic questions. First, if an enemy were really motivated to deliver payloads over the United States in minimum time from launch, he would not limit himself to known space launch sites, but presumable would launch from operational ICBM sites. To then argue that some antisatellite interceptor deployment can destroy these satellites before first passage over the United States, amounts to claiming a solution to the midcourse anti-ICBM problem, and such a claim seems absurd.

It appears much more reasonable to assume known inclination angles (49 and 65 degrees) and to inquire what antisatellite deployment can destroy satellites launched from known sites along known inclinations before their first passage over the United States. This amounts to kill within 4 and 6 revolutions respectively, and, as will be shown, this capability can be achieved quite easily from accessible and non-exotic antisatellite launch sites.

#### 14.2.5 Interception Within One Orbital Period After a Satellite is Designated as a Hostile Target

##### 14.2.5.1 Single Interceptor Launch Site

The lateral reach requirement for a single interceptor launch site is shown in Figure 14-6 for target orbit altitudes of 100, 1000, and 2500 n mi. The maximum required lateral reach of 5400 n mi for each orbit combination occurs at the launch latitude which is complimentary to the inclination angle. The effect of orbit altitude on this plot is illustrated by the dashed lines representing 1000 and 2500 n mi orbit altitudes. The largest effect of increased orbit altitudes on lateral reach requirements occurs for low orbit inclinations and low launch site latitudes.

##### 14.2.5.2 Two Interceptor Launch Site Analyses

An analysis was conducted to determine the latitude and longitude of two interceptor bases which would result in minimum lateral reach requirements against all orbit inclinations (direct orbits only). The analysis was carried out for an orbit altitude of 100 n mi. An increase in orbit altitude would simply result in slightly longer lateral reach capabilities, but would not affect launch site selection significantly.

The analysis was performed in the manner stated in Chapter 4 of the first interim progress report.<sup>\*</sup> It was determined that the minimum required lateral reach for all orbit inclinations was achieved when the interceptor bases were in the same hemisphere (northern or southern) separated by 180 degrees in longitude, and when the latitudes of these bases were complements of one another. It should be noted that the same optimum

---

<sup>\*</sup> "First Interim Progress Report Satellite Interception System Feasibility Study" (U) STL Report No. 5424-6003-RS000, dated 27 June 1963. (S)

can be achieved by placing the two interceptor sites on the same longitude, but placing one base in the northern hemisphere and one in the southern, with the latitudes again complements of one another. In either case, the required lateral reach is 2700 n mi.

#### 14.2.5.3 Multiple Launch Sites

For a nonrotating earth, if all launch sites were placed on the same longitude, but spaced apart equal distances in latitude (i.e., separated by  $180 \text{ degrees}/n$ , where  $n$  equals the number of interceptor launch sites), this would represent one possible combination of sites with minimum lateral reach requirements. This procedure was followed to find the lateral reach requirements for multiple sites ( $n > 2$ ). The result is shown in Figure 14-7. The solid curve represents  $5400/n$ , while the dashed curve represents the actual lateral reach requirement when the earth's rotation is considered. As can be seen, the lateral reach requirement can be fairly well defined by  $5400/n$ .

It should also be pointed out that a similar minimum lateral reach requirement occurs when the sites are on the equator and separated by  $180 \text{ degrees}/n$ .

#### 14.2.5.4 Specific Interceptor Launch Site Combinations

Having shown that the maximum lateral reach requirement for two interceptor sites for coverage of all orbit inclinations is 2700 n mi for suitably placed sites, combinations of AMR and a second interceptor site, and PMR and a second site, have been analyzed to determine the reach requirements of several such combinations. The second launch site was chosen for its favorable position against one of the following two reaction time requirements for satellites launched from present Russian launch sites:

- o Interception during first orbit after launch
- o Interception before the first pass over the continental United States.

The additional interceptor launch site areas considered are shown on the map of Figure 14-5. Johnston Island, Tahiti, Wake Island, and the southern tip of South American (point A on the map) were areas considered mainly in connection with reaction time 1) above. Point Barrow,

Alaska, and the northeast coast of Greenland (point B on the map) were considered in connection with reaction time requirement 2).

Figure 14-8 shows the lateral reach requirement as a function of orbit inclination for combinations of AMR and the above-mentioned launch sites. These curves are based upon the worst possible position of the longitude of the ascending node and the satellite at the time of defined hostility (i. e., that combination of nodal longitude and satellite position which results in the largest lateral reach requirement within one revolution). Note that PMR is of little help when considered with AMR.

The southern tip of South America is the best location for a second interceptor base, when considering only lateral reach requirements. The lateral reach in this particular case is 2800 n mi, almost the minimum that can possibly be obtained. However, this latter site would not give good protection against the reaction time requirement of interception before the first pass over the continental United States. Greenland as a second interceptor base results in a 3600 n mi lateral reach capability. Three interceptor bases—AMR, Greenland, and Wake Island—would require about 2900 n mi lateral reach capability for defense against all orbit inclinations and reaction time requirements.

Figure 14-9 is a similar plot for PMR and a second base. In this case, for protection against all reaction time requirements, the best sites would be PMR, Greenland, and the vicinity of Tahiti. A lateral reach of slightly under 2500 n mi is required for this combination of launch sites.

The lateral reach values shown in Figures 14-8 and 14-9 are worst cases and therefore do not take advantage of knowledge pertaining to enemy launch sites. If one assumes that the launch site location is known (as shown in Figure 14-5), reach requirements become much more modest if it is desired to intercept within one revolution of satellite launch. This fact is made evident by Figures 14-5, and indeed this consideration influenced the choice of launch site locations analyzed. Finally, it should be stated that the specific locations of the distant launch sites studied do not necessarily imply terrestrial bases, but are merely indicative of geographic locations.

### 14.3 EFFECTS OF SYSTEM CONSTRAINTS

The deployment analysis up to this point has been concerned with lateral reach requirements for various launch site combinations and locations without regard for such system constraints as range safety and interceptor-target geometry during homing. The specific constraints which must be considered depend on the interceptor design and specific launch site locations. It is the objective of this section to examine the effects of certain constraints on the launch opportunities available from AMR, Johnston Island, Alaskan, and Puerto Rican launch sites. The following constraints will be considered.

#### 14.3.1 Constraints Considered

##### 14.3.1.1 Range Safety

There are several range safety aspects which must be considered in detail for each vehicle launch. However, for the purpose of this analysis it is assumed that range safety constraints can be specified in terms of permissible launch azimuths and maximum ranges. The permissible launch azimuth limits used in the analysis are listed below:

<u>Launch Site</u>	<u>Launch Azimuth Limits (degrees)</u>
AMR	44 to 110
PMR	170 to 301
Johnston Island	0 to 60 and 81 to 360 (assumed values)
Kodiak, Alaska	120 to 270 (assumed values)
Puerto Rico	15 to 132 (assumed values)
AMR	0 to 360 (assumed values)

##### 14.3.1.2 Interceptor Performance Limitations

The maximum altitude-range capability of the satellite interceptor limits the permissible intercept area. Since the capabilities of the boost vehicles being considered vary over a wide range, the maximum altitude-range capability will be treated parametrically. A minimum range constraint is imposed by range safety considerations, engine cutoff requirements for some booster vehicles, and because (for vehicles incorporating a homing stage) some minimum time is required between booster cutoff and target interception for homing stage separation, warhead deployment.

and target acquisition and homing. A minimum constraint of 500 n mi was assumed for intercepting targets in 100 n mi altitude orbits.

#### 14.3.1.3 Intercept Geometry

There exists two critical parameters pertaining to the intercept geometry:

- Relative velocity,  $V_R$ , between the interceptor and target
- The angle between the target velocity vector and the relative velocity vector.

For a given target orbit and launch site, both parameters are dependent on interceptor trajectory shaping. To simplify the computations and decouple the deployment analysis from the booster performance studies, the intercept geometry constraints are approximated by specifying a maximum permissible interceptor-target track crossing angle (TCA). For a 100 n mi altitude target, a maximum angle of 50 degrees corresponds to a maximum relative velocity of 20,000 fps, if the interceptor flies a flattened trajectory as discussed in Chapter 12. As the target orbit altitude increases, both interceptor and target velocities decrease for near-apogee attacks. This allows for larger interceptor-target track crossing angles while still maintaining a maximum relative velocity of approach of 20,000 fps. For orbit altitudes of 1000 and 2500 n mi, a maximum angle of approximately 55 and 75 degrees, respectively, can be tolerated.

The sun look angle (defined as the angle between the target-interceptor and target-sun vectors) imposes an additional important constraint on those interceptors incorporating a reflected sunlight tracker. The effects of this constraints will be discussed in Paragraph 14.3.7.

#### 14.3.2 Intercept Footprints

If no TCA constraint existed, the "intercept footprint" would consist of the entire area bounded by the launch azimuth and impact range constraints. However, for a given set of constraints, a restricted intercept footprint can be drawn. The footprint defines an area, and each passage of the target over any portion of that area represents one launch opportunity. Footprints for launches from AMR are presented in Figures 14.10 through 14.22 for target orbit altitudes of 100, 1000, and 2500 n mi and various

target orbit inclinations. It is significant to note that launches from AMR are in the same general direction as the target motion (for direct target orbits), so that launch opportunities will occur for targets moving both north to south and south to north except for near polar orbits.

Footprints for PMR are shown in Figures 14-23 to 14-25. The footprints for each target orbit inclination is the area bounded by the contour line representing the maximum allowable TCA and the 170 degree interceptor launch azimuth line. It should be clear that with constrained  $V_R$  these footprints correspond only to targets moving from north to south.

Figures 14-26 through 14-30 represent similar footprints for Johnston Island, Kodiak, Alaska, and Puerto Rico. Figures 14-31 and 14-32 are AMR footprints for a 100 n mi target orbit altitude, but with no interceptor launch azimuth restrictions.

If it is assumed that a launch opportunity will occur if the target passes through the footprint on a given revolution, the probability that a launch opportunity will occur in a specified time interval can be computed if the distribution of the ascending nodal longitudes is known. For the most general case it is reasonable to assume a uniform distribution of nodes (for specific target launch sites and reaction times a probable distribution of nodes could be computed). Then the probability,  $P_1$ , that at least one launch opportunity will occur in a specified time for a given orbit inclination is just the fraction of the total possible orbits, measured in terms of their ascending nodes, that cross an intercept footprint in one revolution.

$P_1$  was evaluated as a function of waiting time for the various assumed launch sites, and for combinations of these sites. This data is presented in Figures 14-33 through 14-52. The change in slope of some curves results from the fact that for some constraints a target can be intercepted only when traveling in one general direction (e.g., north to south), whereas in other cases they can be intercepted when traveling in either direction.

The maximum waiting times required for at least one launch opportunity ( $P_1 = 1.0$ ) were tabulated from these latter figures and are presented in Tables 14-1 through 14-6.



#### 14.3.3 Interception Within 24 Hours

Table 14-7 lists the interceptor launch sites considered and the range of target orbit inclinations that can be intercepted from each site (or combination of sites) for target orbit altitudes of 100 n mi and a TCA of 50 degrees. This is done for interceptor surface range capabilities of 3000 and 5500 n mi. The maximum required waiting times for an interceptor launch opportunity for those sites having complete coverage of all target orbit inclinations are listed. The surface range capabilities of various boost vehicles and various payload weights are influenced by constraints ( $V_R$  for example) and these numbers are presented in Chapter 12.

For a single interceptor launch site, only Johnston Island, Puerto Rico, and AMR (with no launch azimuth restrictions on AMR) are capable of protection against all orbit inclinations. Thus, for the requirement of interceptions within 24 hours, either Johnston Island or AMR (with no launch azimuth restrictions) would be best since these sites already exist. Each of these sites (Johnston Island and AMR) require a maximum waiting time of about 11.5 hours for an interceptor with a 3000 n mi total range capability. Assuming an interceptor site at both of these locations (and again no launch azimuth restrictions on AMR) reduces the maximum waiting time to slightly under 5 hours.

#### 14.3.4 Interception During First Orbit and Before First Pass Over the Continental United States

This analysis was performed only for targets launched from the two present Russian launch sites and was composed of two parts. The first part assumed targets launched from: 1) a site situated at  $48^\circ\text{N}$  latitude and  $46^\circ\text{E}$  longitude (Kapustin Yar) and  $49^\circ$  orbit inclinations, and 2) a site at  $48^\circ\text{N}$  latitude and  $66^\circ\text{E}$  longitude (Tyuratam) and 65 degrees orbit inclinations. The second part assumed polar orbits from both sites.

Table 12-8 is the result of the first part and shows the range of revolution numbers during which an intercept can occur for a target altitude of 100 n mi and a maximum  $V_R$  of 20,000 fps. No one interceptor base allows interception of targets launched from both Russian sites during the first revolution. An interceptor base at Puerto Rico (and 3000 n mi

surface range capability) would give a launch opportunity within one revolution for targets with orbit inclinations of 49 degrees. A site at Johnston Island or Kodiak, Alaska would allow for an interception of targets in a 65 degree inclined orbit.

Passage over the continental United States does not occur until the end of the 6th and 4th revolution of the 65 and 49 degree inclined orbits, respectively. Thus, an interceptor site at AMR, Johnston Island or Puerto Rico would give interceptor launch opportunities prior to a target passing over the United States.

The results of the second part are shown in Table 12-9. Only an interceptor site at PMR (and 3000 n mi surface range capability) allows interception of targets in polar orbits launched from either Russian launch site during the first orbit revolution. Increasing the interceptors surface range capability to 5500 n mi would also give Johnston Island the same capability.

For polar orbits, passage over the continental United States occurs during the first and at the end of the sixth revolution for targets launched from Tyuratam and Kapustin Yar, respectively. Thus, all the interceptor sites considered have intercept opportunities for targets in polar orbits launched from Kapustin Yar prior to passage over the United States, but no site offers such protection for targets launched from Tyuratam. It should be noted that if no intercept is allowed over a land mass, and keeping the  $V_R$  less than 20,000 fps, there seems to be no convenient interceptor site available for this latter case.

#### 14.3.5 Interception Within One Orbital Period After a Satellite is Designated as a Hostile Target

Figures 14-53 through 14-64 present the locus of satellite orbits that can be intercepted within one orbital revolution from each respective interceptor site. The figures are for direct motion orbits only, at an altitude of 100 n mi. It was also assumed that the target was at the ascending node at the instant of defined hostility.

The area of the locus of points of each figure represents the percentage of coverage against all possible combinations of target orbit inclinations and nodal longitudes. These percentages of coverage are

listed in Table 12-10 for each assumed interceptor site. As can be seen, AMR (with no launch azimuth restrictions) and Johnston Island give the best coverages. PMR and the site in Alaska offer the least amount of coverage.

#### 14.3.6 Summary of Constraint Analysis

Table 12-11 is a summary of the reaction time coverage capability of each interceptor base considered. For each interceptor base which provides protection against a specified reaction time requirement (based on the assumption used in this analysis) there is a mark (X). Thus, of the sites considered, none offers complete protection. However, Johnston Island with interceptors of surface range of 5500 n mi can protect against all reaction time requirements except for the unreasonable "AICBM" case. Each of the other sites afford defense against only one or two of the reaction time requirements. It needs to be recognized however, that no interceptor studied is capable of 5500 n mi range performance against the complete spectrum of threat altitudes. Thus, one should not be ensnared by the delusion that a single site on Johnston Island meets all reaction time requirements. It is interesting, however, that the combination of Johnston and, say AMR, can achieve significant reaction time with realistic interceptor designs.

#### 14.3.7 Imposition of Sun-Loop Angle Constraint

An analysis was performed to determine the effects of the sun-loop angle (defined as the angle between the target-interceptor and target-sun vectors) on launch opportunities for those interceptors incorporating a reflected sunlight tracker. It was performed only for a target orbit altitude of 100 n mi. The following assumptions were made:

- At the time of target acquisition, the target and interceptor are separated by a distance of approximately 125 n mi
- From the time of target acquisition to intercept the sun-loop angle had to be equal to or less than 140 degrees.
- Intercepts with an interceptor velocity of 20,000 fps with velocity vector near local horizontal.
- At the time of defined hostility the target was at an ascending node (this assumption has little affect on the analysis).

The analysis was performed only for a target satellite being defined as hostile on June 21 and December 21 for the hours of 0000 hours and 1200 hours (Greenwich time). This was done for an interceptor site at AMR and one at Johnston Island.

Again assuming uniform distribution of nodes, Figures 14-65 and 14-66 show the probability that at least one launch opportunity will occur in a specified time for a given target orbit inclination for an interceptor base at AMR and Johnston Island respectively, for midnight (Greenwich time) of December 20. The curves are quite erratic because of the interplay of all the constraints, especially the sun-look angle limitation and the eclipsing of the target by the earth. Figure 14-64 can be compared with Figure 14-43 to observe the diminishing launch opportunities due to the added sunlight constraint. This comparison reinforces the intensive estimate that the use of a sunlight tracker doubles the average required reaction time.

From Figure 14-65, it can be seen that the second day of waiting time adds little (if any) increase in probability of intercept opportunities. This is the result of the interceptor site being able to intercept only those targets whose nodal longitudes were covered the previous day, thus adding nothing to the probability.

The maximum waiting time required for at least one launch opportunity for the dates and times considered are tabulated in Tables 14-12 and 14-13.

Table 14-1. Maximum Waiting Time Required for at Least One Launch Opportunity from AMR and PMR Without  $V_R$  Restriction  
(Interceptor Maximum Range Capability = 1000, 3000, and 5500 n mi)

A. Target in 100 n mi Circular Orbit

Orbit Inclination	Waiting Time (hr)								
	AMR Only			PMR Only			AMR and PMR		
	(1000)	(3000)	(5500)	(1000)	(3000)	(5500)	(1000)	(3000)	(5500)
0	*	*	<1.5	*	<1.5	<1.5	*	<1.5	<1.5
15	*	15.1	<1.5	*	<1.5	<1.5	*	<1.5	<1.5
30	19.2	14.7	7.5	18.2	7.8	<1.5		6.1	<1.5
45	16.8	13.7	8.5	16.3	8.5	<1.5		6.1	<1.5
60	**	12.8	8.0	22.1	9.0	3.2		5.7	3.2
75	**	11.8	7.9	22.3	8.6	4.4		4.7	4.4
90	**	10.4	7.4	19.2	8.1	4.7		5.8	3.9

B. Target in 1000 n mi Circular Orbit

Orbit Inclination	Waiting Time (hr)								
	AMR Only			PMR Only			AMR and PMR		
	(1000)	(3000)	(5500)	(1000)	(3000)	(5500)	(1000)	(3000)	(5500)
0	*	*	<2.1	*	<2.1	<2.1	*	<2.1	<2.1
15	*	16.0	<2.1	*	<2.1	<2.1	*	<2.1	<2.1
30	19.9	15.6	7.9	19.1	8.5	<2.1		7.0	<2.1
45	17.3	14.3	8.3		9.2	<2.1		7.0	<2.1
60	**	13.3	8.0		9.2	3.1		6.5	3.1
75	**	12.2	7.5		8.9	4.4		5.5	4.4
90	**	10.6	7.5		8.9	6.1		4.5	4.5

C. Target in 2500 n mi Circular Orbit

Orbit Inclination	Waiting Times (hr)								
	AMR Only			PMR Only			AMR and PMR		
	(1000)	(3000)	(5500)	(1000)	(3000)	(5500)	(1000)	(3000)	(5500)
0	*	*	<3.2	*	<3.2	<3.2	*	<3.2	<3.2
15	*	17.5	4.6	*	3.7	<3.2	*	<3.2	<3.2
30	21.4	17.1	8.8	20.4	9.0	<3.2		9.7	<3.2
45	**	15.9	8.9		9.9	<3.2		8.8	<3.2
60	**	14.9	8.5		9.8	3.7		8.1	3.7
75	**	13.8	8.0		9.5	5.1		7.1	5.1
90	**	11.7	9.8		9.7	7.1		5.7	5.7

\* Intercept not possible

\*\* Successive target orbit traces straddle the intercept footprint, waiting time = 24 hrs.

Table 14-2. Maximum Waiting Time Required for at Least  
One Launch Opportunity from AMR and PMR  
With Maximum  $V_R = 20,000$  fps  
(Interceptor Maximum Range Capability = 1000, 3000, and 5000 n mi)

A. Target in 100 n mi Circular Orbit

Orbit Inclination	Waiting Time (hr)								
	AMR Only			PMR Only			AMR and PMR		
	(1000)	(3000)	(5500)	(1000)	(3000)	(5500)	(1000)	(3000)	(5500)
0	*	*	<1.5	*	*	*	*	*	<1.5
15	*	15.2	<1.5	*	*	*	*	15.2	<1.5
30	19.1	15.6	15.1	*	*	*		15.6	15.2
45	**	15.0	15.0	**	22.0	20.7		8.6	7.5
60	**	14.0	14.0	**	22.8	21.0		8.2	6.6
75	**	13.0	13.0	**	22.6	21.6		7.5	6.6
90	**	**	**	**	22.0	19.8		21.0	19.2

B. Target in 1000 n mi Circular Orbit

Orbit Inclination	Waiting Time (hr)								
	AMR Only			PMR Only			AMR and PMR		
	(1000)	(3000)	(5500)	(1000)	(3000)	(5500)	(1000)	(3000)	(5500)
0	*	*	<2.1	*	*	*	*	*	<2.1
15	*	16.0	<2.1	*	*	*	*	16.0	<2.1
30	19.9	16.3	13.8		23.1	23.1		9.2	7.7
45	17.5	15.2	15.2		21.6	20.3		8.9	7.6
60	**	15.2	15.2		22.2	21.3		9.3	8.0
75	**	12.9	12.9		22.6	21.0		8.7	6.7
90	**	**	**		21.4	17.8		15.4	14.5

C. Target in 2500 n mi Circular Orbit

Orbit Inclination	Waiting Time (hr)								
	AMR Only			PMR Only			AMR and PMR		
	(1000)	(3000)	(5500)	(1000)	(3000)	(5500)	(1000)	(3000)	(5500)
0	*	*	<3.2	*	*	*	*	*	<3.2
15	*	17.9	<3.2	*	21.2	21.6	*	8.9	<3.2
30	21.4	17.3	6.7	**	21.2	20.0		9.0	5.3
45	**	16.1	8.8	**	22.2	20.4		9.1	5.2
60	**	15.1	15.1	**	23.0	20.9		8.6	6.2
75	**	14.1	14.1	**	23.0	19.7		8.1	7.4
90	**	11.7	10.9	**	19.8	16.0		11.3	8.1

\* Intercept not possible.

\*\* Successive target orbit traces straddle the intercept footprint, waiting time >24 hours.

Table 14-3. Maximum Waiting Time Required for at Least One Launch Opportunity from Johnston Island and AMR Against Targets in 100 n mi Circular Orbits

A. No  $V_R$  Restriction

Orbit Inclination	Waiting Time (hr)					
	Johnston Island Only			Johnston Island and AMR		
	(1000)	(3000)	(5500)	(1000)	(3000)	(5500)
0	<1.5	<1.5	<1.5	<1.5	<1.5	<1.5
15	12.2	<1.5	<1.5		<1.5	<1.5
30	11.8	<1.5	<1.5		<1.5	<1.5
45	12.7	5.6	1.5		2.2	<1.5
60	12.4	6.2	2.3		3.7	2.7
75	11.9	6.4	3.1		4.7	2.9
90	11.7	6.9	5.8		4.5	3.5

B. Maximum  $V_R = 20,000$  fps

Orbit Inclination	Waiting Time (hr)					
	Johnston Island Only			Johnston Island and AMR		
	(1000)	(3000)	(5500)	(1000)	(3000)	(5500)
0	*	<1.5	1.5	*	1.5	<1.5
15		<1.5	<1.5		<1.5	<1.5
30		7.9	2.7		3.3	<1.5
45		9.9	9.1		4.3	3.4
60		11.4	9.9		4.9	4.7
75		11.0	9.3		5.7	5.7
90		10.3	8.9		10.3	8.9

\* Intercept not possible

Table 14-4. Maximum Waiting Time Required for at Least One Launch Opportunity from Kodiak and AMR Against Targets in 100 n mi Circular Orbits

A. No  $V_R$  Restriction

Orbit Inclination	Waiting Time (hr)					
	Kodiak Only			Kodiak and AMR		
	(1000)	(3000)	(5500)	(1000)	(3000)	(5500)
0	*	*	<1.5	*	*	<1.5
15	*	15.9	<1.5	*	7.5	<1.5
30	*	12.4	<1.5		5.6	<1.5
45	20.5	10.5	2.3		4.4	<1.5
60	16.0	8.8	3.4		3.3	2.9
75	13.0	7.7	3.4		4.5	3.3
90	10.6	6.7	5.5		4.3	3.7

B. Maximum  $V_R = 20,000$  fps

Orbit Inclination	Waiting Time (hr)					
	Kodiak Only			Kodiak and AMR		
	(1000)	(3000)	(5500)	(1000)	(3000)	(5500)
0	*	*	*	*	*	<1.5
15	*	*	21.2	*	15.2	<1.5
30	*	20.3	17.8	19.1	9.1	6.5
45	23.5	18.6	16.7		7.6	5.7
60	23.3	20.3	18.8		9.1	4.7
75	23.0	19.3	17.2		9.0	6.9
90	22.7	18.1	15.9		15.7	14.2

\* Intercept not possible



Table 14-7. The Range of Target Orbit Inclinations that can be Intercepted from Each Assumed Interceptor Launch Site for Targets in 100 n mi Circular Orbits With Maximum  $V_R = 20,000$  fps

Interceptor Site	Target Inclinations Protected Against		Maximum Waiting Time (hr) for Coverage of All Orbit Inclinations	
	(3000)	(5500)	(3000)	(5500)
AMR	15-75	0-75	---	---
PMR	45-90	45-90	---	---
Johnston Island	0-90	0-90	11.4	8.9
Kodiak (Alaska)	30-90	15-90	---	---
Puerto Rico	0-90	0-90	23.5	23.5
AMR (no launch azimuth restrictions)	0-90	0-90	11.6	8.7
AMR - PMR	15-75	0-90	---	19.2
AMR - Johnston Island	0-90	0-90	10.3	8.9
AMR - Kodiak	15-90	0-90	---	14.2
Johnston Island - Puerto Rico	0-90	0-90	8.6	7.3
Johnston Island - AMR (no launch azimuth restrictions on AMR)	0-90	0-90	4.9	3.5

Table 14-8. Revolution Numbers During Which an Intercept Opportunity Occurs for Targets Launched from Present Russian Launch Site

Interceptor Sites	Target Launch Site 1* Inclination = 49°		Target Launch Site 2** Inclination = 65°	
	(3000)	(5500)	(3000)	(5500)
AMR	2-9	2-9	5, 11-13	5, 11-13
PMR	12-13	12-14	16-17	1, 16-18
Johnston Island	6-9, 13-17	1, 6-9 12-17	1-3, 9-11, 17-19	1-3, 9-11, 15-19
Alaska	11-14	11-15	1, 16-18	1-2, 15-19
Puerto Rico	1-4, 8-12	1-4, 8-12	4-6, 11-12	4-6, 10-12
AMR (no launch azimuth restrictions)	2-11	2-11	5-9	4-5

\* Target launch site 1 = Kapustin Yar

\*\* Target launch site 2 = Tyuratam

Table 14-9. Revolution Numbers During Which an Intercept Opportunity Occurs for Targets Launched from Present Russian Launch Sites

Interceptor Sites	Target Launch Site 1* Inclination = 90 deg		Target Launch Site 2** Inclination = 90 deg	
	(3000)	(5500)	(3000)	(5500)
AMR	None	None	None	None
PMR	1-2, 17-18	1-3, 16-19	1-3, 17-19	1-4, 17-20
Johnston Island	1-3, 9-11 17-19	1-3, 9-11, 17-19	2-4, 10-12 18-20	1-4, 10-12 18-20
Kodiak (Alaska)	1-4, 17-21	1-5, 16-21	1-5, 18-22	1-6, 17-21
Puerto Rico	4-5, 20-21	4-5, 20-21	5, 20-21	5, 20-21
AMR (no launch azimuth restrictions)	5-8, 13-16	1, 5-8, 12-17	1, 6-8, 14-17	1-2, 5-9, 13-18

\*Target launch site 1 = Kapustin Yar

\*\*Target launch site 2 = Tyuratam

**Table 14-10. Percentage of Satellite Orbits that can be Intercepted Within One Orbital Revolution**

<u>Interceptor Sites</u>	<u>Percentage of Coverage Within One Orbital Revolution</u>	
	(3000)	(5500)
AMR	33	44
PMR	10	13
Johnston Island	63	72
Alaska	18	28
Puerto Rico	50	56
AMR (no launch azimuth restriction)	65	80

**Table 14-11. Summary of Reaction Time Coverage Capability of Each Assumed Interceptor Site**

	Interceptor Surface Range											
	3000 n mi						5500 n mi					
	Requirement*						Requirement*					
	a	b <sub>1</sub>	b <sub>2</sub>	c <sub>1</sub>	c <sub>2</sub>	d	a	b <sub>1</sub>	b <sub>2</sub>	c <sub>1</sub>	c <sub>2</sub>	d
AMR				X						X		
PMR			X						X			
Johnston Island	X						X	X	X	X		X
Kodiak (Alaska)			X						X			
Puerto Rico	X			X			X			X		
AMR (no launch azimuth restrictions)	X			X			X			X		X

Note: A(X) refers to coverage capability

\* Reaction time requirements are, interception:

- a) Within 24 hours
- b) During first orbit
  - b<sub>1</sub>) Targets launched from Kapustin Yar (inclination = 49°) and Tyuratam (inclination = 65°)
  - b<sub>2</sub>) Targets launched from Kapustin Yar and Tyuratam with inclinations of 90°
- c) Before first pass over the United States
  - c<sub>1</sub>) b<sub>1</sub> above
  - c<sub>2</sub>) b<sub>2</sub> above
- d) Within one orbital period after being defined as hostile (70 percent or greater coverage of all satellite orbits)

Table 14-12. Maximum Waiting Time Required for at Least One Launch Opportunity from AMR and Johnston Island with Both  $V_R$  and Sun-Look Angle Restrictions for December 21

Orbit Altitude = 100 n mi

Time of day of defined hostility: 0000 hours Greenwich time

Orbit Inclination	Waiting Time (hr)					
	AMR Only		Johnston I. Only		AMR and J. I.	
	(3000)	(5500)	(3000)	(5500)	(3000)	(5500)
0	*	7.3	$\leq 1.5$	$\leq 1.5$	$\leq 1.5$	$\leq 1.5$
15	**	10.3	$\leq 1.5$	$\leq 1.5$	$\leq 1.5$	$\leq 1.5$
30	**	20.5	17.6	2.9	10.3	2.9
45	**	23.5	19.1	17.6	14.7	10.3
60	**	**	23.5	17.6	23.5	10.3
75	**	**	23.5	19.1	23.5	10.3
90	**	**	23.5	20.5	23.5	20.5

Time of day of defined hostility: 1200 hours Greenwich time

Orbit Inclination	Waiting Time (hr)					
	AMR Only		Johnston I. Only		AMR and J. I.	
	(3000)	(5500)	(3000)	(5500)	(3000)	(5500)
0	*	$\geq 1.5$	2.9	$\leq 1.5$	2.9	$\geq 1.5$
15	**	$\leq 1.5$	2.9	2.9	2.9	$\geq 1.5$
30	**	22.0	11.7	5.9	7.3	2.9
45	**	22.0	14.7	11.7	8.8	5.9
60	**	42.9	16.1	13.2	10.3	7.3
75	**	**	17.6	17.6	10.3	10.3
90	**	**	16.1	16.1	16.1	16.1

\* Intercept not possible

\*\* Waiting time greater than 50 hrs. — computation stopped

Table 14-13. Maximum Waiting Time Required for at Least One Launch Opportunity from AMR and Johnston Island with Both  $V_R$  and Sun-Look Angle Restrictions for June 21

Time of defined hostility: 0000 hours Greenwich time

Orbit Inclination	Waiting Time (hr)					
	AMR Only		Johnston Island Only		AMR and J. I.	
	(3000)	(5500)	(3000)	(5500)	(3000)	(5500)
0	*	7.3	$\leq 1.5$	$\leq 1.5$	$\leq 1.5$	$\leq 1.5$
15	**	8.8	$\leq 1.5$	$\leq 1.5$	$\leq 1.5$	$\leq 1.5$
30	32.3	19.1	16.1	2.9	8.8	2.9
45	32.3	20.5	14.7	14.7	7.3	7.3
60	22.0	22.0	22.0	22.0	14.6	14.6
75	23.5	23.5	22.0	22.0	16.1	16.1
90	**	**	22.0	22.0	22.0	22.0

Time of defined hostility: 1200 hours Greenwich time

Orbit Inclination	Waiting Time (hr)					
	AMR Only		Johnston Island Only		AMR and J. I.	
	(3000)	(5500)	(3000)	(5500)	(3000)	(5500)
0	*	$\leq 1.5$	2.9	$\leq 1.5$	2.9	$\leq 1.5$
15	20.5	$\leq 1.5$	2.9	2.9	2.9	$\leq 1.5$
30	20.5	20.5	11.7	5.9	7.3	2.9
45	19.1	19.1	14.7	11.7	8.8	5.9
60	20.5	20.5	16.1	13.2	10.3	7.3
75	38.1	36.7	17.6	17.6	10.3	10.3
90	**	**	16.1	16.1	16.1	16.1

\* Intercept not possible

\*\* Waiting time greater than 50 hrs. — computation stopped

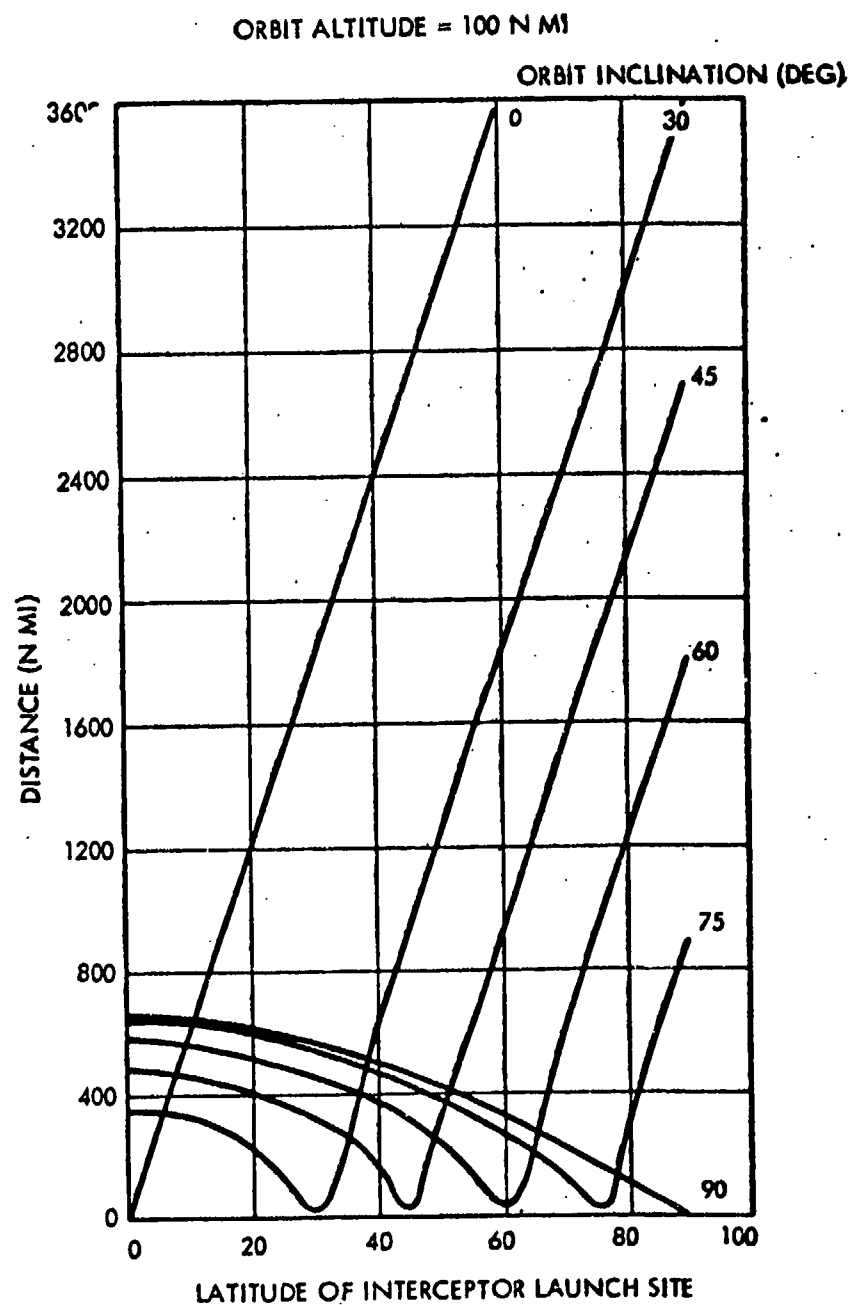


Figure 14-1. Maximum Possible Closest Approach Surface Range within 24 Hours



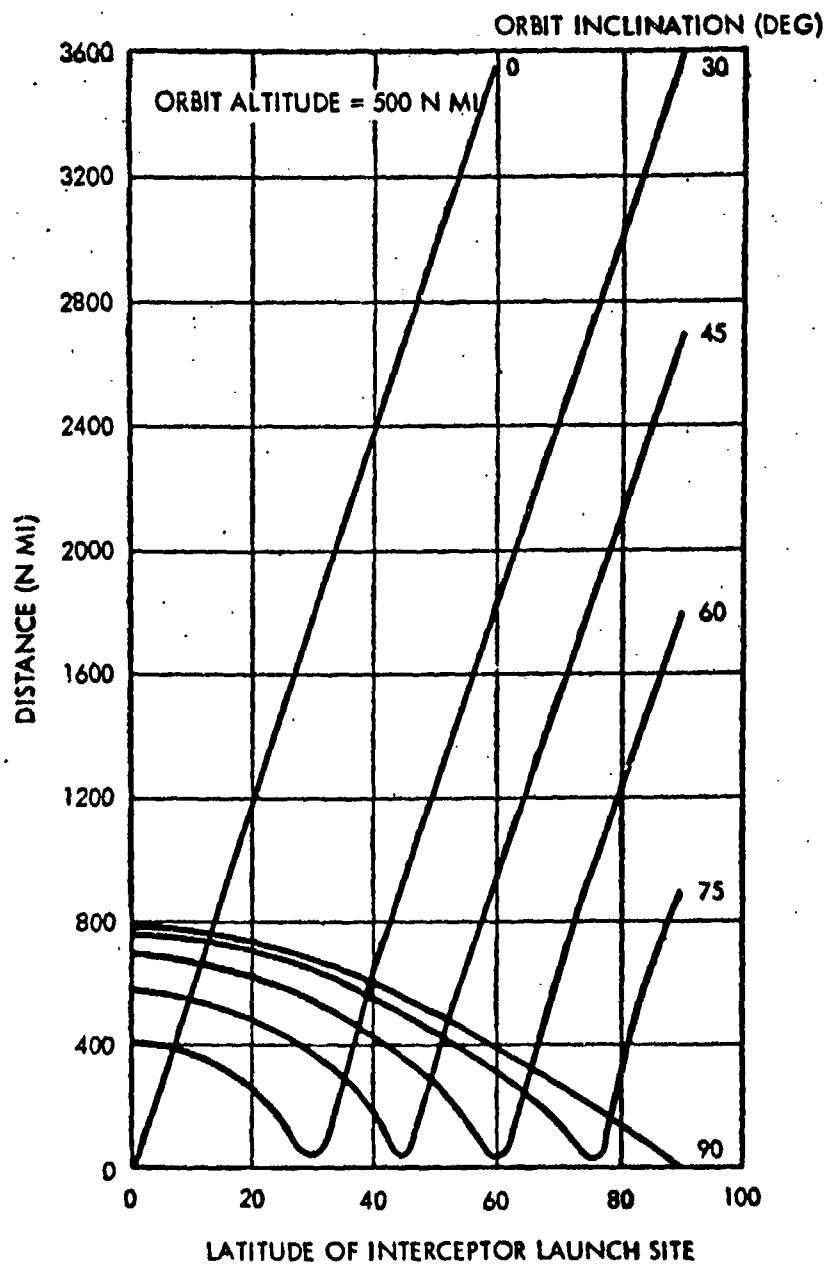


Figure 14-2. Maximum Possible Closest Approach Surface Range within 24 Hours

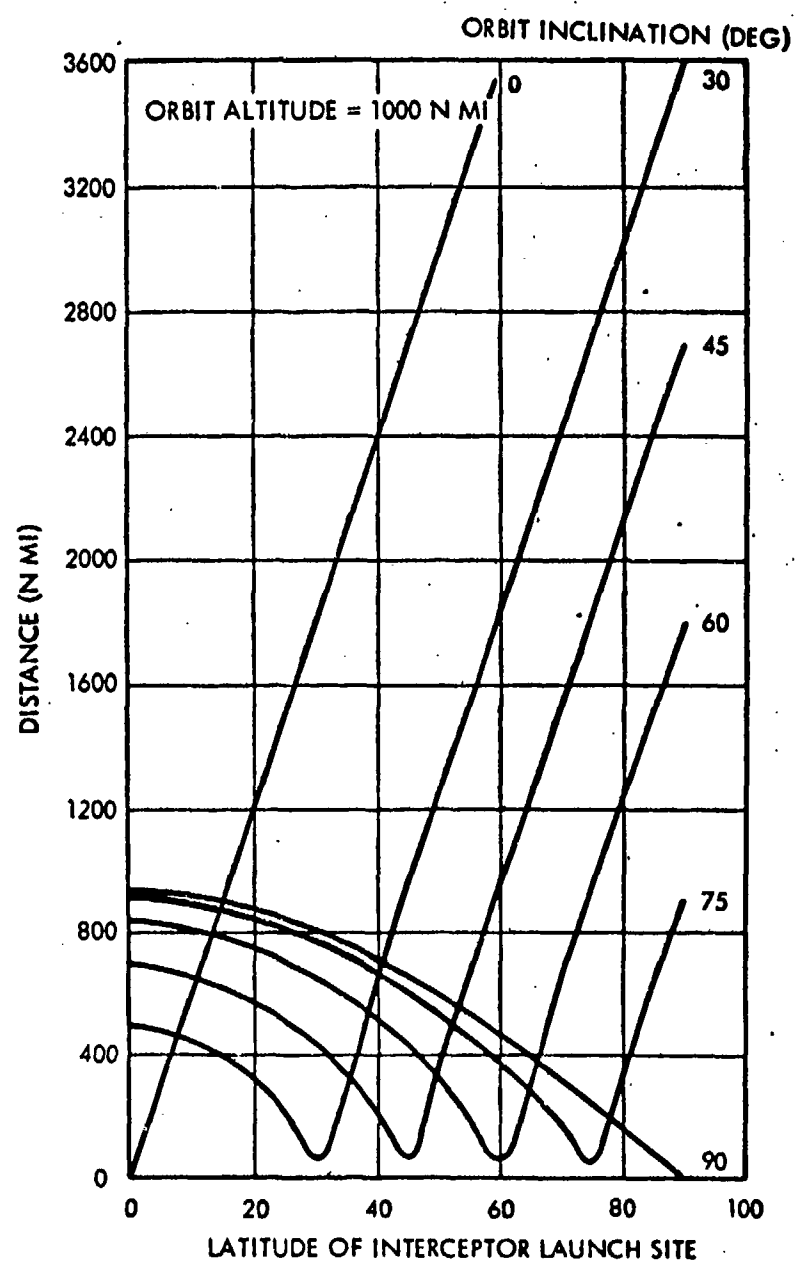


Figure 14-3. Maximum Possible Closest Approach Surface Range within 24 Hours

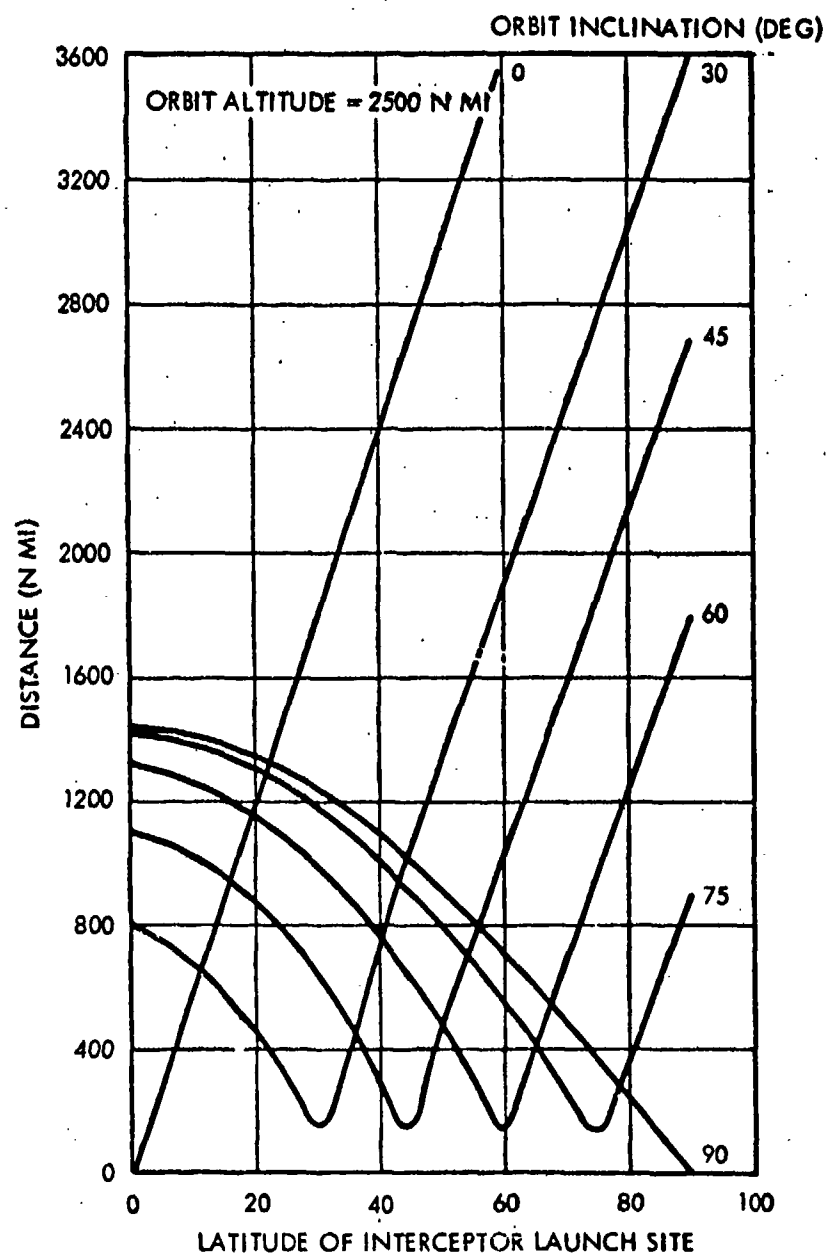


Figure 14-4. Maximum Possible Closest Approach Surface Range within 24 Hours

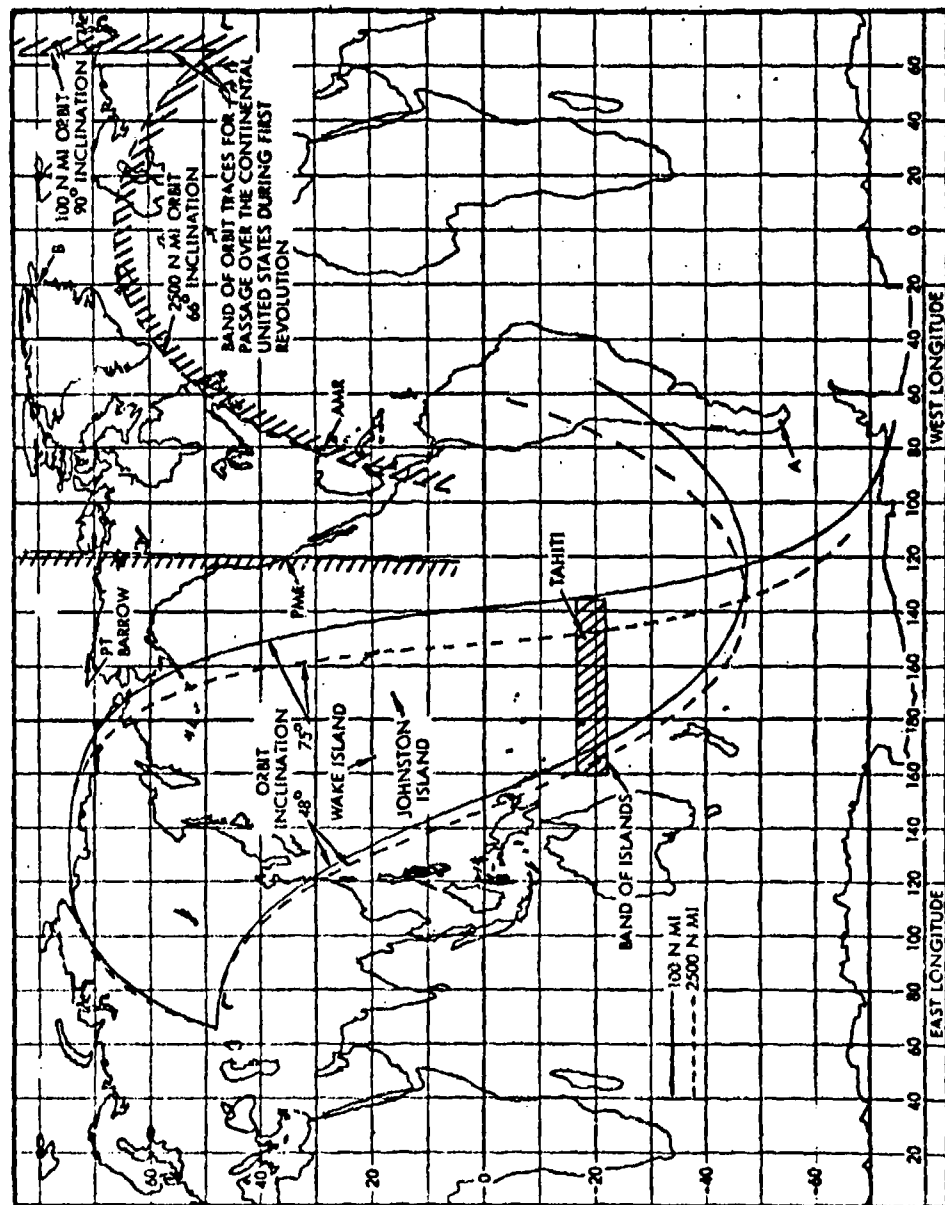


Figure 14-5. Possible Areas for Interceptor Launch Sites

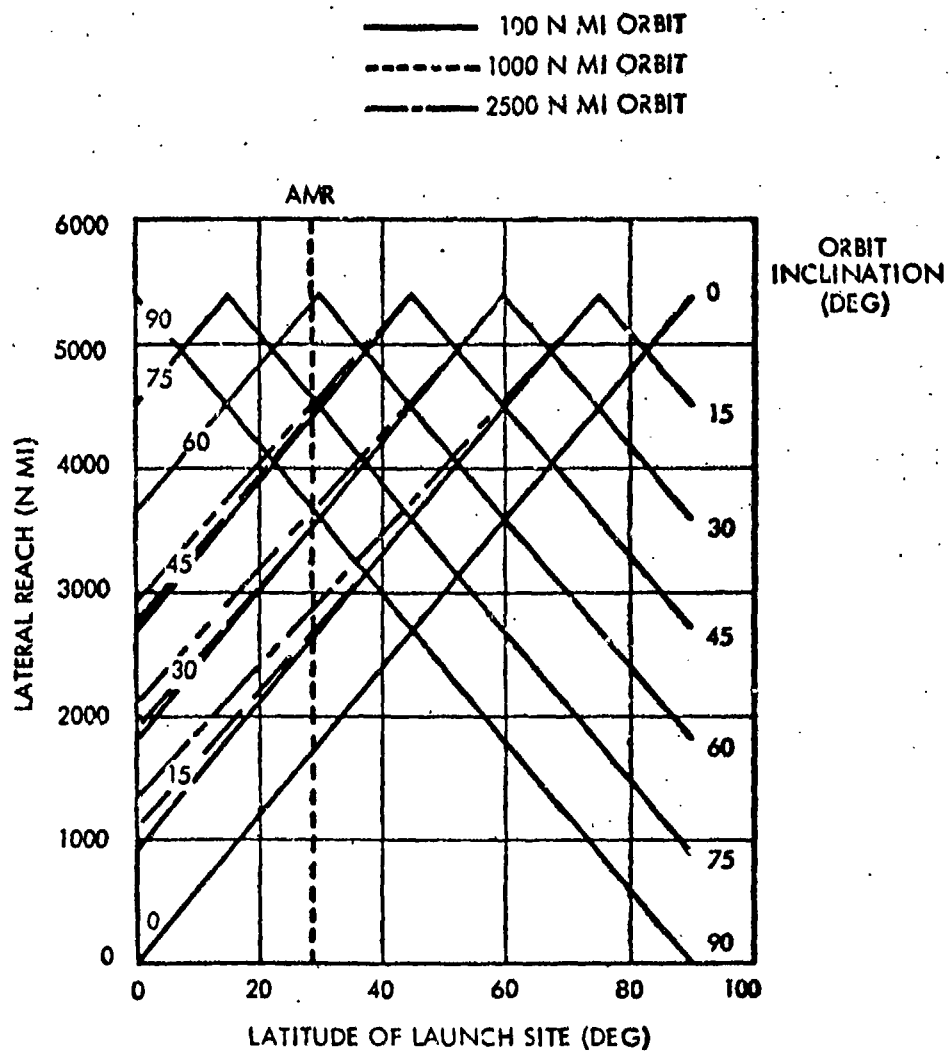


Figure 14-6. Lateral Reach Required for Interception within One Orbit Revolution from One Launch Site

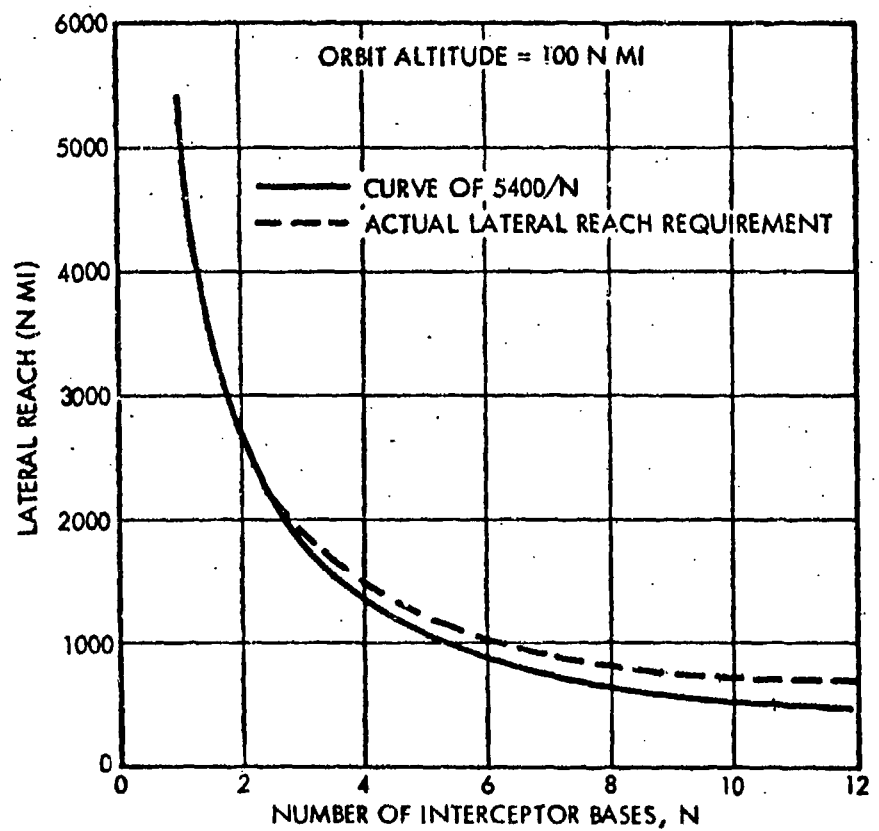


Figure 14-7. Required Lateral Reach for Interception within One Orbit Revolution for All Orbital Inclinations

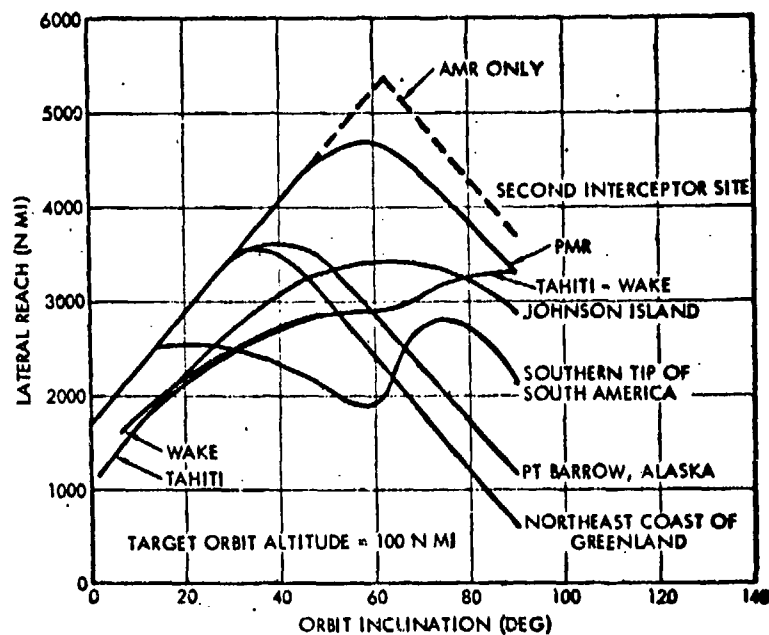


Figure 14-8. Lateral Reach Requirement for AMR and A Second Interceptor Launch Site

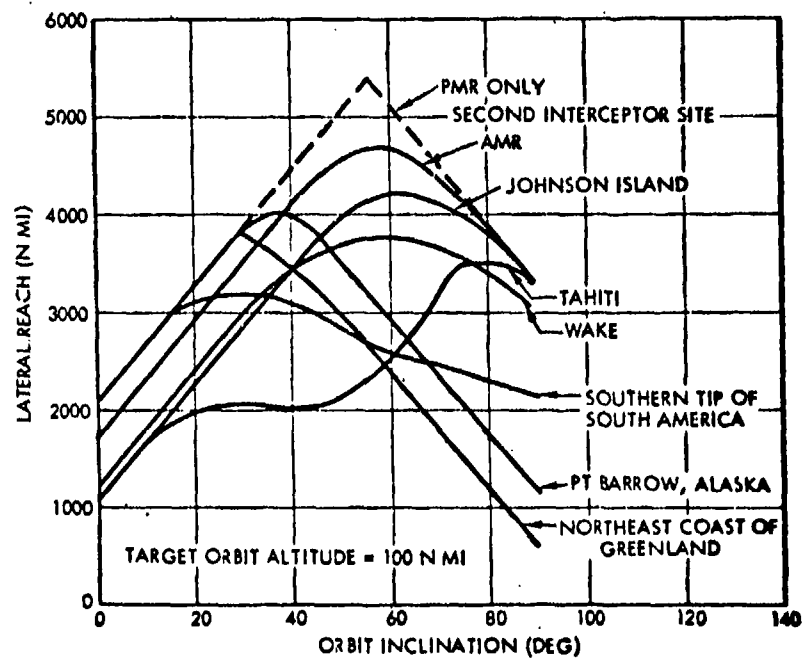


Figure 14-9. Lateral Reach Requirement for PMR and A Second Interceptor Launch Site

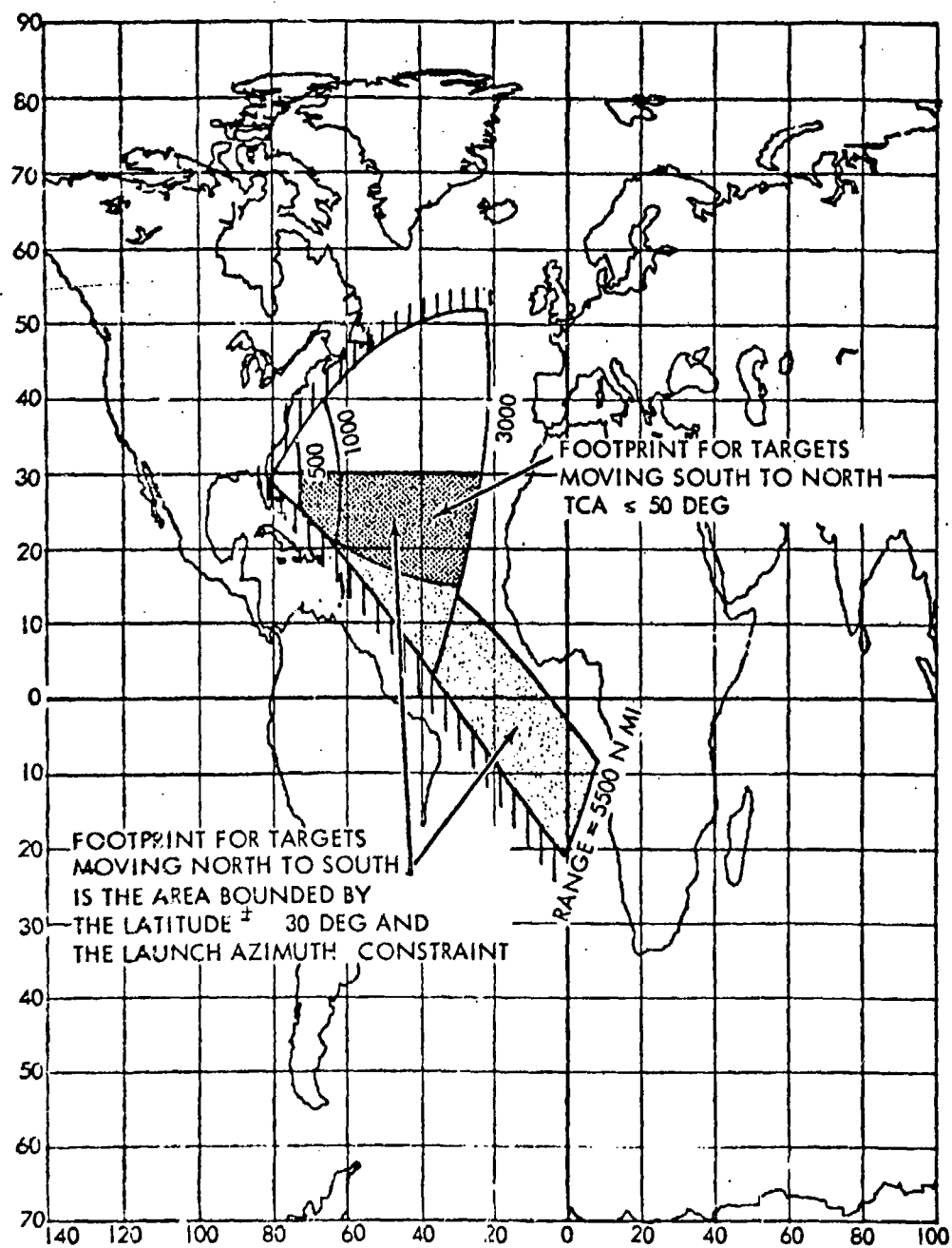


Figure 14-10. AMR Interceptor Footprint for Target Orbit Altitude = 100 N Mi and Target Orbit Inclination = 30 Degrees



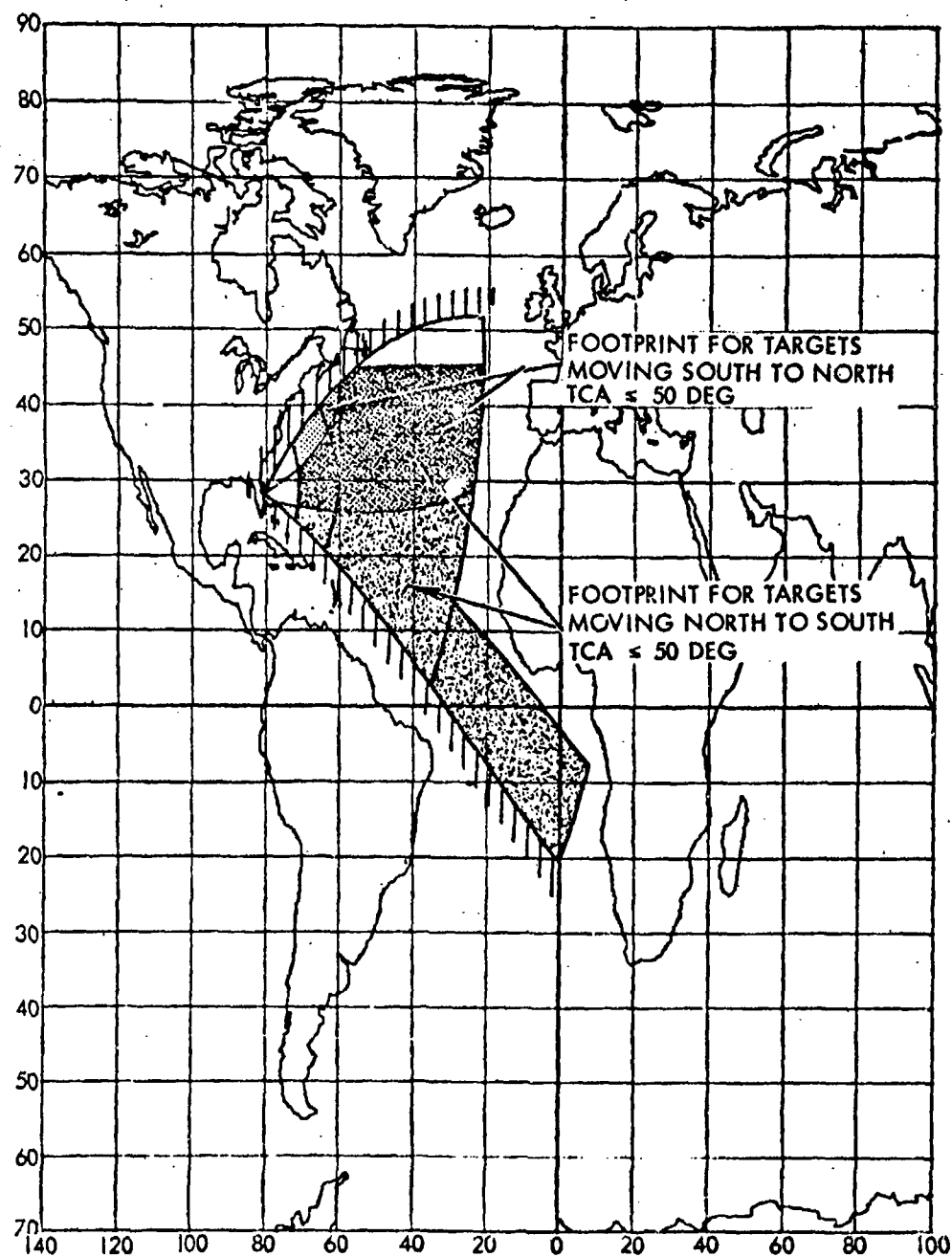


Figure 14-11. AMR Interceptor Footprint for Target Orbit Altitude = 100 N Mi and Target Orbit Inclination = 45 Degrees

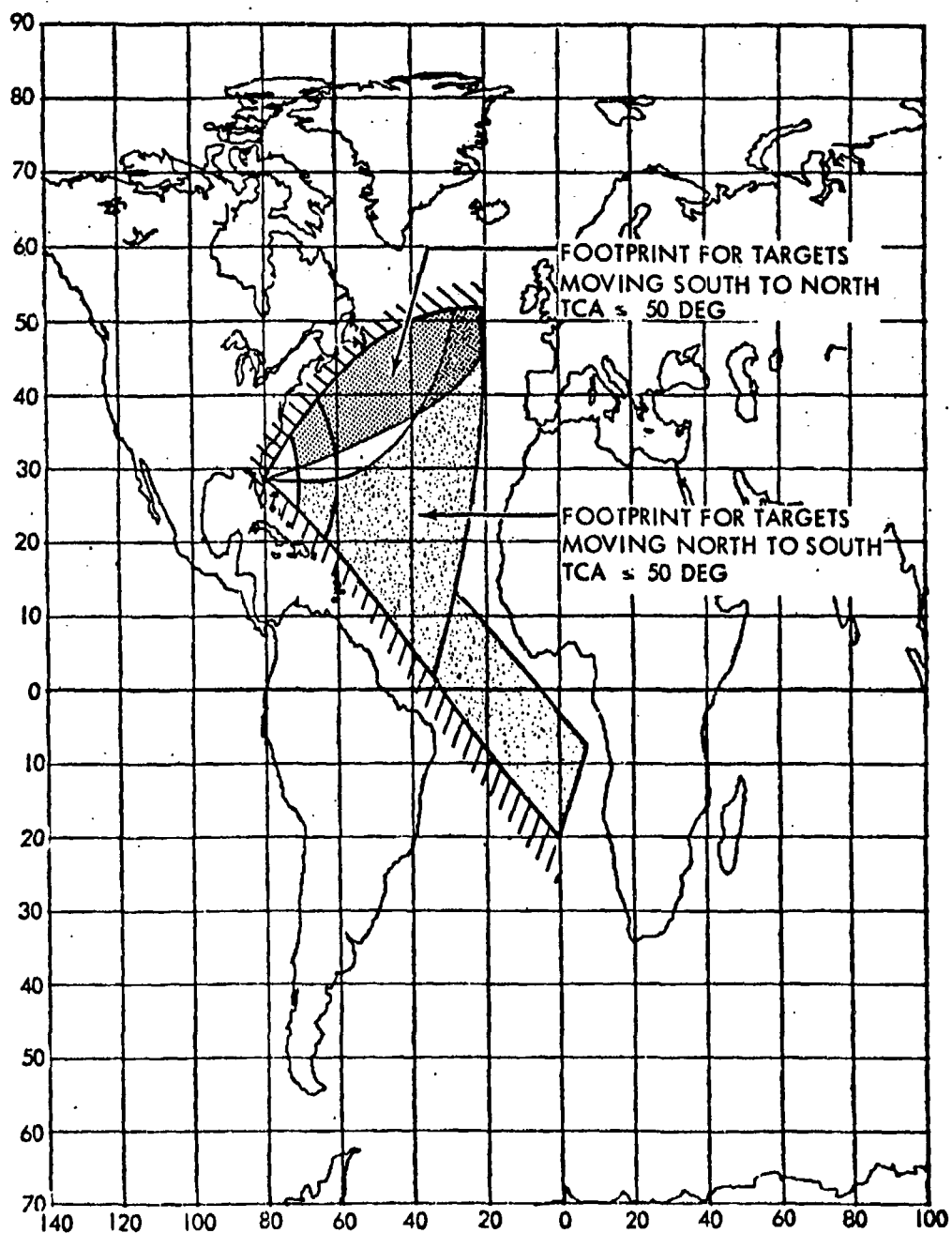


Figure 14-12. AMR Interceptor Footprint for Target Orbit Altitude = 100 N Mi and Target Orbit Inclination = 60 Degrees

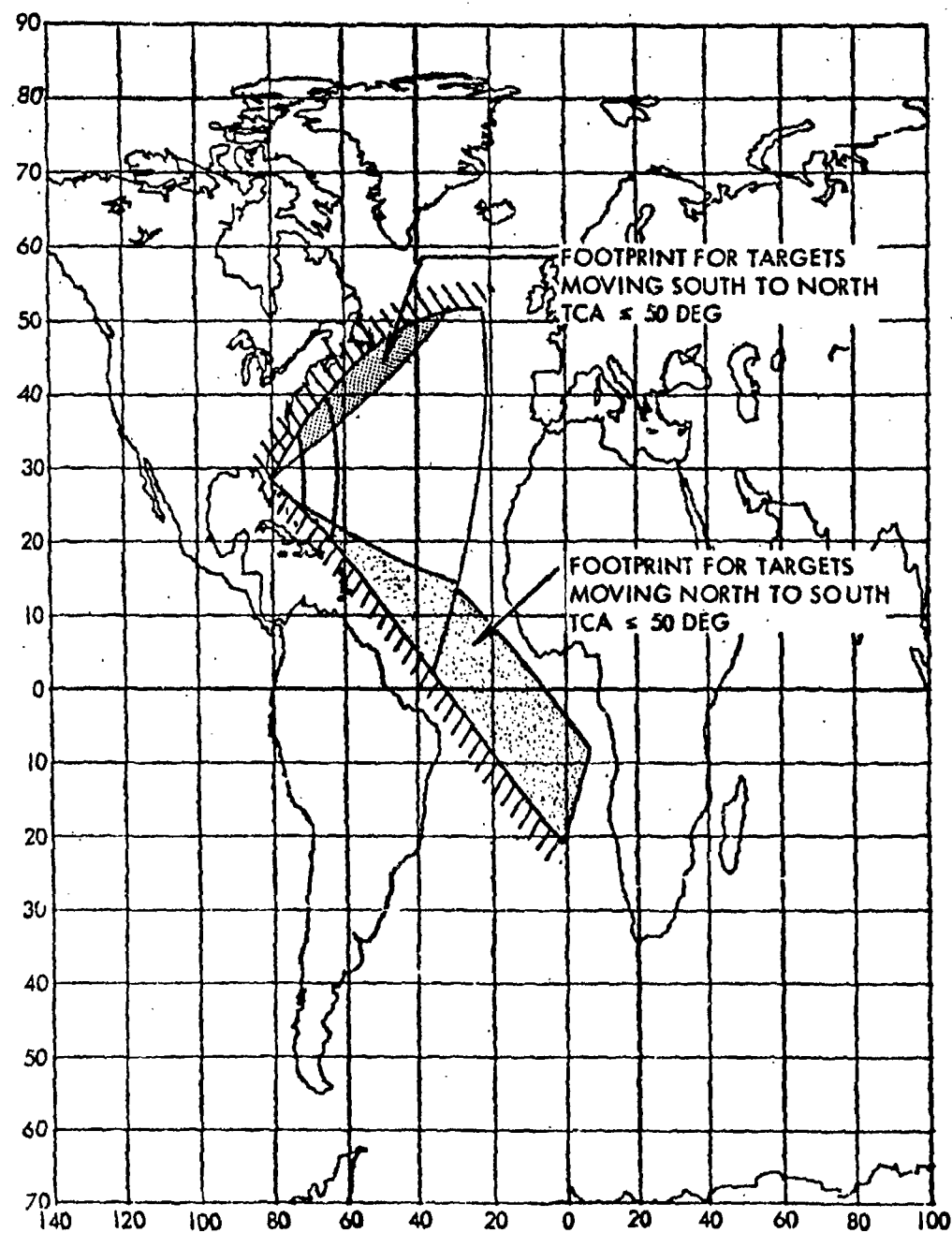


Figure 14-13. AMR Interceptor Footprint for Target Orbit Altitude = 100 N Mi and Target Orbit Inclination = 75 Degrees

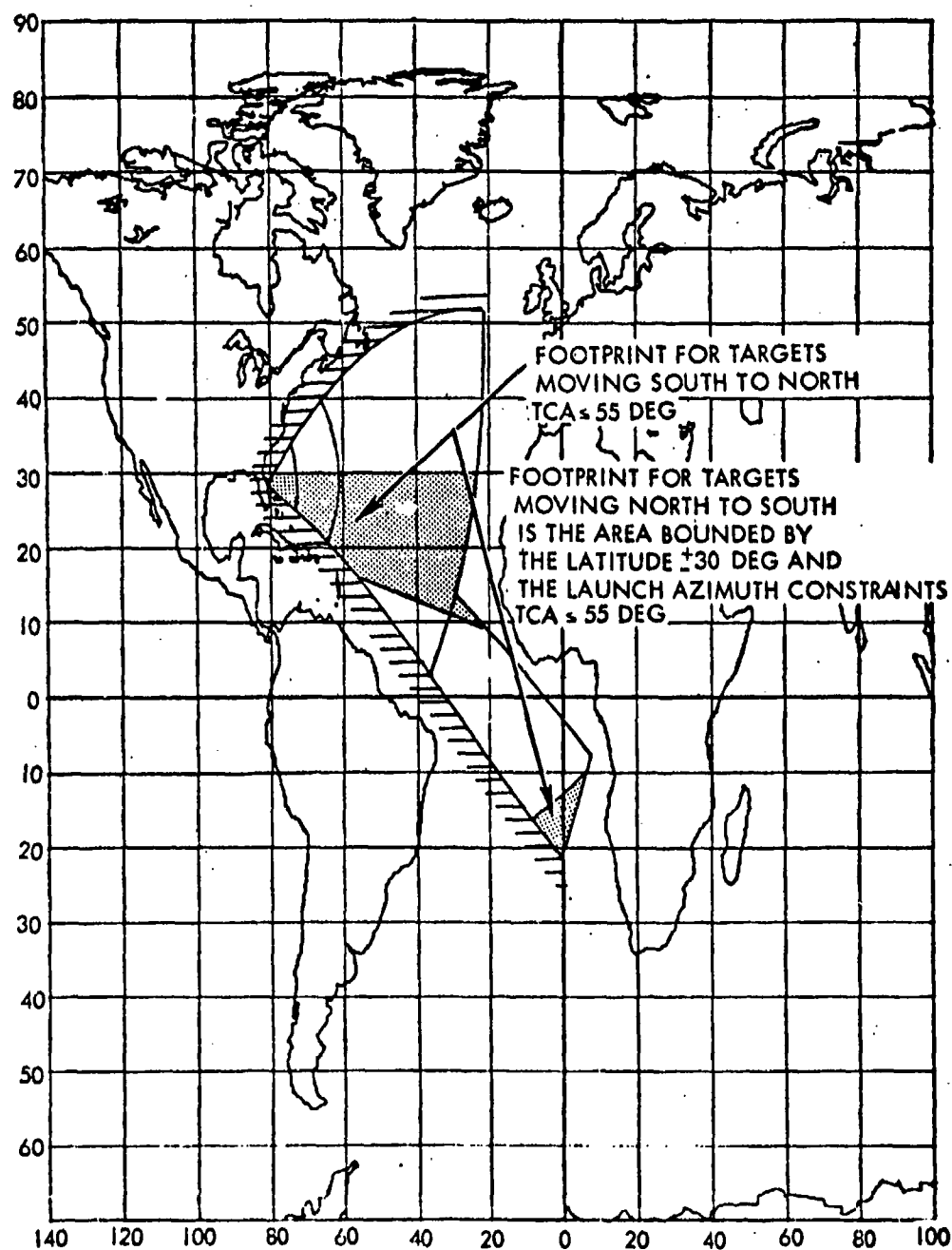


Figure 14-14. AMR Interceptor Footprint for Target Orbit Altitude = 1000 N Mi and Target Orbit Inclination = 30 Degrees

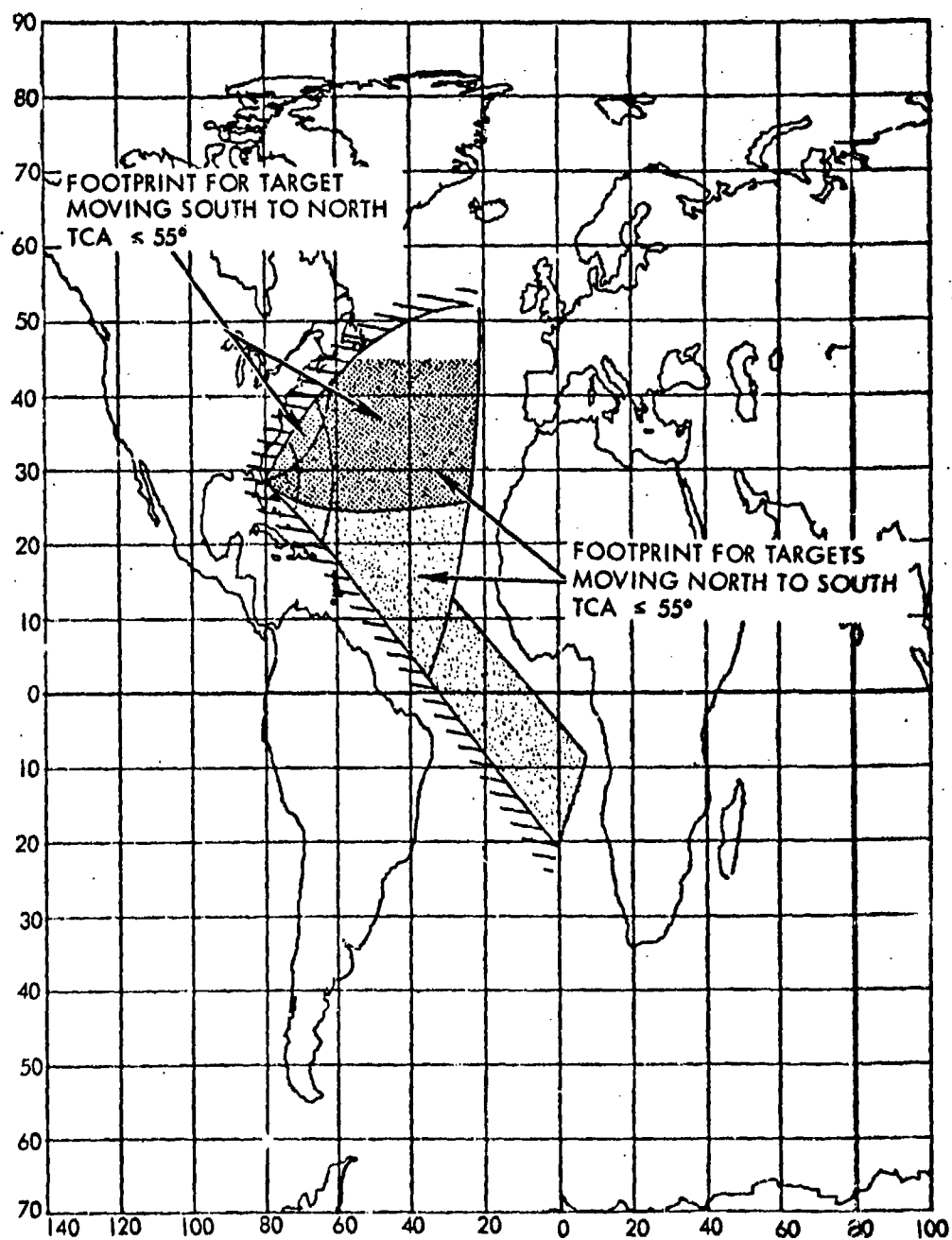


Figure 14-15. AMR Interceptor Footprint for Target Orbit Altitude = 1000 N Mi and Target Orbit Inclination = 45 Degrees

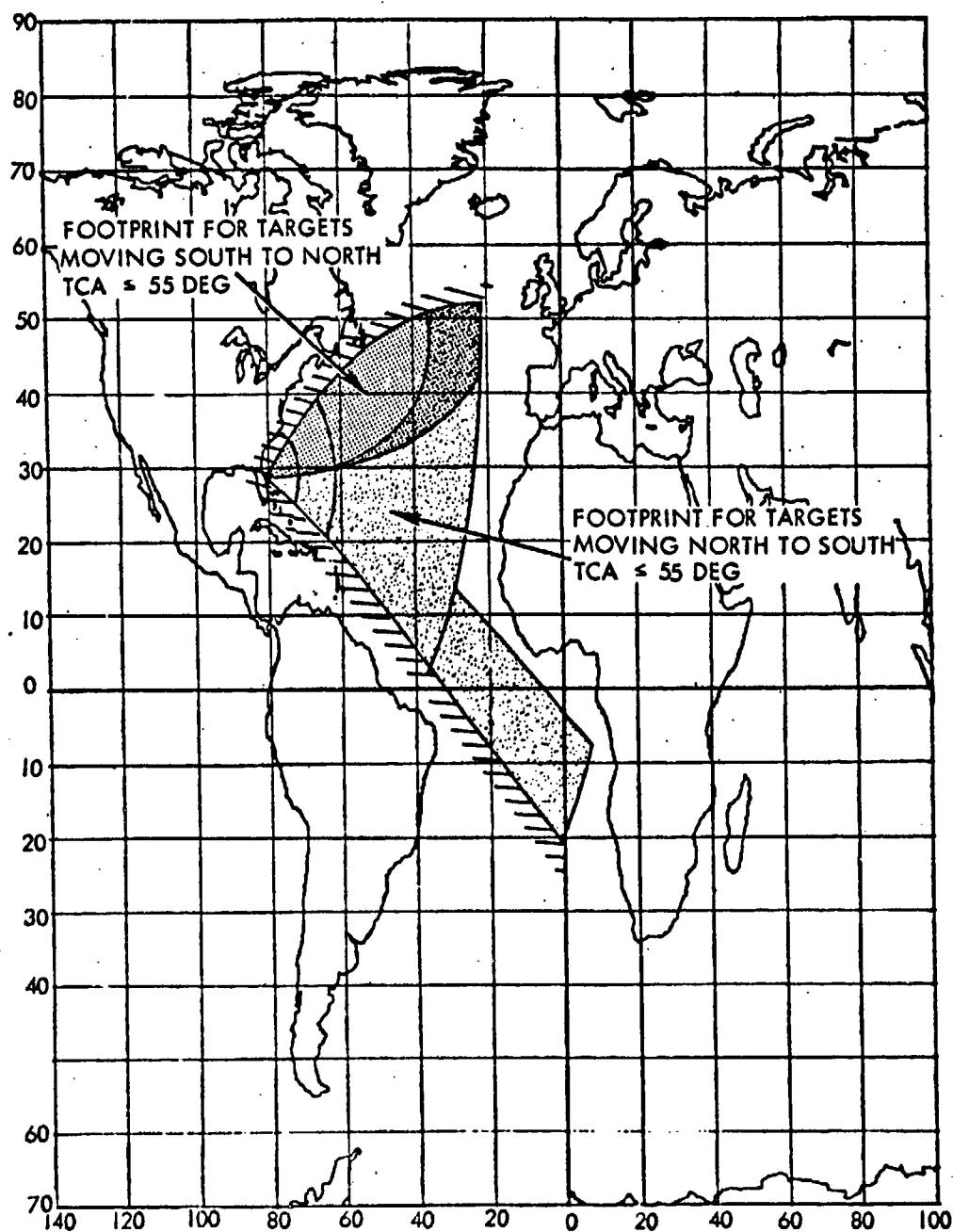


Figure 14-16. AMR Interceptor Footprint for Target Orbit Altitude = 1000 N Mi and Target Orbit Inclination = 60 Degrees

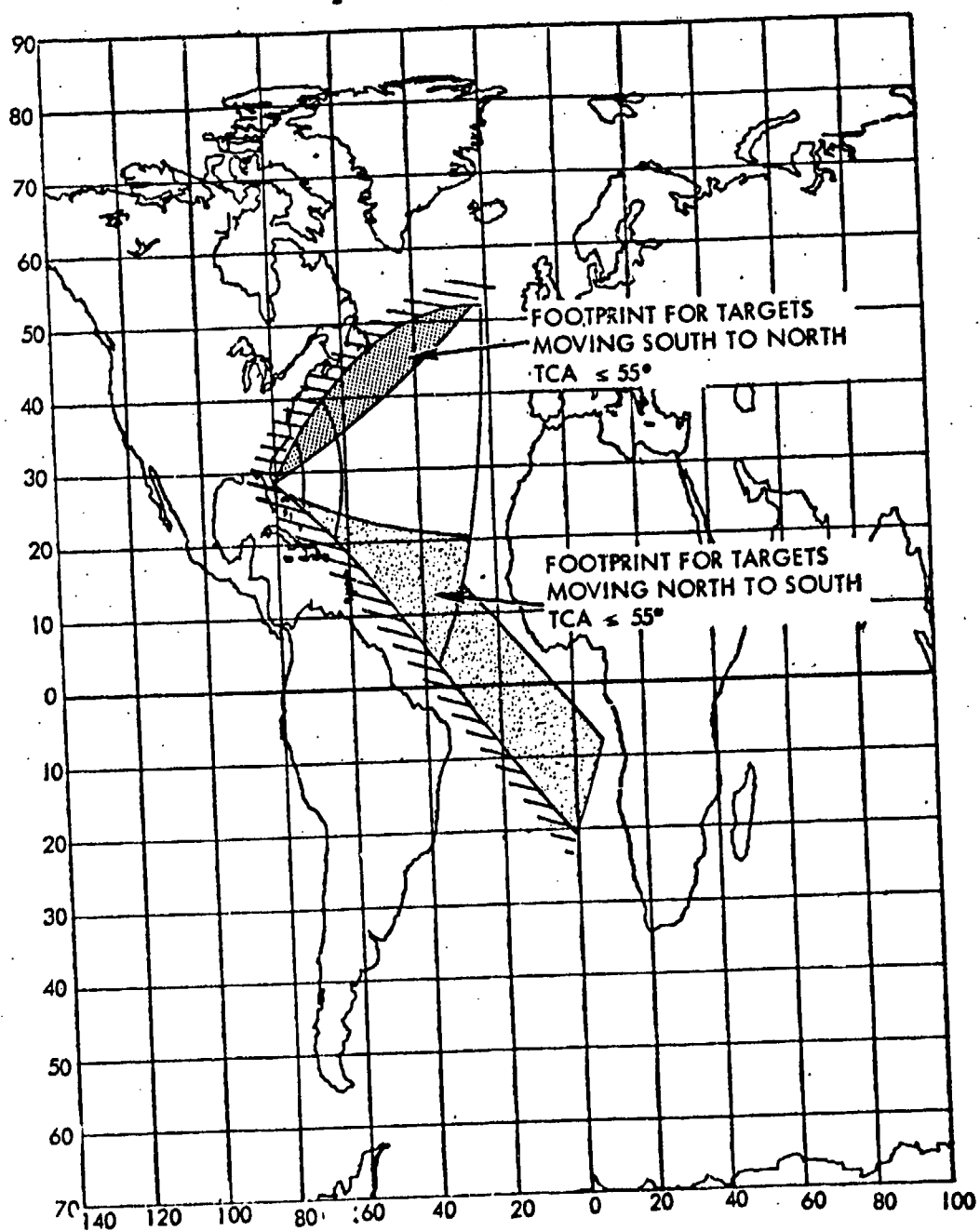


Figure 14-17. AMR Interceptor Footprint for Target Orbit Altitude = 1000 N Mi and Target Orbit Inclination = 75 Degrees

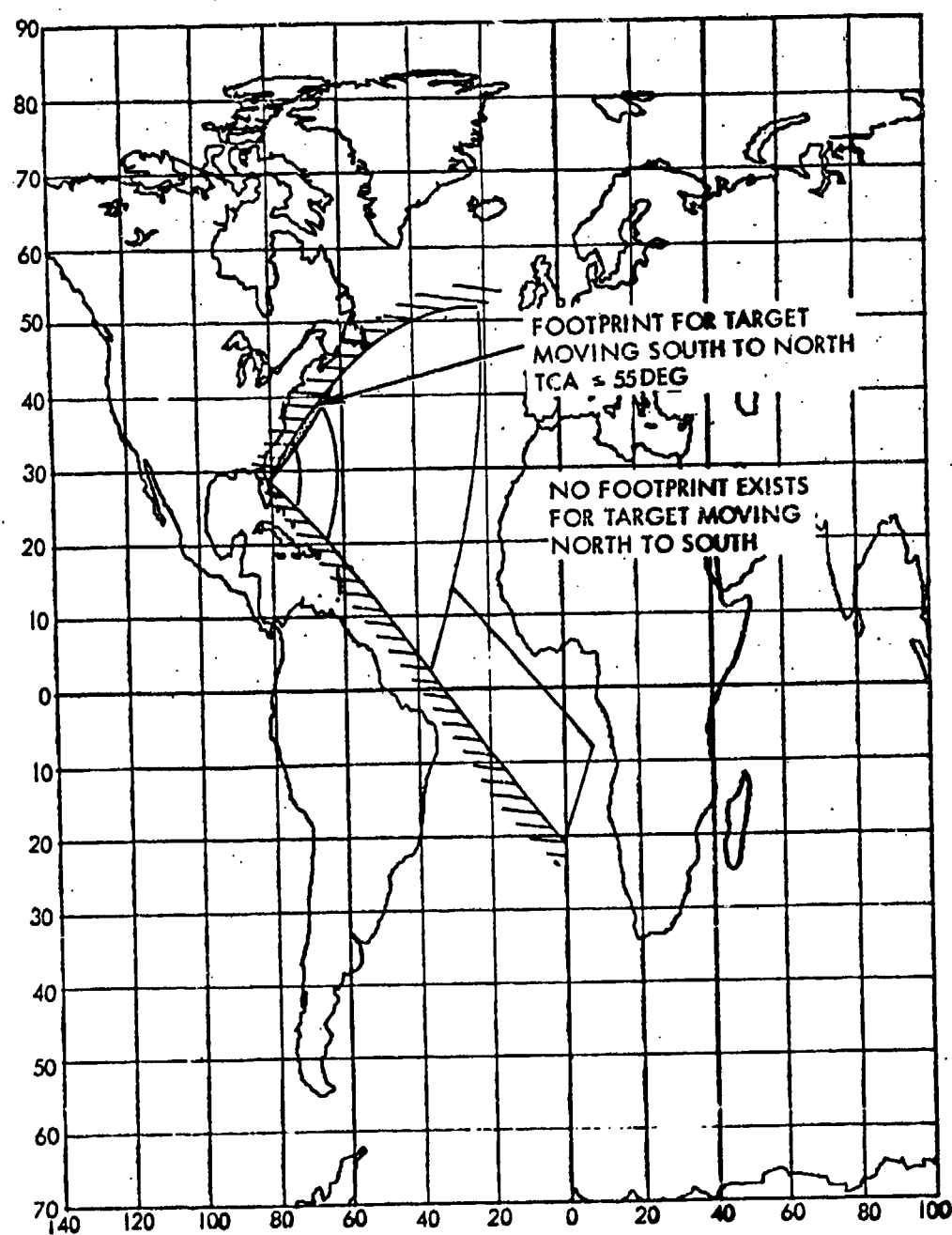


Figure 14-18. AMR Interceptor Footprint for Target Orbit Altitude = 1000 N Mi and Target Orbit Inclination = 90 Degrees



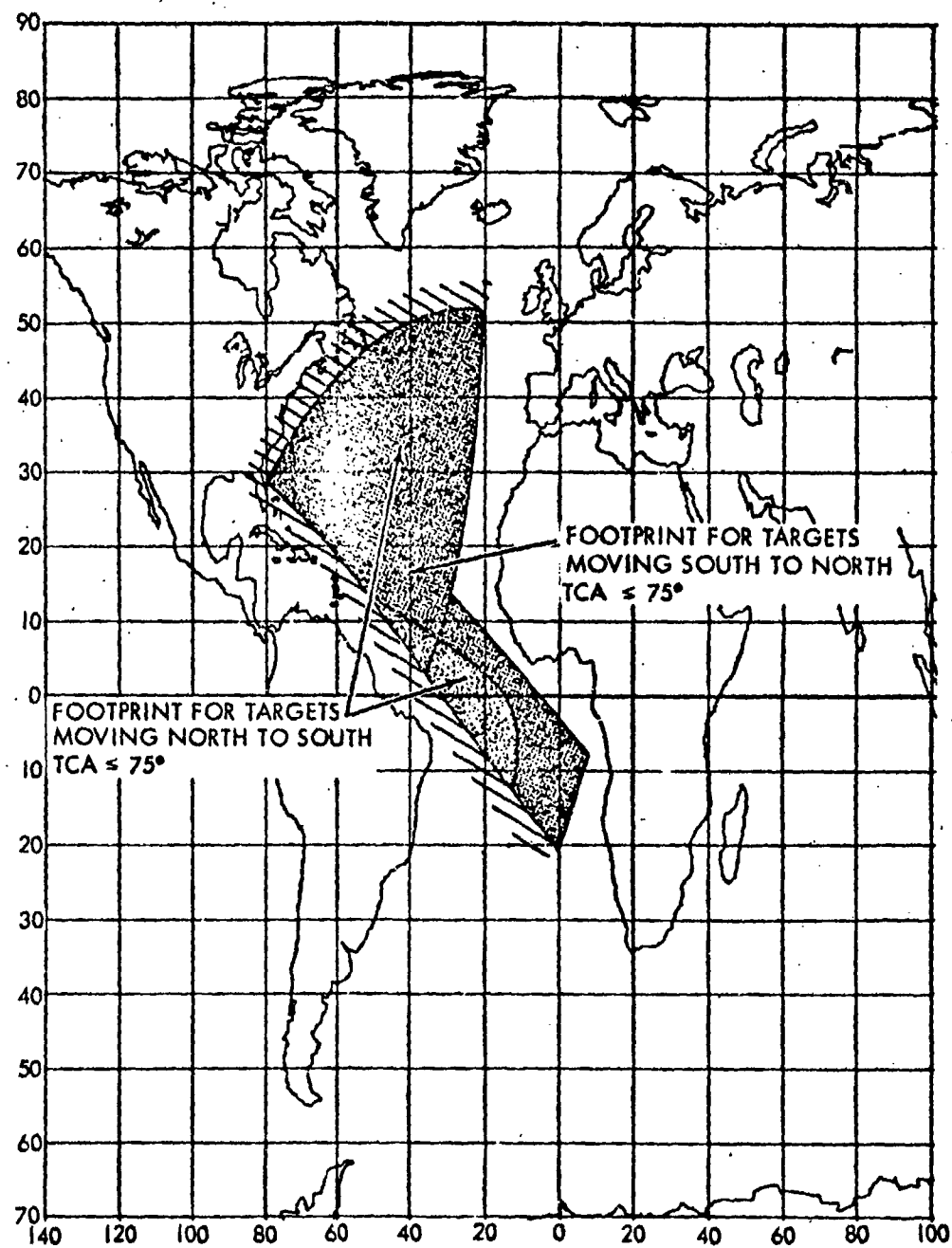


Figure 14-19. AMR Interceptor Footprint for Target Orbit Altitude = 2500 N Mi and Target Orbit Inclination = 45 Degrees

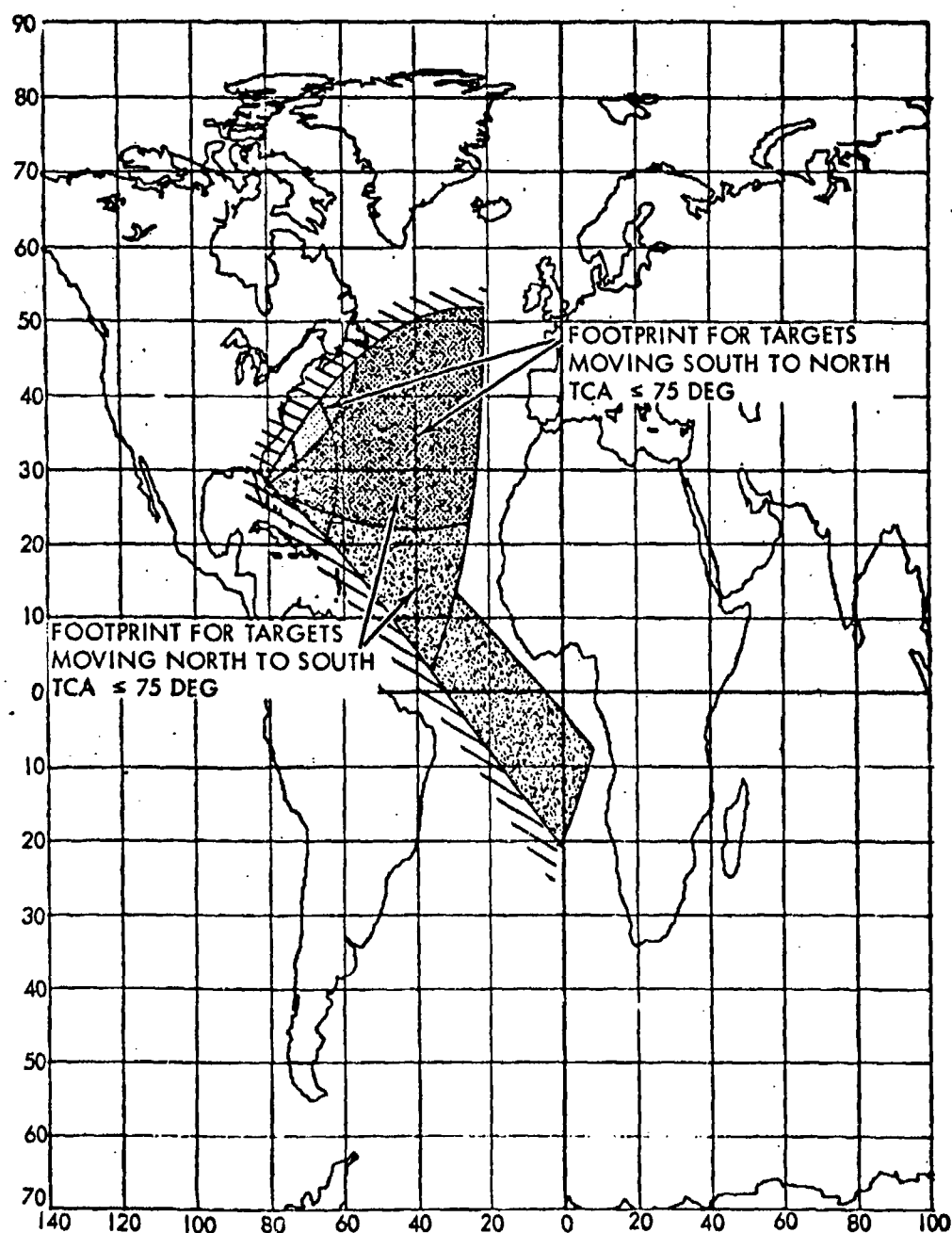


Figure 14-20. AMR Interceptor Footprint for Target Orbit Altitude = 2500 N Mi and Target Orbit Inclination = 60 Degrees

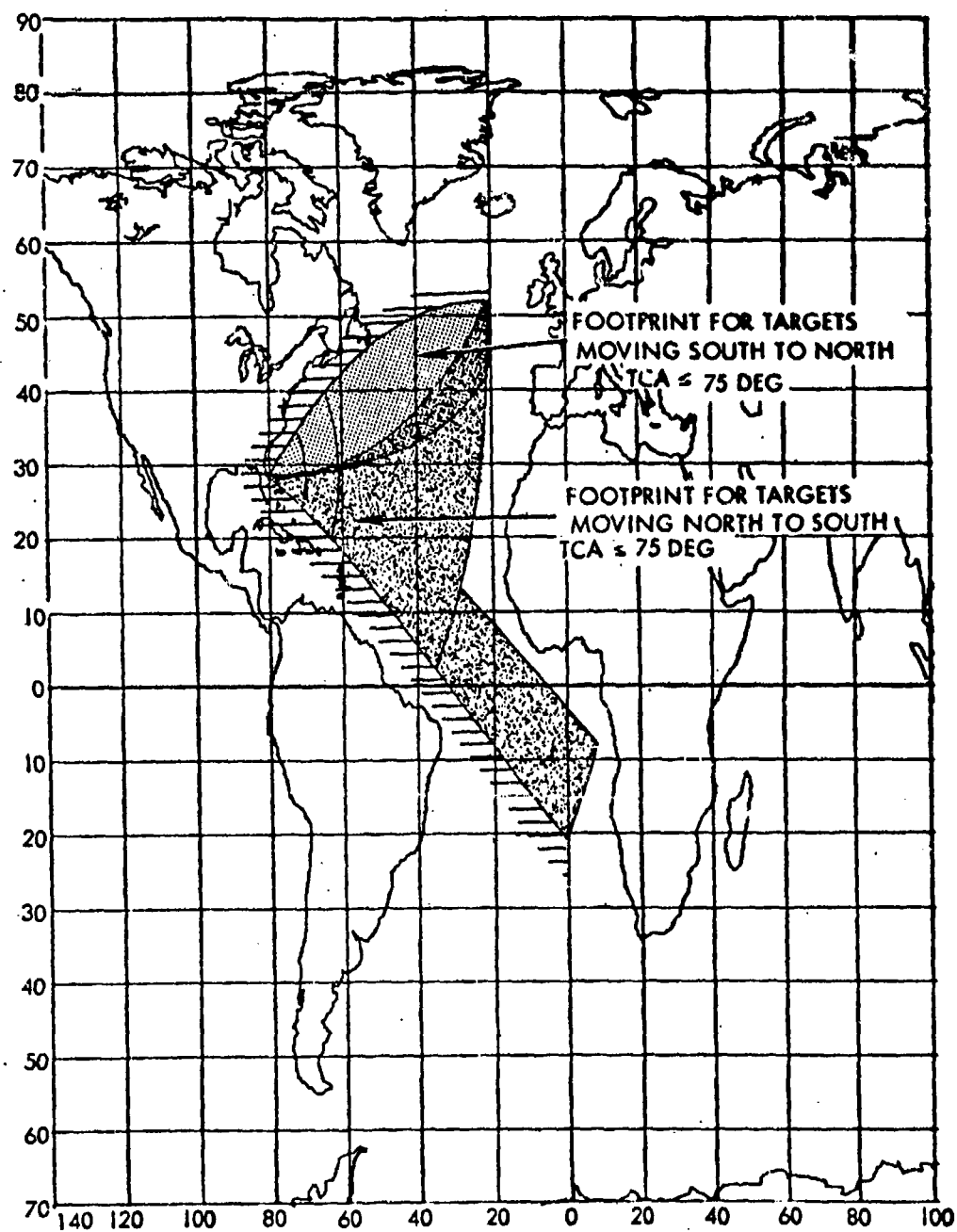


Figure 14-21. AMR Interceptor Footprint for Target Orbit Altitude  
= 2500 N Mi and Target Orbit Inclination = 75 Degrees

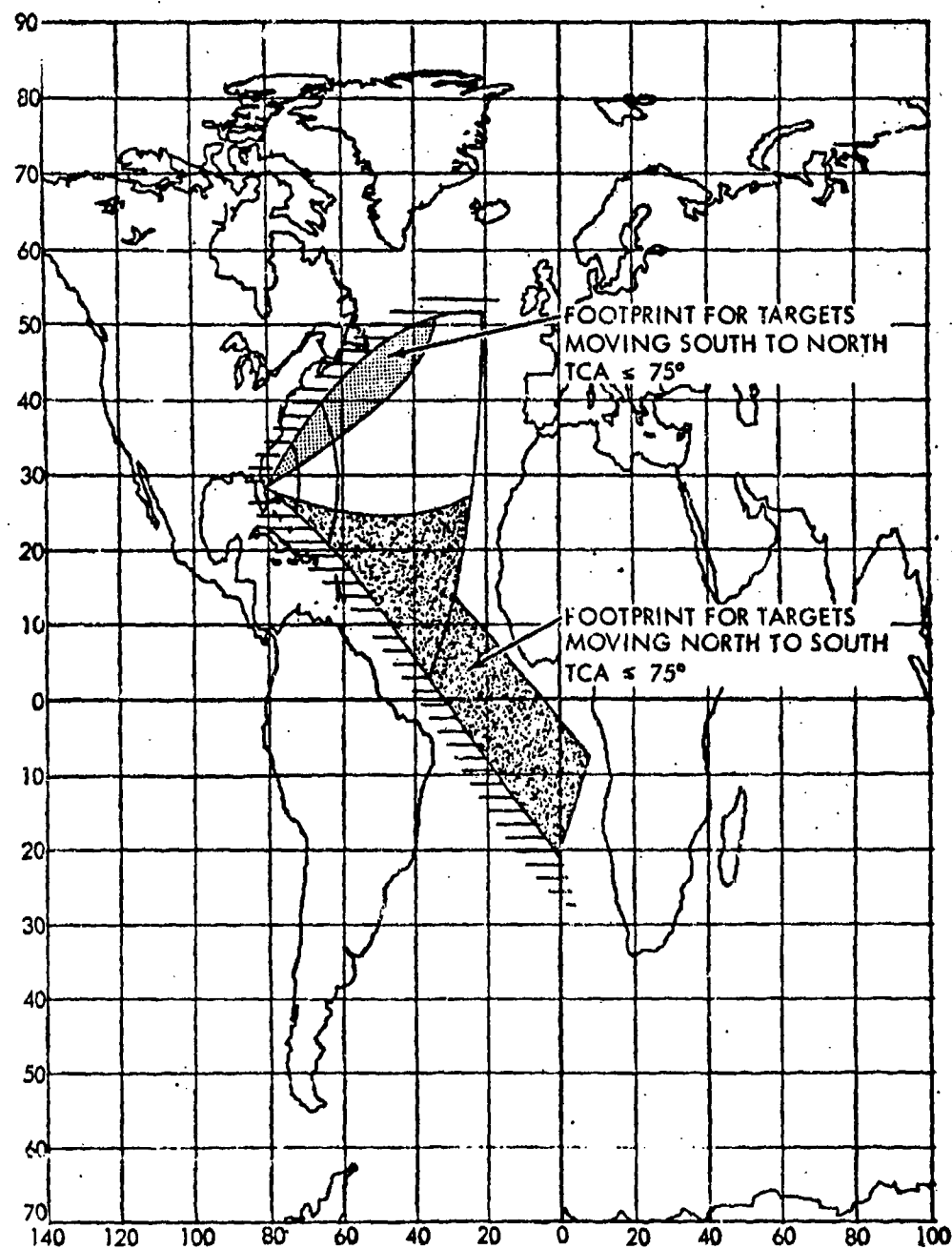


Figure 14-22. AMR Interceptor Footprint for Target Orbit Altitude = 2500 N Mi and Target Orbit Inclination = 90 Degrees

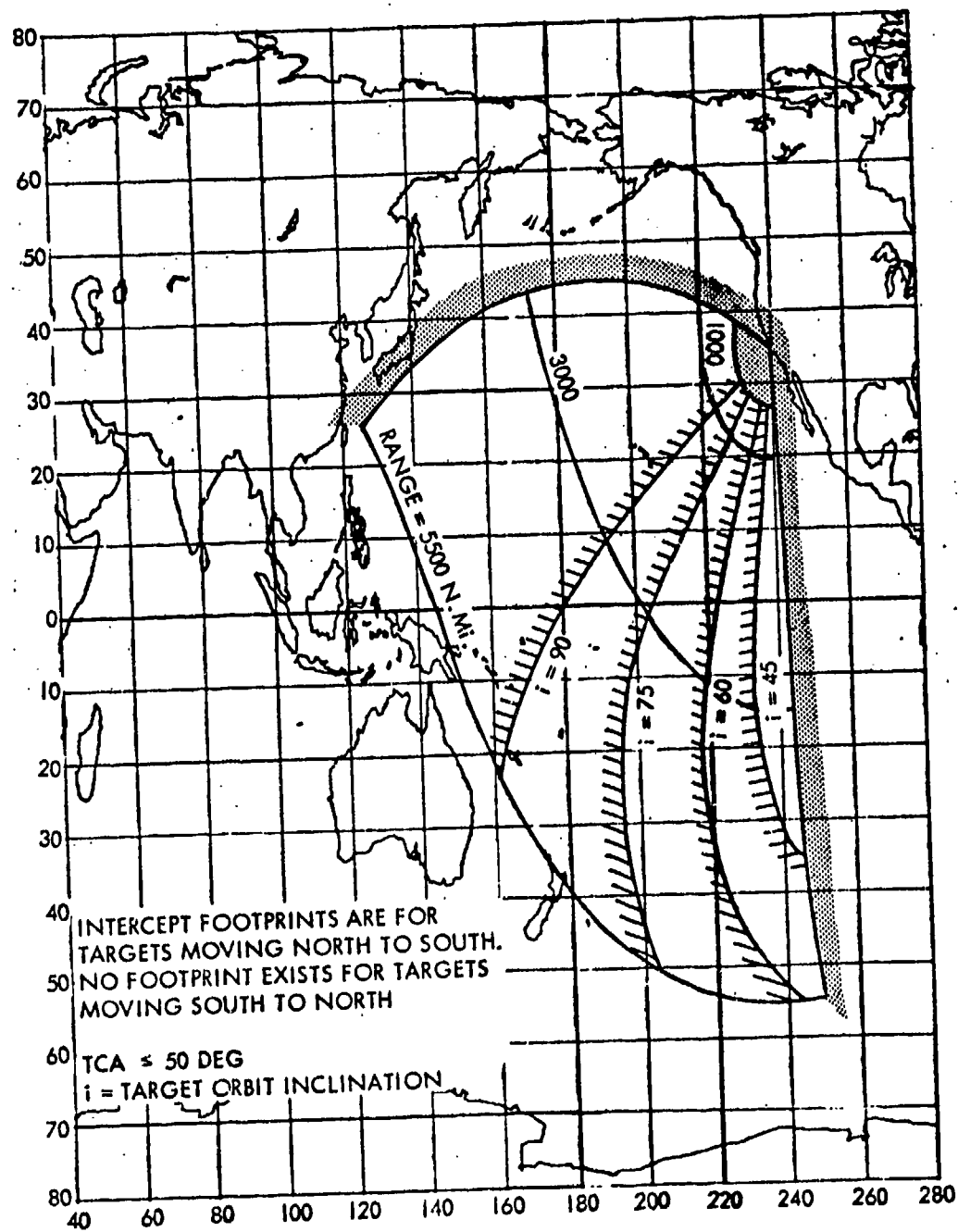


Figure 14-23. PMR Interceptor Footprint for Target Orbit Altitude  
= 100 N Mi

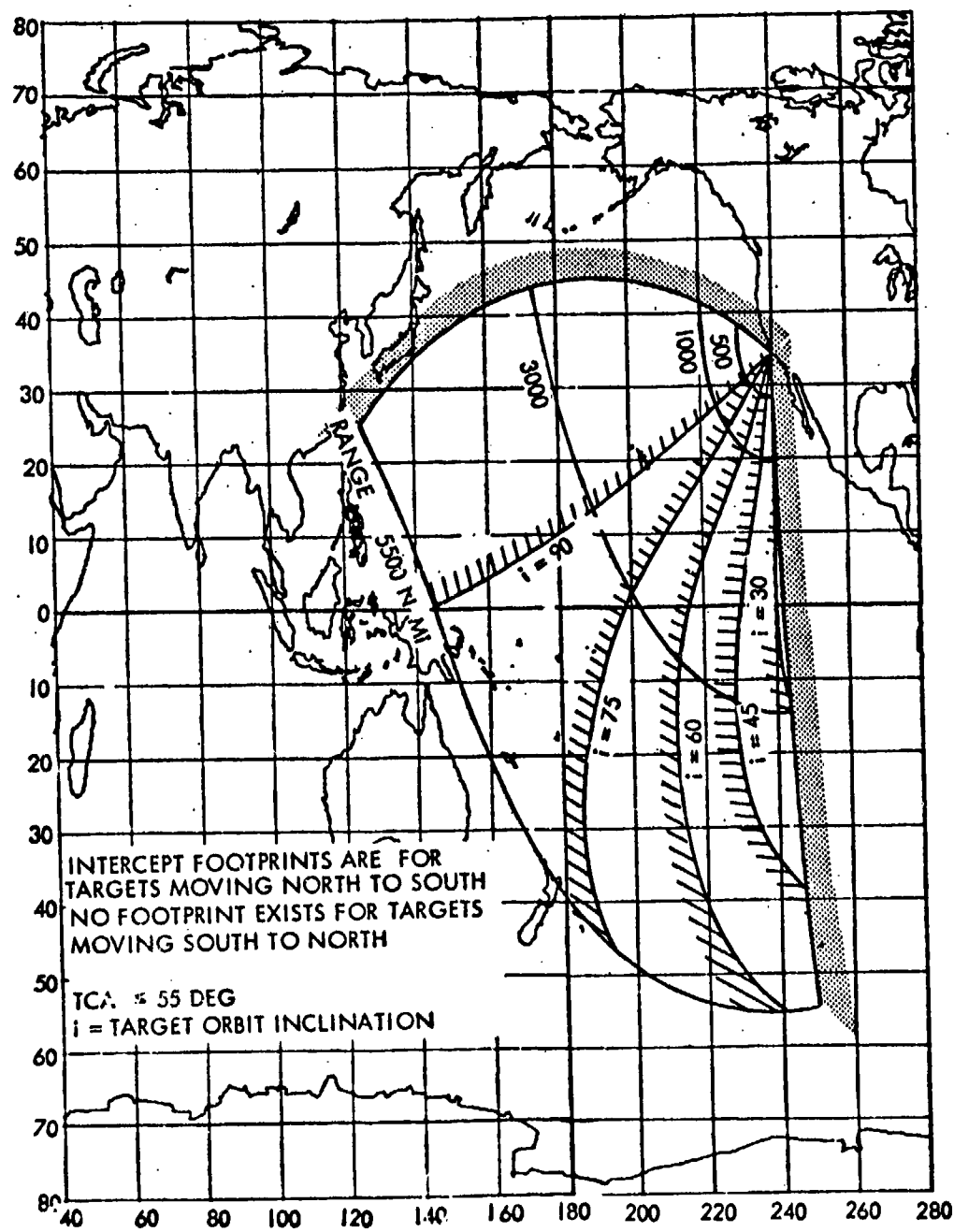


Figure 14-24. PMR Interceptor Footprint for Target Orbit Altitude = 1000 N Mi

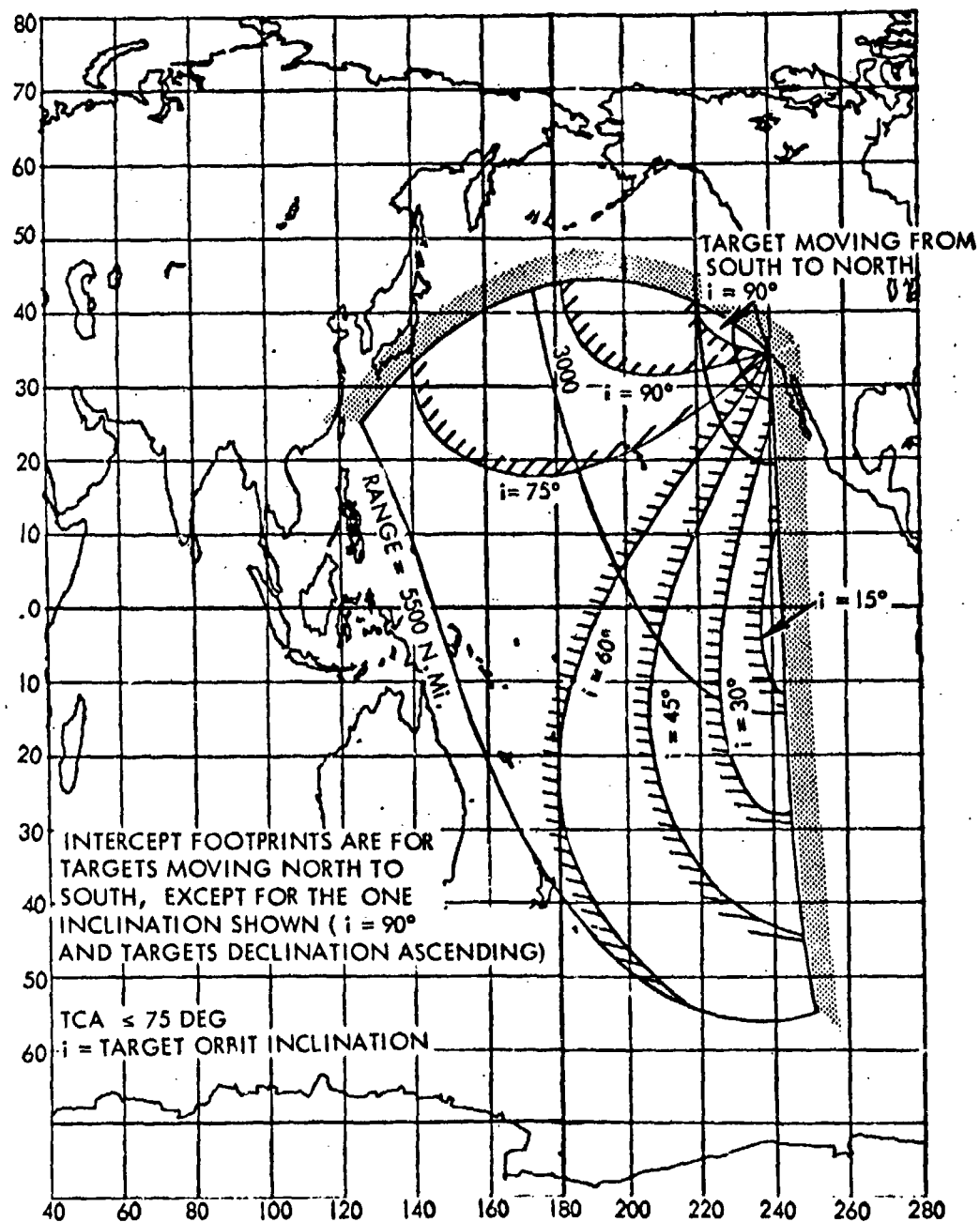


Figure 14-25. PMR Interceptor Footprint for Target Orbit Altitude = 2500 N Mi

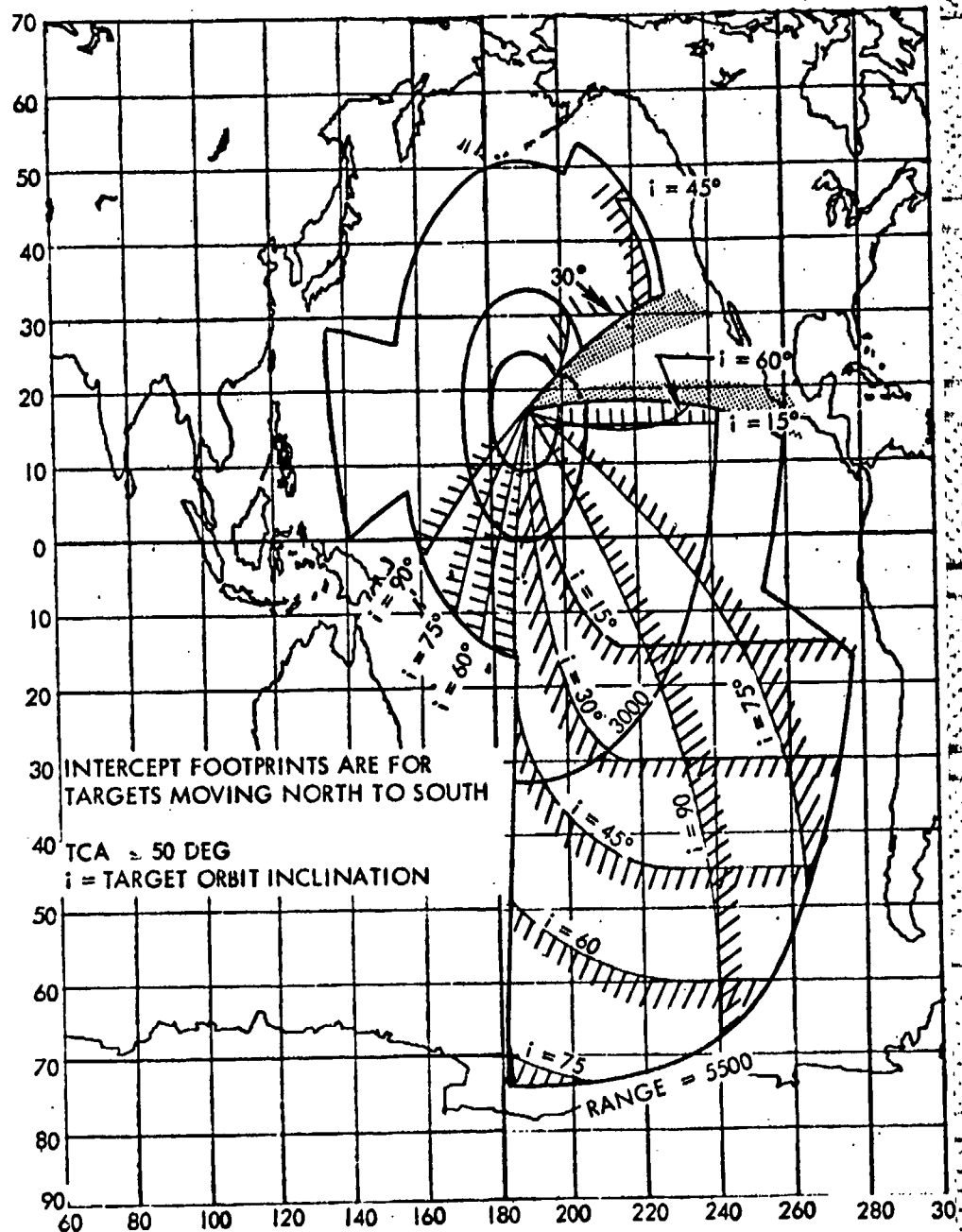


Figure 14-26. Johnston Island Interceptor Footprint for Target  
Orbit Altitude = 100 N Mi



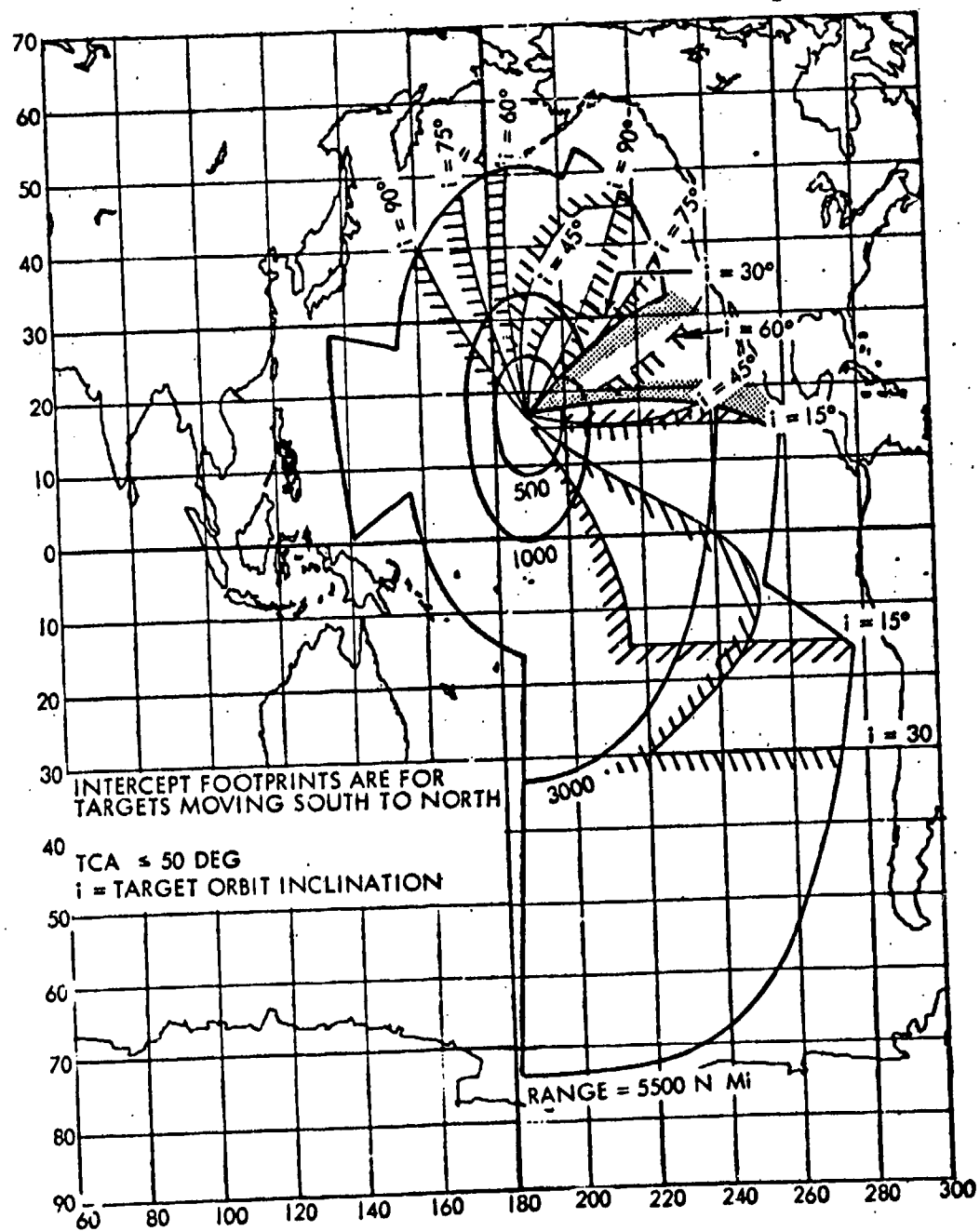


Figure 14-27. Johnston Island Interceptor Footprint for Target  
Orbit Altitude = 100 N Mi

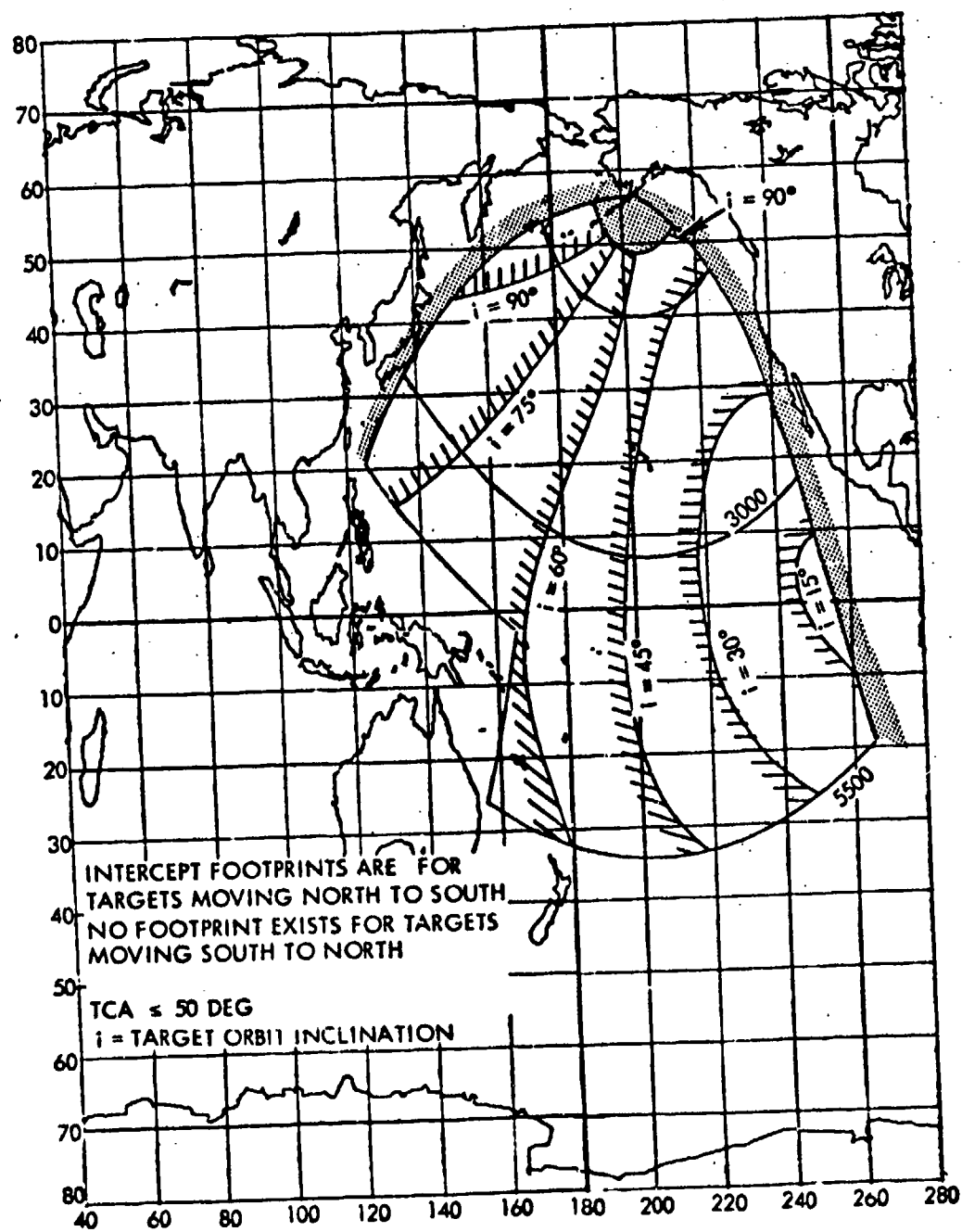


Figure 14-28. Kodiak Alaska Interceptor Footprint for Target  
Orbit Altitude = 100 N Mi

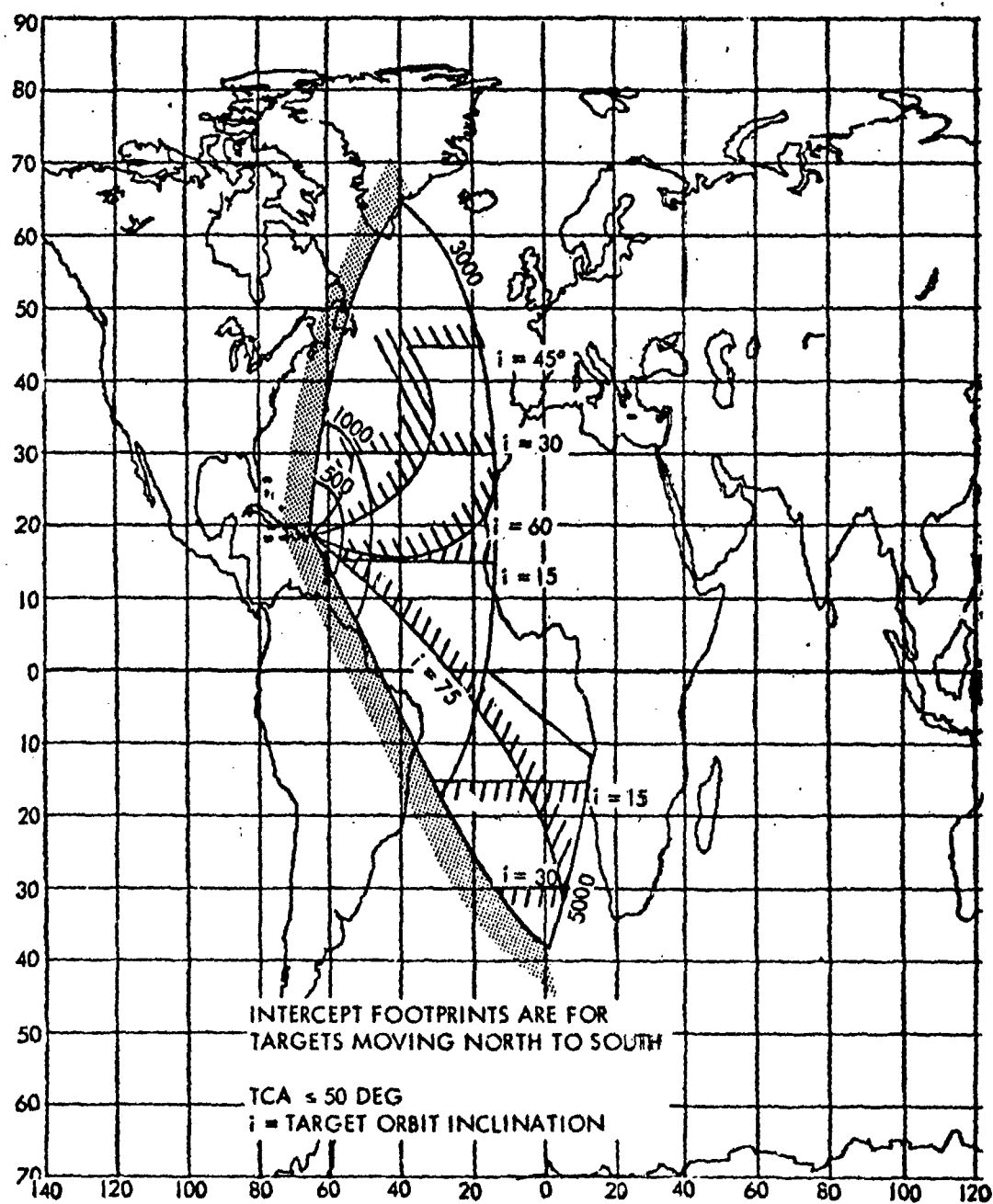


Figure 14-29. Puerto Rico Interceptor Footprint for Target  
Orbit Altitude = 100 N Mi

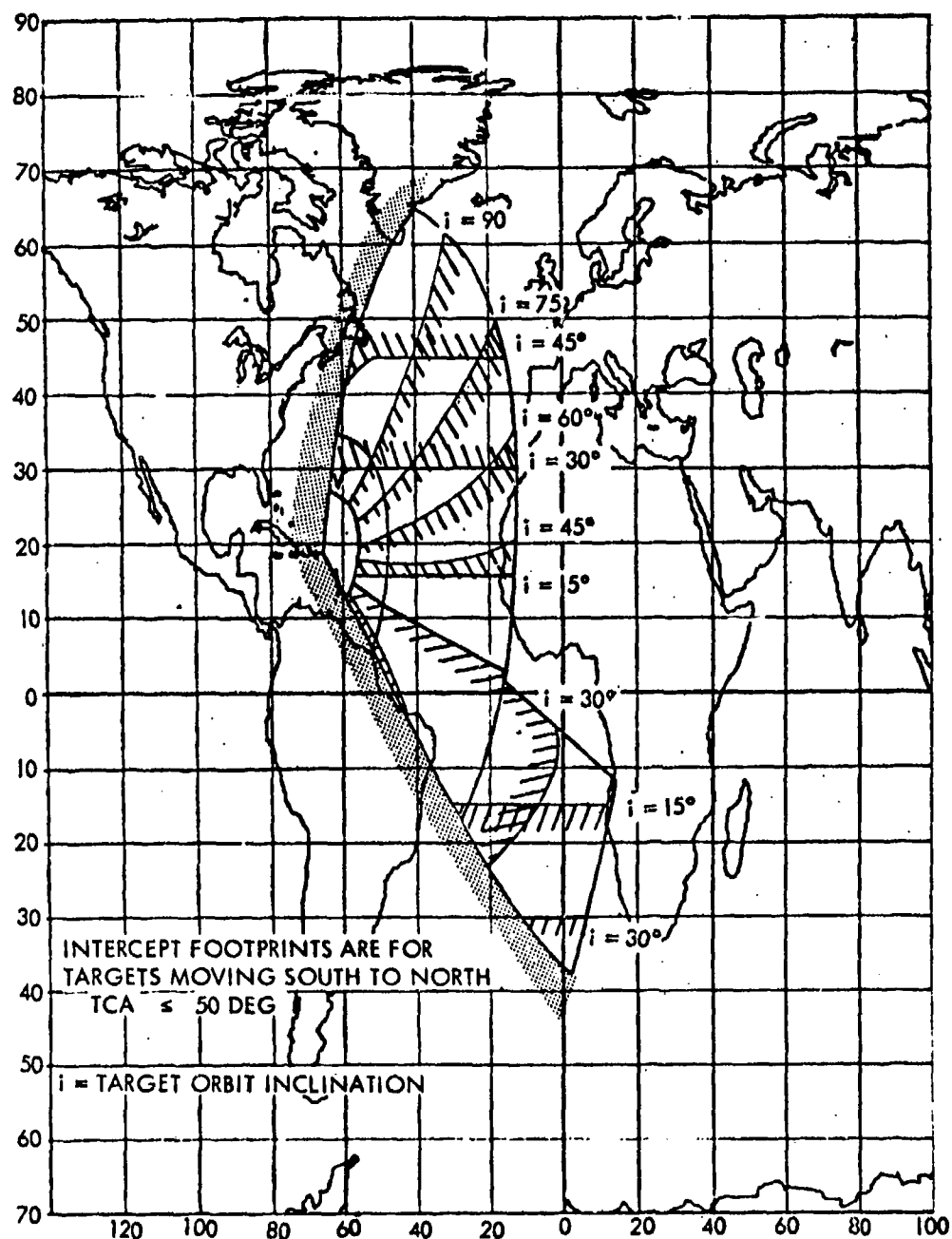


Figure 14-30. Puerto Rico Interceptor Footprint for Target Orbit Altitude = 100 N Mi

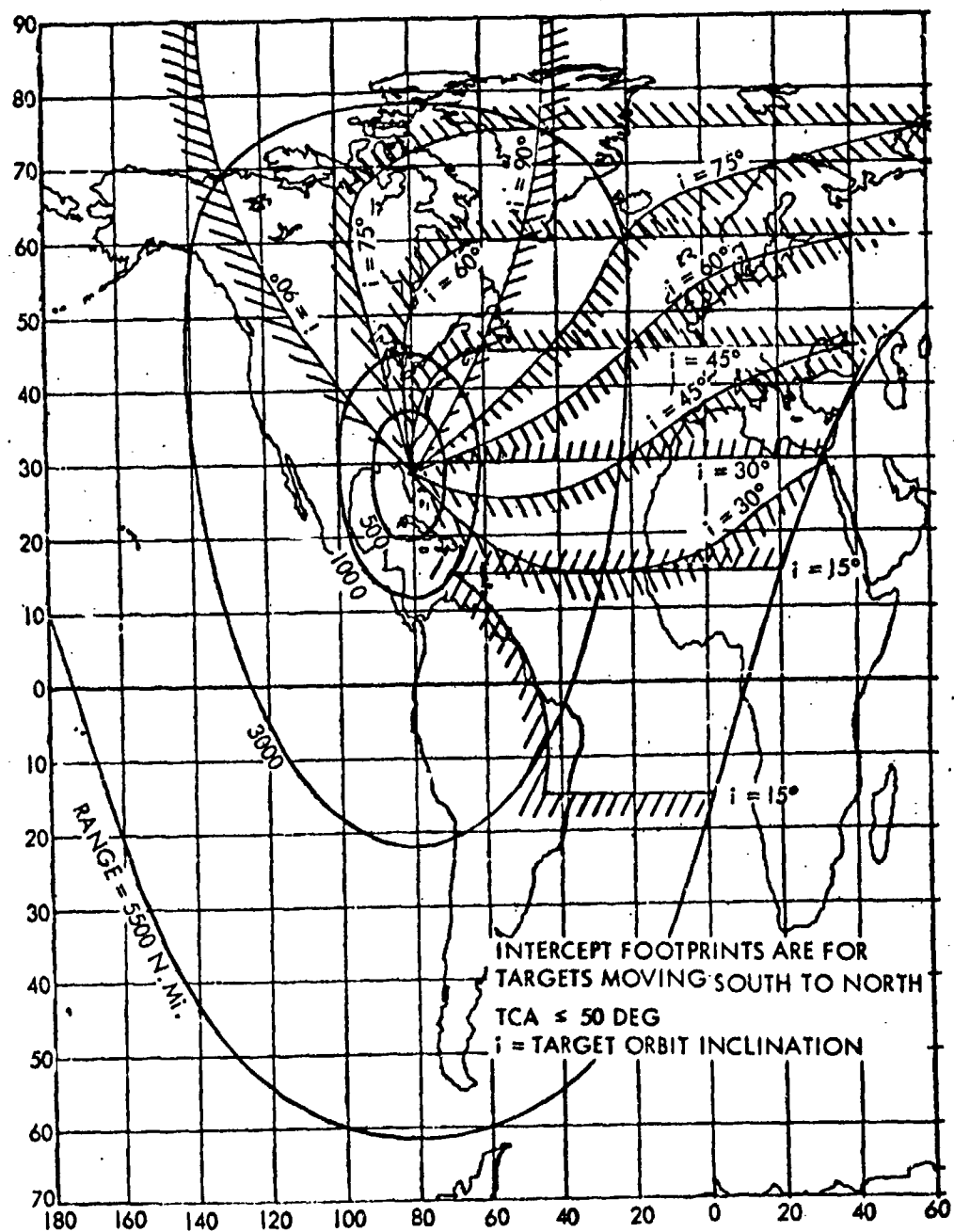


Figure 14-31. AMR Interceptor Footprint for Target Orbit Altitude  
 = 100 N Mi

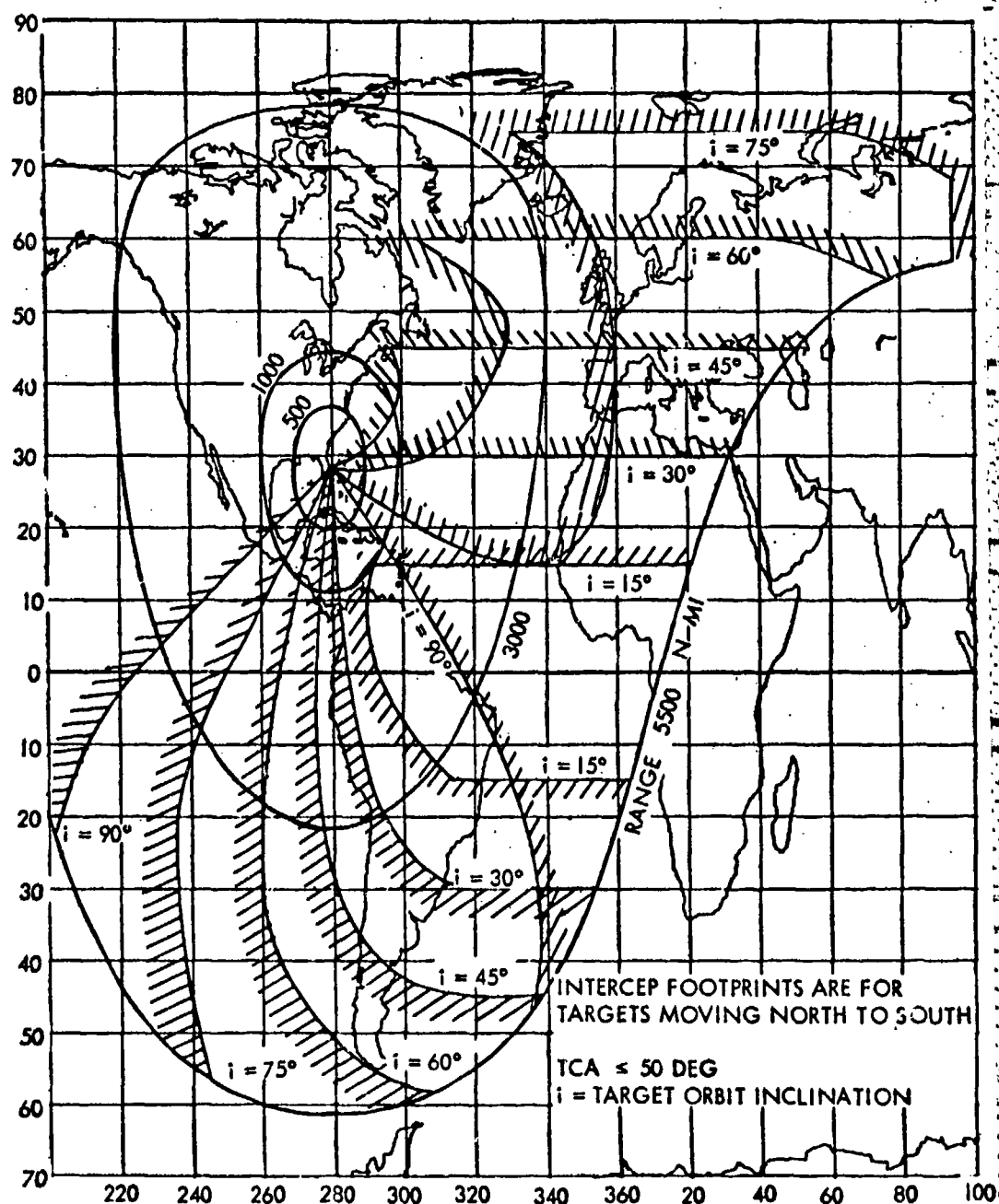


Figure 14-32. AMR Interceptor Footprint for Target Orbit Altitude = 100 N Mi

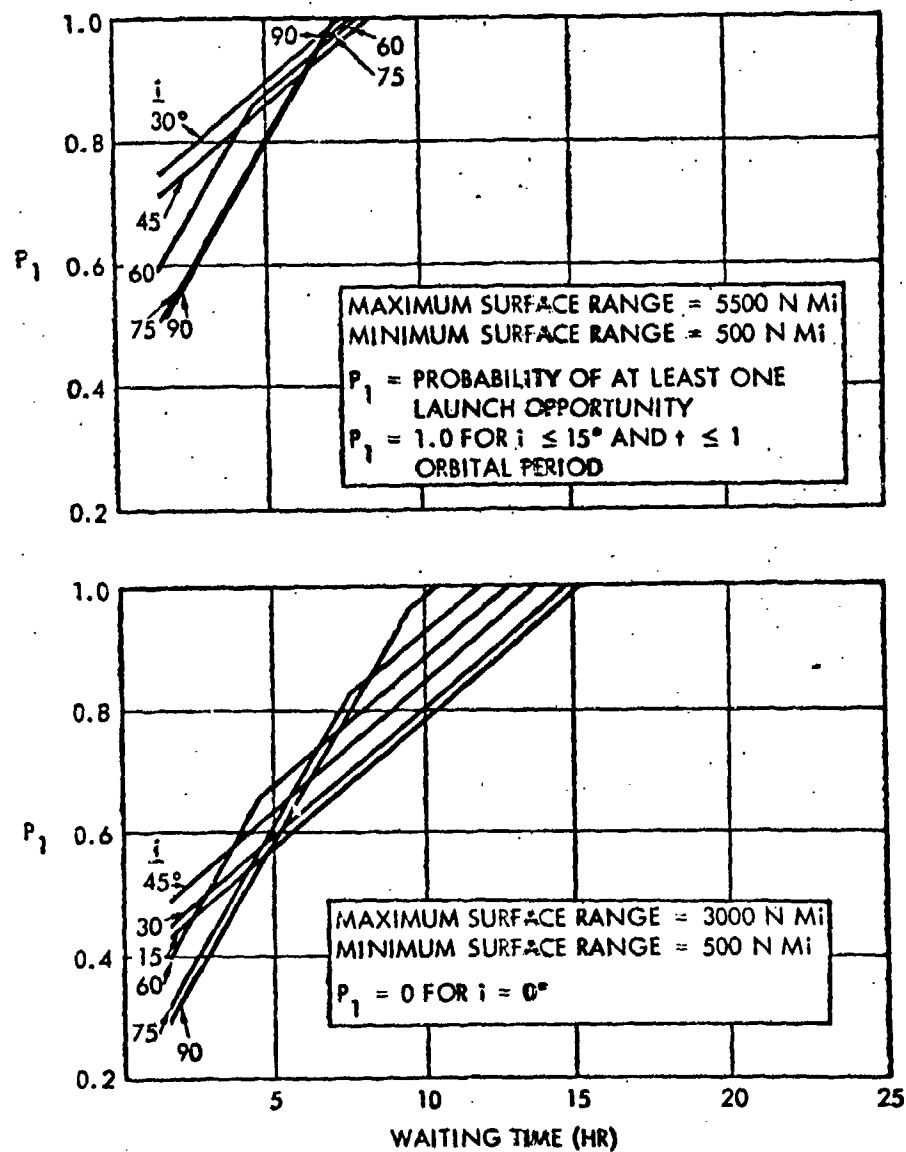


Figure 14-33. AMR Launch Opportunities Against Targets in 100 N Mi Altitude Circular Orbits — No  $V_R$  Restrictions

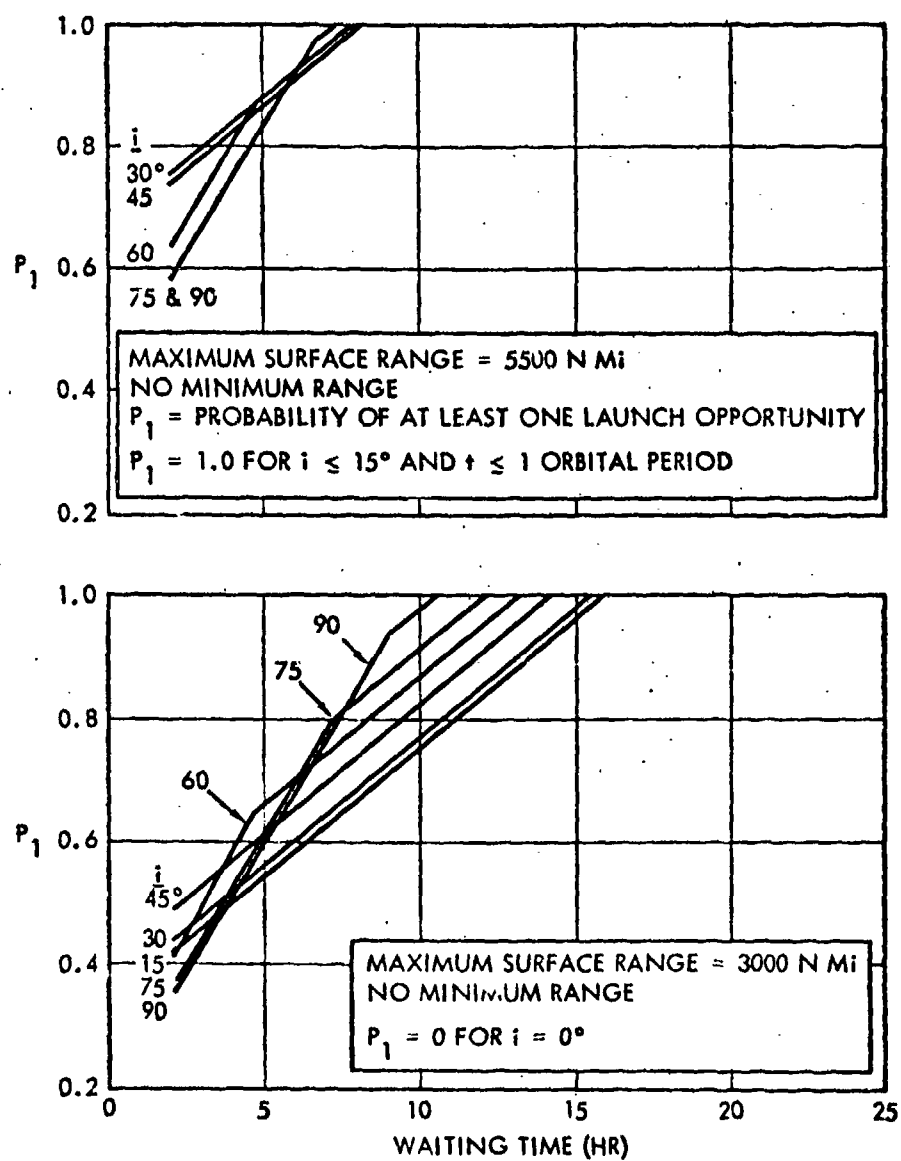


Figure 14-34. AMR Launch Opportunities Against Targets in 1000 N Mi Altitude Circular Orbits — No  $V_R$  Restrictions



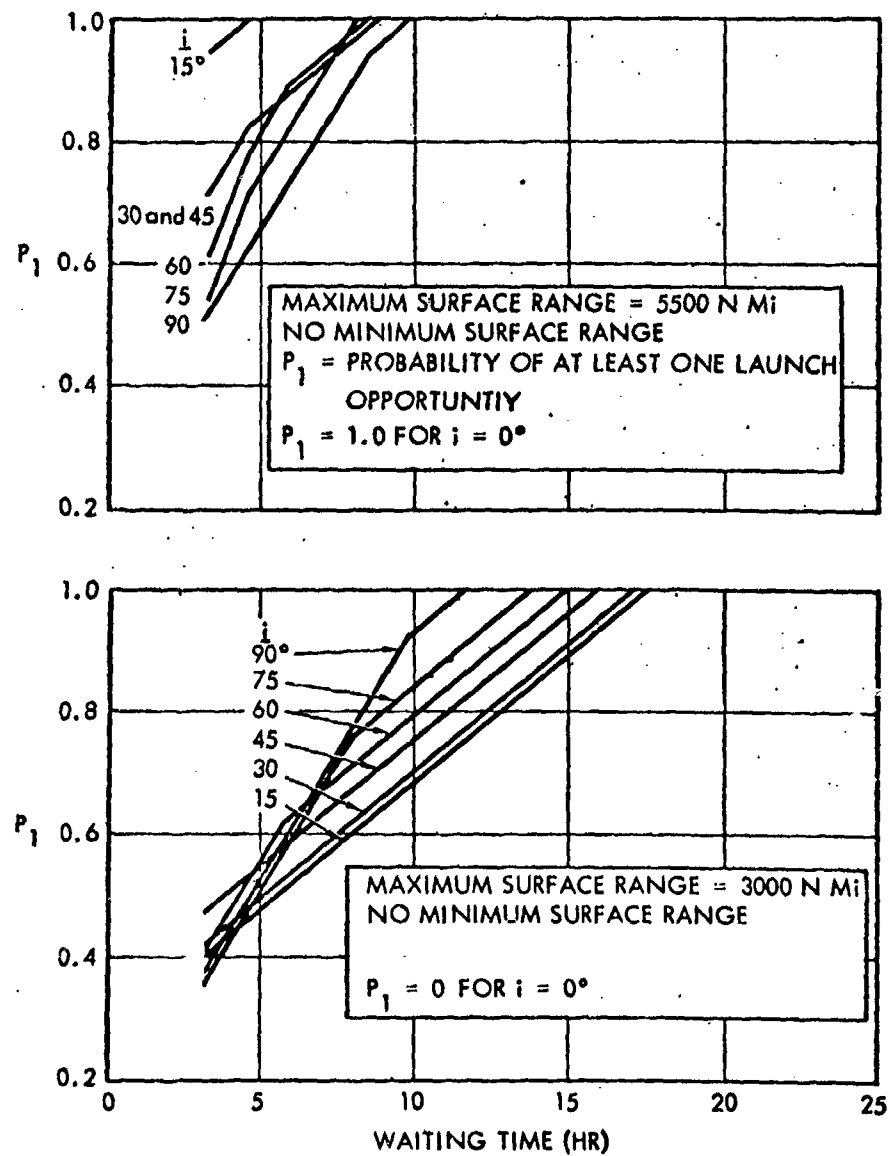


Figure 14-35. AMR Launch Opportunities Against Targets in 2500 N Mi Altitude Circular Orbits — No  $V_R$  Restrictions

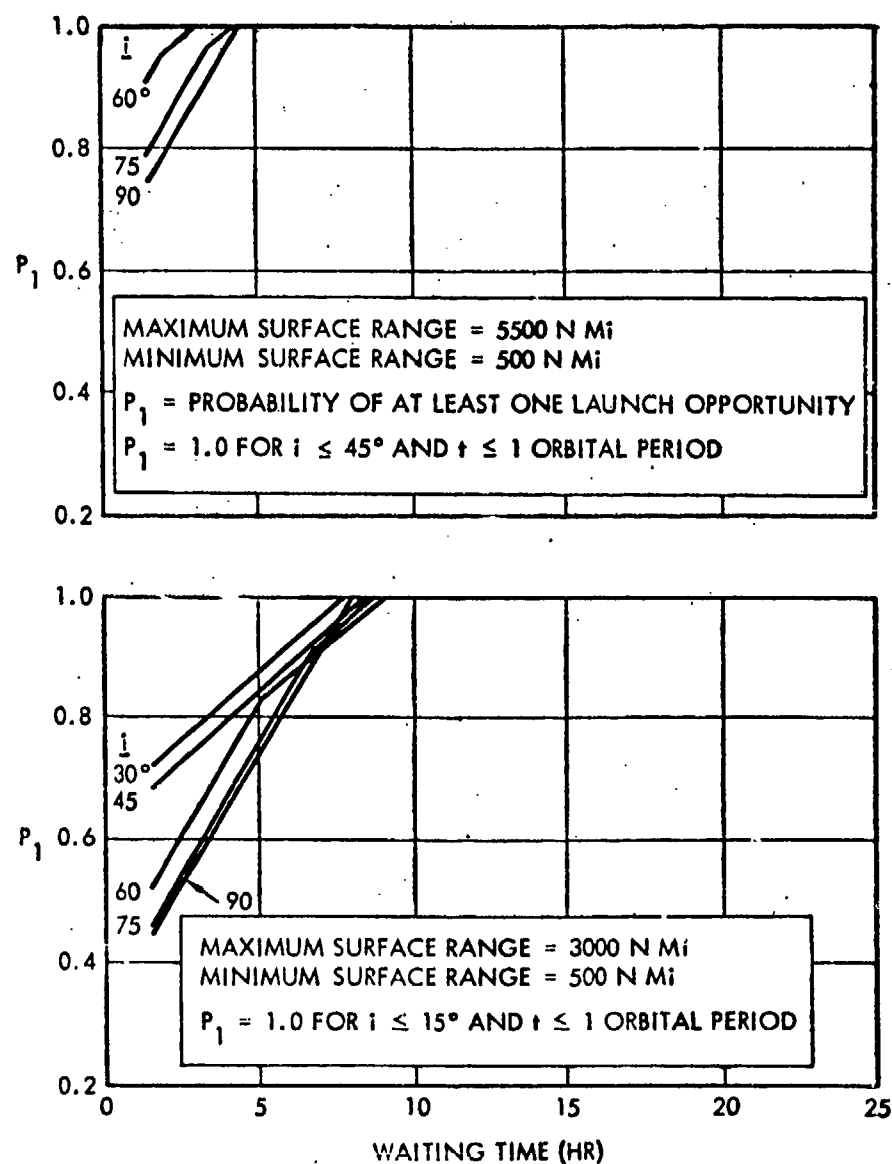


Figure 14-36. PMR Launch Opportunities Against Targets in 100 N Mi Altitude Circular Orbits—No  $V_R$  Restrictions

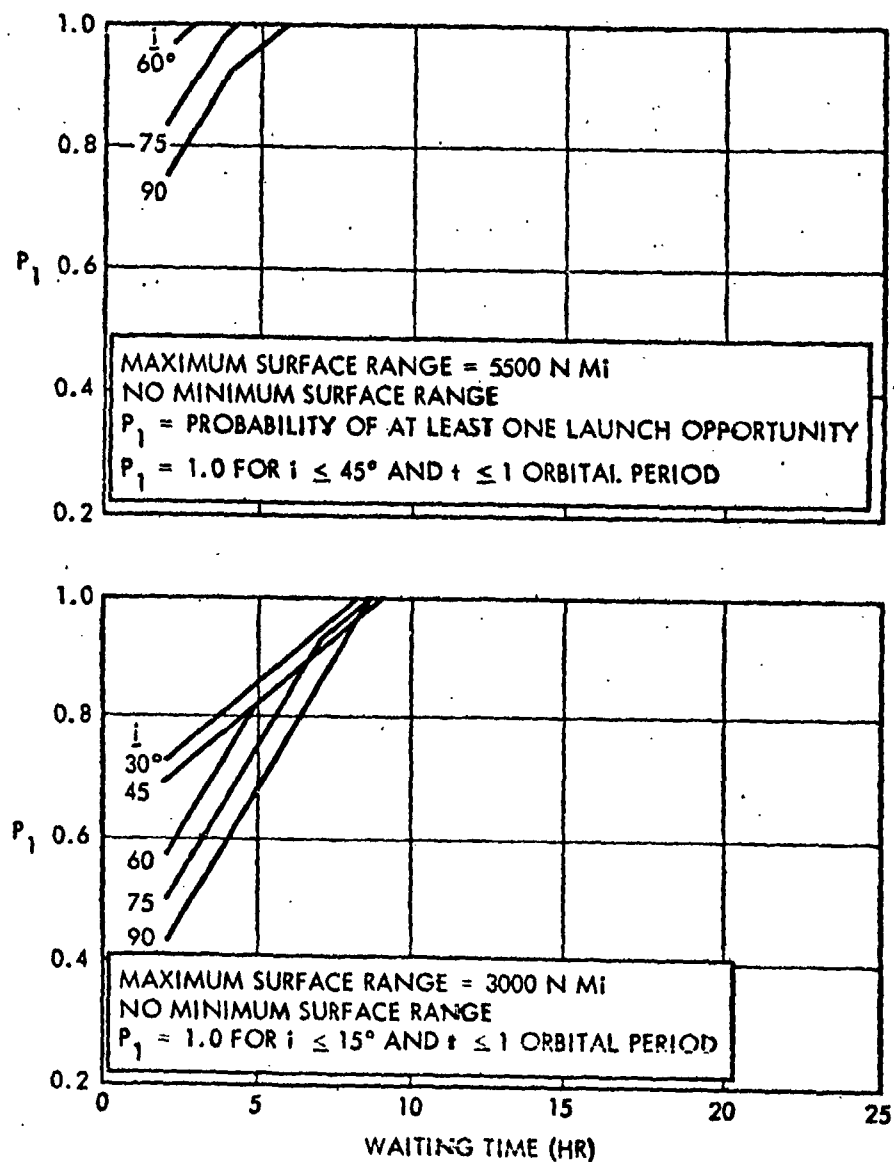


Figure 14-37. PMR Launch Opportunities Against Targets in 1000 N Mi Altitude Circular Orbits—No  $V_R$  Restrictions

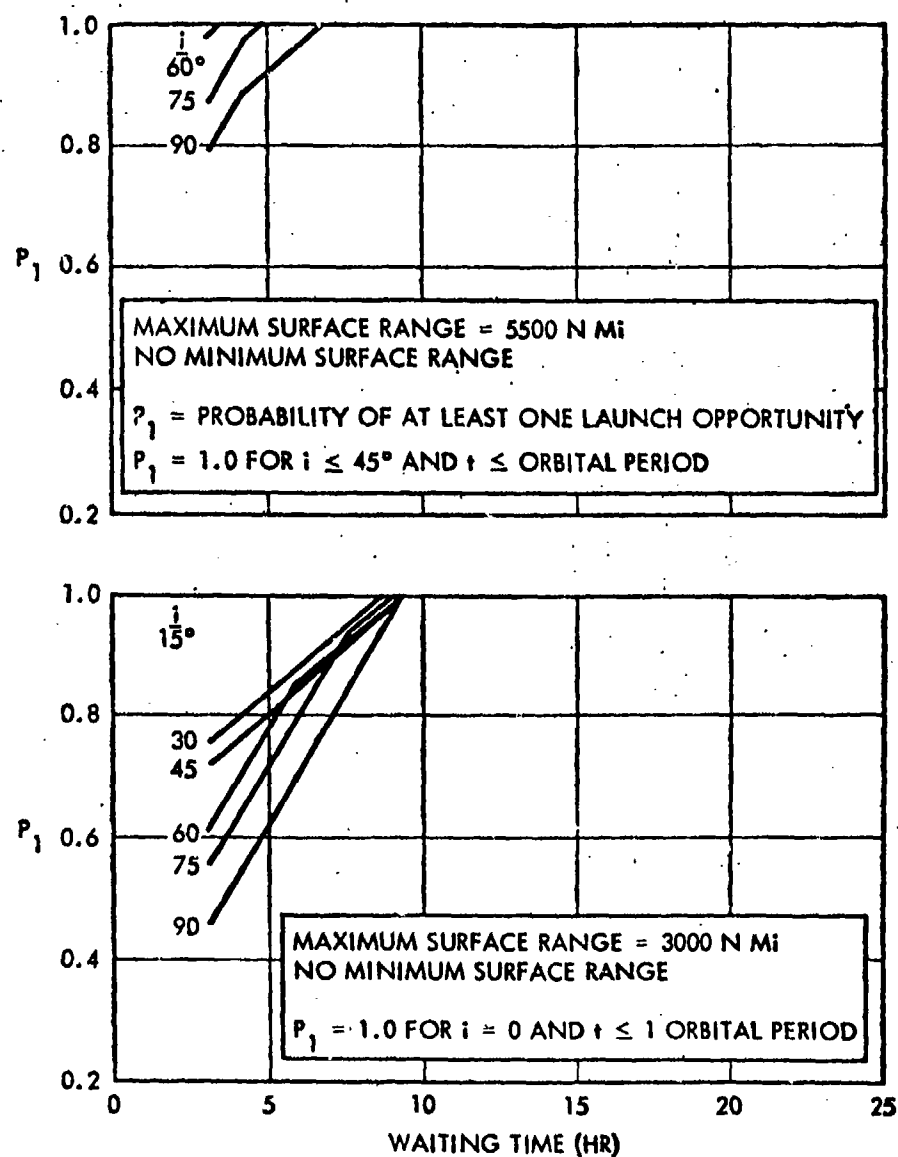


Figure 14-38. PMR Launch Opportunities Against Targets in 2500 N Mi Altitude Circular Orbits-No  $V_R$  Restrictions

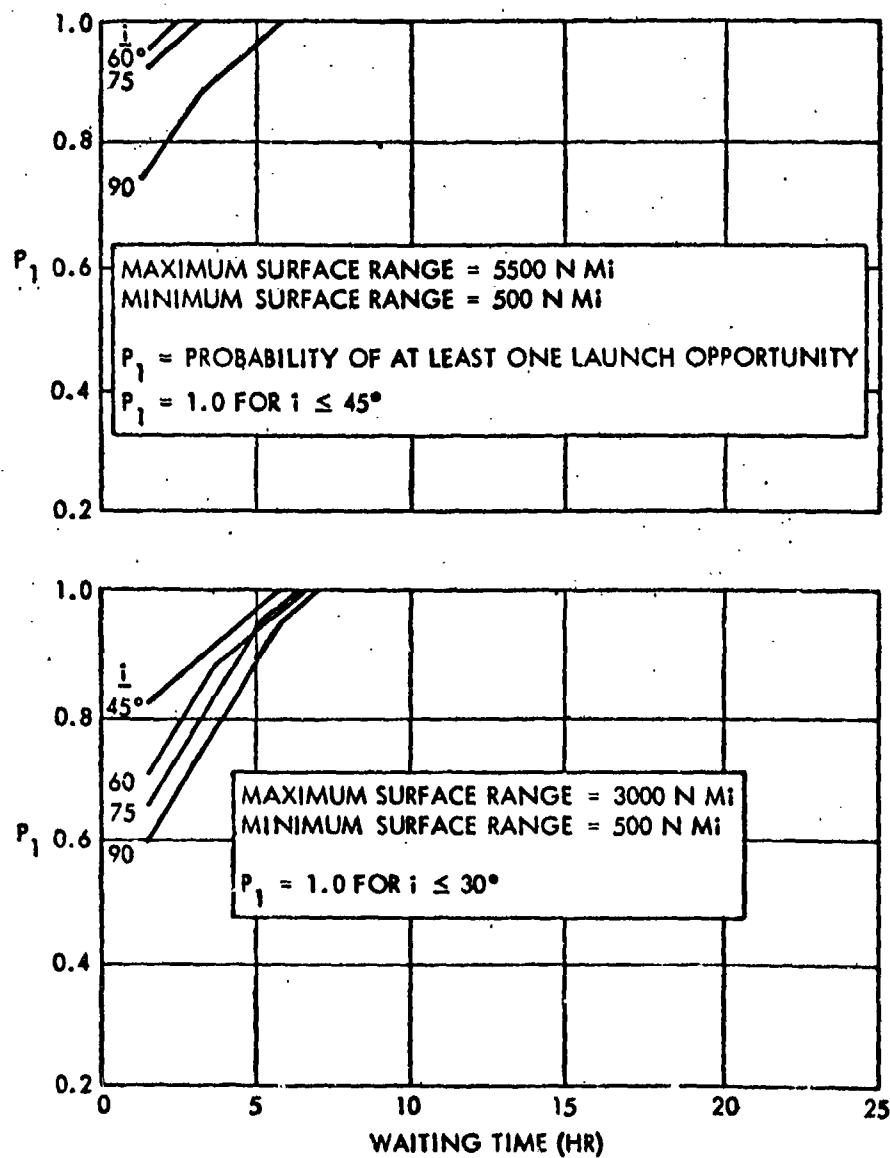


Figure 14-39. Johnston Island Launch Opportunities Against Targets in 100 N Mi Altitude Circular Orbits—No  $V_R$  Restrictions

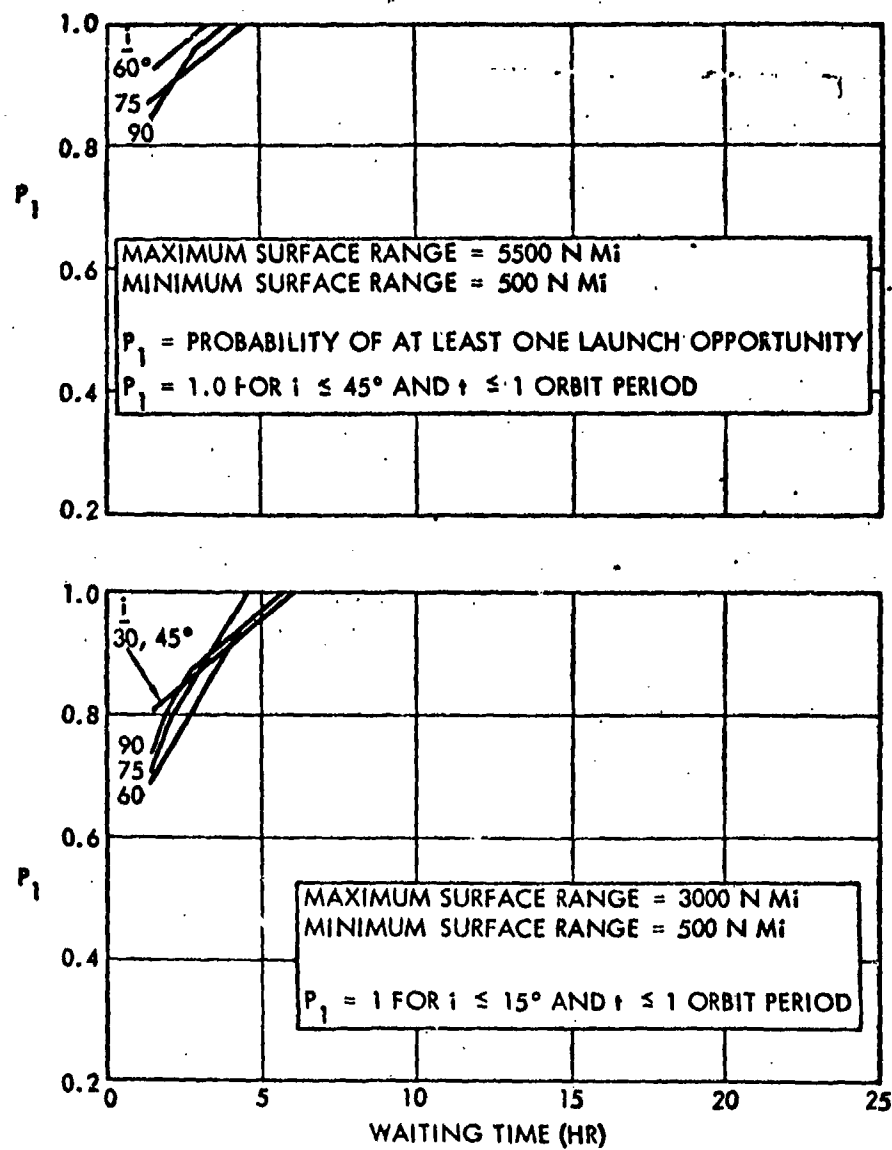


Figure 14-40. AMR and PMR Launch Opportunities Against Targets in 100 N Mi Altitude Circular Orbits—No  $V_R$  Restrictions

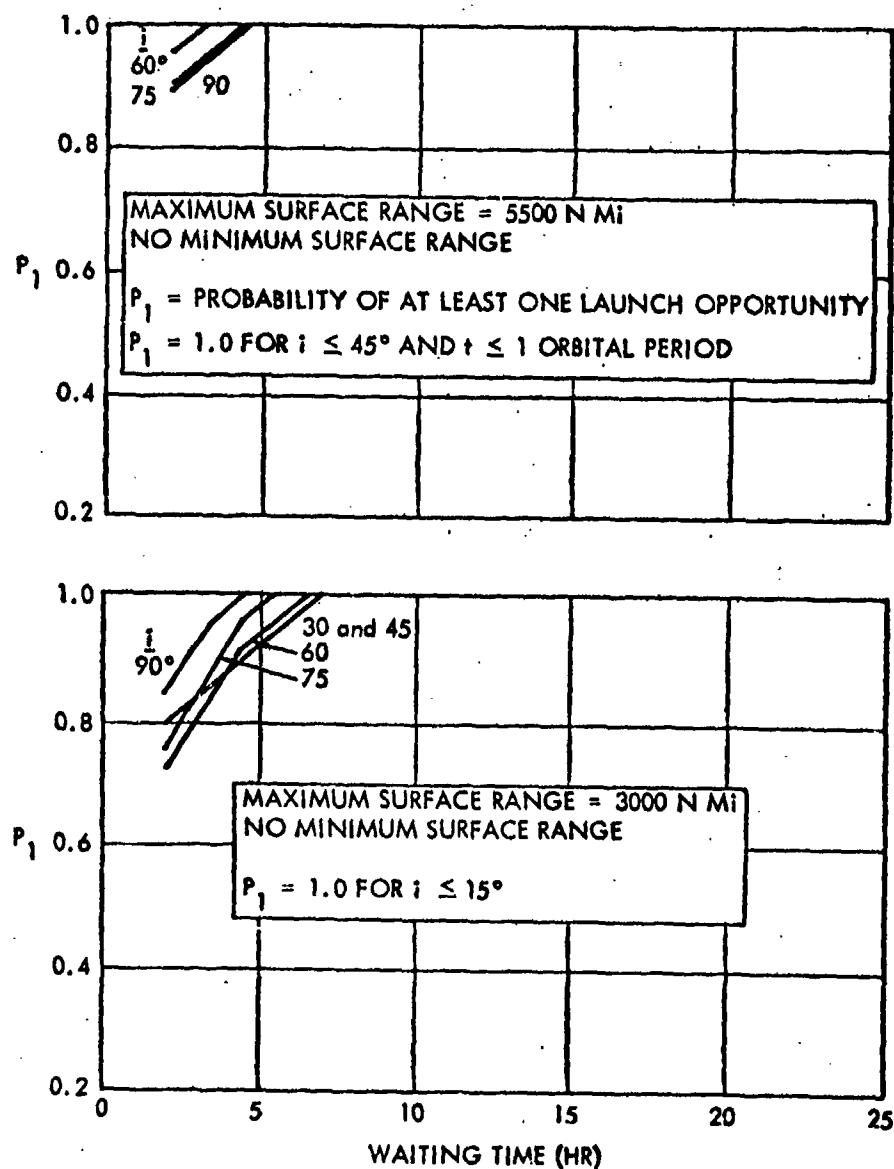


Figure 14-41. AMR and PMR Launch Opportunities Against Targets in 1000 N Mi Altitude Circular Orbits—No  $V_R$  Restrictions

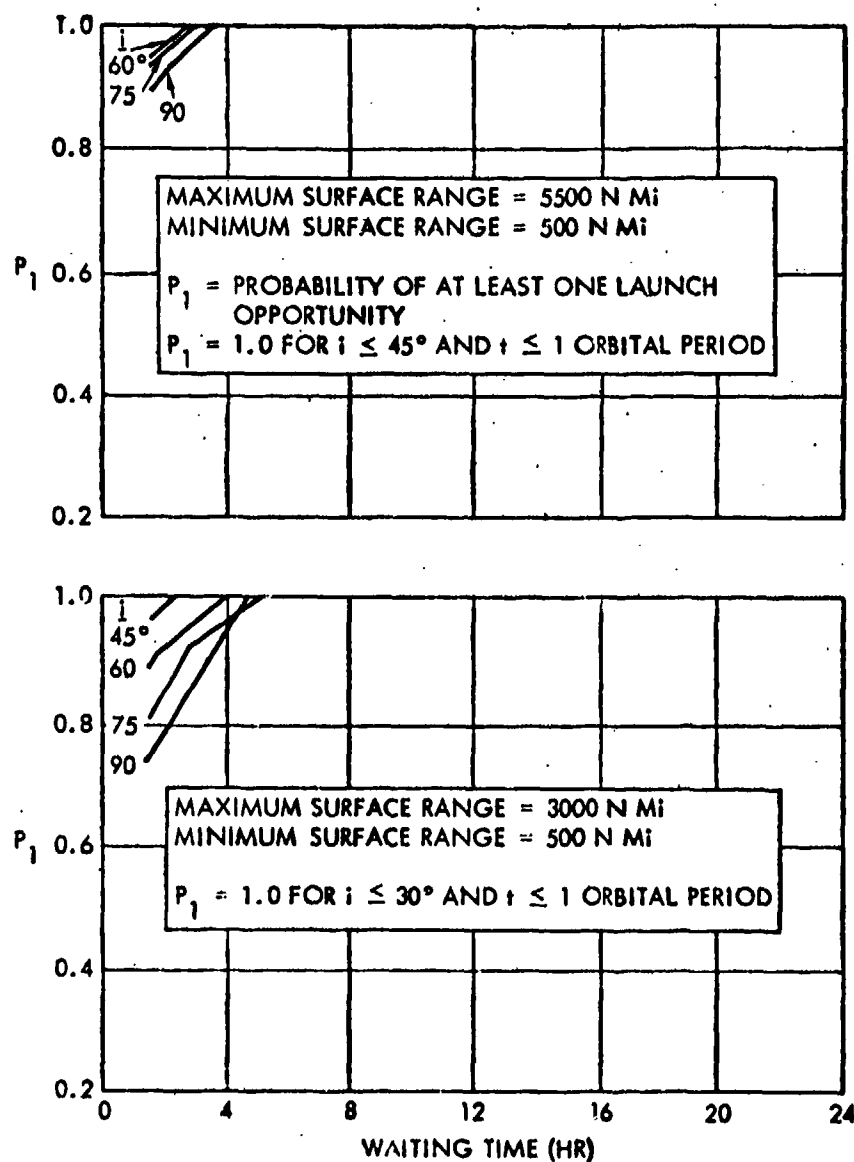


Figure 14-42. AMR and Johnston Island Launch Opportunities Against Targets in 100 N Mi Altitude Circular Orbits—No  $V_R$  Restrictions



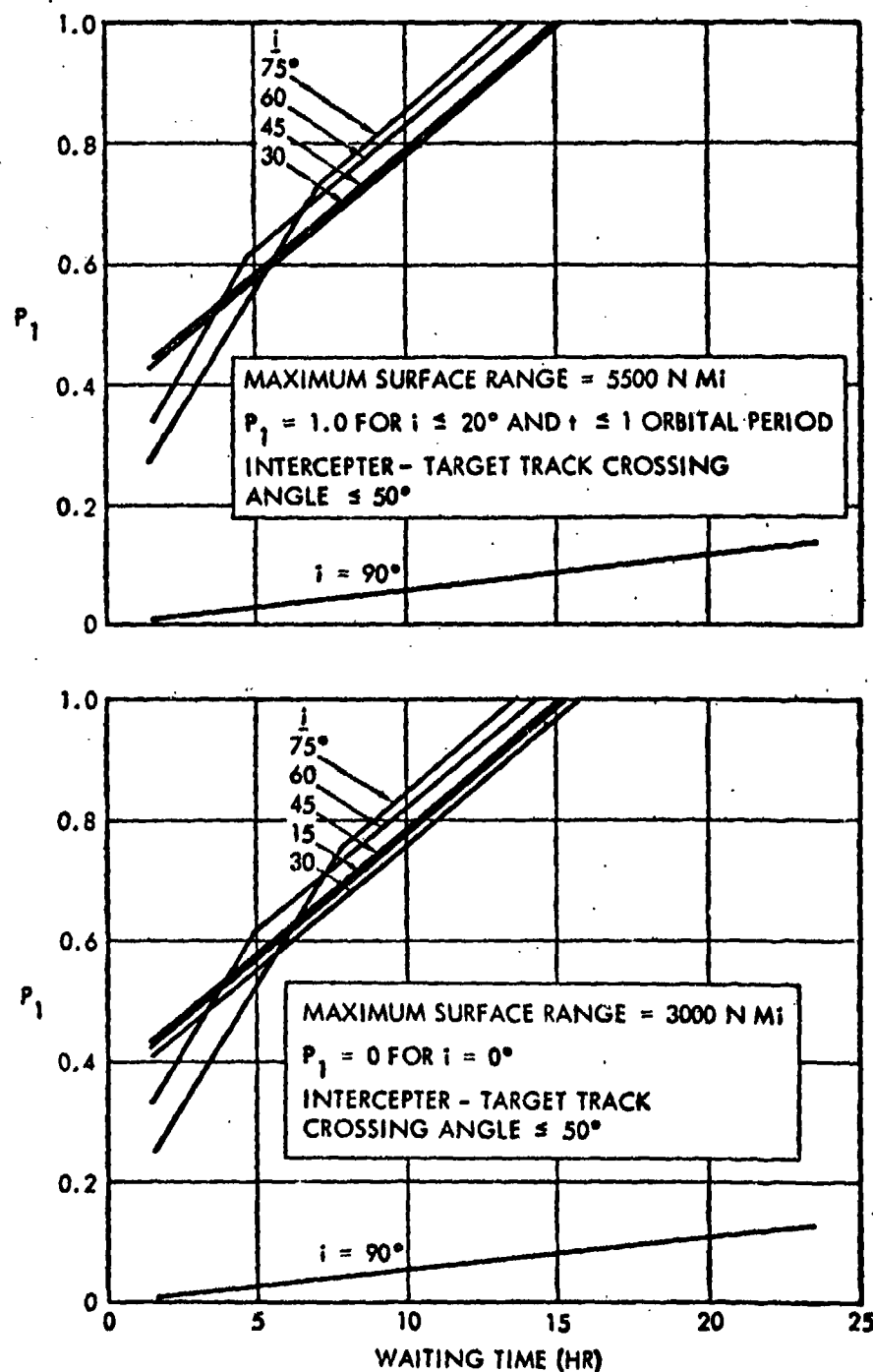


Figure 14-43. AMR Launch Opportunities Against Targets in 100 N Mi Altitude Circular Orbits—With  $V_R$  Restrictions

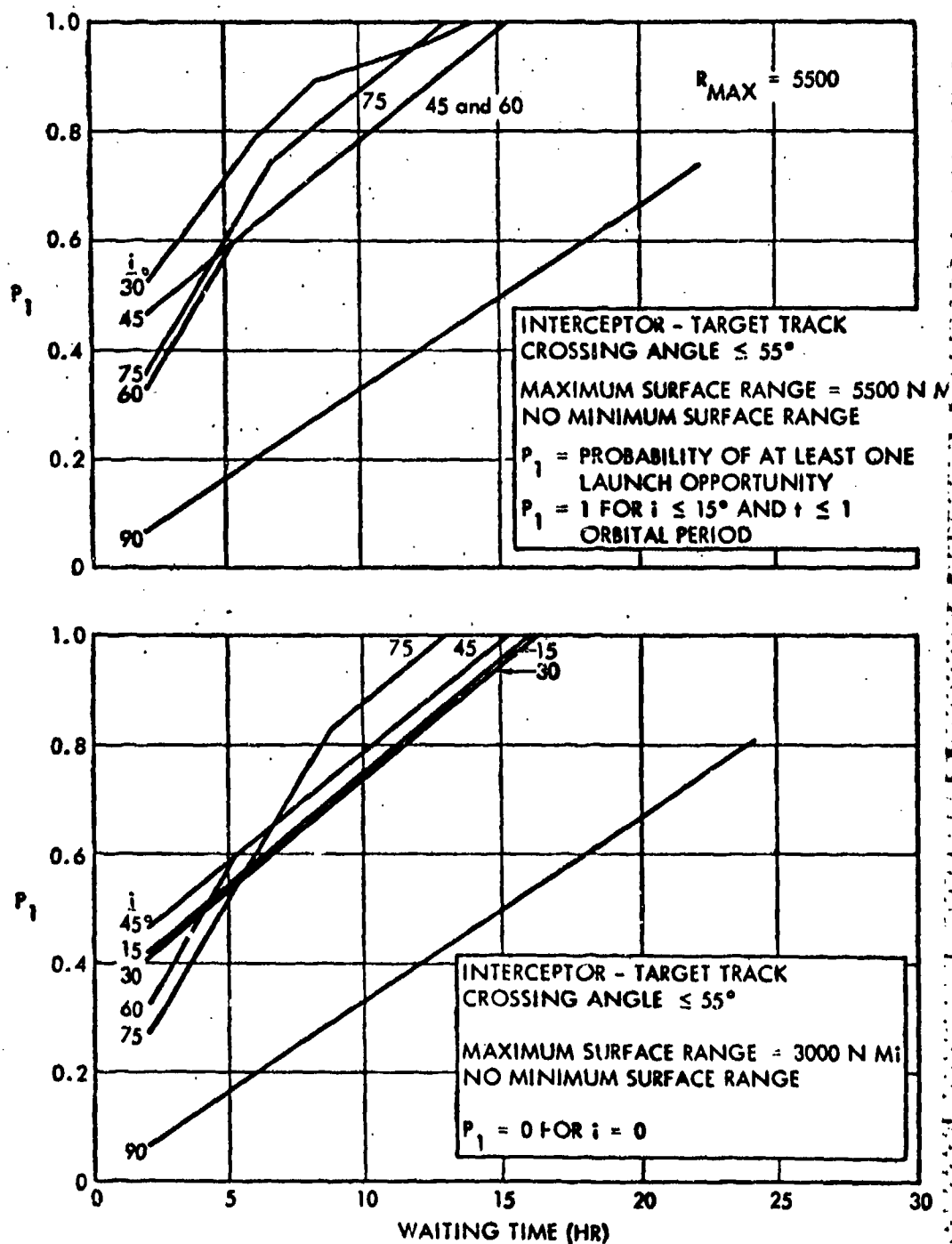


Figure 14-44. AMR Launch Opportunities Against Targets in 1000 N Mi Altitude Circular Orbits—With  $V_R$  Restrictions

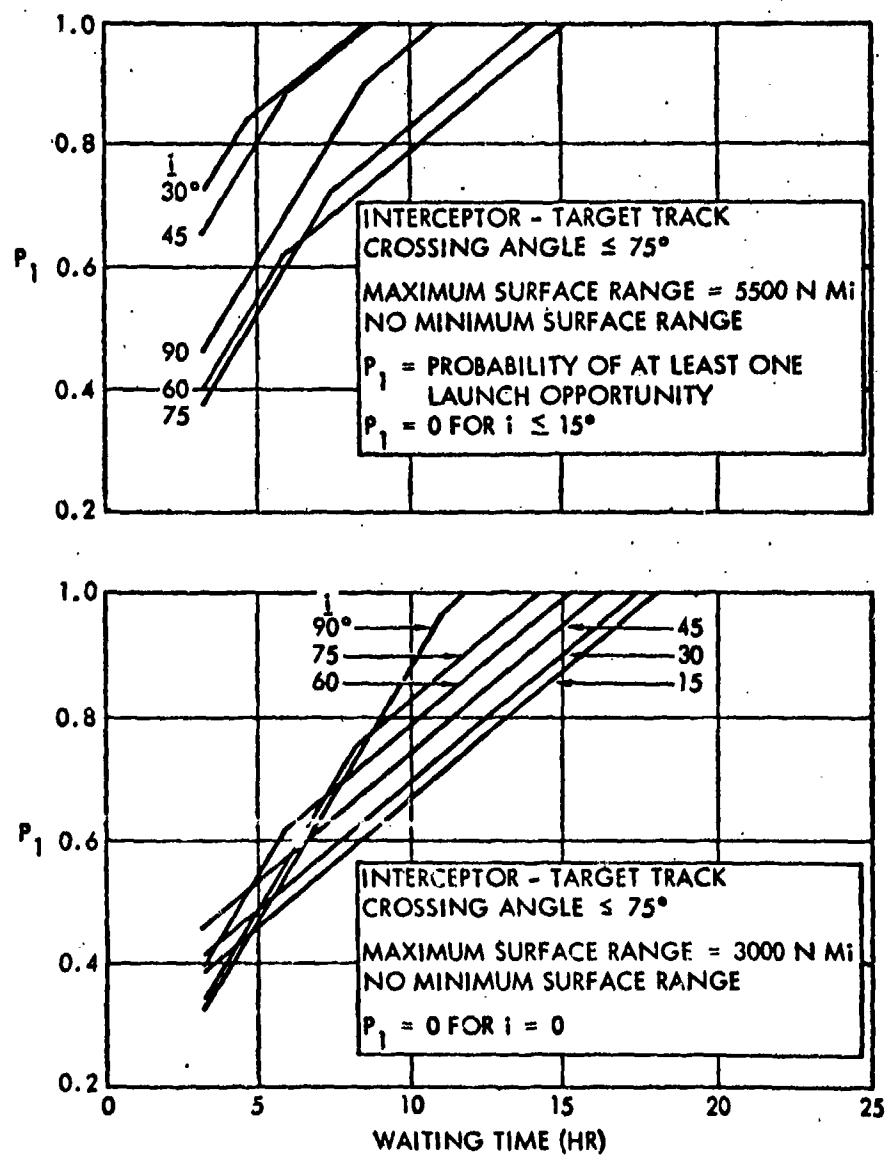


Figure 14-45. AMR Launch Opportunities Against Targets in 2500 N Mi Altitude Circular Orbits—With  $V_R$  Restrictions

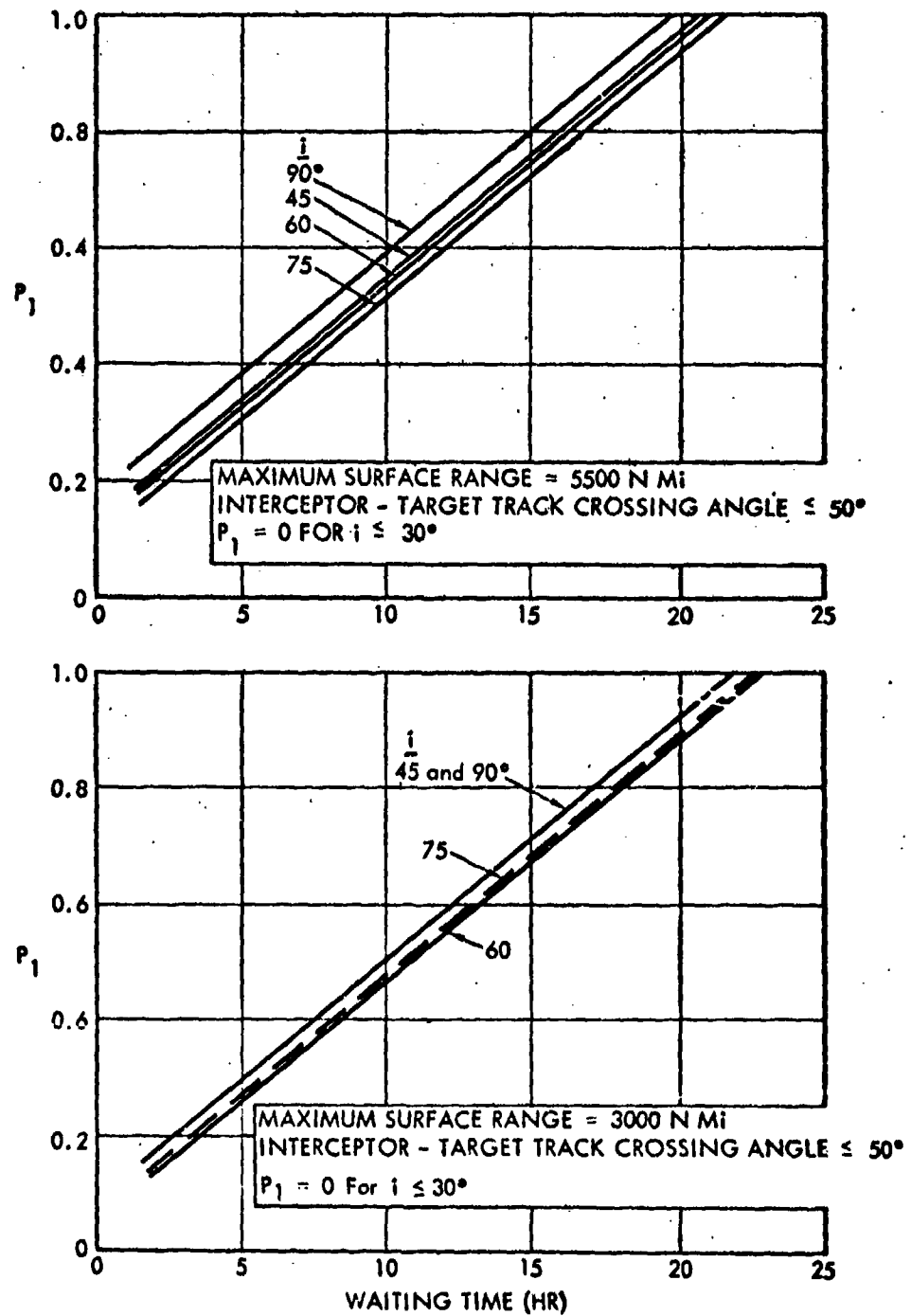


Figure 14-46. PMR Launch Opportunities Against Targets in 100 N Mi Altitude Circular Orbits—With  $V_R$  Restrictions

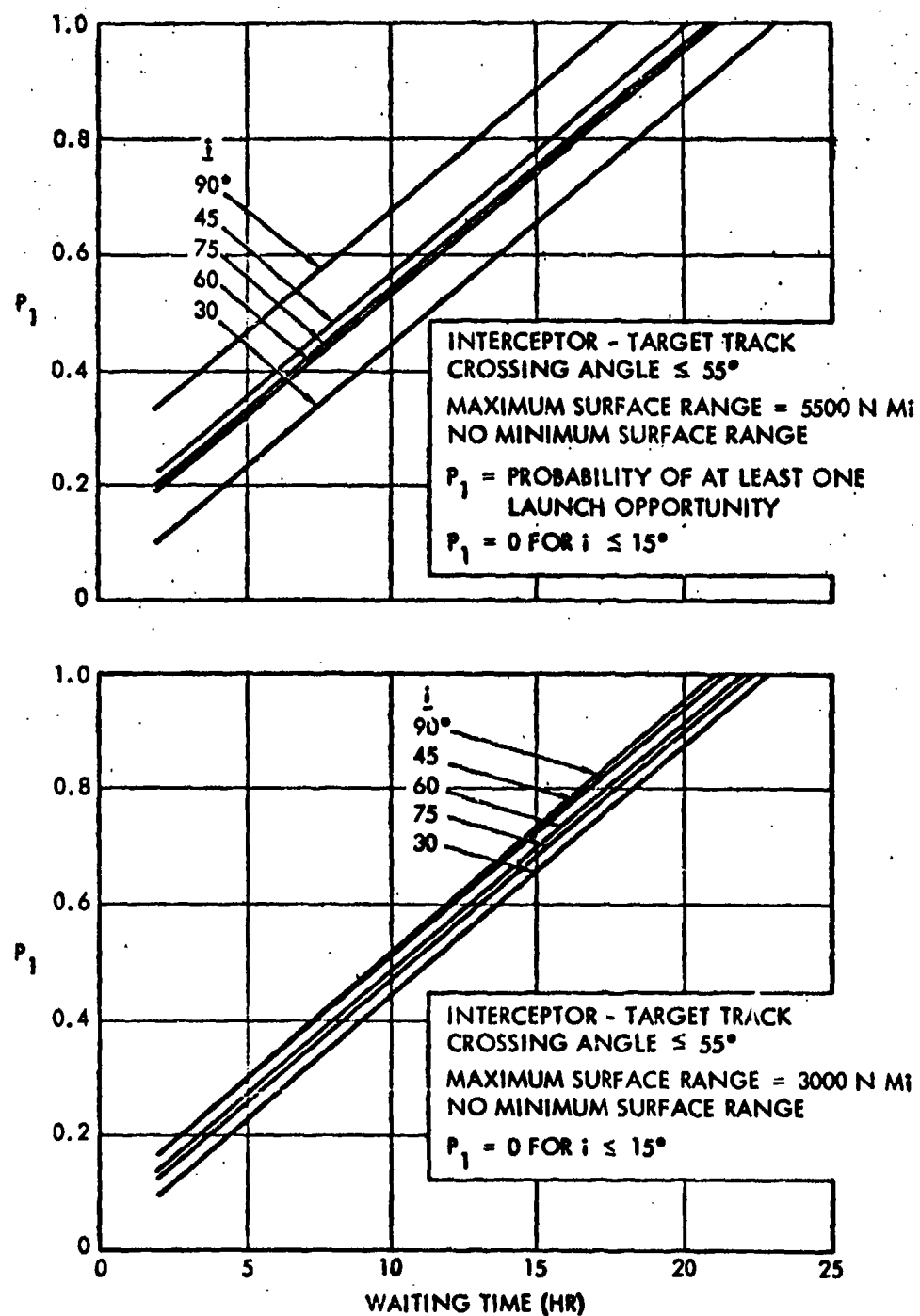


Figure 14-47. PMR Launch Opportunities Against Targets in 1000 N Mi Altitude Circular Orbits—With  $V_R$  Restrictions

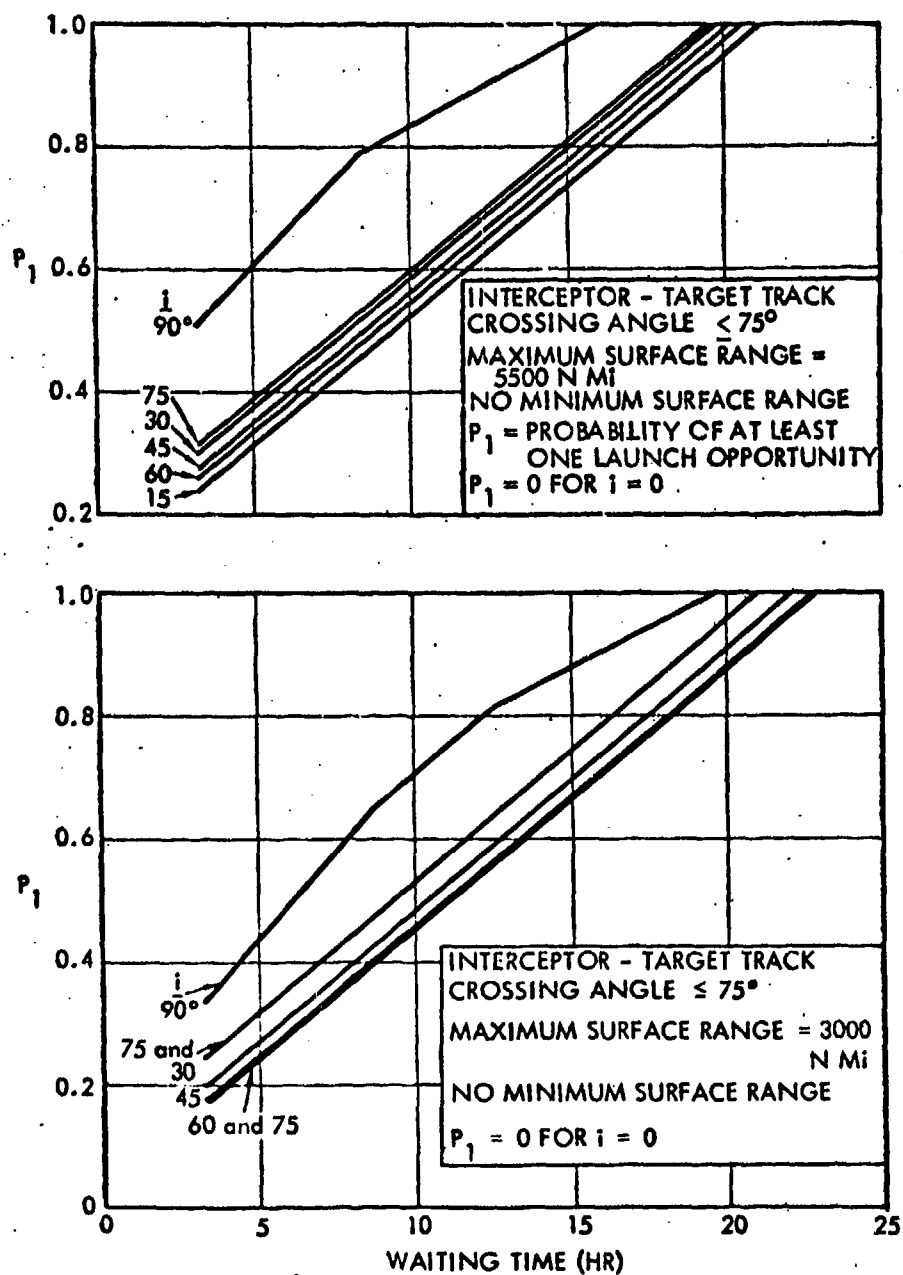


Figure 14-48. PMR Launch Opportunities Against Targets in 2500 N Mi Altitude Circular Orbits—With  $V_R$  Restrictions

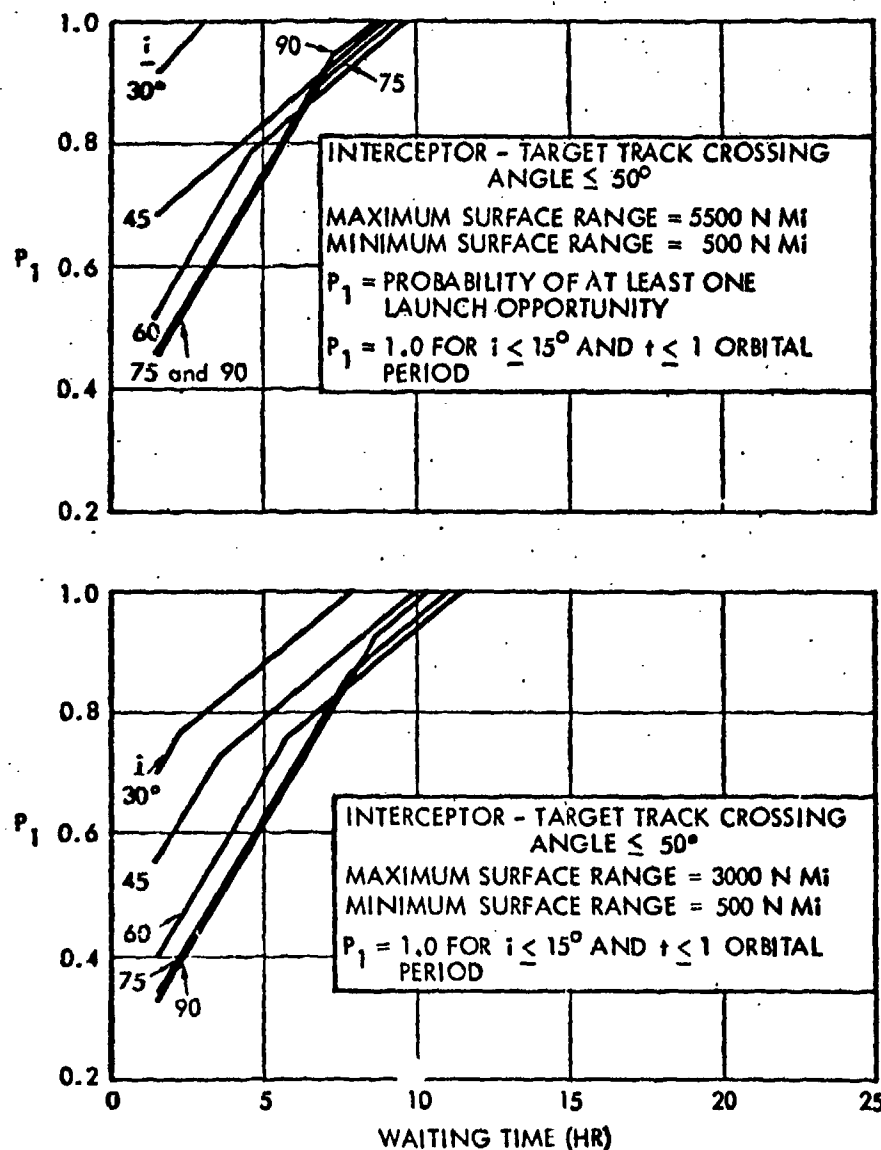


Figure 14-49. Johnston Island Launch Opportunities Against Targets in 100 N Mi Altitude Circular Orbits—With  $V_R$  Restrictions

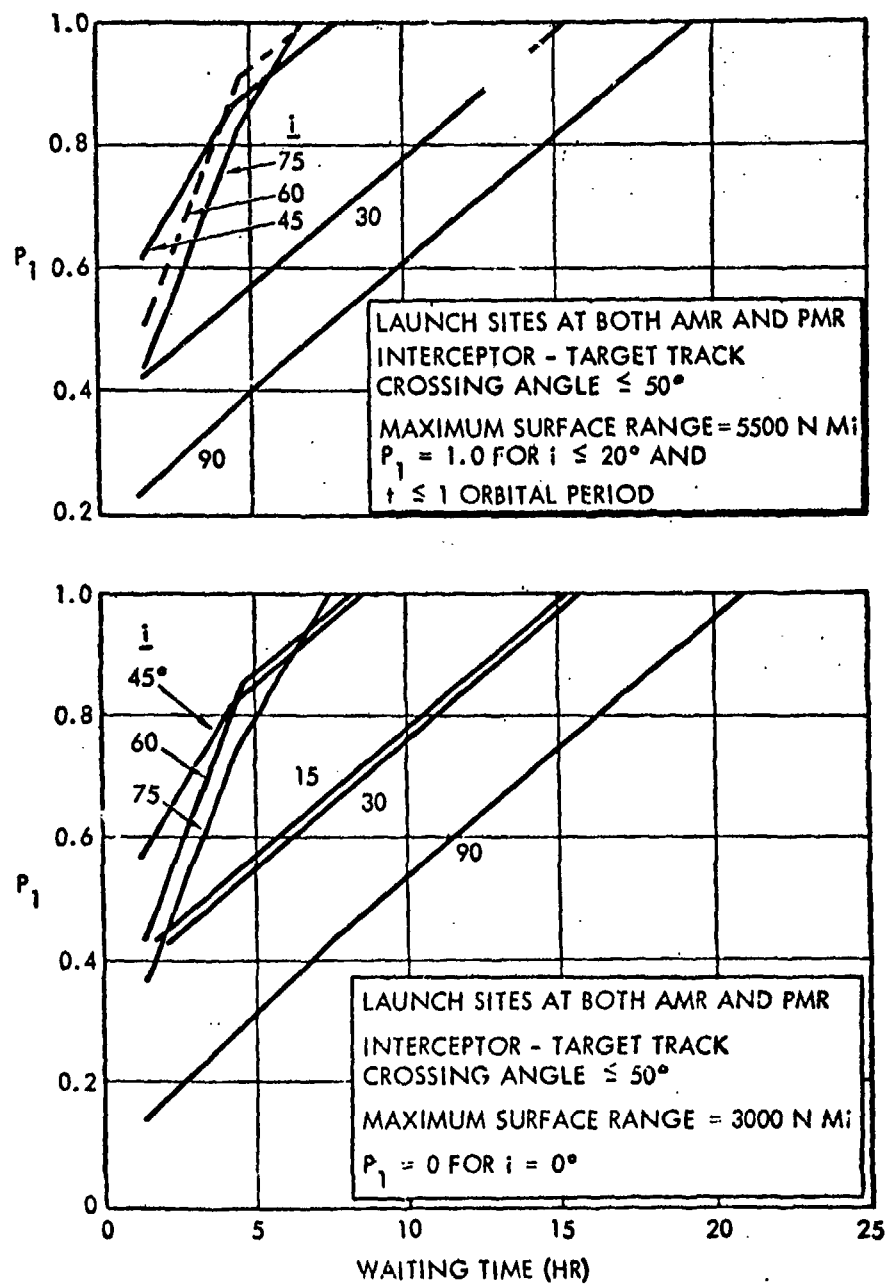


Figure 14-50. AMR and PMR Launch Opportunities Against Targets in 100 N Mi Altitude Circular Orbits—With  $V_R$  Restrictions



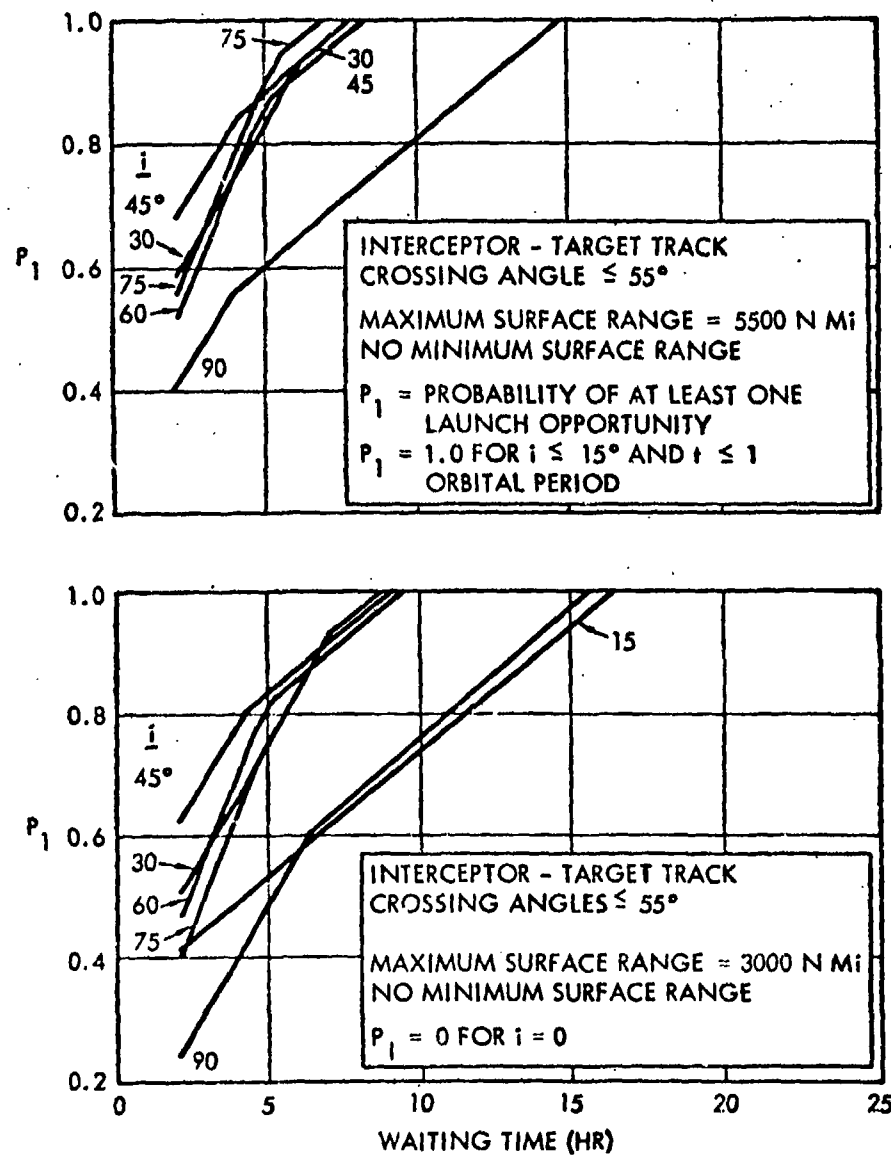


Figure 14-51. AMR and PMR Launch Opportunities Against Targets in 1000 N Mi Altitude Circular Orbits—With  $V_R$  Restrictions

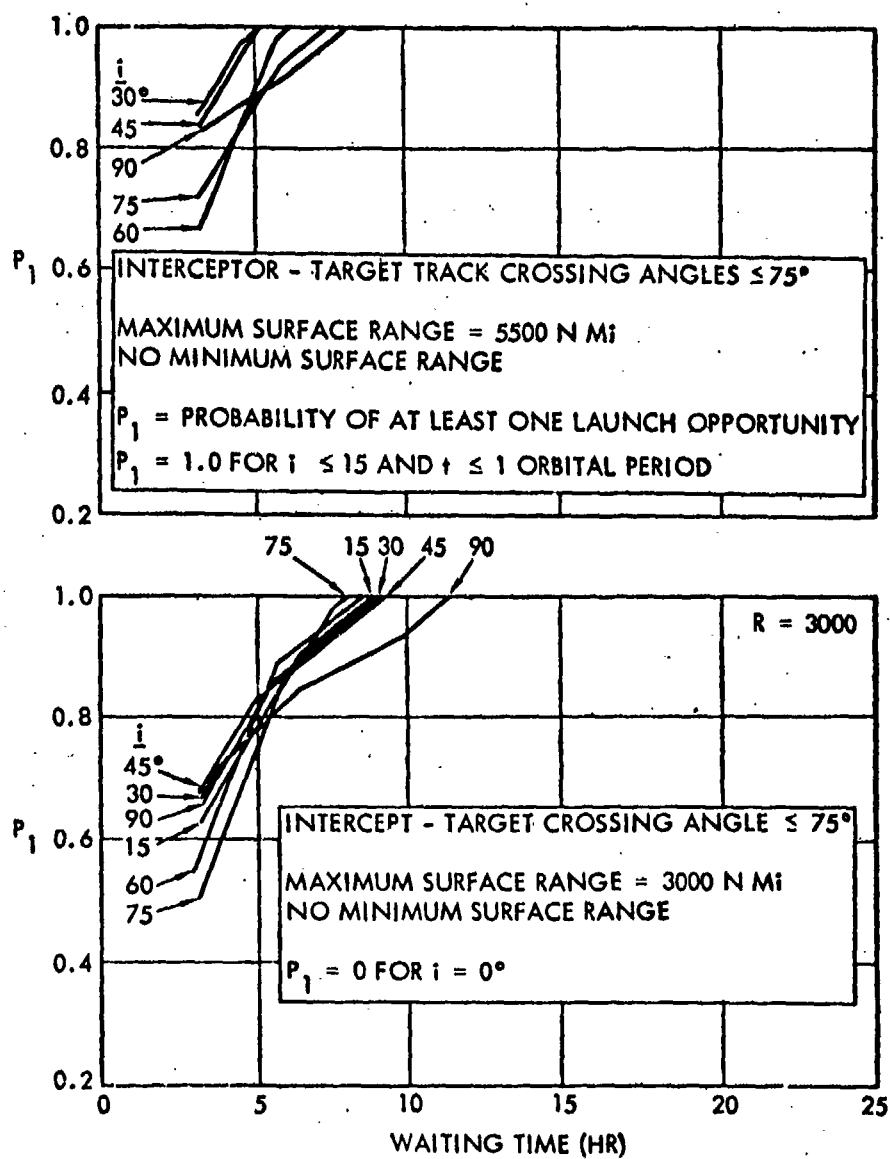


Figure 14-52. AMR and PMR Launch Opportunities Against Targets in 2500 N Mi Altitude Circular Orbits—With  $V_R$  Restrictions

INTERCEPTOR SURFACE RANGE = 3,000 N Mi  
 TARGET ORBIT ALTITUDE = 100 N Mi  
 MAXIMUM  $V_R$  = 20,000 FPS

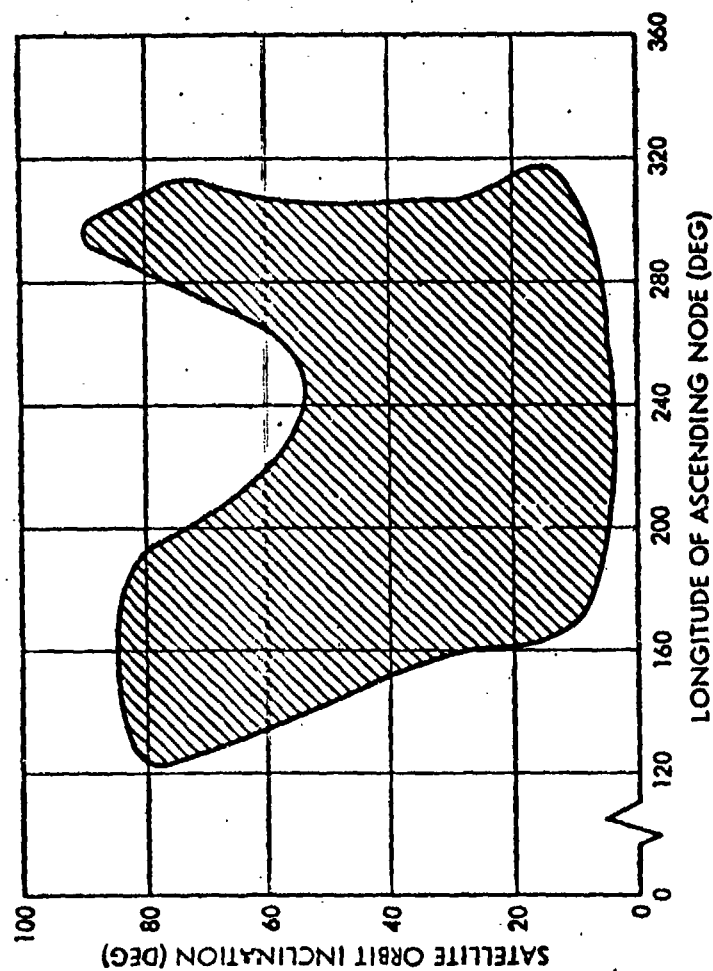


Figure 14-53. Locus of Satellite Orbits That Can Be Intercepted from AMR within One Orbital Revolution

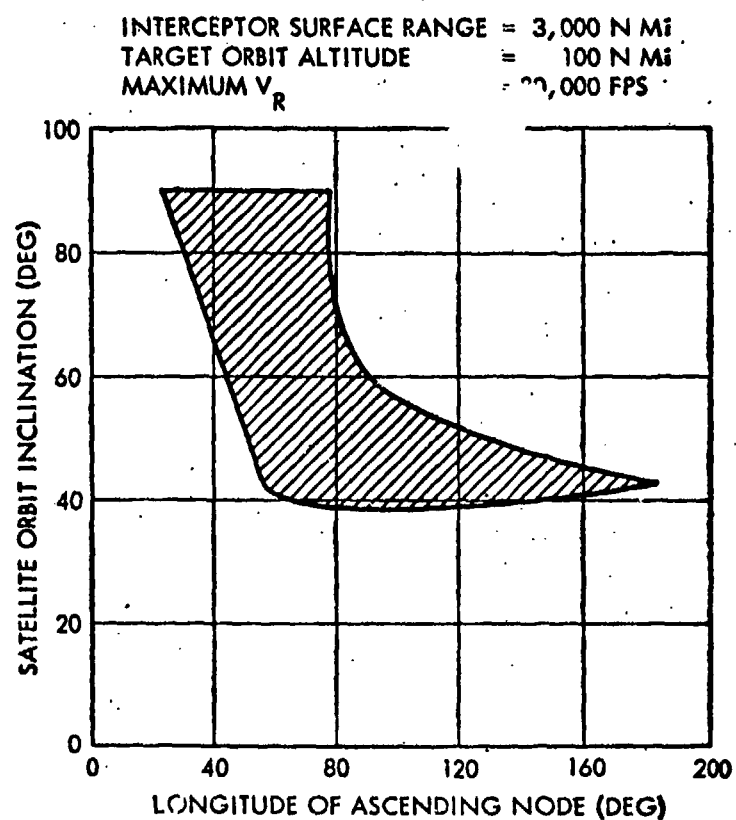


Figure 14-54. Locus of Satellite Orbits That Can Be Intercepted from PMR within One Orbital Revolution

INTERCEPTOR SURFACE RANGE = 3,000 N MI  
TARGET ORBIT ALTITUDE = 100 N MI  
MAXIMUM  $V_R$  = 20,000 FPS

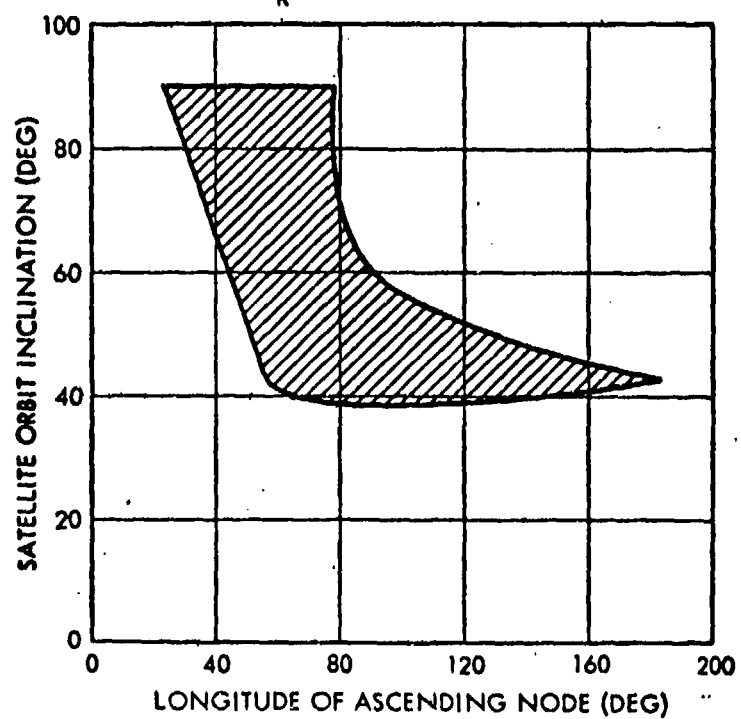


Figure 14-54. Locus of Satellite Orbits That Can Be Intercepted from PMR within One Orbital Revolution

INTERCEPTOR SURFACE RANGE = 3,000 N Mi  
 TARGET ORBIT ALTITUDE = 100 N Mi  
 MAXIMUM  $V_R$  = 20,000 FPS

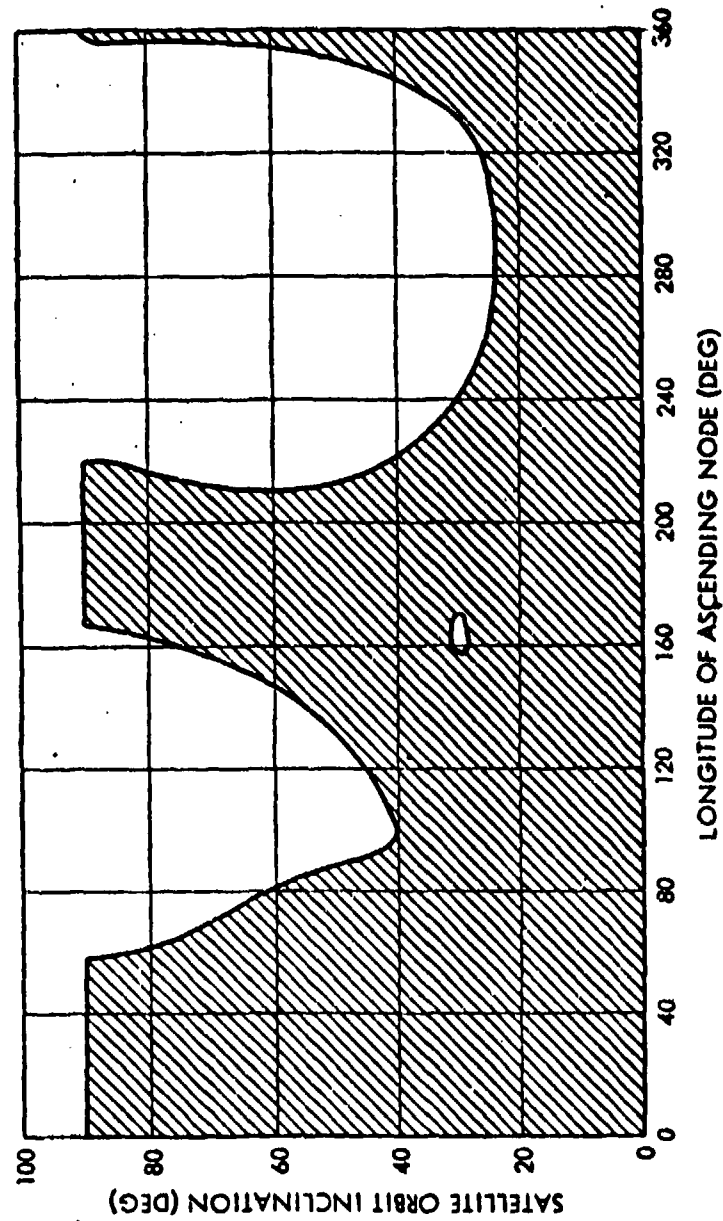


Figure 14-55. Locus of Satellite Orbits That Can Be Intercepted from Johnston Island within One Orbital Revolution

INTERCEPTOR SURFACE RANGE = 3,000 N MI  
 TARGET ORBIT ALTITUDE = 100 N MI  
 MAXIMUM  $V_R$  = 20,000 FPS

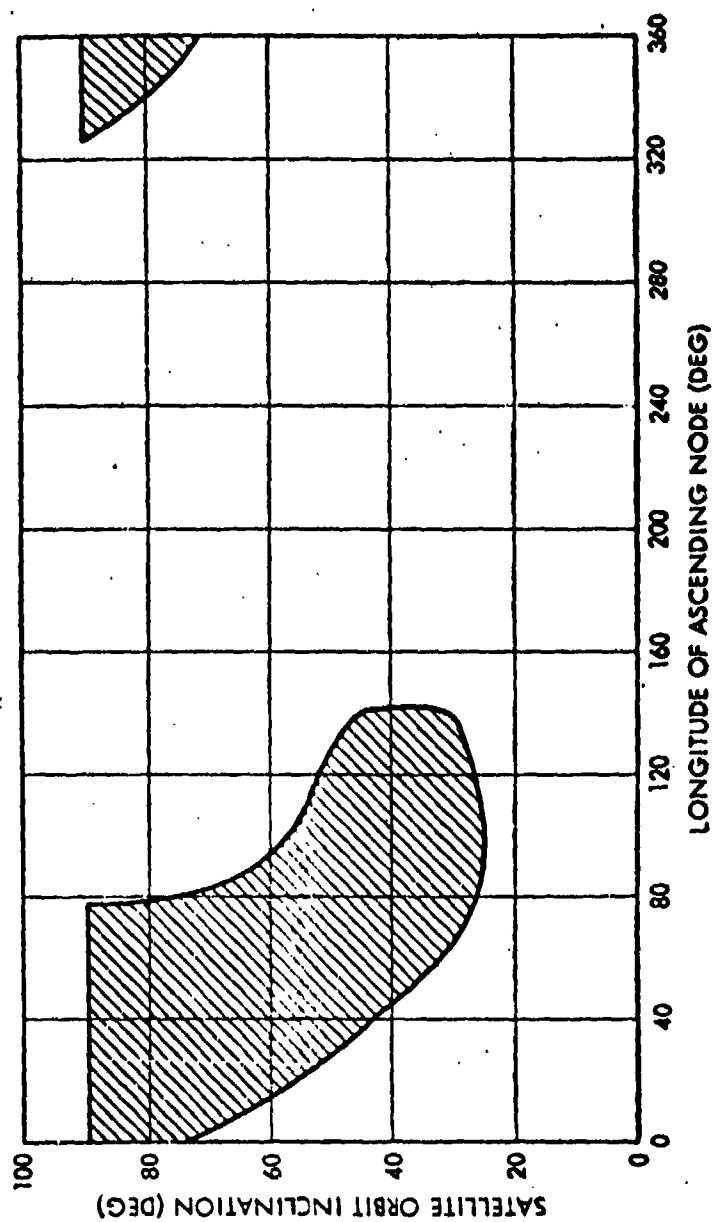


Figure 14-56. Locus of Satellite Orbits That Can Be Intercepted from Kodiak, Alaska within One Orbital Revolution

INTERCEPTOR SURFACE RANGE = 3,000 N MI  
 TARGET ORBIT ALTITUDE = 100 N MI  
 MAXIMUM  $V_R$  = 20,000 FPS

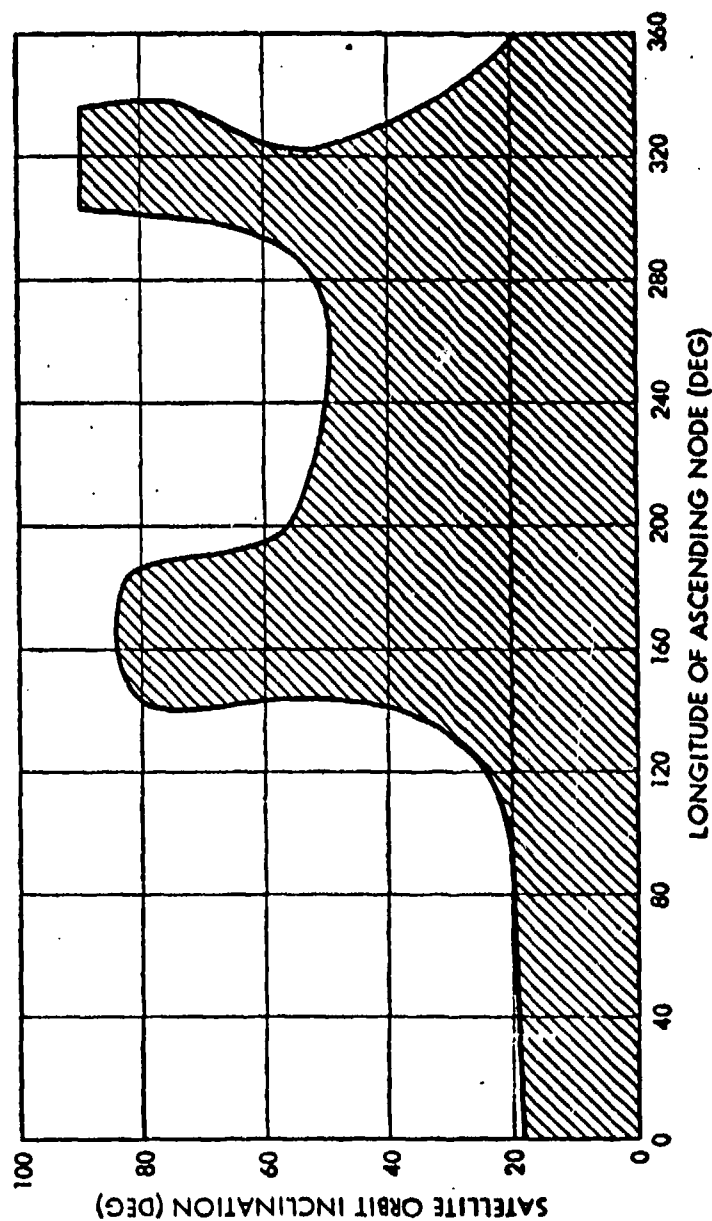


Figure 14-57. Locus of Satellite Orbits That Can Be Intercepted from Puerto Rico within One Orbital Revolution



INTERCEPTOR SURFACE RANGE = 3,000 N MI  
 TARGET ORBIT ALTITUDE = 100 N MI  
 MAXIMUM  $V_R$  = 20,000 FPS

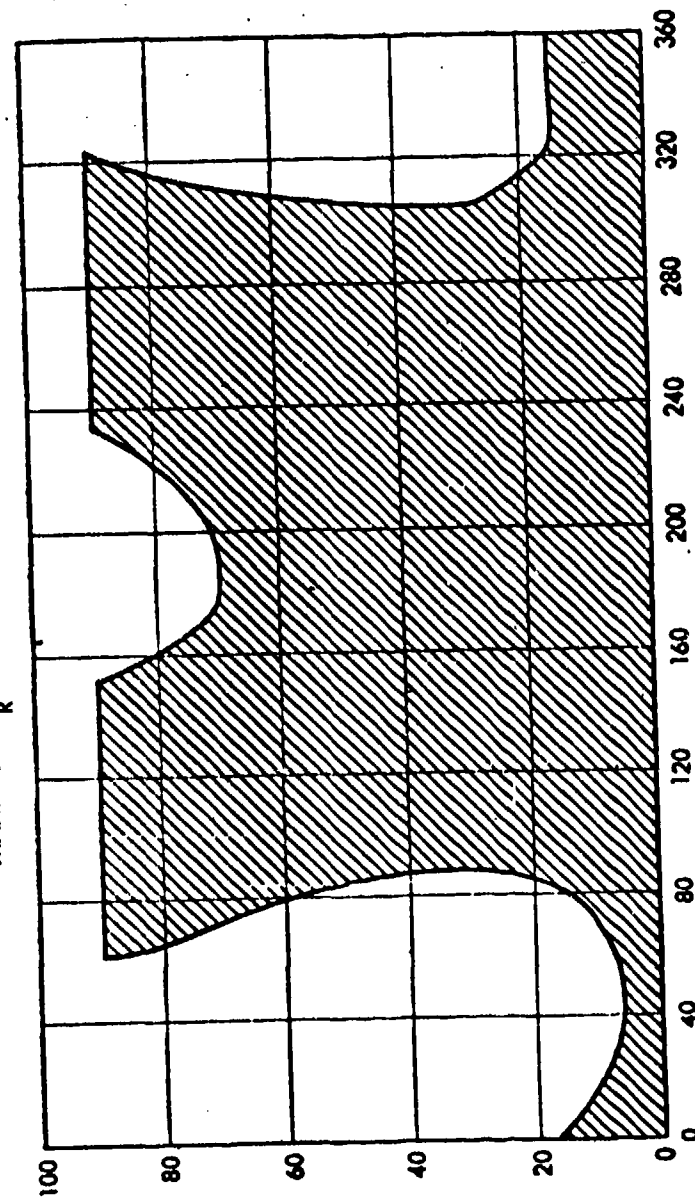


Figure 14-58. Locus of Satellite Orbits That Can Be Intercepted from AMR within One Orbital Revolution (No Launch Azimuth Restrictions)

INTERCEPTOR SURFACE RANGE = 5,500 N MI  
 TARGET ORBIT ALTITUDE = 100 N MI  
 MAXIMUM  $V_R$  = 20,000 FPS

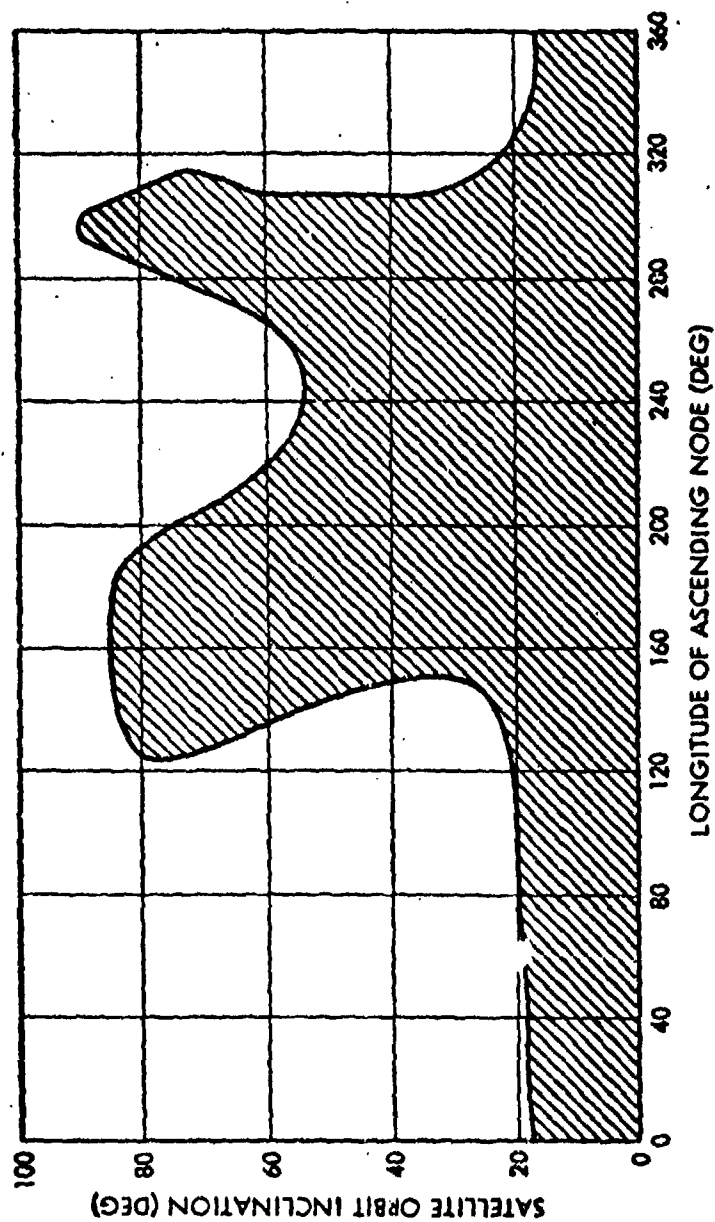


Figure 14-59. Locus of Satellite Orbits That Can Be Intercepted from AMR within One Orbital Revolution

INTERCEPTOR SURFACE RANGE = 5,500 N MI  
 TARGET ORBIT ALTITUDE = 100 N MI  
 MAXIMUM  $V_R$  = 20,000 FPS

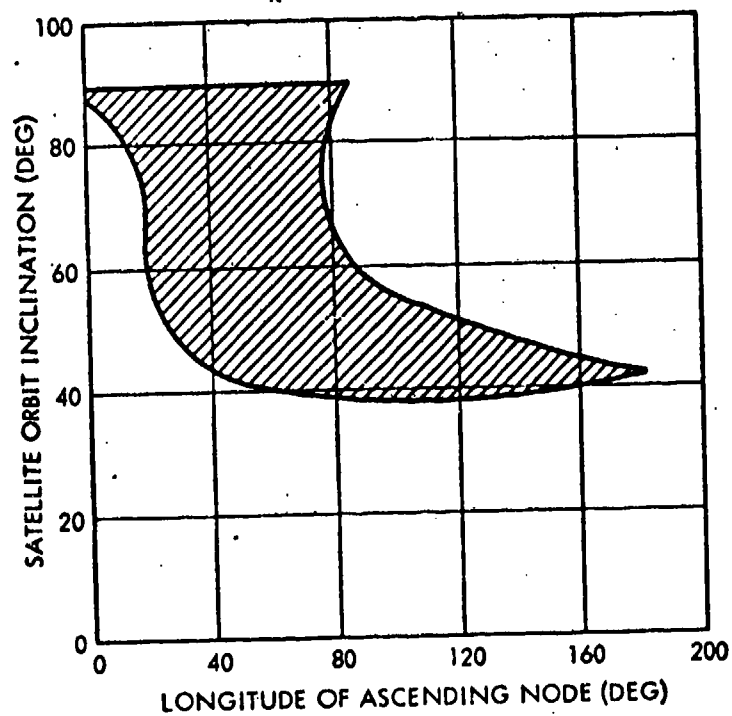


Figure 14-60. Locus of Satellite Orbits Than Can Be Intercepted from  
 PMR within One Orbital Revolution

INTERCEPTOR SURFACE RANGE = 5,500 N Mi  
 TARGET ORBIT ALTITUDE = 100 N Mi  
 MAXIMUM  $V_R$  = 20,000 FPS

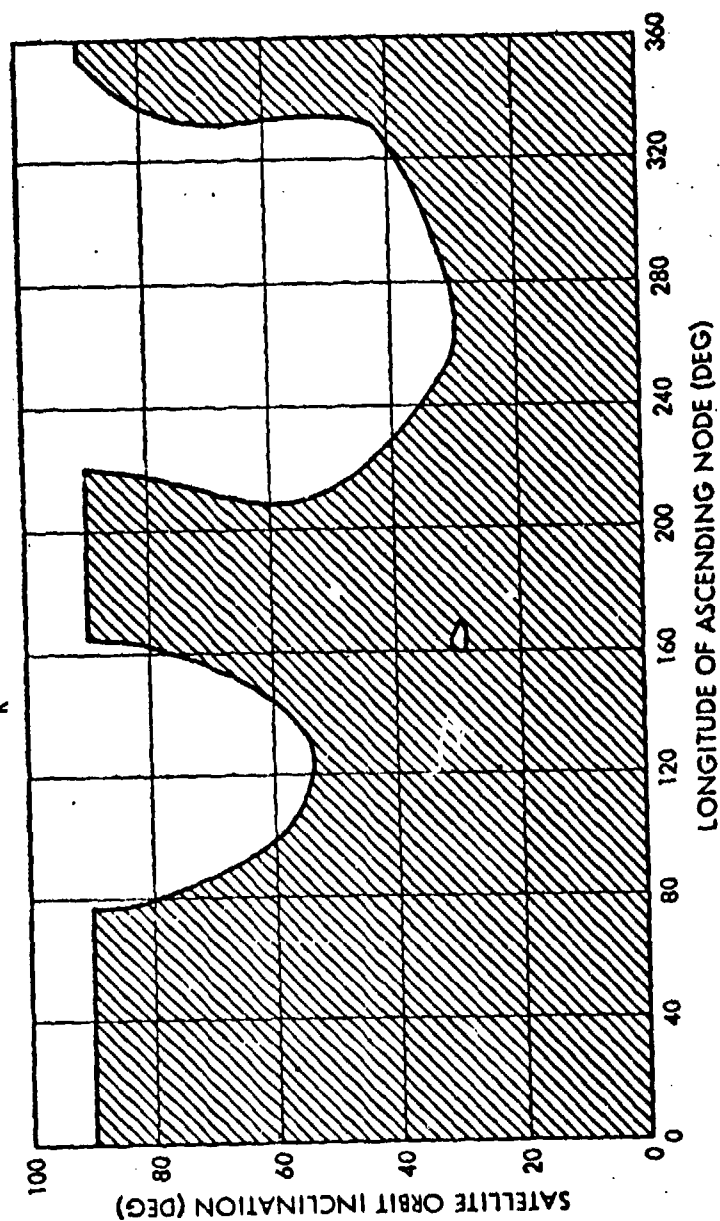


Figure 14-61. Locus of Satellite Orbits That Can Be Intercepted from Johnston Island within One Orbital Revolution

INTERCEPTOR SURFACE RANGE = 5,500 N Mi  
 TARGET ORBIT ALTITUDE = 100 N Mi  
 MAXIMUM  $V_R$  = 20,000 FPS

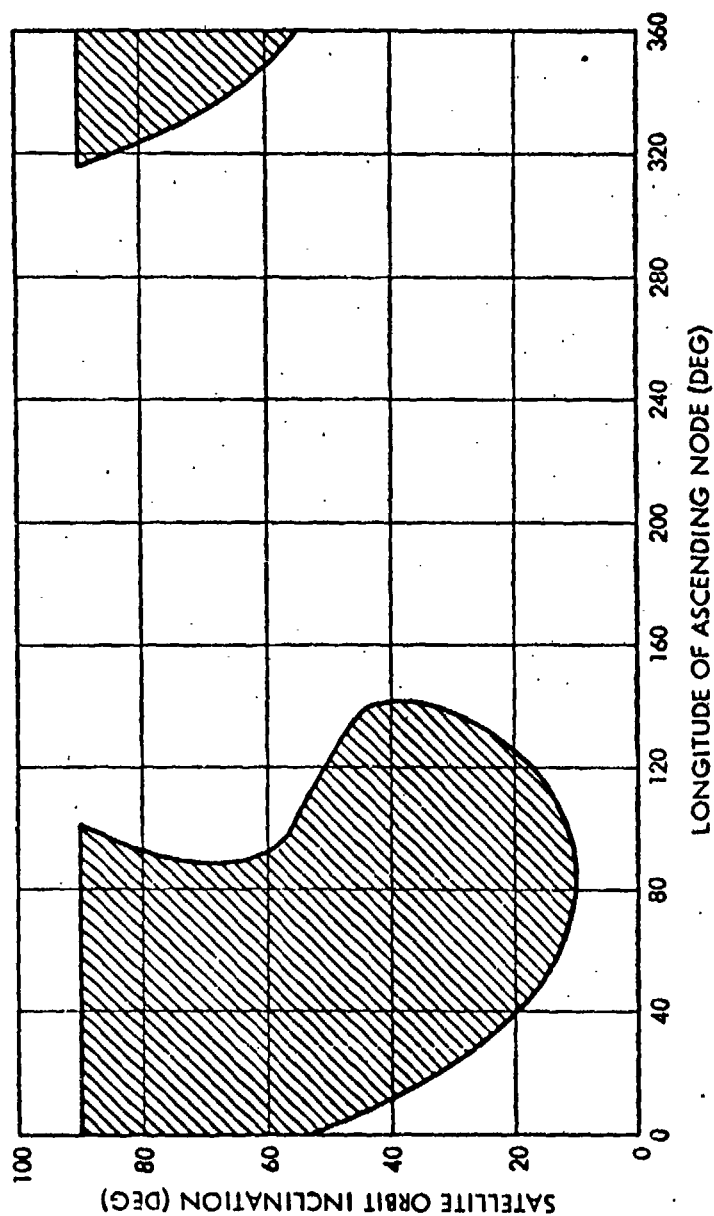


Figure 14-62. Locus of Satellite Orbits That Can Be Intercepted from  
 Kodiak, Alaska within One Orbital Revolution

INTERCEPTOR SURFACE RANGE = 5,500 N MI  
 TARGET ORBIT ALTITUDE = 100 N MI  
 MAXIMUM  $V_R$  = 20,000 FPS

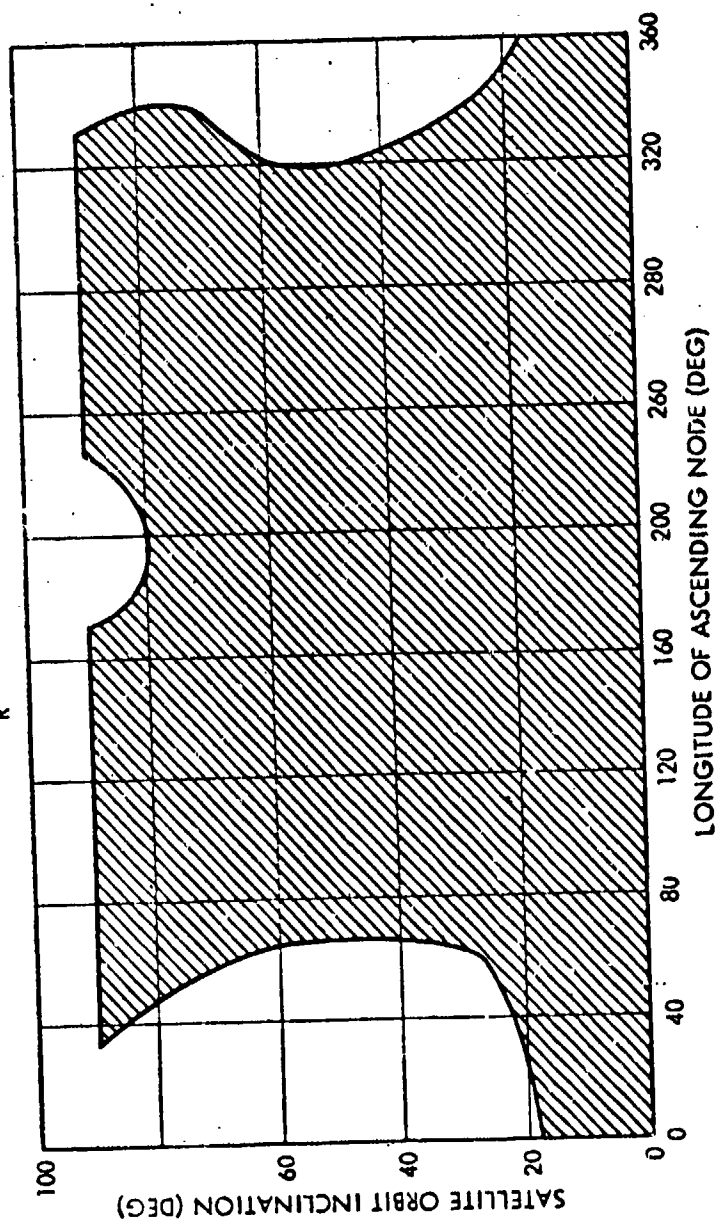


Figure 14-64. Locus of Satellite Orbits That Can Be Intercepted from AMR within One Orbital Revolution (No Launch Azimuth Restrictions)

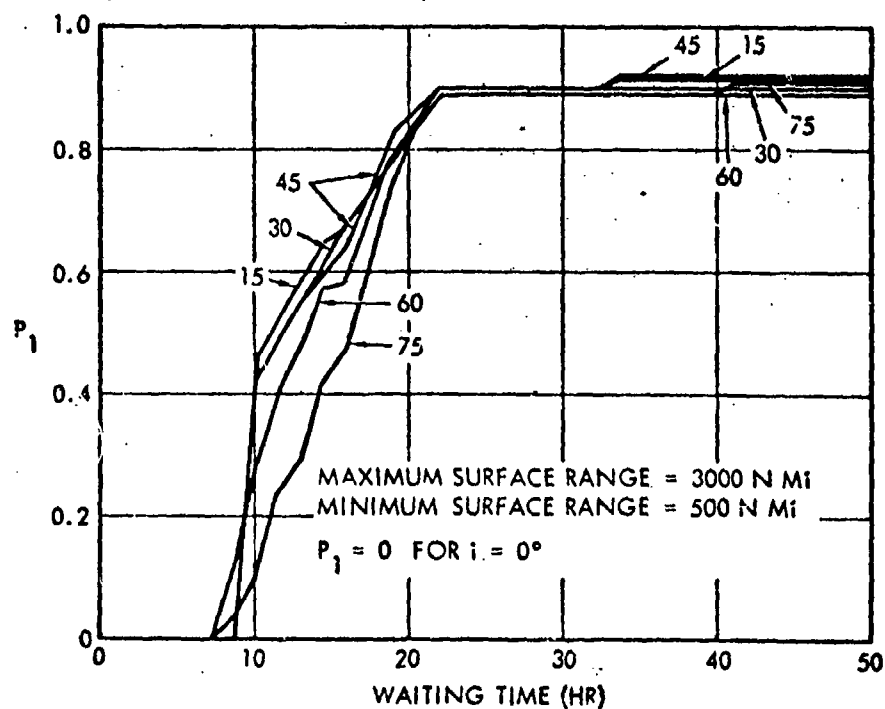
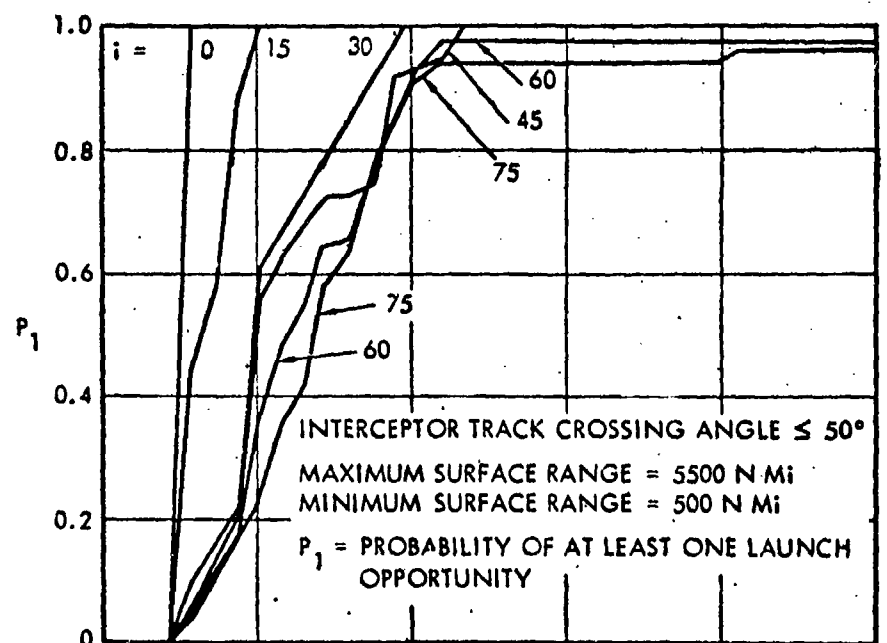


Figure 14-65. AMR Launch Opportunities Against Targets in 100 N Mi Altitude Circular Orbits—With  $V_R$  and Sun-Look Angle Restrictions for Midnight of December 20

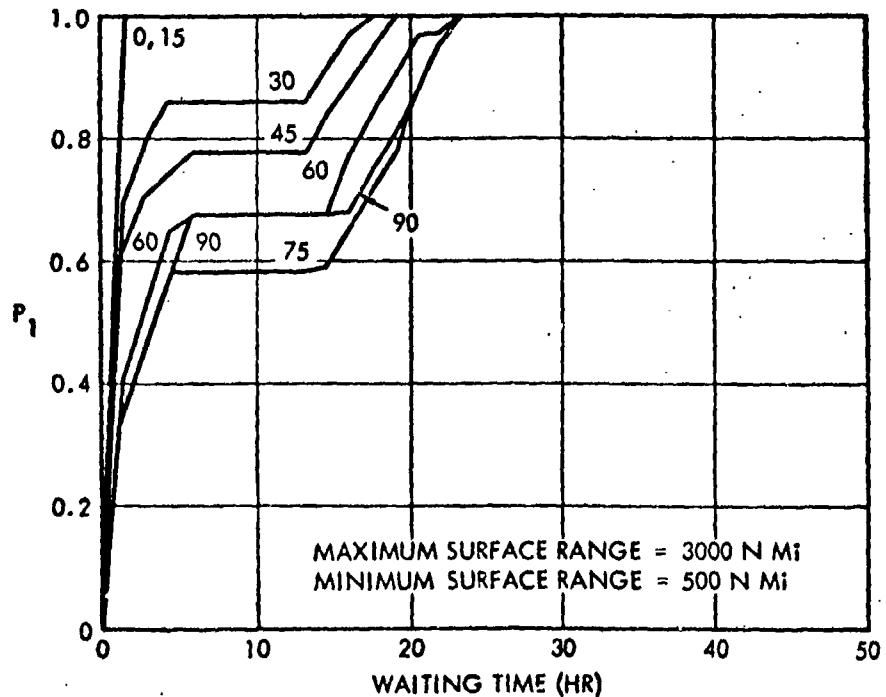
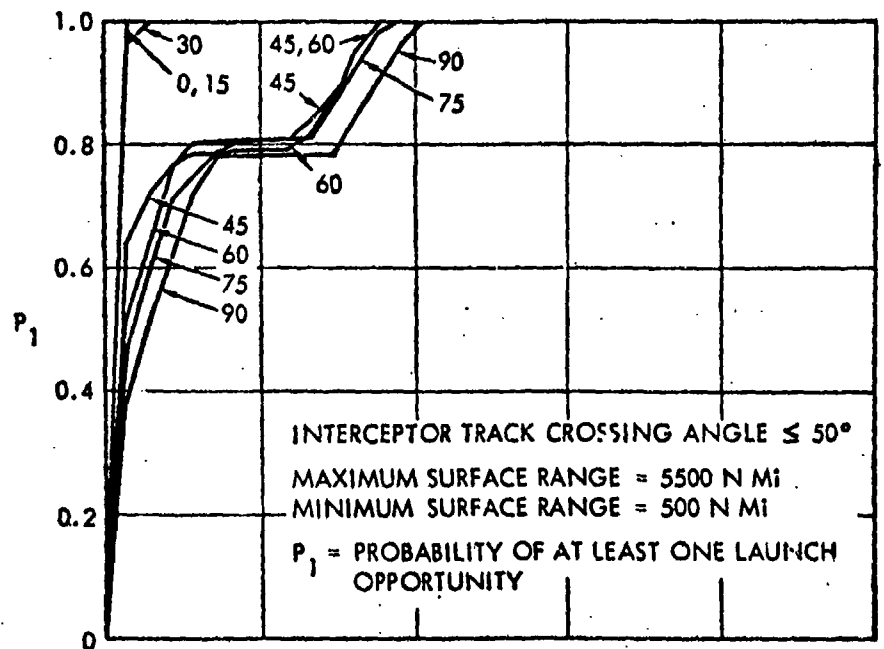


Figure 14-66. Johnston Island Launch Opportunities Against Targets in 100 N Mi Altitude Circular Orbits—With  $V_R$  and Sun-Look Angle Restrictions for Midnight of December 20



## CHAPTER 15

### PROJECTED SYSTEM COSTS

This chapter is concerned with the development of cost estimates for nine proposed interceptor configurations, including three booster systems and three different homing stage designs, namely; the Wing VI Minuteman, Titan II, and Polaris A3 boosters with electro-optical, infrared, and radar sensing homing stages. The cost estimates were developed by the use of scaling factors. Accurate estimates could have been achieved by preparing detailed development plans, but such an effort did not appear warranted in the light of ARPA's interest in only crude cost data.

The cost categories include research, development, test and evaluation, initial investment, and annual operations. The Minuteman and Titan II launch complexes are assumed to be land sites, while the Polaris launch complex is assumed to be a ship based site. Each launch complex is defined as consisting of two ready interceptors and four spares; two launch pads with associated GSE items and one launch control center with its support and control equipments. The estimates do not include cost for command and control equipments necessary to tie the launch complex into an overall global antisatellite system.

Surface ships for the Polaris interceptors are assumed to be GFE from the mothball fleet. The initial investment and annual operations cost for a land complex is assumed to be independent of site location, because the cost difference associated with different launch complex locations is insignificant relative to the total cost. (For example, the estimated cost of land acquisition and site preparation for a Minuteman base at Johnston Island is only  $\$500 \times 10^3$  more than at AMR, and the transportation cost difference is insignificant.)

The results of the analysis are summarized in eight tables\* which provide a means of estimating the total cost of each interceptor configuration, the number of launch complexes, and program years necessary to

---

\*For convenience all tables are placed at the end of the chapter.

achieve a particular objective. This has been done because each interceptor configuration has a different operational capability, causing the number of launch complexes necessary to achieve a given objective to vary with the particular configuration under consideration. No provision has been made for the duty cycle of a ship, which means that in estimating the number of Polaris complexes, additional ships should be included as an allowance for the off-duty time.

The total cost summary is presented in Table 15-1. In summary, it appears that the cost differences between configurations are within the errors associated with the estimating technique employed. The Titan II booster and the radar controlled homing stage appear to be slightly more costly than their respective alternatives. The electro-optical and infrared homing stage cost estimates were virtually identical.

Table 15-2 contains the R, D, T and E cost category breakdown. The cost estimates include a complete launch facility with two launch pads (or tubes) for flight testing. Sixteen interceptors are assumed to be procured for the flight test program, and a provision for targets has been included. Significant cost differences which appear are primarily due to the higher cost of the Titan II booster and the higher cost of development for the radar homing stage.

Table 15-3 presents the initial investment cost per launch complex for the interceptor configurations under consideration. The cost estimates include land procurement and preparation, facilities, GSE, booster, and homing stage procurement. A complex consists of two ready interceptors and four spares. Both the Minuteman and Titan II launch complexes are land-based, while the Polaris launch complex is ship-based. As noted previously, the location of sites for the land complexes is assumed to have an insignificant effect on cost. The results indicate that the Minuteman and Polaris configurations have approximately the same initial investment cost per launch complex.

The costs of the Titan II were expected to be much higher, based on the cost estimates for the weapon system version presented in Chapter 12. However, launching from pads instead of from hardened silos greatly reduces the cost of base construction, facilities, and GSE. Thus the cost

of booster, base construction, facilities, and GSE for one interceptor are about one-third the cost of the operational weapon system version. At the same time, the Minuteman system costs for base construction, facilities and GSE are increased slightly over the weapon system version. The Polaris costs are also lower than the weapon system version due to replacing the submarine with a GFE surface ship.

Table 15-4 shows the annual operations cost per launch complex for the interceptor configurations. The personnel costs are based upon a staff of 65 people per complex for the Minuteman and Titan II systems and 30 people for the Polaris complex, exclusive of ship's crew, at \$7500/man/year. The 65 persons include a three shift operation at the launch control center, plus missile maintenance, security, and on-base logistics support. The 30 persons are for operation of the launch control center and missile maintenance only. The \$7500/man/year includes pay and allowance, replacement training, supply consumption, etc., and is based upon Reference 1. The land facilities maintenance and interceptor system parts consumption costs are based upon 5.8 and 6.6 percent of their respective initial investment costs. The booster and homing stage parts consumption also includes the firing of one missile per complex per year as a readiness demonstration exercise. The ship operation cost is based upon Reference 2. The results indicate that the Minuteman and Polaris configurations have approximately the same annual operations cost per launch complex, while Titan II operations cost slightly more.

Table 15-5 presents the homing stage nonrecurring and recurring cost estimates. Nonrecurring costs are those that do not vary with the number of stages produced, and include a prototype stage. Recurring costs vary with the number of stages produced. The structure subsystem includes two tanks and the basic stage structure. The propulsion system cost is for a pressure-fed variable thrust engine, and the altitude control subsystem includes a hot gas system and the associated control electronics. The power supply system includes batteries, cables, J-boxes, and converters. The warhead for all homing stages is an explosively deployed pellet warhead. The guidance and sensor subsystem for the electro-optical and infrared systems includes a computer, sensor, gimbal platform with gyros, and an electronic control unit. The radar guidance

and sensor subsystem includes a computer, an X-band radar system, and two antennas of which one is gimballed with gyros. The radar controlled homing stage is approximately  $\$20.0 \times 10^6$  and  $\$0.3 \times 10^6$  higher than the other stages in the nonrecurring and recurring cost categories, respectively.

Table 15-6 presents the booster nonrecurring and recurring cost estimates based upon a preliminary analysis of the modifications required. The booster costs include the fairings, interstage adapter, interstage, booster, recurring modifications, and those nonrecurring costs associated with developing the booster system modifications. The Polaris non-recurring cost estimate for booster modifications is highest because of the homing stage separation problems, which have been considered part of the booster system for simplicity.

Table 15-7 presents the Minuteman and Titan II initial investment costs per launch complex for facilities and GSE. The assumed launch pad facilities for Minuteman and Titan II are above ground, which necessitated the addition of an environmentally controlled shield for each of the two ready interceptors. All building costs are based upon a rough estimate of size and a cost of \$30/square foot. The personnel facilities cost is based upon having 65 people at a complex at an initial investment cost of \$14,500/man. The \$14,500 is predicated upon Reference 1 and includes initial training, facilities, original equipment, etc. The GSE costs include two sets of pad related equipment plus the control center related equipment, modified as required.

Table 15-8 presents the Polaris initial investment cost for facilities and GSE, as well as the ship operations cost per year. The ship costs are predicated upon reactivating a GFE C4 ship from the mothball fleet and modifying it extensively, as indicated. The Polaris GSE equipment cost is assumed to be the same as the Minuteman GSE cost.

## REFERENCES

1. "An Analysis of Mobility for Ballistic Missile Systems," Planning Research Corporation, Volume II, PRC R-130, 5 December 1959.
2. "Summary of Trade-off Studies," Hughes Final Report Phase I, Part II, Technical, No. MBM-51, 1 April 1963.

Table 15-1. Total Cost Summary (All Costs in  $10^6$  \$)

Item	Description	Reference Table	Minuteman		Titan II		Polaris	
			EO/IR	Radar	EO/IR	Radar	EO/IR	Radar
1	Research, Development, Test and Evaluation	15-2	176.3	202.8	198.8	225.3	180.9	207.4
2	Initial Investment Per Launch Complex	15-3	27.4	29.5	36.1	38.2	26.9	29.0
3	Annual Operations, Per Launch Complex	15-4	5.6	6.0	6.9	7.3	5.8	6.2
4	Recurring Cost Per Operational Launch	15-5, 6	3.3	3.6	4.1	4.4	3.0	3.3

Table 15-2. Research, Development, Test and Evaluation Costs (in  $10^3$  \$)

Item	Description	Reference Table	Minuteman		Titan II		Polaris	
			EO/IR	Radar	EO/IR	Radar	EO/IR	Radar
1	Systems Engr and Program Mgmt		9,400	10,800	10,600	12,000	9,400	11,000
2	Homing Stage Development	15-5	60,000	80,000	60,000	80,000	60,000	80,000
3	Booster Modification Development	15-6	12,700	12,700	15,000	15,000	20,800	20,800
4	Flight Test							
	Launch Facilities	15-7, 8	2,655	2,655	4,245	4,245	5,000	5,000
	Booster GSE	15-7, 8	2,630	2,630	5,255	5,255	2,635	2,635
	Booster Procurement (16 reqd)	15-6	27,840	27,840	39,440	39,440	21,760	21,760
	Homing Stage GSE	15-5	900	1,200	900	1,200	900	1,200
	Homing Stage Procurement (16 reqd)	15-5	25,600	30,400	25,600	30,400	25,600	30,400
	Launch Operations (16 reqd)	15-5, 6	9,600	9,600	12,800	12,800	9,600	9,600
	Targets		25,000	25,000	25,000	25,000	25,000	25,000
5	Total R, D, T and E		176,325	202,825	198,840	225,340	180,895	207,395

Table 15-3. Initial Investment Costs Per Launch Complex (in  $10^3$  \$)

Item	Description	Reference Table	Minuteman		Titan II		Polaris	
			EO/IR	Radar	EO/IR	Radar	EO/IR	Radar
1	Land Acquisition and Preparation		200	200	400	400	-	-
2	Facilities	15-7, 8	3,600	3,600	5,190	5,190	5,540	5,540
3	Booster GSE (Delivered)	15-7, 8	2,630	2,630	5,255	5,255	2,635	2,635
4	Booster Procurement (Delivered)	15-6	10,440	10,440	14,790	14,790	8,140	8,140
5	Homing Stage GSE (Delivered)	15-5	900	1,200	900	1,200	900	1,200
6	Homing Stage Procurement (Delivered)	15-5	9,600	11,400	9,600	11,400	9,600	11,400
7	Total		27,370	29,470	36,135	38,235	26,855	28,955

Table 15-4. Annual Operations Cost Per Launch Complex (in  $10^3$  \$)

Item	Description	Minuteman		Titan II		Polaris	
		EO/IR	Radar	EO/IR	Radar	EO/IR	Radar
1	Personnel Costs at \$7500/man yr	490	490	490	490	225	225
2	Facilities Maintenance and Ship Operations						
	Land-Based at 5.8 percent of Item 2, Table 15-3	210	210	300	300		
	Ship-Based (See Table 15-8)					1,200	1,200
3	Booster GSE Parts Consumption at 6.6 percent of Item 3, Table 15-3	175	175	345	345	175	175
4	Booster Parts Consumption at 6.6 percent of Item 4, Table 15-3 plus 1 Booster-	2,430	2,430	3,440	3,440	1,900	1,900
5	Homing Stage GSE Parts Consumption at 6.6 percent of Item 5, Table 15-3	60	60	60	60	60	60
6	Homing Stage Parts Consumption at 6.6 percent of Item 6, Table 15-3 plus 1 Homing Stage	2,235	2,650	2,235	2,650	2,235	2,650
7	Total	5,600	6,035	6,870	7,305	5,795	6,230

Table 15-5. Homing Stage Nonrecurring and Recurring Costs (in 10<sup>3</sup> \$)

Item	Subsystem Description	Electro-Optical/Infrared		Radar	
		Nonrecurring	Recurring	Nonrecurring	Recurring
1	System Engr and Program Mgt	\$ 5,000		\$ 7,000	
2	Structures	10,000	110	10,000	110
3	Propulsion	10,000	50	10,000	50
4	Attitude Control	5,000	50	5,000	50
5	Power Supply	1,000	50	1,000	50
6	Warhead	2,000	15	2,000	15
7	Guidance and Sensors	15,000	750	30,000	1,050
8	Integration and Test	5,000	<u>575</u>	5,000	<u>575</u>
9	Total Recurring		\$1,600		\$1,900
10	Prototype Fabrication and Ground Test	2,000		3,000	
11	GSE	5,000	900	7,000	1,200
12	Launch Operations (Flight Test)	—	300	—	300
13	Total Nonrecurring	\$60,000		\$80,000	

Table 15-6. Booster Nonrecurring and Recurring Costs (\$ x 10<sup>3</sup>)

Item	Description	Minuteman		Titan		Polaris	
		Nonrecurring	Recurring	Nonrecurring	Recurring	Nonrecurring	Recurring
1	Systems Engineering & Program Management	\$ 400		\$ 600		\$ 800	
2	Fairings	700	25	700	40		
3	Interstage Adapter	600	15	700	25	3,000	40
4	Booster and Interstage with Spares		1,700		2,400		1,300
5	Booster Modifications	5,000		5,000		10,000	20
6	Booster Modifications (Guidance)	5,000		5,000		5,000	
7	Total Recurring (Booster)		1,740		2,465		1,360
8	GSE Modifications	<u>1,000</u>	<u>10</u>	<u>3,000</u>	<u>15</u>	<u>2,000</u>	<u>15</u>
9	Launch Operations (Flight Test)		300		500		300
10	Total Nonrecurring Cost	\$12,700		\$15,000		\$20,000	



Table 15-7. Minuteman and Titan II Initial Investment Costs for Facilities and GSE for One Launch Complex (In  $10^3$  \$)

Item	Description	No. Req'd Per Launch Complex	Minuteman	Titan II
1	<b>Facilities</b>			
	Launch Pads	2	900	1,100
	Control Center	1	230	340
	Environmental Shielding	2	100	200
	Missile Storage Building	1	110	220
	Spare Parts Storage Building	1	75	150
	Maintenance Building	1	100	225
	Propellant Storage		-	310
	Umbilical Towers	2	200	400
	Roads		100	100
	Powerhouse (Equipped)		840	1,200
	Subtotal		2,655	4,245
	Personnel Facilities		945	945
	Total		3,600	5,190
2	<b>GSE</b>			
	Pad Related	2	1,870	3,740
	Control Center Related	1	750	1,500
	Modifications	1	10	15
	Total		2,630	5,255

Table 15-8. Polaris Initial Investment for Facilities and GSE  
and Ship Annual Operations Cost (In 10<sup>3</sup> \$)

Item	Description	Cost
1	Initial Investment	
	Facilities	
	C4 Ship Reactivation	600
	Ship Engineering	500
	Ship Conversion and Structural Modification	1,600
	Ship Communications	300
	Auxiliary Systems (Hydraulic Electrical)	200
	Navigational System (SINS)	1,800
	Subtotal	5,000
	Personnel Training and Equipment	560
	TOTAL	\$5,560
	GSE	
	Launch Tube Related (2 required)	1,870
2	Control Center Related	750
	Modifications	15
	TOTAL	\$2,635
	Ship Operations Cost	
	Ship Annual Operations Including Crew, Maintenance, Etc.	\$1,200

## APPENDIX A

### LINEAR ANALYSIS OF BODY FIXED TRACKING GYRO MISALIGNMENT

The effects of gyro misalignment on roll stability using a body fixed tracker and gyros and using a single engine, roll-to-maneuver technique are considered. Analytical results are obtained by assuming small angles to linearize the equations.

The results of the analysis show that the effect of the gyro misalignment on roll stability depends on the sign of the misalignment angle. A positive misalignment angle has a pronounced destabilizing effect, while a very small negative misalignment angle has a stabilizing effect. It is shown that the misalignment angle is analagous to a negative roll control system time constant and that with a misalignment  $\beta$  and a roll control system time constant  $\tau$ , the effective roll control system time constant can be considered to be  $(\tau - \beta/\omega)$  where  $\omega$  is the LOS rate.

Tracking loop and guidance system dynamics are neglected. Constant relative velocity is assumed and it is assumed that  $V_R = -\dot{R}$ . Proportional navigation with a dead zone (scalar bias) is considered for the guidance technique. Perfect pitch and yaw attitude control is assumed, thus the interceptor acceleration is always normal to the LOS. A first order lag for roll control system dynamics is considered. The coordinate system used is shown in Figure A-1.

The kinematics equation with the assumptions stated is

$$T\dot{\bar{\omega}} = 2\bar{\omega} + \frac{\bar{r} \times \bar{a}_I}{V_R} \quad (A.1)$$

and the guidance equation is

$$a_I = \lambda V_R (|\bar{\omega}_m| - \omega_b) \quad (A.2)$$

where

$\lambda$  = Navigation constant

$V_R$  = Relative velocity

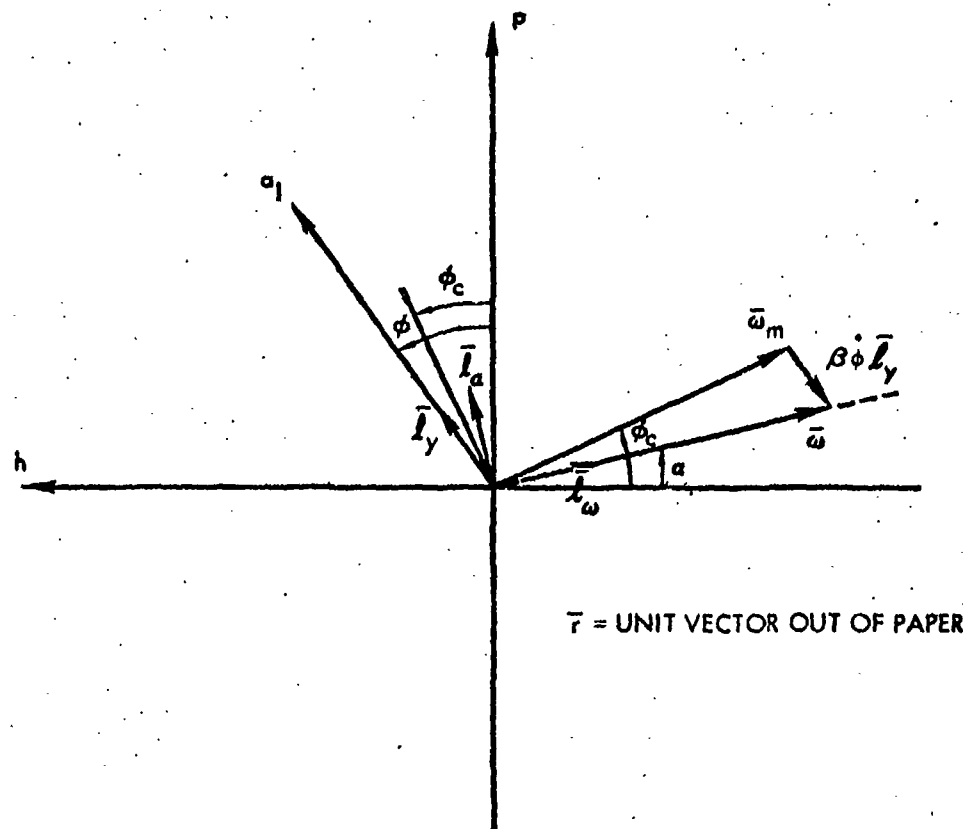


Figure A-1. Coordinate System For Gyro Misalignment Analysis

$\bar{\omega}$  = LOS rate vector

$\bar{\omega}_m$  = measured LOS rate vector

$T = R/V_R$  = time to go

First order roll control system dynamics are considered

$$\tau \dot{\phi} + \phi = \phi_c \quad (A.3)$$

In the presence of a yaw gyro misalignment,  $\beta$ , with respect to the roll axis, the measured LOS rate will differ from the true LOS rate.

$$\bar{\omega}_m + \beta \dot{\phi} \bar{l}_y = \bar{\omega} \bar{l}_\omega \quad (A.4)$$

where  $\bar{l}_y$  and  $\bar{l}_\omega$  are unit vectors.

Referring to Figure A-1, the acceleration  $a_I$  can be resolved into components along and normal to the LOS rate vector, giving

$$\bar{a}_I = -a_I \sin(\phi - \alpha) \bar{l}_\omega + a_I \cos(\phi - \alpha) \bar{l}_\alpha \quad (A.5)$$

Substituting Equations (A.5) and (A.2) into Equation (A.1) and resolving into components along and normal to the LOS rate vector gives

$$T(\bar{l}_\omega \dot{\omega} + \bar{l}_\alpha \omega \dot{\alpha}) = 2 \bar{l}_\omega \omega - \lambda(\omega_m - \omega_b) \left[ \bar{l}_\omega \cos(\phi - \alpha) + \bar{l}_\alpha \sin(\phi - \alpha) \right] \quad (A.6)$$

Decomposing gives

$$T\dot{\omega} = 2\omega - \lambda(\omega_m - \omega_b) \cos(\phi - \alpha) \quad (A.7)$$

$$T\omega \dot{\alpha} = -\lambda(\omega_m - \omega_b) \sin(\phi - \alpha) \quad (A.8)$$

Referring to Figure A-1, the triangle with sides  $\omega$ ,  $\omega_m$ , and  $\beta \dot{\phi}$  has interior angles of  $(\phi_c - \alpha)$ ,  $(90^\circ + \phi - \phi_c)$ , and  $(90^\circ - \phi + \alpha)$ . Using the law of sines therefore gives the following relations:

$$\beta \dot{\phi} \cos(\phi - \phi_c) = \omega \sin(\phi_c - \alpha) \quad (A.9)$$

and

$$\omega_m \cos(\phi - \phi_c) = \omega \cos(\phi - \alpha) \quad (A.10)$$

Now, assume that  $\phi - \phi_c$  remains small, thus either the time constant  $\tau$  defined in Equation (A.3) is small or the roll rate  $\dot{\phi}$  remains small. Also assume that  $\phi_c - \alpha$  remains small, thus  $\beta\dot{\phi} \ll |\bar{\omega}|$ . Thus let  $(\phi - \phi_c) = \delta$  and  $(\phi_c - \alpha) = \rho$  and neglect second order terms in  $\delta$  and  $\rho$ . Equations (A.7) through (A.10) then become

$$T\dot{\omega} = 2\omega - \lambda(\omega_m - \omega_b) \quad (\text{A.11})$$

$$T\omega\dot{\alpha} = -\lambda(\omega_m - \omega_b)(\delta + \rho) \quad (\text{A.12})$$

$$\beta\dot{\phi} = \omega\rho \quad (\text{A.13})$$

$$\omega_m = \omega \quad (\text{A.14})$$

These, along with Equation (A.3) are the equations to be solved.

Substituting Equation (A.14) into Equation (A.11) and solving for  $\omega$

$$T\dot{\omega} = 2\omega - \lambda(\omega - \omega_b)$$

$$T^{\lambda-1} \frac{d}{dt} (T^{2-\lambda} \omega) = \lambda\omega_b$$

$$d(T^{2-\lambda} \omega) = \frac{\lambda\omega_b}{T^{\lambda-1}} dt = -\frac{\lambda\omega_b}{T^{\lambda-1}} dT$$

since  $dt = -dT$

$$T^{2-\lambda} \omega = +\lambda\omega_b \frac{1}{(\lambda-2)T^{\lambda-2}} + K \quad \lambda > 2 \quad (\text{A.15})$$

When  $T = T_0$ , let  $\omega = \omega_0$ . Then

$$K = T_0^{2-\lambda} \omega_0 - \frac{\lambda\omega_b}{\lambda-2} \frac{1}{T_0^{\lambda-2}}$$

and

$$\omega = \frac{\lambda}{\lambda-2} \omega_b + \left( \omega_0 - \frac{\lambda}{\lambda-2} \omega_b \right) \left( \frac{T}{T_0} \right)^{\lambda-2} \quad (\text{A.16})$$

This is the solution for  $\omega$  which is used later in the analysis.

Now, differentiating Equation (A.13) gives

$$\beta \ddot{\phi} = \dot{\omega} \rho + \omega \dot{\rho} \quad (\text{A.17})$$

Substituting for  $\dot{\omega}$  from Equation (A.11) and for  $\rho$  from Equation (A.13) gives

$$\beta \ddot{\phi} = \frac{1}{T} [2\omega - \lambda(\omega - \omega_b)] \frac{\beta \dot{\phi}}{\omega} + \omega(\dot{\phi}_c - \dot{\alpha}) \quad (\text{A.18})$$

Solving for  $T\omega\dot{\alpha}$  and equating to Equation (A.12) gives

$$-\lambda(\omega - \omega_b)(\delta + \rho) = -T\beta\ddot{\phi} + (2\omega - \lambda\omega + \lambda\omega_b) \frac{\beta \dot{\phi}}{\omega} + T\omega\dot{\phi}_c \quad (\text{A.19})$$

Differentiating Equation (A.3) gives

$$\dot{\phi}_c = \dot{\phi} + \tau \ddot{\phi} \quad (\text{A.20})$$

Substituting for  $\dot{\phi}_c$  from Equation (A.20), for  $\rho$  from Equation (A.13), and for  $\delta = \phi - \phi_c$  from Equation (A.3), Equation (A.19) becomes

$$-\lambda(\omega - \omega_b) \left( -\tau \dot{\phi} + \frac{\beta \dot{\phi}}{\omega} \right) = -T\beta\ddot{\phi} + T\omega(\dot{\phi} + \tau \ddot{\phi}) + (2\omega - \lambda\omega + \lambda\omega_b) \frac{\beta \dot{\phi}}{\omega} \quad (\text{A.21})$$

Rearranging gives

$$T\omega(\tau - \beta/\omega)\ddot{\phi} + \left[ -\lambda(\omega - \omega_b)(\tau - \beta/\omega) - (\lambda - 2)\beta + \lambda \frac{\omega_b}{\omega} \beta + T\omega \right] \dot{\phi} = 0 \quad (\text{A.22})$$

The solution of this equation is of the form

$$\dot{\phi} = C \exp \left\{ + \int \frac{[-\lambda(\omega - \omega_b)(\tau - \beta/\omega) - (\lambda - 2)\beta + \lambda \frac{\omega_b}{\omega} \beta + T\omega]}{T\omega(\tau - \beta/\omega)} dT \right\} \quad (\text{A.23})$$

where  $\omega$  is given by Equation (A.16). The integral in Equation (A.23) is not easily solved in general; however, the form of the solution can be obtained by considering the effects of the roll control system and the yaw gyro misalignment separately.

Consider the effect of roll control system dynamics only and no yaw gyro misalignment,  $\beta = 0$ . Equation (A.23) becomes

$$\dot{\phi} = C_1 \exp \left[ + \int \frac{T\omega - \lambda\tau(\omega - \omega_b)}{T\omega\tau} dT \right] \quad (\text{A.24})$$

$$\dot{\phi} = C_1 \exp \left[ + \int \left( \frac{1}{\tau} - \frac{\lambda}{T} + \frac{\lambda\omega_b}{T\omega} \right) dT \right] \quad (\text{A.25})$$

For  $\lambda = 4$  and substituting for  $\omega$  from Equation (A.16)

$$\dot{\phi} = C_1 \exp \left[ + \int \left( \frac{1}{\tau} - \frac{4}{T} + \frac{4\omega_b}{aT + bT^2} \right) dT \right] \quad (\text{A.26})$$

where

$$a = 2\omega_b \text{ and } b = (\omega_o - 2\omega_b)/T_o^2$$

$$\dot{\phi} = C_1 \exp \left[ \frac{T}{\tau} - \ln T^4 + 4\omega_b \frac{1}{2a} \ln \left( \frac{bT^2}{a + bT^2} \right) \right] \quad (\text{A.27})$$

$$\dot{\phi} = C_1 \frac{1}{T^4} \left[ \frac{(\omega_o - 2\omega_b)(T/T_o)^2}{2\omega_b + (\omega_o - 2\omega_b)(T/T_o)^2} \right] e^{T/\tau} \quad (\text{A.28})$$

When

$$T = T_o, \quad \dot{\phi} = \dot{\phi}_o$$

Thus

$$C_1 = T_o^4 \dot{\phi}_o \frac{\omega_o}{\omega_o - 2\omega_b} e^{-T_o/\tau}$$

and

$$\dot{\phi} = \dot{\phi}_o \left( \frac{T_o}{T} \right)^2 e^{-\frac{1}{\tau}(T_o - T)} \left( \frac{\omega_o}{2\omega_b + (\omega_o - 2\omega_b)(T/T_o)^2} \right) \quad (\text{A.29})$$

This result shows that for a nonzero time lag in the roll control system, the roll rate will get large as the time to go  $T$  approaches zero. However, with a zero time lag the roll rate will be zero.



Next consider the effect of yaw gyro misalignment only and a perfect roll control system,  $\tau = 0$ . Equation (A. 23) becomes

$$\dot{\phi} = C_2 \exp \left[ + \int \frac{\lambda(\omega - \omega_b)\beta/\omega - (\lambda - 2)\beta + \lambda\omega_b\beta/\omega + T\omega}{-T\beta} dT \right] \quad (\text{A. 30})$$

$$\dot{\phi} = C_2 \exp \left[ + \int \left( -\frac{2}{T} - \frac{\omega}{\beta} \right) dT \right] \quad (\text{A. 31})$$

Substituting for  $\omega$  from Equation (A. 16) and letting  $\lambda = 4$

$$\dot{\phi} = C_2 \exp \left\{ - \int \left[ \frac{2}{T} + \frac{1}{\beta} 2\omega_b + \frac{1}{\beta} (\omega_o - 2\omega_b) \left( \frac{T}{T_o} \right)^2 \right] dT \right\} \quad (\text{A. 32})$$

$$\dot{\phi} = C_2 \exp \left[ - 2 \ln T - 2\omega_b T/\beta - \frac{1}{\beta} (\omega_o - 2\omega_b) \frac{1}{3} \frac{T^3}{T_o^2} \right] \quad (\text{A. 33})$$

If

$$\dot{\phi} = \dot{\phi}_o \text{ at } T = T_o$$

$$C_2 = T_o^2 \dot{\phi}_o \exp \left\{ \frac{1}{\beta} \left[ 2\omega_b T_o + (\omega_o - 2\omega_b) \frac{1}{3} T_o \right] \right\}$$

and

$$\dot{\phi} = \dot{\phi}_o \left( \frac{T_o}{T} \right)^2 \exp \left\{ \frac{1}{\beta} \left[ 2\omega_b (T_o - T) + (\omega_o - 2\omega_b) \frac{1}{3} \left( T_o - \frac{T^3}{T_o^2} \right) \right] \right\} \quad (\text{A. 34})$$

This result shows that a very small negative misalignment angle,  $\beta$ , has a stabilizing effect, since the exponential goes to zero as  $\beta$  goes to zero from the negative side. However, as  $\beta$  goes to zero from the positive side, the exponential goes to infinity and has a destabilizing effect. Therefore, the overall roll stability with gyro misalignment depends on the sign or direction of the misalignment.

If the case  $\omega_o = 2\omega_b$  is considered, Equation (A. 34) reduces to

$$\dot{\phi} = \dot{\phi}_o \left( \frac{T_o}{T} \right)^2 e^{\frac{2\omega_b}{\beta} (T_o - T)} \quad (\text{A. 35})$$

and Equation (A. 29) reduces to

$$\dot{\phi} = \dot{\phi}_0 \left( \frac{T_0}{T} \right)^2 e^{-\frac{1}{T}(T_0 - T)} \quad (A. 36)$$

Comparing Equations (A. 35) and A. 36) shows that the effect of the gyro misalignment is analagous to a negative roll control system time constant.

Referring to Equation (A. 23), the factor  $(\tau - \beta/\omega)$  may be considered to be an effective open loop roll control system time constant. Therefore if the gyro misalignment angle is positive and large enough to result in an effective negative time constant, a serious instability in roll will result. If the misalignment angle is negative and large in magnitude, a resultant sluggish roll control system exists and the roll rate will get large as the time to go approaches zero.

## APPENDIX B

### STATISTICAL ANALYSIS OF MISS DISTANCE

Because of the nondeterministic inputs to the guidance system, the measured output quantities of interest (the miss distances) must be treated in a statistical manner to arrive at some suitable conclusion with respect to the performance characteristics of a particular system configuration.

Two outputs of each computer run were the terminal misses which are denoted as  $M_h$  and  $M_p$ . From the terminal misses obtained for each set of computer runs for a particular value of noise and system parameters a miss scatter diagram can be generated. This diagram would provide information on how large a nonfused warhead would have to be in order to successfully destroy the target by collision.

The approach to be taken in determining warhead size would then be to simply enclose all miss points in an envelope centered, perhaps, about the tracker axis. This, then, would be the required size of the warhead for a nonexplosive interception. One disadvantage in such a procedure is readily apparent. Since the number of samples (misses) is finite and the miss concentration may not be well defined the warhead size might be grossly undersized or oversized. An undersized warhead would mean that the probability of interception would be small. Conversely, an oversized warhead would probably guarantee a kill but at the expense of an impractically oversized system.

For determining warhead size, it is more convenient to consider the probability that the miss is less than a given number. Then, after selecting a reasonable kill probability the warhead radius could be found. With a nonzero mean miss, however, the derivation of the expression for the miss radius for various interception probabilities is difficult. Therefore, the equations relating the miss radius to the statistical parameters of the miss ensembles will be derived for a zero mean miss.

Several simplifying assumptions were employed to expedite the statistical computations, namely:

- The distribution of the miss in each of two directions,  $h$  and  $p$ , is Gaussian. The mean miss in the  $h$  direction is  $M_{ah}$  with standard deviation  $\sigma_h$  and similarly the mean miss in the  $p$  direction is  $M_{ap}$  with standard deviation  $\sigma_p$ .
- The cross correlation coefficient of the misses  $M_h$  and  $M_p$  is zero. This implies that the two misses are statistically independent.

The equation for the estimate of the magnitude of the mean vector miss is

$$M_a = \left( M_{ah}^2 + M_{ap}^2 \right)^{1/2} \\ = \left[ \left( \frac{1}{n} \sum_{i=1}^n M_{hi} \right)^2 + \left( \frac{1}{n} \sum_{i=1}^n M_{pi} \right)^2 \right]^{1/2} \quad (B.1)$$

where  $n$  is the number of samples (chosen to be 30). The estimated standard deviations of  $M_h$  and  $M_p$  are

$$\sigma_h = \left( \frac{1}{n} \sum_{i=1}^n M_{hi}^2 - M_{ah}^2 \right)^{1/2} \quad (B.2)$$

$$\sigma_p = \left( \frac{1}{n} \sum_{i=1}^n M_{pi}^2 - M_{ap}^2 \right)^{1/2} \quad (B.3)$$

The probability that the miss magnitude  $r$  is less than or equal to  $P(r)$  for the independent random variables  $M_h$  and  $M_p$  with zero means and variances  $\sigma_h^2$  and  $\sigma_p^2$  is

$$P(r) = P(M_h^2 + M_p^2 \leq r^2) \quad (B.4)$$

where  $r$  is the miss distance. Proceeding formally

$$P(r) = \frac{1}{2\pi\sigma_h\sigma_p} \int_0^r \exp\left(-\frac{M_h^2}{2\sigma_h^2} - \frac{M_p^2}{2\sigma_p^2}\right) dM_h dM_p \quad (B.5)$$

$$M_h^2 + M_p^2 \leq r^2$$

Letting

$$M_h = \rho \sigma_h \cos \omega \quad (B.6)$$

$$M_p = \rho \sigma_p \sin \omega$$

with the Jacobian

$$\begin{vmatrix} \partial M_h / \partial \rho & \partial M_h / \partial \omega \\ \partial M_p / \partial \rho & \partial M_p / \partial \omega \end{vmatrix} = \rho \sigma_h \sigma_p \quad (B.7)$$

Equation (5) after substitution becomes

$$P(r) = \frac{1}{2\pi \sigma_p \sigma_h} \int_0^r \int_0^{2\pi} \exp \left[ -\frac{\rho^2}{2} \left( \frac{\sin^2 \omega}{\sigma_p^2} + \frac{\cos^2 \omega}{\sigma_h^2} \right) \right] \rho \, d\rho \, d\omega \quad (B.8)$$

$$= \frac{1}{2\pi \sigma_p \sigma_h} \int_0^r \int_0^{2\pi} \exp \left[ -\frac{\rho^2}{4} \left( \frac{1 - \cos 2\omega}{\sigma_p^2} + \frac{1 + \cos 2\omega}{\sigma_h^2} \right) \right] \rho \, d\rho \, d\omega \quad (B.9)$$

$$P(r) = \frac{1}{\sigma_p \sigma_h} \int_0^r \rho \exp \left[ -\frac{\rho^2}{4\sigma_p^2} \left( 1 + \frac{\sigma_p^2}{\sigma_h^2} \right) \right] \left\{ \frac{1}{\pi} \int_0^\pi \exp \left[ -\frac{\rho^2}{4\sigma_p^2} \left( \frac{\sigma_p^2}{\sigma_h^2} - 1 \right) \cos \xi \right] d\xi \right\} d\rho \quad (B.10)$$

where the bracketed term is a zero order Bessel function of the second kind. Equation (B.10) has been numerically evaluated for several values of  $P(r)$  and is presented in normalized form on Figure B-1. Here, the normalized factor  $u$  which is the ratio of the standard deviations is defined such that it is bounded at the values zero and one. Hence

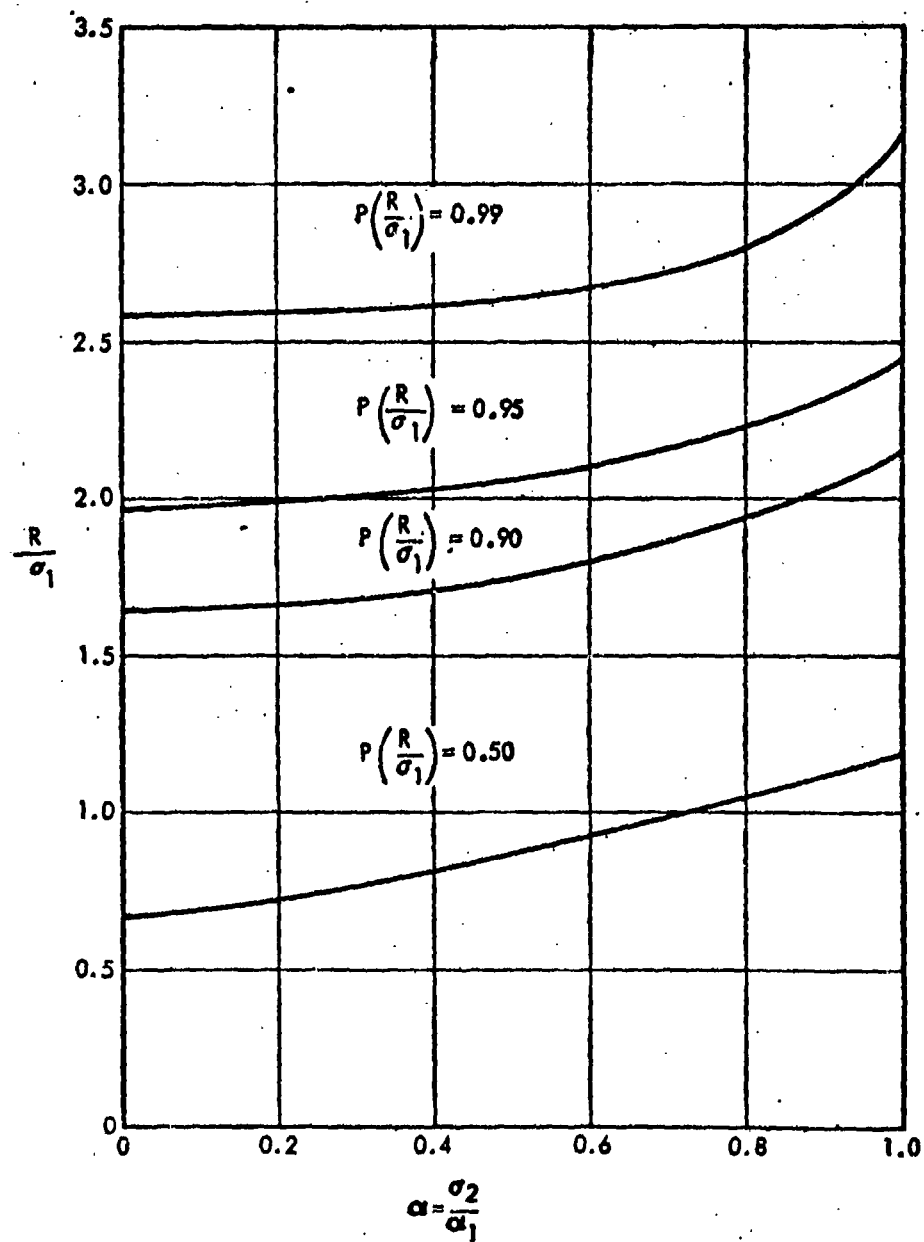


Figure B-1. Ratio of Miss Radius to Larger Standard Deviation as a Function of Interception Probability

$$\begin{aligned}
 \sigma_p &\triangleq \sigma_2 & \text{for } \sigma_p < \sigma_h \\
 \sigma_h &\triangleq \sigma_1 \\
 \sigma_p &\triangleq \sigma_1 & \text{for } \sigma_h < \sigma_p \\
 \sigma_h &\triangleq \sigma_2
 \end{aligned}
 \tag{B.11}$$

The two special cases occur when  $\alpha = 0$  and  $\alpha = 1$ . For  $\alpha = 0$  the distribution is Gaussian and hence

$$P(r) = \frac{1}{\sqrt{2\pi} \sigma_1} \int_0^r e^{-\frac{\rho^2}{2\sigma_1^2}} d\rho
 \tag{B.12}$$

For  $\alpha = 1$  the distribution is Rayleigh and

$$P(r) = 1 - e^{-\frac{r^2}{2\sigma_1^2}}
 \tag{B.13}$$

In addition to the circular probability radii given by Figure B-1 it is useful to place a confidence interval on the miss radius. With this additional information a more conservative estimate of warhead size can be made. For a particular interception probability  $P(r)$  and for a fixed  $\alpha$  the miss radius  $r$  is

$$r = K \sigma_1
 \tag{B.14}$$

For  $\alpha = 1$

$$r = K\sigma = K \sqrt{\frac{\sigma_1^2 + \sigma_2^2}{2}}
 \tag{B.15}$$

The miss radius computed from  $n$  miss samples is denoted by  $r^*$  and is

$$r^* = K \sqrt{\frac{S_1^2 + S_2^2}{2}}
 \tag{B.16}$$

where  $S_1^2$  and  $S_2^2$  are the sample variances.

Hence

$$\frac{r^*}{r} = \sqrt{\frac{S_1^2 + S_2^2}{\sigma^2}} \quad (\text{B.17})$$

For the estimated (i.e., computed)  $r^*$  to be within  $\epsilon$  at its true value

$$1 - \epsilon_1 \leq \frac{r^*}{r} \leq 1 + \epsilon_2 \quad (\text{B.18})$$

Squaring and multiplying by  $n$ , the number of samples

$$n(1 - \epsilon_1)^2 \leq n\left(\frac{r^*}{r}\right)^2 \leq n(1 + \epsilon_2)^2 \quad (\text{B.19})$$

Now

$$n\left(\frac{r^*}{r}\right)^2 = \frac{nS_1^2}{2} + \frac{nS_2^2}{2} \quad (\text{B.20})$$

where  $nS_1^2/2$  is a  $\chi^2$  variate with  $n - 1$  degrees of freedom. Also,  $nS_2^2/2$  is a  $\chi^2$  variate with  $n - 1$  degrees of freedom. Therefore, the sum

$$n\left(\frac{r^*}{r}\right)^2$$

is a  $\chi^2$  variate with  $2n - 2$  degrees of freedom.

Hence

$$P \left[ \chi_1^2 \leq n\left(\frac{r^*}{r}\right)^2 \leq \chi_2^2 \right] = a \quad (\text{B.21})$$

where  $a$  is the confidence (probability) that  $n(r^*/r)$  lies between  $\chi_1^2$  and  $\chi_2^2$ . The bounds  $\chi_1^2$  and  $\chi_2^2$  are chosen in a conventional manner such that

$$\int_0^{\chi_1^2} dF_n(\chi^2) = \int_{\chi_2^2}^{\infty} dF_n(\chi^2) = \frac{1-a}{2} \quad (\text{B.22})$$



where  $F_n(\chi^2)$  is the chi square distribution function. For  $n = 30$  samples,  $\sigma_2/\sigma_1 = 1$  and  $\alpha = 0.95$  (a 95 percent confidence interval),

$$\epsilon_1 \approx \epsilon_2 \approx 0.19 \quad (\text{B.23})$$

Hence

$$0.81 \leq \frac{r^*}{r} \leq 1.19 \quad (\text{B.24})$$

Inverting

$$0.84 \leq \frac{r}{r^*} \leq 1.23 \quad (\text{B.25})$$

This inequality, then, gives the 95 percent confidence interval on the true miss radius as a function of the estimated radius.

The confidence interval derivation for  $\sigma_2/\sigma_1 = 0$  is similar to the preceding.

For  $\sigma_2/\sigma_1 = 0$

$$\frac{r^*}{r} = \frac{S_1}{\sigma_1} \quad (\text{B.26})$$

where  $S_1$  is the estimated standard deviation. Bounding the estimated  $r^*$  as before

$$1 - \epsilon_1 \leq \frac{r^*}{r} \leq 1 + \epsilon_2 \quad (\text{B.27})$$

and

$$n(1 - \epsilon_1)^2 \leq n\left(\frac{r^*}{r}\right)^2 \leq n(1 + \epsilon_2)^2 \quad (\text{B.28})$$

Where  $n(r^*/r)^2$  is the  $\chi^2$  variate with  $n - 1$  degrees of freedom.

Hence

$$P\left[\chi_1^2 \leq n\left(\frac{r^*}{r}\right)^2 \leq \chi_2^2\right] = \alpha \quad (\text{B.29})$$

Where  $\chi_1^2$  and  $\chi_2^2$  are chosen to satisfy Equation (B.22).

For  $a = 0.95$  and  $n = 30$

$$0.81 \leq \frac{R}{\sigma_1} \leq 1.37 \quad (\text{B.30})$$

Since the inequalities of Equations (B.25) and (B.30) do not differ drastically from each other a straight line approximation to the percentage confidence interval for  $0 < a < 1$  has been made. The 95 percent confidence interval for a 0.95 interception probability is shown graphically on Figure B-2. This graph was used in the computation of the miss distance.

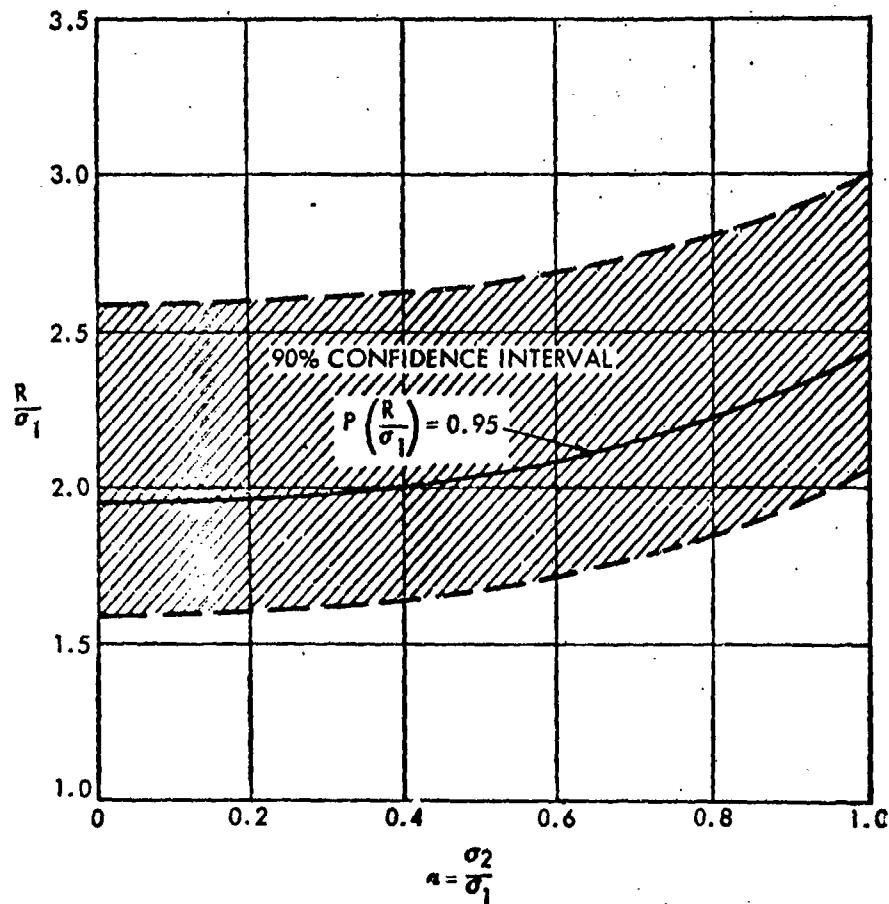


Figure B-2. Ratio of Miss Radius to Larger Standard Deviation for 95 Percent Interception Probability

## APPENDIX C

### DEVELOPMENT OF RADAR PARAMETRIC EQUATIONS

#### 1. PARAMETRIC RELATIONSHIPS FOR A RADAR SEEKER

Let us consider the signal-to-noise ratio per pulse for a conventional pulse radar (starting the analysis with a pulse radar causes no loss in generality).

$$S/N = \left( \frac{P_t^* L G_t}{4\pi R^2} \right) \left( \frac{\sigma}{4\pi R^2} \right) \rho A \left( \frac{1}{KT_e B} \right) \quad (C.1)$$

where

$S/N$  = Peak signal-to-noise ratio per pulse

$L$  = System loss factor

$P_t^*$  = Peak transmitter power

$R$  = Range

$A$  = Antenna area

$\rho$  = Antenna efficiency

$\sigma$  = Target echoing

$B$  = Bandwidth

$K$  = Boltzman's constant - 1.38 watts/cps/°K

$T_e$  = Effective noise temperature of the radar receiver

The terms in Equation C.1 are arranged to illustrate the flow of power. The first bracket represents the power density at the target (power transmitted x antenna gain  $\div$  space loss). The second bracket is simply the received power density per unit power density at the target.

For a single pulse matched filter, the bandwidth  $B$  is approximately the reciprocal of the pulse length  $\tau$ . Substituting, we have

$$S/N = \frac{P_t^* \tau L G_t}{4\pi R^2} \frac{\sigma}{4\pi R^2} \rho A \frac{1}{KT_e} \quad (C.2)$$

If we integrate  $m$  pulses coherently, the resultant output signal to-noise ratio is

$$(S/N)_o = m(S/N) = \frac{L(P_t m \tau) G_t}{4\pi R^2} \frac{\sigma}{4\pi R^2} \rho A \frac{1}{KT_d} \quad (C.3)$$

Now let  $T_i$  be the total time of coherent integration. The basic transmitter quantity of interest is the energy transmitted during the integration time

$$E_i = m P_t \tau = m P_t T_i \quad (C.4)$$

under the assumption of coherent integration, where  $P_t$  is the average transmittal power.

For a CW radar, this is equivalent to assuming that

$$B T_i = 1 \quad (C.5)$$

and the peak transmitted power  $P_t$  equals the average transmitted power  $P_{av}$ .

Consider next the relationships among the antenna related parameters and the field-of-view. The ephemeris errors dictate a certain area  $A_s$  over which the radar must search for the target. At the minimum acceptable detection range  $R_m$  this corresponds to a solid angle

$$\Omega = 4\pi \left( \frac{A_s}{4\pi R_m^2} \right) = \frac{A_s}{R_m^2} \quad (C.6)$$

neglecting curvature corrections. If we assume for the moment a perfect antenna, then the gain  $G_t$  is assumed constant over the solid angle  $\omega$  covered by the antenna beam so that

$$G = \rho 4\pi / \omega \quad (C.7)$$

where  $\rho$  is the aperture efficiency.

The departure of the gain from a constant over the beamwidth will be included in the beam shape and scanning portions of the loss factor  $L$ . In

order to obtain a total time of  $T_i$  for integration, the antenna beam must illuminate the target for  $T_i$  seconds. Therefore a total time of

$$T = T_i \frac{\Omega}{\omega} \text{ seconds} \quad (\text{C. 8})$$

will be required for the antenna beam to scan the required field-of-view. In this amount of time the target, which is traveling toward the interceptor at velocity  $V_c$ , can close a distance of

$$\Delta = V_c T \quad (\text{C. 9})$$

To incorporate these relations, let us return to Equation C.3. The signal-to-noise required after integration  $(S/N)_0$  is determined by the required probability of detection (and vice versa). If we define  $R_0$  as the range at which the  $(S/N)_0$  is unity, then

$$R_0^4 = \frac{P_t T_i G_p A \sigma L}{(4\pi)^2 K T_e} \quad (\text{C. 10})$$

or

$$P_t = \frac{(4\pi)^2 K T_e}{L T_i G_p A \sigma} R_0^4 \quad (\text{C. 11})$$

Substituting the relations in Equations (C.7) (C.8) and (C.9)

$$\begin{aligned} P_t &= 4\pi \left( \frac{K T_e}{L \sigma} \right) \frac{\Omega}{\rho^2 A T} R_0^4 \\ &= 4\pi \frac{K T_e}{L \sigma} \frac{\Omega}{\rho^2 A \Delta} R_0^4 \end{aligned} \quad (\text{C. 12})$$

and then introducing  $R_m$ , we finally obtain

$$P_t = 4\pi \left( \frac{K T_e}{L} \right) \left( \frac{A_s V_c R_m}{\rho^2 A} \right) \frac{(R_0/R_m)^4}{(\Delta/R_m)} \quad (\text{C. 13})$$

In Equation C.13 we have delineated the significant parameters affecting radar performance. The quantities in the first bracket are only

somewhat dependent on system design and choice of frequency. The quantities in the second bracket are dictated by the problem. The third set of quantities

$$\left(R_o/R_m\right)^4/(\Delta/R_m) \quad (C.14)$$

is the ratio of signal-to-noise at  $R_m$  to the fraction of  $R_m$  traveled in a scan time  $T$ . Since the other factors in Equation (C.13) are constants (except for slight variations with choice of frequency), this last ratio [Equation (C.14)] should be minimized to optimize the transmitter power  $P_t$ .

Subsequently we will show that the minimum of Equation (C.14) is a function only of the cumulative probability of detection  $P_c$  required at the specified range  $R_m$ , that is

$$P_t = 4\pi \left(\frac{KT\bar{N}F}{L}\right) \left(\frac{A_s V_c R_m}{\sigma A}\right) \left[\frac{\alpha(P_c)}{\gamma(P_c)}\right] \quad (C.15)$$

where

$\alpha(P_c)$  = optimum signal to noise  $R_o/R_m^4$  required to achieve the cumulative probability of detection  $P_c$

$\gamma(P_c)$  = optimum  $\Delta/R_m$  for the required  $P_c$  (C.16)

Therefore from Equation (C.15) we can see the interrelationship of the primary parameters in system performance. The required radar power varies linearly with the ephemeris uncertainty area, the closing velocity and with the minimum acceptable detection range. It varies inversely with the antenna area and the target nominal area.

The linear dependence of  $P_t$  on  $(A_s, V_c, R_m)$  is most significant. This relationship emphasizes the significance of improving the ephemeris and reducing closing velocity by favorable attack geometrics. It also suggests that improved detection range may be achieved at a rather moderate cost in radar investment, thereby reducing peak homing stage acceleration and fuel requirements.

It is also interesting to note that frequency does not appear explicitly although the terms  $(\bar{N}F, L, \sigma)$  may have frequency dependence. Frequency

does enter in a crucial way, however. We have assumed that the predetection bandwidth  $B$  is matched to the time on target  $T_i$ , thereby achieving coherent signal processing. This requirement is difficult (perhaps impossible) to achieve exactly in practice, requiring extremely narrow antenna beamwidths and hence very high frequencies. These high frequencies are undesirable from the viewpoint of noise temperature  $T_n$ , efficiency of power generation, and the difficulty of pointing and sweeping a narrow beam antenna.

These considerations will force us to consider nonoptimum signal processing. As shown in Section 3, nonoptimum signal processing, i. e., noncoherent or post detection integration, can incur additional penalties of from 1 to 5 db. Also, it is important to note here that with nonoptimum processing the desirable linear dependence of power required with range is spoiled somewhat, perhaps approaching a square relationship.

## 2. OPTIMIZATION OF SCAN TIME

Consider the minimization of Equation (C.14). The object of the radar design is to achieve a certain cumulative probability of detection  $P_c$  at the specified range  $R_m$  with the specified parameters of target size, closing velocity, antenna aperture, etc. From rather extensive analysis by Marcum,<sup>1</sup> Swerling,<sup>2</sup> and others,<sup>3</sup> the probability of detection on a single look, the so-called "blip-scan" ratio, has been determined for constant and fluctuating targets as a function of  $R/R_0$  or equivalently  $(S/N)^{1/4}$ . Denote this ratio (probability) as  $p(R/R_0)$ .

If we assume the target is fluctuating (scintillating) with scan-to-scan independence, then, since the final scan must catch any particular target before it reaches  $R_m$ , the cumulative detection probability for that particular target is

$$P'_c(R', \Delta) = 1 - \prod_{i=0}^n \left[ 1 - p\left(\frac{R' + i\Delta}{R_0}\right) \right] \quad (C.17)$$

where

$$R_m \leq R' \leq R_m + \Delta \quad (C.18)$$

Since the target can be anywhere in the interval specified in Equation (C.18) with equal probability, then the overall cumulative probability is

$$P_c(R_m, \Delta) = \frac{1}{\Delta} \int_{R_m}^{R_m + \Delta} P'_c(R', \Delta) dR' \quad (C.19)$$

The required optimization is to minimize Equation (C.14) by choice of  $\Delta$ , subject to  $P_c(R_m, \Delta)$  from Equation (C.19), being equal to a prescribed value. Increasing the interval  $\Delta$  increases the time for coherent signal integration and thereby improves the signal-to-noise ratio. This results in an increased blip-scan ratio. On the other hand, increasing  $\Delta$  decreases the number of looks at a target, and hence, tends to decrease  $P_c$ . As might be expected, there is an optimum ( $\Delta/R_m = \gamma$ ). This optimization has been addressed by Mallett and Brennan<sup>4</sup> and Dishington.<sup>5</sup> The results of the analysis by Mallett and Brennan are presented in Figure 4-1 and 4-2 of Volume I. Figure 4-1 displays the signal-to-noise ratio required (out of a predetection filter matched to the time-on-target) versus the desired probability of detection  $P_c$  for two false alarm numbers  $n$  of  $10^6$  and  $10^8$ . Figure 4-2 shows the dependence of the optimum scan ratio ( $\gamma = \Delta/R_m$ ) on the desired  $P_c$ . Only the results for the most severe (Swerling Case I) type target fluctuations are presented here.

The false alarm number  $n$  is the reciprocal of the false alarms per look at noise. This number is computed as follows. A practical radar which achieves a performance almost equivalent to the assumed perfectly coherent system will generally have a number  $m$  of narrow band filters (of bandwidth  $B$ ). Each filter is looking at noise and the number of looks per second is  $mB$ . If the average time between false alarms is specified at  $T_{fa}$ , then

$$n = (\text{looks per second}) (\text{false alarm time})$$

or

$$n = mBT_{fa} \quad (C.20)$$

Conservatively,  $m = 100$ ,  $B = 100$  and  $T_{fa} = 10^4$ , so that  $n = 10^8$  or less.



### 3. IMPLICATIONS OF COHERENT SIGNAL PROCESSING

Fundamental to the previous analysis has been the assumption that the radar signal has been processed coherently. This means that in effect the predetection filter is matched to the time-on-target  $T_i$ . The radar system detection configuration comprises a bank of doppler filters of bandwidth  $(1/T_i)$  each of which is followed by a square law detector which directly feeds a threshold circuit. No post detection integration (filtering) is called for. The target echo pulses are thereby integrated coherently in the doppler filter for  $T_i$  seconds. One advantage of this configuration is that since the signal is integrated prior to detection, the signal-to-noise ratio into the square law detector is high, thereby incurring only a small degradation.

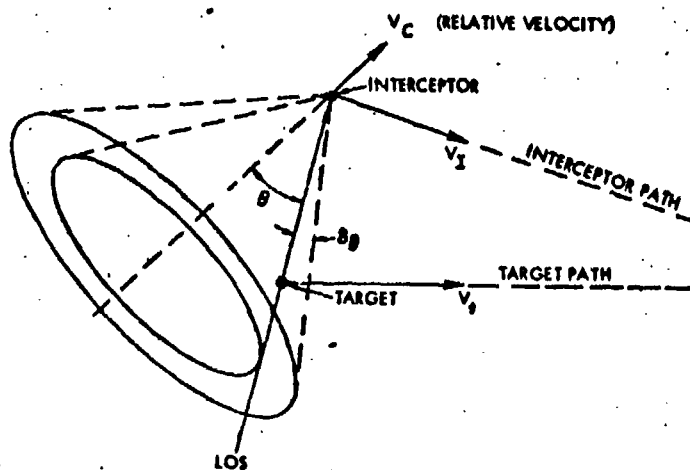


Figure C-1. Typical Geometry at Target Acquisition

The most basic difficulty in achieving the requisite narrow doppler bandwidths is simply the rate of change of doppler shift as the target closes. To illustrate, in Figure C-1 we have shown a typical geometry at target acquisition indicating the LOS to the target and the relative velocity  $V_R$  vector. We shall assume that the magnitude and direction of this relative velocity are accurately known. The doppler shift is proportional to the projection of the relative velocity onto the LOS

$$f = \frac{2V_R}{\lambda} \cos \theta \quad (\text{C.21})$$

where  $\theta$  is the angle between  $V_R$  and the line-of-sight.

Now each filter preceding a detector/integrator must be wide enough so that the received signal remains in the bandpass of the filter for the integration time, i.e.,

$$B \geq \dot{f} T_i \quad (C.22)$$

On the other hand there will be a minimum bandwidth that will be achievable considering carrier spectrum width, availability of components, etc., therefore

$$B \geq B_{\min} \quad (C.23)$$

as well.

From Equation (C.21)

$$\dot{f} = \frac{2}{\lambda} (\dot{V}_R \cos \theta - V_R \sin \theta \dot{\theta}) \quad (C.24)$$

Now

$$\sin \theta = \frac{M}{R} \quad (C.25)$$

where M is the nominal miss and R is the range to the target, so that

$$\cos \theta \dot{\theta} = \frac{M \dot{V}_R}{R^2} \cos \theta \quad (C.26)$$

Substituting m into (C.24), we obtain

$$\dot{f} = \frac{2}{\lambda} \left( \dot{V}_R \cos \theta - V_R^2 \frac{M^2}{R^3} \right) \quad (C.27)$$

In this problem we assume  $V_R$  to be constant (no target maneuvers), so that

$$\dot{f} = -\frac{2}{\lambda} V_R^2 \frac{M^2}{R^3} \quad (C.28)$$

Now, the number of pulses N that must be integrated is given by

$$N = B T_i \quad (C.29)$$

For coherent processing,  $N = 1$ , so that

$$T_i = \sqrt{f} \quad (C.30)$$

This is not usually the case, and we must compute  $N$  as

$$N = \left| \frac{f}{T_i} \right| T_i^2 \geq B_{\min} T_i \quad (C.31)$$

Now, the time on target is

$$T_L = T_s \frac{\omega}{\Omega} = \frac{\gamma R_m}{V_R} \frac{R_m^2}{A_s} \frac{\pi}{4} \left( \frac{\lambda^2}{D_1 D_2} \right) \quad (C.32)$$

assuming a beam dimension of  $\lambda/D$ . Therefore

$$N = \frac{\pi \gamma^2}{2\lambda} \frac{M^2 R^3}{A_s^2} \left( \frac{\lambda^4}{D_1^2 D_2^2} \right) \geq B_{\min} T_i \quad (C.33)$$

However, we can see that  $N$  is largest at the maximum miss  $M$ , so that with  $M = 3\sigma_b$  and recalling that

$$A_s = \pi (3\sigma_a) (3\sigma_b) \quad (C.34)$$

we obtain

$$N = \frac{\gamma^2 R^3 \lambda^3}{72 \sigma_a^2 D_1^2 D_2^2} \geq B_{\min} T_i \quad (C.35)$$

The loss corresponding to  $N \neq 1$  is given in Figure 4-4 of Volume I. For example,  $N = 3$ .

#### 4. OTHER LOSS CONSIDERATIONS

Two other loss phenomena should be considered, eclipsing and modulation. A pure CW system appears to be ruled out by considerations of receiver isolation. An attractive configuration for this intercept task is an ICW system using PRF tracking for range information. In this system, the

transmitter is turned on for the round trip period to the target and then switched off to receive the incoming echo. Before the target has been detected this range is unknown and a programmed PRF must be used. The discrepancy between the actual range and the programmed range will cause the transmitted pulse to overlap the received pulse causing an effective loss in return signal energy. This phenomenon is called eclipsing. An estimate of this loss for the case of detection at 125 n mi with appropriate ephemeris uncertainty in range yielded a loss of 0.5 db.

#### REFERENCES

1. J. I. Marcum, "A Statistical Theory of Target Detection by Pulsed Radar," Rand Research Memo RM-754, December 1, 1947.
2. P. Swerling, "Probability of Detection for Fluctuating Targets," Rand Memo RM-1217, March 17, 1954.
3. J. J. Busgang, P. Nesbeda, and H. Safran, "A Unified Analysis of Range Performance of CW, Pulse, and Pulse Doppler Radar," Proceedings of the IRE, pp. 1753-1762, October 1959.
4. J. D. Mallett and L. E. Brennan, "Cumulative Probability of Detection for Targets Approaching a Uniformly Scanning Search Radar," Proceedings of the IEEE, pp. 596-601, April 1963.
5. R. Dishington, unpublished work.

## APPENDIX D

### RADAR ANGLE ERRORS

#### 1. INTRODUCTION

Two contributors to the tracking noise in a monopulse tracking radar are random fluctuations in the phase front of the received signal called angle noise, and random fluctuations in the amplitude of the received signal called amplitude noise.<sup>1</sup>

The random fluctuations in the phase front of the received signal result from the interference of energy reflected from various scatterers on the target. Because the tracker uses the phase front to determine the radar target direction, the result is an apparent target motion. The return signal amplitude noise causes apparent target motion due to the fact that amplitude fluctuations cannot be completely removed by the automatic gain control.

In this study a target model will be used to assess the effect of AGC and tracking circuit bandwidths on the magnitude of the tracking noise from these two sources. One target model advanced by R. H. Delano,<sup>2</sup> and later used by R. B. Muchmore,<sup>3</sup> assumes that the target consists of an infinite number of scatterers with equal amplitudes and independent, random, phases. Equal amplitudes are assumed to make the results expressible in a readily usable form. Due to the form the approximation takes, the results do not lose appreciable significance as a result of the approximation of equal amplitude scatterers. From this model, conclusions can be drawn about the character of a general target.

#### 2. AMPLITUDE NOISE AND ANGLE NOISE

R. H. Delano<sup>2</sup> determined the error signals introduced into a conically scanned tracking system by the fluctuation of the phase front and amplitude of the received signal. Although the results were obtained specifically for a conically scanned system, the results apply to essentially all linear tracking systems. This is due to the fact that all such systems develop a modulation on the signal from each scatterer which is in phase with the unmodulated signal from that scatterer. From Delano's study, the error signal present, after linear detection of the scattered signal is given by

$$\text{error signal} = E_s = U_a + U_b \quad (\text{D. 1})$$

where

$U_a$  = Gaussianly distributed angle noise with a mean square value of

$$U_a = \frac{1}{2} b_o^2 E^2 \frac{\overline{d_n^2}}{R^2} \quad (\text{D. 2})$$

$d_n$  = Distance from the tracking axis to the individual scatterer  $n$  and  $R$  is the range from the radar to the target

$U_b = E b_o \epsilon - E$  is the Raleigh distributed output of the detector,  $b_o$  is the error signal per unit angle error between the tracking axis and the target, and  $\epsilon$  is the angle between the tracking axis and the mean radar center measured in a signal tracking plane.

For the case of no automatic gain control or a slow AGC, the error signal  $E_s$  is substantially unchanged and is given by

$$E_s = -b_o \epsilon E + U_a \quad (\text{D. 3})$$

which may be written as

$$E_s = -b_o \epsilon \bar{E} + b_o \epsilon (\bar{E} - E) + U_a \quad (\text{D. 4})$$

The first term  $(-b_o \epsilon \bar{E})$  in Equation (D. 4) is a restoring term proportional to the angle  $\epsilon$ , between the tracking axis and the radar center. The second term  $[b_o \epsilon (\bar{E} - E)]$  is an amplitude noise term with a mean value of zero, and a magnitude proportional to the instantaneous value of  $\epsilon$ . The third term is the Gaussianly distributed angle noise.

For a zero time constant AGC, the error signal given by Equation (D. 3) is effectively multiplied by  $\bar{E}/E$ , and hence becomes

$$E_s = -b_o \epsilon \bar{E} + \frac{\bar{E}}{E} U_a \quad (\text{D. 5})$$

The amplitude noise term is not present in Equation (D. 5) to give spurious tracking signals, however, the angle noise term is no longer  $U_a$  but  $\bar{E} U_a / E$ .

$U_a$  is Gaussianly distributed and  $E$  is a Raleigh distributed variable. Then the term  $U_a/E$  is a special case of the Student  $t$  distribution. The resultant distribution is wider than the Gaussian distribution of  $U_a$ . The rms value of a true Student  $t$  distribution is infinite, resulting in an infinite power in the angle scintillation spectrum of a zero time-constant tracking system. This is not a realizable system because the power in the scintillation spectrum will always be finite due to the electric time constants and physical inertia of the system. Thus, a fast AGC while increasing the angle noise, will decrease the tracking noise due to amplitude noise.

Dunn and Howard<sup>4</sup> have assessed the relative merits of slow and fast automatic gain controls. The comparison was made by simulation of an entire tracking system including the AGC, and the closed loop tracking circuit, and the radar target itself. The spectrum of the amplitude noise in the signal simulating the target (with the bandwidth suitably scaled) is shown in Figure 4.11b.

The results of that study indicated that a fast AGC would give less total tracking noise than a slow AGC under practical tracking conditions. This may be seen from Equation (D.4); the amplitude noise induced angle scintillation,  $b_0 \epsilon (\bar{E} - E)$ , with slow AGC is proportional to the angle  $\epsilon$  between the tracking axis and the mean radar center of the target. Because this term is small in a fast AGC, and because the angle noise  $U_a$  is independent of the angle  $\epsilon$ , there is a relatively small value of  $\epsilon$  (about one-half body length), above which the slow AGC tracking noise exceeds the tracking noise with fast AGC.

In Section 4 of this appendix it is shown that the total spectral width of the tracking noise will be 0.4 cps as contrasted with the 1.4 cps total bandwidth noise used in the simulation by Dunn and Howard. However, the results obtained in the simulation will be appropriate to this study if the simulated bandwidths are scaled by the same factor as the noise bandwidths. The results of the radar simulation by Dunn and Howard are shown in Figure 4-11a of this report with the AGC and tracking bandwidths suitably scaled.

#### 5. SERVO DYNAMIC LAG

It was found in Section 2 that the tracking noise induced by target amplitude noise was a function of the antenna pointing error. In this



section, an expression will be given for the tracking lag under proposed tracking conditions of a programmed 2 mr/sec LOS.

For the AN/FPS-16(XN-1)<sup>5</sup> radar, the relationship between the dynamic tracking lag and the tracking-servo bandwidth is given by

$$\Delta\theta \approx \frac{\omega_T}{80B_N} + \frac{\dot{\omega}_T}{2.5B_N^2} + \text{higher order terms} \quad (\text{D. 6})$$

where

$\Delta\theta$  = Tracking lag in mr/sec

$\omega_T$  = Line-of-sight rate in mr/sec

$\dot{\omega}_T$  = First derivative of LOS rate in mr/sec<sup>2</sup>

$B_N$  = Bandwidth of tracking servo

Assuming a similar relationship between the tracking bandwidth and dynamic tracking lag, and for the case

$$\omega_T = 2 \text{ mr/sec}$$

$$\dot{\omega}_T = 0$$

$$B_N = 1.15 \text{ cps}$$

Then

$$\Delta\theta \approx 0.5 \text{ mr} \quad (\text{D. 7})$$

Expressing the tracking lag in feet at the target:

$$\text{at 1 mile range} \quad \Delta\theta(\text{ft}) = 0.11$$

$$\text{at 10 mile range} \quad \Delta\theta(\text{ft}) = 1.1$$

$$\text{at 50 mile range} \quad \Delta\theta(\text{ft}) = 5.5$$

#### 4. SCINTILLATION SPECTRA

The portion of the angle and amplitude scintillation spectra which fall in the bandwidth of the AGC and tracking circuits determine the actual effect of the scintillations on the tracker. It is then quite important to know the widths and general shapes of the spectra.

The actual angle scintillation spectrum shape is a function of the AGC bandwidth. As a result, the angle scintillation spectrum for no AGC will be given here as a guideline for the actual case where a fast AGC might be used. The AGC chosen would not change the width of the spectrum, only the shape. In addition, the total power in the spectrum (area under the spectral density curve) will be a function of the pointing error between the antenna axis and the mean radar center of the target.

Then, as a guideline for the actual spectra, the normalized scintillation spectra for no AGC will be derived for two idealized cases, a closing range on a stabilized target, and a constant range rotating target. The spectra shown are normalized to unity area, the actual area would be equal to the variance of the tracking noise power (which is estimated in the text of this report).

#### 4.1 Spectrum for Closing on a Stabilized Target

Assuming an interceptor to be closing toward the center of a non-rotating target, the spectrum width may be obtained by referring to Figure D-1.

If the closing velocity to the center of the target is  $V_o$ , the closing velocity to the periphery of the target is  $(V_o \cos \theta)$ .

The differential closing velocity is given by

$$V_d = V_o (1 - \cos \theta) \quad (D. 8)$$

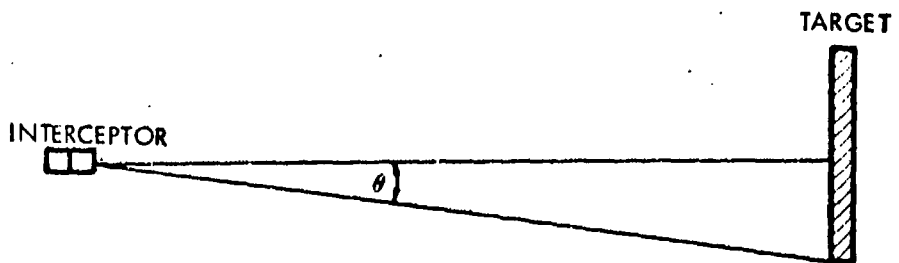


Figure D-1. Target Geometry  
using the approximation for small  $X$

$$\sqrt{1 - X^2} \approx 1 - \frac{X^2}{2} \quad (D. 9)$$

Equation (D. 9) becomes

$$V_d = V_o \left[ 1 - \left( 1 - \frac{\sin^2 \theta}{2} \right) \right] \quad (D. 10)$$

$$V_d = V_o \frac{\sin^2 \theta}{2} \quad (D. 11)$$

for small  $\theta$

$$\sin \theta \approx \theta$$

then

$$V_d \approx \frac{V_o \theta^2}{2} \quad (D. 12)$$

The difference doppler between the center of the target and the periphery is given by

$$f_d = \frac{2V_d}{c} f_o \quad (D. 13)$$

where  $f_o$  is the carrier frequency,  $c$  is the velocity of light.

Combining Equations (D. 12) and (D. 13)

$$f_d = \frac{V_o \theta^2 f_o}{c} \quad (D. 14)$$

For a target diameter of 10 feet, a closing velocity of 10,000 feet per second, and a carrier frequency of 10 kMc

$$f_d \approx \frac{0.09}{R^2} \text{ cps} \quad (D. 15)$$

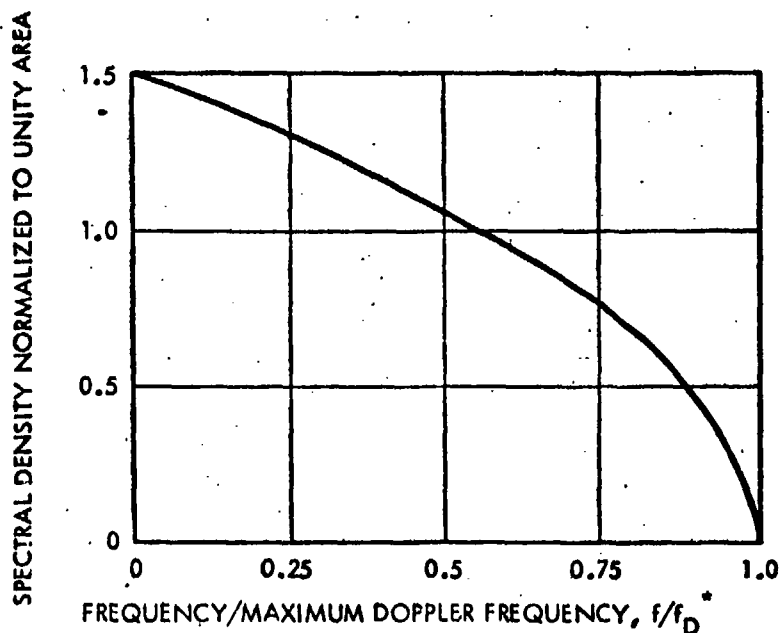
where  $R$  is the range in statute miles,  $f_d$  is the spread of the doppler spectrum for the specified geometry.

From Muchmore, the spectra for  $U_a$ , the Gaussianly distributed error signal is

$$W(U_a) = \frac{3}{2f_d} \sqrt{1 - \frac{f}{f_d}} ; \quad 0 \leq f \leq f_d \quad (D. 16)$$

$$W(U_a) = 0 ; \quad \text{elsewhere}$$

The normalized spectrum  $W(U_2)$ , for a 10 foot target is shown in Figure D-2.



\*FOR A 10 FT TARGET AT A RANGE OF 1 MI,  $f_D = 0.09$  CPS  
 FOR A 10 FT TARGET AT A RANGE OF 10 MI,  $f_D = 0.009$  CPS

Figure D-2. Spectral Density of Angle Scintillation for Closing Range

#### 4.2 Spectrum for a Rotating Target

The width of the angle scintillation spectrum of a rotating target at a large range may be calculated from the expression

$$f_d = \frac{4\pi f_r df_o}{c} \quad (D.17)$$

where

$f_d$  = Spectrum width

$f_r$  = Frequency of rotation of the target in cps

$d$  = Length of the target

$f_o$  = Transmitted frequency

For a 10-foot target, and a transmitted frequency of 10 kMc

$$f_d = 1258 f_r \quad (D. 18)$$

The spectrum is (from Muchmore)

$$W(U_a) = \frac{1}{f_d} \left( 2 - 6 \frac{f}{f_d} + 12 \frac{f^2}{f_d^2} - 8 \frac{f^3}{f_d^3} \right) \quad (D. 19)$$

The normalized spectrum,  $W(U_a)$ , for a 10-foot target rotating at 2 mr/sec, is shown in Figure D-3.

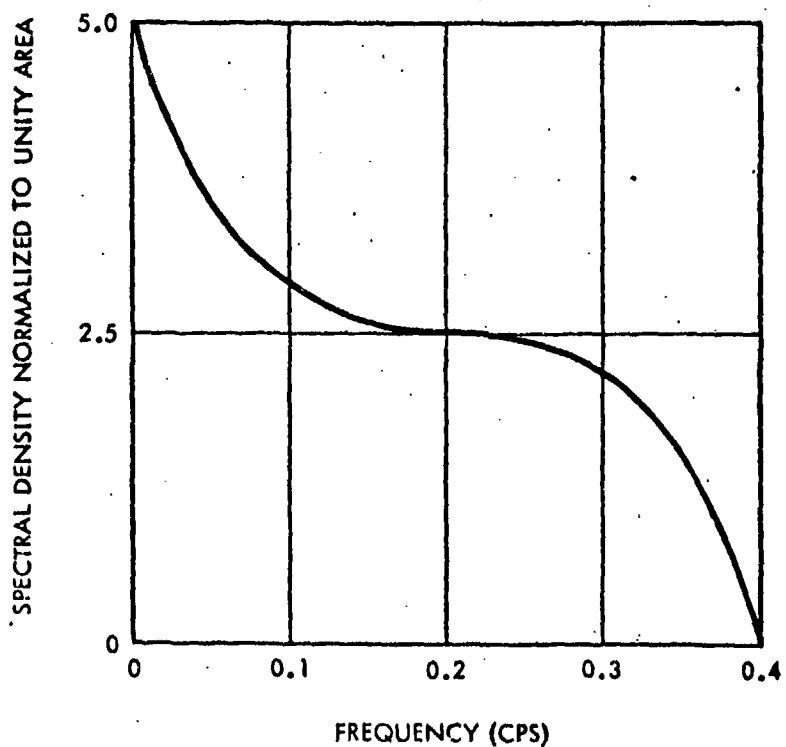


Figure D-3. Spectral Density of Angle Noise for a 10-Foot Target Rotating at 2 mr/sec

## REFERENCES

1. Charles E. Brockner, "Angular Jitter in Conventional Conical-Scanning, Automatic-Tracking Radar System," Proc. IRE, vol. 39 (1951), p. 51.
2. R. H. Delano, "A Theory of Target Glint or Angular Scintillation in Radar Tracking," Proc. IRE, vol. 41 (December 1953) pp. 1778-1784.
3. R. B. Muchmore, "Aircraft Scintillation Spectra," IRE Transactions on Antennas and Propagation, vol. AP-8, No. 2 (March 1960) pp. 201-212.
4. J. H. Dunn and D. D. Howard, "The Effects of Automatic Gain Control Performance on the Tracking Accuracy of Monopulse Radar Systems," Proc. IRE, vol. 47, No. 3 (March 1959) pp. 430-435.
5. "Instrumentation Radar AN/FPS-16(XN-1) Evaluation and Analysis of Radar Performance," Radio Corporation of America. (No date)

## APPENDIX E

### CALCULATION OF TRACKER NOISE EQUIVALENT FLUX DENSITY

#### 1. INTRODUCTION

The noise equivalent flux density (NEFD) of a conventional carrier-type electro-optical tracker is used to express the signal-to-noise ratio at the output of the tracker preamplifier, or intermediate frequency amplifier. A knowledge of NEFD is essential in a determination of the required aperture diameter for given static tracking accuracy or in a discussion of the problems of target acquisition.

Two variations of the same optical system will be discussed, one in connection with the copper-doped germanium detector and the other in connection with the photomultiplier detector. Both systems will employ parabola-flat collecting optics of about  $f/3$  relative aperture. When used with the copper-doped germanium detector, which is background limited, a cone channel condenser will be used in addition to restrict the amount of background radiation falling on the detector and hence decrease the NEFD. Collecting optics alone will be used with the photomultiplier which is also generally background limited by visible spectrum photons.

Although it is an assumption not crucial to the calculation of NEFD, the tracker type to be assumed is a fixed reticle FM system.

#### 2. CALCULATION OF THE NEFD OF A THERMAL TRACKER EMPLOYING CONE CHANNEL CONDENSER OPTICS

A tracker designed for operation against a greybody radiator at  $250^{\circ}\text{K}$  must have a detector capable of operation somewhere in the spectral region of 6 to 30 microns. There are two basic possible choices of detector and filter. One is the spectral region of 6 to 14 microns which includes 40 percent of the radiated power; the other is the spectral region of 8 to 30 microns, which includes 77 percent of the radiated power. Both spectral regions can be covered with copper-doped germanium, the limitation to shorter wavelengths being accomplished with a cold barium fluoride or Irtran II filter. The complete 8- to 30-micron region gives a greater amount of effective target radiation, as well as a decreased

amount of background radiation and is the region to be considered in this calculation. Operation in the 6- to 14-micron band, although not optimum from the point-of-view of maximum signal-to-detector noise or signal-to-background ratios is more convenient in terms of filter and window availability.

The calculation of NEFD is based on the definition of the detectivity,  $D^*$ , of the detector

$$D^* = \frac{\sqrt{A_c} \sqrt{\Delta f}}{NEP} \quad (E. 1)$$

where

$A_c$  = Detector area,  $\text{cm}^2$

$\Delta f$  = Noise equivalent bandwidth, cps

NEP = Noise equivalent power, watts

the NEFD is then

$$NEFD = \frac{4 NEP}{\eta \pi D^2} = \frac{4 \sqrt{A_c} \sqrt{\Delta f}}{D^* \pi D^2 \eta} \quad (E. 2)$$

In this equation

$D$  = Aperture diameter of optical system, cm

$\eta$  = System efficiency

The detector area,  $A_c$ , can be found from the size of the field-of-view and the relative aperture of the collecting optics if the use of a cone channel condenser is assumed. The reduction in detector radius obtained by use of a cone channel condenser is <sup>1</sup>

$$\frac{C}{S} = \frac{1}{2(f/f)}$$

<sup>1</sup> D. W. Williamson, "Cone Channel Condenser Optics," Journal of the Optical Society of America, vol. 42, No. 10, pp. 712-715, October 1952.



where

$C$  = Radius of the detector

$S$  = Radius of the focal plane

$(f/)$  = Relative aperture of the collecting optics

therefore

$$A_c = \pi C^2 = \pi \left[ \frac{S}{2(f/)} \right]^2 = \pi \left[ \frac{\theta_m F}{2(f/)} \right]^2 = \frac{\pi D^2}{4} \theta_m^2$$

The value  $\theta_m$  is the radius of the field-of-view in radians and  $F$  is the focal length of the collecting optics.

The noise equivalent bandwidth,  $\Delta f$ , can be found in the terms of the modulation index,  $M(\theta_m)$ , and the data rate,  $n$

$$\Delta f = 2M(\theta_m) n \quad (E. 3)$$

Substituting for  $A_c$  and  $\Delta f$  in the equation for NEFD gives

$$NEFD = 2 \sqrt{\frac{2}{\pi}} \frac{\theta_m [M(\theta_m) n]^{1/2}}{D^* D \eta} \quad (E. 4)$$

The value of  $D^*$  for a BLIP detector can be found from the equation

$$D^* = D_t^* \frac{(NA)_t}{(NA)} \left[ \frac{\epsilon_{B_t}}{\epsilon_B} \right]^{1/2}$$

which compares the BLIP  $D^*$  in the telescope in question to that under test conditions.  $(NA)_t$  and  $(NA)$  are the numerical aperture under test and operational conditions respectively.  $\epsilon_{B_t}$  and  $\epsilon_B$  are the background emissivities, and  $D_t^*$  is the peak value of specific detectivity measured under test conditions. It has been assumed, as is proper in a cone condenser system, that only thermal energy from the mirrors reaches the detector. This is a good assumption if the cone condenser is cooled to detector temperature.

Therefore Equation (E. 4) becomes

$$NEFD = 2 \sqrt{\frac{2}{\pi}} \frac{\theta_m [M(\theta_m)_n]^{1/2} (NA) \epsilon_B^{1/2}}{D_t^* (NA)_t \epsilon_{B_t}^{1/2} D_\eta} \quad (E. 5)$$

Without the cone channel condenser

$$NEFD = 4 \sqrt{\frac{2}{\pi}} \frac{\theta_m (f/\eta) [M(\theta_m)_n]^{1/2}}{D^* D \eta_1 \eta_2} \quad (E. 6)$$

Using the equation for BLIP  $D^*$ , this equation becomes

$$NEFD = 2 \sqrt{\frac{2}{\pi}} \frac{\theta_m \epsilon_B^{1/2} [M(\theta_m)_n]^{1/2}}{D_t^* (NA)_t \epsilon_{B_t}^{1/2} D \eta_1 \eta_2} \quad (E. 7)$$

which differs from Equation (E. 5) by the factor  $1/NA$ . For an  $f/3$  system, therefore, the NEFD with cone condenser is a factor of six smaller than that without, provided comparable optical efficiencies can be maintained. Generally the optical efficiency with cone condenser is lower than that without so that a net improvement of less than a factor of three can be expected.

Assuming the following values

$$\begin{aligned}\theta_m &= 4 \text{ mrad} & D_t^* &= 3.2 \times 10^{10} \text{ cm sec}^{-1/2} \text{ watt} \\ M(\theta_m) &= 2 & \eta &= 0.2 \text{ with cone channel condenser} \\ f/3 & & \eta &= 0.5 \text{ without cone channel condenser} \\ n &= 50 \text{ sec}^{-1} & (NA)_t &= \sin 30 \text{ degrees} \\ \epsilon_B &= 0.04 \\ \epsilon_{B_t} &= 1.0\end{aligned}$$

the NEFD with and without the cone channel condenser can be plotted (see Figure E-1).

### 3. CALCULATION OF THE NEED OF A REFLECTED SUNLIGHT TRACKER USING A PHOTOMULTIPLIER DETECTOR

Equation (E. 2) can be rewritten in terms of  $(NEP)^*$  the noise equivalent power per unit bandwidth.

$$NEFD = \frac{4\sqrt{\Delta f} (NEP)^*}{\delta_1 \delta_2 \pi D^2} \quad (E. 8)$$

$\delta_1$  and  $\delta_2$  are the optical and electronic efficiencies of the system respectively. Here again the noise equivalent bandwidth is given by Equation (E. 3). The value of  $(NEP)^*$  for a photomultiplier in the background limited or shot-noise limited state is proportional to the square root of the cathode current in the photomultiplier. The cathode current is in turn proportional to the amount of radiation falling on the photocathode, a function of the effective aperture area and the field-of-view of the optical system.

$$(NEP)^* = K \left[ \delta_1 \left( \frac{\pi D^2}{4} \right) (\pi \theta_m)^2 \right]^{1/2}$$

\*D. W. Williamson, "Cone Channel Condenser Optics," Journal of the Optical Society of America, vol. 42, No. 10, pp. 712-715, October 1952.

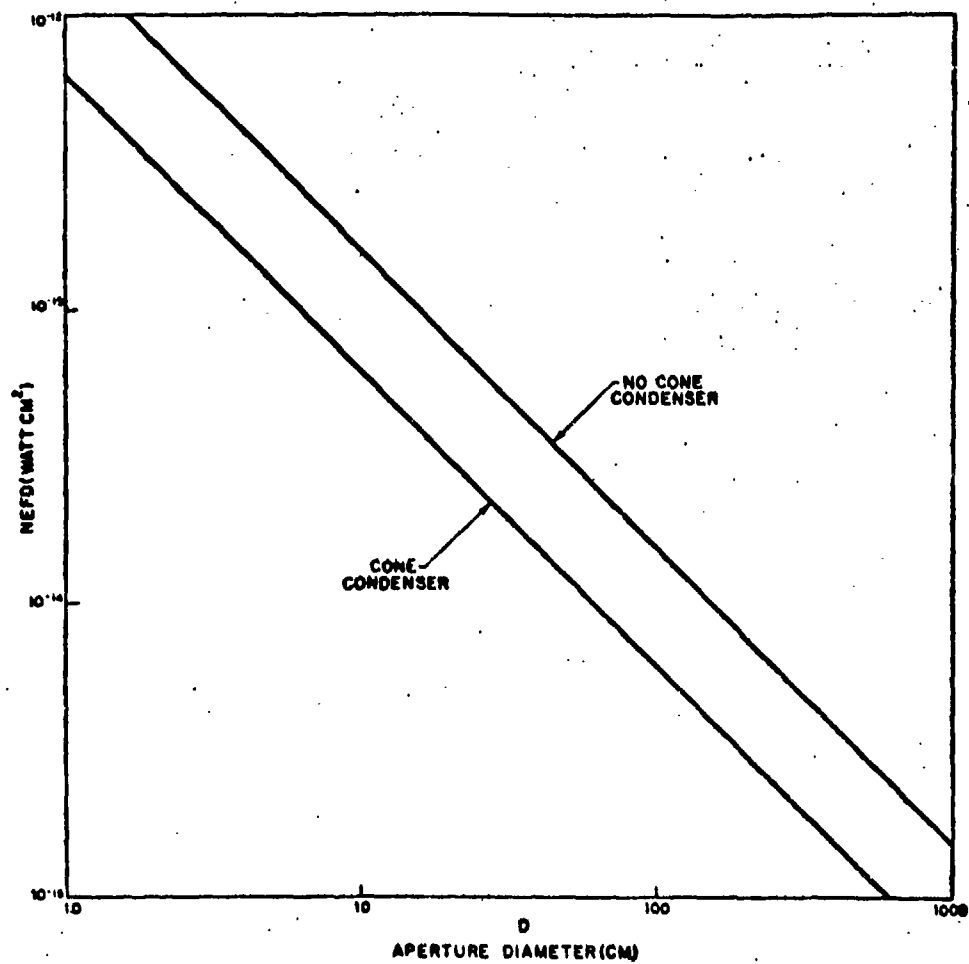


Figure E-1. Noise Equivalent Flux Density Versus Aperture Diameter for Thermal Tracker

The value of K for a 7265 photomultiplier with the night sky as a background is  $3.86 \times 10^{-13} \text{ watt cm}^{-1} \text{ ster}^{-1/2} \text{ cps}^{-1/2}$ .

$$\text{NEFD} = \frac{2K [2M(\theta_m)_n]^{1/2} \theta_m}{\delta_1^{1/2} \delta_2 D} \quad (\text{E. 9})$$

Equation (E. 9) is plotted versus the aperture diameter, D, in Figure E-2.

#### 4. ACQUISITION NEFD

During the acquisition procedure, the tracker telescope will be scanned to cover, in a methodical fashion, the whole ephemeris error volume. The output of the preamplifier will be compared to a fixed threshold and the scan will continue until signal exceeds the threshold. This method is an example of the Neyman-Pearson test of statistical hypotheses in which a threshold is set at a fixed threshold-to-noise ratio determined by an acceptable false alarm rate or probability. The probability of detection of such a test is a function of the excess of signal over threshold in units of rms noise. The rms noise in terms of flux density, the NEFD, must be known before the threshold can be set or the probability of detection determined.

The NEFD is best given for this purpose in terms of the solid angle per channel per second searched during acquisition,  $N \frac{\Omega}{NT}$ . T is the dwell time of the telescope on a point target, N is the number of detector channels, and  $\Omega$  is the instantaneous field-of-view of the telescope. In order to obtain the best possible results during acquisition, given the tracking optics and detector, a separate matched filter preamplifier of bandwidth  $\Delta f$  will be used and

$$\Delta f = \frac{1}{2T}$$

In general this bandwidth will be narrower than that required for the frequency modulation carrier so that the reticle will not be used.

Equation (E. 8) for the photomultiplier case can be re-evaluated using this expression for the noise equivalent bandwidth.

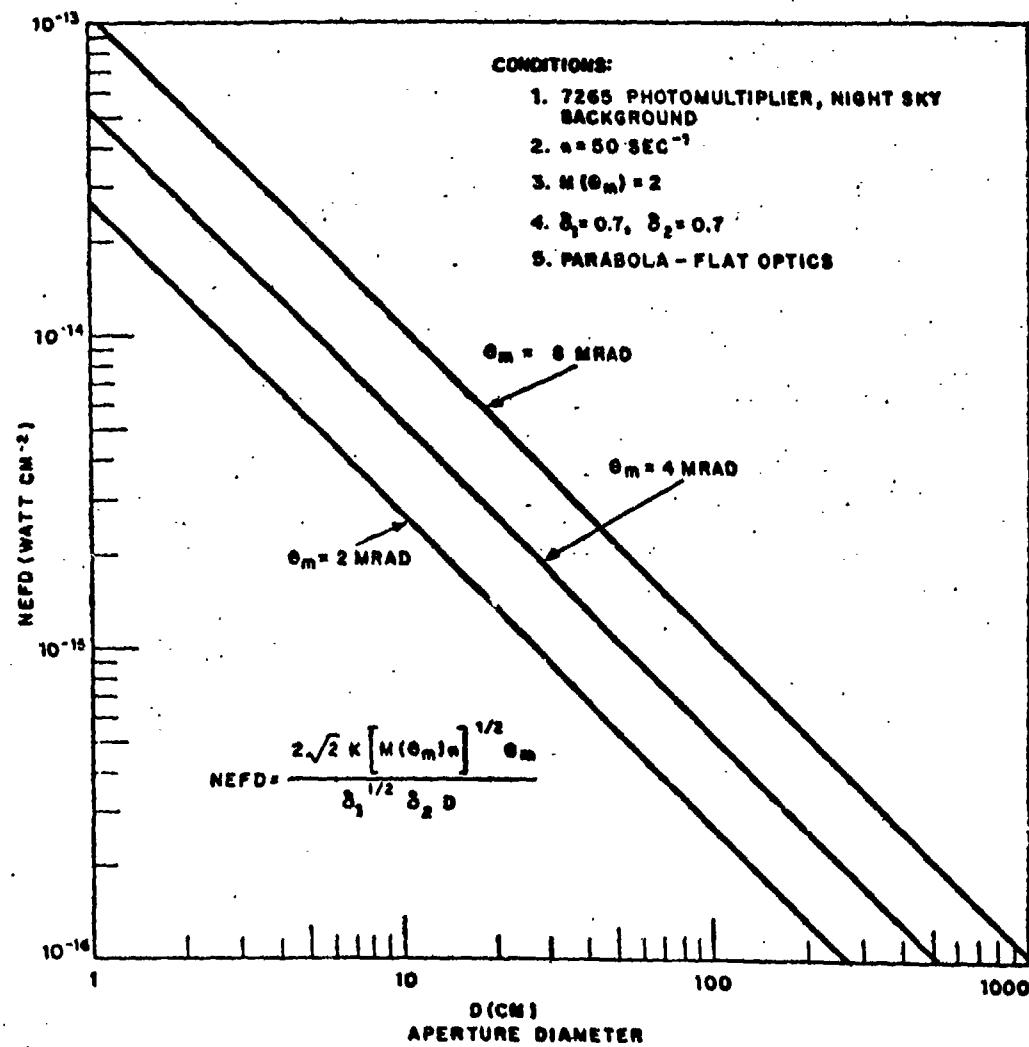


Figure E-2. Noise Equivalent Flux Density for Photomultiplier Tracker Versus Aperture Diameter

$$NEFD = \frac{\sqrt{2K} \sqrt{\frac{\Omega}{NT}}}{\delta_1^{1/2} \delta_2 D} \quad (E. 10)$$

A similar expression can be obtained for the case of a copper-doped germanium detector and cone channel condenser optics using Equation (E. 2) and the equations

$$\Delta f = \frac{1}{2T}$$

and

$$A_c = \frac{\pi D^2}{4} \theta_m^2 = \frac{D^2}{4} \Omega$$

the expression is

$$NEFD = \frac{\sqrt{2} \sqrt{\frac{\Omega}{NT}}}{D_t^* D \eta} \frac{(NA)}{(NA)_t} \left[ \frac{\epsilon_B}{\epsilon_{B_t}} \right]^{1/2} \quad (E. 11)$$

Equations (E. 10) and (E. 11) can be used to determine the peak signal-to-rms-noise ratio at acquisition as a function of solid angle searched per second. The noise at the amplifier output, that at the output of a narrowband linear system, is Gaussian. Hence the false alarm probability and detection probability are easily determined.

## APPENDIX F

### THE EFFECTS OF EARTHSHINE ON TARGET INTENSITY

#### 1. CASE OF A DIFFUSE REFLECTING SPHERICAL SATELLITE

Consider the target-interceptor geometry of Figure F-1. If it is assumed that the interceptor altitude is roughly the same as that of the target, and if acquisition begins at a target-interceptor range of 50 to 100 n mi, then  $P \approx \pi/(2 \pm \beta)$  in the cases of interest. Cunningham<sup>1</sup> has calculated the total reflection radiation on a satellite taking the solar constant as 0.1353 watt/cm<sup>2</sup> and the earth's albedo as 0.34. Looking at the case for  $P = 90$  degrees, at an altitude of 100 n mi, one can use Equation (F. 1)

$$W = \frac{2}{3} \gamma H \left[ (2r + 1/r^2) - (2 - 1/r^2) (r^2 - 1)^{1/2} \right] \cos \beta \quad (\text{F. 1})$$

where

$H$  = Solar constant

$\gamma$  = Earth albedo

$r$  = Target radius from earth center in units of earth radius

$\beta$  = Sun angle from target satellite earth perpendicular

For the parameters stated above

$$W = 90 \text{ milliwatts/cm}^2$$

The area over which the irradiance,  $W$ , is applied is the projected area of a spherical satellite as seen from a point on the earth. The irradiance,  $W$ , is sizable compared to the solar constant of 140 mw/cm<sup>2</sup> even considering the fact that the reflected radiation is nonuniformly distributed over most of the satellite surface, rather than over a hemisphere as in the case of direct solar illumination.

<sup>1</sup>F. G. Cunningham, "Earth Reflected Solar Radiation Input to Spherical Satellites," ARS Journal, 32, 7 (July, 1962)



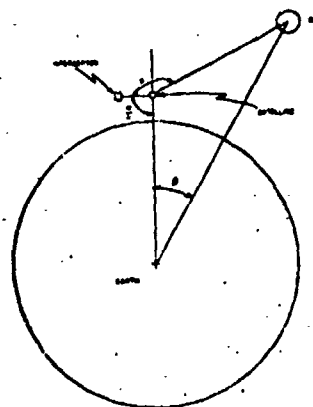


Figure F-1. Geometry for Determining the Effect of Earthshine

To determine how much of this radiation is received by the tracker in the interceptor, some approximations may be made. To a first approximation the earth reflected radiation can be assumed to produce uniform illumination over the lower hemispherical surface of the spherical satellite.

Under this assumption the earth albedo acts as a secondary solar source and for  $P = 90$  degrees, it illuminates the satellite hemisphere away from the sun. Therefore, referring to Figure 5-4, it can be said that the effective irradiance will be increased by a factor of

$$\frac{90 \text{ mw/cm}^2}{H} = \frac{90}{140} = 64 \text{ percent}$$

Although this is an appreciable increase, it applies only to the best conditions for earthshine target illumination. Twilight or night conditions directly below the satellite greatly decrease the effects of earthshine. Furthermore, for larger values of  $P$  when solar reflected radiation is low and earthshine would really be helpful, the earthshine tends to be very low also.

## 2. CASE OF A SPECULAR REFLECTING SATELLITE HAVING PLANE SURFACES

A difficult satellite shape to detect, considering only direct solar illumination, is a rectangular solid having specularly reflecting plane surfaces. Such a vehicle produces irradiance at the interceptor only for certain discrete geometries if the sun alone is considered as light source. The presence of earthshine, however, causes the problem to become much more tractable.

Consider the simple case of the plane side of a satellite which acts as a specular reflector. The image of the earth seen in this reflector has a radiance  $N_{\text{eff}}$  where

$$N_{\text{eff}} = \frac{\rho \gamma H}{\pi}$$

In this equation

$\rho$  = Reflectivity of the surface

$\gamma$  = Albedo of the earth

$H$  = Solar constant

The image occupies a solar angle,  $\omega$ , as seen by an observer at the interceptor of

$$\omega = \frac{\alpha A_T}{R^2} \text{ steradians}$$

$A_T$  is the projected area of the satellite and  $\alpha$  is the fraction represented by the effective surface (that in which the earth's image can be seen).

The effective irradiance at the tracker entrance aperture is then

$$H_{\text{eff}} = \frac{\alpha \rho \gamma H A_T}{\pi R^2} \quad (\text{F. 2})$$

Certain assumptions are contained in Equation (F. 2). First, that the projected surface area of the satellite has a plane portion reflecting the earth in a specular manner, and second, that the amount of satellite effective area is known and is  $\alpha A_T$ . The geometry is shown in Figure F-2.

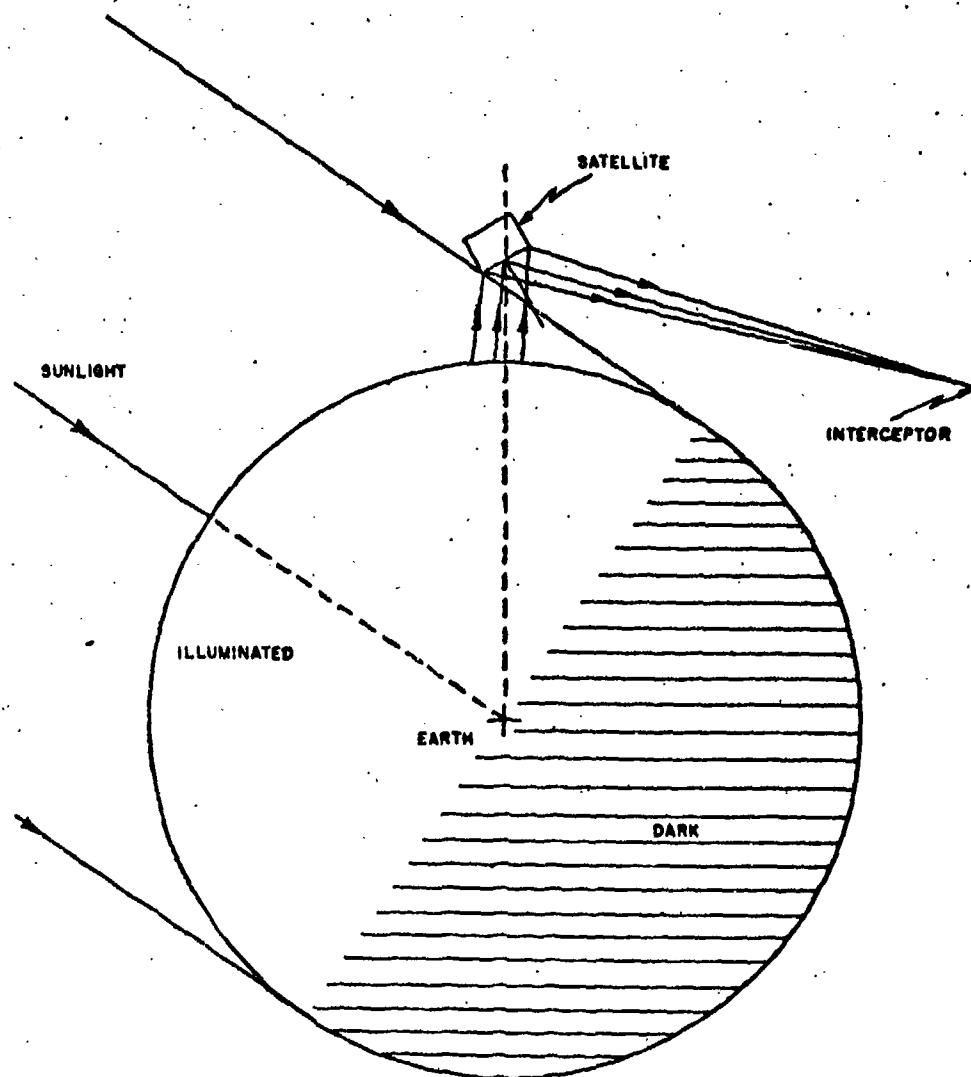


Figure F-2. Geometry Showing Plane Specular Satellite Surface Reflecting Earthshine

Figure F-3 shows the values of  $H_{eff}$  for an S-20 photocathode as functions of  $R$  and  $\rho A_T$  provided there is no direct sunlight reflected by the satellite. This may be compared with the values for a diffuse spherical reflector given in Figure 5-4.

If  $\rho A_T$  equals  $1 \text{ m}^2$  and  $R$  equals 100 n mi, then the plane specular reflector gives  $H_{eff}$  equaling  $1.5 \times 10^{-13}$  S-20 effective watt/cm<sup>2</sup> while the diffuse sphere gives  $H_{eff}$  equaling  $8.5 \times 10^{-14}$  S-20 effective watt/cm<sup>2</sup> for a 90-degree phase angle.

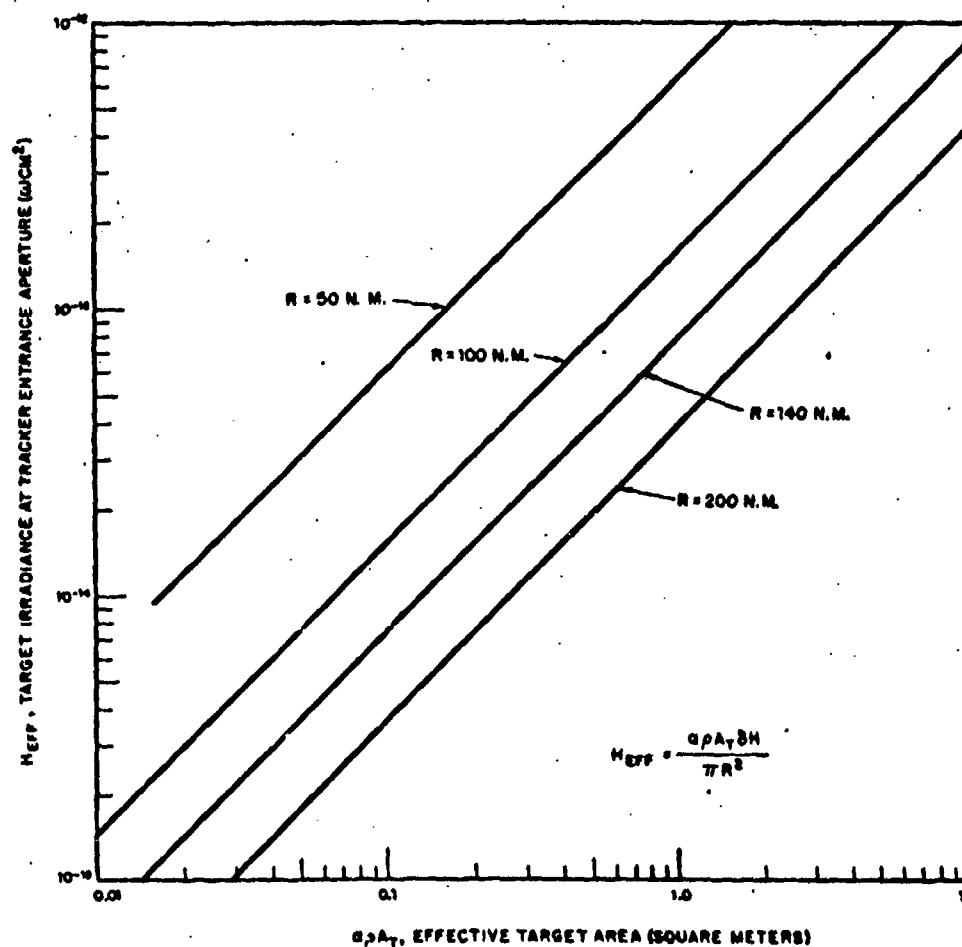


Figure F-3. Effective Irradiance Produced by Earth-Reflected Sunlight From a Plane Specular Surface on a Satellite (S-20 Photocathode)

## APPENDIX G

### TRACKER ACCURACY AS A FUNCTION OF TELESCOPE APERTURE DIAMETER

In order that the satellite interceptor vehicle be capable of a reasonable value of miss distance, specifications must be placed on the angular accuracy of target location of which the tracker is capable. In this particular system the tracker must provide data accurate enough to permit a measurement of the target angular rate with a one sigma accuracy of 0.5 milliradian/second.

The rms angular rate error  $\sigma_\omega$  is related to the low frequency spectral density of angle noise  $Q_0$  and servo filter time lag  $T$  by the equation for a second order lowpass filter

$$\sigma_\omega = \sqrt{\frac{Q_0}{T^3}}$$

The value of low frequency spectral density of angle noise can, of course, be found from the rms angle noise  $\sigma_\theta$  and the noise equivalent bandwidth  $\Delta b$  of the second order filter.

$$\sigma_\theta = \sqrt{Q_0 \Delta b} = \sqrt{Q_0 \frac{T}{4}}$$

Therefore, the relation between rms angle noise and angle rate noise is

$$\sigma_\theta = \frac{\sigma_\omega T}{2} \quad (G.1)$$

For  $T = 0.5$  sec and  $\sigma_\omega = 0.5$  milliradian per second

$$\sigma_\theta = 0.125 \text{ milliradian}$$

This, then, is the angular accuracy required of the tracker.

For the purposes of this discussion, a frequency modulation tracker operating in the large signal mode will be assumed. The angular accuracy for this case is\*

$$\sigma_{\theta} = \left[ \theta_m \frac{2\pi}{M(\theta_m)} \right] \left[ \frac{(NEP)^* (\Delta b)^{1/2}}{P_D} \right] \quad (G.2)$$

In this equation

$\theta_m$  = the radius of the field of view (radians)

$M(\theta_m)$  = the modulation index

$(NEP)^*$  = the noise equivalent power per unit bandwidth (watt cps<sup>-1/2</sup>)

$\Delta b$  = the servo bandwidth (cps)

$P_D$  = the power falling on the detector (watt)

The bracketed quantity in Equation (G.2) can be expressed in terms of the signal and noise at the intermediate frequency amplifier output.

$$\frac{(NEP)^* (\Delta b)^{1/2}}{P_D} = \left[ \left( \frac{S}{N} \right)_{IF} \left( \frac{\Delta f}{\Delta b} \right)^{1/2} \right]^{-1}$$

and

$$\left( \frac{S}{N} \right)_{IF} = \frac{H_{eff}}{(NEFD)}$$

where both  $H_{eff}$  and NEFD have been discussed above and in Appendix E for various targets and detector-optics combinations. Equation (G.2), with these substitutions, becomes

$$\sigma_{\theta} = \theta_m \frac{2\pi}{M(\theta_m)} \left[ \frac{\Delta b}{\Delta f} \right]^{1/2} \frac{(NEFD)}{H_{eff}} \quad (G.3)$$

\* Appendix B, First Semi-annual Technical Report, Signal Modulation Techniques, Space Technology Laboratories, Inc., 24 April 1961, Contract AF04(647)643, Task C.

In Sections 1 and 2, this equation will be evaluated for the thermal target and reflected light target cases, and graphs will be plotted showing the aperture diameter required for a given field of view,  $\theta_m$ , and angular accuracy,  $\sigma_\theta$ .

### 1. THERMAL TRACKER ACCURACY

It has been shown in Appendix E that the NEFD for a thermal tracker using a copper-doped germanium detector at 4.2°K is given by the equation

$$\text{NEFD} = 2 \sqrt{\frac{2}{\pi}} \frac{\theta_m [M(\theta_m)n]^{1/2} (NA)_B \epsilon_B^{1/2}}{D_t^* D \delta_1 \delta_2 (NA)_t \epsilon_{B_t}^{1/2}} \quad (\text{G. 4})$$

Also, it has been shown the available effective flux from a thermal target is

$$H_{\text{eff}} = \frac{\epsilon A_T}{R^2} N^* \quad (\text{G. 5})$$

where

$$N^* = \frac{1}{\pi} \int_0^\infty \frac{D^*(\lambda)}{D_{\text{max}}^*} F(\lambda) W(\lambda, T) d\lambda \quad (\text{G. 6})$$

Substituting Equations (G. 4) and (G. 5) in Equation (G. 3) and solving for the aperture diameter,  $D$ , gives

$$D = \frac{4\pi^{1/2} (\Delta b)^{1/2} \theta_m^2 R^2}{\sigma_\theta M(\theta_m) D_t^* N^* \delta_1 \delta_2} \left[ \frac{1}{\epsilon A_T} \right] \left[ \frac{(NA)_B \epsilon_B^{1/2}}{(NA)_t \epsilon_{B_t}^{1/2}} \right] \quad (\text{G. 7})$$

This equation is shown in Figure G-1 with  $D$  plotted as a function of  $\epsilon A_T$ , the effective target area.

### 2. REFLECTED SUNLIGHT TRACKER ACCURACY

If the tracker operates in the visible region of the spectrum against solar illuminated targets, Equation (G. 3) can again be evaluated using the appropriate values of effective flux and NEFD as derived in Section 2 and Appendix E.

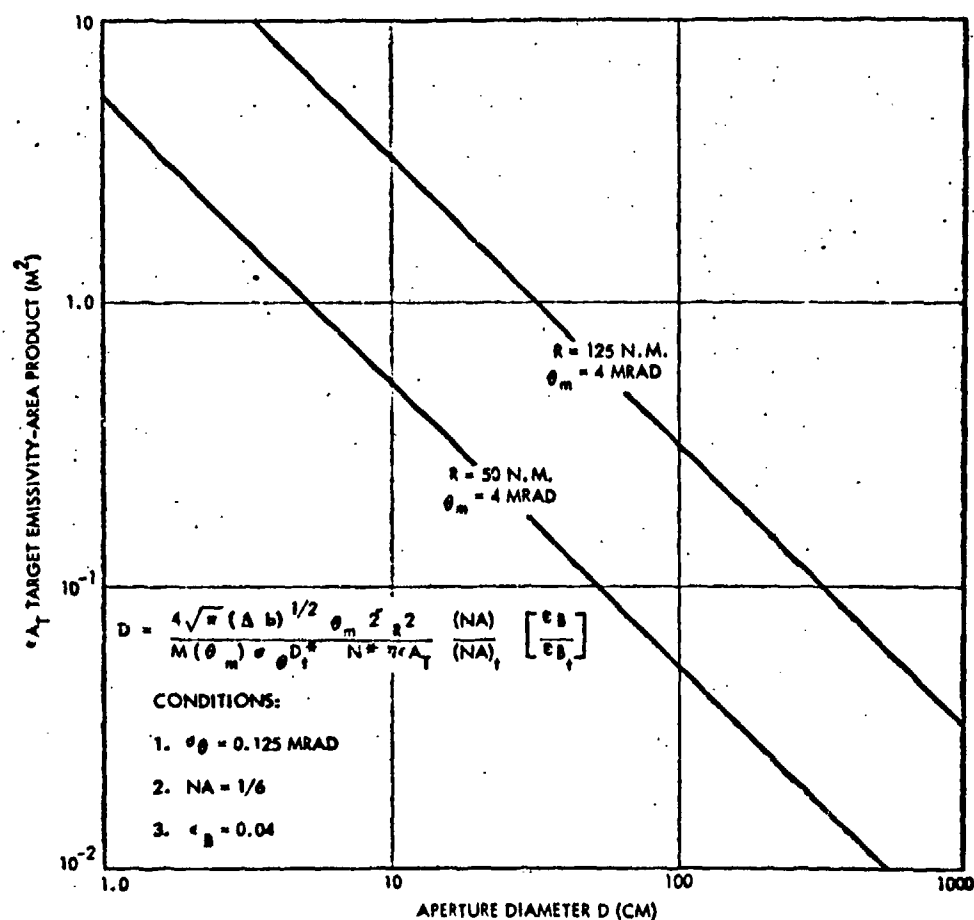


Figure G-1. Aperture Diameter for Single Channel FM Tracker with Cone Condenser versus Target Effective Area for Thermal Target, Ge:Cu Detector and 0.125 Milliradian Tracking Accuracy



These values are

$$H_{\text{eff}} = \frac{2H\rho A_T}{3\pi^2 R^2} [\sin P + (\pi - P) \cos P] \quad (\text{G. 8})$$

and

$$\text{NEFD} = \frac{2K [2M(\theta_m)n]^{1/2} \theta_m}{\delta_1^{1/2} \delta_2 D} \quad (\text{G. 9})$$

Replacing  $H_{\text{eff}}$  and NEFD in Equation (G. 3) with the values given by Equations (G. 8) and (G. 9) leads to an equation for the diameter of the required telescope if an angular accuracy  $\sigma_\theta$  is desired.

$$D = \frac{6\pi^3 (\Delta b)^{1/2} \theta_m^2 R^2 K}{\sigma_\theta M(\theta_m) H \delta_1^{1/2} \delta_2} \left[ \frac{1}{\rho A_T} \right] [\sin P + (\pi - P) \cos P]^{-1} \quad (\text{G. 10})$$

This equation, except for various constants, has the same form as Equation (G. 7) which applies to the thermal target case. It is shown with  $D$ , the aperture diameter of the required telescope, plotted versus the effective target area,  $\rho A_T$ , in Figure G-2.

In order to obtain a feeling for the tracking accuracy requirement and to compare the thermal target and reflected sunlight target cases, assume an effective target size of  $0.1 \text{ m}^2$  and a field-of-view of 4-milliradian radius and then examine Figures G-1 and G-2 to determine the required aperture diameters. In order to obtain 0.125-milliradian 1-sigma accuracy at 50 n mi range, the copper-doped germanium range tracker requires an aperture diameter of approximately 50 cm while the S-20 photomultiplier tracker requires only 7 cm. This result is typical when comparing visible spectrum devices against thermal spectrum devices; the sensitivity of detectors in the visible region is greatly superior. However, as shown in the discussion of the background problem in Chapter 5, Paragraph 5.3, there are definite background-rejection advantages in the thermal spectral region. The applicability of a single channel visible spectrum tracker is severely limited by background stars (Section 5). The thermal target tracker is limited only by target strength and detector sensitivity. If a

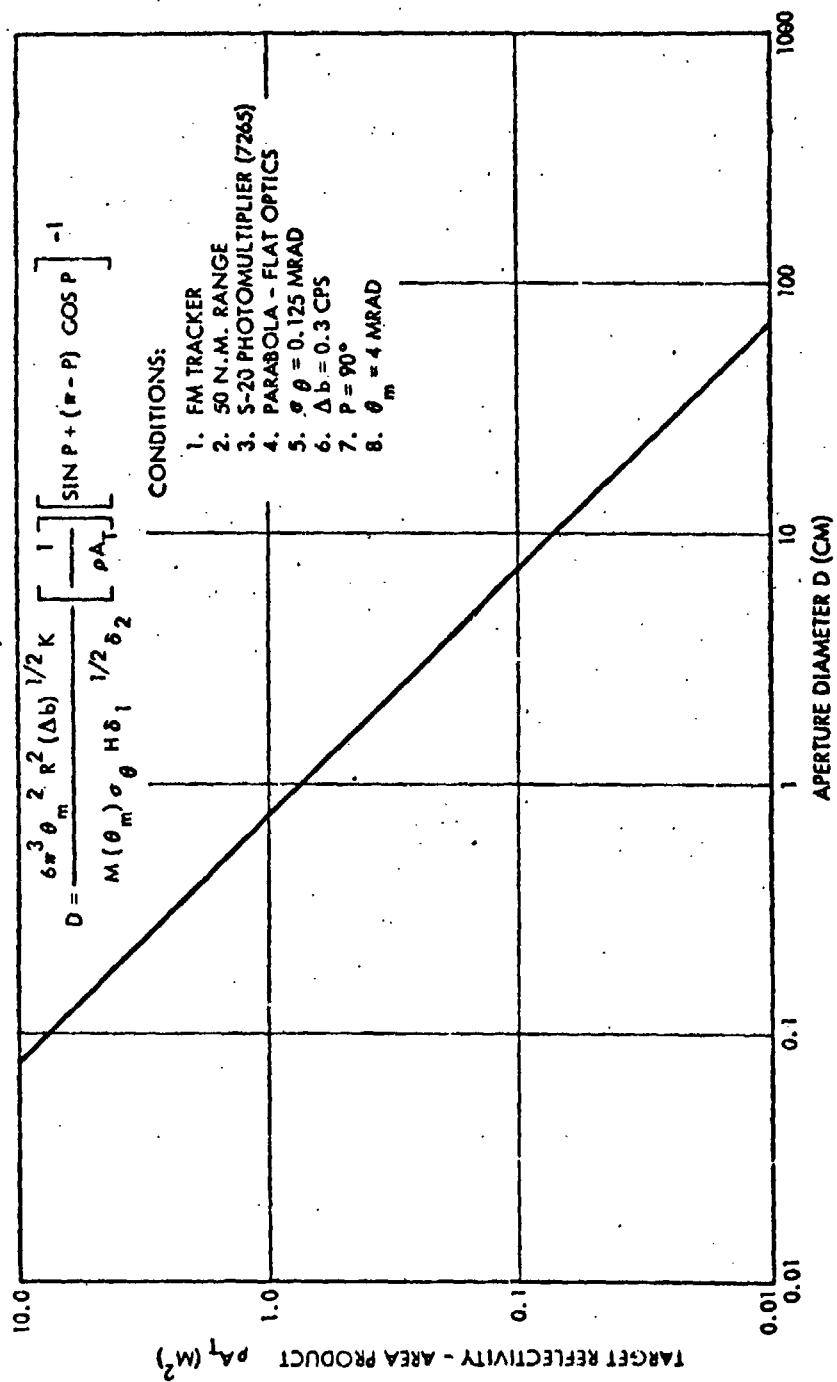


Figure G-2. Required S-20 Photomultiplier Tracking Telescope Aperture Diameter versus  $\rho_A$  for Spherical Diffuse Reflecting Target in Sunlight

30-cm aperture diameter is the largest that can be accommodated by the interceptor vehicle, and if acquisition occurs at 125 n mi, Figure G-1 shows that all thermal targets having effective area more than  $1.0 \text{ m}^2$  can be tracked successfully.

Since a  $5 \text{ m}^2$  effective area target is the largest described by the ARPA Program Guide, the conventional thermal target tracker is not severely limited during track phase. More ramifications in the comparisons of thermal and reflected sunlight track sets will be discussed in the following sections where the problem of target acquisition is examined.

## APPENDIX H

### TYPICAL TARGETING PROGRAM MODIFICATIONS

In essence, the Titan Operational Targeting Program (TOTP) is a digital computer program which has been developed for an IBM 7090 computer to accomplish the weapon system targeting functions that are computer-oriented. The principal targeting function of the TOTP is to generate target tapes which contain the necessary trajectory-dependent information required by the missileborne digital computer in its ground and inflight programs. The Normal Targeting Mode (described below) is the major subdivision of the TOTP which is programmed to accomplish this targeting function.

Several auxiliary targeting functions are mechanized in the three remaining modes of the TOTP. The Target Tape Re-evaluation Mode is designed to re-evaluate existing target tapes and to recommend re-targeting if the existing target tape is unacceptable or cannot be simply modified. The two other auxiliary modes, Sector of Fire Mode and Range Safety Normal Mode, should be combined to generate intercept volumes which satisfy missile, homing stage, and range safety constraints. Once a volume is generated, it should be used in the mission analysis prior to actual missile targeting.

#### 1. NORMAL TARGETING MODE (NTM)

The NTM is the means by which target tapes are generated. Given a launch/target combination, a trajectory must be shaped and optimized; data are then taken from this trajectory to generate all of the launch/target dependent guidance constants. These constants must be verified, placed on magnetic tape in a suitable format, and this tape must then be verified.

The principal part of the TOTP is the Flight Simulation Program (FSP) which generates trajectories (both open and closed-loop). It represents the mathematical model of the missile, its guidance, and its environment (atmospheric and gravitational models). Changes to the FSP are relatively minor. The missile model itself may vary slightly in weight, moment of inertia, and center of gravity but should only alter constants in the present

equations or tables. The re-entry portion of the simulation may be eliminated except for range safety, and it will be desirable to redefine the miss coordinate system. None of these changes present any difficulty.

The Trajectory Shaping and Optimization Subprogram (SOS) iterates (using the FSP) to find an open-loop trajectory for a specified launch/target combination which satisfies the constraints of ascent aerodynamic heating, re-entry, decoy ejection, etc. This subprogram will require major revisions for the SIS mission. Two of the constraints (attitude for decoy ejection and re-entry attitude) are no longer required and the target seeker as written is not applicable to the SIS mission. This subprogram probably should be completely rewritten. The basic outline of a new subprogram, as presented below, retains those constraints essential to the SIS mission.

The target seeker is the mode by which an open-loop, zero lift trajectory is obtained which impacts the target. Variables which affect this trajectory for Titan II are launch azimuth,  $\alpha$ ; kick angle,  $\epsilon$ ; enter-flight mode time,  $t_L$ ; sustainer engine cutoff time,  $t_{seco}$ ; sustainer pitch rate,  $\omega_{ps}$ ; and time of flight,  $\tau$ . These parameters are not entirely arbitrary but are constrained to satisfy certain physical limitations. The azimuth direction will be constrained by range safety requirements and will be reflected in the intercept volume. In addition, the attack geometry may be further constrained because of degradation of homing stage performance at very high closing velocities. Neglecting the closing velocity problem, preliminary azimuth limits may be set by observing where the satellite trajectory crosses the envelope capability. Bounds are also placed on time of flight based on when the satellite enters and leaves the volume.

Another constraint is aerodynamic heating which is a function of kick angle and azimuth. The range probability constraint essentially sets an upper bound on  $t_{seco}$  such that a probability of mass depletion before  $t_{seco}$  is some desired value. This value of  $t_{seco\max}$  may be precomputed, as it is not trajectory dependent. The sustainer pitch rate is constrained because of engine deflection angle and structural constraints and is known a priori.

An open-loop, zero lift trajectory is simulated with the simulation terminated on  $\tau^0$ , when the superscript  $0$  refers to the initial guess for  $\tau$ . The miss is then computed. Each dependent variable is perturbed slightly, one each simulated flight, to calculate the miss sensitivities. New values for the dependent variables are then computed, based on the miss sensitivities and the original values of these variables. Another trajectory is flown using new values of the dependent variables and the miss is again computed. If it is smaller than before, convergence appears likely, and the process repeated until an acceptable limit is achieved using the new "miss" and new values of the dependent variables rather than the initial values. If, at any point, convergence does not appear likely, the free parameters must be varied. The derivatives may not need to be recalculated, however.

When an acceptable miss is achieved, the resultant open-loop trajectory serves as an input to the Guidance Constants Generator Subprogram (GCGS). The GCGS takes the trajectory information from the SOS and generates the inflight guidance constants. Basically, very minor revisions are expected to this subprogram.

First, the issuance of some discretes (e. g., decoy ejection) will be eliminated, and some re-entry vehicle velocity compensations will be changed since the homing stage will replace the present warhead. Another possible change is in the number of perturbations needed to obtain the velocity-required least squares polynomial and in the number of terms necessary in this polynomial. This requirement must be evaluated thoroughly before a targeting program can be developed, but no fundamental changes are expected in the guidance equations or in the targeting computation philosophy.

Once a nominal closed-loop trajectory has been obtained, the homing stage parameters must be generated. This merely amounts to calculating the time from  $t_L$  to the time of acquisition and the homing stage attitude required at acquisition.

When all the guidance constants have been generated, the TOTP currently converts them to the format of the flight computer, verifies the conversion process, writes the constants on magnetic tape, and then verifies the tape writing.

Since direct communication may exist between the targeting center and the launch site for the SIS mission, this subprogram may have to be altered to write a magnetic tape compatible with the communication system. No difficulties are expected in making this modification.

## APPENDIX I

### STRUCTURAL CONSTRAINTS ON MINUTEMAN TRAJECTORIES

#### 1. SUMMARY

The purpose of this appendix is to present the results of a preliminary evaluation of the structural integrity of the Wing II and Wing VI Minuteman systems with three different homing stage configurations. The object of the study was to establish trajectory constraints for each configuration on the basis of the maximum allowable dynamic pressure. Such constraints were determined so that the altitude wind induced loads on the Minuteman booster systems would not exceed their existing structural capabilities.

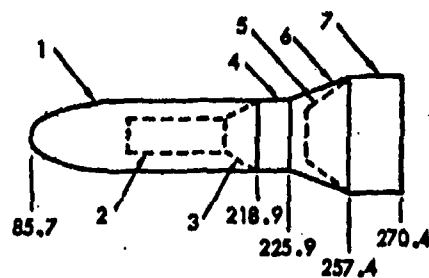
The general conclusions are that 1) the homing stage with the large radar sensor configuration enclosed in the 133 inch ogive fairing has a severe trajectory constraint and therefore is not a feasible configuration without a major structural redesign of the Minuteman boost vehicle; and 2) both the small radar sensor configuration and the electro-optical sensor configuration in the 119 inch cone-cylinder fairing have reasonable trajectory constraints and would require no structural modifications. These results are based on the Minuteman weapon system 99 percent wind criteria and the existing control system design.

#### 2. ANALYSIS

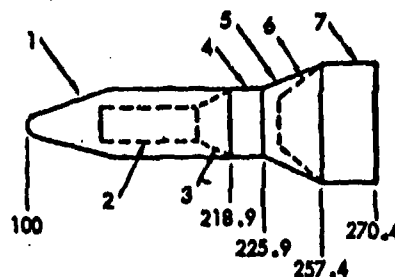
The three homing stage configurations studied are illustrated in Figure I-1 along with the mass and aerodynamic data. The aerodynamic properties for the Wing II Minuteman boost vehicle were extracted from Reference 1.

A complete parametric trajectory study including the effects of altitude winds was not accomplished for this analysis, rather, the results of existing no wind trajectory studies were used. The no wind trajectory parameters at the time of maximum dynamic pressure are shown in Figure I-2 for a Wing II missile with a 1500 pound payload. These parameters are not appreciably changed by introduction of the critical crosswind effects. The resulting yaw plane angle-of-attack was computed as a





CONFIGURATION A  
LARGE RADAR SENSOR



CONFIGURATION B  
SMALL RADAR SENSOR

CONFIGURATION C  
ELECTRO-OPTICAL SENSOR

#### MASS DATA

ITEM	SECTION	CONFIGURATION	WEIGHT	CENTER OF GRAVITY
1	NOSE FAIRING	A	252	151.7
		B	217	169.0
		C	217	169.0
2	PAYLOAD	A	1290	151.7
		B	961	169.0
		C	597.4	176.0
3	PAYLOAD ADAPTER		21	213.0
4	R AND D WAFER		50	222.4
5	G AND C SECTION		67	241.9
6	G AND C EQUIPMENT		253.1	242.7
7	3RD STAGE SKIRT		21.1	264.7

#### AERODYNAMIC DATA

ITEMS	SECTION	CONFIGURATION	$C_{N_d}$ X AR	CENTER OF PRESSURE	$C_A$ X AR
1 AND 4	NOSE TO 226	A	0.308	130.7	2.014
		B AND C	0.2895	147.5	1.68
5 AND 7	226 TO 270		0.146	248.2	0.136

Figure I-1. Configurations, Mass and Aero Data

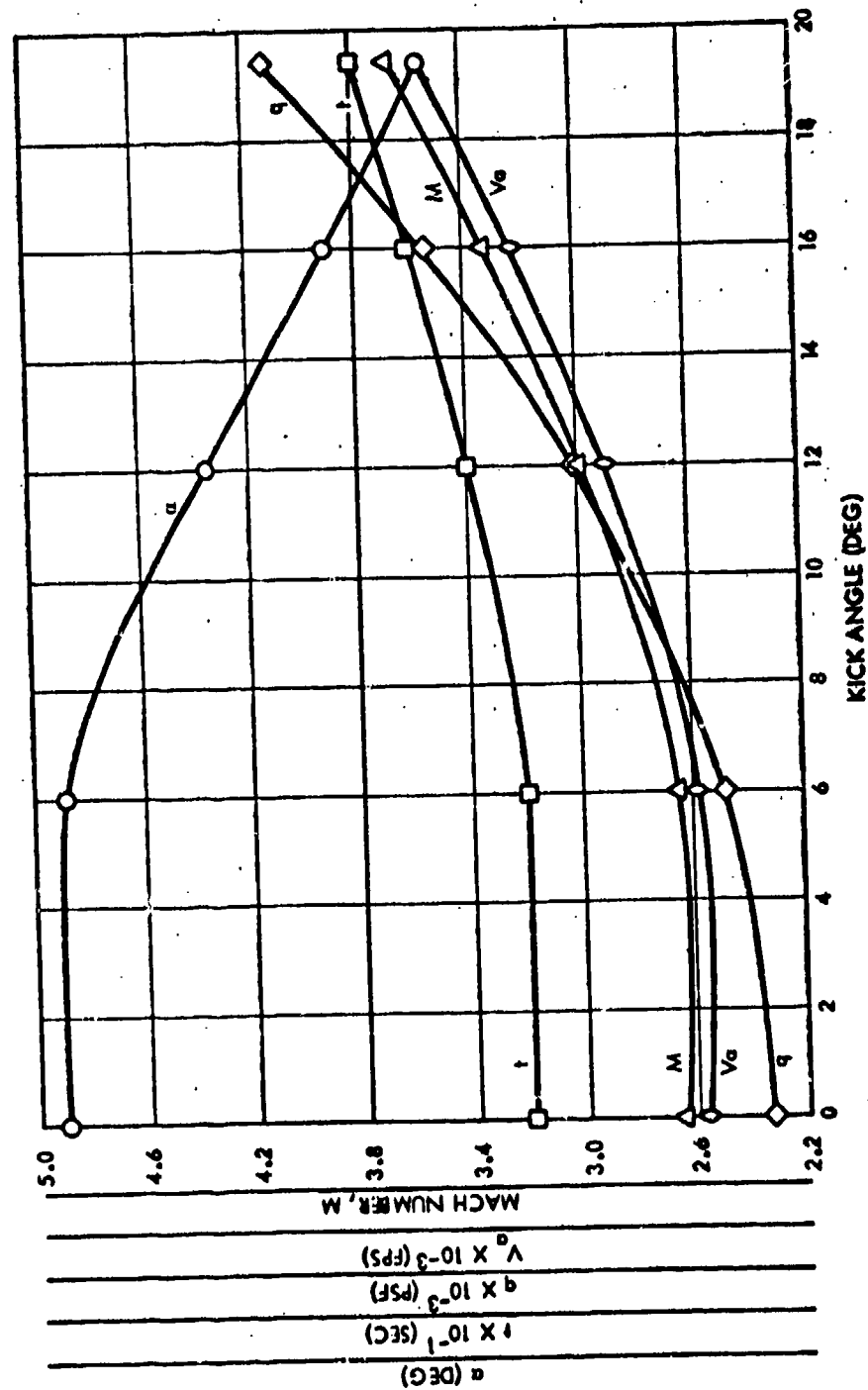


Figure 1-2. Trajectory Parameters at Max  $q$  for a Wing II Minuteman with a Payload of 1500 Pounds

function of the wind velocity and the missile relative velocity after correction for drift. The missile drift velocity with the Minuteman wind criteria was assumed to be 80 ft/sec at maximum  $q$ , which is typical for a Wing II missile. The calculated yaw plane angle-of-attack is also shown in Figure I-2 as a function of the trajectory initial kick angle. These data were assumed to be essentially the same for the Wing VI configurations.

By incorporating the angle-of-attack, drag, thrust, axial acceleration and lateral acceleration (assuming a trimmed missile), structural loads were calculated at maximum  $q$  for various kick angles. These loads were determined for the Minuteman structure at two critical stations: 1) the top of the guidance and control section (Station 226), and 2) the forward tangent line of the third stage engine (Station 270). By comparing these loads with the existing vehicle structural capabilities, it was possible to estimate the trajectory kick angle constraints and the associated maximum dynamic pressures. These results are summarized in Table I-1. The associated design conditions are defined in Table I-2 for each of the homing stage configurations.

It should be noted that the allowable dynamic pressures defined in Table I-1 are based on the Minuteman 99 percent wind criteria and the existing control system. More severe trajectories may be tolerated if the wind criteria were relaxed. Also, the analyses were based on dispersed Minuteman design trajectories which include possible dispersions due to thrust and aerodynamic properties. Thus, each of the allowable  $q$ 's would have to be reduced if a nominal trajectory constraint is desired.

Even if the Wing VI guidance and control section structure were strengthened, the configurations using the large ogive fairing must still be restricted to a 2940 psf maximum dynamic pressure. Such a constraint is not feasible for operational purposes, since the nominal trajectory initial kick angle would be limited to less than 10 degrees. Both configurations using the smaller fairing appear to be feasible, although they are constrained slightly more than the Minuteman weapon systems. The initial kick angle limitations for these configurations would be in the 16 to 17 degree range for a nominal trajectory.

1) Boeing Document, Minuteman Loads Study—Wing II, STL 6120-1737-LS-000 Copy 004, dtd. 10-19-62. (Secret)

Table I-1. Allowable Maximum Dynamic Pressure and Corresponding Angle-of-Attack

		Ogive Fairing		Cone-Cylinder Fairing			
		Large Radar Sensor		Small Radar Sensor		Electro-Optical Sensor	
	Station	Wing II	Wing VI	Wing II	Wing VI	Wing II	Wing VI
Allowable q (psf)	226	5140	2570	6420	4220	6280	4170
	270	2940	2940	4260	4260	4170	4170
Angle-of-Attack (degrees)	226	3.3	4.85	3.3	3.5	3.3	3.5
	270	4.5	4.5	3.5	3.5	3.5	3.5

	Ogive Fairing	Cone-Cylinder Fairing	
	Large Radar Sensor	Small Radar Sensor	Electro-Optical Sensor
Time (sec)	34	38	38
Angle-of-Attack (degrees)	4.5	3.5	3.5
Dynamic Pressure (psf)	2900	4100	4100
Mach Number	3.3	4.1	4.1
Drag (pounds)	12,950	17,000	17,000
Aero. Normal Force (pounds)	16,340	17,800	17,800
Center of Pressure (M <sup>2</sup> Station)	362	369.5	369.5
Weight (pounds)	39,976	36,314	35,950
Center of Gravity (M <sup>2</sup> Station)	519	509	509
Thrust (pounds)	227,000	229,000	229,000
Axial Load Factor (g's)	5.37	5.83	5.9
Lateral Load Factor (g's)	0.664	0.752	0.758

I-25      TABLE I-1  
R.T.

## APPENDIX J

### POLARIS TARGETING ALTERNATIVES

Two types of targeting have been under consideration, the firing table method and the simulation method. Both methods have their advantages and disadvantages, and there appears to be no reason to make a decision between them at this time. Both methods should work for Polaris, and neither should lengthen reaction time. The firing table method requires the transmission of seven parameters to the launch site. If the simulation targeting could be done at the launch site, the transmission burden would be the same; if it could not, less than 20 inflight parameters need be transmitted.

#### 1. FIRING TABLE METHOD

The inflight parameters to be fitted are the initial values of the velocity-to-be-gained  $\vec{V}_g$ , the constants in the Q-matrix, the skew A, the launch azimuth  $\alpha$ , the time of-flight  $\tau$ , and the interceptor velocity  $\vec{V}_H$  at intercept.

A desired intercept surface is defined with respect to the launch point (maximum range for apogee or maximum range satisfying the look-angle constraint). This surface will have an oval shaped horizontal cross section and will not be symmetric with respect to the launch point since there is an initial inertial velocity. Furthermore, the initial inertial velocity varies with latitude, and therefore a surface satisfying certain constraints will vary with latitude. Either the equation of the surface must reflect this, or different surfaces must be generated and assumed to be valid for sectors of latitude. Corresponding to each point on the surface is a latitude, longitude, azimuth, and altitude with respect to the launch point. Each inflight parameter is fitted as a function of these latter variables.

To target a missile, a time of launch,  $t_L^0$ , is chosen to be about minutes prior to the intercept time. The launch point (which is moving) is determined, and the surfaces of intercept fixed with respect to the launch point. The satellite parameters are used to calculate points of interception, if they exist, for each surface. If one exists, then there

exists an absolute time,  $T^0$ , of intercept. A time-of-flight,  $\tau^0$ , can be calculated using the fitted function for  $\tau$ , and  $(T^0 - \tau^0)$  must be equal to  $t_L^0$  for a launch point to be valid. Equality may not exist for  $t_L^0$  since  $\tau^0$  is determined by an equation which is independent of  $t_L$  and  $T$ . Hence, all three quantities are obtained independently and yet dependence must exist. If equality occurs, the missile could then be targeted using these consistent values.

If equality is not obtained, a new value of  $t_L$ , which is an average between  $t_L^0$  and  $(T^0 - \tau^0)$  is used to repeat the above process. Additional iterations may be required. Alternate methods of iteration could be used depending on the constraints.

The values of  $\vec{V}_H$  and  $T$  will be used in conjunction with the target velocity to calculate homing stage acquisition time and attitude when the two objects are some specified distance apart.

The number of surfaces used for targeting is a tradeoff between more surfaces and the additional precomputation and data storage loads. However, at least two surfaces may be used - one representing maximum range for apogee attack, and the other maximum altitude as a function of range, both of which must satisfy the look angle constraint.

## 2. SIMULATION METHOD

The simulation method must determine the same quantities for in-flight guidance as the firing table method. This may be accomplished in two phases.

The first phase is commonly called the target seeker. The object is to find a nominal trajectory which intercepts the target. The parameters which affect the open-loop trajectory for Polaris are time of launch  $t_L$ , time of flight  $\tau$ , kick angle  $\epsilon$ , firing azimuth  $\alpha$ , and booster cutoff time  $t_{bo}$ .

Initial values of the open-loop parameters are judiciously chosen, and a trajectory is obtained by flight simulation on the targeting computer. If a sufficiently small miss occurs, the second targeting phase is begun. If a large miss occurs, new values for three of the five variables may be chosen by obtaining the miss sensitivities of each. This necessitates simulating three open-loop trajectories where each one of the three variables is perturbed successively. The resultant linear equations (linear

Taylor series expansions) can then be used to solve for new values of the three variables such that the miss is zero. Another nominal trajectory is simulated using these new values, and the miss is again computed. If it is sufficiently small, the second phase of targeting is begun. If not, this iteration process is repeated.

The second phase of targeting differs in major aspects from that of the other missile systems because Polaris is a Q-guidance system while the others are "delta" guidance. To obtain the inflight parameters, initial values of the Q's called the  $Q_0$ 's and skew A, are selected. This selection could be done using a loose fit of Q's versus range or some similar variable. Skew is closely related to the attitude of the acceleration vector at burnout because of the steering equations, and, hence, the pitch attitude at burnout from the open-loop trajectory should be a good initial guess. The next step is to obtain the values of  $\dot{V}_g(t_L)$  (the initial conditions for the  $\dot{V}_g$  equation by integrating  $\dot{V}_g$  from  $t_{bo}$  to  $t_L$  using  $\ddot{a}_T$  reversed in time from the open-loop trajectory.

A guided trajectory is now simulated using these initial values of  $\dot{V}_g$ , and the miss is noted. Now guided trajectories (using the same values of Q's and A and initial values  $\dot{V}_g$ ) are simulated using a missile perturbation for each flight (high thrust, specific impulse variation, etc.). If the misses are sufficiently small, the Q's and A may be considered "optimum." If not, they are optimized by perturbing each  $Q_0$  and the value of A and obtaining a linear expansion of miss for each missile perturbation, similar to the target seeker. The new Q's and A are then used in a guided flight simulation with the initial values of  $\dot{V}_g$ . If the miss is not acceptable, this process is repeated. Experience on Polaris indicates that one pass through this procedure would be sufficient.

When the "optimum" Q's and A are obtained, precise values of  $V_g$  are obtained which give very small miss for a nominal flight. The homing stage flight parameters are easily determined since an accurate, nominal, guided trajectory is available.

# APPENDIX K HOMING STAGE GEOMETRY

Figure K-1 depicts the homing phase relative geometry near intercept for an interceptor and satellite on a collision course. The satellite velocity  $V_T$  is horizontal and has the value for a circular orbit. The interceptor velocity is  $V_I$  at an angle  $\beta$  from the local zenith.

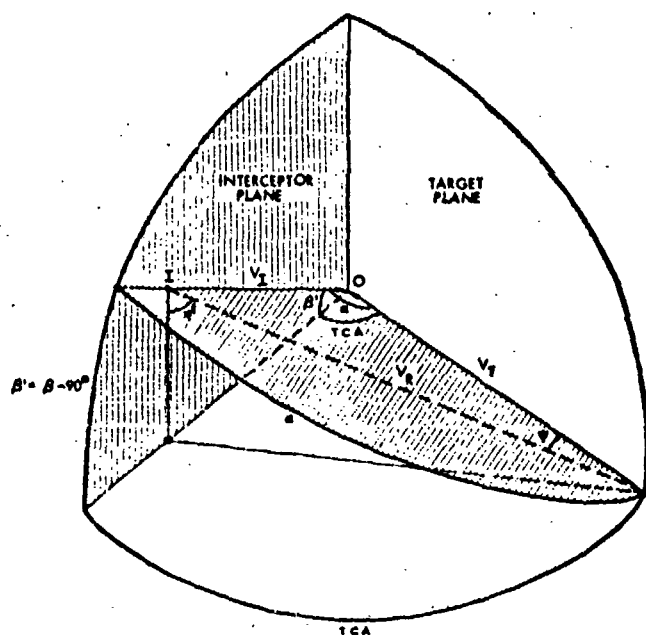


Figure K-1. Homing Phase Geometry



The figure has been drawn for  $\beta = 90$  degrees typical of a post apogee intercept. TCA is the angle between target and interceptor ground traces and is given by

$$TCA = \sin^{-1} \left( \frac{\sin \frac{d}{R_e}}{\sin \frac{R}{R_e}} \right) \quad (K. 1)$$

where

$d$  = Lateral reach (distance of closest approach of satellite trace to launch site) in n mi

$R$  = Downrange distance from launch site to the point of intercept measured along earth's surface in n mi.

$R_e$  = Radius of earth in n mi.

In Figure K-2, define

$V_R$  = Relative velocity vector

$\alpha$  = Angle between target and interceptor velocity vectors

$\psi$  = Angle between target velocity vector and relative velocity vector

$\eta'$  = Angle between relative velocity vector and local nadir

$\beta' = \beta - 90$  degrees (also referred to as  $\gamma_1$ )

From geometry, one has

$$\alpha = \cos^{-1} (\cos TCA \cos \beta') \quad (K. 2)$$

$$V_R = \sqrt{V_T^2 + V_I^2 - 2V_T V_I \cos \alpha} \quad (K.3)$$

$$\psi = \sin^{-1} \left( \frac{V_I \sin \alpha}{V_R} \right) \quad (K.4)$$

$$\eta' = \cos^{-1} \left( \frac{V_I \sin \beta'}{V_R} \right) \quad (K.5)$$

The two most critical parameters of the intercept geometry are  $V_R$  and  $\psi$ .  $V_R$  is important since it determines the time available for acquisition and homing and therefore strongly influences the size of the acquisition sensor, the homing engine thrust level, fuel weight, and tank weight.  $\psi$  is important since it determines the magnitude of the initial ballistic miss distance seen by the interceptor for a given ephemeris error. This miss distance, in turn, strongly influences the size of the acquisition sensor, the homing engine thrust level, fuel weight, and tank weight. The initial ballistic miss distance is defined to be the miss distance measured in the plane normal to  $V_R$  (and therefore also normal to the nominal LOS which is colinear with  $V_R$ ). If neither target nor interceptor accelerate, this miss distance is also the distance of closest approach, neglecting differential gravity effects. The "miss distance" measured along  $V_R$  is not very important for a homing interceptor since its effect is only to advance or delay the time of kill and the position along the track where the kill occurs. (Note that this component of miss distance would be important for a timed warhead burst.) If the precise position of the kill point is not critical (i.e., if there are no strong constraints on the visibility of the kill point from a ground station) the miss distance along  $V_R$  may be ignored.\*

---

\* The miss along  $V_R$  will, however, have a slight effect upon eclipsing loss for an ICW radar, since it represents an error in a priori range estimate. If no range measurements are made during homing, the error remains constant. This error has a slight influence on selection of the nominal range to switch homing phase parameters for the so-called "end game."

In Figure K-1, define two axes  $a$  and  $b$  normal to  $V_R$  and to each other. The  $a$  axis is also normal to  $V_I$ ; the  $b$  axis is in the plane of  $V_R$  and  $V_I$ . The two components of initial ballistic miss distance  $M_a$  and  $M_b$  are the sum of target position uncertainty and interceptor position uncertainty along the  $a$  and  $b$  axes respectively at the nominal time of acquisition. Target and interceptor position uncertainties are independent. For design purposes it is satisfactory to assume that target position uncertainties along the  $z$  axis (track, downrange, or tangential), the  $x$  axis (crosstrack or lateral), and the  $y$  axis (altitude or radial) are independent. The target ephemeris errors are specified in the ARPA guidelines as shown in Table K-1.

Table K-1. Target Ephemeris Errors from ARPA Guidelines

Error Set	Radius (CEP)	Time (1 $\sigma$ )
1	0.3 n mi	0.3 sec
2	1.0 n mi	1.0 sec
3	3.0 n mi	3.0 sec

Assuming Gaussian distributions, and taking  $V_T = 4.2$  n mi/sec for a low altitude target, the 1 $\sigma$  target dispersions along  $x$ ,  $y$ ,  $z$  are given by Table K-2.

Table K-2. Target Ephemeris Dispersions (1 $\sigma$ ) in n mi

Error Set	$\sigma_x$	$\sigma_y$	$\sigma_z$
1	0.254	0.254	1.26
2	0.850	0.850	4.20
3	2.54	2.54	12.6

For purposes of preliminary analysis, assume that the interceptor position uncertainty at acquisition is described by a sphere having a 1 $\sigma$

dispersion of 0.5 n mi in each direction. This assumption\* is somewhat pessimistic for intercepts which take place within 1000 to 2000 n mi from the launch site, but may be slightly optimistic for intercepts which occur many thousands of miles from the launch site.

With the stated assumptions, the initial ballistic miss distances is a function only of  $\psi$  and the ephemeris error set used. One has from geometry

$$\sigma_a = \sqrt{\sigma_x^2 + 0.5^2} \quad (\text{K.6})$$

$$\sigma_b = \sqrt{\sigma_z^2 \sin^2 \psi + \sigma_y^2 \cos^2 \psi + 0.5^2} \quad (\text{K.7})$$

$$\sigma_t = \sqrt{\sigma_a^2 + \sigma_b^2} \quad (\text{K.8})$$

Figure K-2 shows  $\sigma_a$ ,  $\sigma_b$ ,  $\sigma_t$  plotted as a function of  $\psi$  for each of the ephemeris error sets. The numerical subscript on each curve identifies the ephemeris error set.

It is seen that  $\sigma_a$  is independent of  $\psi$  and that  $\sigma_b$  reduces to a value equal to  $\sigma_a$  for small  $\psi$ . Thus, the desirability of small  $\psi$  is apparent. For example, a coplanar apogee attack results in  $\psi = 0$  and  $\sigma_a = \sigma_b = 6000$  ft for Set 2 ephemeris errors. However, a small value of  $\psi$  will not generally occur over the expected range of intercept conditions. Indeed, the value of  $\psi$  which tends to prevail over a wide range of interceptor lateral reach is approximately

\* This assumption, of course, suppresses the influence of interceptor trajectory profile and downrange distance to intercept upon the interceptor positional uncertainty, but is justified for general analysis on the grounds that a) interceptor position errors for all booster guidance systems under consideration are always small compared to ephemeris error Sets 2 and 3; and, b) the dependence of interceptor position errors on trajectory profile and downrange distance to intercept is not extremely strong. If primary attention is to be focused on ephemeris error Set 1, a more careful treatment of interceptor errors would undoubtedly be justified.

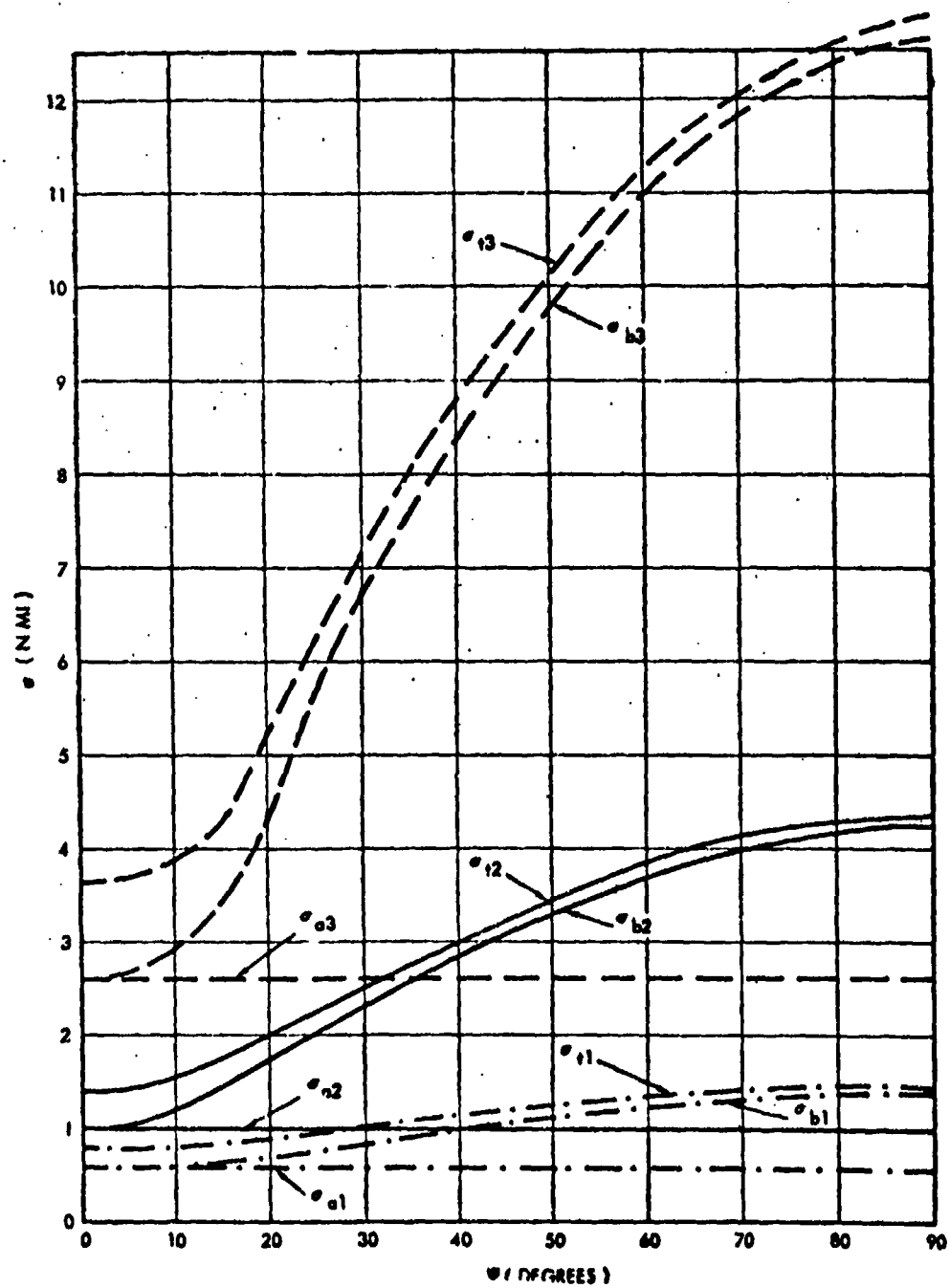


Figure K-2.  $1\sigma$  Initial Miss Distance in Plane Normal to LOS

$$\psi \approx \sin^{-1} \frac{V_1}{V_T} \quad (K.9)$$

$\approx 45 - 60$  degrees

For Set 2 ephemeris errors, the resulting ratio of  $\sigma_b/\sigma_a$  is in the order of 3 or 3.5 to 1. This fact roughly establishes the aspect ratio of the major to minor axes of the required search ellipse.

Another important geometrical parameter is the angle between the LOS and the local horizon during search and track. Just before intercept, this angle is given by

$$ELA = 90 - \eta' + \eta \quad (K.10)$$

where  $\eta'$  is given by Equation (K.5) and  $\eta$  is the angle between the horizontal and the horizon at the target's altitude. By proper shaping of the booster powered flight trajectory ELA can nominally be maintained greater than 5 degrees for lateral reaches as great as 2000 n mi or more (for a Minute-man booster) even for a target altitude of 100 n mi. Now due to ephemeris and booster guidance angles the LOS to the actual target may be somewhat closer to the horizon than the LOS to the nominal target. For the cases of interest the b-axis tends to be nearly horizontal so that the dispersion in angle on ELA at acquisition is approximately

$$\delta(ELA)_{3\sigma} \approx \frac{3\sigma_a}{r_a} \quad (57.3) \text{ degrees}$$

For an acquisition range of 125 n mi, the  $3\sigma$  dispersion is only about 1.4 degrees. Considering the effect of homing stage attitude reference errors as well, the required semiminor axis of the search FOV will still not exceed 2 degrees. Therefore, the bottom edge of the search FOV can be kept at least 3 degrees above the horizon for any interceptor lateral reach up to about 2000 n mi. This will prevent spurious star motion due to atmospheric refraction effects for a visible spectrum sensor, and will prevent the main lobe from seeing the earth for a radar sensor.

## APPENDIX L

### A BOOST-HOME SYSTEM USING A RADAR SENSOR

One potentially attractive system for satellite interception utilizes a homing stage with a radar sensor mounted on a Minuteman Wing II boost vehicle. For the range of parameters being considered in the present ARPA study, however, such a system is rather tight from the point of view of total homing stage weight and volume compared to what the Minuteman can conveniently carry. We would like a system capable of intercepting a target with a one square meter radar cross section at closing velocities as great as 20,000 ft/sec and with ARPA Set 2 ephemeris errors. (There is, of course, some area of tradeoff between the above three parameters; e.g., if the target cross section were greater than one square meter or the ephemeris errors less than those of Set 2, a closing velocity greater than 20,000 ft/sec could be tolerated.) For the desired system performance, previous studies have indicated that

- In order to minimize total homing stage weight, a design acquisition range in the order of 125 n mi is required. For shorter design acquisition ranges the radar sensor weight is reduced, but propulsion and structural weights become much larger.
- In order to achieve a design acquisition range of 125 n mi without grossly excessive radar power, a large deployed antenna must be used for acquisition. A 4 x 6 foot planar array appears feasible for a homing stage carried on Minuteman.
- A large deployed acquisition array which is roll gimbaled will require considerable development time and probably cannot fit on Minuteman without appreciable increase of the nose fairing length. The latter factor may result in a substantial Minuteman modification.
- Closed loop guidance using roll-to-maneuver requires roll gimbaling of the sensor unless extremely tight tolerances can be maintained on angular alignment between the sensor boresight axis and the pitch and yaw gyro input axes.
- Extremely tight angular alignment of the boresight axis of a large array cannot practically be maintained under loads induced by interceptor acceleration and rolling.

The conclusion which can be drawn from the above statements is that closed loop homing at long range cannot readily be achieved on a Minuteman booster using the large acquisition array as a tracking sensor. This conclusion has prompted consideration of a boost plus homing system, where the homing phase begins at a range of about 400,000 feet, such that a small, gimbaled, receiving antenna provides a sufficient signal-to-noise ratio for good tracking. The boost phase corrects most of the initial miss. It can be a fairly coarse open-loop maneuver begun at about 120 n mi and based upon the following data:

- An a priori estimate of relative closing velocity  $V_R$
- A coarse initial range measurement (or even an a priori estimate of initial range as a function of clock time).
- An initial measurement of the magnitude and direction of the angle  $\theta$  between the line-of-sight to the target and the nominal direction of the  $V_R$  vector.

The boost phase would last about 15 seconds or less and would be terminated when a commanded  $\Delta V$  is achieved, based upon a simple accelerometer measurement. An initial thrust to weight ratio of about 4 g appears optimum.

The overall sequence of operations would be as follows: At a sufficiently long range, probably 150 to 175 n mi, search for the target is begun using the large body fixed array. Angular scan is generated by moving the entire interceptor body over an elliptical (or rectangular) pattern. For 2.5 $\sigma$  coverage at an acquisition range of 750,000 feet with Set 2 ephemeris errors and  $\psi = 53$  degrees, the major and minor axes of the total search field-of-view are 8.25 degrees and 3.0 degrees respectively, but the angular motion of the interceptor is somewhat less due to the finite beamwidth. The probability of the target being contained within the search sector at 750,000 feet is 95.6 percent. The two bar scan pattern is centered about the direction of the nominal  $V_R$  vector and is repeated every few seconds until the target is detected. The cumulative probability of detection at 750,000 feet is 98 percent if the target is contained in the search sector, and is at least 93.6 percent if one includes the fact that the target can escape the search sector.



At detection the range is measured; the pitch and yaw angles with respect to the nominal  $V_R$  direction are recorded (by the computer which has been commanding the scan motion by torquing of the pitch and yaw gyros) and the scan motion is stopped as quickly as possible. If the target is in the center of the radar beam at detection, the pitch and yaw angular coordinates establish the magnitude and direction of  $\theta$ . Some beam splitting or phasing technique may be used to reduce target angle uncertainty due to the finite radar beamwidth. Based upon range,  $V_R$ , and angle the computer commands a boost phase  $\Delta V$  to be gained at a constant body orientation and full thrust. The body ACS rolls the engine to the proper angle and maintains constant attitude during boost. Radar contact during boost is not required. During boost the computer determines the nominal direction of the LOS at boost termination. At boost termination, it commands a small reacquisition search pattern centered about that direction in a manner identical to the original search procedure. Owing to the short range and the small search sector, reacquisition takes place during the first scanning frame within 2 to 3 seconds of boost termination. Upon reacquisition the range is in the order of 400,000\* feet and the small dish is capable of beginning angle tracking. Closed loop homing is begun after an additional delay of about one second to reorient the engine in roll. During acquisition, boost, reacquisition, and homing, the body pitch and yaw axes are closely slaved to follow the LOS as indicated by the gimballed antenna platform. This keeps the large array closely on target for illumination.

The initial boost maneuver is admittedly rather coarse and subject to considerable error in magnitude and direction. Nevertheless, if the errors can be held to reasonable levels, the early application of a large boost correction permits the system to be designed with a total homing stage  $\Delta V$  in the order of 3000 to 3500 ft/sec for Set 2 ephemeris errors, and an initial thrust to weight ratio of about 4g. A larger  $\Delta V$  and a much larger thrust level would be required if the boost phase were not used and the system were designed to commence homing at a range of 400,000 feet.

\* The numerical results presented in this appendix were obtained several weeks before the conclusion of the study and time did not permit recalculation of results for a homing phase begun at 375,000 feet rather than 400,000 feet. However the differences should be negligible.

The vector diagram of Figure L-1 portrays how miss correction is accomplished by the boost and homing phases. The plane of the figure is normal to the nominal  $\bar{V}_R$  vector. The b-axis lies in the plane containing  $\bar{V}_T$  and  $\bar{V}_I$ , the target and interceptor velocity respectively. Let

$\bar{M}_0$  = Actual initial miss distance vector

$\bar{M}_{om}$  = Measured initial miss distance vector

$\bar{M}_1$  = Boost phase miss correction vector

$\bar{M}_2$  = Homing phase miss correction vector =  $\bar{M}_0 - \bar{M}_1$

$E_1$  = Initial measurement error vector =  $\bar{M}_{om} - \bar{M}_0$

The boost philosophy is to gain a velocity  $\Delta V$  in the direction of  $\bar{M}_{om}$  such that a distance  $\bar{M}_1$  will be traversed at the instant of interception.  $M_1$  is less in magnitude than  $M_{om}$  since it is intuitively obvious that the boost phase should undercorrect the initial miss. A possible relationship between  $M_1$  and  $M_{om}$  is shown in Figure L-2.  $M_1$  is less than  $M_{om}$  by a fixed amount (a deadzone characteristic), the amount being related to the expected magnitude of the initial measurement error  $E_1$ . In addition  $M_1$  is limited in magnitude regardless of the magnitude of  $M_{om}$ , the limiting value being related to the expected maximum value of the actual miss  $M_0$ . This boost law is empirical but appears to be generally consistent with guidance optimization studies performed by various investigators in the past. As the problem becomes better understood, improved boost laws can be formulated. The present law, though undoubtedly nonoptimum, provides a basis upon which the total  $\Delta V$  requirement for the homing stage can be estimated.

In Figure L-1, T is the actual target position and the actual miss  $M_0$  is given by

$$M_0 = r_0 \theta_0 \quad (L. 1)$$

where

$r_0$  = Range at acquisition

$\theta_0$  = Angle between actual relative velocity vector and LOS to target at time of acquisition.

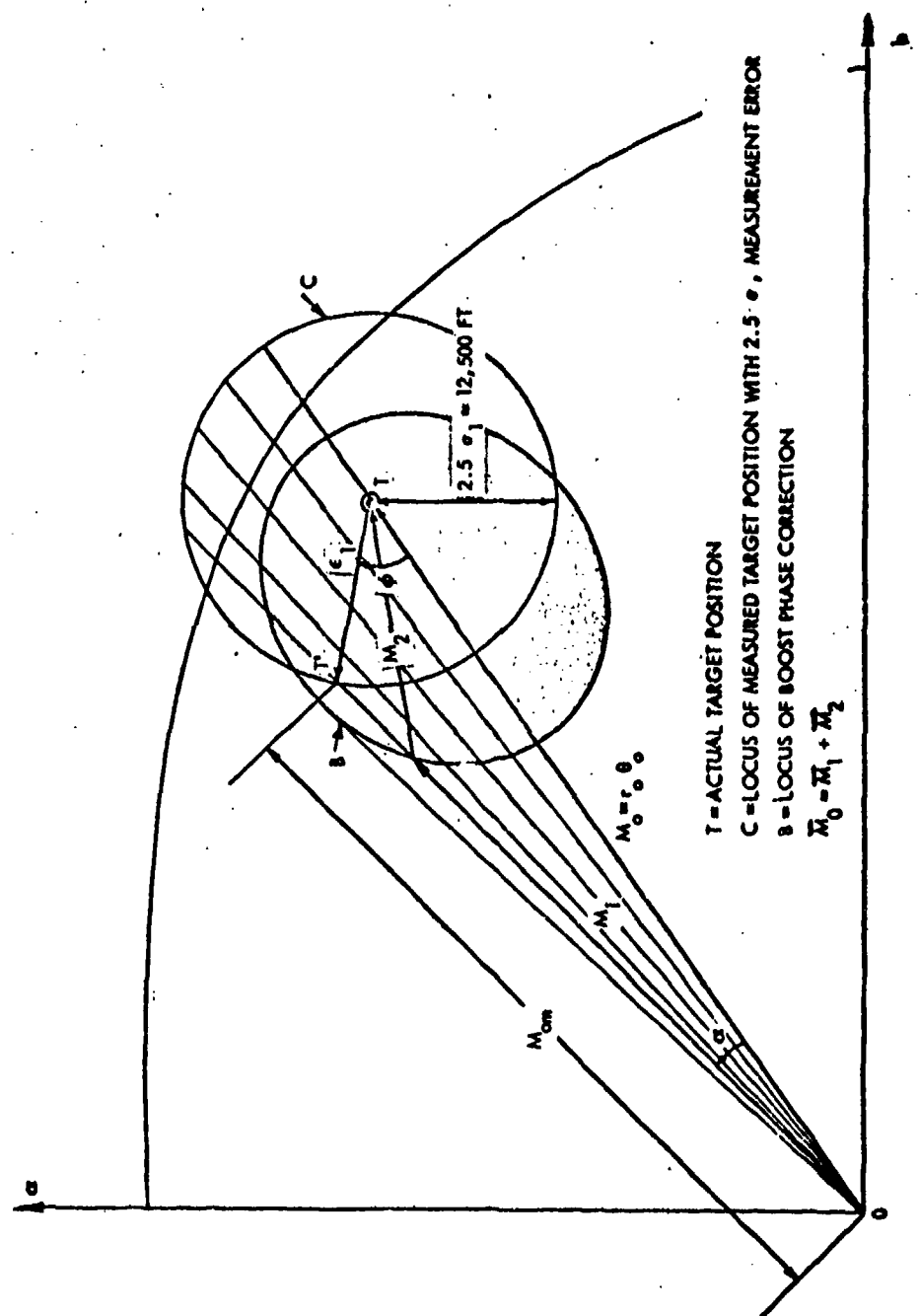


Figure L-1. Miss Distance Vector Diagram (in Plane to Normal Relative Velocity Vector)

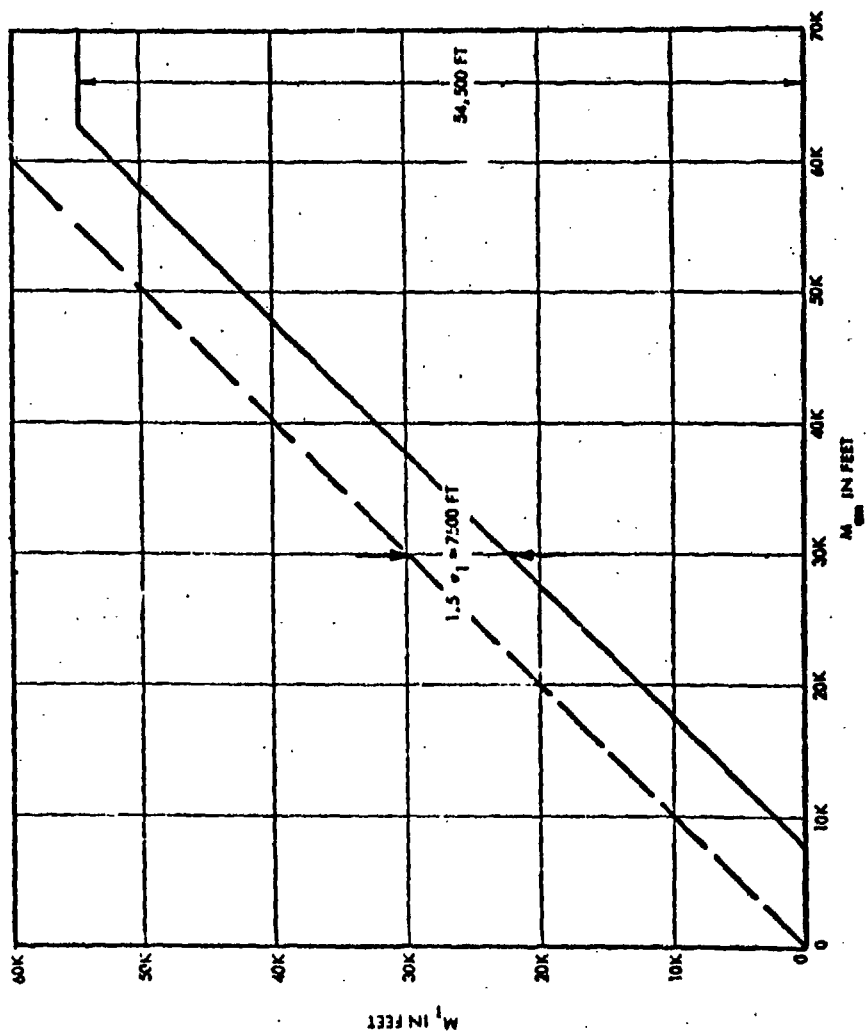


Figure L-2. A Possible Boost Law (Commanded Miss Distance Correction versus Measured Miss Distance)

The interceptor's measurement of  $M_0$  is  $M_{om}$  and is corrupted by errors in range and in angle. The angular error is by far the most significant. Therefore the initial range measurement error will be neglected (as well as all boost phase execution errors) compared with the angular measurement error. The angular error in measuring  $\theta_0$  comes from a number of separate causes. Each contributor gives rise to an angular error along the a-axis and another along the b-axis. It is assumed that the resulting errors along the a-axis and the b-axis are equal and independent. This gives rise to a circular distribution of measurement error about the true target position as shown in Figure L-1.

The causes of angular measurement error are discussed at the end of Chapter 8. Including the error resulting from not knowing where in the beam the target actually is, the 1 $\sigma$  error along each axis has been estimated at 0.4 degree.

Assume that target detection takes place at 750,000 feet (the 98 percent cumulative probability of detection range) and that boost is initiated after a delay of 2 seconds at an initial range  $r_0 = 710,000$  feet. The 1 $\sigma$  angular measurement error of 0.4 degree therefore corresponds to a target position error,  $\sigma_1 = 5000$  feet. In Figure L-1, the circle C represents the locus of measured target positions if the actual target is at T and a  $2.5 \sigma$  measurement error is made. The boost guidance law deadspace (undercorrection) is taken to be  $1.5 \sigma_1 = 7500$  feet, so that the locus of the  $M_1$  vector lies someplace along the contour B, if the angular measurement error is  $2.5 \sigma$  and the actual target is at T.

To estimate the total homing stage  $\Delta V$  requirement, assume first that the ephemeris error is large, resulting in a large initial miss. Let  $M_0 = 2.5 \sigma_t$  where

$$\sigma_t = \sqrt{\sigma_a^2 + \sigma_b^2}$$

$$\sigma_a = 6000 \text{ feet} \quad (\text{Set 2 ephemeris error})$$

$$\sigma_b = 21,000 \text{ feet} \quad (\text{Set 2 ephemeris error with } \psi \cong 53 \text{ degrees})$$

Thus  $\sigma_t = 21,800$  feet and  $M_0 = 54,500$  feet. Further assume that the angular measurement of target position also suffers from a  $2.5 \sigma$  error. (This latter error is essentially independent of the initial miss distance. The  $\Delta V$  requirement will therefore be based on the simultaneous occurrence of two independent error effects, each having a magnitude of  $2.5 \sigma$ .) The total  $\Delta V$  required is the sum of the  $\Delta V$  for the boost and homing phases,

$$\Delta V = \Delta V_1 + \Delta V_2 \quad (L. 2)$$

where

$$\Delta V_1 = \text{Boost velocity to correct } M_1$$

$$\Delta V_2 = \text{Homing velocity to correct } M_2$$

since both phases draw propellant from the same tank. For  $M_0 = 54,500$  feet, the magnitude of  $M_1$  and  $M_2$  can be determined by trigonometry as a function of the angle  $\phi$  in Figure L-1. The case of  $\phi = 0$  degrees corresponds to measuring the target's direction correctly but being low in miss magnitude. A severe undercorrection is made during the boost phase and the homing phase is called upon for a maximum correction. If  $\phi = 180$  degrees, the boost phase overcorrects, but only slightly, so that the homing phase correction is minimized.

The boost phase velocity gain  $\Delta V_1$  can be determined as a function of  $M_1$  (for constant thrust boost) by solution of the following equations

$$\Delta V_1 = -c \ln p \quad (L. 3)$$

$$p = 1 - \frac{a_1}{c} t_b \quad (L. 4)$$

$$t_o = \frac{r_o}{V_R} \quad (L. 5)$$

$$M_1 = \frac{c^2}{a_1} (p \ln p - p + 1) - c \ln p (t_o - t_b) \quad (L. 6)$$

where

$p$  = Boost phase mass ratio

$t_b$  = Boost time

$c = g_{sp}^1$

$a_1$  = Initial boost acceleration

A plot of  $\Delta V_1$  versus  $M_1$  is shown in Figure L-3 for  $c = 10^4$  ft/sec,  $a_1 = 129$  ft/sec<sup>2</sup>,  $r_0 = 710,000$  feet and  $V_R = 20,000$  ft/sec. The homing stage computer need not solve the above set of equations, however, since a simple approximation of the form

$$\Delta V_1 = \frac{M_1 V_R}{r_0} + \text{correction term} \quad (\text{L. 7})$$

will undoubtedly suffice. The correction term would be a simple function of  $M_1$ ,  $V_R$ ,  $r_0$ ,  $c$ , and  $a_1$ . The homing phase velocity gain  $\Delta V_2$  is given by

$$\Delta V_2 = k \frac{\lambda}{\lambda - 1} \left( \frac{M_2 V_R}{r_2} + \omega_b r_2 \right) \quad (\text{L. 8})$$

where

$\lambda$  = Proportional navigation gain  $\approx 4$

$\omega_b$  = Homing phase LOS rate bias  $\approx 10^{-3}$  rad/sec

$k$  = Correction factor to account for noise and other effects  $\approx 1.1$

$r_2$  = Range at which homing phase begins

The homing phase is assumed to begin 4 seconds after boost termination or at 400,000 feet, whichever is smaller (i.e.,  $r_2 = r_0 - V_R(t_b + 4)$  or 400,000 feet, whichever is smaller).

The total  $\Delta V$  requirements have been computed from the above equations for four values of  $\phi$  and are as follows:

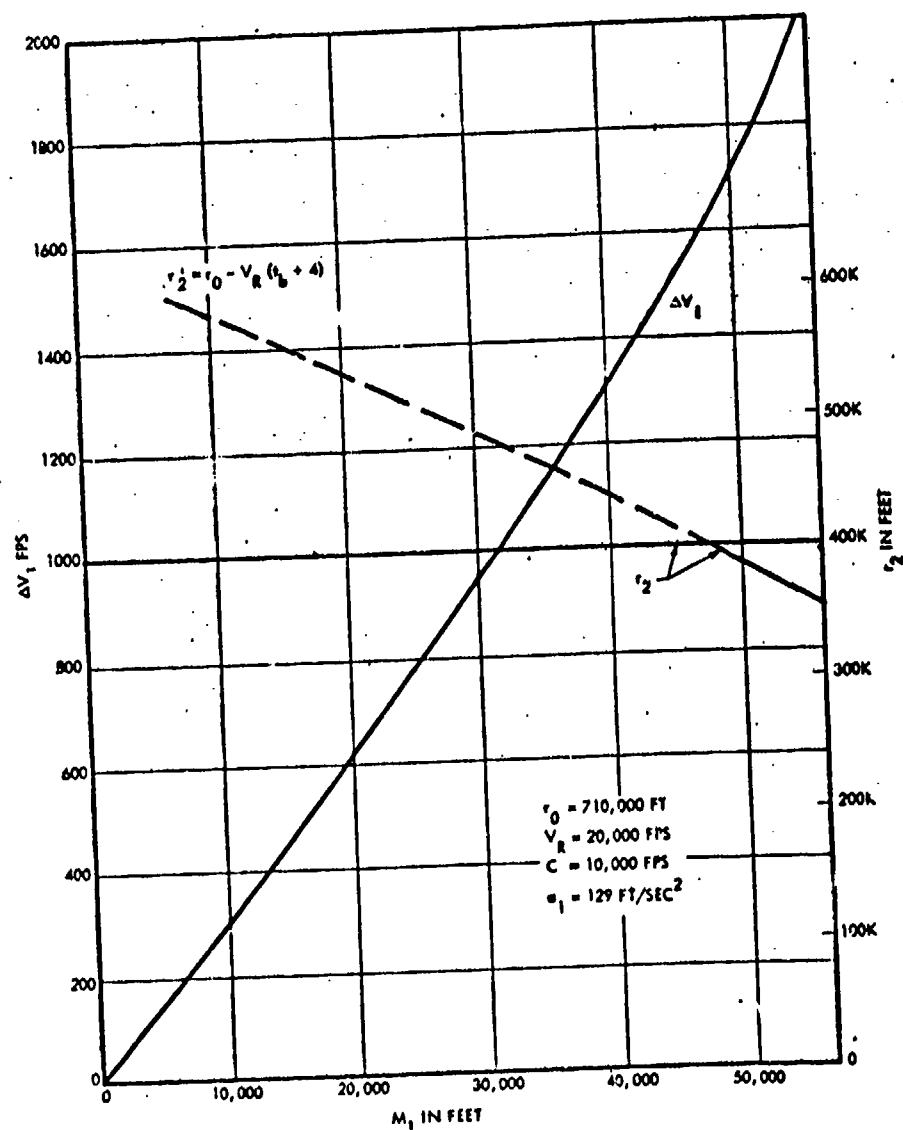


Figure L-3. Boost Phase Velocity Gain versus Commanded Miss Distance Correction (Constant Thrust Boost Phase)



$\phi$ (deg)	$\Delta V$ (ft/sec)
0	3170
30	3175
90	3185
180	2550

These results suggest that the boost guidance law assumed herein is not too far from optimum for the assumed errors, since the required  $\Delta V$  is not a strong function of  $\phi$  over a fairly wide range. The maximum homing stage acceleration required occurs for  $\phi = 0$  and is approximately  $120 \text{ ft/sec}^2$ . This is well within the assumed 4 g initial acceleration capability.

It is interesting to note that if boost were not used and homing were initiated at the initial range of 710,000 with an initial miss of 54,500 feet, that the  $\Delta V$  required (from Equation L. 8) is 3300 ft/sec. This shows that an early corrective maneuver, even if coarse, can be quite effective.

On the basis of this preliminary analysis, a homing stage  $\Delta V$  of 3250 ft/sec and an initial thrust to weight ratio of 4.0 are recommended for the radar design using boost plus homing.

# DISTRIBUTION

	<u>No. of Copies</u>
Director Advanced Research Projects Agency Attn: Capt. Robert B. Greenwood Washington 25, D. C.	2
ZEUS Office Office, Chief of Research and Development Department of the Army Washington 25, D. C.	1
Resident, ARMY ZEUS Project Engineer (AMC) Maj. N. L. Kelley, AFBS Norton AFB, California	1
ZEUS Project Office (AMC) Attn: Mr. Buckholtz Redstone Arsenal Huntsville, Alabama	1
Chief of Naval Operations (OP-761) Department of the Navy Attn: CDr T. Scambos Washington 25, D. C.	1
Chief of Bureau of Naval Weapons Department of the Navy Attn: RTAD-1, Mr. Daniel Brockway Washington 25, D. C.	6
Naval Ordnance Laboratory Attn: Mr. Herb Bulgerin Corona, California	1
Headquarters U. S. Air Force (AFRDP/Lt. Col. Robert O'Clock) The Pentagon Washington 25, D. C.	1
Headquarters U. S. Air Force (AFRAE/Maj. Kenneth Russell) The Pentagon Washington 25, D. C.	1
Commander, Space Systems Division AFSC Attn: Maj. N. McNair Air Force Unit Post Office Los Angeles 45, California	5

# DISTRIBUTION (Continued)

	<u>No. of Copies</u>
Headquarters Air Force Systems Command Attn: SGLDS/Maj. L. Jones Andrews Air Force Base, Maryland	1
Headquarters Air Force Systems Command Attn: MSFA/Maj. S. Kalmus Andrews Air Force Base, Maryland	1
Aeronautical Systems Division Attn: ASR/Mr. Ira Bowker Wright Patterson Air Force Base, Ohio	1
Detachment 4 ASD Attn: AWSQ/Mr. Dale Davis Eglin AFB, Florida	1
Electronics Systems Division Attn: ESS/Col. Sullivan Hanscom Field Bedford, Massachusetts	1
ODDR and E (Defensive Systems) Attn: Mr. John A. Whitman Room 3D132 The Pentagon Washington 25, D. C.	1
Aerospace Corporation Attn: Mr. H. B. Coleman P.O. Box 95085 Los Angeles 45, California	5
Arthur D. Little Company Attn: Dr. R. N. Hazelwood 22 Acorn Park Cambridge, Massachusetts	1
Battelle Memorial Institute Attn: Dr. H. Epstein 505 King Avenue Columbus 1, Ohio	1
Columbia University Electronics Research Labs. Attn: Miss Helen K. Cressman (Dern) 632 West 125th Street New York 27, New York	3

DISTRIBUTION (Continued)

	<u>No. of Copies</u>
Cornell Aeronautical Laboratory Attn: Mr. George Cash Buffalo 21, New York	1
Ford Motor Company Aeronutronic Division Attn: Mr. D. Slager Ford Road Newport Beach, California	1
Institute for Defense Analysis 1666 Connecticut Avenue, N.W. Washington 9, D. C. (one copy Attn: Mr. Pythagoras Cutchis one copy Attn: Mr. Lucien Biberman)	2
Johns Hopkins University Applied Physics Laboratory Attn: Dr. J. W. Follin 8621 George Avenue Silver Springs, Maryland	1
CINCNOAD Attn: NESD-A (Maj. McKinney) Colorado Springs, Colorado	1
DEFENSE DOCUMENTATION CENTER Cameron Station Alexandria, Virginia	20

UNCLASSIFIED

Space Technology Laboratories,  
One Space Park, Redondo Beach, California.  
FINAL REPORT SATELLITE INTERCEPTION  
SYSTEM FEASIBILITY STUDY (UL Project  
Manager: John Mandrow, 6 November 1961,  
438 p., incl. illus. #8424-6018-R5000)  
(Contract No. SD-177) Secret report

This is the final report of an Antisatellite System  
Feasibility Study sponsored by the Advanced  
Research Projects Agency under Contract SD-177.  
The contract performance period extended from  
30 April to 31 October 1961.

The study concerned the feasibility of using homing  
stages launched by ICBM/IRBM launch vehicles to  
achieve satellite kill by non-nuclear means. The  
study concluded that, subject to the practical solu-  
tion of the number of technical problems, the ap-  
proach studied is feasible.

Unclassified Abstract

UNCLASSIFIED

UNCLASSIFIED

Space Technology Laboratories,  
One Space Park, Redondo Beach, California.  
FINAL REPORT SATELLITE INTERCEPTION  
SYSTEM FEASIBILITY STUDY (UL Project  
Manager: John Mandrow, 6 November 1961,  
438 p., incl. illus. #8424-6018-R5000)  
(Contract No. SD-177) Secret report

This is the final report of an Antisatellite System  
Feasibility Study sponsored by the Advanced  
Research Projects Agency under Contract SD-177.  
The contract performance period extended from  
30 April to 31 October 1961.

The study concerned the feasibility of using homing  
stages launched by ICBM/IRBM launch vehicles to  
achieve satellite kill by non-nuclear means. The  
study concluded that, subject to the practical solu-  
tion of the number of technical problems, the ap-  
proach studied is feasible.

Unclassified Abstract

UNCLASSIFIED

UNCLASSIFIED

Space Technology Laboratories,  
One Space Park, Redondo Beach, California.  
FINAL REPORT SATELLITE INTERCEPTION  
SYSTEM FEASIBILITY STUDY (UL Project  
Manager: John Mandrow, 6 November 1961,  
438 p., incl. illus. #8424-6018-R5000)  
(Contract No. SD-177) Secret report

This is the final report of an Antisatellite System  
Feasibility Study sponsored by the Advanced  
Research Projects Agency under Contract SD-177.  
The contract performance period extended from  
30 April to 31 October 1961.

The study concerned the feasibility of using homing  
stages launched by ICBM/IRBM launch vehicles to  
achieve satellite kill by non-nuclear means. The  
study concluded that, subject to the practical solu-  
tion of the number of technical problems, the ap-  
proach studied is feasible.

Unclassified Abstract

UNCLASSIFIED

UNCLASSIFIED

Space Technology Laboratories,  
One Space Park, Redondo Beach, California.  
FINAL REPORT SATELLITE INTERCEPTION  
SYSTEM FEASIBILITY STUDY (UL Project  
Manager: John Mandrow, 6 November 1961,  
438 p., incl. illus. #8424-6018-R5000)  
(Contract No. SD-177) Secret report

This is the final report of an Antisatellite System  
Feasibility Study sponsored by the Advanced  
Research Projects Agency under Contract SD-177.  
The contract performance period extended from  
30 April to 31 October 1961.

The study concerned the feasibility of using homing  
stages launched by ICBM/IRBM launch vehicles to  
achieve satellite kill by non-nuclear means. The  
study concluded that, subject to the practical solu-  
tion of the number of technical problems, the ap-  
proach studied is feasible.

Unclassified Abstract

UNCLASSIFIED